Multi-scale experimental study on the nanoparticles chemistry by shock tube techniques

Fabian Esneider Cano Ardila

UNIVERSITÉ D'ORLÉANS

ÉCOLE DOCTORALE ÉNERGIE, MATÉRIAUX, SCIENCES DE LA TERRE ET DE L'UNIVERS

INSTITUT DE COMBUSTION, AÉROTHERMIQUE, RÉACTIVITÉ ET ENVIRONNEMENT

THESIS dissertation by :

Fabian Esneider CANO ARDILA

presented on : **22 June 2023**

In partial fulfillment of the requirements for the degree of : **Doctor of Philosophy**

Discipline/ Speciality : **Energy**

Multi-scale experimental study on the nanoparticles chemistry by shock tube techniques

Thesis directed by:

COMANDINI Andrea	Associate Researcher, Université d'Orléans

EXAMINATORS:

ROTAVERA Brandon	Assistant professor, University of Georgia
DE IULIIS Silvana	Associate Researcher, CNR-Italy

JURY :

CATOIRE Laurent	Professor, Université Paris-Saclay, President of jury
COMANDINI Andrea	Associate Researcher, Université d'Orléans
CHAUMEIX Nabiha	Director of Research, ICARE-CNRS
TRANTER Robert Simon	Director of Research, Argonne National Laboratory
ROTAVERA Brandon	Professor, University of Georgia
DE IULIIS Silvana	Chargé de recherche, CNR-Italie

European Research Council
Established by the European Commission

UNIVERSITÉ D'ORLÉANS

ÉCOLE DOCTORALE ÉNERGIE, MATÉRIAUX, SCIENCES DE LA TERRE ET DE L'UNIVERS

INSTITUT DE COMBUSTION, AÉROTHERMIQUE, RÉACTIVITÉ ET ENVIRONNEMENT

THÈSE présentée par :

Fabian Esneider CANO ARDILA

soutenue le : **22 Juin 2023**

pour obtenir le grade de : **Docteur de l'Université d'Orléans**

Discipline/ Spécialité : **Energétique**

Etude expérimentale multi-échelle sur la chimie des nanoparticules par les techniques du tube à choc

THÈSE dirigée par :

COMANDINI Andrea	Chargé de Recherche, Université d'Orléans

RAPPORTEURS :

ROTAVERA Brandon	Professeur assistant, University of Georgia
DE IULIIS Silvana	Chargé de recherche, CNR-Italie

JURY :

CATOIRE Laurent	Professeur, Université Paris-Saclay, Président du Jury
COMANDINI Andrea	Chargé de Recherche, Université d'Orléans
CHAUMEIX Nabiha	Directrice de recherche, ICARE-CNRS
TRANTER Robert Simon	Directeur de recherche, Argonne National Laboratory
ROTAVERA Brandon	Professeur assistant, University of Georgia
DE IULIIS Silvana	Chargé de recherche, CNR-Italie

European Research Council
Established by the European Commission

Fabian Esneider CANO ARDILA

Etude expérimentale multi-échelle sur la chimie des nanoparticules par les techniques du tube à choc

Résumé : Différentes techniques de tubes ont été utilisées pour étudier les mécanismes cinétiques impliqués dans la formation de suie à partir des principaux composants des combustibles et intermédiaires. En particulier, un nouveau tube à choc à taux de répétition élevé (HRRST) est présenté ainsi que son couplage à des détecteurs i^{2}PEPICO dans les synchrotrons européens. Cette technique a été mise en œuvre pour étudier la pyrolyse de l'éthanol, du toluène, de l'éthylbenzène et du styrène, en accordant une attention particulière à la chimie des HAP. Les expériences HRRST complètent les nouvelles données obtenues dans des tubes à chocs à plus grande échelle avec différentes concentrations de combustible et diagnostics, depuis les mesures chromatographiques en phase gazeuse des profils de HAP jusqu'aux mesures d'extinction de la formation de nanoparticules. Les résultats fournissent de nouvelles informations sur les processus complexes conduisant aux nanoparticules pour les de modèles cinétiques.

Mots clés : tube à choc, diagnostic du synchrotron, chimie des nanoparticules, cinétique chimique, extinction laser, chromatographie en phase gazeuse

Multi-scale experimental study on the nanoparticles chemistry by shock tube techniques

Summary : Different laboratory-based and synchrotron-based shock tube techniques were used to study the kinetic mechanisms involved in soot formation from key fuel components and intermediates. In particular, a new high repetition rate shock tube (HRRST) is presented together with its coupling to double imaging photoelectron/photoion coincidence spectroscopy detectors in European synchrotrons. This technique was implemented to study ethanol, toluene, ethylbenzene and styrene pyrolysis with particular attention to polycyclic aromatic hydrocarbon chemistry. The HRRST experiments complement new data obtained in larger scale shock tubes with different fuel concentrations and diagnostics, from gas chromatographic measurements of PAH profiles up to four rings to time-history laser-based extinction measurements of nanoparticles formation. The results provide new information on the complex processes leading to the nanoparticles for future developments of predictive chemical kinetic models.

Keywords : shock tubes, synchrotron diagnostics, nanoparticles chemistry, chemical kinetics, laser extinction, gas chromatography.

ICARE - CNRS
1C Avenue de la Recherche Scientifique
45071, Orleans Cedex 2

Résumé

Différentes techniques expérimentales, basées sur la technique du tube à choc, ont été utilisées pour étudier les mécanismes cinétiques impliqués dans la formation des suies à partir des principaux composants des combustibles et intermédiaires et de combustion. En particulier, un nouveau tube à choc, automatisé avec un taux de répétition élevé (HRRST), est présenté ainsi que son couplage à des détecteurs i^{2}PEPICO dans les synchrotrons européens. Cette technique a été mise en œuvre pour étudier la pyrolyse de l'éthanol, du toluène, de l'éthylbenzène et du styrène, en accordant une attention particulière à la chimie des HAP. Les expériences HRRST complètent les nouvelles données obtenues dans des tubes à chocs à plus grande échelle avec différentes concentrations de combustible et diagnostics, depuis les mesures chromatographiques en phase gazeuse des profils de HAP jusqu'aux mesures d'extinction de la formation de nanoparticules. Les résultats fournissent de nouvelles informations sur les processus complexes conduisant aux nanoparticules pour le développement des modèles cinétiques détaillés.

Mots-clés : tubes à chocs, diagnostics synchrotron, chimie des nanoparticules, cinétique chimique, extinction laser, chromatographie en phase gazeuse.

Introduction et motivation

Les matières particulaires (PM) constituent l'un des polluants les plus nocifs pour la santé humaine et l'environnement [3]. D'un point de vue fondamental, une compréhension détaillée et précise de la formation des particules dans les conditions propres aux dispositifs de combustion est un élément clé de la mise en œuvre de techniques d'atténuation efficaces pour réduire les émissions. En particulier, le noyau carboné des PM, appelé suie, provient de l'oxydation incomplète du combustible dans les régions de la flamme où les concentrations en oxygène sont insuffisantes par rapport aux concentrations de carbone.

La formation de suie est un processus très complexe qui implique plusieurs étapes multiphases et multi-échelles, à commencer par la décomposition des composants du combustible et la formation et la croissance ultérieures des structures à cycles multiples, les hydrocarbures aromatiques polycycliques (HAP), à partir des aromatiques à cycle unique [4], [5]. Les modèles actuels de formation de la suie suggèrent "en soi" un ordre cinétique des intermédiaires de la phase gazeuse, y compris l'apparition et l'évolution des HAP, comme le montre la **Figure** 1.1. Le processus se poursuit avec l'apparition des particules et leur croissance ultérieure par coagulation et réactions de surface. Enfin, les particules primaires s'agglomèrent et s'oxydent pour former les structures matures de la suie. Les études cinétiques sur la formation de la suie sont nombreuses et impliquent des recherches expérimentales sur les molécules de HAP, précurseurs de la suie, et sur la chimie en phase solide des particules carbonées dans diverses configurations. En particulier, les tubes à chocs constituent des réacteurs idéaux pour étudier la chimie de la suie dans les conditions typiques rencontrées dans les dispositifs de combustion modernes [7], [8].

Différentes techniques analytiques telles que les systèmes de chromatographie en phase gazeuse/spectrométrie de masse (GC/MS) [13], la spectrométrie de masse à temps de vol (TOF-MS) [14], [15] et les mesures d'absorption laser in situ [16] ont été couplées à des tubes à chocs pour fournir des informations cinétiques détaillées sur la chimie en phase gazeuse, tandis que des techniques basées sur l'interaction matière-laser [17] ont été employées pour mesurer la formation et la croissance des particules. Cependant, malgré les capacités remarquables de ces techniques, il existe certaines limites qui

ne peuvent être surmontées qu'avec des solutions innovantes basées sur des diagnostics synchrotron récents. La combinaison des tubes à chocs avec ces diagnostics permettrait d'ajouter les avantages des deux installations. Malheureusement, l'installation d'un tube à choc dans un accélérateur de particules pose plusieurs problèmes liés aux faibles niveaux de signal et à l'espace disponible limité [18], [19]. Récemment, une nouvelle catégorie de tubes à chocs, les tubes à chocs miniaturisés à haut taux de répétition (ANL-HRRST), a été développée par R. Tranter au Argonne National Laboratory, spécifiquement pour une utilisation dans les installations synchrotron, démontrant une excellente répétabilité des conditions thermodynamiques atteintes dans le tube à chocs (essentielles pour le calcul de la moyenne du signal) et une fiabilité de fonctionnement [21]. En particulier, l'ANL-HRRST a été couplé à la spectrométrie de masse par photoionisation dans l'ultraviolet sous vide du synchrotron (VUV-PIMS), ce qui démontre le potentiel de ces techniques combinées [22]. En revanche, jusqu'à présent, les études réalisées avec l'ANL-HRRST n'ont pas été appliquées à la chimie des HAP ou des suies.

Le présent travail de thèse est basé sur une approche multi-échelles pour clarifier certains aspects liés aux différentes étapes de la formation et de la croissance des HAP et des particules, avec l'utilisation de techniques conventionnelles et innovantes de tubes à chocs. En fait, l'un des principaux objectifs de ce travail est de concevoir, construire, développer et caractériser un nouveau tube à choc miniaturisé à haut taux de répétition (ICARE-HRRST), le premier en Europe, destiné à être utilisé dans les Synchrotrons pour compléter les capacités expérimentales du laboratoire ICARE qui comprend déjà plusieurs tubes à chocs conventionnels. L'ICARE-HRRST a ensuite été couplé pour la première fois à un diagnostic avancé basé sur le synchrotron, la spectroscopie de coïncidence de photoélectron-photoion à double imagerie (i2PEPICO) [23], dans le but d'étudier la chimie des HAP dans des environnements pyrolytiques à haute pression. i^2PEPICO est l'une des techniques les plus avancées capables de résoudre des mélanges complexes d'isomères de HAP, comme l'ont démontré des études antérieures sur les flammes et les réacteurs à flux [24]-[26]. Par conséquent, l'application d'i^2PEPICO à l'étude de la formation des HAP dans des conditions similaires à celles d'un moteur a le potentiel de démêler la chimie complexe qui relie la formation de petits HAP et l'apparition de nanoparticules de carbone et d'aider à résoudre les controverses de longue date sur les mécanismes impliqués. Les premières études réalisées avec i2PEPICO/HRRST seront également présentées, y compris les résultats de la pyrolyse des principaux composants des carburants et des intermédiaires cruciaux dans la formation des nanoparticules de suie comme le toluène, l'éthylbenzène, le styrène et l'éthanol.

Pour compléter les mesures effectuées dans les installations synchrotron par des expériences réalisées avec des tubes de choc conventionnels à grande échelle, la formation de petits hydrocarbures aromatiques polycycliques (jusqu'à trois cycles, tube de choc à impulsion unique) et de nanoparticules carbonées (techniques basées sur l'interaction matière-_laser) à partir de différents intermédiaires de combustible tels que l'éthylbenzène et le styrène a été examinée. Les différents types de données seront analysés en fonction des caractéristiques spécifiques des installations. Ces résultats étendront les travaux antérieurs du laboratoire concernant la chimie des HAP et des particules provenant d'une variété de carburants aromatiques et de mélanges avec de petits intermédiaires aliphatiques, dans le cadre de la subvention européenne ERC FUN-PM.

Etude bibliographique

La compréhension de la formation et de la croissance des molécules de HAP est cruciale et influe fortement sur la précision de l'ensemble du modèle de formation de la suie. Malheureusement, la chimie

des HAP n'est pas encore bien comprise en raison du grand nombre de voies et de mécanismes de réaction possibles [27] et des limites des techniques expérimentales et théoriques [28]. L'un des mécanismes les plus acceptés est le schéma HACA, dans lequel plusieurs additions d'acétylène (C2H2) sur des sites radicaux conduisent à des structures cycliques et, par conséquent, à la croissance des HAP [29]. Des mécanismes similaires sont également impliqués dans la croissance des particules solides. Le mécanisme HACA repose sur la stabilité de l'acétylène dans des conditions de flamme à haute température, et il est limité par la concentration de l'espèce dans l'environnement de combustion.

Le mécanisme HACA est toujours l'une des principales voies dans de nombreuses applications pratiques, bien que plusieurs études expérimentales et de modélisation dans le passé aient montré comment sa mise en œuvre en tant que processus de croissance unique est incapable de prédire le taux de croissance correct, en particulier pour les HAP de grande taille ([30], [31]). Par exemple, Miller et al. [32] et Marinov et al. [33] ont constaté dans les années 90 que le mécanisme HACA était trop lent par rapport à leurs résultats expérimentaux. Comme alternative, ils ont proposé un mécanisme pour décrire la croissance rapide de grandes molécules complexes, basé sur l'ajout de radicaux stabilisés par résonance. Les radicaux stabilisés par résonance comprennent le propargyle (C3H3), l'allyle (C3H5), le cyclopentadiényle (C5H5), le benzyle (C6H5CH2) et l'indényle (C9H7).

D'autres mécanismes importants de croissance des HAP impliquent des réactions entre les radicaux aromatiques et les molécules aromatiques, accompagnées d'une abstraction d'hydrogène et d'une cyclisation, ce que l'on appelle la coagulation réactive [37]-[39]. Il s'agit d'une généralisation de la réaction entre le radical phényle et le benzène, observée dans le cadre de la formation des HAP lors des études antérieures [33], [40]. Récemment, Shukla et Koshi [41], [42] ont reproposé ce mécanisme sous un nom légèrement différent, à savoir la cyclisation par addition de phényle (PAC). Les mêmes auteurs ont également proposé le mécanisme dit HAVA [43] impliquant des radicaux C2H3, mais l'efficacité de ce mécanisme dans des conditions de combustion est limitée par la courte durée de vie du radical. D'autres mécanismes de croissance proposés comprennent l'addition de méthyle et cyclisation (MAC), comme indiqué par plusieurs auteurs [44]-[47], dont la contribution n'est cependant pas aussi efficace que les mécanismes mentionnés précédemment en raison de la faible masse moléculaire du radical méthyle, et la cycloaddition diradicale / fragmentation (CAF) [48]-[51], qui concerne principalement certaines réactions pyrolytiques des combustibles.

Dans la pyrolyse de combustibles réels, ces mécanismes de croissance se produisent en même temps et leur importance relative dépend de la composition du combustible et des conditions thermodynamiques (pression et température). Les recherches en laboratoire ont permis d'identifier ces mécanismes et de développer des modèles cinétiques chimiques détaillés capables de reproduire les observations expérimentales. En particulier, les tubes à chocs ont été couplés à différents systèmes analytiques pour réaliser des études de spéciation. Aujourd'hui, ces systèmes permettent de détecter, d'identifier et de quantifier un grand nombre de molécules dans les conditions rencontrées derrière les ondes de choc réfléchies. De nombreuses études antérieures sur la chimie pyrolytique appliquée à la formation de suie impliquent la décomposition thermique de molécules d'hydrocarbures aromatiques. Les molécules aromatiques sont présentes dans les carburants réels et les substituts de carburants, et sont formées comme intermédiaires dans la croissance moléculaire vers les particules solides. Ainsi, une

compréhension détaillée de la décomposition pyrolytique de ces molécules dans des conditions similaires à celles d'un moteur représente une étape importante dans la compréhension des processus de formation des HAP. Certains de ces travaux sont examinés en détail dans la section 2.1.1. En outre, la section 2.1.2 présente des travaux récents associant des tubes à chocs à taux de répétition élevé à des détecteurs synchrotron avancés afin de surmonter les limites des techniques actuelles. Une revue de la chimie des HAP pyrolytiques utilisant d'autres dispositifs expérimentaux est présentée à la section 2.1.3.

Les expériences menées en laboratoire et dans les synchrotrons sur la mesure des grands produits intermédiaires en phase gazeuse pertinents pour la formation des nanoparticules de suie peuvent aider à clarifier les voies qui mènent à la croissance des cycles. Cependant, le chemin vers la formation et la croissance des nanoparticules de carbone comprend plusieurs étapes qui doivent encore être clarifiées sur la base de techniques complémentaires axées sur la chimie en phase solide. Une revue de la littérature sur les tubes à chocs couplés à des diagnostics laser pour les mesures de particules est présentée à la section 2.2, en mettant l'accent sur les méthodes d'extinction laser, utilisées pour sonder l'évolution temporelle de la croissance des nanoparticules de suie provenant de la décomposition pyrolytique de multiples composants et mélanges de combustibles.

Techniques expérimentales

Les tubes à chocs sont des réacteurs adiabatiques idéaux, fermés et à volume constant, qui fournissent des conditions de pression et de température presque constantes au moyen d'ondes de choc [20]. La nature d'un tube à choc conventionnel est relativement simple. Au départ, les gaz chargés dans les deux sections, la section haute pression et la section basse pression, sont séparés au moyen d'un diaphragme. La section haute pression est remplie d'un gaz (généralement de l'hélium) à l'état 4, tandis que la section basse pression est remplie du gaz d'essai à une pression inférieure, appelée état 1. Après la rupture de la membrane, une série d'ondes de compression se forme. Ces ondes se déplacent dans un milieu comprimé par les ondes précédentes, de sorte que les ondes de compression suivantes ont des vitesses croissantes. Enfin, les ondes de compression se rejoignent pour former une forte onde de choc. Cette onde de choc se propage dans la section basse pression, augmentant soudainement la pression du gaz d'essai P1 jusqu'à l'état P2. L'onde de choc se propage le long de la section entraînée jusqu'à ce qu'elle soit réfléchie à la paroi d'extrémité. Derrière l'onde de choc réfléchie, les conditions sont T5 et P5. La **Figure** 3.2 montre un exemple de profil de pression obtenu dans le tube à choc à impulsion unique du laboratoire ICARE avec 92 ppm de styrène dans de l'argon.

Installations de tubes à chocs en laboratoire à ICARE

Récemment, une nouvelle technique expérimentale a été conçue et développée au laboratoire ICARE pour l'étude de la chimie des HAP. Cette technique est basée sur le tube à choc conventionnel à impulsion unique de haute pureté couplé à la chromatographie en phase gazeuse et à la spectrométrie de masse (HPST-GC/MS). Cette technique a été largement utilisée pour mesurer les intermédiaires stables issus de la pyrolyse et de l'oxydation des combustibles [8]. Un schéma du tube à choc conventionnel à impulsion

unique ICARE couplé au système analytique est présenté à la **Figure** 3.3. En outre, des techniques d'extinction laser ont été couplées au tube à choc chauffé du laboratoire ICARE (HST-LE) en tant qu'équipement de diagnostic optique pour étudier la formation transitoire et la croissance des nanoparticules de suie après la décomposition de plusieurs composants et mélanges de combustibles dans des conditions pyrolytiques. Le système HPST-GC/MS peut être utilisé pour étudier la chimie des aromatiques et des HAP dans les étapes de la phase gazeuse vers les particules de suie jusqu'aux espèces à trois/quatre cycles. D'autre part, en ce qui concerne la chimie en phase solide, le système HST-LE peut révéler des informations très utiles sur l'apparition et la croissance des nanoparticules de suie.

Tube à choc miniaturisé et installations au synchrotron

Le tube à choc miniaturisé couplé à des détecteurs synchrotron a le potentiel de surmonter certaines des limitations des systèmes GC, de compléter les techniques conventionnelles et de dévoiler la chimie des structures HAP à cycles multiples. Un nouveau tube à choc miniaturisé à haut taux de répétition (ICARE-HRRST) est présenté pour la première fois. L'ICARE-HRRST a été développé sur la base d'une conception antérieure des Dr Tranter et Dr Lynch (ANL-HRRST) afin d'accéder aux détecteurs de spectroscopie de coïncidence photoélectron/photoion à double imagerie (i2PEPICO) situés dans différentes installations synchrotron européennes (SOLEIL et SLS). Sa conception et son fonctionnement ont été examinés en détail (section 4.1), ainsi que la caractérisation de ses performances. Les défis à relever pour réaliser le couplage HRRST/i2PEPICO sont également décrits. En particulier, le tube de choc miniaturisé, caractérisé par un diamètre interne de 8 mm, est construit de manière modulaire, ce qui permet de varier sa longueur de ~84 cm (**Figure** 4.4). Le gaz d'essai et les gaz produits sont chargés/évacués vers/depuis la section basse pression du tube à choc au moyen de cinq vannes pneumatiques fabriquées sur mesure (une pour le remplissage et quatre pour l'évacuation) qui sont des éléments clés du système. La vanne de remplissage utilisée pour introduire les mélanges est équipée de deux réservoirs pour garantir que la pression P1 est pratiquement constante pendant le fonctionnement continu. Les deux réservoirs sont reliés à une cuve de 6 litres qui est automatiquement remplie de nouveau mélange en cas de besoin. Le mélange frais est préparé à l'aide de trois régulateurs de débit massique et d'un système de barbotage. Le tube à choc est équipé de 8 détecteurs de choc également espacés et situés le long de l'axe de la section entraînée afin de mesurer le temps de passage de l'onde de choc, tandis que la vitesse est extrapolée jusqu'à la paroi d'extrémité afin de calculer T5 et P5 en résolvant les équations de conservation. Le tube de choc peut être équipé à son extrémité soit d'un transducteur de pression PCB pour mesurer l'historique de la pression, soit d'une buse divergente en acier inoxydable pour le couplage par échantillonnage du faisceau moléculaire avec des détecteurs synchrotron. Le fonctionnement automatique du HRRST est garanti par un code, sous LabVIEW, qui gère également l'acquisition des données. L'ICARE-HRRST peut fonctionner à des taux allant jusqu'à environ 1,5 Hertz.

Les performances du système HRRST ont été caractérisées par des mesures de l'historique de la pression effectuées par un transducteur PCB situé à l'extrémité de la paroi. Les résultats ont mis en évidence la présence de dP/dt dans les expériences sur les mini-tubes à choc plus importants (dus à la croissance de la couche limite derrière les ondes de choc réfléchies) par rapport aux systèmes conventionnels, ce qui constitue le principal inconvénient de la réduction de la taille (**Figure** 4.9). Cela n'est pas préjudiciable à la qualité des résultats car les historiques de pression peuvent être pris en compte lors des simulations

cinétiques. Les expériences en laboratoire ont démontré une excellente reproductibilité des conditions expérimentales, non seulement pour la température T5 et la pression P5, avec des écarts types généralement inférieurs à 20 K et 0,15 bar, respectivement, mais aussi pour les historiques de pression. Ceci est essentiel pour le moyennage ultérieur du signal requis lors de l'utilisation de diagnostics à faible rapport S/B (signal/bruit) comme ceux du synchrotron.

Le couplage entre le HRRST et les détecteurs i2PEPICO à SOLEIL et à PSI a été réalisé avec succès, bien que les résultats expérimentaux de la campagne PSI n'aient été que préliminaires et ne soient pas présentés dans cette thèse. L'alignement mécanique entre le HRRST et la station terminale SAPHIRS située dans la branche A du monochromateur VUV DESIRS au synchrotron SOLEIL a été l'un des principaux défis, ainsi que la sécurité des opérations du HRRST à l'intérieur de la chambre à vide. Une chambre à vide différentielle sépare la chambre principale, où le HRRST est inséré, et la chambre à vide du spectromètre de masse DELICIOUS III i2PEPICO pour une extraction efficace des produits en réduisant le risque d'endommager les instruments du spectromètre de masse en cas d'accident ou de dysfonctionnement (**Figure** 4.12). L'optimisation de la technique expérimentale a été obtenue de manière empirique, y compris la sélection des meilleurs modèles de buses et du skimmer ainsi que la distance entre eux, pour des niveaux de pression sûrs à l'intérieur de la chambre du spectromètre de masse pendant le fonctionnement du HRRST et un faisceau moléculaire de bonne qualité avec des niveaux de signal suffisants. L'alignement entre la buse HRRST et les skimmers SAPHIRS a également été affiné avec la conception d'un système de serrage et l'utilisation de rails en aluminium de haute précision pour une insertion/extraction précise du HRRST avec une reproductibilité de l'alignement. Le couplage entre ICARE-HRRST et la ligne de faisceaux SLS/VUV X04DB est également présenté, y compris les principaux défis et les développements futurs (**Figure** 4.18).

Résultats et discussions

Pyrolyse d'éthanol – implémentation de la technique

La première campagne expérimentale à SOLEIL s'est concentrée sur la pyrolyse de l'éthanol, le principal biocarburant actuel. En général, quatre conditions expérimentales comprenant plus de 54 000 expériences ont été examinées, démontrant plusieurs fonctionnalités du couplage HRRST/i2PEPICO dans une large gamme de conditions de températures (1232 K - 1525 K), de pressions (6,2 bar-7,5 bar), de concentrations de carburant (0,25%-2,7%), de taux de répétition (1Hz-1,5Hz), et d'énergies de photons (10,0 eV-11,0 eV). Les données spectrales ont été enregistrées en utilisant le mode d'acquisition de données pulsé dans des conditions de pré-choc et de post-choc. Pour chaque ensemble de données expérimentales, des matrices de temps de vol des ions/électrons et des images photoélectroniques sélectionnées en fonction de la masse ont pu être obtenues, ce qui a permis d'extraire des spectres de masse, des profils cinétiques temporels (**Figure** 5.1) et, en outre, des spectres photoélectroniques sélectionnés en fonction de la masse (PES), une caractéristique unique pour l'identification des espèces isomériques (voir **Figure** 5.2).

Dans le premier ensemble de données expérimentales, environ 15 000 expériences sur tube à choc ont été réalisées à une température moyenne T5 de 1232 K et à une pression moyenne de 7,4 bar avec une énergie des photons de 11 eV et une concentration d'éthanol de 2,7 %. Le système HRRST/i2PEPICO a été mis en œuvre pour obtenir des PES d'une qualité suffisante pour identifier la plupart des principaux isomères produits pendant la pyrolyse de l'éthanol, y compris les concentrations relatives des principales espèces isomériques (voir **Figure** 5.5). Cependant, les niveaux du signal n'étaient pas toujours suffisants pour distinguer les espèces avec des PES similaires, voir par exemple la **Figure** 5.3. Certaines améliorations du signal ont pu être obtenues afin d'augmenter la résolution de la PES et différentes énergies de photons ont également été utilisées. Cela a permis d'augmenter la sensibilité de détection pour les espèces mineures observées dans le spectre de masse. En outre, les profils temporels ont permis de déterminer les concentrations relatives entre les espèces de masses différentes et les résultats ont été comparés aux simulations cinétiques utilisant le modèle cinétique chimique CRECK avec une bonne concordance (voir **Figure** 5.4). Les simulations ont aidé à l'interprétation des résultats expérimentaux, montrant le grand potentiel de cette technique pour l'étude cinétique de mélanges complexes d'espèces gazeuses isomères.

La deuxième série d'expériences a été réalisée dans des conditions similaires à celles des expériences réalisées à 11 eV présentées précédemment (T5 = 1234 K et P5 = 7,5 bar, valeurs moyennes, éthanol 2,7 %). Un nombre d'expériences de 27 000 a été obtenu afin d'augmenter le rapport S/N pour les petits produits. L'énergie de photoionisation a été réduite à 10,0 eV afin de diminuer le bruit de fond dû aux fausses coïncidences de l'ionisation de l'éthanol et des principaux produits (principalement l'éthylène) et de pouvoir capturer les espèces mineures, y compris les espèces aromatiques, qui s'ionisent en dessous de cette valeur énergétique (voir **Figure** 5.6 et **Figure** 5.7). Cette série d'expériences a mis en évidence l'un des potentiels de la technique proposée, à savoir la capacité d'identifier des isomères spécifiques à l'intérieur d'un mélange complexe si l'énergie de photons correcte est sélectionnée.

Une troisième série de 32 000 expériences dans les conditions de réaction suivantes : T5 = 1525 K, P5 = 7,5 bar et éthanol 2,7 % a été réalisée pour tenter d'identifier les produits HAP. La température a été augmentée pour permettre la production et la détection des espèces de HAP afin de tester les capacités du système HRRST/i2PEPICO sur ces espèces aussi. Même si le rapport S/B est faible pour les pics mineurs comme m/z 116 dans la **Figure** 5.10d, le PES expérimental a permis de réduire autant que possible la quantité de candidats pour les isomères, ce qui est également une contribution très précieuse pour l'étude de ces mélanges complexes avec des espèces de HAP en très faibles concentrations.

Enfin, la concentration d'éthanol a été réduite de 2,7 % à 0,25 %, car les mélanges fortement dilués sont généralement préférés pour les études cinétiques. Un ensemble d'environ 9 000 expériences à T5 de 1354 K, P5 = 6,2 bar, à une énergie des photons de 11 eV a été réalisé. Afin de tester la fiabilité de l'utilisation du système HRRST/i2PEPICO pour des concentrations de réactifs aussi faibles, une nouvelle configuration d'interface d'échantillonnage par faisceau moléculaire a été mise en œuvre, comme le montre la **Figure** 4.16. La nouvelle configuration d'échantillonnage par faisceau moléculaire a considérablement réduit le temps global nécessaire pour obtenir des données spectrales avec un bon rapport signal/bruit, même pour des mélanges fortement dilués (voir **Figure** 5.11). Cette caractéristique particulière du couplage unique HRRST/i2PEPICO permet de mieux planifier les campagnes expérimentales où une large gamme de conditions peut être explorée en prêtant attention aux ensembles spécifiques qui nécessitent un niveau de détail plus élevé.

Malgré le caractère innovant des résultats expérimentaux sur la pyrolyse de l'éthanol, deux défis ont été identifiés afin d'améliorer les capacités expérimentales. Tout d'abord, la nécessité d'obtenir des ensembles de données quantitatives sur les profils temporels des espèces a été mise en évidence lors de la première campagne à SOLEIL, malgré la valeur des informations qualitatives. Plus précisément, les mesures quantitatives doivent prendre en compte les variations de pression à l'intérieur de la chambre du spectromètre de masse afin de corriger le signal. L'autre problème concerne les niveaux de signal PES limités en mode d'acquisition de données pulsé, même avec un alignement optimisé. Cette limitation rend difficile l'identification de plusieurs isomères, en particulier pour les espèces mineures comme les HAP.

Méthode d'étalonnage standard externe pour l'analyse cinétique quantitative

Comme indiqué précédemment, les données expérimentales brutes ne pouvaient pas être utilisées pour extraire des profils cinétiques à des fins de quantification. Une nouvelle méthode utilisant un étalon externe est proposée dans ce chapitre pour corriger le signal des variations de pression à l'intérieur de la chambre du spectromètre, applicable à toute expérience HRRST/TOF-MS. En particulier, la méthode s'est avérée capable de fournir des profils de concentration pour les expériences HRRST couplées à la spectrométrie de masse basée sur le rayonnement synchrotron, d'un intérêt particulier pour les études cinétiques chimiques et la validation de modèles. À cette fin, le CO2 a été proposé comme étalon externe de référence, et deux carburants largement étudiés ont été considérés pour mener cette analyse: le toluène et l'éthylbenzène. En ce qui concerne les conditions expérimentales, le mode d'acquisition de données pulsé a été utilisé, couvrant 8 ms de conditions de pré-choc et de post-choc. Le taux de répétition était de 1 Hz et l'énergie des photons utilisée pour ioniser les molécules de carburant et le dioxyde de carbone était de 10 eV et 14,5 eV, respectivement.

Le comportement du signal peut être formulé en fonction de la section efficace de photoionisation, de la concentration, du facteur de discrimination de masse, du nombre d'expériences, du coefficient d'efficacité et d'une fonction de correction des variations temporelles de pression à l'intérieur du spectromètre de masse, voir l'équation (5.3). Les données spectrales brutes utilisées avec cette méthodologie contiennent plus de 107 000 expériences moyennées avec 1 % de toluène dilué dans de l'argon à T5 et P5 égal à 1362±22 K et 6,6±0,2 bar, respectivement. L'évolution des profils temporels des espèces, depuis les espèces légères jusqu'aux cycles à 5 membres, a été obtenue en utilisant le mode d'acquisition de données pulsées à une énergie des photons de 10 eV. Pour déterminer si l'historique de la pression a un effet sur les profils temporels des espèces, 6 042 expériences ont été menées en utilisant la technique ICARE-HRRST/i2PEPICO avec l'étalon de calibration externe, le CO2 (0,1 % dans l'argon). Pour que la méthode soit précise, des conditions thermodynamiques (T5 = 1376±12 K et P5 = 6,6±0,1 bar,) et l'historique de la pression ont été maintenus similaires aux expériences sur le toluène, mais l'énergie des photons a été augmentée à 14,5 eV pour permettre l'ionisation du dioxyde de carbone. Les premiers résultats obtenus en utilisant la technique d'étalonnage avec étalon externe sont présentés dans la **Figure** 5.13. Les profils de concentration sont comparés aux simulations réalisées avec le modèle cinétique chimique ICARE pour la formation et la croissance des HAP à l'aide du logiciel ANSYS CHEMKIN-Pro 2021, réacteur à pression variable, suivant le profil de la **Figure** 5.12a. Il existe un excellent accord global entre les expériences et les simulations pour la décomposition du combustible et la formation des principaux produits aromatiques à cycle unique, notamment le benzène (m/z = 78), le styrène (m/z = 104), le phénylacétylène (m/z = 102) et un pic à m/z = 91, correspondant au radical benzyle. Les profils des espèces pour les produits HAP plus importants, tels que l'indène (m/z = 116) et le naphtalène (m/z = 128), sont présentés dans la **Figure** 5.13d, et les résultats sont tout à fait satisfaisants compte tenu de la complexité

de la chimie impliquée dans la formation des HAP et des incertitudes expérimentales. La même analyse a été réalisée pour un combustible plus réactif, l'éthylbenzène (27 000 expériences, T5 = 1327±18 K, P5 = 6,7±0,2 bar). Comme pour le cas du toluène, un bon accord a été obtenu entre les données expérimentales et les simulations. Plusieurs paramètres pertinents pour la méthodologie, y compris l'alignement entre les profils de CO2 et de carburant et le nombre d'expériences, ont été pris en compte et analysés en termes de qualité des résultats expérimentaux. Dans l'ensemble, il a été déterminé que la méthode de l'étalon externe est une technique polyvalente pour obtenir des informations cinétiques à partir d'expériences HRRST/TOF-MS menées dans des synchrotrons, y compris le couplage HRRST/i2PEPICO.

Pyrolyse du toluène avec HRRST/i2PEPICO

Les résultats de la première étude pyrolytique sur la chimie aromatique utilisant la combinaison HRRST/i2PEPICO sont présentés dans ce chapitre, démontrant les capacités de la technique, en particulier en ce qui concerne la détection et la mesure de produits HAP importants. Le toluène (C7H8) a été choisi comme combustible à cette fin, car il s'agit d'un important composant des combustibles et d'un intermédiaire lors de la formation et de la croissance des HAP. Cette étude complète les travaux cinétiques de la littérature sur la pyrolyse du toluène en utilisant différents systèmes conventionnels de spéciation tels que le tube à choc/GC-MS [59], [63] et les réacteurs à flux atmosphérique et sub-atmosphérique [95], [102].

Deux conditions expérimentales sont présentées dans ce chapitre avec les deux modes d'acquisition de données disponibles pour DELICIOUS III. La première condition est également celle utilisée pour valider notre méthode d'étalonnage externe développée pour l'analyse de la concentration des espèces en fonction du temps, discutée précédemment. La seconde condition est similaire, avec 0,1 % de toluène dans l'argon à T5= 1351 ± 13 K et P5=6,4 ± 0,1 bar, mais une énergie des photons de 8,5 eV a été utilisée cette fois-ci avec plus de 41 000 expériences. Cette énergie des photons a permis la photoionisation de la plupart des espèces de HAP, ce qui a permis d'obtenir des PES pour des masses plus importantes au détriment de la détection de la molécule de carburant et de certains intermédiaires (section 5.3.2). En outre, le mode d'acquisition de données en continu du détecteur i2PEPICO a été utilisé et exploité afin d'obtenir des niveaux de signal PES plus élevés. Ce mode ne permet pas d'extraire des informations cinétiques car les informations sont acquises en continu sans référence à l'arrivée de l'onde de choc. Cependant, des spectres de masse bien définis et des PES plus nets ont été obtenus pour des HAP plus gros, permettant l'identification d'isomères qui n'auraient pas pu être obtenus sans i2PEPICO. Les résultats du mode pulsé et du mode continu sont présentés parallèlement au cours de la discussion.

L'identification par sélection de masse d'un grand nombre de composés d'hydrocarbures aromatiques polycycliques issus de la décomposition pyrolytique du toluène en utilisant la configuration HRRST/i2PEPICO a été présentée et comparée aux résultats expérimentaux précédemment rapportés en utilisant le tube à choc à impulsion unique ICARE couplé à la GC/GC-MS. Cela a été possible grâce au développement d'une nouvelle méthodologie analytique qui met en œuvre des calculs de chimie quantique ab-initio sur les caractéristiques spectrales détaillées des isomères possibles. Sur la base des résultats et des connaissances cinétiques actuelles, plusieurs voies communes ont été identifiées, notamment la voie HACA, l'addition de radicaux stabilisés par résonance (C3H3, C7H7), l'addition du radical phényle et la cyclisation, la méthylation et l'addition de diacétylène aux radicaux aromatiques. En outre, la détection de grands produits PAH jusqu'à m/z 426 a été possible, fournissant des informations

qualitatives sur la croissance des grands précurseurs de suie (**Figure** 5.19). Ces informations constituent un progrès substantiel pour la compréhension des premières étapes en phase gazeuse de la chimie de la formation des suies, et complètent les données obtenues avec les techniques conventionnelles de laboratoire en termes d'identification des isomères et de détection des grosses molécules. Ces nouveaux résultats illustrent également les capacités de cette technique expérimentale innovante qui ne peuvent être atteintes avec des études analytiques régulières en laboratoire.

Pyrolyse de l'éthylbenzène et du styrène avec HRRST/i2PEPICO

Cette étude exhaustive utilisant la technique HRRST/DELICIOUS III-i2PEPICO a été étendue à d'autres molécules intermédiaires de suie importantes. Plus précisément, les résultats de la décomposition pyrolytique de l'éthylbenzène (C8H10) et du styrène (C8H8) ont été comparés aux données relatives au toluène afin de mettre en évidence l'influence de la structure du combustible sur la croissance des HAP. L'éthylbenzène est le plus petit des hydrocarbures aromatiques alkylés et un composant important du combustible, tandis que le styrène a été identifié comme un sous-produit abondant de la pyrolyse de l'éthylbenzène et un intermédiaire clé pour la formation de grosses molécules de HAP. En fait, comme indiqué dans des études précédentes portantsur la pyrolyse de l'éthylbenzène à l'aide d'un tube à choc à impulsion unique connecté à la GC/MS [66], les réactions du styrène avec le radical phényle (C6H5) jouent un rôle important dans la formation du phénanthrène par la production de dihydro-phénanthrène. Une étude comparative entre les résultats de l'éthylbenzène et du toluène est présentée sur la base du spectre de masse afin qu'une analyse qualitative puisse être effectuée sur l'influence de la longueur de la chaîne latérale sur la distribution des produits pyrolytiques (**Figure** 5.52). En outre, le styrène a une structure similaire à celle de l'éthylbenzène, bien qu'il présente une double liaison dans sa chaîne alkyle latérale. Compte tenu de l'analogie et pour mettre en évidence l'influence de la saturation des liaisons sur la distribution des produits, les données du styrène sont comparées aux résultats de l'éthylbenzène (**Figure** 5.66). Cette analyse est essentielle pour comprendre les différentes voies de réaction impliquées dans la décomposition thermique des différents combustibles, et pour les futurs développements de modèles pour la chimie des combustibles de substitution.

Deux conditions expérimentales différentes ont été prises en compte dans l'étude sur la pyrolyse de l'éthylbenzène et du styrène. Un ensemble d'expériences a été moyenné en utilisant le mode d'acquisition pulsé afin de réaliser des profils cinétiques chimiques avec une énergie de photon de 10 eV. Les conditions sont relativement proches de celles utilisées pour la pyrolyse du toluène afin d'effectuer des comparaisons valables. Le même dispositif expérimental a été mis en œuvre pour la deuxième partie de l'étude. Une autre série d'expériences a été moyennée en utilisant le mode d'acquisition dit continu à une énergie de photon de 8,5 eV. Une concentration de combustible de 0,1 % dilué dans l'argon a de nouveau été considérée pour l'éthylbenzène et le styrène, et la décomposition pyrolytique thermique a été étudiée dans des conditions similaires en ce qui concerne le toluène. Les données ont été utilisées pour obtenir un grand nombre de PES expérimentaux pour l'identification des isomères de HAP sur une large gamme de m/z comme dans l'étude de la pyrolyse du toluène. Les PES expérimentaux sont ensuite comparés aux spectres photoélectroniques d'isomères convolus et aux PES expérimentaux respectifs sélectionnés en fonction de la masse provenant de la pyrolyse du toluène (pour le cas de l'éthylbenzène, par exemple, comme dans la **Figure** 5.56) et de la pyrolyse de l'éthylbenzène (pour le cas du styrène, comme dans la **Figure** 5.69) dans des conditions similaires. La comparaison met également en évidence les effets de la chaîne latérale sur la distribution des produits en fonction de l'abondance relative des isomères et des contributions à chaque signal PES. Ces nouveaux résultats complètent les bases de données

expérimentales disponibles dans la littérature à partir de techniques conventionnelles en laboratoire, pour une meilleure compréhension de la chimie complexe des hydrocarbures alkylés et de la pyrolyse du styrène et la validation de modèles cinétiques chimiques détaillés pour la chimie des précurseurs de suie.

Pyrolyse du styrène avec HPST/ GC-MS

Une étude comparative entre les techniques de tube à choc basées sur le synchrotron et les techniques conventionnelles de tube à choc basées sur le laboratoire a été réalisée dans le cadre de cette thèse afin de mettre en évidence la complémentarité des différentes installations. Plus précisément, la première étude pyrolytique sur la décomposition du styrène à l'aide du tube à choc ICARE à impulsion unique couplé à la GC/GC-MS a été présentée pour des produits allant jusqu'à quatre cycles (profils d'espèces). Les expériences à impulsion unique ont été réalisées à une température comprise entre 1168 et 1734 K et à une pression nominale de P5 = 20 bar avec un temps de réaction d'environ 4 ms. La concentration initiale du combustible est de 92 ppm dilués l'argon.

Les résultats expérimentaux sont accompagnés de résultats de simulation numérique obtenus avec la version la plus récente du modèle cinétique chimique ICARE pour la formation et la croissance des HAP (voir **Figure** 5.73). Les simulations ont été effectuées à l'aide du module de réacteur homogène de CHEMKIN Pro. La complémentarité entre les informations obtenues à l'aide du HRRST couplé au détecteur i2PEPICO et les résultats obtenus avec des techniques conventionnelles bien établies a été illustrée. Ainsi les nouvelles données confirment les résultats des études conventionnelles e tout en donnant davantage d'informations sur la chimie de formation des grandes espèces de HAP. Les résultats constituent une contribution importante au domaine de la chimie des suies en raison du rôle important que joue le styrène dans la formation des HAP à partir de combustibles réels et de substitution typiques. En outre, ces nouvelles données, ainsi que les résultats sur le toluène et l'éthylbenzène tirés de la littérature, constituent le point de référence pour la validation du modèle, ainsi qu'une référence pour la comparaison avec les résultats de la HRRST (**Figure** 5.74).

Pyrolyse de l'éthylbenzène et du styrène avec HST/LS

Enfin, les données sur le temps d'extinction du tube à choc/laser de la pyrolyse de l'éthylbenzène et du styrène sont comparées aux données précédentes sur le toluène, et servent, avec les données sur les HAP, à clarifier les principaux mécanismes liés à la formation de suie à partir de ces combustibles, pour les futurs développements de modèles cinétiques chimiques, qui font partie des activités en cours du groupe ICARE. Environ 76 expériences ont été réalisées pour les deux combustibles avec la même concentration initiale de carbone [C] que celle utilisée dans l'étude précédente sur la pyrolyse du toluène, ce qui correspond à des concentrations molaires de 0,0613 % d'éthylbenzène et de styrène dans l'argon. Les conditions ont été maintenues à une pression nominale de 17,6 bars et la température a varié entre 1560 K et 1942 K.

La discussion est basée sur l'analyse des densités optiques de suie (**Figure** 5.76). Les délais d'induction (τind) sont également présentés, fournissant une estimation de la tendance du combustible à former plus ou moins rapidement les premières nanoparticules (voir **Figure** 5.77). Les résultats montrent notamment que le toluène a une propension plus élevée à former de la suie que le styrène et l'éthylbenzène. En général, deux facteurs influencent la chimie de la suie d'après les analyses de données : i) la formation de radicaux stabilisés par résonance à partir de la décomposition thermique de la molécule de carburant dans la région à basse température ; ii) le rapport C/H dans la région à haute température. Les ensembles

de données présentés dans la section précédente fournissent des informations essentielles pour améliorer notre compréhension des différents processus responsables de la formation de suie à partir de combustibles clés, en fonction des conditions de température et de la structure/chimie du combustible, et pour l'estimation des paramètres cinétiques correspondants.

Conclusions

Afin de développer des modèles cinétiques chimiques prédictifs ciblant la formation et la croissance des suies et qui peuvent être utilisés comme outils théoriques pour la conception des dispositifs de combustion de la prochaine génération, notre compréhension fondamentale des différents processus chimiques et physiques connexes doit être affinée. Des efforts récents pour améliorer les techniques expérimentales conventionnelles ont permis de mesurer des composés d'hydrocarbures aromatiques polycycliques (HAP) relativement grande taille, précurseurs des particules de suie, et d'évaluer avec précision la chimie en phase solide. D'un autre côté, ces techniques présentent des limites qui ne peuvent être surmontées que par des solutions innovantes basées sur des diagnostics modernes.

Le présent travail de thèse utilise trois tubes à chocs de différentes échelles couplés à des techniques de laboratoire et de synchrotron pour étudier expérimentalement la chimie des HAP et des particules de suie à partir de composants et d'intermédiaires de combustibles réels et de substitution. En particulier, un nouveau tube à choc miniaturisé à taux de répétition élevé (ICARE-HRRST) a été conçu et construit. L'ICARE-HRRST est capable de travailler à des taux de répétition allant jusqu'à 1,5 Hz, avec d'excellentes performances en termes de reproductibilité des conditions expérimentales.

L'ICARE-HRRST a également été couplé à des détecteurs de spectroscopie de coïncidence photoélectron/photoion à double imagerie (i2PEPICO) situés dans différentes installations synchrotron européennes (SOLEIL et SLS). Les premiers résultats de la combinaison HRRST/i2PEPICO ont été obtenus à SOLEIL sur la pyrolyse de l'éthanol, le principal biocarburant actuel. Des expériences ont été réalisées pour tester la fonctionnalité de la technique, à différentes énergies de photons, dilutions de carburant et températures. Pour chaque ensemble de données expérimentales, des matrices de temps de vol d'ions/électrons et des images photoélectroniques sélectionnées en fonction de la masse ont pu être obtenues, ce qui a permis d'extraire des spectres de masse, des profils cinétiques temporels et, en outre, des spectres photoélectroniques sélectionnés en fonction de la masse (PES), une caractéristique unique pour l'identification des espèces isomériques.

Les limitations spécifiques du couplage HRRST/i2PEPICO rencontrées lors de la première campagne expérimentale à SOLEIL ont été résolues lors de la campagne suivante axée sur la chimie des HAP issus de la pyrolyse du toluène, de l'éthylbenzène et du styrène. Les résultats, obtenus en faisant la moyenne de plus de 300 000 expériences HRRST, ont été analysés pour obtenir des informations détaillées sur la chimie de la formation des HAP à partir de la décomposition thermique du toluène, grâce à l'identification des isomères des principales espèces de HAP sélectionnées en fonction de leur masse. Cela a été possible grâce au développement d'une nouvelle méthodologie analytique qui met en œuvre des calculs de chimie quantique ab-initio sur les caractéristiques spectrales détaillées des isomères possibles. Les résultats ont permis de déterminer les principales voies de réaction associées. En outre, la détection de grands produits PAH jusqu'à m/z 426 a été possible, fournissant des informations qualitatives sur la croissance des grands

précurseurs de suie. La comparaison entre les résultats expérimentaux pour les différents carburants a également été effectuée pour mettre en évidence l'influence de la structure du carburant sur la croissance des HAP. Dans le cadre du développement de la technique expérimentale, une nouvelle méthode d'étalonnage standard externe pour les études cinétiques quantitatives utilisant la HRRST couplée à des systèmes de spectrométrie de masse basés sur le synchrotron a également été formulée et développée.

Les expériences synchrotron ont été complétées par des expériences conventionnelles de tube à choc à impulsion unique pour les mesures des produits stables jusqu'à quatre cycles issus de la pyrolyse du styrène (profils d'espèces). Ces nouvelles données, ainsi que les résultats sur le toluène et l'éthylbenzène de la littérature, constituent le point de référence pour la validation du modèle, ainsi qu'une référence pour la comparaison avec les résultats du HRRST. Enfin, les données du tube à choc/laser de la pyrolyse de l'éthylbenzène et du styrène sont comparées aux données précédentes sur le toluène, et servent, avec les données sur les HAP, à clarifier les principaux mécanismes liés à la formation de suie à partir de ces combustibles, en vue de futurs développements de modèles de cinétique chimique.

Abstract

In order to develop predictive chemical kinetic models for soot formation and growth that can be used as part of theoretical tools for the design of next-generation combustion devices, our fundamental understanding of the different related chemical and physical processes needs to be refined. Recent efforts in improving conventional experimental techniques have allowed the measurement of relatively large polycyclic aromatic hydrocarbon (PAH) compounds, precursors of the soot particles, and accurate evaluation of the solid-phase chemistry. On the other hand, these techniques present limitations which can be overcome only with innovative solutions based on up-to-date diagnostics.

The present thesis work uses three shock tubes of different scales coupled to both laboratory-based and synchrotron-based techniques, to experimentally investigate PAH and soot particle chemistry from key real and surrogate fuel components and intermediates. In particular, a new miniature high repetition rate shock tube (HRRST) is presented for the first time. Details on the mechanical design and operation are discussed together with the characterization of its performances. In addition, the coupling between the HRRST and double imaging photoelectron/photoion coincidence spectroscopy (i^2PEPICO) detectors located in different European synchrotron facilities (SOLEIL and SLS) is described together with the related challenges.

The first ever results from the HRRST/i^2PEPICO combination were obtained at SOLEIL on the pyrolysis of ethanol, the current main biofuel. Experiments were performed to test the functionality of the technique, at different photon energies, fuel dilutions, and temperatures. For each experimental dataset, ion/electron time of flight matrices and mass-selected photoelectron images could be obtained, which allowed the extraction of mass spectra, time kinetic profiles, and, additionally, mass-selected photoelectron spectra (PES), unique feature for isomeric species identification.

Specific limitations of the HRRST/i^2PEPICO coupling encountered during the first experimental campaign at SOLEIL were solved in the following campaign focused on PAH chemistry from toluene, ethylbenzene, and styrene pyrolysis. The results, obtained by averaging more than 300 000 HRRST experiments, were analyzed to derive detailed information on the PAH formation chemistry from toluene thermal decomposition through isomer identification of the main mass-selected PAH species. This was possible thanks to the development of a new analytical methodology that implements ab-initio quantum chemistry calculations on the detailed spectral characteristics of possible isomers. The main related reaction pathways are discussed based on the current kinetic knowledge. In addition, the detection of large PAH products up to m/z 426 was possible, providing qualitative information on the growth to the large soot precursors. The comparison between the experimental results for the different fuels was also performed to highlight the influence of the fuel structure on the PAH growth. As part of the experimental technique development, a new external standard calibration method for quantitative kinetic studies using HRRST coupled to synchrotron-based mass spectrometry systems was also formulated and developed.

The synchrotron experiments were complemented with conventional single-pulse shock tube experiments for measurements of stable products up to four-rings from styrene pyrolysis (species profiles). These new data, together with the results on toluene and ethylbenzene from the literature, provide the benchmark for the model validation, as well as a reference for comparison with the HRRST

results. Finally, shock tube/laser extinction time-history data from ethylbenzene and styrene pyrolysis are compared to previous toluene data, serving together with PAH data to clarify the main mechanisms related to soot formation from these fuels, for future chemical kinetic model developments.

Keywords: shock tubes, synchrotron diagnostics, nanoparticles chemistry, chemical kinetics, laser extinction, gas chromatography.

Acknowledgments

Institutionality provides every researcher with a sense of belonging. Thanks to the laboratory ICARE-CNRS, Université d'Orléans and members of doctoral school EMSTU. Thanks to the European Research Council for funding this project.

Good luck is when opportunity and capability get combined. Happy to meet you Dr. Andrea Comandini. Thanks for sharing confidence, help and a lot of memories… Thanks for making me a luckier person.

Knowledge and inspiration are the sustain for a learner and should be transmitted effectively with vocation and the best of the dispositions. Thanks to Dr. Nabiha Chaumeix for being a gentle director inside and outside the laboratory. To Prof. Abid Said, Dr. Mahmud Idir and Dr. Robert Tranter for the will to help and for the respect, that is inspiring. Thanks to the members of the Jury, Prof. Brandon Rotavera and Dr. Silvana De Iuliis for the revision of this thesis and thanks to the president of the Jury Prof. Laurent Catoire.

They say that who finds a friend, finds a treasure. I have found several at ICARE. Thanks to Dr. Alaa Hamadi, Dr. Alka Karan, Dr. Leticia Carneiro Piton, Dr. Sharath Nagaraju and Dr. Alejandra Palomino Martinez. You can always count on me.

Collaboration is where things become possible and is essential for the stability of humanity. Thanks to members of *shock waves team* specially to Dr. Anthony Oswaldo Roque Ccacya, Tullio Viola and Ayan Mousse Rayaleh for the hospitality and fun. Thanks to ICARE administrative staff, informaticians, technicians and other permanents, specially to Prof. Fabian Halter who shared my CV to end up in this PhD position. Big thanks also to postdocs, PhD students and CNRS colleagues with whom I exchanged either help, conferences or discussions during the development of the thesis. Thanks to SOLEIL, PSI and ARGON members with who I had the pleasure to collaborate, who directly or indirectly helped a lot to make this on-going process to be enjoying. To all of them I wish success and recognition.

What is inside you, is shared outside too. Thanks to my great family, my incredible wife, and my supportive friends for the pleasant company through the best and most challenging moments of this adventure in Orleans. You are part of my joy, you are with whom the story started, and it goes… the merit of this thesis is also yours!

Contents

Table of Figures

List of Tables

1 Introduction and motivation

Particulate matter (PM) constitutes one of the most harmful pollutants for human health and the environment. The presence of particulates suspended in the atmosphere has been undeniably related to health issues like lung diseases and cancer as well as to global warming. PM is associated to inefficiencies on energy conversion in thermal engines used in transportation, boilers or turbines for energy production. Additionally, in the context of transportation, PM can be produced from 'non-exhaust' sources like brake dust and tire/road abrasion [1]. Despite the development of mitigation techniques like particle filters [2], [3], some projections show a dramatic increase on premature deaths from 1 million worldwide in 2000 to 3.5 million in 2050 due to suspended PM in the air [4]. For this reason, the international regulations on particulate emissions are becoming more and more stringent, and the development of more efficient and cleaner combustion devices is an urgent need for modern societies. From a fundamental perspective, a detailed and accurate understanding of the particulate formation at conditions relevant to combustion devices is a key element towards the implementation of effective mitigation techniques for reduced emissions, including design optimization or fuel reformulation with use of additives. In particular, the carbonaceous core of particulates, called soot, derives from the incomplete fuel oxidation in regions of the flame where the oxygen concentrations are deficient compared to the carbon concentrations.

As known so far, soot formation is a very complex process that involves several multi-phase, multi-scale steps starting from the decomposition of the fuel components and subsequent formation and growth of the multi-ring structures, the so-called polycyclic aromatic hydrocarbons (PAHs) from the single-ring aromatics [5], [6]. The current soot formation models suggest *'per se'* a kinetic order of the gas-phase intermediates to soot including the appearance and evolution of PAHs as shown in **Figure** 1-1. The following steps include particle inception with formation of the primary nanoparticles (1-5 nm in size), one of the main unresolved questions in the combustion field and focus of the major research groups worldwide. In fact, no consensus could be reached yet regarding basic understanding of the nature of the soot precursors and their size or the relevance of different physical processes behind the inception (clustering by physical or ionic forces, PAH bridging, PAH-PAH bonding, reaction-based processes) [7]. The nascent nanoparticles subsequently undergo surface growth by reaction (similar to gas-phase chemistry involving PAHs and small intermediates like acetylene) and coagulation by sintering to form larger particles. Once the particles reach a certain size, they start to agglomerate and form long chains of hundreds of primary particles with size 10-100 nm. In flames, such agglomerates are finally transported to regions of the flame where oxygen is present in considerable concentrations and they undergo oxidation to form the so-called mature-soot.

Literature kinetics studies on soot formation are numerous and they involve experimental investigations on the soot precursor PAH molecules and solid-phase chemistry of carbonaceous particles in various set-ups (flames, perfectly stirred rectors, shock tubes, flow reactors, etc), kinetic modeling development and validation (fuel decomposition, PAH formation and growth, soot inception-growth-oxidation), theoretical ab-initio calculations mainly focused on the fuel decomposition and only recently on PAH chemistry, and reactive molecular dynamics simulations. The scope of these investigations is to provide predictive comprehensive models for particle chemistry to be used in CFD codes and validated against laboratory-based results. In particular, shock tubes constitute the ideal apparatuses for investigating soot chemistry at the typical conditions encountered in modern combustion devises [8], [9]. The advantages of shock

tubes compared to other set-ups include: 1) possibility to obtain any combination of well-defined pressure and temperature conditions within few microseconds of rise time; 2) homogeneous and adiabatic reactor; 3) the chemistry is dissociated from any fluid dynamic aspect (the gases behind reflected shock waves are still); 4) possibility to run any dilution condition and in absence of oxygen (essential to isolate the soot chemistry).

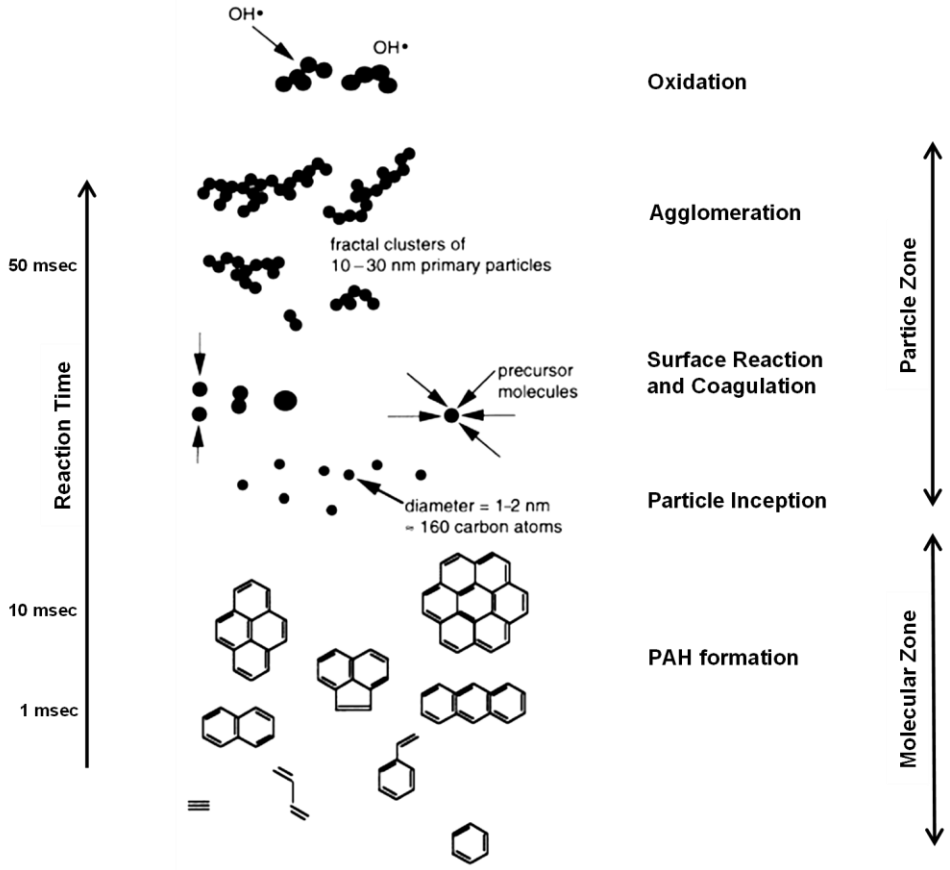

***Figure** 1-1. Physical processes involved in soot formation.* [5], [6]

Since the appearance of first apparatus which can be considered as a progenitor of modern shock tubes in 1899 [10], [11], the diagnostics which have been coupled to shock tubes have evolved over time along with the need of more accurate and comprehensive kinetic results. This need follows the advances in kinetic modeling as nowadays the kinetic models are able to capture detailed chemistry not only of the main fuels and products but also of the minor intermediates, including PAHs. One of key factors in reaching such predictive capabilities lies in the possibility to access computational capabilities and theoretical methods which, at least for systems constituted by a reasonable number of atoms, can provide results as accurate as the ones obtained in the experiments [12], [13]. Among the different techniques

capable to provide detailed kinetic information relevant to soot formation, gas chromatography/mass spectrometry systems (GC/MS) coupled to shock tubes operated in a single-pulse fashion have been extensively implemented to detect, separate and quantify a large number of PAHs mainly up to three aromatic rings [14]. These results are very helpful and fundamental for understanding PAH formation chemistry but there are some limitations in the technique that make it impossible to be used for large compounds beyond three-four rings which are interesting for the soot nucleation process. In fact, heavy species can condense in the lines during transfer from the shock tube to the analytical system, and often, the identification and separation of isomers is quite challenging due to the similar retention times and low signals. Other complementary techniques capable to measure time-history species profiles without the problems related to the physical transfer of the sample to the analytical system include the time-of-flight mass spectrometry (TOF-MS) with supersonic jet sampling at the shock tube end-wall [15], [16] and in-situ laser absorption measurements [17]. Despite the remarkable capabilities of these techniques, there exist some intrinsic limitations especially relative to PAH measurements. For example, the laboratory-based TOF-MS has reduced sensitivity, inability to distinguish between structural isomers, and unwanted molecular fragmentation during ionization, while the possibility to detect and measure a specific species by laser absorption technique depends on its absorption bands and possible interference with other compounds present in the mixture (which, for the case of large molecule, constitutes an undeniably unsolvable constrain). Thus, the only conventional shock tube technique capable to investigate in detail the gas-phase soot precursor molecules is by gas chromatography.

Shock tube techniques have been also fundamental to study particle formation and growth by implementing laser-based techniques [18]. In this case, the major limitations derive from the interference of the signal with the fluorescence from the PAH precursor molecules and the low laser intensities. Indicatively, these experiments cannot detect particles below 10-15 nm. Thus, once again, the processes between the appearance of the three-ring structures and the presence of relatively large nanoparticles cannot be monitored.

In addition to the laboratory-based techniques, researchers in the chemical kinetic field have tried to take advantage of the extraordinary capabilities of particle accelerators-based diagnostics to overcome the limitations of conventional techniques. This is particularly valid for stationary set-ups like flames, perfectly-stirred reactors and flow reactors, where the signal can be collected over long-times. On the other hand, the kinetics of the fuel decomposition and product formation can not be followed but only inferred from subsequent measurement at different conditions and/or positions in the reactor. Combining shock tubes with these up-to-date detection techniques would add the advantages of the two set-ups. Indeed, the experiments at accelerators, such as synchrotron and XFELs, would constitute an extension of the laboratory-based studies with a level of detail never attained before. Unfortunately, there are several challenges to be addressed in order to bring a shock tube to a particle accelerator. First of all, these detectors are very low signal-to-noise ratio detectors [19], [20], which means that averaging over tens of thousands of experiments needs to be performed in order to get a meaningful signal for non-stationary conditions as in shock tubes. With conventional shock tubes, each cycle takes approximately one hour mainly because of the need to replace the diaphragm [21], consequently obtaining around 10 000 shocks would be required more than 5 years of experiments. In order to shorten the cycle, it is mandatory to reduce the shock tube size to be able to fill, fire and evacuate in less than one second, ideally. In addition, space at accelerators is very limited and the small dimensions are a requirement for transportation and

installation. Recently, a new category of shock tubes, the miniature high-repetition-rate shock tube (ANL-HRRST), has been developed by R. Tranter at Argonne National Laboratory, specifically for use at synchrotron facilities, demonstrating great repeatability of the thermodynamic conditions attained in the shock tube (essential for signal averaging) and reliability of operation [22]. Specifically, the ANL-HRRST has coupled to synchrotron vacuum ultra violet photoionization mass spectrometry (VUV-PIMS) demonstrating the potential of these combined techniques [23]. On the other hand, up to now the studies performed with the ANL-HRRST were not applied to PAH or soot chemistry.

The present thesis work is based on a multi-scale approach for clarifying certain aspects related to the different steps of PAH and particle formation and growth, with the use of conventional and innovative shock tube techniques. In particular, the term "multi-scale" not only refers to the different experimental conditions employed in the various installations (mainly in terms of fuel concentrations and reaction times), but also to the physical sizes of the shock tubes. In fact, one of the main goals of the work is to design, build, develop, and characterize a new miniature high-repetition-rate shock tube (ICARE-HRRST), the first in Europe, for use at Synchrotrons to complement the experimental capabilities of the laboratory ICARE which already includes several conventional shock tubes. The ICARE-HRRST was then coupled for the first time to an advanced synchrotron-based diagnostic, the double imaging photoelectron photoion coincidence spectroscopy (i^2PEPICO) [24], with the goal of studying PAH chemistry in pyrolytic, high-pressure environments. i^2PEPICO is one of the most advanced techniques capable to solve for complex mixtures of PAH isomers, as demonstrated in previous studies on flames and flow reactors [25]–[27]. Therefore, applying i^2PEPICO to study PAH formation at relevant engine-like conditions has the potential to unravel the complex chemistry that links the formation of small PAHs and the inception of carbonate nanoparticles and help to resolve existing long-standing controversies over the mechanisms involved. The first studies with i^2PEPICO/HRRST will also be presented, including results on pyrolysis of key fuel components and crucial intermediates in the formation of soot nanoparticles like toluene, ethylbenzene, styrene, and ethanol.

To complement the measurements at the synchrotron facilities with experiments performed with large-scale conventional shock tubes, the formation of small polycyclic aromatic hydrocarbons (up to three-rings, single-pulse shock tube) and carbonaceous nanoparticles (laser-based techniques) from different fuel intermediates such as ethylbenzene and styrene was considered. The different type of data will be analyzed based on the specific characteristics of the installations. These results will extend the previous works in the laboratory concerning PAH and particle chemistry from a variety of aromatic fuels and mixtures with small aliphatic intermediates, as part of the European Starting Grant FUN-PM.

2 Literature review on pyrolytic soot formation kinetic studies

In this chapter, a review of experimental studies related to soot formation chemistry is presented, while the oxidation studies with flames, jet-stirred rectors, etc. are beyond the scope of this work.

The first part will focus on the chemistry of PAH formation and growth. In particular, previous results obtained coupling conventional shock tubes to different diagnostic techniques like mass spectrometry and gas chromatography will be analyzed with particular focus on the corresponding capabilities with respect to the detection and quantification of gaseous aromatic molecules and multi-ring species. Subsequently, a brief overview of miniature shock tubes at synchrotron facilities, as implemented before the present thesis work, will be reported together with the future needs. Other experimental set-ups, including flow reactors, will also be considered in this section.

Finally, a review on solid soot measurements using shock tubes with laser-based extinction techniques applied to the decomposition of well-known hydrocarbon fuel molecules and surrogates will conclude the chapter.

2.1 Chemistry of gas-phase soot precursors

The brief description presented in the chapter 1 highlights the central role of the chemistry involved in the formation and growth of PAH intermediates as building blocks for the nascent particles and factors for the particle growth. Thus, the understanding on the formation and growth of these PAH molecules is crucial and it strongly affects the accuracy of the entire soot formation model. Unfortunately, the PAH chemistry is still not well understood because of the large number of possible reaction pathways and mechanisms [28] and limitations in experimental and theoretical techniques [29]. One of the most accepted mechanism is the hydrogen-abstraction carbon-addition scheme (HACA) where several acetylene (C_2H_2) additions on radical sites lead to ring structure and PAH growth [30]. For instance, two hydrogen abstractions and two acetylene additions in different adjacent sites can lead to the formation of the naphthyl radical ($C_{10}H_7$, radical of naphthalene) from a single-ring molecule like benzene (C_6H_6). The naphthyl radical ($C_{10}H_7$) can react with a hydrogen atom to form naphthalene or with another acetylene to form directly acenaphthylene ($C_{12}H_8$) or ethynylnaphthalene ($C_{10}H_7C_2H$). Following the same pathway, the HACA mechanism can lead to the formation of the three-ring structure phenanthryl radical ($C_{14}H_9$) from ethynylnaphthalene, subsequently to phenanthrene ($C_{14}H_{10}$) or larger four-ring structures from reactions of the phenanthryl radical with H or C_2H_2, respectively. Similar mechanisms are also involved in the solid-particle growth. The HACA mechanism relies on the stability of acetylene at the high-temperature flame conditions, and it is limited by the concentration of the species in the combustion environment.

The HACA mechanism is still one of the main pathways in many practical applications, although several experimental and modeling studies in the past showed how its implementation as unique growth process is unable to predict the correct growth rate especially for large PAHs (i.e. [31], [32]). For example, Miller et al. [33] and Marinov et al. [34] found in the 90's that the HACA mechanism is too slow in relation to the experimental results. As alternative, they proposed a mechanism to describe the fast growth of complex

large molecules based on the addition of resonantly stabilized radicals. These studies were supported by previous investigations where the role of the main resonantly stabilized radicals was highlighted, such as the recombination of cyclopentadienyl radicals to form naphthalene [35], of indenyl radicals to form $C_{18}H_{12}$ isomers [36], the benzyl radical with the propargyl radical to the second-ring structure [37], and the clustering of hydrocarbons by radical-chain reactions (CHRCR) [38]. The resonantly stabilized radicals include propargyl (C_3H_3), allyl (C_3H_5), cyclopentadienyl (C_5H_5), benzyl ($C_6H_5CH_2$) and indenyl (C_9H_7).

Other important PAH growth mechanisms involve the reactions between aromatic radicals and aromatic molecules, accompanied by hydrogen abstraction and cyclization, the so-called reactive coagulation [39]–[41]. This is a generalization of the reaction between phenyl radical and benzene as observed relevant to PAH formation in previous investigations [34], [42]. Recently, Shukla and Koshi [43], [44] have re-proposed such mechanism with a slightly different name, as the phenyl addition cyclization (PAC). The same authors have also proposed the so-called HAVA mechanism [45] involving C_2H_3 radicals, but the efficiency of such mechanism at combustion-like conditions is limited by the short lifetime of the radical. Additional proposed growth mechanisms include the methyl addition/ cyclization (MAC) as reported by several authors [46]–[49] whose contribution though is not as effective as the previously mentioned cases due to the low molecular mass of the methyl radical, and the diradical cycloaddition fragmentation (CAF) [50]–[53], relevant mainly for certain pyrolytic fuel reactions.

In pyrolysis of real fuels, these growth mechanisms will occur at the same time with relative importance dependent on the fuel structure and the thermodynamic conditions (pressure and temperature). The laboratory-based investigations allowed the identification of such mechanisms and the development of detailed chemical kinetic models able to reproduce the experimental observations.

2.1.1 Shock tubes coupled to gas chromatography/mass spectrometry

Speciation studies using shock tubes are first analyzed, including the advances made on the development of the up-to-date analytical systems which nowadays allow to detect, identify, and quantify a large number of molecules withdrawn from the shock tube after the reaction time at conditions encountered behind the reflected shock waves. In order to achieve the separation and identification of the different compounds, methods like gas chromatography / mass spectrometry (GC/MS) are typically used. In recent experimental investigations, the direct connection between shock tubes and GC systems have been highlighted as the optimal solution for accurate sample recovery [14]. The possibility to use resin trapping methods for detection of absorbed species could also be considered and it is expected to provide qualitative information on the large species product distribution [14]. The GC/MS raw data are further processed offline and they constitute precise quantitative information on chemical kinetics pathways that yield to the formation of PAHs. In particular, many of the previous studies on pyrolytic chemistry applied to soot formation involve the thermal decomposition of aromatic hydrocarbon molecules. Aromatic molecules are present in real fuels and fuel surrogate, as well as formed as intermediates in the molecular growth towards the solid particles. Thus, a detailed understanding of the pyrolytic decomposition of these precursor molecules at engine like conditions represents an important step in understanding also the PAH formation processes.

In order to clarify the pyrolysis mechanisms of aromatic molecules like benzene (C_6H_6) and toluene (C_7H_8), in year 1982, Kern et al. reported product profiles from the decomposition of these important soot precursor molecules using a shock tube coupled to time-of-flight mass spectrometry (TOF-MS) [54]. The gases eluted through a nozzle of an orifice of 0.1 mm diameter and 1 mm apex entering the ionization chamber. The mass spectrum range of these experiments covered m/e 12-300. The peak heights of each product was converted to concentrations by making use of calibration plots obtained with peak height ratios of compounds with known concentrations and under no reactive conditions. Typical observation time was between 700 μs and 1000 μs and reflected shock conditions were variated from 1400 K to 2200 K by using helium as driver gas and from 2200 K to 2600 K by using H_2 driver gas, in a pressure range of 0.21-0.57 atm. With this configuration the authors were able to measure species up to C_8H_2 and for the case of benzene and toluene decomposition, the major detected products were acetylene and polyacetylenes. The technique did not allow to detect PAH molecules. For the case of butadiene, it produces small concentrations of benzene who decomposed to form acetylene and polyacetylenes. By applying carbon balance, the study showed that the maximum soot yield reported in previous literature investigations with laser extinction-shock tube experiments should have been less than 10% for toluene, compared to the previously reported value of ~ 80% [55], [56].

Similarly, between 1986 and 1987 Pamidimukkala et al., performed pyrolytic high temperature shock tube experiments on toluene (C_7H_8) and ethylbenzene (ETB-C_8H_{10}), the simplest methyl- and alkyl-substituted aromatic molecules [57], [58]. The experiments were carried out at very low pressures ranging between 0.2 and 0.5 atm. In the work on toluene [57], Pamidimukkala at al. used time-of-flight mass spectrometry (TOF-MS) to detect and identify major species like acetylene (C_2H_2), diacetylene (C_4H_2), methane (CH_4), and benzyl radical (C_7H_7), along with smaller amounts of ethylene (C_2H_4), triacetylene (C_6H_2), and benzene (C_6H_6) in a range of temperatures 1550-2200 K. Compared to toluene pyrolysis, ETB decomposition starts at lower temperatures (range of 1350-2080 K) and the major products reported are toluene (C_7H_8), benzyl (CH_4), benzene (C_6H_6), diacetylene (C_4H_2), ethylene (C_2H_4), acetylene (C_2H_2) and methane (CH_4); styrene (C_8H_8) was detected as a minor product. Once again, no PAHs could be detected.

In 1996, Laskin and Lifshitz studied the pyrolytic decomposition of benzene (C_6H_6) behind reflected shock waves by using a single-pulse shock tube in the temperature range of 1400-2000 K, pressure around 5 atm, and reaction time of 2 ms [59]. The gas sample was withdrawn and sent through a heated injection system to a gas chromatograph operating with flame ionization detectors (FID). Both, the shock tube and the transmission system were heated at 150 °C in order to avoid condensation of heavy PAHs. The identification of reaction products was done by analyzing the GC retention times while the concentrations were determined by integrating the GC peaks relatives to benzene from standard mixtures. In this work the authors could detect small molecules and aromatic products like acetylene (C_2H_2), diacetylene (C_4H_2) and phenylacetylene (C_8H_6) until biphenyl ($C_{12}H_{10}$), the main two ring molecule produced from the recombination of two aromatic rings. The experiments were used to develop a kinetic mechanism which contains 15 species and 22 reactions reproducing the experimental species profiles.

Later, in 2006, Sivaramakrishnan et al. also performed single-pulse shock tube experiments of benzene pyrolytic decomposition (65-800 ppm in argon) but at higher pressures of 30-50 bar and temperatures in the range 1200-1800 K [60]. After reaction times of around 1.2-1.5 ms, the stable species were sampled though heated lines using a gas sampling valve and stored in heated vessels for subsequent off-line analysis using GC techniques. Only species profiles for the fuel decay and primary products like C_2H_2 and

C_4H_2 were obtained but no PAH molecules. This is mainly due to the loss of heavy species during transfer to the analytical set-up.

In the same year, Sivaramakrishnan et al., also performed high pressure shock tube experiments on pyrolytic decomposition of toluene (below 100 ppm in argon), one of the most abundant aromatic component of commercial and jet fuels [61], [62]. The tests were done using the same single-pulse shock tube-GC/MS system used in the previous benzene study in a temperature range of 1200-1900 K and high pressures (27-45 bar). These experiments allowed to detect and quantify a variety of stable species ranging from small hydrocarbons to principal single and two-ring aromatics like phenylacetylene (C_8H_6) and indene (C_9H_8). With experimental data obtained in this work, a detailed kinetic model for toluene pyrolysis was developed including the decomposition chemistry of the benzyl radical. This model was validated against the stable species profiles of toluene (C_7H_8), benzene(C_6H_6), and methane (CH_4) as well for key soot precursors as C_2H_2 (acetylene), C_4H_2 (diacetylene), phenylacetylene (C_8H_6), and indene (C_9H_8). Toluene pyrolysis was also the target of the previous work by Colket and Seery in 1994 [37]. The authors carried out experiments in a single-pulse shock tube at approximately 10 atm, temperatures ranging from 1200 to 1850 K for a mixture of 1% toluene diluted in argon and residence times near 600 µs. These relatively-high fuel concentrations resulted in production of large mole fractions of PAH intermediates detectable by GC. The shock tube was connected to the GC system through a transfer line heated up to 150 °C to avoid condensations and products up to pyrene ($C_{16}H_{10}$) could be measured. More than 50 individual peaks were identified in this work and a detailed chemical kinetic model was developed to help clarify uncertain ring growth kinetic sequences. The author stated that concentrations for larger PAHs may be in error by a factor of 2, but they did not discuss the effects of soot production (expected at these fuel concentrations) on carbon balance and PAH measurements.

Recently, Comandini et al. re-designed the analytical set-up and the “on-line” coupling with the high pressure single-pulse shock tube (HPST) present at the University of Illinois at Chicago to be capable to perform measurements of PAHS down to sub-ppm levels [14]. This is essential in order to perform studies at very low initial fuel concentrations which limit soot formation keeping on the other hand the possibility to detect minor products as the PAHs. The species calibration curves were inferred by a combination of analyses of standard liquid samples and measurements of the reference molecule naphthalene both in gas-phase and in liquid solution. The estimated errors in the measurement of species up to naphthalene ($C_{10}H_8$) were between 5−10%, 15-20% for C12 hydrocarbons, 20-25% for C14 and for larger compounds up to four rings was as high as a factor of 2. The system was implemented to study the pyrolytic reactions of the phenyl radical also in the presence of acetylene [63]. Speciation measurements were obtained at typical conditions found in modern combustion devices over a pressure range of 25-50 atm and temperatures of 900-1800 K, with initial fuel mole fractions between 25 and 100 ppm. Both small hydrocarbon products including single-ring aromatics and a large variety of multi-ring PAH compounds were measured as a function of temperature. In this case, for the higher dilution conditions, the carbon recovery was higher than 90% at all temperatures. These results contributed to clarify the role of several reaction pathways, established and new ones, involved in the formation and growth of PAHs. In particular, modelling suggested that formation of PAH is strongly influenced by benzyne chemistry and the reactions involving the o-benzyne diradical.

The same experimental set-up was subsequently used for various studies, including the pyrolysis of an important component of surrogates for jet fuels, n-propylbenzene (C_9H_{12}) [64]. The temperature range

was 1027-1678 K at a nominal pressure of 50 atm and initial fuel mole fractions below 100 ppm. The authors measured a large number of PAHs, from the major species indene (C_9H_8), naphthalene ($C_{10}H_8$), anthracene/phenanthrene ($C_{14}H_{10}$) and acenaphthylene ($C_{12}H_8$), to smaller products relevant to the fuel molecule, including 1-ethynylnaphthalene ($C_{12}H_8$), bibenzyl ($C_{14}H_{14}$), methylfluorene ($C_{14}H_{12}$), diphenylacetylene ($C_{14}H_{10}$), methylanthracene ($C_{15}H_{12}$), phenylnaphthalene ($C_{16}H_{12}$), o-, m-, p-terphenyl ($C_{18}H_{14}$) and acenaphthylene ($C_{12}H_8$). The reported kinetic model presents good agreement with experiments for the fuel decay as well as the formation of the major aliphatic, monoaromatic and PAHs as a function of the reaction temperature.

A similar analytical system was subsequently reproduced at the laboratory ICARE-CNRS as part of the ERC-Starting Grant FUN-PM with additional modifications to improve the accuracy of the measurements. Specifically, the ICARE high-purity single-pulse shock tube has been lately modified to work in a single pulse fashion by adding a dump tank, with an additional gas sampling valve that allows withdrawal of gas samples and subsequent transfer through a heated line to the analytical system. The transfer line is usually heated to 150 °C and the shock tube is heated up to 90 °C. The analytical system is composed of two gas chromatographs, one specifically designed and developed at ICARE to measure PAHs with an external oven heated to 300 ^{o}C to avoid condensations, the second used to measure light species. A DSQ mass spectrometer is also connected to the transfer line and used to help the identification of the PAH products. Direct calibration in gas-phase was also extended up to the three-ring species, with errors of the order of 10% even for these large molecules. Difficulties still remain for the measurement and identification of larger species, although detection and identification of several four-ring structures, including fluoranthene, pyrene, chrysene, is possible. These difficulties depend on the species condensation and the impossibility to perform a gas-phase calibration.

Recent studies implementing this set-up include pyrolysis of a large number of aromatic compounds, such as toluene, phenylacetylene, benzene, C8-C10 linear alkylbenzenes and xylene isomers [65]–[68], straight-chain alkane n-heptane[69], cycloalkenes like cyclopentene and its mixtures with acetylene[70], intermediates like propene and propyne [71], and mixtures of key aromatics (benzene, toluene, phenylacetylene) with small C2 and C3 compounds [67], [71]–[74].The experiments were all performed at a nominal pressure of 20 bar and initial fuel concentrations between 100 and 500 ppm. A comprehensive and detailed PAH predictive model was developed and optimized based on the experimental results of all these fuel components and mixtures with the goal of probing a large number of kinetic pathways. The experimentally validated model was used to improve our fundamental understanding on the chemistry involved in the formation of these intermediates.

Future work should be addressed to extend this analysis and study to larger gas-phase intermediates, with the goal of filling the gap between the appearance of the three-ring structures and the particle inception. This is particularly challenging for a system where the gas sample needs to be physically transferred to the analytical system as the case of the single pulse shock tube with GC and GC/MS. In addition, the isomer selectivity of these instruments is limited, while it is impossible to detect and measure radicals. The implementation of a new innovative set up based on synchrotron-based detectors for PAH studies will be presented in this thesis.

2.1.2 Shock tubes coupled to synchrotron light-based diagnostics

The synchrotron-based techniques are routinely used to selectively identify the components of complex mixtures including isomers as synchrotron light offers easy and wide tunability, high resolution of the mass spectra, and high photon fluxes. These are considerable advantages over conventional techniques [75], [76]. For instance, because molecular electronic transitions are induced when UV/Vis radiation interacts with gas-phase dilute matter found in nature, several VUV beam lines have been constructed and coupled to different diagnostics. For example, the synchrotron vacuum ultra violet photoionization mass spectrometry technique (SVUV-PIMS) has been extensively used in astrophysics, chemistry and more specifically to probe combustion chemistry [77][75], [76]. SVUV-PIMS has the advantage of minimizing fragmentation interference compared to conventional TOF-MS apparatuses that use high energy electron-impact ionization, where high signal levels are obtained but with limited isomer selectivity [78]. On the other hand, signal levels from synchrotron detectors are very low and signal averaging needs to be performed to get sufficient signal-to-noise (S/N) ratios. This is of course particularly challenging in kinetic studies such as the ones performed with shock tubes compared to stationary reactors.

Recently, high-temperature and high-pressure pyrolytic studies have been published using the new generation of high repetition rate shock tubes (HRRST) developed by Tranter et al. at Argonne National Laboratory (ANL) in 2013 [22]. These shock tubes were specifically designed for use at synchrotron facilities demonstrating great repeatability of the experimental conditions. The authors reduced the shock tube size by minimum a factor ten compared to conventional shock tubes, as the internal diameter was designed at 6.35 mm while the length at 687 mm. Transportation and mounting at synchrotron beamlines could be possible. More importantly, reduced shock tube size and automated operation were mandatory requirements in order to physically be able to reduce the cycle operation time, run thousands of experiments for signal averaging, and optimize the limited beam time available for SVUV-PIMS measurements. The ANL-HRRST can operate up to 4 Hz, 4 shock every seconds, compared to 1 shock per hour in conventional shock tubes.

The miniaturized ANL-HRRST was coupled with VUV-PIMS at the Advanced Light Source (Lawrence Berkeley National Laboratory), trying to exploit the capabilities of this technique [22]. The end part of the driven section, equipped with a nozzle of 0.03-0.07 mm diameter orifice, was aligned to a 2 mm orifice skimmer allowing a molecular jet flowing into the ionization chamber of the TOF-MS where it was intersected by the VUV light. In this work, Tranter et al. presented two mass spectra of dimethyl ether (C_2H_6O) pyrolysis obtained from averaging over 1500 experiments at temperature of 1530 ± 50 K and pressure of 8 ± 0.5 bar with a photon ionization energy (IE) of 10.5 eV. One of the mass spectra was obtained for pre-shock conditions and the other at post-shock conditions with very weak signal levels. They attributed this to the long distance between the nozzle and the skimmer which reduces the jet density. This distance was chosen, in fact, in order to minimize the pressure build up in the vacuum chamber and avoid damages to the mass spectrometer. Despite these limitations, comparison between the two mass spectra showed how dimethyl ether (C_2H_6O) dissociates to compounds with mass over charge ratio m/z 15 which corresponds to methyl radicals (CH_3), m/z 30 which is likely a combination of ethane (C_2H_6) and formaldehyde (CH_2O), m/z 28 which corresponds to ethylene (C_2H_4), and m/z 26 (acetylene, C_2H_2), products mainly derived from the recombination of methyl radicals [79], [80].

A more extended study on dimethyl ether pyrolysis (2% CH_3OCH_3/Ar) was reported by Lynch et al. in 2015 using the same ANL-HRRST at temperature range of 1400-1700 K, and pressure 3-16 bar with ionization energies between 10 and 13 eV [23]. Despite the low signal levels, the authors were able to well resolve product species and radical intermediates when averaging over hundreds of shocks. In particular, they were able to detect the same species reported by Tranter et al. [22] with the addition of diacetylene (C_4H_2), methane (CH_4), and certainly propargyl radical (C_3H_3). The authors also included time profiles for some of these species although not quantitative.

In 2020 and 2021, works performed by Randazzo et al. [81] and Banyon et al. [82] applied the same ANL-HRRST/VUV-PIM configuration to explore reactions mechanisms involving radicals, the four butyl radicals and the propyl radical, respectively. In order to increase S/N levels, this time the authors increased the nozzle orifice diameter from 0.070 mm to 0.2 mm, reduced skimmer diameter from 2 mm to 0.2 mm and reduced separation between nozzle and skimmer from 4 mm to 2 mm, keeping a distance of ∼10 times the diameter of the nozzle orifice. The authors also highlighted how a short distance between the skimmer and the ion source minimizes the molecular beam diameter in the ion source leading to increased sensitivity and reduced mass discrimination effects as described by Cool et al. [19]. In the study by Randazzo et al. [81], experiments were performed at 805 K and 8.7 bar, being able to detect iso-butyl radicals (C_4H_9) and masses up to m/z 72 with relatively good signals, while Banyon et al. [82] obtained product analyses to probe the decomposition mechanisms of n-butyl nitrite (n-$C_4H_9NO_2$) and isobutyl nitrite (i-$C_4H_9NO_2$) at elevated temperatures and pressures (600–900 K and 5–8 bar). They were able to detect n-propyl (n-C_3H_7) and iso-propyl (i-C_3H_7) radicals and their precursors, providing relevant experimental information to support pyrolytic reactions of these radicals. Banyon et al. also presented identification of some isomers by using photoionization spectra, not possible in conventional laboratory-based techniques [82].

Same procedure was implemented in the last work reported using the ANL-HRRST set-up by Sikes et al. [83] on styrene (C_8C_8) pyrolysis, using the same technique but with different temperature and pressure ranges (1660–2260 K, 11 bar). Photoionization spectra was useful to identify styrene decomposition products like diacetylene (C_4H_2), triacetylene (C_6H_2), benzene (C_6H_6), and phenylacetylene (C_8H_6) demonstrating the efficiency of VUV-PIMS technique.

Despite the great qualities of the HRRST/VUV-PIMS coupling, as the number of possible isomers grow, the capability of fitting a photoionization spectrum to identify and quantify complex mixtures of isomers may become challenging in view also of the low signal-to-noise ratios, and more sensitive and/or accurate methods have to be employed to overcome this limitation. Compared to photoionization mass spectrometry (PIMS), photoelectron photoion coincidence spectroscopy (PEPICO) and double imaging photoelectron photoion coincidence spectroscopy (i^{2}PEPICO) can provide more detailed information of the molecular and electronic structures of species. PEPICO was proposed for the first time by Brehm and von Puttkammer in 1967 [84], [85] and it is a combination of photoelectron spectroscopy [86] and photoionization mass spectrometry. The enhanced capabilities of these techniques derive from the fact that both the ion kinetic energies and the corresponding electron kinetic energies are measured, from which the total energy of the parent molecules can be derived and consequently the mass-selected photoelectron spectra (PESs) [76]. Photoionization efficiency curves (PIE), which are constructed from PIMS information to identify molecules, can be derived by integrating a specific PES, making PIM and PES very powerful and complementary techniques. However, PES offers much more sensitivity and selectivity

for each m/z, since it is like an improved fingerprint for each molecule (compared to PIE) as it is linked to the different vibrational states, represented by sharp peaks. This allows excellent isomer identification capabilities. Double imaging photoelectron photoion coincidence spectroscopy, available in very few synchrotron VUV beamlines [24], [87], [88], is one of the most advanced diagnostic technique capable to solve for complex mixtures of PAH isomers.

Photoelectron spectroscopic studies of relevant PAH intermediates have been carried out with these techniques by direct injection of the species into the ionization chamber [25]–[27]. Additionally, several studies characterizing PAH chemistry have been conducted using steady state reactors like flat premixed flame burners [89], catalytic pyrolysis reactor [90], low pressure premixed sooting flames [91] and pyrolysis hot tube microreactor [92] demonstrating the impressive capabilities of the technique. The method is anyway dependent on the availability of photoelectron spectra of each pure isomer and, for quantification, of their photoionization cross sections (PICS), which are usually obtained from very scarce PIMS experiments or not accurate estimations. However, there has been significant progress on theoretical methods based on quantum chemistry to the calculation of PICS [93]. Regarding the photoelectron spectra, these can be derived: i) by measurements obtained with pure compounds; or ii) from high-level *ab initio* quantum chemical calculations and Franck-Condon (FC) simulations, in order to get high-quality theoretical PESs.

Double imaging photoelectron photoion coincidence spectroscopy (i^2PEPICO) has never been exploited using synchrotron-based shock tube techniques, placing the present thesis as the first one presenting the implementation of the coupling between these two powerful techniques [94]. In particular, the goal of the present work is to develop a tool for accurate kinetic measurements of large gas-phase intermediate products relevant to soot nanoparticle formation, to complement the measurements conducted at the laboratory scale on PAH formation and soot inception and growth.

2.1.3 Pyrolytic PAH chemistry in other experimental set-ups

In the previous two sections the works performed with shock tubes on high-temperature gas-phase reactions were presented. However, there are other experimental setups that have been also employed to study pyrolytic PAH chemistry. Among them, flow reactors and jet stirred reactors coupled to different analytical methods have been widely used to study key reaction mechanisms related to the formation and growth of soot precursor molecules. In this section, some of these experimental studies and the insights that have been gained through the use of these reactors with different aromatic fuels will be briefly presented. A detailed list of these studies is presented in **Table** 2-1.

One of the first experimental works to study PAH formation at pyrolytic conditions was reported in 1965 by Hou and H. B. Palmer [95]. The authors used a heated flow system connected to a vapor fractometer to probe benzene thermal decomposition and identify the related products. One of the main conclusions of this work was that biphenyl is produced at low temperatures during benzene decomposition. Later on in 1979, R.D Smith [96] used quartz and tungsten Knudsen cells to study toluene pyrolysis at low pressures using electron-impact ionization (EI) mass spectrometry (MS) finding that at higher pressures C1-C7 products will form heavy compounds up to $C_{20}H_{12}$. Subsequently, in a study by Bruinsma et al. (1988) [97]

a coiled tube reactor coupled to GC was used to investigate the pyrolytic decomposition of a number of aromatic fuels including benzene, toluene, ethylbenzene, styrene, phenylacetylene. The authors highlighted the importance of the dimerization reactions through radical intermediates at temperatures below 1100 K while above 1200 K the addition of acetylene and benzene plays an important role in the increase of C/H ratio of the produced species.

Between 2007 and 2012, Shukla et al. published works using flow reactor coupled to VUV-SPIMS to investigate toluene/acetylene pyrolysis [98] and benzene/acetylene pyrolysis[43] and toluene/benzene pyrolysis [99]. The authors were able to detect PAH species up to m/z 522 ($C_{42}H_{18}$), m/z 454 ($C_{36}H_{22}$) and m/z 304 ($C_{24}H_{16}$) for toluene/acetylene, benzene/acetylene and toluene/benzene, respectively, suggesting possible mechanisms for the formation of these species. Specifically, the efficiency of phenyl addition cyclization (PAC) mechanism in PAH growth [43], [99] compared to HACA was proposed. Shukla et al. [45] also reported experiments using a quartz reactor tube coupled to a linear TOF-MS to probe acetylene and ethylene pyrolysis, two significant intermediates which are PAH promotors. The authors pointed two main mechanisms for PAH growth: addition of acetylene/ethynyl (C_2H_2/C_2H) (HACA) during acetylene pyrolysis and addition of ethylene/vinyl radical (C_2H_4/C_2H_3), known as HAVA, for ethylene pyrolysis.

These studies provided insights into the reaction pathways and mechanisms involved in the formation and growth of PAHs. However, due to the lack of possibility to identify the detected species isomers, more recent works have been carried out in order to overcome the limitation of the techniques. Among the most recent pyrolysis studies using flow reactors are the ones where the reactor is coupled to VUV beamlines in synchrotron light facilities.

For instance, between 2009 and 2020, Zhang et al. has employed flow reactor coupled to synchrotron VUV-PIMS to investigate the pyrolysis of toluene [100], [101] and butylbenzenes [102]–[104] detecting species up to m/z 202 ($C_{16}H_{10}$), including radicals up to m/z 165 ($C_{13}H_9$). Speciation profiles are presented from indene C_9H_8 (m/z 116) up to bibenzyl $C_{14}H_{14}$ (m/z 182) suggesting relevant decomposition pathways and PAH formation and growth mechanism.

Similarly, flow reactor coupled to SVUV-PIMS is used by Yuan et al. as found in literature between 2015 and 2021 on the pyrolysis of toluene [105], [106], ethylbenzene [107], n-propylbenzene [108] and o-xylene [109]. A series of PAH compounds were detected in the serial work of Yuan et al. starting from indene. Pyrene ($C_{16}H_{10}$, m/z 202) speciation profiles was reported in o-xylene and toluene pyrolysis while chrysene ($C_{18}H_{12}$, m/z 228), was detected and quantified in toluene pyrolysis helping to the elaboration of validation of a chemical kinetic model [106].

In recent works by Jin et al, a flow reactor coupled to SVUV-PI-MBMS has been used to investigate PAH pyrolysis chemistry of indene [110] and α-methylnaphthalene[111], [112]. The researchers found the dominant PAHs in the indene pyrolysis up to m/z 230 ($C_{18}H_{14}$) attributing it mostly to 3,3-bi-indene. The experimental results were used to validate a chemical kinetic model that was updated later with the results on α-methylnaphthalene pyrolysis. In the experiments the sum of the mole fractions of m/z 282 ($C_{22}H_{18}$) and m/z 156 ($C_{12}H_{12}$) was comparable to the monocyclic aromatic (MCA). The authors considered in the model two isomers for each mass associating methyl-(naphthyl-methyl)-naphthalene and dinaphthyl-ethane to m/z 282 while dimethyl-naphthalene and ethyl-naphthalene to m/z 156.

***Table 2-1**. List of pyrolytic studies on PAH chemistry using experimental set-ups different to shock tubes*

Author/year	***Fuel***	***System***	***Temperature***	***Pressure***	***Residence time***
Hou and H. B. Palmer (1965)[95]	Benzene	Flow reactor/ vapor fractometer	1173-1523 K	735 ± 5 torr	20-250 ms
R.D. Smith (1979)[96]	Toluene	Quartz-tungsten Knudsen cells/ MBMS	<1800 °C	10^{-5} to 1 torr	-
Bruinsma et al. (1988)[97]	Benzene, toluene, ethylbenzene, styrene, phenylacetylene, n-decane	Coiled tube reactor/ GC	900-1250 K	-	5 s
Shukla et al. (2007-2008)[98], [99]	Toluene, toluene/acetylene, toluene/benzene	Flow reactor/ VUV-SPIMS	1136-1507 K	8.15-15.11 Torr	0.56 s
Zhang et al. (2009-2010) [100], [101]	Toluene	Flow reactor/ VUV-MBMS / VUV-PIMS	1270-1870 K	10 Torr	0.22-0.29 ms
Shukla et al. (2010)[43]	Benzene, benzene/acetylene, acetylene	Flow reactor/ VUV-SPIMS	1140-1500 K aprox	10 Torr	0.56-0.61 s
Shukla et al. (2012)[45]	Acetylene, ethylene	Quartz reaction tube/ linear TOFMS	1100-1500 K	12.33-35 torr	0.69 s
Yuan et al. (2015) [105], [106]	Toluene	Flow reactor/ VUV-PIMS	1100-1730 K	5-760 torr	-
Yuan et al. (2016)[107]	Ethylbenzene	Flow reactor/ SVUV-PIMS	850-1500 K	0.04-1 atm	-
Yuan et al. (2017)[108]	n-propylbenzene	Flow reactor/ SVUV-PIMS	800-1500 K	0.04-1 atm	-
Zhang et al. (2017)[102]	n-butylbenzene,	Flow reactor/ SVUV-PIMS	800-1300 K	30-760 torr	-
Shao et al. (2019-2020) [113], [114]	n-heptane/iso-octane/toluene	Jet-stirred reactor/GC, Flow reactor/ SVUV-PI-MBMS)	850-1250 K	1 atm	1 s
Jin et al. (2019) [110]	indene	Flow reactor/ SVUV-PIMS	1000-1500 K	30-760 torr	20-500 ms
Zhang et al. (2020)[103], [104]	iso-butylbenzene, tert-butylbenzene, sec-butylbenzene	Flow reactor/ SVUV-PIMS	780-1300 K	0.04-1 atm	-
Yuan et al. (2021)[109]	o-xylene	Flow reactor/ SVUV-PIMS	1050–1600 K	0.04-1 atm	-
Jin et al. (2021) [111], [112]	α-Methyl-naphthalene	Flow reactor/ SVUV-PI-MBMS	1000-1550 K	30-760 torr	20-500 ms
Liu et al. (2022) [115]	Toluene/allene, Toluene/propyne	Flow reactor/ SVUV-PIMS	647-1510 K	0.04-1 bar	9.12-11.6 ms

Finally, recent works performed by Shao et al. [113], [114] have used flow reactor coupled to SVUV-PIMS and jet stirred reactor coupled to GC to study pyrolytic PAH chemistry of a fuel surrogate containing n-heptane/iso-octane/toluene. The study reported mole fraction profiles of reactants, aromatics and PAH compounds up to four rings. The last work found in literature regarding pyrolytic PAH chemistry using the flow reactor/SVUV-PIMS combination was reported in 2022 by Liu et al. (2022) [115] on toluene/C_3H_4 isomers co-pyrolysis reporting channels leading to the formation of PAHs up to two rings like indene and naphthalene.

2.2 Laser diagnostics for particle measurements

2.2.1 Shock tubes coupled to laser diagnostics

The experiments conducted in the laboratory and in synchrotron on the measurement of large gas-phase intermediate products relevant to soot nanoparticle formation can help clarifying routes that lead to the ring growth. However, the pathway to the formation and growth of carbon nanoparticles includes several steps which still need to be clarified based on complementary techniques focused on the solid-phase chemistry.

Spectroscopic techniques have been routinely used for the measurement of soot parameters since they are non-intrusive diagnostic techniques, a very important aspect for combustion phenomena which are inherently easy to be perturbed [116]. For instance, laser extinction and Rayleigh scattering techniques can be coupled to shock tubes to probe the temporal evolution of soot nanoparticle growth relative to the shock wave passage from the pyrolytic decomposition of multiple fuel components and mixtures. A review on soot measurements using shock tubes with laser-based techniques applied to the decomposition of well-known hydrocarbon fuel molecules and surrogates will conclude the present literature review chapter.

Soot volume fraction (f_v) and soot yield (Ys) are important soot parameters that can be obtained from laser extinction measurements. These two variables depend on the intensity of the transmitted laser beam after light has been introduced, absorbed and scattered by the homogeneous distribution of nanoparticles in the control volume. The extinction measurement is correlated to the refractive index of the media and the wavelength (λ) of the laser which is much larger than the average particle diameter [117]. The mean diameter and number of particles produced in the control volume can be related to f_v. Rayleigh scattering technique is a complementary technique to laser extinction since it allows the determination of the diameter and density number of particles that scatter light. Laser extinction technique coupled to shock tubes is sometimes complemented by transmission electron microscopy analysis (TEM) characterizing the collected soot, determining both average primary particle diameters and internal microstructure, aspects that are related to soot coagulation, growth by reactions, and agglomeration processes [118]. Soot induction delay time (τ) is also an important soot parameter that can be extracted from laser extinction measurements; it is related to the time of appearance of the first

detectable particles from the time arrival time of the shock wave to the observation window, and it provides kinetic information on soot inception [31].

Concerning previous literature investigations, the use of shock tubes coupled to laser diagnostics to measure soot formation during the pyrolysis of benzene has been already reported. Among these, the works performed between the 70s and 80s by Graham et al. [55] reported soot yields and growth rates using laser extinction and Rayleigh scattering (1600-2300 K, $2x10^{17}$ atoms/cm^3), by Frenklach et al. [119] on soot yields by laser extinction (1430-3490 K, 0.20 to 3.14 bar, $2×10^{17}$ and $5×10^{17}$ atoms/cm^3), and by Evans et al. [120] who used laser extinction to determine relative soot yields (1012-2588 K,74-177.3 kPa, 1% benzene by volume diluted in argon) and TEM analyses. Subsequently, in 1996 benzene/acetylene pyrolysis and acetylene/hydrogen pyrolysis were investigated by Knorre et al. [118] employing laser extinction coupled to a shock tube to determine induction delay times and soot yields; the authors also used TEM to determine particles size (1560- 2580 K, 6 and 60 bar, $1–16x10^{16}$ mol/cm^3).Other studies on benzene pyrolysis using shock tubes coupled with lasers have been conducted on the last two decades. Among them, in 2004 Naydenova et al. [121] reported soot yields, soot particle growth, induction time and mean particle radius by using continuous-wave (CW)-laser extinction technique and by the time-resolved laser-induced incandescence (LII) method. Later on, Agafonov et al. [122], [123] reported soot yields and modeling study on benzene pyrolysis (1640-2680 K, 1.8-2.4 $×10^5$, mol/cm^3) and Drakon et al. [124] reported soot yields not only for benzene but also for acetylene and with additions of CH_4, H_2, CO and O_2 (1400–2400 K, 1.6–2.7 bar). Utsav et al. [125] reported in 2017 soot volume fractions, particle size and number densities by using laser extinction and scattering coupled to shock tube (1600–2200 K, 3–5 bar). Bauerle et al. [126] has also measured induction periods, soot growth rate constants and soot yields for benzene and ethylene as well as for n-hexane using laser extinction coupled to a shock tube. In 2022, Nativel et al. [127] reported optical densities D_{633nm} and inception times for benzene mixtures with oxygenated additives (1670–2680 K, ~1.4 bar). The most recent study on benzene pyrolysis is the one reported by Carneiro et al. [128] who presented optical densities D_{633nm}, induction delay times, soot growth rates and TEM analyses. This analysis was extended to toluene, ethylene, acetylene, propene, propyne, cyclopentene, cyclopentadiene and mixtures among them. Specifically, toluene set is of special interest in section 5.7 for comparisons with the results produced in this thesis work.

Some of the discussed studies also investigated soot parameters for toluene and ethylbenzene pyrolysis using similar methods. Among them, the works of Graham et al. [55], Evans et al. [120] and Agafonov et al. [123] extended the analysis for toluene, while the works of Graham et al. [55] and Agafonov et al. [123] for ethylbenzene, the last one also reporting the soot parameters for methane, propane, and propylene pyrolysis. Several other works on toluene and ethylbenzene pyrolysis using shock tubes coupled to laser diagnostics can be found in literature. Specifically, for toluene pyrolysis, the work by Alexiou et al. [129] reporting soot induction times, rates of soot formation and soot yields by using laser extinction coupled to a shock tube for toluene and its mixtures with ethanol and methanol (1447-2426 K, 1.63-3.77 bar, and $5.5\text{-}8.7×10^{17}$ atoms/cm^3), and by Partker et al. [130] reporting soot initiation times and soot yields measured in a shock tube between 1500 and 2500 K and high pressures of 10-30 atm. Agafonov et al. [131] performed laser extinction measurements using shock tubes for toluene pyrolysis as well as for mixtures with propane presenting time profiles and soot yields (1700-2450 K, 5-5.5 bar). D'Alessio et al. [132] also reported soot yields and soot induction times (1500-2300 K, 8-13 bar, $3.7\text{-}5.7x10^{17}$ atom/cm^3) including real-time high-speed absorption spectroscopy in the wavelength range 300–800 nm. De Iuliis et

al. [18] reported simultaneous extinction/scattering measurements on toluene and ethylene pyrolysis using shock tubes along with TEM analyses (1650-2200 K, 500 kPa). Among the reported results are mean diameter of the primary particles obtained with TEM, temporal soot particle diameters and density numbers, soot yields, induction delay times and soot diameters versus temperature. Ly et al. [133] also measured soot yield for toluene compared to methylcyclohexane over a range of temperatures and pressures of 1630-2273 K and 2-4 atm, respectively.

Other recent studies reporting optical densities D_{633nm} and soot particle size and soot-inception times have been carried out using near infrared laser extinction and laser-induced incandescence (LII) for nanoparticle sizing coupled to shock tubes (1840-2815 K, 2.1-4.2 bar) for the pyrolytic decomposition of different hydrocarbon fuels, among them ethylene [134] and a gasoline surrogate [135] both under the influence of several oxygenated co-reactants like methanol and butanol. Another work found in literature for a diesel surrogate fuel was reported by Mathieu et al. [136] using the heated shock tube available in ICARE over a wide range of temperatures and almost constant pressure conditions (1456-2670 K, 1.09-1.87 MPa, 1.7-2.8x7x10^{18} atom/cm^3). In this work, the authors reported soot volume fractions, induction delay times and soot yields not only for the diesel surrogate fuel but for each single component of the surrogate.

As shown before, conventional shock tubes coupled to laser extinction can reveal very useful information on the soot nanoparticles inception and growth, although detailed information on the nascent particles (1-10 nm size) cannot be obtained. In fact, Rayleigh scattering cannot measure such small particles mainly due to interference with PAHs and laser power, while extinction measurements are not size selective and inaccurate at low extinction levels. In addition, these techniques are not capable to provide information concerning the internal structure of the nascent particles. Thus, there is a gap between the formation of relatively large PAHs and the appearance of 10-15 nm primary particles.

The miniature shock tube coupling with synchrotron detectors has the potential to overcome some of these limitations. For instance, coupling miniaturized shock tubes to X-Ray Free-Electron Laser Facilities (XFELs) to study morphology of single soot particles by means of particle diffraction patterns among with TOF-MS can reveal important kinetic characteristics of carbonaceous nanoparticles surrounded by PAH species [137]. Anyway, more insights on soot and PAH formation chemistry will be gained as more access to different accelerator-based light sources is obtained. Additionally, continuous improvement on the coupling of shock tubes to these diagnostics is mandatory for the progress of soot chemistry models. Based on these statements, developing laboratory-based and synchrotron-based shock tube techniques are of special interest in this thesis in order to go beyond the detection limits of the current methods and clarify uncertain features involved in soot chemistry process. The processes intended to be studied are located in the molecular and the solid levels, more specifically the formation and growth of PAHs and carbonaceous nanoparticles, respectively. The detailed description of these techniques will be presented in the following chapters.

2.2.2 Particle measurements in other experimental set-ups

Most of the available works on soot measurements other than in shock tubes have been performed using flame set-ups although few also implemented well stirred reactors (WSR), plug flow reactors (PFR), or rapid compression machines (RCM). In particular, similar techniques used with shock tubes have been coupled to flames gaining useful information on the soot tendencies as well as to perform kinetic studies [138]. This section contains a brief overview on some of the main results obtained in the literature with particular focus on examples which highlight the different diagnostics and capabilities. It is beyond the scope of this work to provide a detailed literature analysis.

Among the non-intrusive techniques coupled with flames, laser induced incandescence (LII) [139],[140], laser extinction[141],[142], emission computed tomography [143], and two-color method [144] were applied. Additionally, soot produced in flames has been studied by implementing intrusive methods like thermocouple particle densitometry (TPD) [145], scanning electron microscopy (SEM) or transmission electron microscopy (TEM) [146],[147] and electron spectroscopy for chemical analysis (ESCA)[148]. Some remarkable works performed using the previously mentioned techniques are listed in **Table 2-2**, including details as reaction conditions, studied mixtures and measured variables.

In 1983, Santoro et al. [149] reported measurements on particle size and soot volume fraction by coupling a coannular laminar diffusion flame burner with both laser extinction and laser scattering techniques. The work was performed with ethene/air flames at atmospheric conditions as the majority of soot measurements found in **Table 2-2**. Similarly, based on the coannular burner used by Santoro et al, in 1987 Samson et al. [150] performed particle counting, and obtained structural data of soot agglomerates by implementing transmission electron microscopy (TEM), this time using acetylene/air diffusion flames. In 1994, the same kind of reactor was coupled by Quay et al. [151] to laser induced incandescence (LII) technique being able to measure soot volume fractions and particle size obtaining good agreement with laser extinction/ and scattering techniques. The measurements were performed using ethylene/air mixtures.

Between 1994 and 1998, Vander Wal et al. has reported measurements on soot volume fractions and soot morphology using laminar flat premixed flame using McKenna burner or laminar coflow diffusion flames with several fuel mixtures of acetylene/ ethylene/ air. These measurements were achieved by using LII technique [152]–[154], gravimetric sampling [154], and TEM [153]. Parallel to Vander Wal et al. other authors also performed soot measurements during the same period of time including Will et al. in 1995 [155] using time-resolved LII (TIRE-LII) in a coannular laminar diffusion flame for particle diameters, Bengtsson et al. in 1995 [156] using LII coupled to a laminar premixed porous-plug burner to obtain soot volume fractions and Choi et al. in 1995[157], Xu et al. in 1997 [158] and Zhou et al. In 1998 [159] using gravimetric sampling and laser extinction in a premixed McKenna burner to measure soot volume fractions, primary diameters and particle temperatures and dimensionless extinction constants, respectively. In 1997, Kasper et al. used a coannular laminar diffusion flame burner coupled to scanning mobility particle sizer (SMPS) to measure size distributions in metal aerosol/CH_4/Ar/air flames.

Numerous subsequent studies were performed implementing similar detection techniques. For example, SMPS has also been employed by other authors between 1999 and 2017 to measure particle size distributions in laminar flames [160],[161],[162] as well as the probability density function in turbulent

flames [163]. In same manner, classical LII, laser extinction and scattering, gravimetric sampling and TEM techniques continued being implemented during this period to measure soot volume fractions, diameters, temperatures, aggregate size and fractal dimensions in laminar [164]–[175] and turbulent flames[176], [177].

Most recent works remarked in the literature come from Mishra et al. in 2020 on simultaneous LIF-LII measurements using a single camera [178]; Mannazhi et al. in 2021 [179] who measured soot volume fractions using 2D-LII at high pressures up to 5 bar in a methane/air coflow diffusion flame; Xu et al. in 2022 [180] determining the sooting limits of propane/air flames using three different methods: laser extinction and scattering, LII, and flame luminosity; and Zhang et al. in 2022 [181] who measured soot particles morphology and size distribution in anisole/ n-heptane/ air coflow diffusion flame using TEM.

Despite the great importance of the soot measurements performed using flame set-ups, in this case the chemistry is coupled to the fluid dynamics, which needs to be accounted for during data analysis and treatment. In addition, non-uniform concentration and temperature fields as well as limited spatial resolution lead to uncertainties in the measurements. Finally, for certain applications, the set-up can provide only a narrow equivalence ratio range.

Between 2005 and 2009, soot measurements were also performed using different reactors like well stirred reactors (WSR) and plug flow reactors (PFR). These experimental set-ups were combined with Nano Differential Mobility Analyzer (Nano-DMA) and TEM by Manzello et al. [182],[183] and Lenhert et al. [184] on ethylene/ benzene/ naphthalene/methanol/CO/air flames in order to obtain the soot size distributions at atmospheric conditions. In addition, Crua et al. in 2003[185] coupled LII technique to RCM in order to determine the time dependent soot formation of low sulfur diesel/air mixtures at a temperature of 373 K and pressures ranging 60-90 bars. Kitsopanidis et al. in 2006[186] coupled laser extinction technique to RCM to obtain soot volume fractions from n-butane/ O_2 /Ar mixtures at a temperature of 765 K and 14 bar. Similarly, RCM/laser extinction experiments were performed by Ketterer et al. in 2019[187] using gasoline/ toluene/air mixtures at a temperature of 657-695 K and pressure of 8.09-9.25 bars to determine soot yields from these important aromatic fuels.

Table 2-2. List of studies on particle measurements using other reactors than shock tubes.

Author/year	*Fuel*	*System*	*Temp.*	*Pres.*	*Measured*
Santoro et al. (1983)[149]	ethene/ air	coannular laminar- diffusion flame burner / laser extinction/ scattering technique	Atm	Atm	particle size, soot volume fraction
Samson et al. (1987)[150]	acetylene/ air	coannular laminar diffusion flame burner/ TEM	Atm	Atm	particle counting, structural data of agglomerates
Quay, et al. (1994)[151]	ethylene/ air	coannular laminar diffusion flame burner/ LII	Atm	Atm	soot volume fraction, particle size
Vander Wal et al. (1994)[152]	ethylene/ air	premixed flat flame,laminar coflow diffusion flame/ 2D-LII	Atm	Atm	soot volume fraction
Will, et al. (1995)[155]	ethene/ air	coannular laminar diffusion flame/ time-resolved LII (TIRE-LII)	Atm	Atm	particle diameters
Bengtsson et al. (1995)[156]	ethene/ air	laminar premixed porous-plug burner/ LII	Atm	Atm	soot volume fraction
Choi, et al. (1995)[157]	acetylene/ air	premixed McKenna burner/ gravimetric sampling/laser Extinction	Atm	Atm	soot volume fraction
Vander Wal et al. (1996)[154]	acetylene/ ethylene/ air	McKenna burner/ LII/ gravimetric sampling	Atm	Atm	soot volume fraction
Xu F et al. (1997)[158]	ethylene/ air	laminar premixed flat-flame burner/ laser extinction / gravimetric	294 K	Atm	soot volume fraction, primary diameters, temperatures
Kasper et al. (1997)[188]	Metal aerosol/ CH4/ Ar/air	coannular laminar diffusion flame burner/ SMPS	Atm	Atm	size distributions
Zhou et al. (1998)[159]	acetylene/ air	premixed flat fame McKenna burner/gravimetric sampling / laser extinction	Atm	Atm	dimensionless extinction constant, soot volume fraction
Vander Wal et al. (1998)[189]	acetylene/ air	premixed McKenna burner/ LII	Atm	Atm	soot volume fraction
Vander Wal et al. (1998)[153]	ethylene/ air	coflow diffusion flame/LII/ TEM	Atm	Atm	morphology and LII signals
Skillas et al. (1999)[160]	ferrocene/ air	coflow diffusion flame/ SMPS/ TEM	Atm	Atm	size distribution, monodisperse particles
Bryce et al. (2000)[164]	diesels/ air	coflow diffusion flame/ LII	Atm	Atm	soot volume fraction
Axelsson et al. (2000)[165]	ethylene/ air	premixed McKenna burner/ LII/ laser extinction/ scattering	Atm	Atm	soot volume fraction, particle diameter
Zhao et al. (2003)[161]	ethylene/ oxygen/ argon	porous plug burner/ SMPS	Atm	Atm	particle size distribution function
Yang et al. (2005)[176]	ethylene/ air	non-premixed turbulent flame/ laser scattering and extinction	Atm	Atm	soot volume fraction, spherule diameter,

					aggregate size and fractal dimension
Yang et al. (2005)[177]	acethylene / air	non-premixed turbulent flame/ laser scattering and extinction	Atm	Atm	soot volume fraction, spherule diameter, aggregate size
Bladh et al. (2006)[168]	methane/ air	diffusion McKenna burner/ LII	Atm	Atm	LII signals
Charwath et al. (2006)[169]	acetylene/ air	premixed flat flame/ time-resolved LII (TIRE-LII)	Atm	Atm	particle heating
Iyer et al. (2007)[170]	ethylene/ air	coannular laminar diffusion flame burner/ laser scattering and extinction	Atm	Atm	total scattering coefficient, primary particle size
De Iuliis et al. (2007)[171]	ethylene/ air	coannular laminar diffusion flame burner/ 2D-2C-LII	Atm	Atm	soot volume fraction
Williams et al. (2007)[172]	methane/ ethylene/ kerosene/ air	coannular and slot laminar diffusion flame burner/ gravimetric sampling/ laser extinction/ TEM	Atm	Atm	dimensionless extinction coefficient
Hadef et al. (2010)[173]	ethylene/ air	premixed McKenna burner/ TIRE-LII/ 2D-LII	Atm	Atm	soot volume fraction, primary particle sizes
Bladh et al. (2011)[162]	propane/ air	coannular laminar diffusion burner/ SMPS and DMA-APM/ TEM	Atm	Atm	particle size distribution
Chan et al. (2011)[174]	ethylene/ air	non-premixed, premixed coannular laminar burner/ NTLAF/ LII	Atm	Atm	temperature, soot volume fraction
Migliorini et al. (2011)[175]	ethylene/ air	premixed plug McKenna burner, Gülder laminar coannular burner/ (Spec-LOSA)/ TEM	Atm	Atm	refractive index absorption function
Merchan et al. (2012)[166]	CME/SME/ SME-AF/ diesel/air	wick-generated open-air laminar diffusion flame/ TEM/ HR-TEM	Atm	Atm	particle diameters
Sirignano et al. (2017)[167]	ethylene/ air	stabilized capillary burner, McKenna burner/ LIE/ LII / DMA	Atm	Atm	particle size distribution
Chowdhury et al. (2017)[163]	ethylene/ air	turbulent coflow piloted jet burner/ (SMPS)	Atm	Atm	probability density functions
Mishra et al. (2020)[178]	ethylene/ air	Bunsen-type burner/ LII	Atm	Atm	LII signals
Mannazhi et al. (2021)[179]	methane/ air	coflow diffusion flame burner/ 2D-LII	Atm	0.1-0.5 Mpa	soot volume fraction
Xu et al. (2022)[180]	propane/ air	counterflow diffusion flame/ laser extinction and scattering/ LII/ flame luminosity	293 K	Atm	sooting limits
Zhang et al. (2022)[181]	anisole/ n-heptane/ air	co-flow diffusion burner/ TEM	Atm	Atm	soot particles morphology, size distribution

Manzello et al. (2005)[182]	co/air	well stirred reactor (WSR),plug flow reactor (PFR)/ Nano-DMA/ TEM	Atm	Atm	soot size distributions
Manzello et al. (2007)[183]	co/air	well stirred reactor (WSR),plug flow reactor (PFR)/ Nano-DMA/ TEM	Atm	Atm	soot size distributions
Lenhert et al. (2009)[184]	ethylene/ benzene/ naphthalene /methanol/CO/air	well stirred reactor (WSR),plug flow reactor (PFR)/ Nano-DMA/ TEM	Atm	Atm	soot size distributions
Crua et al. (2003)[185]	Esso AF1313 /air	RCM/ LII	373 K	6-9 Mpa	time dependent soot formation
Kitsopanidis et al. (2006)[186]	n-butane/ O2 /Ar	RCM/ Laser Extinction	765 K	14 bar	soot volume fraction
Ketterer et al. (2019)[187]	gasoline/ toluene/air	RCM/ Laser Extinction	657–695 K	8.09-9.25 bar	soot yield

3 Laboratory-based shock tube set ups at ICARE

This chapter presents the conventional shock tube techniques available at ICARE. First, a brief overview of the principles behind shock tubes will be provided. Then, the ICARE single pulse high-purity shock tube (HPST, also abbreviated as SPST) coupled to GC-GC/MS will be briefly described together with its applications to studies at highly diluted pyrolytic conditions. Finally, the ICARE heated shock tube (HST) coupled to laser extinction diagnostics will be described for the studies on particle formation and growth.

3.1 Principles of shock tubes

Shock tubes are ideal closed, constant-volume, adiabatic reactors which provide nearly constant pressure and temperature conditions by means of shock waves [21]. Its invention can be traced back to the 19th century with applications to acoustic studies but they were mostly exploited during the 20th century. During this period the type of gases and initial conditions were characterized and varied, with different applications including aerodynamics, chemistry, astrophysics, and physics [190]–[193].

Concerning the combustion field, shock tubes have been proven excellent instruments for kinetic studies as the thermodynamic temperature and pressure conditions can be brought to well-defined values almost instantaneously [194]. In addition, it is possibility to attain a wide range of temperatures and pressures (typically 600-4000 K and 0.1-1000 bar) and to run experiments at ideally any dilution condition as well as in oxidation or pyrolytic conditions. Typical observation times of the order of few ms allow the implementation of different optical and analytical techniques to monitor various variables and processes. Few of these studies will be presented in the next chapters. The small effects of thermal and velocity boundary layers on the reaction conditions inside the shock tubes are another advantage over other conventional set-ups, like flames or burners, where the fluid dynamics is strongly coupled to the chemistry.

The nature of a conventional shock tube is relatively simple. Initially the gases loaded into the two sections, driver and driven sections, are separated by means of a diaphragm. The driver section is filled with a gas (usually helium) at state 4, while the driven section is filled with the test gas under study at a lower pressure, denominated state 1. Namely, the pressure nomenclature for these two conditions are P4 and P1, respectively. After the rupture of the diaphragm a series of compression waves are formed. These waves travel through a medium compressed by the previous waves, thus subsequent compression waves have increasing speeds. Finally, the compression waves coalesce to form a strong shock wave. This shock wave propagates into the driven section suddenly increasing the test gas pressure P1 to the state P2. The shock wave travels along the driven section till it is reflected at the end-wall. Behind the reflected shock wave the conditions are T5 and P5. At the same time expansion waves propagate in the opposite direction of the shock wave without any abrupt change in the pressure while. The zone that includes the expansion waves is called ‘rarefaction fan’. The rarefaction fan is used in combustion applications to quench the reactions (for single pulse operation). The expanded driver gas conditions are referred to as state 3, while the moving interface between the test gases and the expanded driver gas is called contact surface. The position of the contact surface with respect to the shock wave varies in time as the shock wave travels at higher velocity. The time evolution of the position of the contact surface, shock front and

rarefaction fan are illustrated in the x-t diagram on **Figure** 3-1a and b. **Figure** 3-1c and d show an example of pressure and temperature distribution along the shock tube at a determined time t1.

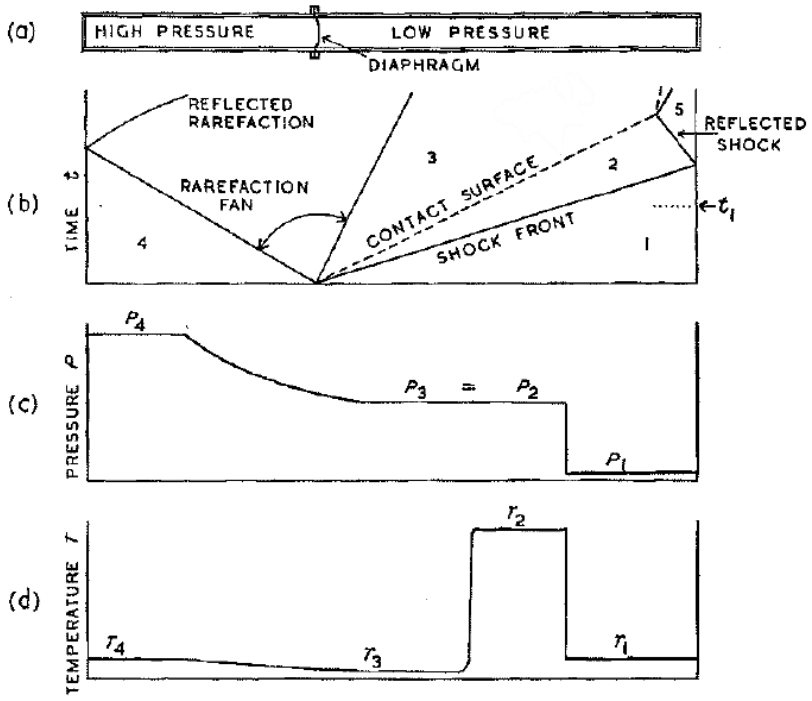

***Figure** 3-1. a) conventional shock tube, b) x-t diagram c) Pressure distribution at time t1* [21]

Ideally, when a shock wave passes through a quiescent gas, the molecules undergo an irreversible abrupt increase of the pressure, temperature and density as molecules can only transmit perturbations at a unique molecular velocity, the speed of sound, which is much slower than the shock wave velocity. The speed of sound can be determined in each medium and it depends on density, temperature and specific heat capacity ratio (γ) of the gas. In particular, since the experiments presented in this work were performed behind reflected shock waves, an accurate estimate of the state 5 should be obtained in order to determine the thermodynamic conditions during the test reaction time. This can be done by applying the conservation of mass, momentum, and energy in a unit area of the shock front between states 1 and 2, without momentum and heat transfer though the walls, and assuming that the flow is inviscid and that gases obey the ideal gas law.

$$\rho_1 u_1 = \rho_2 u_2 \tag{3-1}$$

$$P_1 + \rho_1 u_1^2 = P_2 + \rho_2 u_2^2 \tag{3-2}$$

$$H_1 + \frac{1}{2}u_1^2 = H_2 + \frac{1}{2}u_2^2 \tag{3-3}$$

where the initial density (ρ_1), pressure (P_1) and enthalpy (H_1) of the test gas ahead the shock wave are known. If additionally, the shock velocity u_1 is measured experimentally, then the exact values for T_2, P_2 and ρ_2 can be derived from system of equations 2.1 to 2.3. The following equations can be obtained by applying Ranking-Hugoniot method [195], [196]:

$$\frac{P_2}{P_1} = \frac{2\gamma M_1^2 - (\gamma - 1)}{\gamma + 1} \tag{3-4}$$

$$\frac{\rho_2}{\rho_1} = \frac{(\gamma+1)M_1^2}{(\gamma-1)M_1^2+2} \tag{3-5}$$

$$\frac{T_2}{T_1} = \frac{p_2\rho_1}{p_1\rho_2} = \frac{(\gamma M_1^2 - \frac{\gamma-1}{2})(M_1^2\frac{\gamma-1}{2}+1)}{\frac{(\gamma-1)^2}{4}M_1^2} \tag{3-6}$$

where M_1 is the incident shock wave Mach number defined as $M_1=u_1/a_1$, a_1 is the speed of sound in the test gas defined as $a1 = \sqrt{\gamma R T_1/Mw}$ and Mw is the molar mass of the test gas. Moreover, and considering that after the rupture of the diaphragm no gas flow takes place through the contact surface during the isentropic expansion, we can assume that velocities and pressure are equal between state 2 and state 3 since they need to be continuous (P2=P3). With this in mind we can correlate the unexpanded driver gas at initial state 4 with the initial test gas state 1 and derive the well-known shock tube equation [21]:

$$\frac{P_4}{P_1} = \frac{2\gamma_1 M_1^2 - (\gamma_1 - 1)}{\gamma_1 - 1} * \left\{1 - \frac{\gamma_4 - 1}{\gamma_1 + 1} * \frac{a_1}{a_4} * \left(M_1 - \frac{1}{M_1}\right)\right\}^{-\left(\frac{2\gamma_4}{\gamma_4 - 1}\right)} \tag{3-7}$$

This equation shows the relation between the strength or Mach number of the shock and the initial pressure ratio loaded across the diaphragm. Which means that while variating the initial pressure conditions, we can obtain different shock strengths. In order to obtain stronger shocks, a driver gas having a high speed of sound and low specific heat ratio should be used. For this reason, helium is commonly used in shock tube studies.

Finally, and similar to the analysis described to derive equations 2.4-2.6, between states 2 and 5 there is another pressure and temperature rise. The conditions behind the reflected shockwave can be derived in terms of the initial state 1 and incident shock Mach number as follows:

$$\frac{P_5}{P_1} = \left\{\frac{2\gamma M_1^2-(\gamma-1)}{\gamma+1}\right\}\left\{\frac{(3\gamma-1)M_1^2-2(\gamma-1)}{(\gamma-1)M_1^2+2}\right\} \quad (3\text{-}8)$$

$$\frac{T_5}{T_1} = \frac{\{2(\gamma-1)M_1^2-(3-\gamma)\}\{(3\gamma-1)M_1^2-2(\gamma-1)\}}{(\gamma+1)^2 M_1^2} \quad (3\text{-}9)$$

As already stated, this reflected conditions are kept almost constant during a test time, also named observation time. The observation time mainly depends on the size of the shock tube and the nature of the driver and driven gases. For combustion studies, this is the available time for the measurements. **Figure** 3-2 shows an example of PCB pressure profile obtained in the single pulse shock tube at the laboratory ICARE with 92 ppm styrene in argon. Behind the reflected shock wave, constant pressure and temperature conditions P_5 = 21 bar and T_5 = 1339 K are observed during a reaction time of around 4 ms [65]. At this time most of the reactions are quenched due to the cooling by the arrival of the rarefaction waves. Measurements can be performed in-situ during the nearly 4 ms observation time or off-line if samples are taken.

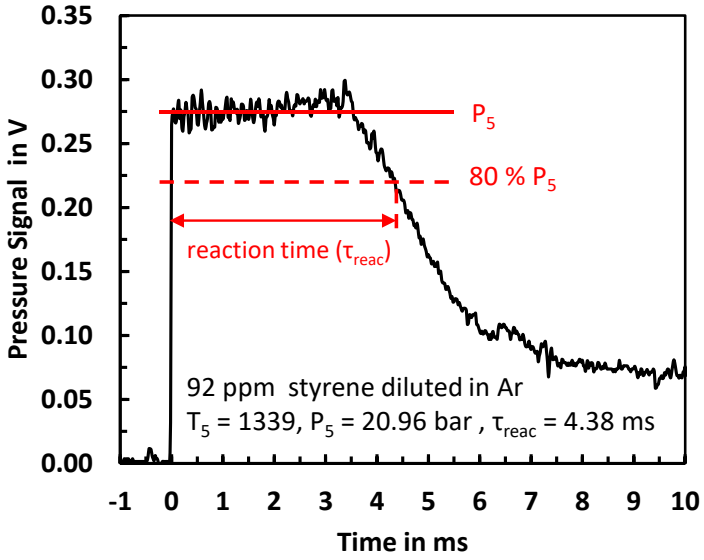

***Figure** 3-2. Typical end wall pressure profile in ICARE single pulse shock tube and definition of reaction time* [65]

Compared to other experimental techniques, the characteristics presented in the previous paragraphs make shock tubes an interesting reactor for pyrolytic studies on soot chemistry at relevant thermodynamic conditions and at different time scales, in the molecular and solid phase regimes. For instance, in flow reactors temperature gradients and pressure limitations reduce the experimental capabilities compared to shock tubes. The advantages and capabilities of coupling conventional shock

tubes to different diagnostics focused on PAH chemistry and soot formation and growth that are part of the motivation of this thesis work will be systematically discussed as follows.

3.2 Single pulse high purity shock tube and GC/MS

Recently, a new experimental technique has been designed and developed at ICARE laboratory dedicated to the study of PAH chemistry. The technique is based on a conventional single pulse shock tube coupled to gas chromatography and mass spectrometry. This technique has been widely implemented in the measurement of stable intermediates produced from the pyrolysis and the oxidation of fuels [9]. A schematic of the ICARE single pulse conventional shock tube coupled to the analytical system is presented in **Figure** 3-3. The ICARE single pulse high-purity shock tube (HPST) is composed of a driven section of 78 mm bore and 6 m length, and a driver section of around 2 m length. The driven section is electropolished and heated up to 90 °C in order to avoid the wall condensation of heavy PAH products and fuels before the experiment. During operation, initially the driven section is evacuated until 10^{-5} torr by means of a turbomolecular pump and then loaded with the test gases under study at the desired pressure P1 while the driver section is filled with helium at higher pressure P4. The two sections are separated by a double diaphragm section filled at P4/2. The 150 L dump tank, installed close to the diaphragm, is also filled at a pressure P1 with argon, before the ball valve connecting the dump tank to the driven section is opened. When the system is loaded and ready for an experiment, the double diaphragm is suddenly evacuated by opening a line to an evacuated chamber. This generate the bursting of the diaphragm and the formation of the shock wave downstream and rarefaction fan upstream.

Typical test gases are composed of highly diluted mixtures of hydrocarbon fuel (aromatic, straight-chain alkane, cycloalkenes, and their mixtures with C2-C3 intermediates) in argon bath gas and they are usually stored in a leak free gas mixture electro-polished cylinder. Special attention before mixture preparation is paid to assure the absence of fuel condensation on the walls based on the vapor pressure of the compounds. Tests are also performed to check that the partial pressure of the fuel once introduced into the tank does not drop but remains constant over time. Before the mixture preparation, the tank is evacuated until 10^{-5} torr, then filled up with the fuel vapor or gas to the desired partial pressure and subsequently diluted with argon at a typical pressure of 16 bar. Usually, with this tank pressure limit a set of 24 experiments can be obtained although the tank can be filled at higher pressures if desired. No mixer is at the moment installed inside the tank so a minimum waiting time of 5 hours is required for the mixture to homogenize.

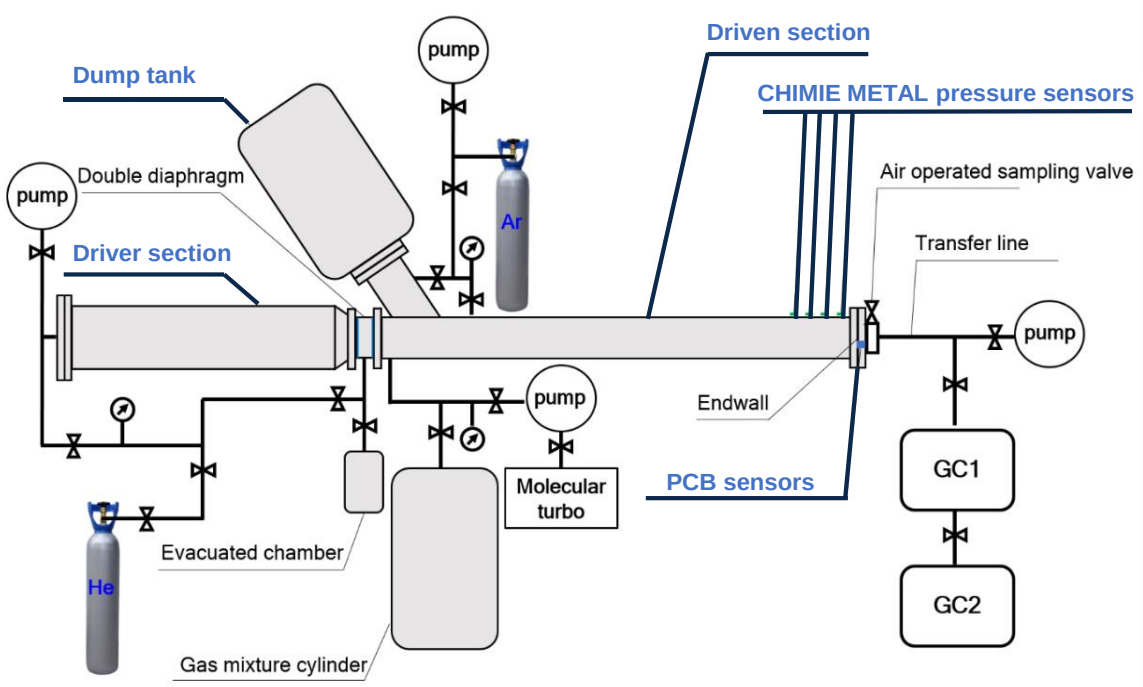

***Figure** 3-3. A schematic view with description of the ICARE single pulse shock tube coupled to the analytical system*

The shock tube is equipped with four CHIMIE METAL pressure sensors mounted on the last part of the driven section to track the passage times of the incident shock wave and derive the shock wave velocity extrapolated to the end wall. This information is required to calculate temperature T5 and P5 at which the reactions take place. One last PCB pressure sensor covered with a thin layer of RTV is used to record the pressure time history. An example of a typical end wall PCB pressure profile obtained in the single pulse shock tube at laboratory ICARE with 92 ppm styrene in argon was discussed in **Figure** 3-2. In this profile, initially the test gas is kept at 90 °C and around atmospheric pressure, then the arrival of the shock wave generates an instantaneous increase of the pressure to 21 bar and the gases are heated to 1339 K in less than one micro second. This condition stays almost constant during the observation time, which is around 4 ms, before the arrival of the rarefaction waves leads to a fast decrease in the pressure and temperature of the gases and to the quenching of the reactions. The reaction time is taken as the time between the arrival of the shock wave at the end-wall and the time when the pressure drops to 80% of its maximum value [197]. The ICARE HPST can be considered as an ideal adiabatic reactor at constant pressure conditions. This is related to the large diameter of the tube which reduces the non-idealities and avoids the need for chemical thermometers to be implemented [198]. On the other hand, certain reactions involving resonantly stabilized radicals may continue during the quenching [65], [199]. In this case, the pressure profile needs to be introduced in the kinetic simulation.

After the quenching of the reactions, a pneumatic sampling valve (HIP 30- 11HF4) is triggered by the PCB signal around 10 ms after the arrival of the shock wave at the end-wall. This allows the withdrawal of the gases and their transfer to the analytical system through a SilcoTek line heated up to 150 °C. The analytical system is composed of two gas chromatographs, one specifically designed and developed at ICARE to

measure PAHs that have been formed at pyrolytic, high-pressure, high-temperature, highly-diluted conditions (see detailed description in chapter 2.1.1). A DSQ mass spectrometer is also connected to the transfer line and used to help the identification of the PAH products.

Gas chromatograms are obtained and used to analyze the gas mixtures produced in the shock tube. **Figure** 3-4 shows an example of gas chromatogram from the decomposition of 100 ppm of styrene in argon bath gas at pyrolytic conditions (reaction time of 4 ms, T_5 of 1517 K and P_5 of 21.14 bar). It can be noticed that the system is capable to detect and separate many different polycyclic aromatic structures ranging from two-ring species like indene and naphthalene passing by three-ring compounds like phenanthrene and anthracene up to four-ring species like pyrene, fluoranthene or chrysene.

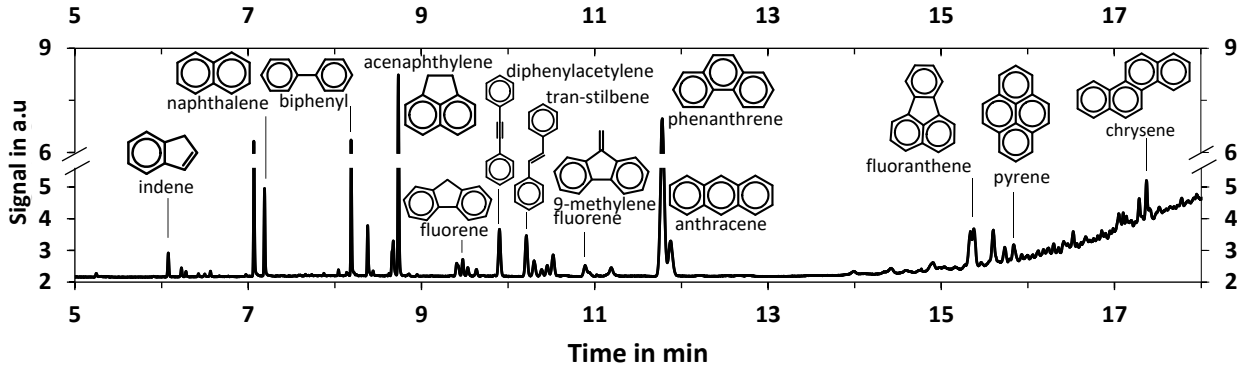

***Figure** 3-4. Example of gas chromatogram for 92 ppm styrene decomposition in argon bath gas at T_5 = 1553 K and P_5 = 21.1 bar. Experiment M1529.*

Species separation takes place as a function of the retention time on the column (DB-17ms in the case of **Figure** 3-4) and for each of the species up to three-rings included it is possible not only to identify but also to quantify the concentrations by integrating the peaks areas and applying a calibration coefficient. The calibration curves are obtained using custom-made mixtures of known PAH concentrations in argon which are directly injecting to the GC. Up to three ring compounds included, these curves are very accurate and linear over the range of mole fractions obtained in the experiments. If the measurement is repeated at different T5 conditions it is possible to obtain species concentration profiles as a function of temperature for the fuel decay as well as the formation of the major and minor products, including PAHs. These temperature dependent species profiles can then be used for the development and validation of detailed chemical kinetic models regarding, in the specific case, the formation of the gas-phase soot precursors. Once the models have been optimized based on the experimental results, they can be used to improve our fundamental understanding of the PAH chemistry through kinetic analyses (rate-of-production and sensitivity analyses) and as a base for the coupling of the solid-phase soot code.

Despite the limitations described in the previous chapter, mainly related to condensation of heavy species and reduced isomer selectivity, the single-pulse shock tubes are powerful techniques that allow the measurement of PAH products produced from the decomposition of fuel molecules. The results can be complemented with those produced in synchrotron-based investigations.

3.3 Heated shock tube and laser-based extinction measurements

Laser extinction technique was coupled to the heated shock tube of ICARE laboratory (ICARE-HST) as the optical diagnostic equipment for probing the transient formation and growth of soot nanoparticles after the decomposition of several fuel components and mixtures at pyrolytic conditions. The ICARE-HPST is shown schematically in **Figure** 3-5. The driven section is 52.5 mm bore with 5.25 m long and it is covered by heating elements and 5 cm thick glass fiber insulation. The shock tube has the possibility to be heated up to 130 ^{o}C but the shock tube was kept at room temperature in this work. The driver section is 114.3 mm bore and 2 m long and it is rigidly attached to a recently home-made antivibration structure by means of a set of 16 screw bolts. Other 16 screw bolts are also used to connect the end part of the driven section to a second home-made antivibration structure. The operation of the heated shock tube is similar to the HPST with few differences.

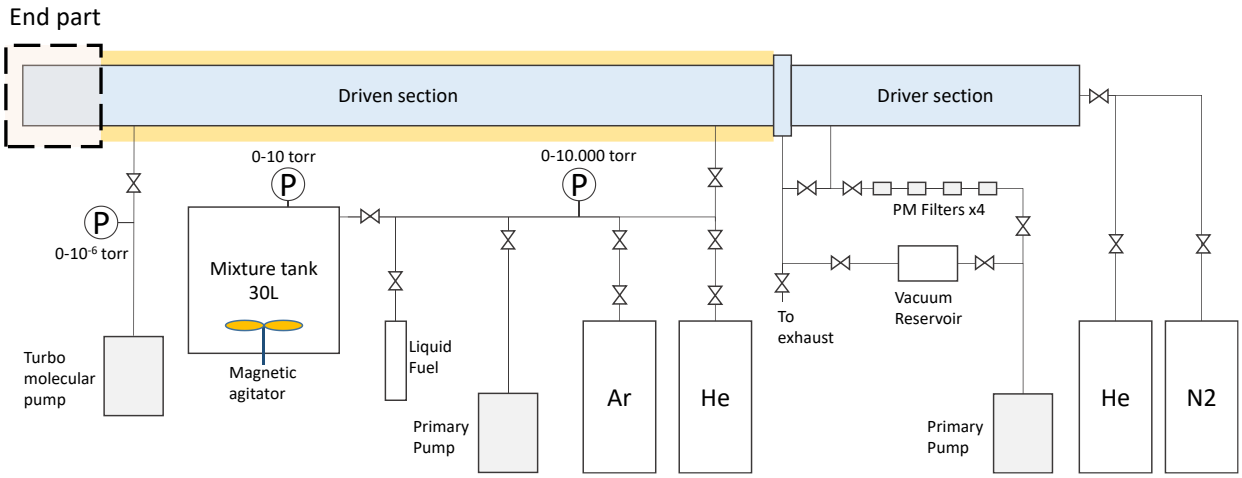

***Figure** 3-5. Schematics of the high-pressure heated shock tube set up showing mixing rig, pumping systems, pressure gauges, four particulate matter filters, and gas bottles.*

First, the mixing rig is attached to the beginning of the shock tube driven section and the mixtures are stored inside a 30 L mixture tank. The tank is evacuated below 0.01 torr before the liquid fuel is vaporized and introduced to the required partial pressure which is normally less than 10 torr. Then the 0-10 torr pressure gauge and the tank are closed, the lines flushed with argon (> 99.9999% purity) before the tank is filled with argon to a total pressure of 2450 ± 2 torr. This pressure allows a maximum of four experiments per mixture preparation. After the preparation, a magnetic agitator homogenizes the mixture for minimum 20 minutes. Just before each experiment, the shock tube walls are passivated with the fuel mixture for 5 minutes to avoid any undesired fuel adsorption which may occur at room temperatures. This means that initially, the shock tube is evacuated down to 10^{-5} torr using a turbo molecular pump, then it is filled with the fuel mixture under study to 740-760 torr, and finally re-evacuated and re-filled at the desired pressure condition. This pressure condition is lower than P1 as 24 % of helium (by volume) is added as a buffer gas in order to increase the observation time.

When both P_1 and the acquisition system are ready, the driver section is filled with helium and a relatively small amount of nitrogen (11-17%). The nitrogen addition postpones the arrival of the rarefaction fan and it improves the quality of the pressure profiles [200], [201]. Shock tube is closed and a double diaphragm section initially filled at a pressure of P4/2 is evacuated to generate the shock wave. The driven section if equipped with 4 equally spaced CHIMIE METAL (A25L05B) piezoresistive pressure sensors used to record the passage of the incident shock wave and a PCB pressure sensor (PIEZOTRONICS Model482C series) covered with a thin layer of RTV installed at the end-wall. An example of a typical raw PCB pressure history and extinction signals are shown in **Figure** 3-6. It can be noticed that although a pressure bump at 2 ms is presented, in average almost constant pressure conditions are achieved in the HPST during a reaction time of around 4.5 ms, in the specific case for an experiment at T5 = 1661 K and P5 = 16.6 bar with 0.0613% ethylbenzene in argon bath. The PCB signal is also used to trigger data acquisition (pressure measurements and extinction signal).

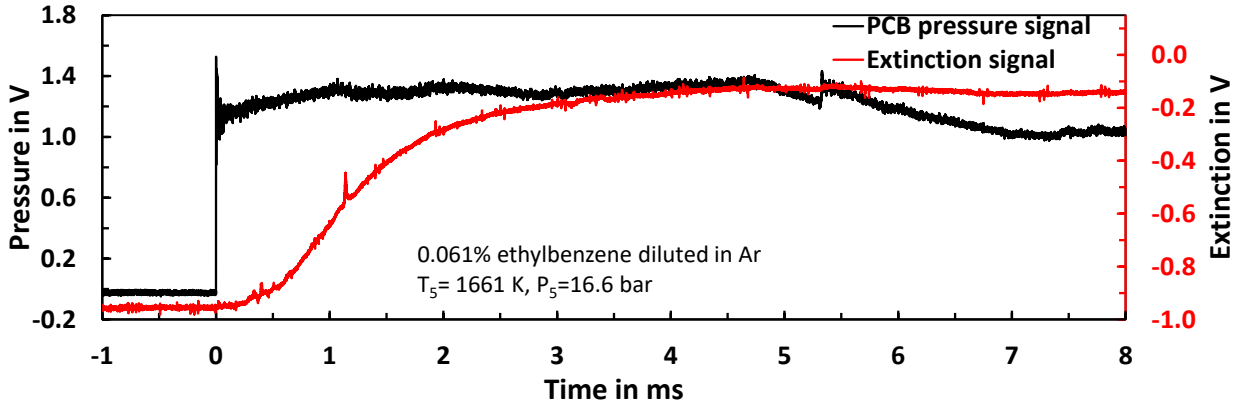

***Figure** 3-6. Typical PCB pressure time history and extinction signal obtained in ICARE – HST. Obtained at T_5 1661 K and P_5 16.6 bar, Ma= 2.6, attenuation 4.5 %. Experimental condition M1244.*

After each experiment, the shock tube is vented through a series of four filters (15, 7, 2 and 0.5 microns) to capture the soot before going to the extraction system. In addition, the inner surface of the shock tube is cleaned with acetone several times. The end wall is also carefully removed from the end part to extract soot nanoparticles by using ultrasound bath with acetonitrile solvent. The soot particles are stored and labeled in darkened glass recipient for future transmission electron microscopy (TEM) analyses. TEM allows the obtain primary soot particle diameters in the final aggregates and atomic scale structure organization, fundamental parameters for the validation of the soot models.

The crucial variables that can be studied using laser extinction are soot volume fraction or optical densities as well as soot yield, induction delay time, and soot growth rate, all as a function of the reaction temperature T5. **Figure** 3-7 presents a schematic of the end part of the driven section where the optical access is located. The location of the flush mounted CHIMIE METALS used for the incident shock wave velocity measurements is also shown. At 10 mm from the end-wall, five quartz windows are placed at different angles (0^o, 90^o, 180^o, 235^o, 335^o). The two windows at 0^o and 180^o are used to enter and exit a 633 nm red Helium-Neon laser (Melles Griot, 15 mW). The laser wavelength of 633 nm is large enough

compared with the size of the expected nanoparticles so that the light will be mainly absorbed according to the Beer-Lambert law for gases. In addition, the contribution due to the absorption from other species, in particular the gas-phase PAH precursors, is minimized.

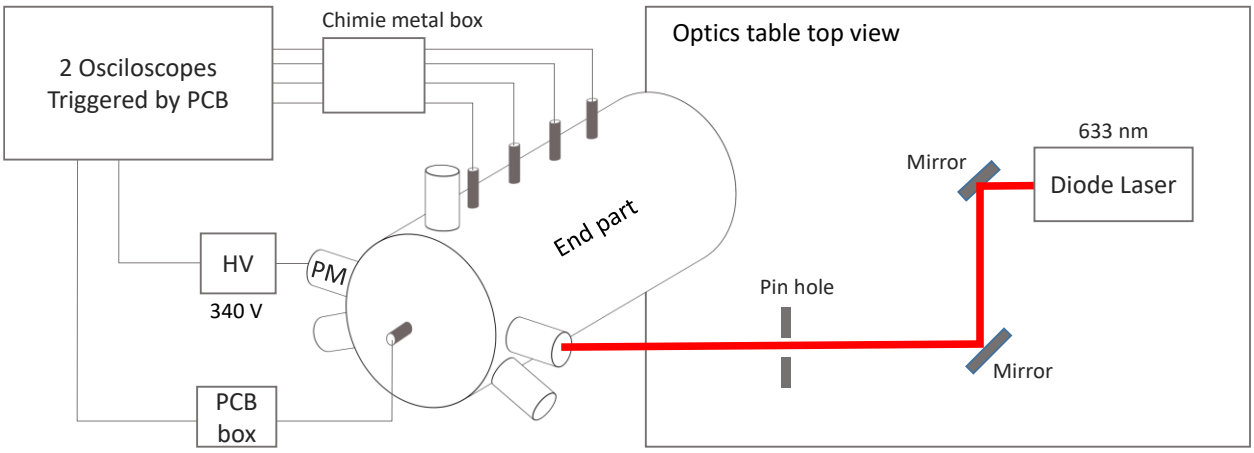

***Figure** 3-7. Schematics of heated shock tube (HST) end section showing pressure transducers connections, photo multiplier, and laser extinction configuration mounted on the optics table.*

The laser is installed on an antivibration optical table very close to the end section of the shock tube, and the light is directed inside the shock tube using optical mirrors. Just before the inlet, a pinhole is installed facilitating the alignment as well as a convex lens in order to focus the laser beam at the center of the shock tube (necessary for future technique developments). The laser beam crosses the control volume perpendicularly to the shock tube axis and parallelly to the floor. The exiting monochromatic light is collimated and detected by a photo multiplier (PM, model: HAMAMATSU R5938P) connected in parallel to a 10 kΩ resistance for enhanced time resolution. The signal is amplified using a high-power supply (HV, BERTRAN 230). A voltage of 340 volts was chosen based on the output extinction signal in order to guarantee linearity of the response. The photo multiplier is physically attached to the structure holding the shock tube.

The methods and equations implemented in [18] can be employed to determine the soot induction delay times, soot volume fractions, and soot growth rates, while the data treatment presented in [124] can be used to characterize the optical densities at 633 nm (D_{633}). Assuming monodispersed and homogeneously-distributed spherical particles of average diameter much smaller than the wavelength of the beam light ($d_p << \lambda$), the soot volume fraction (f_v) can be defined as the volume of particles per unit volume (m^3/m^3). It can be expressed as function of the ratio between the incident (I_0) and transmitted (I_L) intensity of the laser light. Additionally, if scattering contribution is negligible, the extinction coefficient (K_{ext} in cm-1) can be assumed as the absorption coefficient (K_{abs}) obtaining the commonly used expression for (f_v) presented in equation (3-10).

$$f_v = \frac{\lambda}{6\,\pi\,L\,E(m)}\,ln\left(\frac{I_0}{I_L}\right) = \frac{\pi \cdot d_p^3 \cdot N_p}{6} \qquad 3\text{-}10$$

where N_p is the number density of soot particles (in #/m^3), L the optical length assumed as the shock tube bore, and E(m) function of the refractive index (m) of the particles. This last factor introduces important uncertainties to the measurements for several reasons: 1) the measurements of E(m) in the literature are based on soot which is mature, not incipient as in the shock tube experiments; 2) E(m) varies with time for the same fuel and thermodynamic conditions; 3) E(m) varies with the temperature/pressure conditions and with the fuel. Comparing the values proposed in the past for E(m), for average real (n) and imaginary (k) values of the refractive index (m=n-ik), a value of E(m) = 0.19 is obtained, which can result in a factor 4 uncertainty in the final measurement [202]–[207]. Recent shock tube works use a value equal to 0.36 [127], [134], [135].

Despite the uncertainties in their absolute values, f_v profiles can be used to derive soot induction delay times and surface growth rates as their measurements are independent of the optical properties and their characterization is possible with the following expressions [208]–[210]:

$$ln\left(\frac{f_{v\,max}}{f_{v\,max}-f_v}\right) = k_f \cdot t = f(t) \qquad 3\text{-}11$$

where k_f is the soot growth rate constant by surface reactions assuming that no coalescence neither agglomeration of particles occurs. It is extracted from the slope of function f(t) and can also be represented in an Arrhenius form as it follows:

$$k_f = A\,exp\left(-\frac{E_f}{RT}\right) \qquad 3\text{-}12$$

where A and E_f are the preexponential factor and the activation energy of the soot growth, respectively.

Soot induction delay times τ_{ind}, defined as the time necessary to form the first soot particles, can be used to characterize the process of nucleation. It represents the time interval between the instant when the fuel is brought to the desired conditions and the instant when the first particle is produced. It can be extracted from the f_v signal by extrapolating the maximum slope of the soot volume fraction profile to the baseline. Soot induction delay time can also be expressed in Arrhenius form to account for variation in temperature, pressure and initial concentration [18], [211]:

$$\tau_{ind} = A\left[C_xH_y\right]^a[O_2]^b[Diluent]^C\,exp(E_{ind}/RT) \qquad 3\text{-}13$$

where A is the pre-exponential factor, $[C_xH_y]$, $[O_2]$ and [diluent] the initial fuel, oxygen and diluent concentrations, respectively, in mol/m^3. E_{ind} is the activation energy of the induction process in J·mol^{-1} and R is the ideal gas constant (8.314 J·K^{-1}·mol^{-1}). The coefficients a, b and c are exponents to fit the experimental results. Since in this work almost constant fuel and diluent concentrations were utilized in the test section and additionally, no oxidation was considered, these coefficients are equal to zero.

One parameter that is not affected by the optical properties is the optical density (D, in m^2/mol) at a determined wavelength, in this case 633 nm. It depends only on the logarithmic ratio between the transmitted light (I_L) and the incident light (I_0) intensities, the concentration of carbon atoms in the mixture ([C]), and the optical path L. The optical density can be calculated by the next equation [212]:

$$D_{633} = \frac{ln\left(\frac{I_0}{I_L}\right)}{[C]L} \qquad 3\text{-}14$$

where the carbon concentration [C] in #carb/mol is defined as a function of the fuel molar fraction x_{hc}, Boltzmann's constant (K_B= 1.38·10^{-23} J·K^{-1}), reflected T5 and P5 conditions and initial number of fuel carbon atoms n_c:

$$[C] = \frac{x_{hc}P_5}{k_B T_5} n_c 10^{-6} \qquad 3\text{-}15$$

In the experiments presented below, a nominal pressure of 17 ± 1.2 bar was selected for all experiments together with similar fuel concentrations and fuel composition (in terms of carbon atoms per molecule), thus the carbon concentration [C] will mainly depend on the temperature T5.

4 Miniature shock tube and synchrotron-based set ups

In order to introduce the development of a new miniature shock tube and its applications with synchrotron-based diagnostics, the laboratory-based shock tube facilities described in the previous chapter coupled with different measurement systems are schematically shown in **Figure** 4-1.

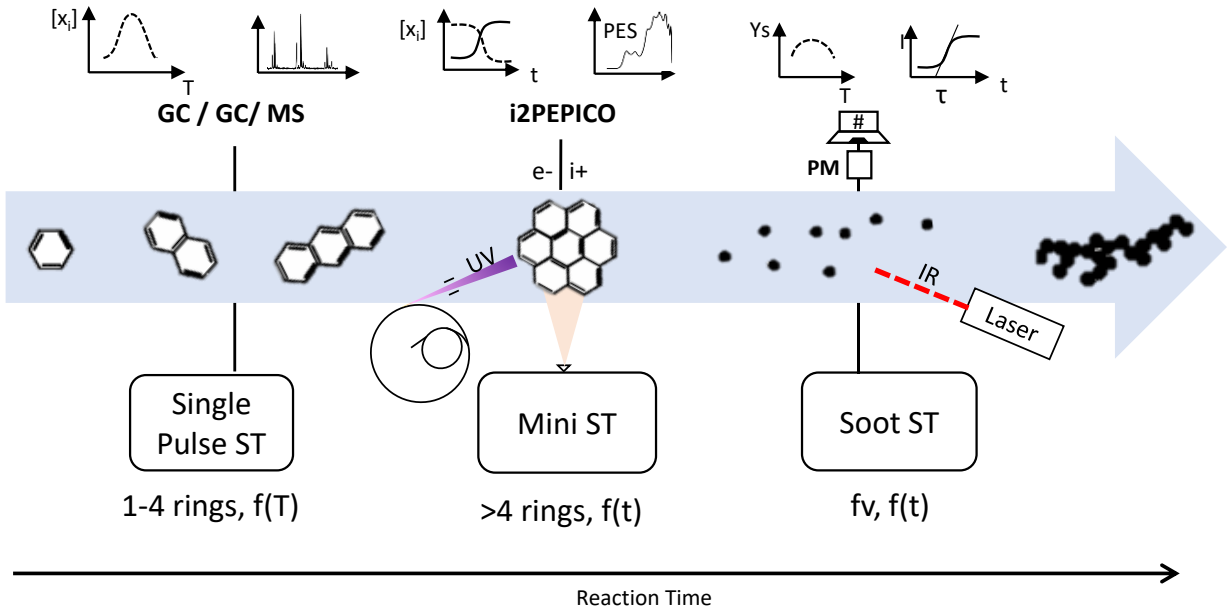

***Figure** 4-1. Experimental facilities used in the thesis and expected results.*

The single pulse shock tube coupled to GC/GC/MS can be used to study aromatic and PAH chemistry in the gas-phase steps towards the soot particles up to three-/four-rings species. On the other side, concerning the solid phase chemistry, the shock tube coupled to laser extinction can reveal very useful information on the soot nanoparticles inception and growth, although detailed information on the nascent particles (1-10 nm size) cannot be obtained. In fact, Rayleigh scattering cannot measure such small particles mainly due to interference with PAHs and laser power, while extinction measurements are not size selective and inaccurate at low extinction levels. In addition, these techniques are not capable to provide information concerning the internal structure of the nascent particles. Thus, there is a gap between the formation of relatively large PAHs and the appearance of 10-15 nm primary particles. The miniature shock tube coupling with synchrotron detectors has the potential to overcome some of the limitations of the GC systems and unveil the chemistry of multi ring PAH structures.

In this chapter, the design, functioning, and characterization of the ICARE high repetition rate shock tube (ICARE-HRRST) will be described. In particular, its capability to run automatically thousands of very reproducible experiments necessary for signal averaging will be shown. This is a requirement to implement and exploit the strengths of i^{2}PEPICO, despite its low signal-to-noise ratio signals.

Additionally, the installation of the ICARE-HRRST at different European light source facilities will be described. For instance, the coupling with SAPHIRS vacuum chamber of DESIRS VUV beamline in SOLEIL Synchrotron will be presented in detail as well as the installation at the X04DB VUV beamline (SLS/VUV) available in the Swiss Light Source (SLS) at Paul Scherrer Institut (PSI). All the challenges faced during the successful campaigns will also be discussed for the first time in this thesis manuscript.

4.1 ICARE high repetition rate shock tube facility

The first governing parameter in the design of a shock tube that is intended to be coupled with synchrotron detectors is to be sufficiently small in order to fit in very restricted space available at the beamlines. Additionally, the system has to be compact and modular since campaigns to synchrotron require transportation of the different pieces from the laboratory to the different facilities, with the need of modifying the length and design of the shock tube based on the geometry of the beamline. The last design condition to meet is to be able to run shocks at high repetition rate as beamtime at synchrotrons is very reduced and its efficient use is mandatory. The experiments need also to be reproducible for signal averaging. All these conditions can be met only with a miniaturized, automated, modular shock tube, despite the fact that reducing shock tube size can yield to larger non-idealities of the reaction conditions compared to regular shock tubes.

With all this in mind, the miniature high repetition rate shock tube at ICARE laboratory (ICARE-HRRST) was designed and constructed based on the design developed by Tranter et al. [22] specifically for use at synchrotron facilities. There are several subsystems interconnected with the experimental section of the ICARE-HRRST as shown in **Figure** 4-2. These comprise electronics boxes for automated control of the operations, reagent mixture preparation rig, pneumatic circuits, gas and fuel supply, vacuum system, and the coupled measurement techniques. Detailed information about all the coupled subsystems will be presented in detail as follows in this chapter.

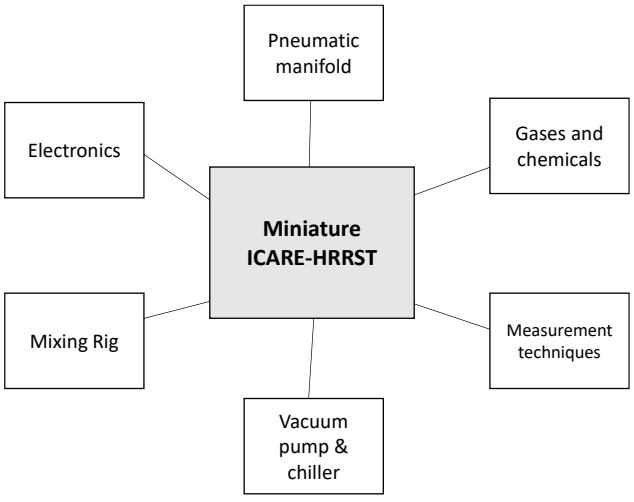

***Figure** 4-2. Different elements designed for the functioning of the ICARE-HRRST.*

4.1.1 Shock tube design

The ICARE-HRRST was designed to work at laboratory and at synchrotrons. However, dimensions were specifically chosen to fit inside the restricted space of the SAPHIRS chamber at DESIRS beamline. ICARE-HRRST is a fully automated shock tube that can operate at repetition rates up to 2 Hz, compared to regular shock tubes which can be operated up to around 1 experiment per hour. **Figure** 4-3 shows a 3D view of the experimental section of the shock tube set up. It is ~ 10 times smaller than regular shock tubes but its operation is very similar with a driven and a driver section separated by an element which is removed to generate the shock wave.

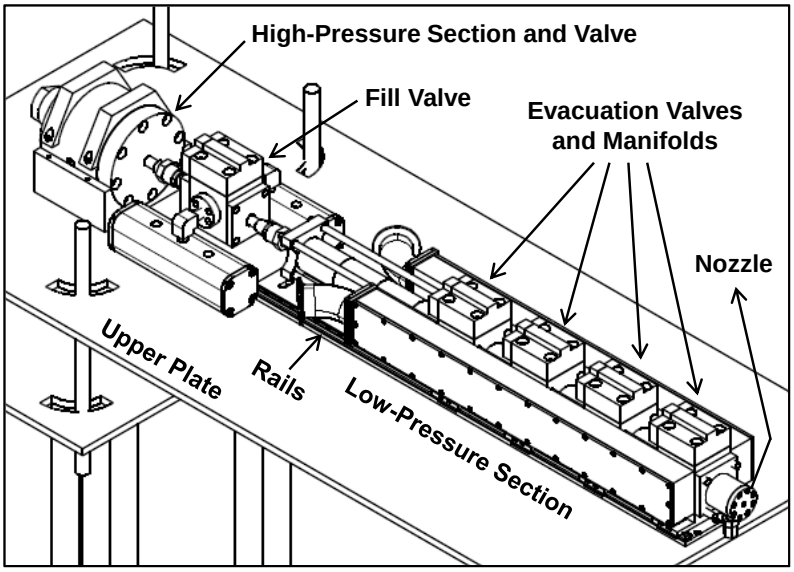

***Figure** 4-3. 3D view of the ICARE-HRRST.*

4.1.1.1 Driven section

The driven section was designed to be able to slide on high-precision aluminum rails in a modular fashion in order to obtain different system configurations and meet specific length needs. It has a bore of 8 mm and its total length from the high-pressure section to the end wall is variable, starting from a minimum value of ~84 cm. It is quite simple to add elements to make the shock tube longer. In fact, the driven section is constituted of 60 mm long custom-made stainless steel pneumatic valves (end-valve EV, middle-valves MVs and fill-valve FV in **Figure** 4-4a) and spacers (S in **Figure** 4-4a) of the same length used to increase or reduce the length as needed. Both, spacers and valves are joined and aligned through low-tolerance male-female coupling, with viton o-rings placed between the different elements to avoid leaks from the shock tube to the outside and entrance of atmospheric air into the shock tube. To hold all the valves and spacers together threaded rods are used as shown in the **Figure** 4-3.

A detailed cross-sectional view and top view of the assembled driven section including the notation for the different elements is shown in **Figure** 4-4a. Eight CHIMIE METAL A25L05B pressure sensors are located in the bottom part of each pneumatic valve and spacer to detect the moment when the shock wave passes and calculate the shock wave velocity. These are placed every 60 mm by means of screwed adaptors which hold the sensors by means of o-rings. The last pressure sensor located in the end part (T) is 20 mm from the end wall. The velocity at the end wall is obtained by extrapolation of the single measurements. Notice that the inner surfaces of the sensors are flush-mounted to reduce the perturbances on the shock propagation.

The four exhaust valves (EV and three MVs) are used to evacuate the tube through two separate evacuation manifolds, while the fill valve (FV) is used to introduce reagent fresh mixture into the shock tube. All the valves have the same design and they are built based on previous design by Tranter and Lynch [22]. These are controlled by compressed air through the two ports in the valve cap (B) shown in **Figure** 4-4b. Port P1 is used to push down the piston (C) while P2 is used to lift it. The movement of the piston closes or opens the ports F, and the sealing is obtained with an o-ring inside a dovetail groove in the bottom part of the piston. In the case of valves EV and MVs, the ports are connected to the two vacuum manifolds to evacuate the gases, one on each side of the valves. In the case of the valve FV, the port joins the shock tube with two reservoirs which store the mixture close to the tube in sufficient amount for having a pressure P1 nearly constant during operation at high repetition rates.

The piston movement is guided by two CHESTERTON 22KN5-AWC860 lip seals (D) separated by Teflon spacers. The CHESTERTON seals prevent compressed air for valve operation to enter the shock tube. An o-ring is located radially in the head of the piston to separate the two compartments connected to P1 and P2. In this case the groove is designed for dynamic applications. Finally, another o-ring is placed between the valve body for holding the compressed air from exiting the valve. The ICARE-HRRST was designed to run experiments at a maximum frequency of 2 Hz.

The driven section end part (T) is designed to hold a nozzle (100-400 µm orifice diameters) in order to couple the shock tube with the mass spectrometers at synchrotrons as it will be discussed in next chapter. These nozzles are perfectly aligned with the shock tube axis. Due to the difference between the pressure P5 inside the shock tube and the pressure inside the vacuum chamber connected to the mass spectrometer, the gas elution generates a supersonic jet flow that will expand on the surrounding ambient. This expansion cools down the reaction products withdrawn from miniature ICARE-HRRST freezing the kinetic reactions. For the case a diagnostics with mass spectrometers, a skimmer or a series of two skimmers (for double stage pumping systems) is precisely aligned and placed just after the nozzle in order to capture the central part of the jet and create a collimated molecular beam that will be introduced into the mass spectrometer vacuum chamber, as discussed later. In order to obtain an effective cooling effect, the minimum distance between the nozzle and the skimmer is around 10 times the nozzle orifice diameter.

The end part (T) can also be configured to hold a 113B24 PCB pressure transducer covered with a thin layer of room-temperature-vulcanizing silicone (RTV) to perform experiments in the laboratory and to characterize the pressure time-histories behind reflected shock waves. The PCB transducer cannot be mount simultaneously with the nozzle due to the small bore of the shock tube.

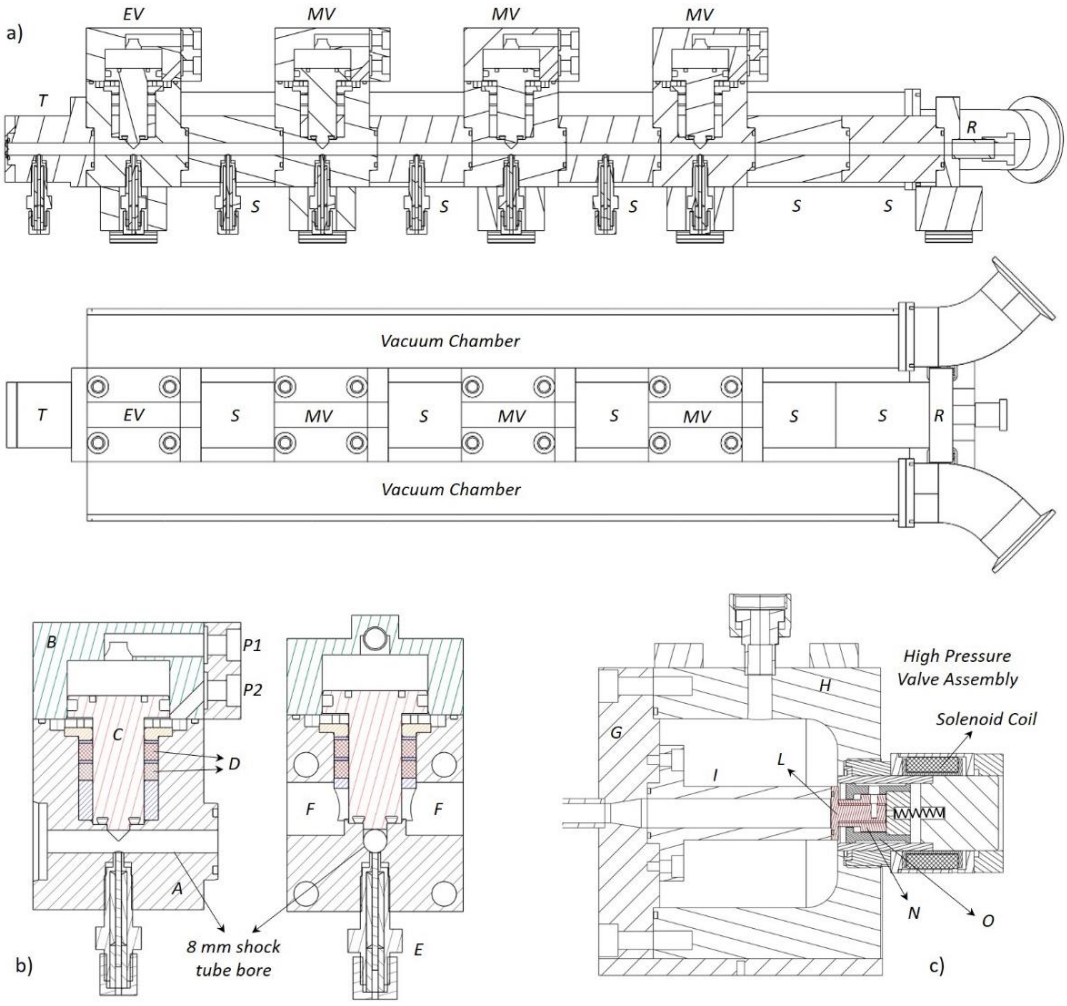

***Figure** 4-4. a) Cross-sectional view and top view of the driven section of the ICARE-HRRST. EV: end valve; MV: middle valves; T: end section; S: spacers; R: connection element. b) Cross-sectional views of the pneumatic valves EV and MV and FV which are identical in design. Compressed air is connected to ports P1 and P2. A: valve main body; B: valve cap; C: piston; D: lip seals; P1: valve closing port; P2: valve opening port; F: exhaust ports for evacuating HRRST driven section; E: pressure sensor holder. c) Cross-sectional view of the driver section showing the high-pressure chamber and solenoid actuated valve. G: flange with convergent section; H: main chamber body; I: leading part of the driven section; L: poppet; N: outer body; O: armature body. Parts L, N and O form the armature.*

4.1.1.2 Driver section

The driver, or high pressure section is shown in **Figure** 4-4c, its design is similar to the one of Tranter and Sikes [213]. It consists of a 0.334 L and 78 mm i.d., 304 stainless steel cylindrical chamber (H) surrounding the first part of the driven section (I). The maximum pressure rating is 100 bar. Compared to conventional shock tubes, the diaphragm is here replaced by a poppet (L) highlighted in red in **Figure** 4-4c. This allows multiple subsequent operations without the need for opening the tube between experiments. Part (L) is screwed into part (N) which can move axially inside the armature body (O). The poppet contains an O-ring in a dovetail grove that seals against the entrance of the shock tube by the force of a spring. Additionally,

at initial conditions, the poppet is automatically pushed by the difference between the high pressure in the driver chamber and the low pressure in the shock tube.

An external solenoid valve installed on the high-pressure section governs the poppet movement. The valve opens and closes by the rapid action of the magnetic field which is produced and held for a period of time of around 2 ms, moving back the poppet by around 1.5 mm compared to the close position, while the armature travels for 4.5 mm total. The 2 ms opening time is sufficient for allowing enough driver gas to expand into the driven section and to subsequently form the shock wave. Since the movement of the armature acts like a hammer on the poppet, a set screw is inserted to avoid unscrewing between pieces L and N and to prevent misfunctioning of valve or poppet destruction. The insertion of the set screw has to be performed after all armature is installed and it is done through a side hole in the armature body O.

The driver section extends into the driven section through the piece (I) whose design includes a conical reduction on cross sectional area of 2.25 (from 12 mm to 8 mm). This reduction results in higher Mach numbers compared to straight tube for the same P4/P1 ratio [214]. There is a 2.2 L reservoir tank connected to the entrance of the driver section in order to keep a constant P4 during the high repetition rate operation. P4 is measured by means of a Honeywell LM-BP211DL gauge pressure sensor located just before the helium reservoir tank. A pneumatic ball valve is inserted between the reservoir tank and the high-pressure chamber. This valve is triggered and closed if any misfunctioning occurs in the operation of the shock tube, in order to avoid high-pressure gases to keep flowing into the system and potentially damage not only the shock tube parts but also the diagnostics coupled to the HRRST.

4.1.1.3 Vacuum system

For each cycle, the gases inside the shock tube must be rapidly extracted through the manifolds shown in **Figure** 4-4a. The vacuum chambers are communicating to the ports F of each pneumatic valve (EV and MVs) and to a vacuum system. The vacuum system is composed of a vacuum booster coupled to a dry root vacuum pump (3900 m^3/hr, Edwards EH500/GV-80 combination) which is connected to the vacuum manifolds using stainless steel flexible bellows and KF 40 fittings. An ISO 100 butterfly valve is located at the exit of the pump to isolate the pump when needed. The vacuum pump is never stopped while the experiments are running since miniature shock tube is designed to run experiments continuously for several hours. However, pump heating needs to be avoided and a reliable refrigeration system has to be implemented in order to reduce operation temperature and subsequent possible damages. This is solved using a water chiller. There is a dust filter just before the water entrance to the chiller to trap big particles that come from the pump and to prevent chiller damages too. Additionally, the vacuum root pumps need a compressed air flow-rate to purge the system in case of “dirty” gases.

4.1.1.4 Reagent mixture preparation and mixing rig

The fill valve FV in **Figure** 4-3 is connected to two reservoirs which have the function to feed fresh mixture into the shock tube at a sufficient rate so that P1 stays nearly constant during operation. The reservoirs are equipped with a security rupture disk and an additional port; one side of the reservoirs is opened and

function as inlet for the mixture. An MKS 722B capacitance manometer is installed on one of the additional ports to measure the absolute pressure in the driven section. The picture of the fill valve and its connection to one of the reservoir is shown in **Figure** 4-5.

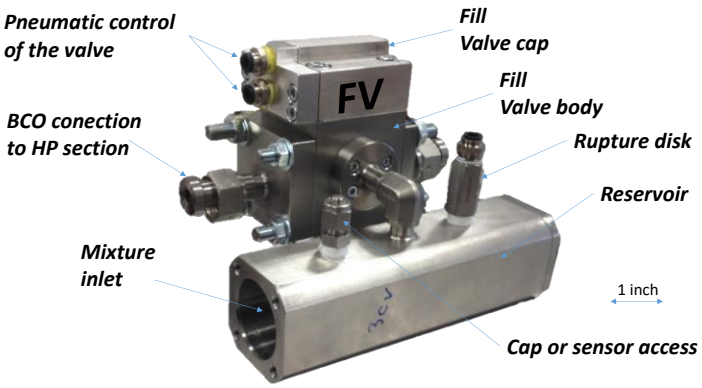

***Figure** 4-5. Photography and description of one side of the assembled fill valve FV*

New reagent mixture is continuously provided to the driven section of the HRRST by means of a homemade automatic mixing rig system. Most of the elements of the mixing rig are mounted on a compact aluminum frame built with Bosch Rexroth profiles and equipped with wheels for easy transportation and installation at synchrotrons and laboratories. As presented below, the mixing rig is a versatile set-up capable to prepare different mixtures at high flow rates for a large number of subsequent experiments as in the case of application to high repetition rate shock tube set-ups. On the other hand, it can be used for any other scientific purpose.

The mixing rig system design comprises three MKS mass flow controllers of different scales (MFC, model 1179A) connected to a common 946 MKS vacuum system controller box which is also connected to the analog P1 signal. A schematic diagram of the whole mixing rig system is presented in **Figure** 4-6b. The rig is capable to generate different gaseous mixtures including vapor from liquid fuels. In particular, the mixtures with liquid fuel vapors are produced in a bubbler. In the bubbler, a carrier gas (argon > 99.9999% pure in this case) passes through a porous frit that is immerged into the liquid fuel. During this process, schematically shown in **Figure** 4-6a, the carrier gas entrains the fuel vapor till its saturation pressure. The fuel concentration depends on the mass flow rate of the carrier gas, thus it is required to maintain a constant inlet pressure in the bubbler line (around 4.1 ± 0.1 bar for most of the cases reported here). The bubblers could be also heated up using a hot water bath heater to increase the fuel concentration.

The carrier gas + liquid fuel are then introduced into a second bottle, called the catch pot, where the excess fuel droplets, if any in the carrier gas, are trapped. The carrier gas/fuel mixture is now ready to be send to the mass flow controller. Normally, no liquid is deposited in the catch pot after running thousands of experiments. This was observed for many fuels, including toluene, styrene and ethylbenzene; however, it can be taken as a security measure to avoid liquid going to the lines or to the mass flow controller. During operation, the liquid level must be constantly checked to refill when needed while running

experiments. Once the mixture exits the catch pot, it is directly to the respective mass-flow controller (MFC) which, along with the gases from the other two MFCs, can produce different desired mixtures, i.e. reduce the fuel vapor concentration by dilution with argon or prepare mixtures with oxygen/air and/or mixtures with other fuel components.

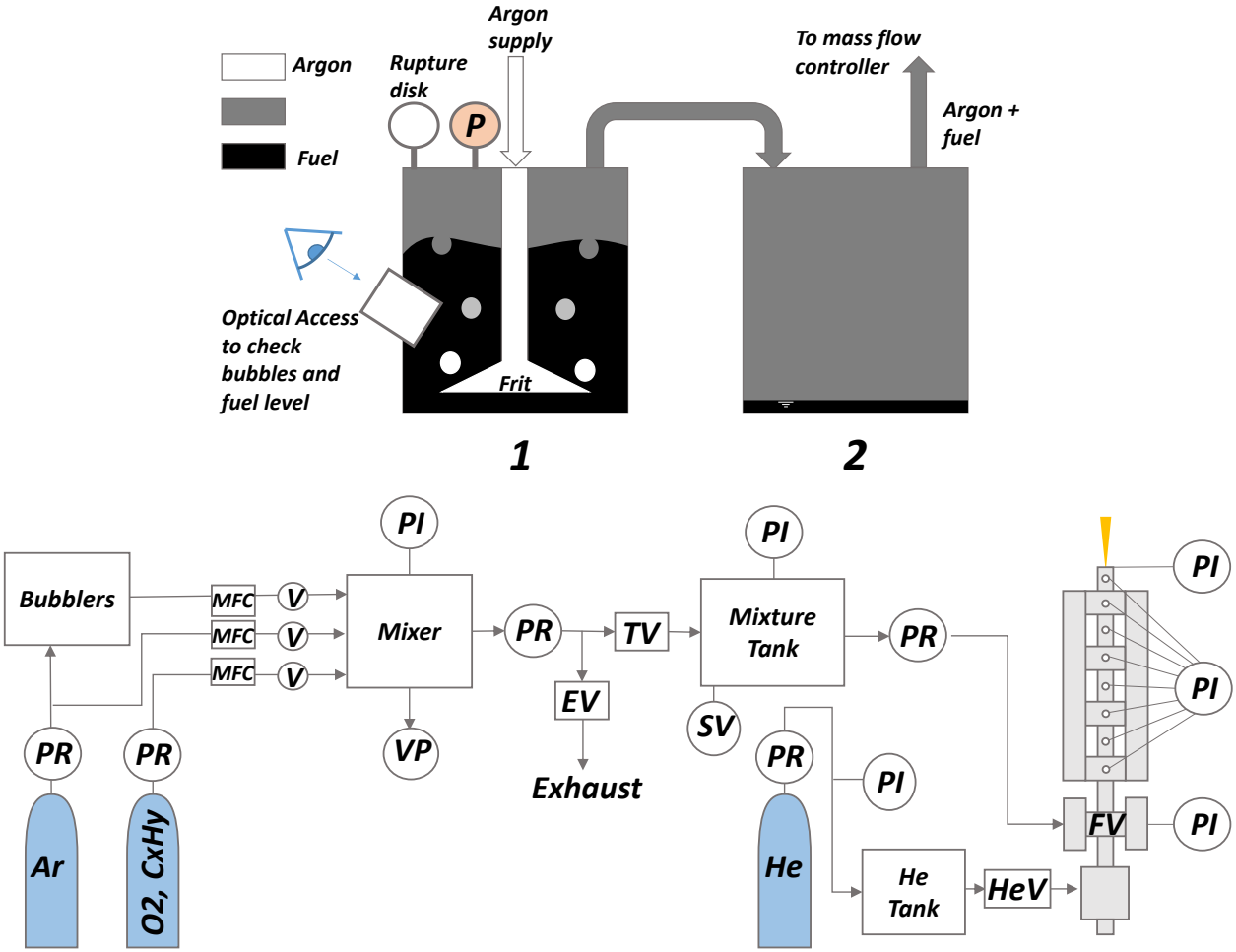

***Figure** 4-6. a) Schematics of functioning of bubbler for liquid fuel vapor production and b) Schematics of instrumentation used in the mixing rig.*

After passing through the MFCs, the mass flows are introduced into a manifold equipped with a static mixing element (mixer) and a Honeywell pressure sensor (PI) usually employed to check leak rates in the lines and eventually to trigger the security valve stopping the MCFs in case of overpressures inside the manifold. The flow can be started/stopped by acting solenoid valves (V) placed just after the MFCs. The fresh reagent mixture coming from the manifold is stored in a six-liters tank, which is equipped with a security valve (SV) with a rupture disc and a Honeywell gauge pressure sensor (PI). The signal of the pressure sensor allows the pressure inside the tank to be monitored, so that this is maintained in certain

desired range during HRRST operation. The tank can be refilled several times during the course of the batches of experiments (usually including thousands of runs). The mixing rig operation is entirely automated by making use of a LabVIEW application and an electronic control box. In particular, part of the mixture just after the opening of the solenoid valves Vs is vented through EV as the MFCs require some time before reaching the desired flow values. The procedure and technique have been proven to be very reliable in producing fuel mixtures with accurate concentrations [215].

The tank outlet is directly connected to a Matheson vacuum regulator which controls the pressure P1 below the atmospheric pressure. Between the vacuum regulator and the FV reservoirs, a check valve is connected to prevent breaking of the pressure regulator in case of back overpressure due to failure on the operation of the fill valve (FV). In that case, the 946 MKS vacuum system controller box will also send a relay signal taken from P1 sensor (usually set at 750 torr) to the mixing rig electronic box in order to close the helium valve (HeV) shown in **Figure** 4-6b and stop helium supply to the high-pressure driver section. In addition to this safety measure, an external manual Stop button is connected to the mixing rig box and it is placed close to the persons operating the system in order to stop mixing rig operation and close Helium valve (HeV) in case of emergency. In that case, a reset button is installed in the valve box to restart operation when required. Finally, the reagent supply line is connected to the reagent reservoirs of the fill valve (FV) at the desired pressure P1. Normally, in the postprocessing the first 20 shocks in a batch are not considered as this time is required to reach stable values of P1 and P4 for continuous operation of the shock tube.

4.1.1.5 Control and data acquisition

The ICARE-HRRST functioning is fully automatic. Control of the operations and the data acquisition are possible by making use of a LabVIEW software and a set of electronic and electro-pneumatic elements presented in **Figure** 4-7. Similar to the mixing rig, most of the elements are placed inside a portable and compact aluminum electronic rack (40x40x150 cm^3) that can easily be installed as a sole module and that is equipped with wheels allowing transportation during synchrotron campaigns. All the aluminum structures of the ICARE-HRRST are grounded during operation.

The control of the five custom-made pneumatic valves located in the driven section (EV, MVs, and FV) is done through a set of three double acting 5/2 electro-pneumatic valves (Parker-Viking Xtreme P2LCX513EEHDDN) all placed in a common pneumatic manifold. The three middle valves (MVs) are connected to a single 5/2 electro-pneumatic control valve, while the fill valve (FV) and the end valve (EV) are controlled individually. Two flexible lines go from each 5/2 electro-pneumatic valve outlet to the respective custom-made valve port entrance to supply/remove compressed air (minimum 5 bar) that controls the opening and closing position of the piston as shown in **Figure** 4-4b.

In total, six 12 Volt electrical signals actuate the solenoids of the three 5/2 electro-pneumatic valves. These are supplied by a home-made electronic valve box controller shown in **Figure** 4-7. The valve box receives six digital control signals generated by the LabVIEW software via a multifunction DAQ card (National Instruments PCIe-6361) through a BNC-2110 block adapter also shown in **Figure** 4-7 and accordingly, the electrical signals are delivered governing the operation sequence of the ICARE-HRRST.

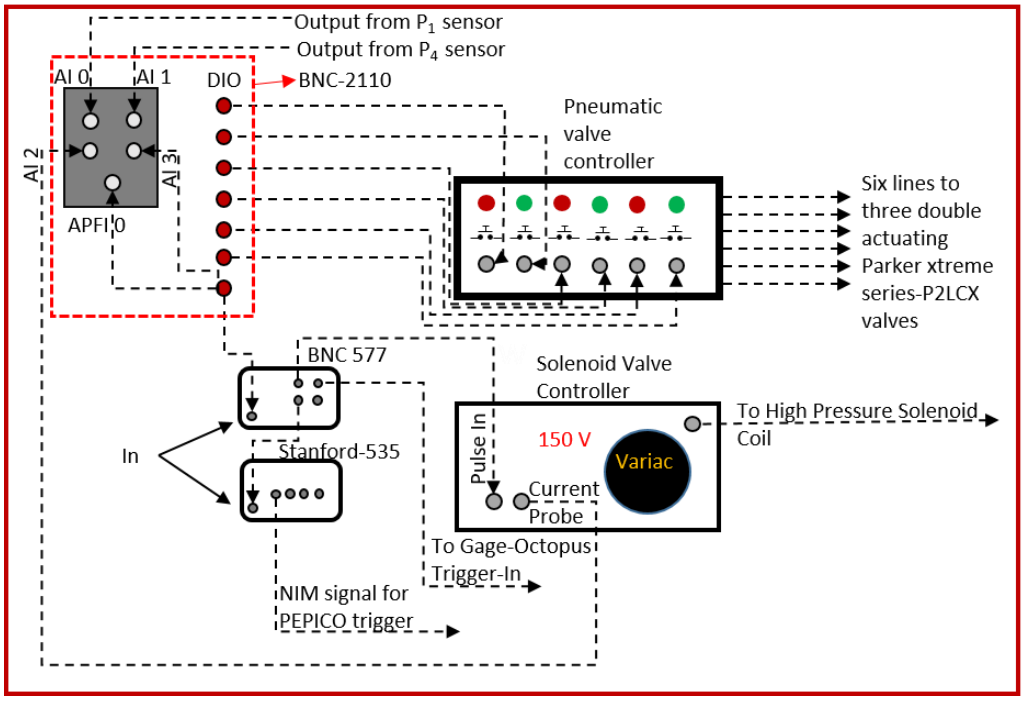

***Figure** 4-7. Schematic showing the connections between various components in the electronic system. The BNC-2110 is the connector block of the Pcie-6361 card.*

The shock tube is operated in a sequence similar to the strategy used in ANL-HRRST [22] and UIC-HRRST [216]. **Figure** 4-8 shows the digital pulse pattern over 1 Hz operation using the DAQ card which is also employed to record several analog signals like MKS 722B capacitance manometer (P1), Honeywell LM-BP211DL gauge pressure sensor (P4), 113B24 PCB pressure transducer PCB pressure sensor (P5) or even current probe from the high voltage box (HVB) to check current delivery status.

The majority of the cycle time is occupied by extracting the gases from previous experiments. Evacuation of the gases is obtained by opening the four custom pneumatic vent valves (EV and MVs). This is specified by the digital control signals EVo and MVo where the subscripts 'o' represent opening of the valve. After evacuation of the shock tube, the three middle valves MVs are closed using the same digital control signal MVc and after 100 ms the fill valve opens (FVo) for 300 ms. Valve EV remains open and overlaps with FV opening for 25 ms, after which signal EVc closes the venting valve. This overlap between EV and FV was chosen just to ensure flushing with fresh reagent mixture. Once the valve FV is closed, the driven low-pressure section is completely isolated and filled with new reagent gas mixture. In this moment P1 and P4 analog signals are recorded by the software via the DAQ and 100 ms after, a digital signal, also shown in **Figure** 4-8, is sent by the software to a BNC-577 DPG pulse generator that subsequently produces a 2-3 ms pulse. This pulse is used to trigger a high voltage box (HVB) shown in **Figure** 4-7. The high voltage is applied to activate the bobbin located in the high-pressure diaphragmless valve (driver section) opening the poppet for ~ 2 ms. During this very small opening time, the shock wave forms. 20 ms after the high-

pressure valve closure, the vent valves EV and MVs open again to evacuate the product gases. This is the start of a new cycle.

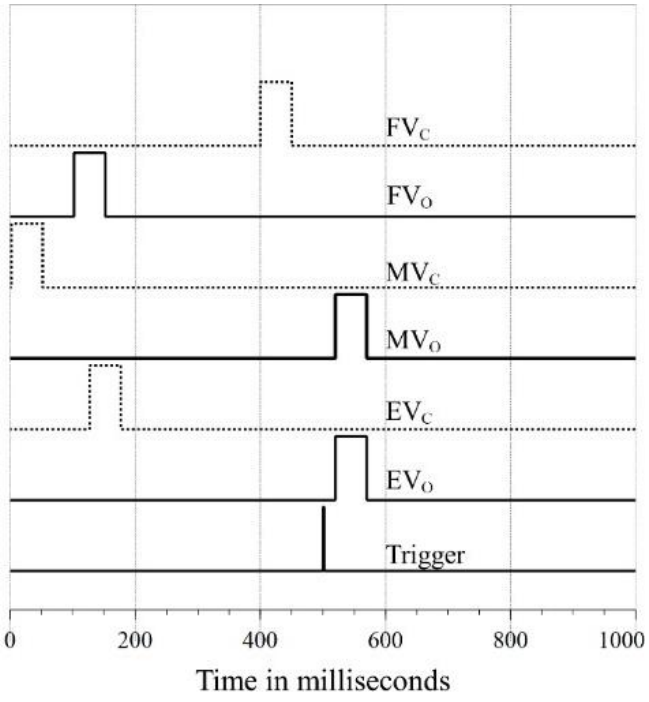

***Figure** 4-8. Pulse pattern, 1 Hz operations. EV, MV and FV denote end, middle and fill valves, respectively, subscripts O and C the open and close control signals.*

In addition to the pulse to the high voltage box, the BNC-577 DPG pulse generator produces a second pulse with a time delay of 3-4 ms with respect to the first one. This second pulse is used: i) as a trigger signal to start the spectral data acquisition in PEPICO detectors via a Stanford DG535 DPG; ii) to start recording all eight CHIMIE METAL pressure sensor analog signals via a 25 MS/s, GAGE-Applied Octopus digitizer PCIE card that is installed in the computer board. The eight CHIMIE METAL signals need to be amplified before being registered by the Octopus card. This is done by means of two home-made amplifier boxes each one with four available channels. For each channel, the software is capable to locate the incident shock, getting the time intervals and hence derive the shock wave velocity on-the-fly, allowing the monitoring of HRRST performance during continuous operation. Each cycle, all analog signals being acquired and calculated by the software (e.g. T5, P5, T2, P2, P1, P4) are stored in excel files in different groups of data, as preferred, for eventual post-processing.

4.1.2 Shock tube performances

As already stated, the ICARE-HRRST can operate at rates up to 2 experiments per second. Since averaging of the signals is mandatory for practical use with low signal-to-noise detectors, the shock waves have to be reproducible and desired temperature T5 and pressure P5 conditions to be kept almost constant over thousands of subsequent experiments. In addition, consistent time-history pressure profiles need to be obtained for kinetic purposes. In order to test the capabilities and characterize the performances of the shock tube, two different conditions, each one comprising one thousand experiments, were conducted in the laboratory using helium and argon as driver and driven gas, respectively.

Figure 4-9 presents the PCB pressure time-histories for temperatures T5 of 1509 K and 1297 K and pressures P5 of 7.3 bar and 7.8 bar, respectively, demonstrating that the ICARE-HRRST is capable to generate thousands of very reproducible experiments. It is shown in black the average over 1000 experiments which perfectly corresponds to one randomly chosen single pressure profile, which had to be offset +1 bar and -20 µs in order to be recognized. The only major difference between the single shot profile and the average one lies in the noise after the passage of the shock wave.

A larger dP/dt is present in comparison to ICARE single pulse conventional shock tube where nearly constant pressure conditions are obtained during the reaction time as shown in **Figure** 4-9. In fact, reducing the internal diameter from 78mm to 8 mm leads to non-ideal test conditions related to boundary layer growth which results in increasing pressure profiles from around 7 bar to 12 bar during the reaction time before a subsequent drop due to rarefaction waves. The non-idealities constitute a major disadvantage of using such a small apparatus. However, because these pressure profiles are very reproducible for a given range of T5 and P5, the time profiles can be introduced into chemical kinetic simulations without having significant consequences on the validity of the experimental results.

Another implication of having such high increase on pressure is the need to consider pressure variation inside the mass spectrometer chambers at synchrotron beamlines as it will be described on the following chapters where quantitative measurements are attempted. Additionally, since shock tube bore is very small, PCB and nozzle cannot be installed simultaneously during synchrotron campaigns.

Considering the observation time as the time before the arrival of the rarefaction waves, for the higher temperature case with T5 = 1509 K and P5 = 7.3 bar, the test time is shorter, around 500 µs, compared to the lower temperature experiment with T5 = 1297 K and P5 = 7.8 bar (test time around 650 µs). This is consistent with observation times reported for ANL-HRRST of ~300 µs with a smaller bore of 6.3 mm[23], UIC-HRRST of ~700 µs with bigger bore of 12.7 mm [216] and HRRST designed by Matsugi of ~500-650 µs observation time and the largest bore of 15 mm [217]. On the other hand, the rarefaction waves in this case do not generate a fast drop in the temperature and pressure conditions as for the case of the single-pulse shock tube in **Figure** 3-2. Thus, in reality, the reactions will continue for some time after the pressure reaches its maximum value, and the observation time can be extended as it will be shown in the next chapter concerning the kinetic measurements from aromatic fuel pyrolysis.

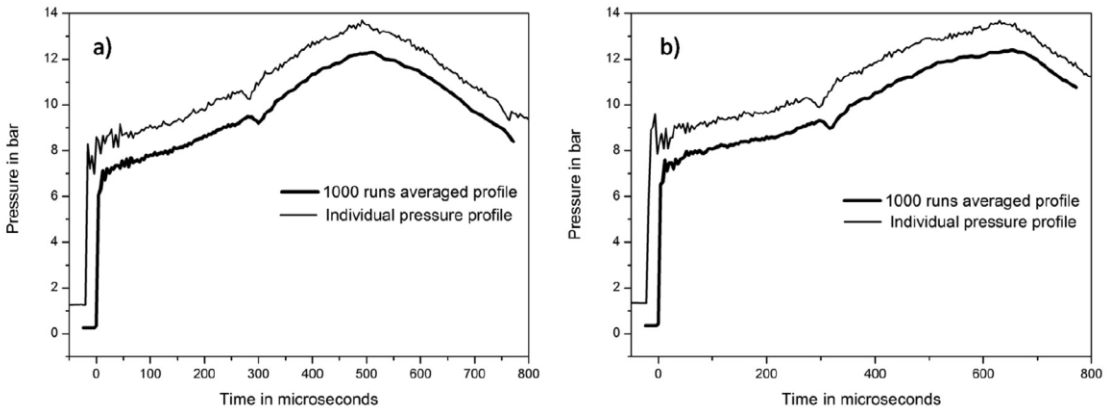

***Figure** 4-9. Pressure time-histories for a single experiment and an average pressure over 1000 experiments for the following conditions: a) T 5 = 1509 K, P 5 = 7.3 bar; b) T 5 = 1297 K, P 5 = 7.8 bar. For clarity, the individual pressure profiles are offset relative to the averaged profile (+ 1 bar, -20 µs). Without the offset, the profiles would be largely indistinguishable.*

The shock tube length may also influence the observation time and attenuation. For instance, as will be discussed later, SAPHIRS vacuum chamber at the DESIRS beamline allows the installation of the miniature HRRST only with longer driven section length compared to the one employed in the laboratory for the experiments in **Figure** 4-9. **Figure** 4-10 shows the average over thousand pressure profiles for T5 of 1351 K and P5 of 6.4 bar obtained with shock tube length as used at SOLEIL Synchrotron (~129.5 cm). The larger shock tube length results in similar observation times of ~650 µs for the conditions studied. Additionally, the pressure profile shape remains similar to the case in **Figure** 4-9b with comparable pressure increase from 6 bar to 11 bar, in this case.

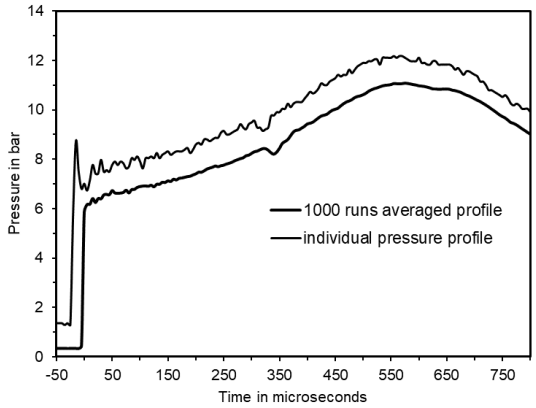

***Figure** 4-10. Pressure time-histories for a single experiment and an average pressure over 1000 experiments for T5 = 1351 K, P5 = 6.4 bar and standard deviations of 13 K and 0.13 bar, respectively. For shock tube length used in SOLEIL.*

The measured reflected conditions P5 for each shock in **Figure** 4-9 are determined by averaging the first 40 µs of the pressure signal after the arrival of the shock wave. Additionally, the reflected pressures P5

were also calculated by extrapolating velocities based on last five CHIMIE METAL sensors to the end-wall of the shock tube and solving the conservation equations. Measured and calculated P5 are reported in **Figure** 4-11a presenting an excellent agreement. It can be seen that at two different conditions (1509 K and 7.3 bar, 1297 K and 7.8 bar) the standard deviation for the measured pressure is lower than 0.14 bar.

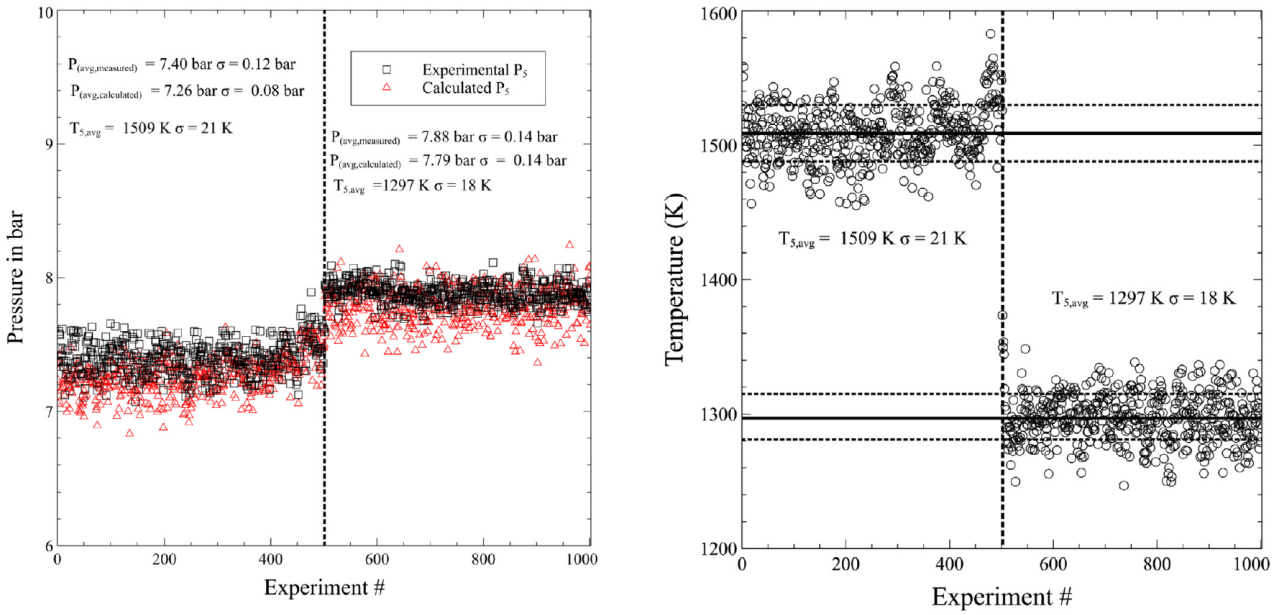

***Figure** 4-11. a) Distribution of measured and calculated reflected shock pressures using extrapolated velocities to the end-wall of the shock tube, b) Distribution of calculated reflected shock temperatures using extrapolated velocities to the end-wall.*

Figure 4-11b reports the calculated temperatures behind the reflected shock waves using extrapolated shock velocity. The variation of T5 and P5 can be due to the variation of P1 and P4. Particularly, P5 has similar behavior of P1 variation and P1 may change as the filling reservoir tank empties and start a new filling shift. However, for both cases the standard deviation is less than 21 K, which is a remarkable result with respect to the reproducibility that can be obtained with regular shock tubes which is around 30-40 K. This demonstrates the great performance capabilities of ICARE-HRRST in terms of reproducibility of temperature and pressure at reflected shock conditions.

4.2 HRRST/i^{2}PEPICO coupling

4.2.1 HRRST at DESIRS VUV beamline

With 354.097 m circumference and dedicated to the study of matter at atomic level since year 2013, Synchrotron SOLEIL is the 2.75 GeV third generation French national light source facility located near Paris, France. Injection and subsequent acceleration of electrons along a circular path provide synchrotron radiation (SR) to 29 beamlines, including an extremely stable VUV photon beamline [218], named DESIRS [75]. The miniature ICARE-HRRST design is conceived to be small enough in order to be coupled with SAPHIRS permanent photoionization molecular beam end-station located at the monochromatic branch A of a VUV undulator-based beamline DESIRS [75].

DESIRS VUV undulator-based beamline covers a wide range of energies of 5-40 eV offering very high-resolution spectroscopy, high photon flux (10^{10} to 10^{13} photons/sec) and precisely calibrated polarization control. During experimental campaigns in DESIRS, high spectral purity was obtained by adding an argon gas filter that eliminates high harmonic contamination. Once high order photons are removed, a 200 g/mm low dispersion grating is used to deliver photons with resolution of ~15-25 meV for typical photon energy range of 8.5 – 11 eV employed in this work.

The photoionization process takes place inside the mass spectrometer vacuum chamber of SAPHIRS end-station where double imaging particle photoelectron photoion coincidence (i^{2}PEPICO) spectrometer, DELICIOUS III, is installed [24], [76]. It combines a velocity map imaging device (VMI) for photoelectrons detection and a modified Wiley-McLaren time of flight (WM-TOFMS) momentum imaging analyzer for photoions detection. Then electrons and ions are extracted from the ionization region to the electron and ion analyzers by means of an electric field. On the ions side a full 3D ion momentum distribution is obtained from its TOF, each ionization event is tagged and correlated with ion position on a 40 mm position-sensitive detector (PSD) and the arrival time of each electron on the electron PSD. Photoelectron kinetic energy images are collected in the electron side using an additional 80 mm PSD and then filtered by ion mass and momentum using a coincidence scheme. Electron images can be Abel inverted to reconstruct the photoelectron's Newton sphere using the pBasex algorithm [219]. By applying this procedure, it is possible not only to determine the mass of the ions like any other mass spectrometer, but also the photoelectron spectra for each mass, allowing the identification of complex mixtures of PAH isomers as the ones produced pyrolytically in the miniature ICARE-HRRST.

4.2.1.1 Mechanical coupling

The miniature ICARE-HRRST was coupled to the ionization vacuum chamber where DELICIOUS III is installed, via a double differentially pumped molecular beam sampling interface [76]. A schematic view of the installation at SOLEIL is shown in **Figure** 4-12. In particular, part of the driven section containing the four exhaust valves of the shock tube is placed inside the inner vacuum chamber (in red) with the nozzle facing two skimmers. The inner vacuum chamber is a continuation of the main vacuum chamber.

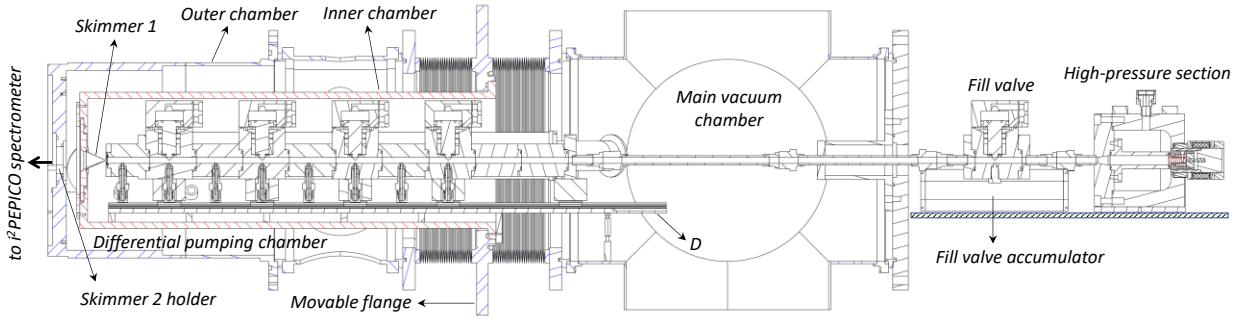

***Figure** 4-12. ICARE-HRRST coupled with DESIRS-SAPHIRS. A : DESIRS-SAPHIRS outer chamber; B : DESIRS-SAPHIRS inner chamber; C : movable support flange for chamber B; D : slab with linear guides*

The nozzle/skimmers alignment represents the first challenge to be faced in order to obtain optimal conditions in HRRST/i^{2}PEPICO coupling. The complication in the alignment is due to the fact that DELICIOUS III spectrometer is relatively far from the entrance of the main vacuum and any misalignment translate into either low quality of the molecular beam, or incorrect sampling of the gases eluting from the nozzle which leads to a decrease in the signal level. Additionally, the fill valve and high-pressure section are kept outside due to space restrictions in the main vacuum chamber and safety precautions, this fact has added more difficulty to the mounting/dismounting and alignment processes.

Gas extraction towards the spectrometer chamber is made through different adiabatic expansion stages. The main vacuum chamber is where the supersonic jet first expansion is taking place. A second expansion occurs between the two skimmers in a differential vacuum chamber allowing the entrance of the molecular beam to the i^{2}PEPICO spectrometer vacuum chamber characterized by high vacuum performance [76]. A gate valve isolates the spectrometer vacuum chamber from the differential chamber and can be used when the main vacuum chamber is opened for routine maintenance or modifications in the set-up. All the three vacuum chambers of SAPHIRS are evacuated by turbomolecular pumps with a reference pressure in the range of 10^{-8} torr without gas load. During normal shock tube continuous operation, the pressure levels inside the main chamber, the differential chamber and the spectrometer chamber were always monitored during shock tube operation and kept below the 10^{-4}, 10^{-6} and 10^{-7} torr safe ranges, respectively. The double differential pumping constitutes a great advantage of SAPHIRS end-station for high pressure - high repetition rate experiments where efficient gas extraction is needed to significantly reduce the risk of damaging the instruments due to overpressures.

In order to be able to maintain a good alignment between the nozzle and the skimmers even after several mounting/dismounting of the HRRST and considering that big part of the weight of the shock tube is supported by the inner vacuum chamber, a new custom-made inner chamber design was developed. **Figure** 4-13 shows how the miniature, ICARE-HRRST is mounted on an 80 mm wide aluminum plate (P1) equipped with two 720 mm PBC Mini Rails in order to allow shock tube displacement inside the chamber for easily removal/insertion. Each pneumatic valve (EV, MVs) and one connecting element (R) are equipped with a support with two sliding carriages allowing the shock tube to move axially over the two

PBC Mini Rails. Other four carriages are used as stoppers that precisely fix the desired relative position of the shock tube with respect to the skimmer.

The plate P1 is mounted inside the inner vacuum chamber with seven aluminum supports (A, L1 and L2) fixed to it. The five supports (A) are curved in the bottom taking the shape of the internal diameter of the chamber. Plate position is fixed to the vacuum chamber by means of a pin and two screws between L1 and the vacuum chamber flange. The adjustable support (L2) was conceived to support the initial part of plate P1 on the inner surface of the main chamber, as can also be noticed in **Figure** 4-12. All seven supports transfer the weight held by plate P1 to SAPHIRS inner and main vacuum chambers. In addition, six threaded rod supports are inserted at end part of the inner chamber close to the skimmers. These can be regulated until they are in contact with the differential chamber's internal surface once the shock tube alignment is optimized. Thus, these supports add rigidity to the inner vacuum chamber. The inner chamber is also equipped with a flange attached to SAPHIRS movable flange (XYZ). This allows the isolation between the differential chamber and main vacuum chamber and the optimization of the alignment between the shock tube axis and the second skimmer axis.

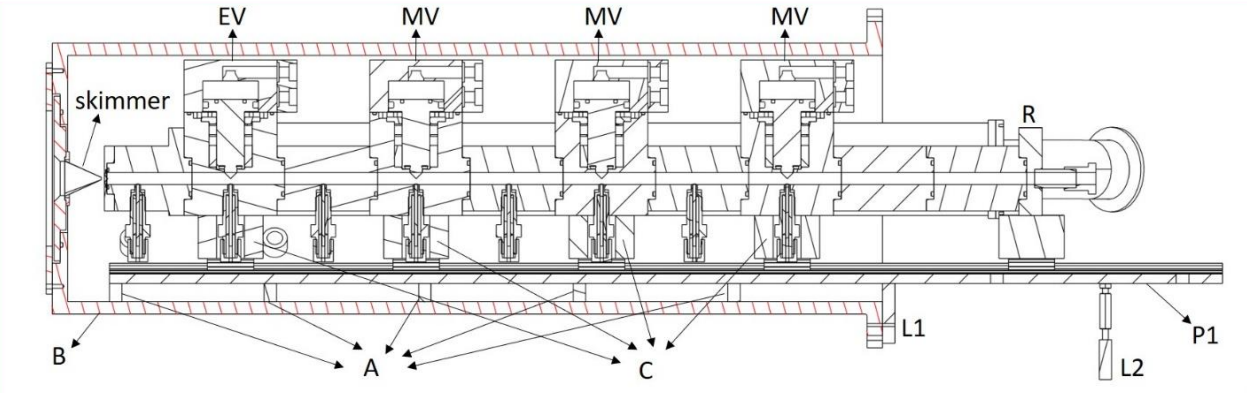

***Figure** 4-13. ICARE-HRRST inside SAPHIRS. A: support for the plate; B: internal chamber; C: supports with two sliding carriages; P1: plate with two PBC Mini Rails; R: connecting element; L1: plate support fixed to the cylinder B; L2: adjustable support; EV: end valve; MV: middle valves.*

When dismounting of the shock tube is required, a second plate P2 is added to extend plate P1 length until the exit of SAPHIRS. Both plates, with similar dimensions, have small tolerance machined slots used to precisely fit with an aligning slab. The slab is screwed on P1 and P2 top side and a third plate (P3) is screwed on their bottom side, adding rigidity. A detailed 3D view of these details when shock tube is mounted inside SAPHIRS during experiments and when dismounting operation is required can be found in annex **A 1**. During shock tube removal, plate P2 is supported on a custom-made external structure by means of three adjustable feet. The custom-made external structure was specifically built to, i) sustain the external parts of the ICARE-HRRST, ii) facilitate displacement of main external parts during mounting/dismounting of the shock tube, iii) align high pressure section and fill valve and connect them with the part of the shock tube inside SAPHIRS. A schematic isometric view of the support structure built around SAPHIRS is shown in **Figure** 4-14. An aluminum plate P4 is used to hold the fill valve (FV) with its

two reservoirs and the high-pressure section. Although the helium reservoir tank is placed on a higher-level plate, it is solidary with the rest of the main parts sharing the same movements. Because the plate P4 needs to be displaced in function of the movements of the inner vacuum chamber during skimmer 1 and skimmer 2 alignment, P4 can move up, down and even rotate relative to SAPHIRS. For this reason, P4 is connected to another aluminum plate (P5) by means of four threaded rods. The rods are fixed on plate P5 using nuts on its upper and bottom sides. The angle and level of P4 relative to SAPHIRS is regulated with respect to P5 as needed to maintain the alignment between the shock tube parts inside and outside SAPHIRS. In particular, the fill valve FV is connected to the shock tube part inside SAPHIRS through a set of two tubes equipped with BCO connections until the connecting element R of **Figure** 4-13. The assembly is presented in **Figure** 4-12. The first tube connected to FV is attached to a flexible bellow acting as feedthrough that isolates the vacuum chamber from the external ambient. At the same time, the bellow allows relative movement of the inner chamber with respect to the main vacuum chamber. The feedthrough is mounted on the center of a custom-made flange labeled as *end-flange* in **Figure** 4-14 which has a circular clearance to freely move and align the external parts with the inner parts as evidenced in **Figure** 4-12. The end-flange is also attached rigidly to the custom-made external structure by means of Bosch profiles. Thus, during dismounting, the flange can move together with the external structure in all directions.

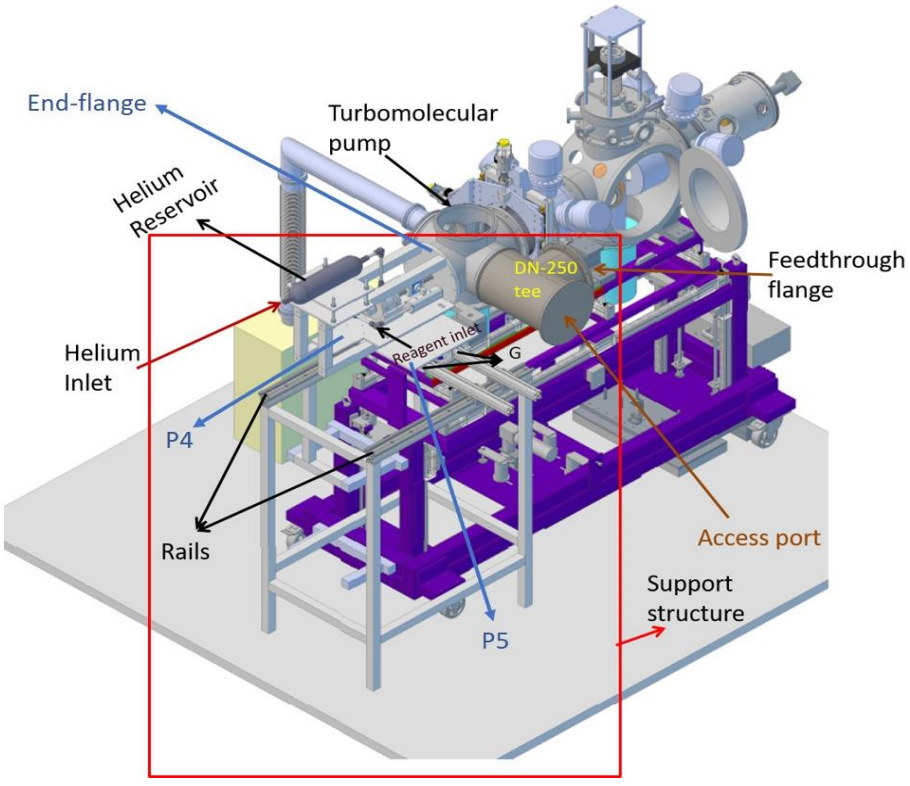

***Figure** 4-14. Isometric view of the structure built around SAPHIRS to aid removal of the HRRST. G: Eco-slides. Feedthrough flange contains ports for pressure sensor feedthrough, air supplies, and vacuum lines. End-flange. Helium and reagent inlet. Plate P4 and Plate P5.*

To allow external maneuvering, two movements parallel to the floor were enabled in the external support structure design. P5 is equipped with four Eco-slides (G) that allow transversal movement over two Bosch Rexroth profiles that at the same time are carrying four sliders placed on two aluminum rails that are parallel to the shock tube axis. The axial and lateral movements are used to remove the complete fill-valve/HP-valve/he-tank/end-flange subsystem and clear the space for access to the main vacuum chamber and for introducing or removing the shock tube. The accuracy of the sliding system is sufficient for allowing subsequent operations with consistent alignment between the different elements. The load of all the elements is supported by a structure with aluminum columns and beams that is accommodated around SAPHIRS/DESIRS beamline and connected to the DESIRS structure or to the floor.

Another challenge on the installation is to prevent leaks inside the main vacuum chamber since several pneumatic lines, vacuum bellows, pressure and temperature sensors were introduced inside SAPHIRS. This was possible by making use of vacuum feedthroughs and Swagelok connections mounted in a DN-250 flange that was coupled to a DN-250 *tee* installed perpendicularly to the shock tube and main chamber's turbo molecular pump axes. This position allows the minimization of bending and curvature of the vacuum bellows from the exhaust vacuum manifolds of the ICARE-HRRST and easy access to the shock tube from the lateral side during mounting and dismounting. In addition, easy access to the custom-made feedthrough element for the CHEMIE METAL signals and the quick-connect fittings for the compressed air lines is granted through the free side of the DN-250 tee, named access port in **Figure** 4-14. By using a transparent blank flange, this access functions also as a monitoring window when the system is operating under high vacuum conditions.

As mentioned above, the first challenge on the installation of the HRRST at SOLEIL consists in the alignment between the nozzle and the skimmer 1 of the SAPHIRS two-stage differential pumping system. Initially, this was obtained in the laboratory using a regular laser to center both nozzle and skimmer orifices prior to the experiments in SOLEIL. Multiple mounting and dismounting of the HRRST did not modify the alignment. **Figure** 4-15 shows an expanded view of one of the nozzle/skimmer 1 configuration employed in the coupling of ICARE-HRRST with SAPHIRS molecular beam sampling interface. Here, the shock tube end-wall section is holding the divergent nozzle, while parts A, B and C keep skimmer 1 position fixed relative to the end-wall of the inner vacuum chamber. The base of the skimmer 1 is held by a movable plate B and the clamp ring A that are attached together by a circular pattern of eight screws. Radial and angular movement of skimmer 1 is then allowed since plate B has a clearance (3 mm) with respect to the groove machined on the inner chamber end-wall external surface. To avoid leaks between the main vacuum chamber and the differential chamber, an o-ring is placed between part B and the inner vacuum chamber surface. Once the skimmer 1 is aligned by laser, plate B can be permanently clamped by tightening 8 screws between plate C and the external face of the inner chamber end-wall. Thus, skimmer 1 will be fixed and aligned with the shock tube and nozzle axes.

Once the shock tube is mounted on the plate P1 inside the inner vacuum chamber and the stoppers correctly placed in the rails, the nozzle and skimmer will be separated at the desired distance. Additionally, since nozzle is perfectly aligned with the shock tube axis, they will be automatically parallel with the inner chamber axis because of the geometrical restriction given by the five curved supports A and L1 shown in **Figure** 4-13. This alignment will not change with shock tube displacement since rails cannot move relative to the inner chamber.

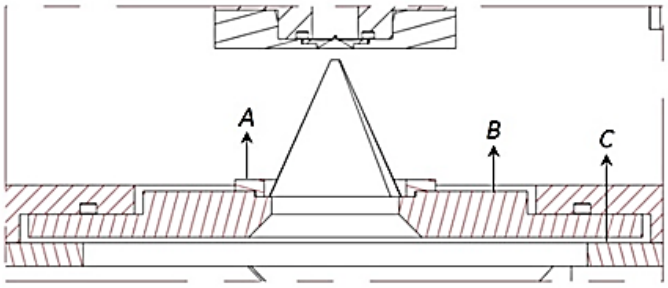

***Figure** 4-15. Expanded view of the HRRST end-wall section showing the nozzle and skimmer 1.*

As a first approach to the implementation of the technique, the configuration presented in **Figure** 4-15 allows the variation of the position of the nozzle with respect to the skimmer 1 while keeping them aligned over several shock tube removals/insertions into the inner chamber. However, in the case the skimmer 1 needs to be replaced during the course of an experimental campaign, it is better to reduce the time invested in the laser alignment procedure, even more for synchrotron campaigns where the beam time and space are very reduced and an optical system cannot always be easily set-up.

Several improvements can be done to this system in order to obtain a more versatile alignment method that would allow the change between different skimmers and nozzles to facilitate determining their optimal diameters/separations that maximize the signal-to-noise ratio. For this reason, a different configuration is presented in **Figure** 4-16a where a sort of aluminum *bird cage* was designed to be attached to the plate holding the skimmer. The *Bird cage* and skimmer holder are rigidly connected keeping their axes perfectly aligned and fixed with low tolerances. Subsequently, the end part of the shock tube is introduced inside the *bird cage* and since the tolerance between them is very small (< 0.01 mm) the alignment between nozzle and skimmer 1 will be ensured. Finally, and similar to the method shown in **Figure** 4-15, the plate C can be clamped to the inner chamber end-wall to fix skimmer 1 to it.

An additional adjustable clamp was attached to the end part of the shock tube acting as a stopper when shock tube is introduced. Thus, the desired axial separation between nozzle and skimmer 1 is also guaranteed. **Figure** 4-16b and **Figure** 4-16c show a 3D section of the inner chamber with the *bird cage* installed on it and end part of the shock tube inserted into the *bird cage.*

Once shock tube and nozzle axes are aligned with the skimmer 1 axis inside the inner chamber, it is required to align the whole system with skimmer 2 too. Skimmer 2 position is fixed and aligned with the ionization region of the mass spectrometer vacuum chamber. The alignment is done by partially pressurizing the inner chamber with argon so that a supersonic jet is created between skimmer 1 and skimmer 2 and a molecular beam is introduced to the i^2PEPICO ionization region. Once argon gets ionized by the synchrotron radiation, the ion and electrons signals can be maximized by moving the inner chamber axis. This procedure can be done under high vacuum with SAPHIRS motor driven movable flange (XYZ) with a very high precision. However, since the inner chamber axis moves together with the flange and the shock tube is relatively heavy, the HRRST could not be mounted inside SAPHIRS for alignment of skimmer 1 with skimmer 2. Nevertheless, measurement of the signal intensity with and without the shock tube

inserted into the inner chamber showed that the alignment was kept. The distance between the two skimmers is also set-up as needed. All diameters and distances chosen for the nozzles and skimmers are discussed in the results section showing how these dimensions impact the signal quality.

During dynamic high repetition operation, the shock waves warm up the end part. More importantly, under vacuum conditions convective heat loss is negligible and avoiding excessive heating up is required. Therefore, two thermocouples are mounted in the end part and EV during synchrotron campaigns not only to measure the initial temperature T1 but also to monitor the temperature of the valve. The thermocouple cables are connected to a KF 40 K-type feedthrough, while the temperature measurements are acquired as an analog signal input via the DAQ PCIe-6361 card.

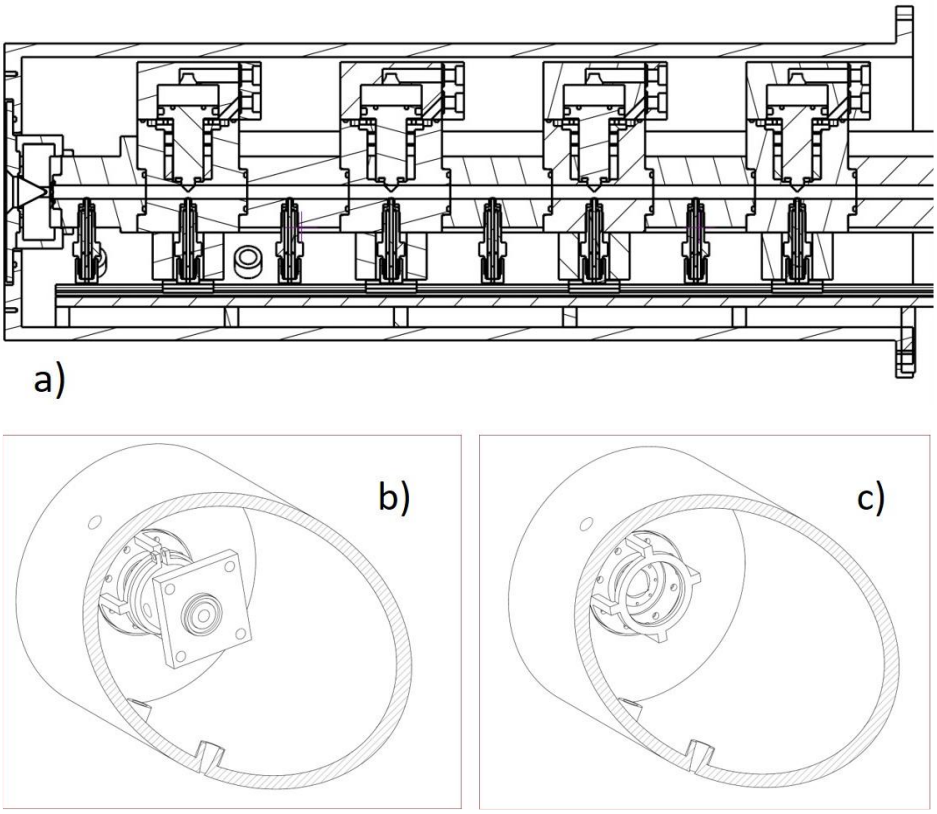

***Figure** 4-16. Cross-sectional view of the HRRST inside SAPHIRS showing the mechanical alignment system (a). 3-D section of the chamber showing the HRRST terminal section inserted into the cage (b) and the cage mounted at the end of the chamber (c).*

4.2.1.2 Data acquisition and processing

In order to trigger the DELICIOUS III acquisition with respect to the HRRST operation, for every experiment a NIM signal needs to be produced. For this purpose, a Stanford DG535 DPG was used to generate the NIM signal as triggered by the BNC-577 DPG controlling the shock tube running cycle. This allows the shock

tube and detector to be synchronized. The NIM signal is sent to a Time to Digital Converter (TDC) to start the recording of the signal from the mass spectrometer. Photoionization events release ions and electrons that fly to the position sensitive detectors PSD and that are associated with each experiment. These events are counted by the TDC with a time step of 120 psec immediately when they arrive to the detectors. The time and position information are acquired, accumulated and stored for post-processing using IGOR software and DELICIOUS III subroutines developed by DESIRS beamline scientists. Averaged signals can be also monitored on-line while acquisition is running to check for any eventual problem.

In particular, the IGOR software allows a flexible analysis of the acquired spectral information. For example, the ion masses which are related to ion times and electron times can be filtered by interval of experiments also called '*pulses'*. This constitutes a good advantage of the post-processing tool, since experiments or events that do not correspond to the desired conditions can be excluded from the analysis without affecting the quality of the resulting averaged signal. For instance, if shock tube nozzle is blocked during a period of time while running, the gases introduced into the spectrometer will be reduced and thus, the ion and electron counts on TDC will be reduced, decreasing the average signal level during that interval of time. Or if beam light intensity is varied during some moment of the operation, this spectral data can be excluded from the analysis too. Similarly, in synchrotron campaigns several adverse possibilities can be presented during data acquisition and information can be binned or chosen as desired also based on T5 and P5 ranges. Finally, the i^{2}PEPICO data can be filtered by coincidence events in order to produce electrons and ions time of flight matrixes, projected mass spectra, projected mass selected time profiles or photoelectron spectra.

Spectral data acquisition from DELICIOUS III mass spectrometer can be performed in two different ways. In the first mode, also called *"pulsed mode"*, for each experiment a trigger signal is sent to the TDC to acquire data over a time span of 8 ms that contains the pre-shock and post-shock conditions. The raw data is accumulated over thousands of runs and a matrix of single ionization events as function of ion time-of-flight, and the electron time of flight can be produced. **Figure** 4-17 shows an example of raw spectral data obtained averaging around 107 000 experiments for an initial toluene concentration of 0.1% in argon, initial temperature around 1362 K and pressure of 6.6 bar. Thus, since arrival of the photoelectrons is relative to the shock arrival, they contain the kinetic information for the respective ion TOF which is linked to the mass-to-charge ratio (m/z). This assumption is possible since the electron time-of-flight is in the order of nsec, being independent of its initial kinetic energy and negligible to the ion kinetics time scale which is in the order of µs. Thus, ion mass kinetics information and mass spectra can be extracted from raw spectral data by projecting the electron/ion TOF matrix with respect to the electron TOF axis for each ion mass and with respect to the mass-to-charge ratio axis, respectively, as will be discussed in the results section.

The data obtained using the pulsed acquisition mode can be used to obtain mass spectra, time-history profiles for selected m/z ratios, and mass selected photoelectron spectra (PES) tagged by experiment number, ion mass and reaction time. However, due to the specific pulsed character of the HRRST operation, considering the limited time available at the accurate PES signals can be obtained only for species with relatively high concentrations while they are somehow relatively low and poorly defined for heavier low concentration species like PAHs. In order to overcome this limitation and obtain larger PES signals for the PAH species, a second acquisition mode was evaluated called "*continuous mode*". In this mode the acquisition does not stop between the experiments and data is continuously saved and

averaged helping in increasing the number of electron and ion counts and thus the signal-to-noise ratio for low concentration products as the PAHs. Additionally, if the photon energy is chosen close to the ionization energies of most PAH compounds (typically PI < 8.5 eV), PES signal for the PAH products will be maximized obtaining sharper peaks that allow the identifications of isomers of each m/z. In general, the energies chosen for the pulsed mode are intended to allow the measurement of the fuel as well as the main aromatic intermediates and certain small products, while the continuous mode is focused specifically on the PAH species.

As evident and unfortunate, kinetic information cannot be extracted from data obtained using the continuous acquisition mode since there is not synchronization between the shock tube experiment and the mass spectrometer data acquisition. Another fact that needs to be taken in mind is that the PES signals from the continuous mode can not be exactly associated with the kinetic profiles from the pulsed mode as the PESs are obtained from signals covering not only 8 ms but larger experimental times. On the other hand, in the case where PES signals are large enough for both methods, the spectral features are similar even if better defined in the continuous mode case.

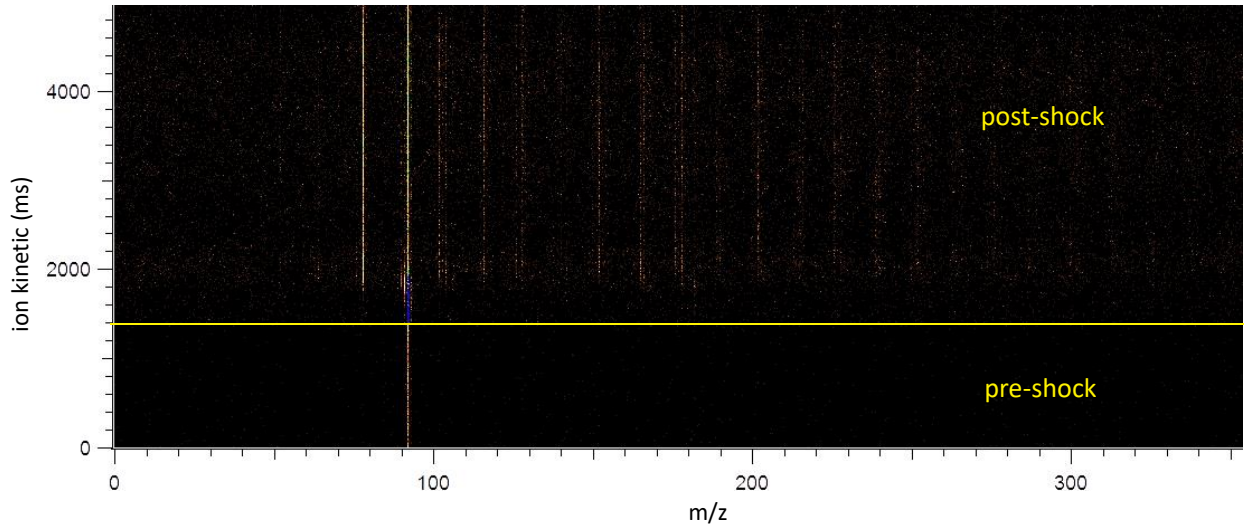

***Figure** 4-17. Example of raw spectral data obtained using an initial toluene concentration of 0.1% in argon, initial temperature around 1362 K and pressure of 6.6 bar.*

Another aspect which was raised during the first experimental campaigns is related to the accuracy of the kinetic profiles. In particular, the challenge relates to the capability to extract not only qualitative but also quantitative profiles. First, the pressure inside the mass spectrometer is subject to a strong variation after the passage of the shock wave. But, due to restriction in the flow though the nozzle, this variation is slow relative to the sudden rise in pressure from P1 to P5 inside the shock tube. The pressure build-up inside the mass spectrometer chamber must be considered in order to reflect the changes on species composition inside the shock tube. In addition, due to the non-idealities behind the reflected shock waves, the variations in pressure during the observation time are large and may lead to changes in the mass

spectrometer pressure and consequently in the signal levels. These changes have to be corrected too. In conventional shock tubes / TOF-MS apparatuses, the problematic of corrections for the kinetic profiles has been already addressed, where an internal standard (often argon) is added to the initial mixture [15]. On the other hand, the internal standard technique is not very practical at synchrotrons, as the photon energies usually employed are relatively low and internal standards capable to ionize at these energies but not participate to the reactions are difficult to find. An external calibration method is presented in the results section where CO_2 is used as an external standard to consider for pressure fluctuations inside the mass spectrometer chamber.

The discussion presented in the previous paragraphs indicates how obtaining a sufficient signal-to-noise ratio signal is somehow challenging for a dynamic system as the HRRST. In fact, the maximum repetition-rate is 1-1.5 Hertz by overheating of the valves and especially by the limited pressure allowed inside the mass spectrometer chamber. These limitations cannot be avoided. Although this repetition rate range is very high for a shock tube it is a low repetition rate pulsed source resulting in an effectively low duty cycle for the i^{2}PEPICO instrument. Still this rate is not dissimilar to pulsed photolysis sources (4–10 Hz) used with other experiments that employ VUV- PIMS [220].

On the other side, a bigger number of counts and thus a greater signal can be obtained by increasing the photon flux. However, considering that i^{2}PEPICO works at very low ionization events per photons pulse (<0.01), increasing the photon flux by changing the slit and cache can increase the so-called false coincidences increasing the noise and consequently decreasing the S/N ratio. In general, a relatively-low photon flux is necessary for i^{2}PEPICO measurements. For the experiments presented here the grating *slits* were kept mainly in the range of 200-400 µm (average around 300 µm) and *cache* was set between 0.8 and 1.

There are conditions for which the photon flux was varied intentionally with the goal of keeping the same average counts per shock during continuous operation. One example is the drop in the average counts due to partial nozzle blockage. This drop could be compensated by increasing the photon flux. When the number counts become too small or the nozzle is fully blocked, the HRRST has to be dismounted and the end part including the nozzle have to be fully cleaned. The procedure of venting the chamber, dismounting the shock tube, cleaning the nozzle, mounting the shock tube, and evacuating the chambers until de desired vacuum levels takes approximately 1 hour and 30 minutes.

For continuous acquisition mode where no kinetics is intended to be obtained, lowering the repetition rate and delaying the products extraction from the shock tube was observed to increase the number of counts and the signal level. This is probably linked to the residence time of the species inside the shock tube and consequently to the amount of gas injected into the i^{2}PEPICO chamber. This hypothesis needs to be proven in future synchrotron campaigns.

4.2.2 HRRST at X04DB VUV beamline

Although the dimensions of the ICARE-HRRST were predetermined to make it fit at the DESIRS beamline of synchrotron SOLEIL, some modifications can be performed in order to couple it with other European synchrotrons. For instance, the coupling of the ICARE-HRRST with the i^{2}PEPICO detector available at the

X04DB VUV beamline (SLS/VUV) of the Swiss Light Source (SLS) at Paul Scherrer Institut (PSI) presented different challenges that had to be faced before and during the experimental campaign. Even the simplest aspects like the logistics involved in bringing the equipment to the SLS facility in Switzerland are different, considering customs clearance and rules for scientific equipment shipment, larger travel hours and lower error margin compared to SOLEIL which is close to the ICARE laboratory. However, the experience already gained during the implementation of the technique at SOLEIL was crucial for the development and implementation at the specific conditions at SLS where the i^{2}PEPICO detector was coupled for the first time with a high repetition rate shock tube. Only one campaign could be completed at the moment.

At SLS, electrons are accelerated along a circumference of 288 m. The synchrotron radiation (SR) is directed to the X04DB SLS/VUV beamline using bending magnets. Then, the light is collimated and passed through gratings being capable to produce ultraviolet monochromatic light in the range of 5-30 eV. If the desired photon energy is higher than 15.759 eV, a 80 cm gas filter can be filled with Ne or Ne/Ar in order to filter out higher harmonics [221]. Since photon energies used during the implementation of the technique were kept below this level, no gas filter was used in the campaign at SLS.

The beam light enters the mass spectrometer chamber and it is aligned with the mass spectrometer's skimmer so that ionization of the molecular beam can occur. Electro valves and manual valves are available after the gas filter and just at the entrance of the mass spectrometer (MS) chamber in order to isolate the chamber from the ultra-high vacuum of the beam line when necessary. For example, when it is required to open the mass spectrometer, venting with N_2 needs to be performed and isolation of the beam line is mandatory. This is the case for the alignment between the MS's skimmer and the externally coupled HRRST parts or for the change/cleaning of the HRRST nozzle. Unfortunately, a gate valve that isolates the MS's skimmer with the outside ambient could not be designed and constructed for this campaign. It is clearly recommended to install a gate valve for future campaigns in order to avoid shut down of all the system when a change in skimmers/nozzles configuration is required.

The i^{2}PEPICO detector configuration available in X04DB SLS/VUV beamline is similar to DELICIOUS III, it is a cross between TPEPICO and PEPICO apparatuses where the electron kinetic energy analysis and the ion TOF analysis are carried out simultaneously. Electrons fly vertically into an electron flight tube to a 40 mm position sensitive delay (PSD) line detector while ions are extracted and fly until they are detected by another 40 mm detector. All electron and ion signals (arrival times at the detectors and image coordinate positions) product of the ionization events are recorded by a HPTDC8 acquisition card employing a continuous acquisition mode and the information is correlated at the same time using a coincidence scheme. Here, the electrons provide the start signal for the respective ion TOF, and their position is required in TOF mass selected analysis.

A Microsoft Visual C code is available to couple the HPTDC8 acquisition card driver and the measurement user interface and this last is also integrated with the beamline control system. Spectral data obtained from the campaign in May 2022 is still to be processed. However, the HRRST-i^{2}PEPICO coupling presented here is already an important contribution to the scientific community and preliminary results on ethylene pyrolysis, a simple organic compound, will be analyzed as soon as possible.

As in SOLEIL, an external NIM trigger signal can be sent by using a Stanford DG535 DPG pulse generator in order to use it as reference to perform chemical kinetic experiments obtaining ion TOF profiles at ns resolution and relative to the shock arrival. On the other hand, compared to SOLEIL, the mechanical

installation at PSI is simpler since the shock tube is placed outside the mass spectrometer vacuum chamber, reducing the installation time, the complexity of the solutions, the time for mouting/dismounting, and the risks for the equipment. Since no differential chamber was available in X04DB SLS/VUV beamline, a home-made differential vacuum chamber was designed and constructed in order to obtain a double differentially pumped molecular beam sampling interface which allows better vacuum performance and protection of the i^{2}PEPICO equipment. A schematic of the assembly between the miniature ICARE-HRRST end part with the differential chamber being coupled to the i^{2}PEPICO detector of SLS/VUV is presented in **Figure** 4-18.

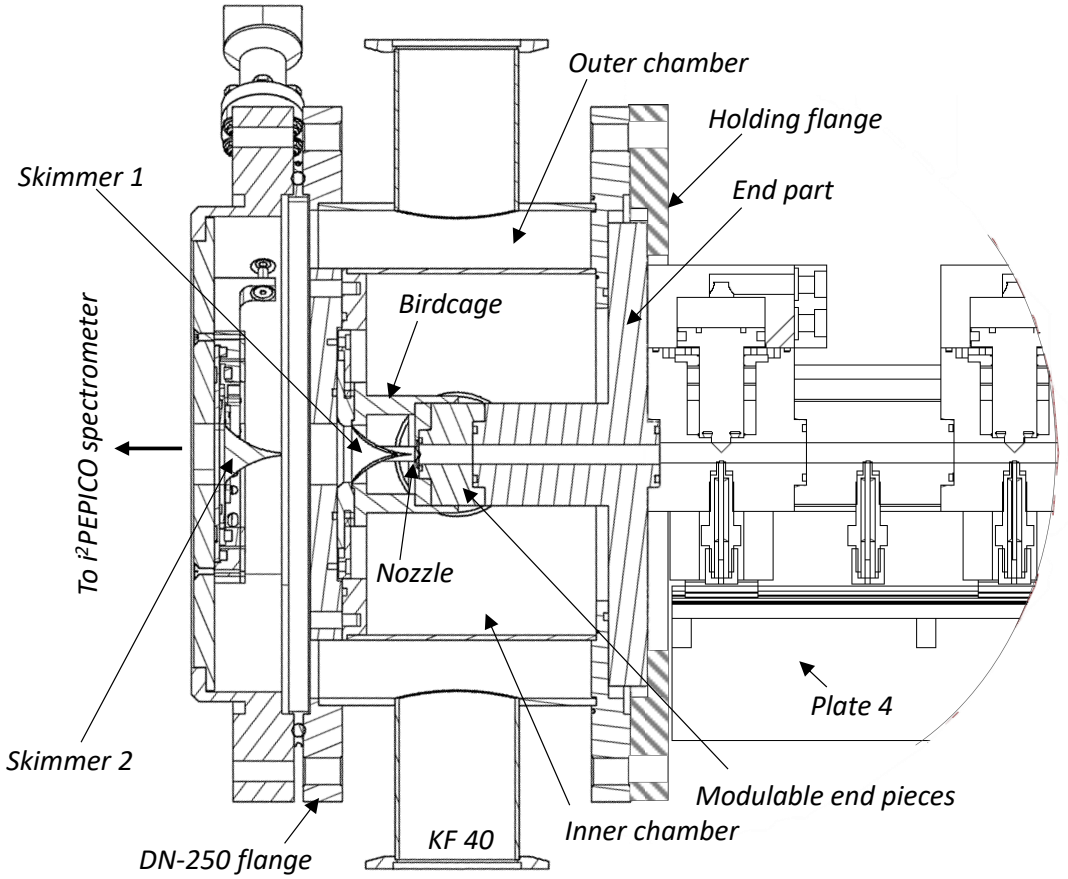

***Figure** 4-18. Profile section view of the end part of ICARE-HRRST being coupled with i^{2}PEPICO spectrometer available in the X04DB SLS/VUV beamline through the use of a custom-made differential vacuum chamber.*

The ICARE differential vacuum chamber is constituted of an outer chamber and an inner chamber and each volume was conceived to have two symmetrical and opposite accesses in order to improve conductance for pumping purposes. It is connected to the MS chamber by using a DN-250 centering ring and bolts ensuring its alignment with the skimmer 2 as shown in **Figure** 4-18. The dimensions are such that the internal volume is optimized and at the same time the maneuvering inside the inner chamber is possible. This is a special requirement since after the alignment between the skimmers and the end part

of the HRRST access to the inner chamber is necessary in order to tighten the screws that clamp the *birdcage* to the plate.

The HRRST end part is introduced into the inner chamber with the nozzle facing the two skimmers, one of them held by the *birdcage* that is mounted inside the inner chamber (skimmer 1) and the other being installed at the entrance of the MS chamber (skimmer 2) constituting an interface between the outer chamber and the MS chamber. A specific end part was designed so that is can be inserted into the *birdcage* with small clearance and low tolerances, assuring automatic alignment between nozzle and skimmer 1. Also, modular terminal pieces of different lengths can be installed to set up predefined nozzle/skimmer 1 distances, as needed. The end part, and thus the entire shock tube, is axially stopped when it touches the differential chamber outer's face. A flange holds the HRRST in place. No CHIMIE METAL pressure sensor was installed at the end part and longer shock wave velocity extrapolation are required, but the uncertainty resulting from such extrapolation of within the experimental errors.

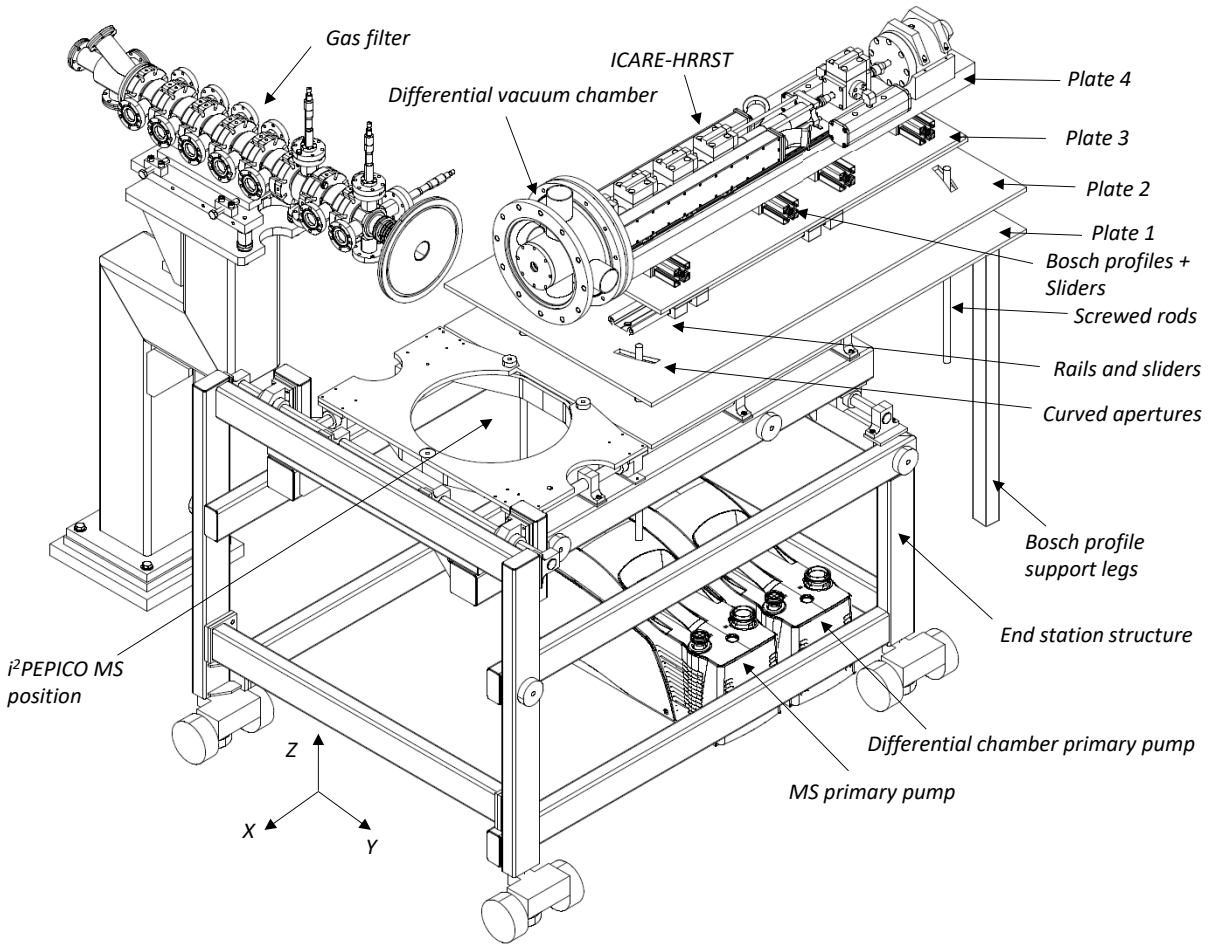

***Figure** 4-19. Isometric view of ICARE-HRRST coupled with X04DB SLS/VUV beamline including support and sliding plates.*

Alignment of the skimmer 1 with skimmer 2 is done by using a laser pointer from the exterior of the mass spectrometer vacuum chamber and when the shock tube is dismounted. An external support structure shown in **Figure** 4-19 had to be designed and constructed in order to hold all the elements located outside, including the shock tube. For the alignment, the laser is located on an aluminum platform (shown as plate 2) and axially far from the two skimmers in order to minimize long distance misalignment. The orthogonal distance from the platform to the laser axis is the same as the distance from the platform to the shock tube axis. The HRRST is installed on a structure that can slide relative to the surface of plate 2 over axes X and Y.

Plate 2 can be rotated over small polar angles (θ) and small azimuthal angles (ϒ) relative to the Z-axis which is perpendicular to the floor. The height can be also adjusted. These movements are possible because four vertical screwed rods fixed on a plate 1 pass through curved apertures in plate 2. Each rod is fixed to the plate 1 by using 2 nuts in both sides of the plate. Plate 1 at the same time is fully fixed to the end station structure by a set of 16 screws. This plate is equipped with two attached Bosch profile legs that extend to the floor taking part of the shock tube and structure weight although most of the weight is transmitted from the plate 1 to the end station structure. The legs are equipped with adjustable feet in order to regulate the final length and keep plate 1 perfectly horizontal.

Plate 2 can be leveled and tilted by means of four nuts that support it from the bottom face and are screwed to the four vertical rods. During the procedure for the first alignment, each nut can be regulated independently making the laser arrive to the center of the ionization region of the MS by passing through skimmer 1 and 2. Skimmer 1 can also be moved to the desired position since there is a radial clearance in the groove where the birdcage is placed against the inner vacuum chamber as discussed for the configuration at SOLEIL.

The alignment needs to be kept when moving the laser pointer towards and from the ionization region at distances equal to the shock tube length. Once the skimmer 1 is aligned, the *birdcage* that is holding it is then clamped to the face of the inner chamber by using screws. Additionally, four nuts are tightened on the top of plate 2 to fix it and maintain the alignment of the structure.

In order to insert the end part of the shock tube in the *birdcage*, a sliding structure containing the shock tube driven and driver sections as well as with the helium tank was built. The driven and driver sections are fixed to plate 4 that is attached to four Eco-sliders allowing the Y movement over four Bosch profiles that are attached to a horizontal plate 3. This movement is perpendicular to the shock tube axis. Plate 3 is supported on four sliders that can move on two rails attached to platform plate 2. These two rails are parallel to the shock tube axis (X) so axial movement of at least 40 cm is allowed for the HRRST. The helium tank is placed in a upper structure similar to the one in SOLEIL. The described configuration allows the whole shock tube to be fully movable on the XYZ axes and with the possibility to adjust angles relative to Z axis too. This makes the mounting and dismounting operations relatively simple and fast while conserving the alignment between the skimmers and the nozzle.

When the end part is being inserted into the birdcage it is stopped by the outer face of the differential chamber and an external holding flange can be clamped to the differential chamber DN-250 flange with screws in order to compress the end part against the differential chamber's outer face as can be noticed in **Figure** 4-18. After this procedure is finished, the shock tube is completely fixed to the differential

chamber and the mechanical coupling between the HRRST and i^{2}PEPICO detector is aligned and ready to perform other tests and experiments.

Concerning the pumping of the system, two vacuum circuits were built *in situ* for the differential chamber. Both inner and outer vacuum chambers are pumped independently by three turbo molecular pumps. A set of two turbos constituted by one 145 l/s air cooled Leybold TurboVac 151C and one 60 l/s water cooled Pfeiffer vacuum TMU 071 were connected to the two accesses of the outer chamber by means of 40 KF connectors and reductions while one 300 l/s air cooled Leybold TurboVac MAG W 300 iP was connected to the two accesses of the inner chamber using a reduction from ISO 100 to KF 40, an ISO 100 tee and KF 40 bellows. One of the two inner chamber accesses was also used to install a K type feedthrough connected to a K type thermocouple. Th thermocouple is introduced inside the inner chamber and attached on the end part of the shock tube close to the end-wall in order to measure and record T1 by the shock tube LabView software via a NI-DAQ temperature module.

A bypass between the mass spectrometer chamber and the inner chamber of the differential chamber was constructed by using KF 40 bellows and clamps. Initially, the bypass is opened and the primary pump of the mass spectrometer chamber among with the primary pump of the differential chamber are started together. After the pressure levels are in the range of 10^{-1} torr, the MS and differential chamber turbos are started all together. After pressure in the differential chamber reaches ranges of 10^{-3} torr the bypass is closed to isolate the pumping circuit of the MS and the inner chambers and obtain the desired vacuum levels and pumping capacities for the specific required load in the different supersonic jet expansion stages. This operation allows a faster pumping of the vacuum chambers when system is restarted since the i^{2}PEPICO vacuum chamber is pumped by a robust system composed of a 1500 l/s COOLVAC 1500 CL cryopump and a 500 l/s Pfeiffer TMH 521 YP turbomolecular pump. During the initial tests, several shock tube experiments were run making attention that the different vacuum chamber minimum level ranges are kept in the safe ranges (10^{-5} torr for the MS chamber and 10^{-2} torr for the inner chamber). No gauge was installed in the outer chamber during this campaign.

All the auxiliary electronics of the shock tube were kept the same as in SOLEIL. All the structures were grounded and a chiller was provided by SLS to cool down the Edwards-EH500 root vacuum pumps used to evacuate the shock tube.

The first campaign at SLS was useful to test the coupling between the ICARE-HRRST and the X04DB VUV beamline (mechanical and electronic) as well as to improve our understanding of the system and necessary improvements for future campaigns. Indeed, the system constructed to hold the HRRST and to align the nozzle with the two skimmers through the double differential pumping chamber was accurate and of easy utilization. On the other hand, the SLS software required certain modifications for data acquisition synchronized with the HRRST operation and the general functioning of the electronic controls faced several challenges. In particular, ground loop noise appeared several hours after the start of the experiments triggering the opening of the high-pressure valve at random times during the HRRST cycle and thus preventing the correct functioning of the system. Despite several attempts to solve the problem, a solution could not be found. Thus, only preliminary data on ethylene pyrolysis could be obtained before the ground loop issue appeared. Future tests are necessary with the HHRST electronic system at SLS before next campaigns can be planned.

5 Experimental Results

In this chapter, the experimental results obtained during the present thesis work are presented and discussed. The experimental campaigns with the HRRST coupled to the i^{2}PEPICO spectrometer available at synchrotron SOLEIL are the main core of the work, including development and implementation of a state-of-the-art experimental technique. The first ever campaign was concluded in January-February 2020 where ethanol pyrolysis was studied. The results are presented to highlight the functionality of this novel experimental coupling and the potential utilization in kinetic studies. Following improvements in the method, the campaign of September 2021 was focused on pyrolytic PAH chemistry from aromatic fuels, for the first time probed in such details with this analytical system. The work includes also the development of an external calibration method for quantitative studies. During the campaign, an impressive amount of time dependent spectral information on toluene, ethylbenzene, and styrene decomposition was retrieved, and the experimental results will be extensively discussed here. No experimental results will be presented from the campaign to PSI in Switzerland in May 2022 where ethylene pyrolysis was studied. However, all the description of the system, including the challenges encountered during the implementation of the technique, can be found in the methodology section.

Results on pyrolytic PAH formation from the decomposition of styrene using the SPST coupled to GC-GC/MS will be then presented together with preliminary prediction results obtained with the ICARE PAH chemical kinetic model. Finally, results on soot nanoparticles measurements using the HST coupled to laser extinction techniques will be discussed in order to provide further understanding on the soot tendency of the ethylbenzene and styrene fuels. The list of all the experimental conditions presented in this chapter are shown in the next table:

***Table 5-1**. List of evaluated conditions using different laboratory-based and synchrotron-based shock tube techniques*

Fuel and % molar concentration	***Conditions***	***ST/Technique***	***# exps ~***
Ethanol 2.7 % in argon	1232 K, 7.4 bar, 11eV, pulsed mode	HRRST/i^{2}PEPICO	15 000
Ethanol 2.7 % in argon	1234 K, 7.5 bar, 10 eV, pulsed mode	HRRST/i^{2}PEPICO	27 000
Ethanol 2.7 % in argon	1525 K, 7.5 bar, 10 eV, pulsed mode	HRRST/i^{2}PEPICO	32 000
Ethanol 0.25 % in argon	1354 K, 6.2 bar, 11 eV, pulsed mode	HRRST/i^{2}PEPICO	9 000
Toluene 0.1% in argon	1362 K, 6.6 bar, 10 eV, pulsed mode	HRRST/i^{2}PEPICO	107 000
Toluene 0.1% in argon	1351 K, 6.4 bar, 8.5 eV, continuous mode	HRRST/i^{2}PEPICO	41 000
Ethylbenzene 0.1% in argon	1326 K, 6.7 bar, 10 eV, pulsed mode	HRRST/i^{2}PEPICO	27 000
Ethylbenzene 0.1% in argon	1339 K, 6.8 bar, 8.5 eV, continuous mode	HRRST/i^{2}PEPICO	29 000
Styrene 0.1% in argon	1345 K, 6.5 bar, 10 eV, pulsed mode	HRRST/i^{2}PEPICO	22 000
Styrene 0.1% in argon	1355 K, 6.5 bar, 8.5 eV, continuous mode	HRRST/i^{2}PEPICO	41 000
CO_2 0.1% in argon	1376 K, 6.6 bar, 14.5 eV, pulsed mode	HRRST/i^{2}PEPICO	6 000
Styrene 100 ppm in argon	1170 K-1733 K, 20 bar	SPST/GC-GC-MS	34
Ethylbenzene 0. 0613% in argon	1560 K-1939 K, 17.6 bar	HST/laser	34
Styrene 0. 0613% in argon	1567 K-1942 K, 17.9 bar	HST/laser	42
			356 100

5.1 Pyrolysis of Ethanol using HRRST/i²PEPICO

The experiments on ethanol (C_2H_5OH) pyrolysis were carried out with the DELICIOUS III i²PEPICO spectrometer available at the SAPHIRS end station of the DESIRS beamline at synchrotron SOLEIL. This was the first time a shock tube was coupled to an i²PEPICO detector. The description of the installation was previously discussed. The rationale behind the focus on ethanol is the fact that ethanol is one of the main biofuels already used blended with conventional fuels, and a widely studied molecule, with available experimental [222]–[227] and theoretical [225], [228]–[230] literature, that can help in the selection of the experimental conditions and in the understanding of the produced results. Besides, by changing the reaction temperatures, ethanol pyrolysis can pass from non-sooting to sooting regimes, exhibiting a wide range of detectable molecules from small hydrocarbon to large PAH species, respectively. This characteristic allowed the exploration of different functionalities of the technique.

Four experimental conditions were evaluated to test the capabilities of the system in a temperature range of 1232 - 1525 K, pressures of 6.2 - 7.5 bar, with high and low ethanol concentrations (2.7% and 0.25% in argon bath gas, respectively), and photon energy of 10.0 eV and 11.0 eV. The four experimental conditions tested in this section are listed in **Table** 5-2 specifying the number of averaged shocks for each case:

Table 5-2*. The four experimental conditions tested in ethanol pyrolysis experiments at SOLEIL synchrotron*

Exp cond.	$T_{5,\,mean}$	$P_{5,\,mean}$	***Ethanol %***	***Photon energy***	***#of exps***
Eth 1	1232 K, σ=19 K	7.4 bar, σ=0.2 bar	2.7	11 eV	15 000
Eth 2	1234 K, σ=19 K	7.5 bar, σ=0.2 bar	2.7	10 eV	27 000
Eth 3	1525 K, σ=55 K	7.5 bar, σ=0.2 bar	2.7	10 eV	32 000
Eth 4	1354 K, σ=23 K	6.2 bar, σ=0.1 bar	0.25	11 eV	9 000

The reason why a photon energy of 11 eV was chosen for this campaign comes from the fact that ethanol has a photoionization energy of 10.41 ± 0.05eV [231] and its detection was initially desired together with ethylene (C_2H_4, 10.50 ± 0.01 eV [232]), one of the major products from reaction R 5-1. However, since the concentrations of the fuel and the main products are relatively high, the false coincidences from their respective photoions generate an increased background noise that can produce a masking effect for the small concentration species, lowering the sensitivity and quality of the results. For this reason, experiments at a lower photon energy of 10 eV were conducted in order to be able to detect species present in lower concentrations like PAHs, without ionization of the fuel molecule and ethylene. Additionally, based on the current knowledge of three main channels for the thermal decomposition of ethanol at high temperatures [224]–[226], [229] (R 5-1 – 5-3), the expected products include acetaldehyde from the thermal decomposition of CH_2OH, and the relatively stable CH_3 radicals. CH_2OH and C_2H_5 are not so probable to be detected because the dissociation rates (> 10^7 s^{-1}) are very high at the studied temperatures. The same happens with OH radicals which are very low concentration with very short life. C1-C6 hydrocarbons can be detected with a photon energy of 11 eV while PAHs can be detected using 10 eV, as mentioned above.

$$C_2H_5OH = C_2H_4 + H_2O \qquad \textit{R 5-1}$$

$$C_2H_5OH = CH_3 + CH_2OH \qquad \textit{R 5-2}$$

$$C_2H_5OH = C_2H_5 + OH \qquad \textit{R 5-3}$$

In addition to variating the reaction temperatures and the photon energies, two different ethanol concentrations were tested. Initially, the concentration was set at 2.7 % ethanol in argon in order to obtain sufficient signal levels, so these results are presented first. However, highly diluted mixtures are preferred for kinetic analysis as more accurate experimental conditions are obtained. The second mixture was then diluted around ten-times, down to 0.25% ethanol in argon. The signal levels were kept acceptable even for a lower fuel concentration because of adjustments performed to the molecular beam sampling strategy. In particular, the choices of the skimmers and nozzle diameters and the separation distances were also part of the learning experience as they strongly influence not only the signal levels but also the quality of the results. In the first experiments, such parameters were chosen with the goal of assuring the integrity of the mass spectrometer during operation, while in the following studies they were optimized based on the experimental results. All the details of the nozzle/skimmers configurations will be presented in the discussions including the best sizes and separations found during the campaign. Similarly, several weak points to be improved were also identified and discussed here. In general, this section focuses in how to exploit the experimental capabilities of the unique HRRST/i^{2}PEPICO coupling and not to present a detailed kinetic analysis on ethanol pyrolytic decomposition. The results presented in this chapter constitute a demonstration of the potential of the developed methodology and they are the basis of subsequent studies presented later in the thesis.

5.1.1 Experiments with high ethanol mole fractions (0.027)

A molar concentration of 2.7% ethanol diluted in argon was used for three experimental conditions. Two electroformed nickel nozzles (Servometer) with diameters of 0.35 mm and 0.4 mm were used. Regarding the skimmers, the skimmer 1 was a Beam Dynamics Model 2 of 0.5 mm orifice diameter while the orifice of skimmer 2 located at the entrance of the MS chamber was 2 mm. The distance between the tip of skimmer 1 and the nozzle was set to 3.2 mm since it is the point where the maximum quenching of the reactions can be reached for the supersonic jet [233] while keeping safe pressure levels inside each vacuum chamber as discussed in the methodology. The repetition rate was kept at 1 Hz and at the end of the experimental campaign it was increased to 1.5 Hz without degradation in the performance of the system and without risks for the instruments.

5.1.1.1 Low temperature, 11.0 eV photon energy

Around 15 000 shock tube experiemnts were performed at an average temperature T_5 of 1232 K and average pressure of 7.4 bar (P5/P1 ~ 25) with a photon energy of 11 eV. The data were acquired using the so-called *pulsed mode* already discussed in the methodology and all the experiments were averaged obtaining a matrix of single ionization events as function of ion time-of-flight, and the electron time-of-flight (eiTOF), as the one presented in **Figure** 4-17. The eiTOF matrix was integrated over 7.8 ms, including the ionization events occurred during 1.25 ms of the pre-shock, and the resulting mass spectrum is shown in **Figure** 5-1a.

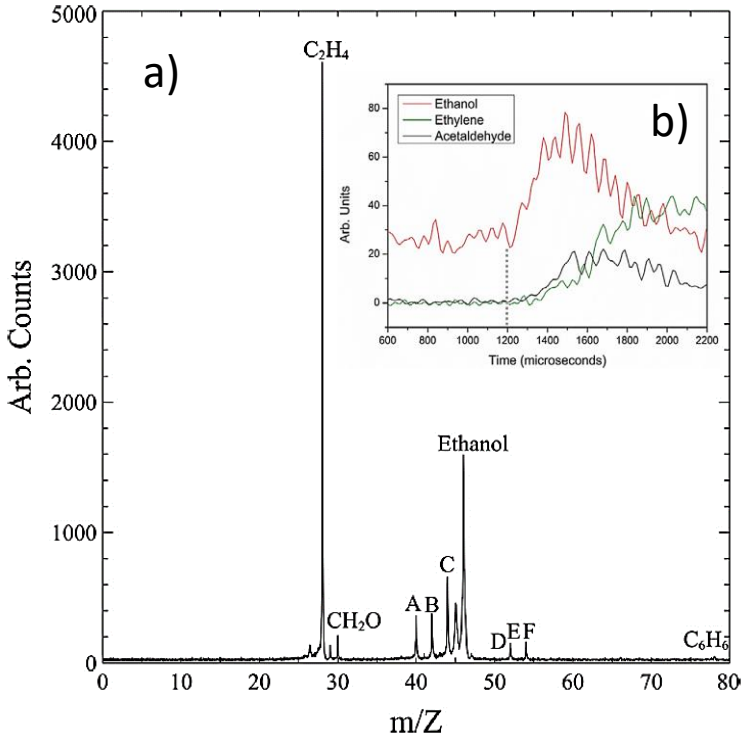

***Figure** 5-1. a) Mass spectrum obtained for $T_{5,mean}$ = 1232 K, $P_{5,mean}$ = 7.4 bar, 2.7% ethanol in argon. A: propyne, B: propene/ketene, C: acetaldehyde + vinyl alcohol, D: diacetylene, E: vinylacetylene, F: 1,3 butadiene, also possibly 1-butyne. Photon energy 11.0 eV. b) temporal profiles of ethanol (red), ethylene (green), and acetaldehyde (black), with a vertical line distinguishing pre-shock and post-shock area.*

The mass spectra has signal contributions from ionization events occurred in the pre-shock region and the post-shock conditions including after the arrival of the rarefaction waves. Before the shock arrival the only expected species contributing to the mass spectrum would be the parent ion of ethanol (m/z 46) and $C_2H_5O^+$ (m/z 45) since dissociation of ethanol can occur at a photon energy of 11 eV considering the photoionization energy of $C_2H_5O^+$ as 10.8 eV [234]. At post-shock conditions the pyrolysis products from the decomposition of ethanol start appearing and they are reflected in the mass spectrum. As expected, there are two big signals at mass over charge ratio m/z 28 and m/z 46 attibuted to ethylene (C_2H_4, m/z

28) and ethanol (C_2H_5OH, m/z 46). The i^{2}PEPICO technique has the unique characteristic to confirm this attribution by providing the VMI-photoelectron images of each mass in the mass spectrum. For example, for the case of m/z 28 the 2D Abel-inverted photoelectron image is presented in **Figure** 5-2a. The 2D Abel-inverted photoelectron images contain information on the vibrational states of the molecules and are used to extract the photoelectron spectra (PES) as a function of the binding energy. The binding energy is related to the energy required to remove an electron from the compound and comes from energy balance between the inlet photon energy (in this case, 11 eV) and the measurement of the ion and electron kinetic energies at the position sensitive detectors PSD. For the i^{2}PEPICO detector available at SOLEIL, the binding energy range spans 3-4 eV from the applied photon energy. The PES is denoted in arbitrary units like the one presented for m/z 28 in **Figure** 5-2b were literature PES for ethylene was compared with the obtained PES for m/z 28. The two signals can confirm that effectively ethylene is the molecule that corresponds to the measured m/z 28 since they match perfectly the positions and relative heights of the three sharp peaks.

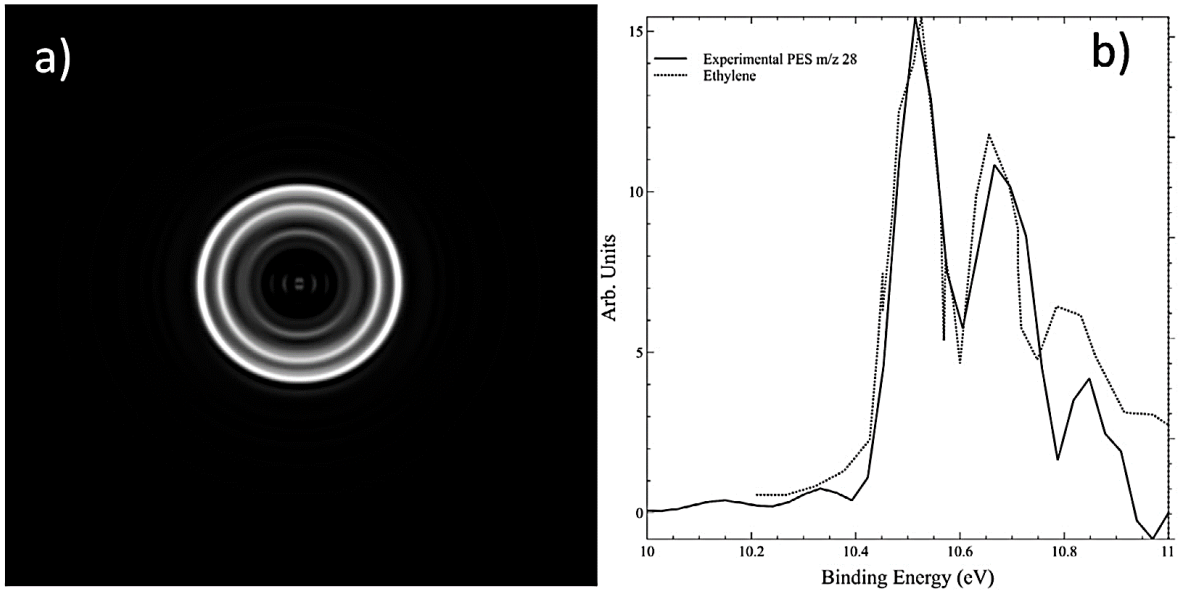

***Figure** 5-2. a) Photoelectron image corresponding to m/z 28; b) comparison of photoelectron spectra for m/z 28 (experimental) and ethylene* [235]

Other products were also identified by using the correspoding PESs as presented in the supplementary material where the photoionization energies of these species match the experimental data. This is the case for formaldehyde (CH_2O, m/z 30), propyne (mz 40), propene/ketene (m/z 42), acetaldehyde/vinyl alcohol (CH_3CHO and CH_2CHOH, m/z 44), and vinylacetylene (m/z 52). From the available PES data it can be concluded that the S/N level obtained is big enough to provide reliable identification with the HRRST/i^{2}PEPICO coupling. Specifically for isomers of C_4H_4 (m/z 52), three possibilities could contribute to the signal as shown in **Figure** 5-3a but the peaks locations and heighs confirm that vinylacetylene is the predominant species. The reason why the experimental PES peaks for m/z 52 are too broad compared to

the literature one is because the signal is small in this condition, as can be noticed in the m/z peak '*E*' of the mass spectrum of **Figure** 5-1a. Thus, PES resolution is decreased because the available photoelectron images had to be binned during the Abel inversion process in order to increase the S/N per pixel. It is possible that there could be a small contribution from 1,2,3-Butatriene to the overal signal around 9.25 eV, fact that can be confirmed with the next experimental condition where the PES will be cut at 10 eV and a better resolution in that zone will be obtained. Last thing that can be seen is that the presence of cyclobutadiene can be excluded from the analysis since none of the spectral characteristics of the respective literature PES matches the ones in the obtained experimental PES for m/z 52.

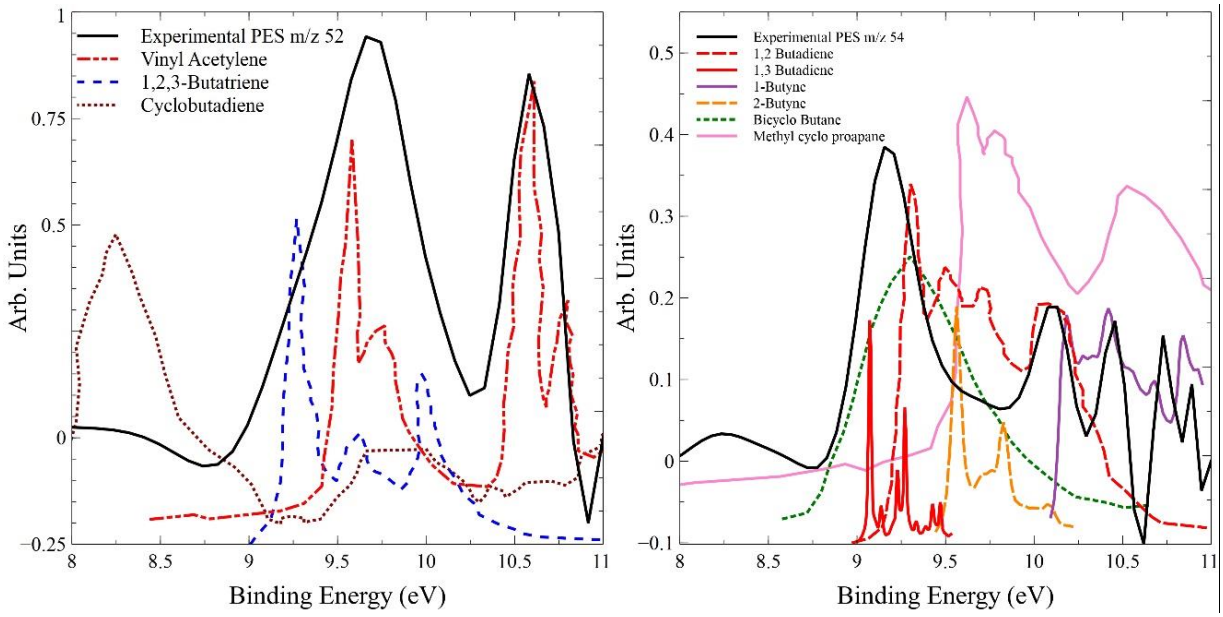

***Figure** 5-3. a) Photoelectron spectra for m/z 52 (experimental), vinylacetylene* [236]*, 1,2,3- butatriene* [237]*, and cyclobutadiene* [238]*. Photon energy equal to 11.0 eV. b) Photoelectron spectra for m/z 54 (experimental), 1,2 butadiene* [239]*, 1,3 butadiene* [240]*, 1-butyne* [240]*, 2-butyne* [240]*, bicyclo butane* [241]*, methyl cyclo proapane* [242]*.*

Oppositely, for m/z 54, it is not possible to exclude with certainty the presence of 1-butyne isomer since the first two peaks of 1-butyne literature PES could be associated to the two peaks at 10.1 eV and 10.4 eV in the experimental PES as shown in **Figure** 5-3b. The only candidate isomer peaking exactly at the same position of the first peak in the experimental PES for m/z 54 is 1,3 butadiene. For a case like this, more experiments need to be done in order to increase S/N and thus the PES resolution.

Figure 5-5b presents the case of m/z 44, another major peak in **Figure** 5-1a. Acetaldehyde (C_2H_4O) was attributed as main product for m/z 44 while ethylene oxide (C_2H_4O) can be excluded. However, a minor species vinyl alcohol (CH_2CHOH) was detected, as some of the characteristics from the literature PES coincide with the experimental profile. In the following sections, the use of different experimental conditions will clarify the presence of such species, demonstrating at the same time the capabilities of the experimental method. This result complements the data found using shock tubes coupled to TOF/MS where based on modeling, the peak at m/z 44 was attributed only to acetaldehyde at similar temperature

conditions, excluding the presence of vinyl alcohol [223]. This ability to distinguish isomers at very different concentrations, including low concentration ones, constitutes one of the main advantages of the HRRST/i^{2}PEPICO technique coupled to a tunable light source.

For the case of m/z 42, two isomer candidates are shown in the annex **A 2** (propene and ketene), but for both of them the literature PES seems to peak at similar points making more challenging to identify which can be assigned to the experimental PES. Different experiments should be implemented in order to be able to discriminate between the two species in such a challenging task. In general, identifying species with similar PESs can be very challenging if the corresponding features match with the experimental results, and this constitutes one of the disadvantages of the HRRST/i^{2}PEPICO technique.

As discussed before, ion kinetics studies can be addressed if the eiTOF matrix is projected to the ion TOF for each selected mass. Embedded to the mass spectrum, **Figure** 5-1b presents time profiles (raw data) for the three main peaks of the mass spectrum which correspond to ethanol (in red, m/z 46), ethylene (in green, m/z 28), and acetaldehyde + vinyl alcohol (black, m/z 44). The vertical line represents the shock wave arrival dividing the pre-shock and post-shock regions.

It is well known that large and rapid pressure fluctuations inside the shock tube as well as inside the MS chamber induce changes in species concentrations inside the mass spectrometer chamber that are reflected in these time profiles. For this reason, an external calibration method will be presented later where an inert gas (CO_2) can be implemented to run shocks and correct the i^{2}PEPICO time profiles signals by considering for pressure fluctuations and changes in concentration inside the vacuum chamber. This will allow the quantification of species concentration using HRRST/i^{2}PEPICO technique. Nevertheless, the temporal profiles shown in **Figure** 5-1b can be considered as pseudo-concentration profiles and serve as a qualitative indicator of how species evolve during the reaction time. For the ethanol profile, the baseline shows the measurement of species at pre-shock P1 conditions and then an immediate increase of the signal occurs when the shock wave arrives around 1.25 ms due to the sudden increase in the post-shock pressure. In ideal conditions the signal should increase rapidly in less than 1 microsecond but in this case the signal does not follow the rise in P_5 due to the pressure build up inside the mass spectrometer chamber. Additionally, because of the stochastic nature of the formation of shock waves and their arrival at the end-wall, the resulting time profile rise from the averaged spectral information can be influenced and broadened. An additional postprocessing can be performed to the kinetic data to account for such factor. In particular, every ionization event is tagged by shock tube experiment number and time arrival, so that all the ion signals can be re-adjusted with respect to the shock wave arrival time. This could produce better time profiles in terms of initial rise slope. However, this would imply huge amount of data postprocessing. Instead, the external calibration method proposed later reduces this problematic.

It can also be noticed that parallel to ethanol decomposition, ethylene and acetaldehyde are formed. These time profiles can be qualitatively compared with closed homogenous reactor simulations in order to validate models, similar to the assessments in previous HRRST/VUV-PIMS works [81], [82]. For example, modeling of ethanol pyrolysis was performed in COSILAB using the CRECK model at same T_5 = 1232 K and P_5 = 7.4 bar conditions [243], [244]. In these simulations, the PCB pressure profile obtained at similar conditions averaging thousand experiments in the laboratory was included to assure correct interpretation of the experimental results. The shape of the pressure profile from the shock arrival until 700 µs is presented in **Figure** 4-9b.

The simulated and filtered experimental time profiles over 700 µs for certain products, e.g. ethylene (m/z 28), acetaldehyde (m/z 44), and formaldehyde (m/z 30), are presented in **Figure** 5-4. A very good qualitative correspondence between both information is found in terms of appearance order, raising velocity and relative concentration variation over time for the species. These analyses are quite simplified, as the relative response can be affected by the PI cross section of the specific species, but the results give confidence in the validity of the data.

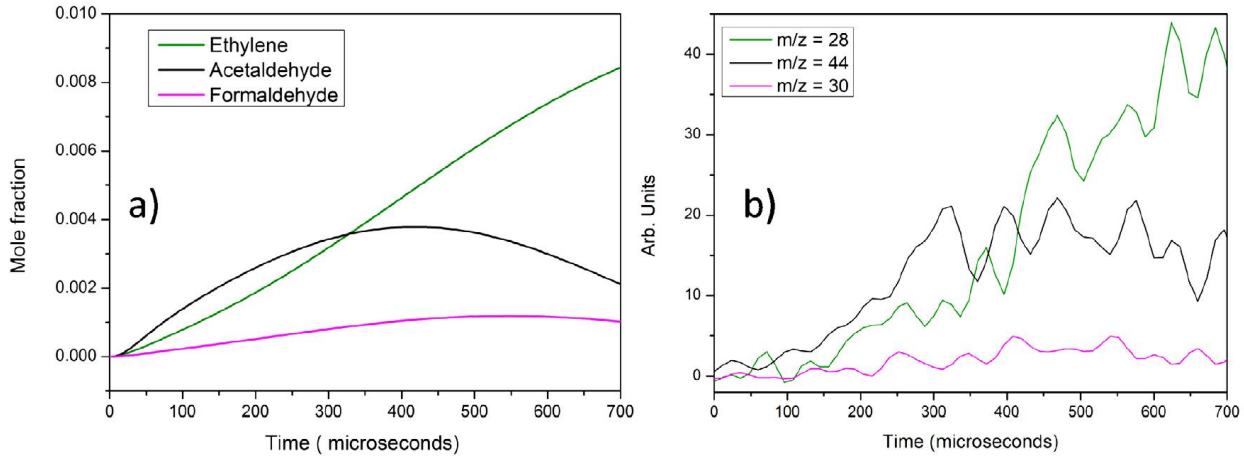

***Figure** 5-4. Time profiles for ethylene and m/z 28 (green), acetaldehyde and m/z 44 (black) and formaldehyde and m/z 30 (pink). a) Simulations with CRECK model* [244]*; b) experimental profiles.*

In order to further advance in the analyses on the capabilities of the new HRRST/i^{2}PEPICO technique, a qualitative comparison between experiments and simulations need to be performed. First, the rate-of-production analyses with the integrated rates over 700 µs reaction time were extracted from the COSILAB simulations and shown in **Figure** 5-5 to identify the formation of the main products observed experimentally. No production of vinyl alcohol (CH_2CHOH) is predicted in the main primary reaction pathways of ethanol. Vinyl alcohol may indeed come from the H-loss/abstraction from the terminal carbon atom of the CH_3CHOH radical and from the central carbon atom of the CH_3CH_2OH radical. The integrated rate of production scheme shows how 15 % of the fuel decomposes directly to ethylene (C_2H_4) while 24 % also goes to ethylene though the formation of the CH_2CH_2OH radical. Around 7 % of the fuel decomposition leads to the formation of formaldehyde (CH_2O) while the production of acetaldehyde (CH_3CHO) mostly comes from the decomposition pathways of CH_3CHOH, which is produced by H-abstraction reactions (49% of the fuel decomposition rate).

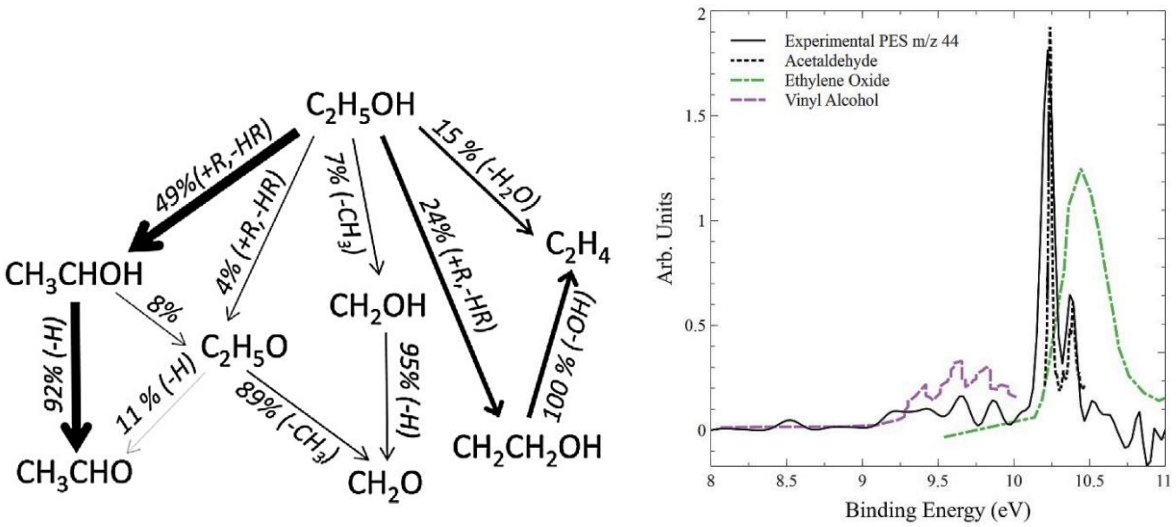

***Figure** 5-5. a) Integrated rates of production, 2.7% C_2H_5OH in argon, T_0 = 1232 K, P_0 = 7.4 bar. The percentages refer to the consumption of the reactant species, the arrow thickness is proportional to the corresponding flux. CRECK model* [244]*. b) Experimental PES for m/z 44, literature PES for Acetaldehyde* [245]*, Vinyl alcohol* [245]*, Ethylene oxide* [246]*.*

As mentioned, ethylene, acetaldehyde (CH_3CHO) and formaldehyde (CH_2O) are predicted as main products of the ethanol pyrolysis, while vinyl alcohol formation is not considered in the CRECK model. On the other hand, before comparing the relative concentrations of experiments and simulations, the contribution of the vinyl alcohol to the experimental PES needs to be determined first and subtracted from the total signal. For this, a convolution process can be realized where the two literature PES for acetaldehyde and vinyl alcohol are combined and best-fitted to get a sum of convolved isomer PES that matches the experimental PES using the following equation:

$$PES_{(m/z=\,44@11\,eV)} = c1 \cdot \sigma_{acetaldehyde\ @11eV} \cdot PES_{acetaldehyde} + c2 \cdot \sigma_{vinyl\ alcohol\ @11eV} \cdot PES_{vinyl\ alcohol} \qquad 5\text{-}1$$

In this equation, σ represents the photoionization cross sections (PICs) of each isomer at the photon energy used, in this case at 11 eV. PICs are function of the tendency of the molecule to get ionized at an specific photon energy, and it is expressed in megabarn (1 Mb = 10^{-18} cm^2). The constants c1 and c2 are proportionality constants that minimize the mean squared error (MSE) between the convolved curve and the overall experimental curve and the relative concentration to the signal between the species is denoted by the ratio between them (c1/c2). Since the available literature and experimental PES are found in arbitrary units, all signals are normalized to 1 for the analyzed range of binding energies before starting the optimization of the constants. The relative concentration between acetaldehyde and vinyl alcohol was found to be (4±1):1. This procedure can be applied to each m/z of the mass spectrum where even more than two species are present. For instance, the analysis can be extended to cases where numerous

options of isomers are being identified by adding new terms to the Equation (5-1) corresponding to the different compounds whose relative concentrations for the same m/z are required.

In order to get the relative concentrations between species of different m/z like ethylene (C_2H_4), acetaldehyde (CH_3CHO), and formaldehyde (CH_2O), an integration of the corresponding mass spectrum peaks or time profiles can be performed. In this way, an integration of the time profiles shown in **Figure** 5-4 was realized which is representative of the branching ratios for the fuel decomposition pathways. Although a full chapter is dedicated later on the quantification of species concentrations, for simplicity, the equation (5-2) is here employed in first approximation. The signal value of a species x (S_x) is proportional to the product concentration ([x]), the photoionization cross section of the respective species (PICS, $\sigma_{x,@11eV}$) and the mass discrimination factor (D_x), among other factors that will be discussed in detail in the next chapter. With this approximated procedure, the relative concentration ethylene: acetaldehyde: formaldehyde was found to be 54:36:10 for the simulations and 59:35:5 for the experiments after vinyl alcohol contribution is subtracted.

$$S_x \; \alpha \; [x] \cdot \sigma_{x,@11eV} \cdot D_x \qquad 5\text{-}2$$

Although the time dependent signal (S_x) is influenced by the pressure variations in the mass spectrometer chamber, the uncertainty is reduced by applying an integration over 700 µs. Additionally, there is an uncertainty associated to the value of the PICS that usually can reach values higher than 20%. Experimentally determined PICS employed for ethylene, acetaldehyde, and formaldehyde at 11 eV are 8.1 Mb [247], 7.9 Mb [248], and 9.6 Mb [249], respectively. In addition, the mass discrimination factor was assumed 1 since these effects, associated to the molecular beam sampling, introduce small error in the determination of the concentrations. Cool et al. have determined a mass discrimination factor of 0.6-1.0 for a m/z range of 28-44 for a molecular beam sampling with similar characteristics using VUV-PIMS [19]. Even like this, the agreement between the relative concentrations for the simulations and experiments is good, especially considering that CRECK model has not been validated at the conditions studied here.

To summarize, the HRRST/i^{2}PEPICO system was implemented to obtain PESs with enough quality to identify most of the main isomers produced during ethanol pyrolysis including the relative concentrations of main species with the same molecular masses. However, signal levels were not always enough to distinguish species with similar PESs. Some signal improvements can be obtained in order to increase the PES resolution and different photon energy can be used as presented next. This will also increase detection sensitivity for minor species observed in the mass spectrum. Additionally, the time profiles allowed the determination of the relative concentrations between species of different masses and results were compared with kinetic simulations using CRECK model with good agreement. An external calibration method will be discussed in next chapters in order to obtain more detailed qualitative information.

5.1.1.2 Low temperature, 10.0 eV photon energy

The photoionization energy was reduced to 10.0 eV in order to reduce the background noise due to the false coincidences from ionization of ethanol and main products (mainly ethylene) and be able to capture minor species, including aromatic species, that ionize below this energy value. The experimental set was conducted at similar conditions than the experiments realized at 11 eV previously presented (T_5 = 1234 K and P_5 = 7.5 bar, average values). An increased number of experiments of 27 000 was obtained in order to increase the S/N ratio for the small products. All the experiments were averaged over a time span of 7.8 ms (1.25 ms pre-shock, 6.55 ms post-shock) to obtain the mass spectrum presented in **Figure** 5-6. Several differences can be found when analyzing the mass spectrum obtained at 10 eV compared to the one obtained at 11 eV. The first big difference is that the major species (ethylene, m/z 28, ethanol, m/z 46, and m/z 45) don't appear in the mass spectrum of 10 eV due to their photoionization occurs threshold greater than 10 eV. Several other masses with minor concentrations appear to be detected at 10 eV like m/z 66, which was identified mainly as cyclopentadiene although the presence of other isomers could not be completely discarded as shown in the annex **A 3**. The same situation for m/z 78, where benzene can be attributed as the major species although other isomers could be also associated to this mass. For other peaks like m/z 50, 56, 58 and 68 the experimental PES signal is too small to obtain a correct identification of the species involved in the ethanol chemistry. It is important to notice from the mass spectrum obtained at 10 eV that a new peak observed at m/z 15 corresponds to the methyl radical confirming ethanol decomposition pathway through the reaction R 5-4. Considering the short life and small concentration of a radical like methyl, its detection using the HRRST/i^{2}PEPICO configuration is a very good achivement since at this stage these initial experiments were still in an exploratory stage.

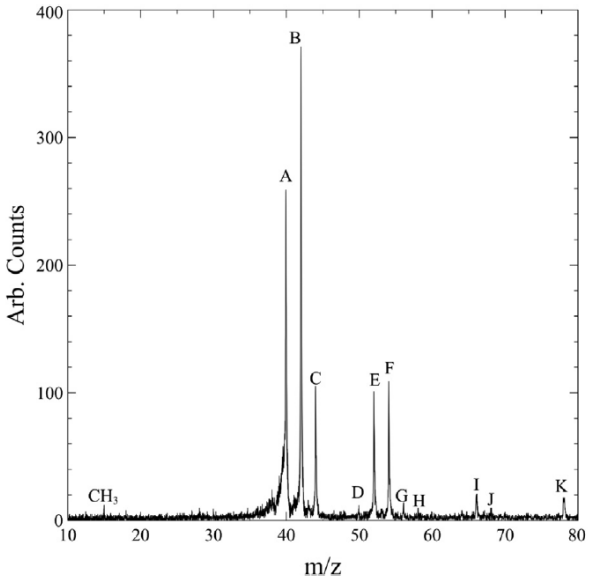

***Figure** 5-6. Mass spectrum obtained for $T_{5,mean}$ = 1234 K, $P_{5,mean}$ = 7.5 bar, 2.7% ethanol in argon. A: allene, B: propene/ketene, C: vinyl alcohol, D: mass 50, E: vinylacetylene, F: 1,3-butadiene (possible contribution from 1,2-butadiene), G: m/z 56. H = m/z 58, I: cyclopentadiene, J: m/z 68, K: benzene. Photon energy 10.0 eV.*

These results demonstrate that complex mixtures of gaseous species cannot be fully resolved with the use of only one photon energy. In addition to the detection of different species, the capability to determine the isomers might be affected by the photon energy. For example, in 11 eV data, because of the low concentration of vinyl alcohol, it was difficult to confirm the presence of this isomer for m/z 44. The photoelectron spectra comparison for m/z 44 obtained with photon energy equal to 11.0 eV and 10.0 eV is presented in **Figure** 5-7. It can be seen that the PES obtained at 10 eV clearly confirms the presence of vinyl alcohol in the mixture since the reference PES for this species perfectly coincide with the spectral characteristics of the experimental PES for m/z 44. No contribution from other isomers is found in 10 eV PES for m/z 44 since the photoionization of these species are higher than 10 eV. Thus, vinyl alcohol is the only species contributing to the peak located at m/z 44 in the mass spectrum of **Figure** 5-6.

Similarly, another situation where the experiments at 10 eV helped to clearly identify the species concerns m/z 52. The photoelectron spectra comparison for m/z 52 obtained with photon energy equal to 11.0 eV and 10.0 eV are presented in **Figure** 5-8. The PES obtained at 10 eV is much sharper than the one obtained at 11 eV because the photoionization energy of the isomers of m/z 52 are less than 10 eV. Then, a better correspondence between the reference PES of vinylacetylene and the experimental PES for m/z 52 is obtained at 10 eV, in comparison with the one at 11 eV. However, for cases where there is not possibility to run experiments at different photon energies intending to targeting different species, the experiments at higher photon energies are still useful to determine the identification of some crucial species. This is the case for vinylacetylene, whose identification is possible with 11 eV PES for m/z 52 only, even if the PES for m/z 52 obtained at 10 eV is much more well resolved as represented in **Figure** 5-8. Anyway, the combined information obtained at different photon energies provide more insights compared to a study realized using only one photon energy because it allows the identification of a number of species with very different masses like the fuel molecule, the major products, and several other minor compounds.

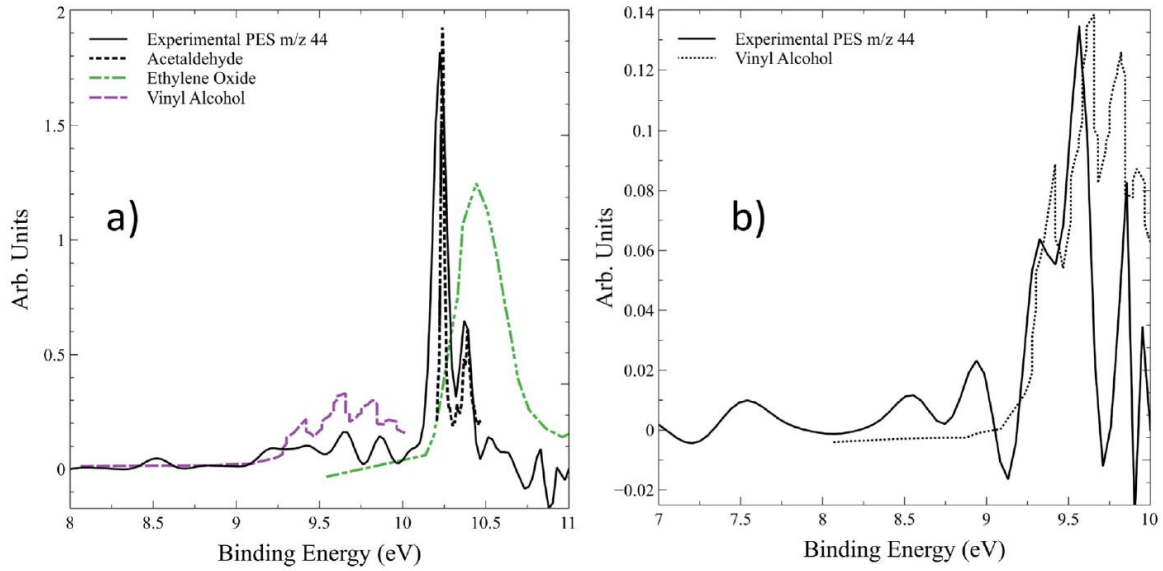

***Figure** 5-7. Photoelectron spectra comparison for m/z 44 (experimental), acetaldehyde* [245] *, ethylene oxide*[246] *and vinyl alcohol* [245] *. Photon energy equal to a) 11.0 eV, b) 10.0 eV.*

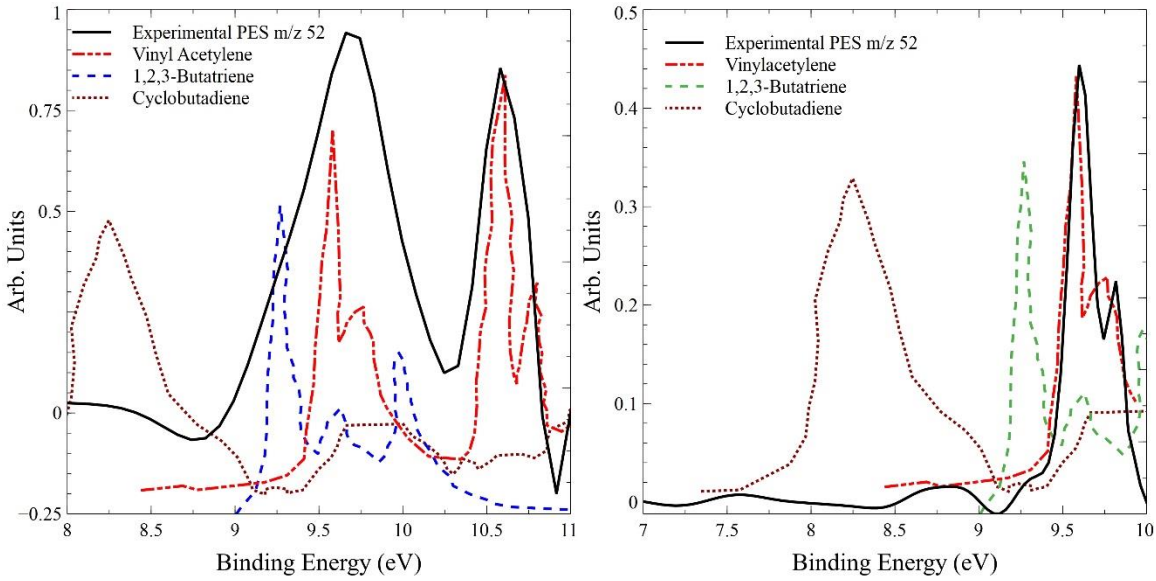

***Figure** 5-8. Photoelectron spectra comparison for m/z 52 (experimental), vinylacetylene* [236]*, 1,2,3- butatriene* [237]*, and cyclobutadiene* [238]*. Photon energy equal to a) 11.0 eV, b) 10.0 eV.*

For other cases, the identification of isomers is more challenging. For instance, the corresponding signal contribution for m/z 40 from allene can be guessed when analyzing the experimental PES. As presented in the supplementary material on the 10 eV results, the experimental PES signal obtained for m/z 40 is very noisy which complicates the assignation of allene to this mass. In addition, the photoionization energy of allene is very close to 10 eV and the PICS is very small [245]. However, one of the main peaks in the reference PES for allene clearly matches one of the peaks for the experimental PES obtained at 10 eV photon energy as well as other peak of this species matches the experimental spectra obtained at 11 eV where propyne is the major species as shown in the supplementary material (11 eV results). Better results could have been obtained if a slightly higher photon energy of 10.2 eV was used instead of 10 eV. In any case, propyne does not contribute to the peak located at m/z 40 in the mass spectrum presented in **Figure** 5-6 because it ionizes after 10 eV and the PES evidence leads to the conclusion that allene is the main contributor in that peak of mass spectrum obtained at 10 eV.

These examples evidence one of the potentials of the proposed technique, which is the capability to identify one specific isomer inside a complex mixture if the correct photon energy is selected. Unfortunately, it does not work for all the cases. Even if a better resolution of the experimental PES for m/z 42 is obtained at 10 eV compared to the one obtained at 11 eV, the differentiation between propene and ketene is impossible with the current configuration due to the fact that both isomers have similar spectral characteristics and their reference PESs are very similar. Other efforts should be addressed in order to resolve this challenge.

5.1.1.3 High temperature, 10.0 eV photon energy

An attempt for the identification of PAH products was performed with the aim of testing the capabilities of the HRRST/i^{2}PEPICO system on such relevant subject. In this case, the temperature was increased to allow production and detection of the PAH species. A new set of 32 000 experiments at reaction conditions of T_5 = 1525 K, σ= 55 K, and P_5 = 7.5 bar, σ= 0.2 bar was conducted in order to obtain the mass spectrum presented in **Figure** 5-9. The photon energy was kept at 10 eV because this allows the photoionization of PAH molecules while hiding the major species that ionize at higher energy and that could increase the background noise. The physical configuration of the molecular beam sampling system remained the same for this set compared to the previous cases.

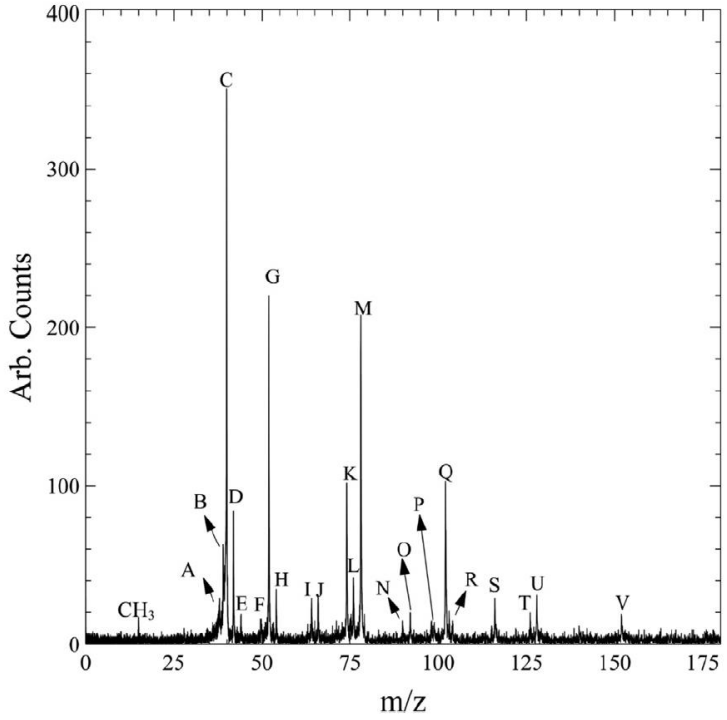

***Figure** 5-9. Mass spectrum obtained for $T_{5,mean}$ = 1525 K, $P_{5,mean}$ = 7.5 bar, 2.7% ethanol in argon. A: m/z 38, B: propargyl radical, C: allene, D: propene/ketene, E: vinyl alcohol, F: m/z 50, G: vinylacetylene, H: 1,3 butadiene/2-butyne, I: 1,3-pentadiyne, J: cyclopentadiene, K: triacetylene, L: m/z 76, M: benzene, N: m/z 90, O: m/z 92, P: m/z 98, Q: phenylacetylene, R: styrene, S: indene/p- methylphenylacetylene, T: m/z 126, U: m/z 128, V: m/z 152. Photon energy 10.0 eV.*

Regarding the detected masses, several peaks are common to the low temperature experiments like the ones assigned to methyl radical (m/z 15), vinyl alcohol (m/z 44), cyclopentadiene (m/z 66), vinylacetylene (m/z 52), allene (m/z 40), propene/ketene (m/z 42). However, several new peaks are noticed in the mass spectrum compared to the lower temperature experiments realized at 10 eV. Specifically, another radical was found at this temperature conditions. This is the case of propargyl radical (m/z 39) as well as linear compounds like 1,3-pentadiyne (m/z 64), triacetylene (m/z 74), and the C_6H_4 isomers (E)- and (Z)-1,5-hexadyine-3-yne (m/z 76). A contribution to m/z 76 coming from o-benzyne could not be confirmed due

to the lack of sharpness of the obtained experimental PES for this peak that did not allow the assignment of the features of the reference photoionization energies for this diradical intermediate. The corresponding photoelectron spectrum comparisons for these masses are presented in the corresponding annex **A 4** for this case and any improvement in signal could be done by increasing the number of experiments or by increasing the amount of mass that enters the photoionization region in order to increase the number of ionization events.

On the other hand, very well resolved photoelectron spectra for several masses greater than m/z 78 was obtained and these are presented in the PES comparisons of **Figure** 5-10. Due to the relatively high concentration of benzene at higher temperatures also evidenced in the mass spectrum, the PES for m/z 78 presents higher S/N and thus very sharp spectral characteristics which exactly coincide with the reference PES for this single-ring aromatic molecule as shown in **Figure** 5-10a. From the comparison, other C_6H_6 isomers could be excluded except for the presence of fulvene whose second peak of its reference PES located at a binding energy of around 9.55 eV coincides with the second larger peak of the experimental PES for m/z 78. However, the addition of this species would generate an additional peak located at 8.5 eV that is not clearly observed in the experimental PES. Experiments at photon energies close to 8.8 eV would clarify the presence of fulvene as found in a similar study using a low pressure premixed sooting flame [91]. Other monoaromatic compounds like phenylacetylene (m/z 102) and styrene (m/z 104) were also identified with excellent correspondence by using well defined experimental photoelectron spectra as presented in **Figure** 5-10b and **Figure** 5-10c, respectively.

Regarding the multi-ring structures, several PAH compounds were detected with m/z up to 152 using the HRRST/i^2PEPICO combination at high temperatures including m/z 116, 126, 128, and 152. For instance, **Figure** 5-10d compares the experimental PES obtained for m/z 116 with the reference PES for several isomer candidates. The comparison resulted in the exclusion of several isomers as well as the identification of indene, phenylpropadiene and p-methylphenylacetylene. In order to be able to discriminate between these three isomers a more resolved experimental PES should be obtained. Anyway, even if the S/N ratio is small for these minor peaks, the experimental PES serves, in this case, to reduce the amount of isomer candidates as possible which is also a very valuable contribution for the study of these complex mixtures with PAH species which are in very small concentrations. The experiments presented in subsequent sections focused on PAH chemistry with “continuous mode” acquisition will provide a substantial improvement in the data quality and capabilities of the technique concerning PAH identification.

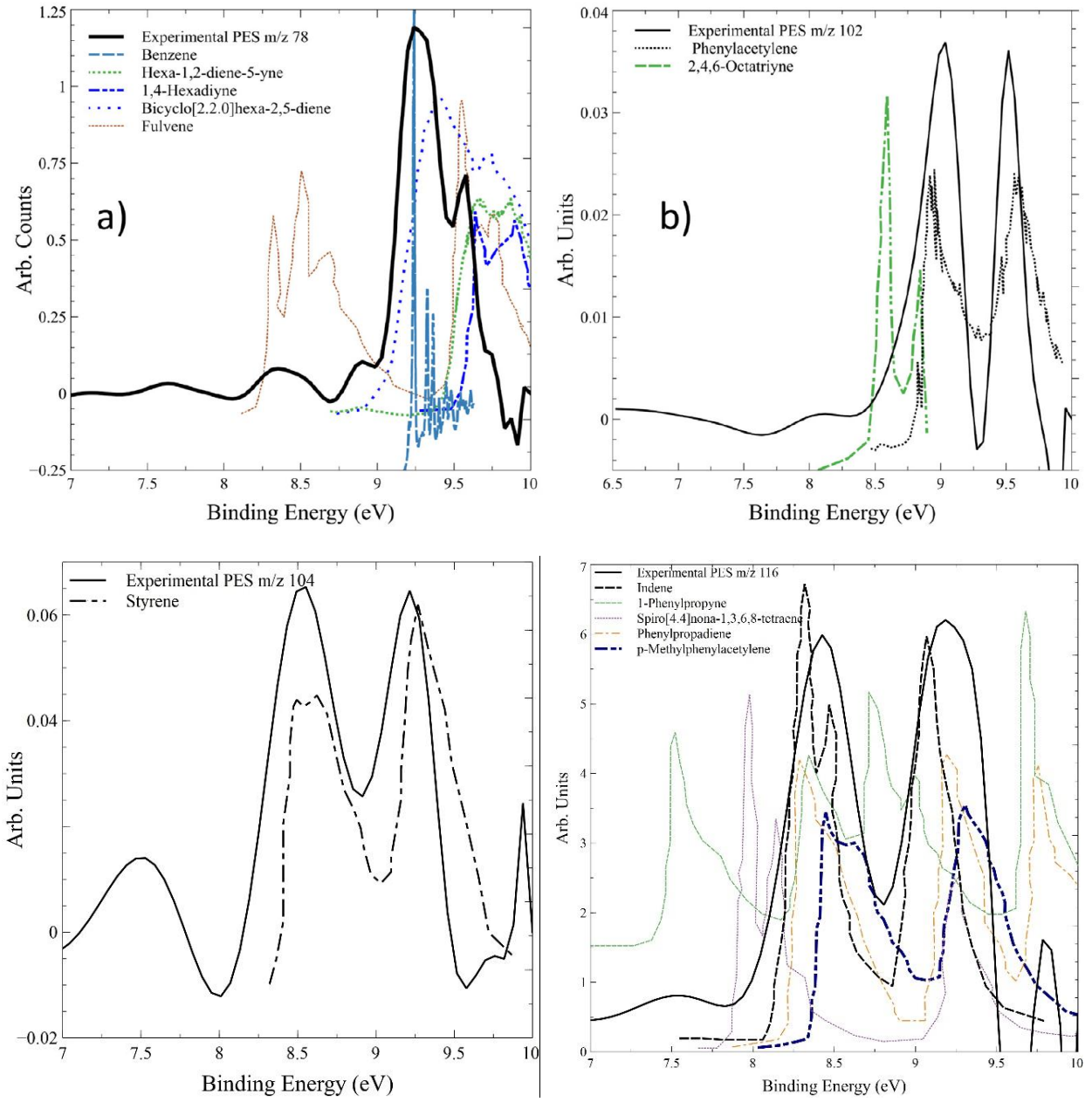

***Figure** 5-10. a) Photoelectron spectra for m/z 78 (experimental), benzene* [250], *fulvene* [251], *1,2-hexadiene-5-yne* [252], *1,4-hexadiyne* [253], *and bicyclo[2.2.0]hexa-2,5-diene* [254]. *b) Photoelectron spectra for m/z 102 (experimental), phenylacetylene* [255], *and 2,4,6-octatriyne* [256]. *c) Photoelectron spectra for m/z 104 (experimental) and Styrene* [257]. *d) Photoelectron spectra for m/z 116 (experimental) and selected isomers (indene* [258], *1-phenylpropyne* [259], *spiro[4.4]nona-1,3,6,8-tetraene* [259], *phenylpropa- diene* [260], *p-methylphenylacetylene* [261]*).*

5.1.2 Experiments with low ethanol mole fractions (0.0025)

Highly-diluted mixtures are typically preferred for kinetic studies as they tend to conserve ideal conditions with respect to less diluted mixtures. For the experiments presented here, the concentration of ethanol was reduced to 0.25%, ten times less the value used in the previous cases. In order to test the reliability of using the HRRST/i^{2}PEPICO system for such low reagent concentrations, a new molecular beam sampling interface configuration was implemented with the use of a *birdcage* for more reliable and precise alignment between the nozzle and the skimmers, as also discussed in the methodology section. In addition, the skimmer 1 was replaced by a Beam Dynamics model-1 skimmer with a larger hole of 1 mm and shorter length compared to the one used before (model-2 with a conservative hole of 0.5 mm). The increase in the skimmer 1 orifice combined with the decrease of the distance between skimmer 1 and skimmer 2 can create an increase of mass flux as well as an increase of pressure in the mass spectrometer chamber. Thus, the nozzle was reduced to 0.3 mm and its separation to the skimmer 1 tip was set to be 3 mm, which is ten times the nozzle diameter. This configuration ensures that the supersonic jet coming from the shock tube will achieve the maximum cooling during the expansion, for maximum gas density from the frozen reactions.

A set of around 9 000 experiments at T_5 of 1354 K, σ= 23 K, and P_5 = 6.2 bar, σ= 0.1 bar were performed in order to obtain a low temperature condition. A photon energy of 11 eV was chosen to capture the fuel molecule and the major products like ethylene for comparison with the resulting mass spectrum in **Figure** 5-1. Additionally, the photon resolution was intentionally improved to 15 meV but at expenses of losing some photon flux. To do this, the size of the photon beam was reduced to 65% by changing the position of a variable aperture device.

Figure 5-11 presents the mass spectrum resulting from the accumulation of all the experimental data which is integrated over 7.8 ms of acquisition time compared to the already discussed mass spectrum obtained at similar temperature and pressure conditions but with 2.7 % ethanol. Due to the high dilution and to the significant decrease in the number of experiments from 15 000 to 9 000, the mass spectrum obtained at 0.25% ethanol in argon is noisier than the one for 2.7%. However, the peaks are well-defined and the small differences in relative heights between peaks of different m/z ratios can be attributed to the differences in the temperature and pressure conditions in the two cases.

Following the same methodology where the branching ratios were extracted by integrating the species time profiles over 700 µs, for the experiments at lower concentration it was obtained 0.69:0.06:0.25 for ethylene, acetaldehyde, and formaldehyde, respectively. The simulations using the CRECK model at T = 1354 K with variable pressure profile delivered reasonable integrated values of 0.82:0.08:0.1.

The photoelectron spectra for the observed peaks ranging from m/z 28 until m/z 54 are presented in the annex **A 5** for this section. In general, they are very similar to the ones for 2.7% ethanol experiments which means that the quality of the highly-diluted data is almost the same as the one of the high concentration experiments despite the lower number of experiments. On the other hand, the experimental PES for m/z 52 did not present enough resolution in order to fully correlate with the reference PES for vinylacetylene due to the lack of the second peak located at 10.5 eV. Similarly, the m/z 54 peak for 1,3 butadiene is very small compared to the one obtained in high concentration experiments. Oppositely, the experimental PES for m/z 50 is much larger than in 2.7% experiments which allows a clearer assignation to the reference PES for diacetylene. These results are clearly influenced by the temperature conditions, 1354 K in **Figure**

5-11 vs 1232 K in **Figure** 5-1. Indeed, at higher temperatures, the conversion by dehydrogenization of C4 intermediates (vinylacetylene and 1,3-butadiene) to diacetylene is favored.

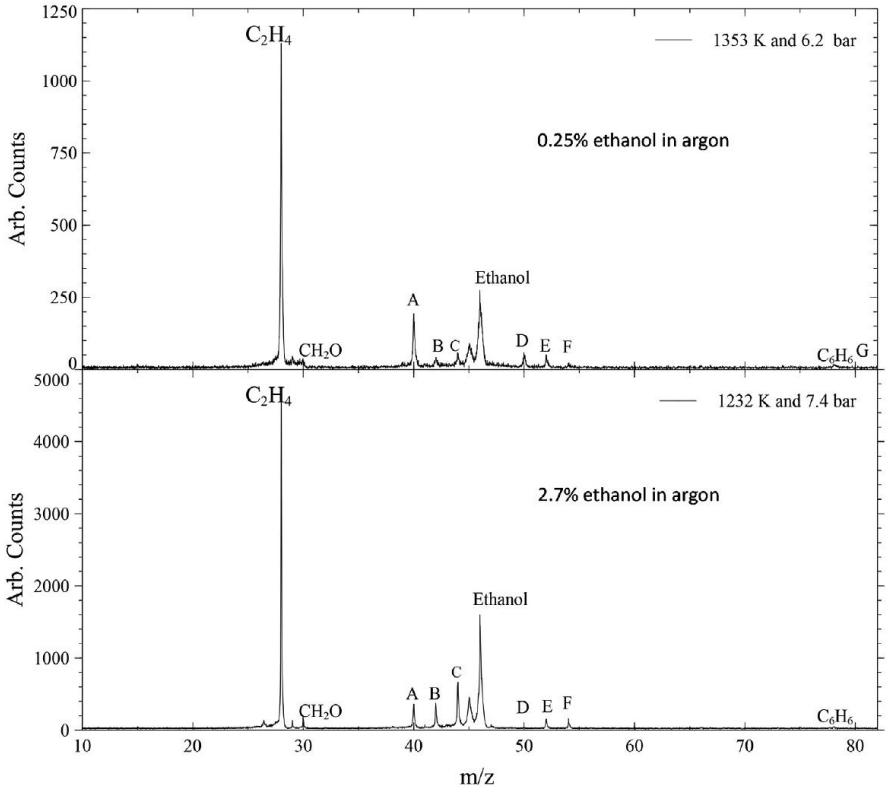

***Figure** 5-11. (Top) Mass spectrum obtained with 0.25% ethanol in argon. A: propyne, B: propene/ketene, C: acetaldehyde + vinyl alcohol, D: diacetylene, E: vinylacetylene, F: 1,3 butadiene (possible contribution from 1-butyne). (Bottom) Mass spectrum obtained with 2.7% ethanol, for comparison. Photon energy 11.0 eV.*

The new molecular beam sampling configuration has significatively reduced the overall time to get spectral data with good S/N even for highly-diluted mixtures. This, by making use of an auto-aligning *birdcage* together with the changes in skimmer 1, nozzle dimensions, and beam light resolution. This special feature of the unique HRRST/i^{2}PEPICO coupling gives the possibility to better plan experimental campaigns where a broad range of conditions can be explored with attention to specific sets that require a higher level of detail.

In general, the four experimental conditions discussed in this chapter have demonstrated the different functionalities of the HRRST/i^{2}PEPICO coupling in a wide range of conditions of temperature (1232 K – 1525 K), pressure (6.2 bar-7.5 bar), concentrations (0.25%-2.7%), repetition rates (1Hz-1.5Hz) and photon energies (10.0 eV-11.0 eV). Simulations performed with CRECK chemical kinetic model helped the interpretation of the experimental results showing the great potential of this technique for the kinetic study of complex mixtures of isomeric gaseous species. The spectral information was used to extract mass

spectrums, photoelectron spectra and species time profiles for a number of masses being able to identify radicals, isomers of monoaromatic compounds and to help the identification of PAHs.

Nevertheless, two challenges need to be faced in order to improve the experimental capabilities. First, the need to obtain quantitative datasets of temporal species profiles has to be highlighted in this first campaign to SOLEIL, despite the value of the qualitative information. Specifically, the quantitative measurements must take into consideration the pressure variations inside the mass spectrometer chamber in order to correct the signal from the dynamic behavior of the shock tube. The other problem concerns the limited PES signal levels in this data acquisition mode, even with optimized alignment. This limitation makes difficult the identification of several isomers, specially for minor species like PAHs.

In order to overcome these limitations, a new campaign to SOLEIL synchrotron was realized on toluene, ethylbenzene and styrene pyrolysis that allowed to solve these two aspects. First, in the next chapter the external calibration technique to solve the problematic of pressure fluctuations inside the mass spectrometer chamber is presented. In addition, the new *continuous* data acquisition mode of i^{2}PEPICO already explained in the methodology section was also employed and exploited in order to obtain sharper PESs and allow the selective identification of isomers.

5.2 External standard calibration method for Kinetic quantitative analysis

In the previous chapter on ethanol pyrolysis, it has been demonstrated how the raw spectral signal could be used to obtain species time profiles for selected m/z's. As stated, the experimental raw data could not be used to extract kinetic profiles for quantification purposes. However, a set of corrections to the raw signals could be implemented in order to derive accurate temporal species concentration profiles. If an internal standard gas is introduced in the initial mixture, a calibration procedure could be employed to use this unreactive species as reference for photoionization experiments, as already performed in laboratory-based TOF set-ups [15]. However, it is quite challenging to find an internal gas that does not participate in the reactions while ionizing at photon energies lower than most of the organic molecules produced in the pyrolysis.

Therefore, a new method using an external standard is proposed in this chapter to correct signal for pressure variations inside the spectrometer chamber, applicable to any HRRST/TOF-MS experiment. In particular, the method will be proven to provide concentration profiles for HRRST experiments coupled to synchrotron-based mass spectrometry of special interest for chemical kinetic studies and model validation. For this purpose, CO_2 was proposed as a reference external gas, and two widely-studied fuels were considered as test cases: toluene and ethylbenzene. Chemistry-related aspects for these two important fuels and PAH precursors will be discussed in next chapters. Here, only the development of the methodology for the extraction of the kinetic information is presented, specifically tested for the HRRST/i^{2}PEPICO coupling. The corrected experimental results are compared with the simulations provided by the current version of the ICARE PAH model in order to prove the reliability of the methodology.

Regarding the experimental conditions, the pulsed data acquisition mode was employed spanning 8 ms of pre-shock and post-shock conditions. The repetition rate was 1 Hz and the photon energy used to ionize the fuel molecules and the carbon dioxide was 10 eV and 14.5 eV, respectively.

5.2.1 Formulation of the external calibration method

For any species x, the mass spectrometer signal (S_x) was simplified in equation 5-2. Now, the expression is expanded in detail as:

$$S_x = \sigma_x \cdot [x] \cdot n_{exp} \cdot D_x \cdot \eta_{set} \cdot f(P,t) \qquad \textit{Equation (5.3)}$$

indicating that the signal (S_x) is proportional to the product of the concentration [x], the photoionization cross section of the respective species at the specific photon energy (PICS, σ_x), the mass discrimination factor D_x, the number of experiments n_{exp}, an efficiency coefficient η_{set} which is function of the beamline intensity and the sampling configuration for the specific set. Finally, f(P,t) is a correction function including temporal pressure changes inside the mass spectrometer chamber. In order to derive f(P,t), it is enough to apply the equation to the specific case of the CO2 external standard gas, obtaining

$$f(P,t) = \frac{S_{CO_2}}{\sigma_{CO_2} \cdot [CO_2] \cdot n_{CO_2\_set} \cdot D_{CO_2} \cdot \eta_{CO_2\_set}} \qquad \textit{Equation (5.4)}$$

If both equations are combined, the concentration of any species can be derived from

$$[x] = [CO_2] \cdot \frac{S_x}{S_{CO_2}} \cdot \frac{\sigma_{CO_2}}{\sigma_x} \cdot \frac{n_{CO_2\_set}}{n_{set}} \cdot \frac{D_{CO_2}}{D_x} \cdot \frac{\eta_{CO_2\_set}}{\eta_{set}} \qquad \textit{Equation (5.5)}$$

The concentration of CO_2, the number of experiments and the ratio of the experimental signals are known. If the discrimination factors can be estimated based on previous measurements with different interface sampling system [262] and the literature PICS are measured or estimated, the only unknown term is the ratio between the efficiency coefficients which is the same for all species of the dataset, including the fuel molecule. The initial concentration of the fuel molecule $[fuel]_0$ and the external standard gas $[CO_2]_0$ are known. Thus, applying the equation 5-5 with the fuel at time zero after the passage of the shock wave, the ratio between the efficiency coefficients can be derived as

$$\frac{\eta_{CO_2\_set}}{\eta_{set}} = \frac{[fuel]_0}{[CO_2]_0} \cdot \frac{S_{CO_2,t=0}}{S_{fuel,t=0}} \cdot \frac{\sigma_{fuel}}{\sigma_{CO_2}} \cdot \frac{n_{set}}{n_{CO_2\_set}} \cdot \frac{D_{fuel}}{D_{CO_2}} \qquad \textit{Equation (5.6)}$$

5.2.2 Experimental results and discussion

As it will be explained in detail in the following chapters, the raw spectral data used with this methodology contains more than 107 000 averaged experiments with 1 % toluene diluted in argon at T_5 and P_5 equal to 1362±22 K and 6.6±0.2 bar, respectively. The evolution of species time profiles ranging from light species up to 5-member rings has been obtained using the pulsed data acquisition mode at a photon energy of 10 eV.

For this dataset, meaningful kinetic profiles require a signal level at least as high as the one for m/z = 350, even though the maximum detectable limit for the raw spectral data is around m/z 426. This is due to the specific signal/noise ratios. However, just to illustrate the external calibration methodology and due to the lack of precise literature information for the photoionization cross sections of large PAHs, the time profiles studied here do not overpass m/z 128.

For instance, **Figure** 5-12a contains species time profiles for the fuel molecule, toluene (m/z 92) and one of the main toluene pyrolysis products, benzene (m/z 78), together with the pressure profile from averaging of 1000 experiments with PCB mounted on the HRRST end-wall, at thermodynamic conditions corresponding to the specific reaction conditions of the toluene experiments.

The species profile for toluene (m/z 92) shows that initially, the concentration corresponds to the fresh gases prior to the arrival of the shock wave at time zero. This is followed by a steep increase corresponding to the reflected conditions. Once the mixture reaches shocked conditions, the concentration of toluene stays constant for around 400 µs and then it starts decreasing gradually as the fuel is pyrolyzed. Finally, at around 500 µs, a sharp decrease is observed to nearly its baseline.

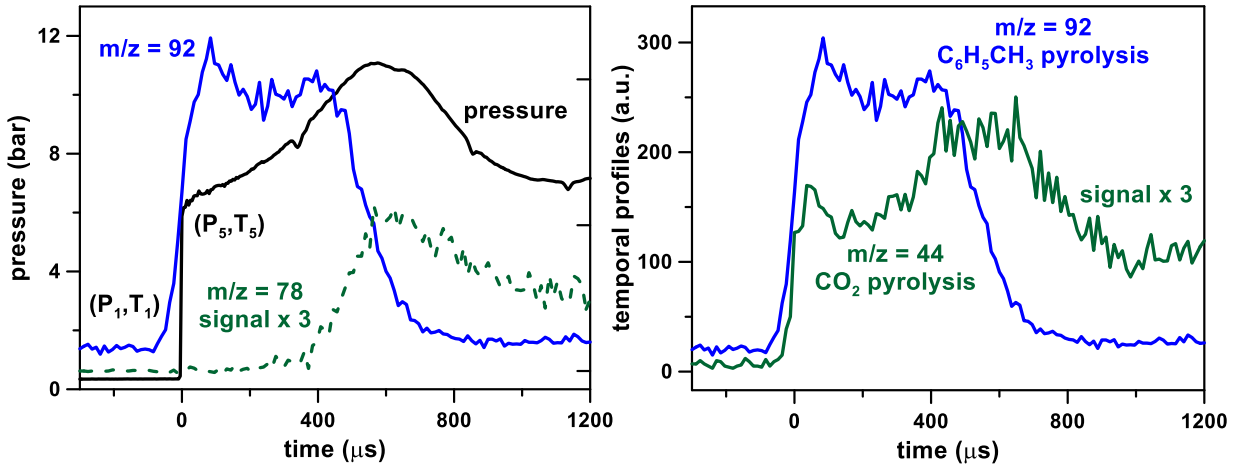

***Figure** 5-12. a) Species time profiles for m/z 92 and m/z 78. Toluene pyrolysis, 0.1% in argon, results obtained from averaging 107 000 experiments at T = 1362±22 K and P = 6.6±0.2 bar, photon energy 10.0 eV; pressure profile from averaging 1000 experiments at same condition. b) Temporal species profiles, m/z = 92 from toluene pyrolysis (0.1% in argon), average over 107 000 experiments at T = 1362±22 K and P = 6.6±0.2 bar, photon energy = 10.0 eV; m/z = 44 from carbon dioxide pyrolysis (0.1% in argon), average over 6 000 experiments at T = 1376±12 K and P = 6.6±0.1 bar, photon energy = 14.5 eV.*

As the fuel profile decreases, the appearance of products can be observed. Benzene (m/z 78), one of the main products, is formed after a certain delay reaching its maximum at approximately 600 µs. It is then consumed at a slower rate. However, based on the temporal profiles of toluene and benzene, it is evident that these profiles are affected by the pressure history during the observation time, in particular in correspondence with the initial rise in the fuel profile (slower than the rise from P_1 to P_5 inside the HRRST) and the later drop in m/z 78 which corresponds also to the drop in pressure due to the arrival of the rarefaction waves. Indeed, the pressure profile presented indicates that there is a rise in pressure behind the reflected shock wave, which lasts for approximately 500 µs. Subsequently, there is a decrease in pressure that lasts for approximately 500 µs after arrival of the rarefaction waves. The changes in the thermodynamic conditions lead to variation of the molecular beam gas density and species concentrations as the non-idealities in the HRRST are larger than those found in conventional shock tubes. As the mass spectrometer signal is directly proportional to the gas density, it is important to consider the pressure time histories in the analysis.

As mentioned before, the species profile for m/z 92 shows a slow buildup of pressure inside the mass spectrometer chamber mainly due to the rapid transition from state P_1 to state P_5. In addition, the shape and starting points of the temporal profiles are influenced by the time of arrival of each shock wave front to the end wall. These times have a stochastic behavior which can vary within ±50 µs around the average. Consequently, the averaged signal is smoother in comparison to a single measurement. As a result, in order to align the fuel profile with the pressure profile, a translation has been performed such that the time corresponding to the half of the maximum value of the fuel profile matches the time zero of the pressure profile.

To determine if the pressure history has an effect on the temporal species profiles, 6042 experiments were conducted using the ICARE-HRRST/i^{2}PEPICO technique with the external calibration standard, CO_2 (0.1% in argon). For the method to be accurate, similar conditions (T_5 = 1376±12 K and P_5 = 6.6±0.1 bar,)

and pressure history used in the actual experiments were kept constant, but the photon energy increased to 14.5 eV to allow ionization of the carbon dioxide.

Since CO_2 does not react at these thermodynamic conditions, its mole fraction will be kept constant even at reflected conditions. Thus, the CO_2 profile varies due to the pressure variation inside the shock tube (and consequently inside the MS chamber) and the resulting signal was monitored and presented in **Figure** 5-12b together with m/z 92 species profile. It appears that the CO_2 profile follows a similar trend as the pressure profile history. Compared to the toluene profile, it seems that CO_2 rises faster than toluene. The difference in the rise slope between the CO_2 and m/z 92 profiles may be an artifact of the difference in number of experiments (~ 6 000 vs 107 000) and the large difference in signal levels. However, this hypothesis has to be demonstrated in future campaigns.

The first results obtained using the external standard calibration technique for analyzing toluene pyrolysis are presented in **Figure** 5-13. The alignment between the fuel and CO_2 profiles is a major uncertainty in the technique, as their initial rise times differ slightly. Actually, misalignment can amplify signal noise during data processing, leading to increased uncertainty.

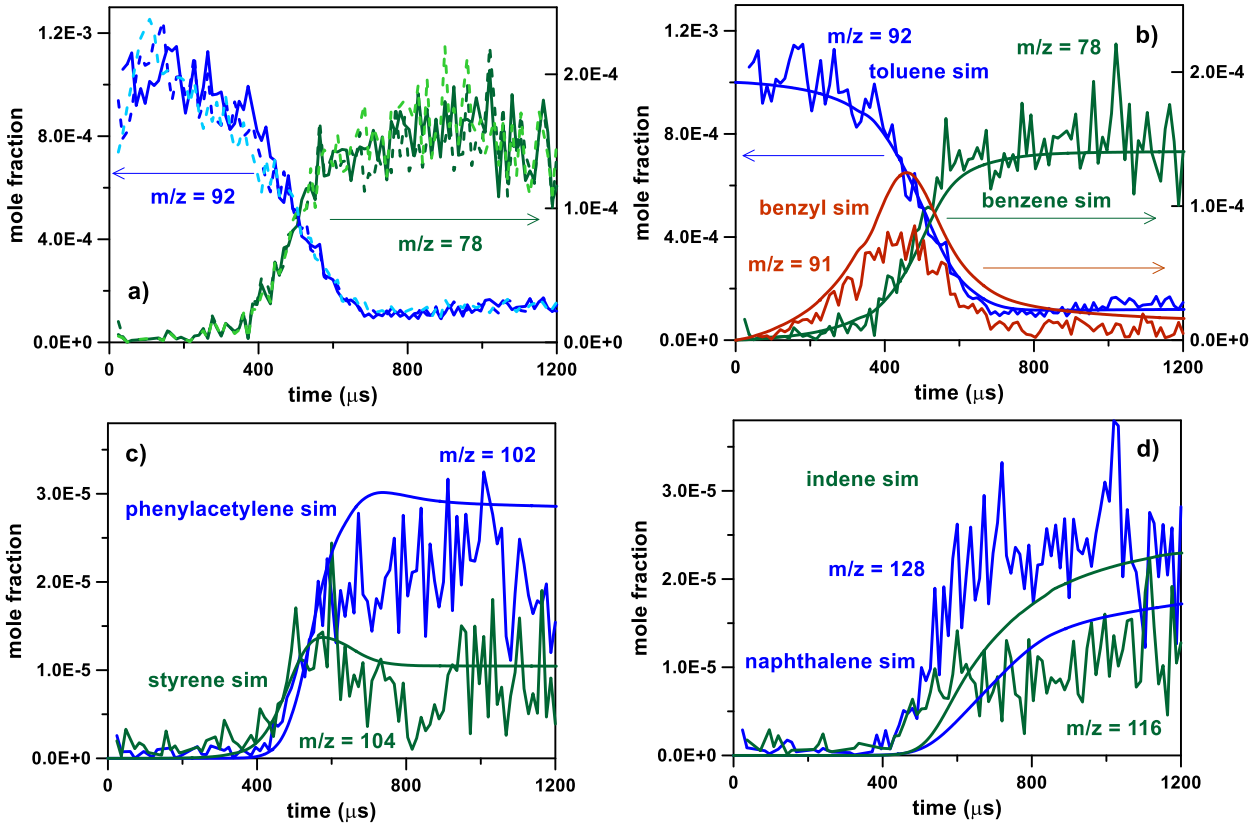

***Figure** 5-13. Temporal species profiles from toluene pyrolysis (0.1% in argon), average over 107 000 experiments at T = 1362±22 K and P = 6.6±0.2 bar, photon energy = 10.0 eV. In a), different matching between fuel and CO2 profiles: solid line at the peak, light dashed line at start of the rise, dark dashed line at 50% rise. Lines in b)-c)-d) represent kinetic modeling with ICARE PAH chemistry model.*

Figure 5-13a shows the fuel profile (m/z = 92) and benzene profile (m/z = 78) with the CO2 profile shifted to match i) the times at the half of the signal rises as in **Figure** 5-12 (dark dashed lines), ii) the times matching the two main peaks (solid lines, CO2 profile shifted +36 µs), and iii) the times at which the two profiles start rising (light dashed line ,CO2 profile shifted by -24 µs). The first 200 µs of the fuel profile are mostly affected by different treatments, resulting in less oscillations for the second case (ii). The noise in the treated signal before time zero is large, rendering the derived information useless. The product profiles are not significantly affected by the alignment procedure, as their appearance occurs at late times. Finally, the method ii) was preferred due to reduced noise at early stages.

The corrected temporal species profiles for the fuel and some of the main products are presented in **Figure** 5-13b, c, and d. These species were chosen based on their abundancy compared to other minor isomers, and also because their identification was easily achieved by comparing their reference photoelectron spectra with the experimental ones obtained in this study which will be presented in the next chapter. Moreover, the photoionization cross sections (PICS) of these species are available in literature, with some being measured and others estimated. The measured PICS at 10 eV for toluene, phenylacetylene, styrene, indene, and ethylbenzene was obtained from Zhou et al.[263], benzene from Rennie et al. [264] while the estimated value for naphthalene was taken from [265]. The PICS at 14.5 eV for CO2 is taken from Hitchcock et al. [266]. A list of photoionization cross sections used in this work is presented in annex **A 6**.

The concentration profiles are compared with simulations performed with the ICARE chemical kinetic model for PAH formation and growth using ANSYS CHEMKIN-Pro 2021 software, batch reactor with variable pressure following the profile in **Figure** 5-12a. The model has been validated against species profiles vs temperature conditions from single-pulse shock tube experiments for pyrolysis of a large number of single fuels at nominal pressure of 20 bar, including toluene, ethylbenzene and their mixtures with small aliphatics. There is an overall excellent agreement between experiments and simulations for the decomposition of the fuel and the formation of the main single-ring aromatic products, including benzene (m/z = 78), styrene (m/z = 104), phenylacetylene (m/z = 102) and a peak at m/z = 91, corresponding to the benzyl radical, also detected and measured for which the same parameters as for m/z = 92 were used as first approximation. The shape of the m/z = 91 profile is correctly captured by the model, as well as its concentration considering the related uncertainties. The species profiles for larger PAH products, such as indene (m/z = 116) and naphthalene (m/z = 128), are shown in **Figure** 5-13d, and the results are quite satisfactory considering the complexity of the chemistry involved in the PAH formation and the experimental uncertainties. A complete and detailed description of the pyrolytic products and their chemistry will be presented in the next chapter, and the examples presented here serve the purpose of demonstrating the capability of the external standard calibration method.

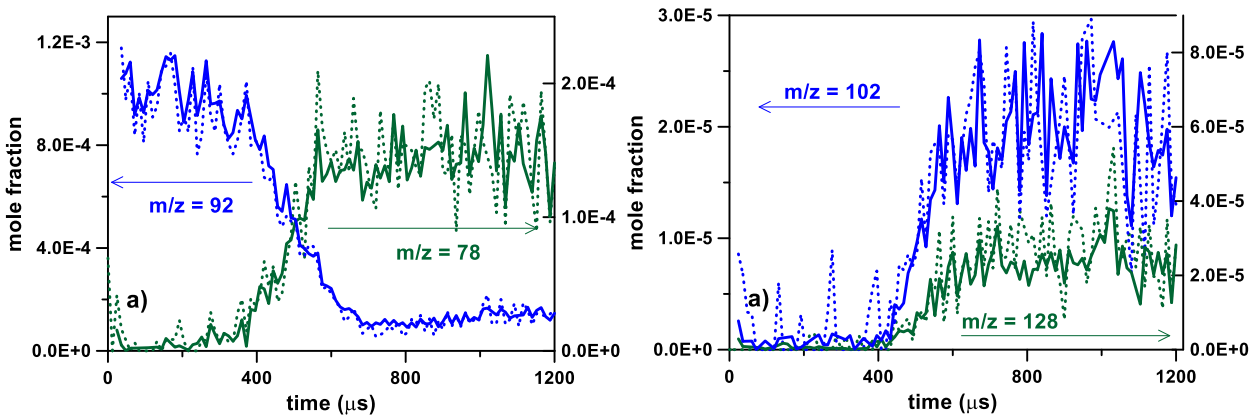

***Figure** 5-14. Temporal species profiles from toluene pyrolysis (0.1% in argon), average over 107 000 (solid lines) and 27 000 (dashed lines) experiments at T = 1362±22 K and P = 6.6±0.2 bar, photon energy = 10.0 eV.*

Figure 5-13 presented the experimental species profiles, which were obtained by averaging roughly 107,000 experiments. To evaluate the effects of decreasing the number of experiments on the signal quality, a set of 27,000 experiments was selected to derive species time profiles using the same methodology. **Figure** 5-14 presents the results of this set for various m/z ratios in dashed lines along with the results from averaging 107,000 experiments in solid lines. The overall profiles are very similar in the two cases in terms of shape and concentrations even if the noise is less for larger amount of experiments. Thus, it can be affirmed that the external standard calibration method is not significantly affected by the signal levels or number of experiments and that even a band pass filter could be used in order to smooth the signals with lower amount of experimental information without losing quality. This is of especial interest for experimental campaigns where the time limitation in beamlines has to be rapidly optimized and accurate signal levels for target species has to be obtained.

To demonstrate the validity of the proposed external standard calibration method with different fuel molecules characterized by different kinetic properties, a more reactive fuel than toluene was tested, i.e. ethylbenzene. The fuel was pyrolyzed at similar conditions than the case of toluene (T_5 = 1327±18 K and P_5 = 6.7±0.2 bar, 0.1% in argon). More than 27,000 were obtained with a photon energy of 10.0 eV.

The raw fuel profiles of ethylbenzene (m/z = 106) and toluene (m/z = 92) presented in **Figure** 5-15a demonstrate that ethylbenzene is more reactive than toluene. Additionally, the ICARE model simulations showed in **Figure** 5-15b, c and d, seem to well reproduce the shape and concentration of the fuel molecule and main products like benzene (m/z = 78), toluene (m/z = 92), styrene (m/z = 104), phenylacetylene (m/z = 102) and the benzyl radical (m/z = 91). Nevertheless, there is a minor discrepancy in the time at which the toluene peak occurs. Finally, there is a satisfactory match between the experimental and simulated profiles for larger PAHs such as naphthalene (m/z = 128) and indene (m/z = 116), although the relative concentrations were not perfectly captured as for the case of toluene. Despite this, the simulated profiles accurately capture the overall experimental data.

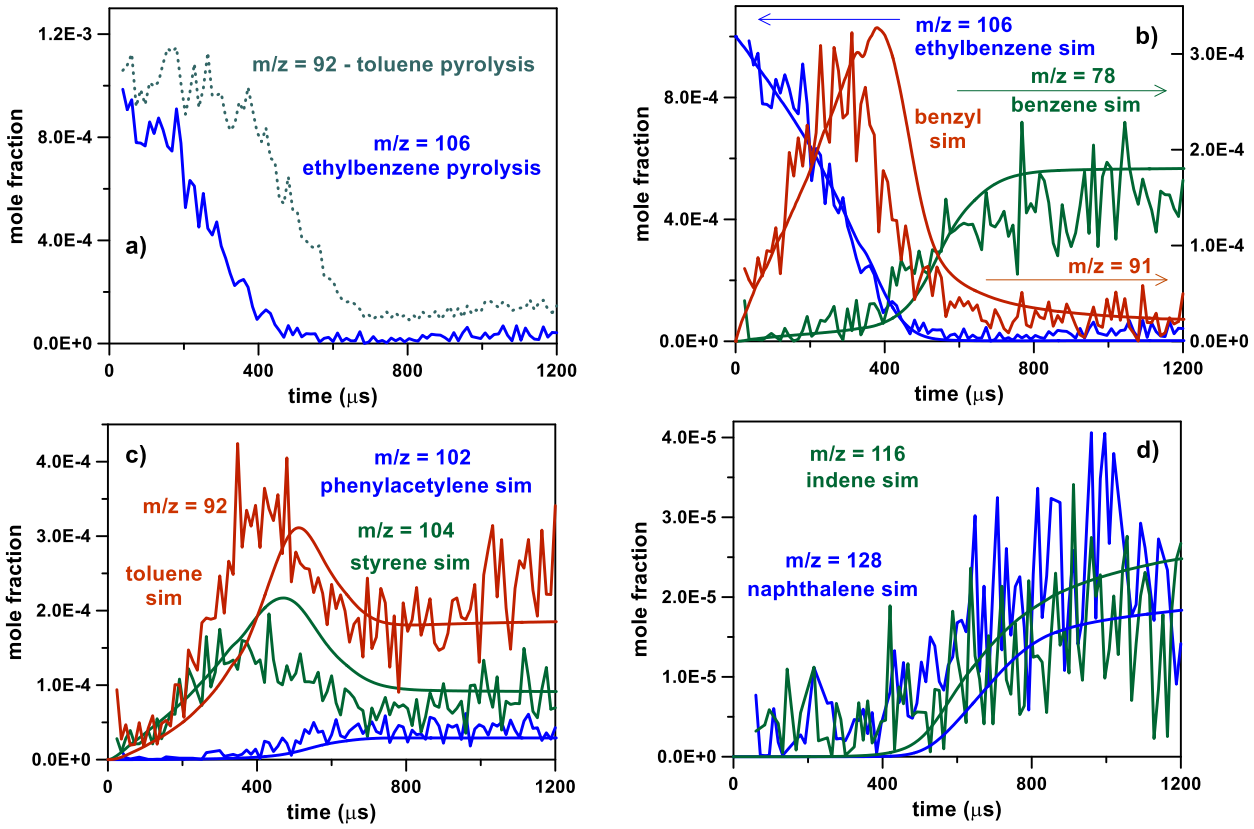

***Figure** 5-15. Temporal species profiles from ethylbenzene pyrolysis (0.1% in argon), average over 27 000 experiments at T = 1327±18 K and P = 6.7±0.2 bar, photon energy = 10.0 eV. a) includes the m/z = 92 from toluene experiments as in **Figure** 4. Lines in b)-c)-d) represent kinetic modeling with ICARE PAH chemistry model.*

In this chapter, a new methodology for correcting concentration profiles obtained from miniature high-repetition-rate shock tubes coupled to Synchrotron-based mass spectrometry diagnostics has been proposed. The method utilizes CO_2 as an external standard gas to correct for pressure variations within the mass spectrometer due to the inherent dynamic behavior of the HRRSTs. The validity of the method was evaluated based on experiments for the thermal decomposition of toluene and ethylbenzene. The corrected profiles for fuels and main products resulted in excellent agreement with simulations obtained employing the most updated version of the ICARE PAH model, demonstrating the reliability of the procedure. It has been determined that the external standard method is a versatile technique to obtain kinetic information from HRRST/TOF-MS experiments conducted at synchrotrons, including the HRRST/i^{2}PEPICO coupling.

5.3 Pyrolysis of toluene using HRRST/i^{2}PEPICO

The results from the first pyrolytic study on aromatic chemistry using the HRRST/i^{2}PEPICO combination is presented in this chapter, demonstrating the capabilities of the technique, specifically in relation to detection and measurement of large PAH products. Toluene (C_7H_8) was chosen as a fuel for this purpose because it is an important fuel surrogate component and intermediate during the formation and growth of PAHs. This study complements the literature kinetics works on toluene pyrolysis using different conventional speciation systems such as shock tube/GC-MS [61], [65] and atmospheric and sub-atmospheric flow reactors [98], [105].

Regarding the experimental installation, the set-up components and parameters were kept constant during the campaign. Nevertheless, compared to the first installation used in the ethanol campaign, some improvements were implemented. The *birdcage* used here allows the easy variation of the distance between the nozzle tip and the skimmer tip as discussed in the methodology section. Skimmer 1 and skimmer 2 have orifices diameters of 1 and 2 mm, respectively. The employed nozzle has a 400 µm orifice and the optimal distance between the nozzle and the skimmer 1 tips is found to be around 9.5 mm. Indeed, the first tests with distance of around 4 mm (equal to 10 times the nozzle orifice diameter) showed very weak signal levels. The 9.5 mm distance allows the pressure inside the mass spectrometer chamber to remain at acceptable levels even when the shock tube runs at 1.5 Hz (between 10^{-8} and 10^{-6} mbar during operation). Despite this, all the experiments presented here are performed at 1 Hz repetition rate.

Additionally, during the previous ethanol campaign a noise appeared after several thousand HRRST runs which affected the ability to obtain data from the system. With the aim of resolving the issue, the new installation includes the possibility to apply a voltage to skimmer 1, electrically isolated from the ground. In particular, a voltage of -120 V was chosen in order to avoid possible electrically charged ions carried by the molecular beam entering the mass spectrometer chamber. While the low temperature experiments (1300-1400 K) could be run without problems, the higher temperature ones (1700-1900 K) still showed noise. The reasons behind this noise is still under evaluation. Strategies to include charged parallel plates through which the molecular beam passes before entering skimmer 2 will be tested in the next experimental campaign.

Two experimental conditions are presented in this chapter with the two data acquisition modes available for DELICIOUS III. The first condition is also the one used to validate our external calibration method developed for analysis on species concentration vs time presented in section 5.2. Briefly, the experimental pyrolytic decomposition of 0.1 % toluene diluted in argon bath gas was evaluated at T_5= 1362 ± 22 K, P_5=6.6 ± 0.2 bar and photon energy of 10 eV. The selection of this specific photon energy allowed the photoionization of the fuel molecule as well as key aromatic intermediates. The data was recorded during 8 ms comprising the pre-shock and post-shock regions by using the so-called *pulsed mode* for data acquisition. More than 107 000 experiments were averaged at this condition.

The second condition is similar, with 0.1 % toluene in argon at T_5= 1351 ± 13 K and P_5=6.4 ± 0.1 bar, but a photon energy of 8.5 eV was employed this time. This allowed the photoionization of most of the PAH species obtaining PES for larger masses at expenses of detecting the fuel molecule and some intermediates. More importantly, because of the natural pulsed operation of the shock tube, the data acquisition *pulsed mode* allowed obtaining accurate PES signals only for high concentration species which corresponds to small aliphatics and single-ring aromatics. Therefore, the *continuous* acquisition mode was

employed in this second case, which means that the acquisition does not stop between shock runs. This allows increased S/N for the minor species compared to the pulsed mode, as well as sharper features of the PES profiles. More than 41 000 experiments were averaged. The results of the pulsed mode and continuous mode are presented parallelly during the discussion of the results, considering that temperature and pressure conditions were kept the same for both cases.

5.3.1 Mass spectrum and identification of small aromatic products

The mass spectrum averaged over 8 ms for the pulsed mode is shown in the **Figure** 5-16, from the pyrolysis of 0.1 % toluene evaluated at T5= 1362 ±22 K, P5=6.6 ± 0.2 bar and photon energy of 10 eV. The mass spectrum has been divided into four regions for better visualization. Starting from the major peaks at small mass to charge ratio, m/z 40 derives from the second order harmonic of argon, followed by peaks corresponding to the aromatic ring fragmentation. In particular, m/z = 52 corresponds to vinylacetylene (PI = 9.63 eV[236]), m/z = 54 to 1,3 butadiene (PI = 9.07 eV[267]), m/z = 64 to 1,3-pentadiyne (PI=9.5 eV[268]), and m/z = 74 to triacetylene (PI = 9.5 eV[268]). **Figure** 5-18 contains the related experimental PESs and the literature profiles for these species. Vinylacetylene presence has been previously attributed to the acetylene (C_2H_2) self-reaction via vinylidene which can lead also to the production of 1,2,3-butatriene [269]. In the experimental PES for m/z 52 it is obvious how 1,2,3-butatriene [237] and cyclobutadiene [270] can be excluded as products of toluene pyrolysis at the conditions presented here. Regarding m/z 64, previous studies using potential energy surface method have shown that 1,3-pentadiyne formation can be due to the decomposition pathway from fulvenallene (m/z 90, C_7H_6) to 1,3-pentadiyne and acetylene [271]. It is in fact interesting how the present mass spectrum contains not only a peak at m/z = 91 (corresponding to the fuel resonantly stabilized benzyl radical (C_7H_7)) but also a peak at m/z 90. The set obtained at 8.5 eV is used for identification purposes in this case since the PES signal for the peak at m/z 90 (C_7H_6) is too small in the set at 10 eV. It can be seen in the **Figure** 5-17 that the literature PES for fulvenallene exactly corresponds to the experimental PES obtained for m/z 90, in particular the ionization energy for this molecule (8.22 ± 0.005 eV[272]) matches the peak present at 8.24 eV in the experimental PES. Since the literature PES for fulvenallene has much greater resolution than the experimental PES for m/z 90, a binning procedure was applied to the available PES in order to compare with the experimental profiles and confirm that the peak shape differences are just an artifact of the technique. This can be seen with the binned literature PES in red dotted line, proving the reliability of the binning procedure which converts the reference PES resolution to the experimental resolution. This procedure will be discussed more in detail later. Fulvenallene has been proposed in the past as one of the main decomposition products of benzyl radical fragmentation at high temperatures [273]. In m/z 74 (C_6H_2), 1,3,5-hexatriyne also known as triacetylene was identified. The pathways involved in the formation of this species is still not well understood. A reaction pathway was proposed indicating that triacetylene could be produced through a polymerization process but the research could not clarify this [63] especially at the temperatures considered here, where C_2H_2 and C_4H_2 do not decompose. Thus, this study concluded that triacetylene is mainly produced through the decomposition of the C_6H_3 radical by the reaction $C_6H_3 \leftrightarrow C_6H_2 + H$. C_6H_3 is mainly formed from isomers/ring opening/fragmentation of C_6H_4 which was detected here as m/z = 76. Due to lack of literature PES for this mass, it was not possible to clearly identify the C_6H_4

intermediate, although o-benzyne from the thermal fragmentation of the benzyl radical [274] is a very probable candidate.

A small peak at m/z 54 is also evidenced in the mass spectrum which corresponds to isomers of C_4H_6. In that case, the experimental PES peaks at around 9.15 eV proving the presence of 1,3 butadiene (PI = 9.07 eV[267]) even with such low resolution, but the peak at 9.8 eV cannot be clearly attributed to any of the isomers shown in the **Figure**. The most probable product is from 2-butyne (PI = 9.6 eV [240]) but other isomers should be considered before reaching a conclusion.

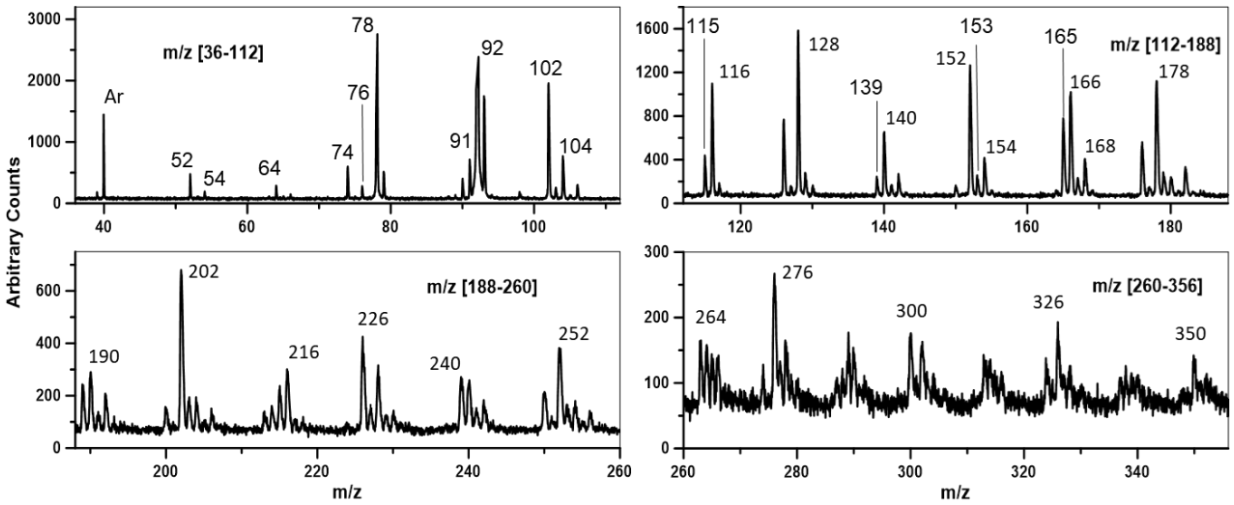

***Figure** 5-16. Mass spectrum obtained in pulsed mode, averaging over 107 000 experiments. 0.1% toluene in argon, photon energy 10 eV. T5= 1362 ±22 K, P5=6.6 ± 0.2 bar.*

Concerning the single ring aromatics, in previous work using single pulse shock tubes coupled to gas chromatography it was possible to measure toluene (C_7H_8), the fuel, and the largest product benzene (C_6H_6) which is a relevant species during soot formation and initiation through the HACA mechanism. Benzene is produced from toluene pyrolysis mainly through the ipso-substitution reaction $C_7H_8+H = C_6H_6+CH_3$ [65]. Similarly, in the present study m/z 92 and m/z 78 are the biggest peaks corresponding to toluene and benzene, respectively. **Figure** 5-18 presents the comparisons of the photoelectron spectra corresponding to m/z 92 and m/z 78 with the literature ones for toluene and benzene, respectively. In the laboratory-based work [65], large amounts of phenylacetylene (C_8H_6, also $C_6H_5C_2H$) and styrene (C_8H_8, also $C_6H_5C_2H_3$) were measured which are confirmed in the mass spectrum at m/z 102 and m/z 104, respectively, plus a small amount of ethylbenzene (ETB, C_8H_{10}, also $C_6H_5C_2H_5$) as a minor single ring species (m/z 106). Following HACA mechanism, phenylacetylene comes from the addition of acetylene to phenyl, the benzene radical, through the reaction $C_6H_5 + C_2H_2 \rightarrow C_6H_5C_2H + H$ [275]. ETB and styrene are produced from the recombination of the fuel radical, benzyl (C_7H_7), with one methyl (CH_3) [65], and subsequent thermal decomposition of the resulting ETB intermediate, respectively. These three species are clearly identified by the PES comparison presented in **Figure** 5-18. The peaks at 8.75 in the experimental PES for m/z 102 confirms the presence as major contributors of phenylacetylene whose photoionization energy (PI) is 8.75 eV[276]. This allows to exclude the presence of different other isomers also shown in the **Figure**

like benzocyclobutadiene [277] and 2,4,6-octatriyne[256]. The same applies for the experimental PES of m/z 104 and m/z 106 whose peaks coincide with literature photoionization energies for styrene (PI = 8.464 eV[278]) and ethylbenzene (PI 8.77 = eV[279]), respectively. In particular, while examining the experimental PES for m/z 104, the exclusion of benzocyclobutane [26] is possible based on the shape of the profiles (the experimental profile has two major peaks, the one for benzocyclobutane is flat in this photon energy range). However, it is not possible to exclude the presence of the xylylene isomers (o-m-p-C_8H_8[280], [281]) as the signal is quite noisy at photon energies lower than 8 eV. On the other hand, by modifying the binning of the signal (see the embedded image), clear features in correspondence with the xylylene isomers appear. Actually, there is evidence from a previous study realized with the single pulse shock tube coupled to GC-GC/MS on xylene chemistry that o-xylylene following dehydrogenation of o-xylyl isomers is an intermediate to styrene formation [66]. Globally, the contribution from the xylylene isomers is minimal compared to the styrene one.

Concerning m/z 106, although the corresponding signal is small, the peak at around 8.5 eV confirm that not only ethylbenzene is produced but also the xylene isomers. Xylenes [255], [282]contribute to the m/z 106 signal for around 38% against the remaining 62% associated to ethylbenzene (ETB). According to recent studies realized with SPST/GC system, the production of xylene comes from the recombination reaction of the toluene radical ($CH_3C_6H_4$) with methyl (CH_3) [74]. Additionally, the latest study on pyrolysis of xylene isomers realized with HPST/GC-GC/MS revealed that xylenes decompose mainly via hydrogen abstraction reactions by H, CH_3 and C_7H_7, forming toluene and xylyls (m-o-p-C_8H_9) which are resonantly stabilized radicals. Xylyls (m-o-p-C_8H_9) directly decompose to o-m-p-xylylene (o-m-p-C_8H_8) through the chemical reaction (o-m-p-C_8H_9) -> (o-m-p-C_8H_8) + H, which supports the observation of the presence of xylylene isomers in the experimental PES of m/z 104.

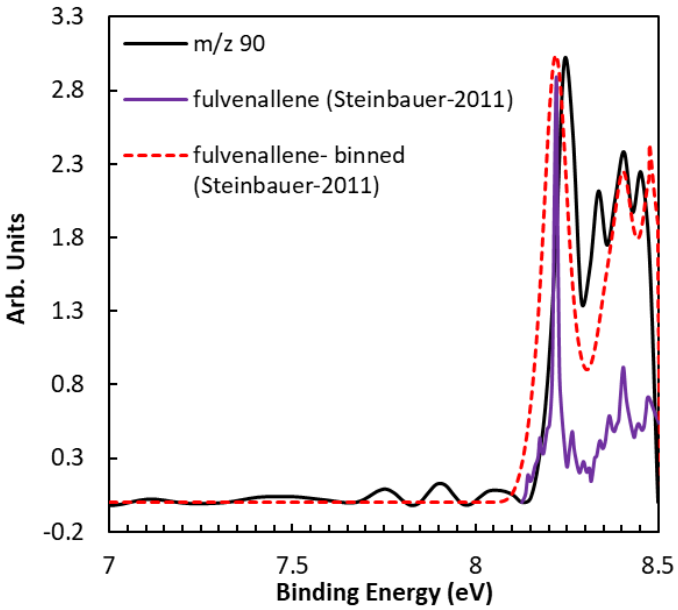

***Figure** 5-17. Photoelectron spectra for m/z 90 obtained at 8.5 eV. Literature PES for fulvenallene and binned literature PES for fulvenallene*[272].

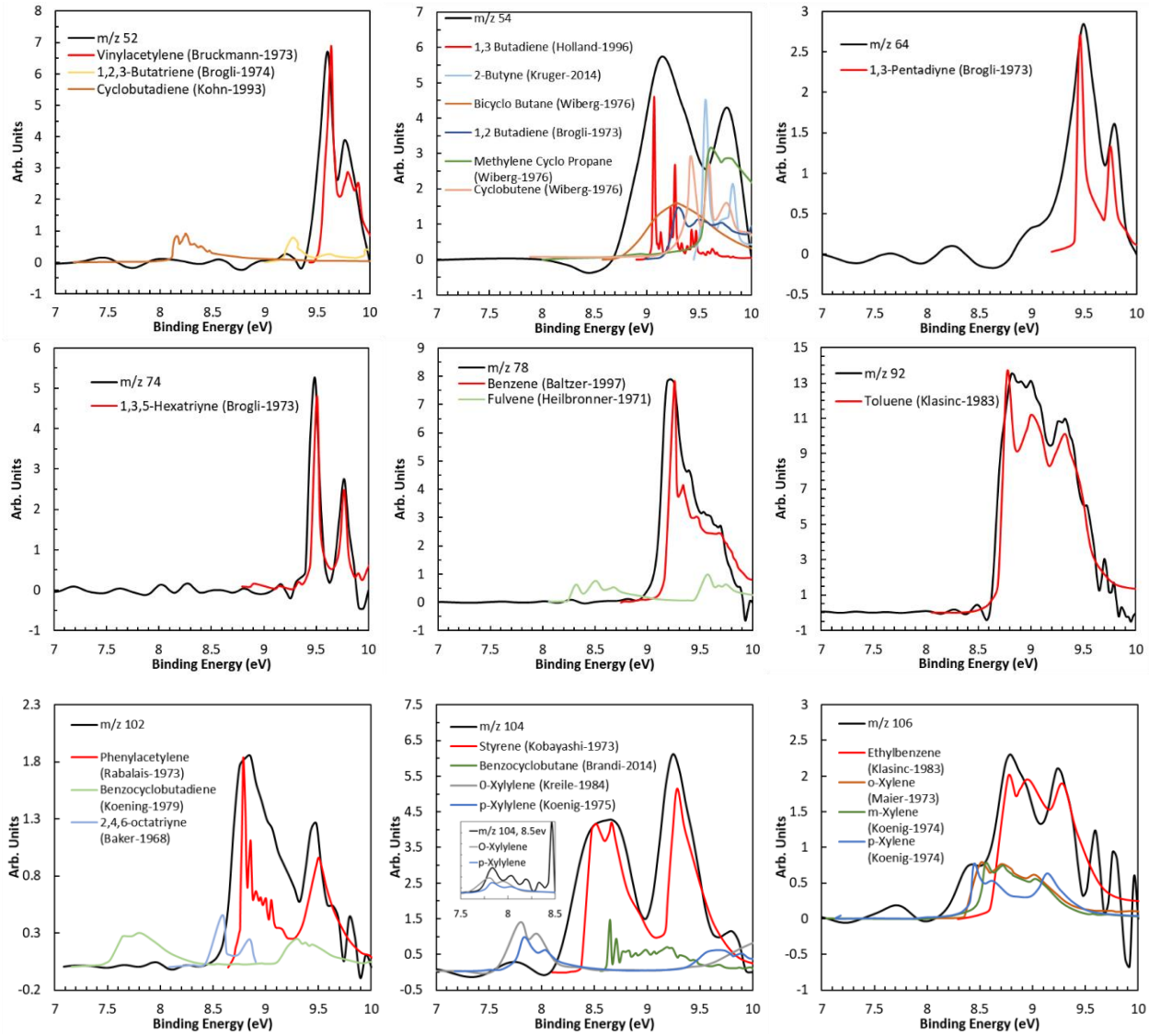

***Figure** 5-18. Photoelectron spectra of product molecules with m/z ranging from 52 to 106. Photon energy of 10 eV.*

Concerning the two and three rings PAH molecules, the gas chromatographic measurements in [65] showed some major products including indene (m/z 116), naphthalene (m/z 128), acenaphthylene (m/z 152), fluorene (m/z 166), phenanthrene/anthracene (m/z 178), and of course bibenzyl from the benzyl recombination (m/z 182) with the presence also of minor isomers like 1-methylene indene (m/z 128) and 1-ethynylnaphthalene (m/z 152). These compounds are also the major peaks in the mass spectrum of **Figure** 5-16, confirming the importance of the related kinetic pathways. However, in this work, additional isomeric compounds could be identified by analyses of the mass selected photoelectron spectra presented on the following section.

In addition to the major species in common with the previous HPST/GC-GC-MS work, other masses are present for two and three ring minor species, including m/z 168, m/z 126, m/z 140, m/z 142, m/z 176 and m/z 180, and other peaks corresponding to radical molecules, e.g. m/z 115 and m/z 165 which should correspond to indenyl and fluorenyl resonantly stabilized radicals, respectively. The correspondence of the m/z 154 with acenaphthene/biphenyl will be discussed based on the PES.

For larger PAHs, m/z 202 is the major product. Products with similar mass/charge ratio were identified as the four ring products pyrene and fluoranthene in the previous work [65]. From the mass spectrum, clearly defined peaks corresponding to four-five ring species, larger than what can be achieved in the conventional shock tube/GC system, can also be observed. These peaks correspond to m/z 190, m/z 216, m/z 226, m/z 228, m/z 240, m/z 250, m/z 252, m/z 254 and m/z 280. The exhaustive species identification for these peaks will be discussed in the following section. Bigger species are also visible but with lower signal levels as can be seen in the mass spectrum. For the kinetics profiles, discernable trends can be obtained for m/z up to 350, although the identification starts becoming very challenging from m/z = 230 due to low signal and lack of literature data on PES profiles. Additional experiments would have been necessary to increase the definition of the peaks for these large molecular weight species. Peaks from the integrated mass spectrum were also measured for m/z up to 426 although small, while periodic groups of peaks providing broad featured signal rises are visible for larger masses (**Figure** 5-19).

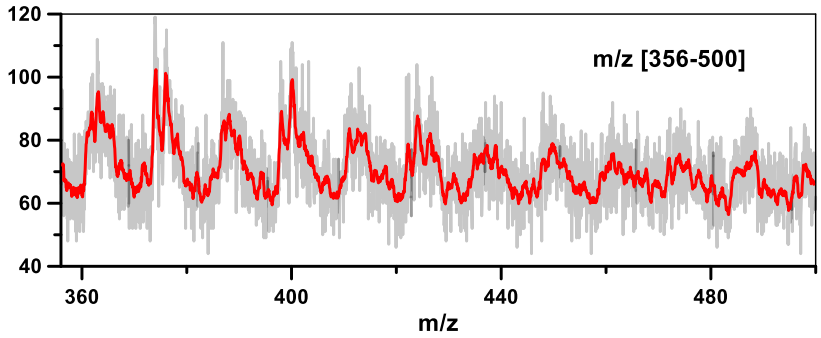

***Figure** 5-19. Zoomed region of the mass spectrum obtained in pulsed mode comprising signals from m/z 356 to m/z 500. 0.1% toluene diluted in argon, photon energy 10 eV. T5= 1362 ±22 K, P5=6.6 ± 0.2 bar*

In general, the number of isomers increases exponentially with the m/z ratio, thus a complete characterization of the large products is beyond the current capabilities. On the other hand, the following analyses will provide additional information on the major growth mechanisms based on the observations on the small PAH molecules. These growth mechanisms include CH_3 addition forming 3-carbon ring structures as well as stable intermediates with methyl moieties (as methylbiphenyls), the possible propargyl radical addition to form benzo-like structures, and the common HACA mechanism for the growth of number rings and the formation of 5-member rings in the PAH bays (as from naphthalene to acenaphtylene $C_{10}H_7+C_2H_2 = C_{12}H_8+H$). The addition of PAH radicals will also play a key role.

In the following section, detailed analyses of the relatively-small PAHs based on the photoelectron spectra for major m/z ratios will be presented.

5.3.2 Mass selected identification of polycyclic aromatic hydrocarbons

The data obtained with the *pulsed* mode may be used to obtain the photoelectron spectra of polycyclic aromatic hydrocarbons (PAH) but a more efficient way involving the data acquisition in *continuous* mode and with reduced photon energy (8.5 eV) has been implemented to obtain improved signal to noise ratio and sharper PES features for better isomer selectivity at a given m/z. Of course, kinetic analyses cannot be performed with the extracted data since the acquisition is *continuous,* without a time reference for the shock runs, opposite to the pulsed mode where ion kinetics analyses till 8 ms relative to shock wave arrival can be performed, including quantification of species, as explained in section 5.2 relative to the calibration method.

The average mass spectra over 41 000 runs, for an ionization energy of 8.5 eV, is illustrated in **Figure** 5-20. At a first glance, it is clear how the mass spectrum is very different from the one at 10 eV. First of all, the small species are not detected because most of them ionize at higher energies, while here the photon energy of 8.5 eV is close to the ionization energy of larger PAHs. In addition, the cross-sectional areas at 10 eV and at 8.5 eV might change differently depending on the species, thus modifying the relative signals for the same concentrations. Thus, the same PAH molecules are common to both mass spectra at 8.5 eV and 10 eV, although with different proportions.

In reality, the choice of the photon energies is a trade-off between need of ionizing a specific group of compounds (PAHs in this case) reducing the noise for better detection of the low-concentration species and keeping in mind that the signal level decreases at lower photon energies. For example, the ionization of the fuel and major products (e.g. benzene) is not desired as it would lead to the occurrence of false coincidences and thus noise in the signal. This is the reason why cleaner signals for low-concentration species is noticed in the mass spectrum of **Figure** 5-20 compared to **Figure** 5-16.

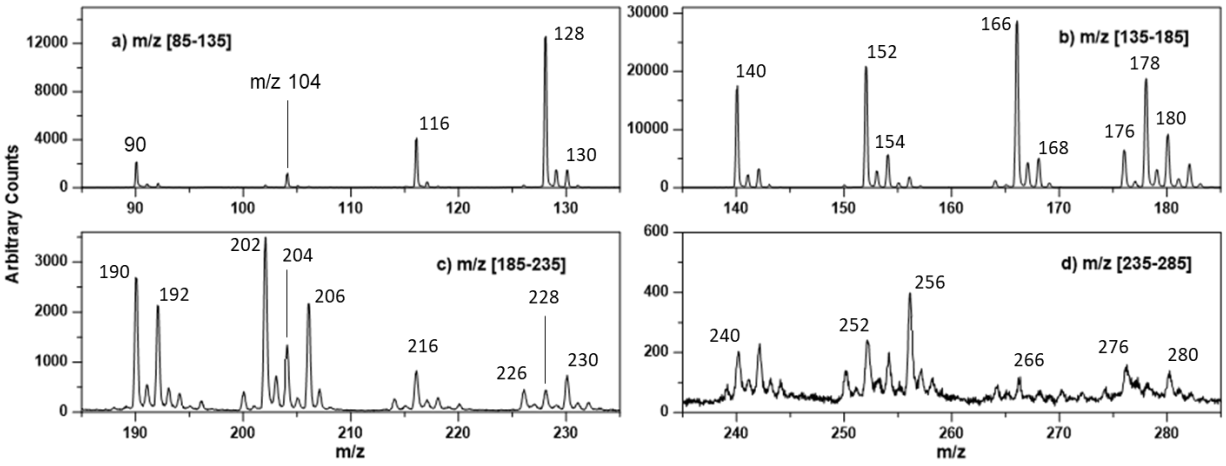

***Figure** 5-20. Mass spectrum obtained in continuous mode, averaging around 41 000 experiments. 0.1% toluene in argon, photon energy 8.5 eV. T_5= 1351 ± 13 K and P_5=6.4 ± 0.1 bar.*

The PES analysis presented here is based in previously discussed Equation (5-1), where a semi-automatic optimization procedure has to be applied in order to produce a sum of convolved PES spectra to well fit the experimental PES curves. This allows to determine the relative concentrations of the isomers present at each m/z by exporting the constants (C_i) in Equation (5-1). Nevertheless, for most of the PAHs presented here, either no experimental works on the determination of photoionization cross section (PICS) are available in the literature or only estimated information could be found, which introduce large uncertainties to the relative concentration determination. Thus, an exhaustive analysis based on signal ratios (i.e. S_1/S_2) will be presented here. Depending on the evolution of the research on PICS and mass discrimination effects, future investigations will focus on the accurate quantification of the relative concentrations by applying Equation (5-2).

More importantly, due to the limitations in the number of PESs studied in the literature, the analyses will evidence how several features of the experimental PESs would not be reproduced based on the available data. Since the main advantage of investigating the i^2PEPICO photoelectron spectra is to identify the different isomers present in a specific m/z signal, new information on the photoelectron spectra had to be obtained in order to fully exploit the technique. Therefore, a recent collaboration with Dr. Jasper at Argon National Laboratory (ANL), USA, has allowed the determination of theoretical PESs of large PAHs compounds by complementary high-level ab-initio quantum calculations based on Frank Cordon parameters. The uncertainties associated to the assessment of the spectral characteristics of the PAHs, related to the different vibronic states, can be estimated smaller than 0.05 eV when the calculation is based on the higher-level methods (HL). Since some of the calculations based on HL required very large computational resources, a 'medium-level' theory was implemented for certain PAH compounds with uncertainties lower than 0.1 eV.

The uncertainty in the definition of the PESs will affect the convolution of the experimental signal and the derivation of the different contributions from the various isomers. The development of an automatic code capable to provide a large number of fitting parameters by shifting the PESs within their uncertainties should be envisioned for determining the experimental uncertainties related to this aspect. This is though beyond the scope of this thesis work. At the present, the best option is to manually fit the relative heights of the peaks even if not exactly located at the exact binding energy, if required. An example is provided in the following sections related to m/z 128. Another source of uncertainty in the fitting procedure is the selection of the isomers. In fact, the simulation can be run considering a different number of isomers or a different combination of isomers, in particular with respect to the minor components. In general, the possibility to run several fitting procedures provides a way to estimate the experimental uncertainty for the different contributions to the signal. An example is provided as related to the contribution of fluorene to m/z 166 (section 5.3.2.10).

With the aim to correctly compare the experimental and literature/calculated PESs for each m/z, the resolution of the simulated PESs along with the literature ones were binned to the resolution of the respective experimental PES. The binning process consists on the conversion of the reference PES into gaussian functions that take into consideration the spectral resolution of the reference PES. Then, the spectral characteristics are spread accordingly with the experimental PES resolution in order to get a binned reference PES that will be used for comparison. This process is realized by using an IGOR subroutine developed by the DESIRS beamline scientists. The contribution of this ongoing collaboration with ANL is essential for providing novel, high-quality databases for accurate PES analyses.

The data presented in the following sections will be ordered by increasing m/z values and not based on the relative importance as observed in the mass spectra. This will allow an easier discussion on the kinetic pathways involved in the formation of the different isomers, based on simulations with the ICARE PAH model and on chemical intuition. The PAH identification will also provide an important contribution not only for the combustion science but also for astrophysics [283], [284]. The full list with the nomenclature and structures for the species involved in the mass-selected isomer identification can be found in annex **A 7**.

5.3.2.1 Species at m/z 116

The m/z 116 is in general present in all the studies performed with mass spectrometry techniques on PAH chemistry. For this mass to charge ratio, an excellent fitting was found between the experimental PES and the literature spectra for indene (C_9H_8, [26]). Almost 88% of the experimental signal derives from the indene spectra as evidenced in **Figure** 5-21. According to previous work using ST coupled to GC and rate of production analyses at the current conditions, indene is mainly produced from the reaction between the benzyl radical (C_7H_7) and acetylene (C_2H_2) [65] as well the isomerization of $C_6H_5C_3H_3$ isomers. Indene is consumed by thermal decomposition and H-abstraction to form the resonantly stabilized indenyl radical. A relatively large peak at m/z 115 is indeed observed in **Figure** 5-16.

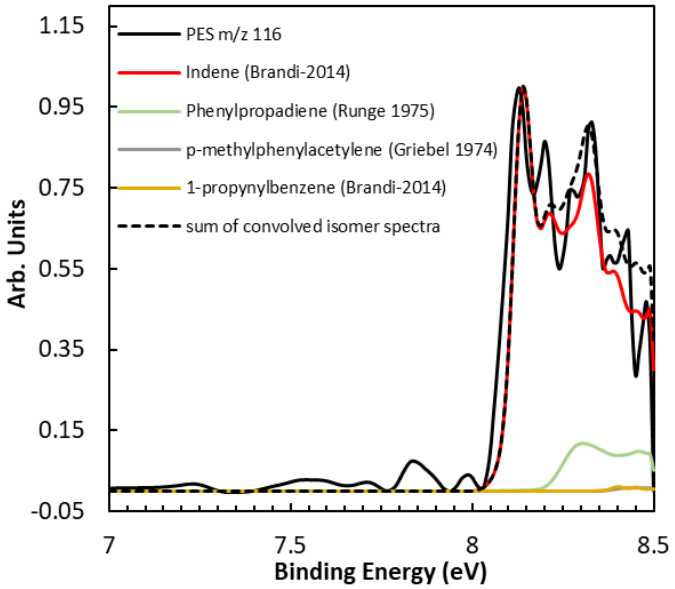

***Figure** 5-21. Experimental and reference photoelectron spectra for m/z 116 obtained at 8.5 eV.*

A relatively small amount of phenylpropadiene ($C_6H_5CHCCH_2$, $PI_{vertical}$ = 8.29 ±0.03 eV, [260]) was found to contribute to the second signal peak located at 8.31 eV. This species is produced from the reaction of C_3H_3 with phenyl (C_6H_5). Additionally, from the sum of convolved spectra analysis the presence of p-

methylphenylacetylene ($C_6H_5(CH_3)C_2H$, [285]) and 1-propynylbenzene ($C_6H_5CCCH_3$, [26]) can be excluded. In fact, the optimization procedure indicates almost neglectable signal contributions from these PAHs.

The relative PES signal contributions to m/z 116 coming from indene : phenylpropadiene : p-methylphenylacetylene : 1-propynylbenzene (1-phenyl-1-propyne) are 88 : 10 : 1 : 1.

5.3.2.2 Species at m/z 126

For this mass, the experiments performed at photon energy equal to 8.5 eV and continuous acquisition mode did not allow the identification of isomers as the main contributors have photoionization energies higher than this value. Indeed, the PES at 8.5 eV shows no peaks but a start of signal rise close to the maximum energy. On the other hand, the experimental PES acquired at 10 eV with the pulsed mode could be used to identify the major compounds for m/z 126 and also to exclude a group of candidate isomers. First, the photoelectron spectra of the three didehydronaphthalene isomers were calculated and plotted in order to compare with the experimental PES for m/z 126 (**Figure** 5-22a). It is clear how the corresponding PES features do not correspond to the peaks observed in the experimental PES. Thus, this group of isomers was excluded from the analysis.

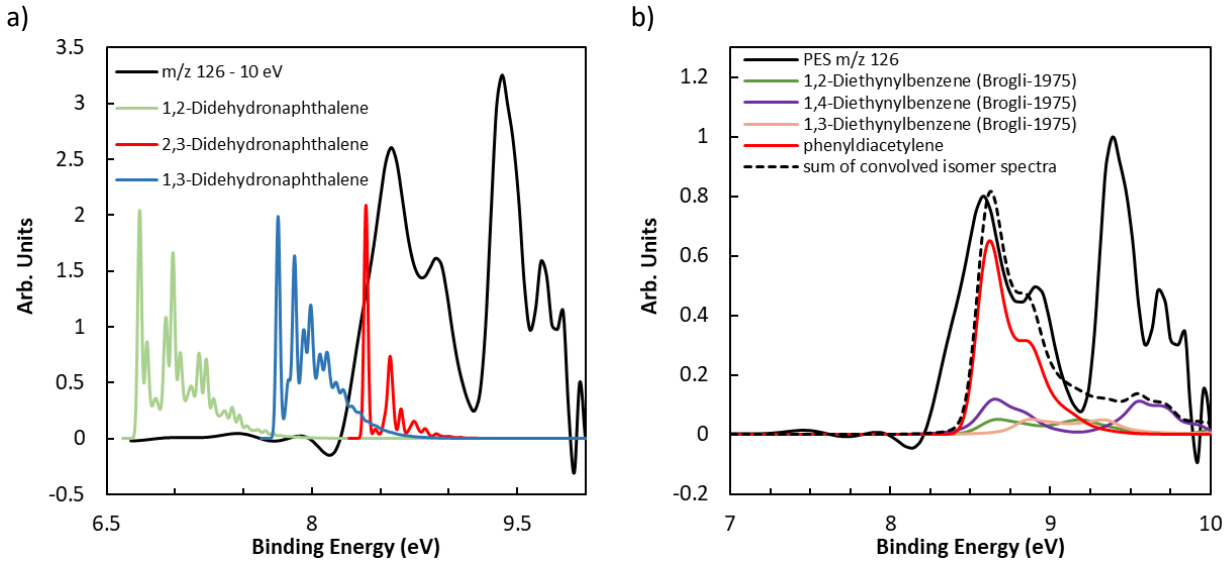

c)

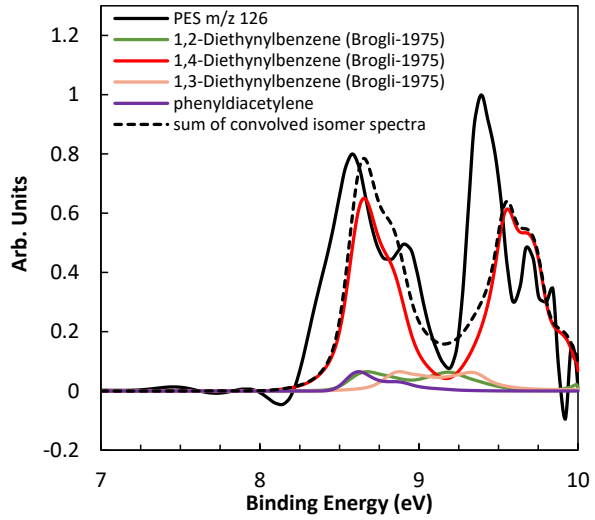

***Figure** 5-22. Experimental and reference photoelectron spectra for m/z 126 obtained at 10 eV, a) comparison with didehydronaphthalene isomers, b) and c) comparisons with diethynylbenzene isomers and Phenyldiacetylene.*

On the other hand, literature PESs for the diethynylbenzene isomers ($C_6H_5(C_2H)_2$, [253]) were plotted together with the calculated PES for phenyldiacetylene ($C_6H_5C_4H$). Phenyldiacetylene comes from the reaction of the phenyl radical with diacetylene, while the diethynylbenzene isomers from the HACA route starting from phenylacetylene (H-abstraction and C_2H_2 addition to the different carbons in the ring). From an experimental point of view, the PES shows a huge drop separating the peak at 8.58 eV to the one at 9.39 eV. This behavior in the experimental PES suggests that 1,2- and the 1,3- diethynylbenzenes should not significantly contribute in the reconstruction of the second part of the spectrum as the PESs of these isomers do not decrease as the experimental profile. According to the PES simulation, phenyldiacetylene has a photoionization energy of 8.59 ± 0.05 eV which coincides with the first peak of the experimental PES located at 8.58 eV. If this PES is used as the main contributor to the profile below 9.2 eV, the results in **Figure** 5-22b would be obtained. In this case, the second peak at 9.39 eV is completely neglected. The use of 1,4-diethynylbenzene PES to fit the first peak would lead to a slight better description of the PES features at higher binding energies, as shown in **Figure** 5-22b. On the other hand, the second peak is still underpredicted. It is not so clear at the moment why 1,4-diethynylbenzene would be favored compared to the 1,3-diethynylbenzene isomer, while the HACA step in position 2 would definitely lead the formation of the second aromatic ring ($C_{10}H_7$) and not of 1,2-diethynylbenzene. It is also not clear if other isomers are present which would provide an additional contribution to the region around the 9.39 eV peak. All these questions will require further calculations and/or experiments.

5.3.2.3 Species at m/z 128

The identification process for m/z 128 is another good example together with m/z 116 where the majority of the signal comes from one single PAH molecule (**Figure** 5-23a). There is no doubt that naphthalene ($C_{10}H_8$, PI = 8.09 ± 0.03 eV, [279]) is the most abundant PAH in this case, peaking at almost the same energy

of the experimental PES (around 8.12 eV). The slight shift does not allow an automatic fitting to be performed if the relative height of the peaks is selected as the reference target. Thus, the relative contributions from the different isomers was manually adjusted. In particular, the relative height between the experimental peak at 8.12 eV and the second one at 8.31 eV cannot be accurately reproduced by the literature PES for naphthalene. Additionally, the literature PES for naphthalene is characterized by a marked drop above 8.3 eV compared to the overall experimental curve of m/z 128. These observations suggest the possible presence of other PAHs different than naphthalene. Naphthalene is produced mainly by the dehydrogenation and ring-rearrangement steps from the $CH_3C_9H_6$ and $C_9H_6CH_3$-1 radicals and from methylindene ($C_9H_6CH_2$) as shown in the scheme of **Figure** 5-23b. The recombination between the naphthyl radicals and H and the H-abstraction by the naphthyl radicals to other products also play a major role. The naphthyl radicals derive mainly from the reaction between C_6H_5 and C_4H_2, while the $CH_3C_9H_6$ radicals from stepwise pathways starting from the fuel radical C_7H_7 reacting with the propargyl radical. $CH_3C_9H_6$ decomposition also leads to the formation of 1H-Indene-1-methylene which is also formed by the H-loss from $C_9H_6CH_3$-1, another precursor of naphthalene. $C_9H_6CH_3$-1 is one of the possible radicals of 1H-Indene-1-methylene, and it derived from the reaction of indenyl radical with CH_3. Other pathways to naphthalene include the cycloaddition fragmentation (CAF) mechanism [53] where o-benzyne comes from the direct fragmentation of the fuel radical (C_7H_7 = o-C_6H_4+CH_3), and the reaction of C_7H_5 (from the benzyl radical decomposition) with the propargyl radical.

a)

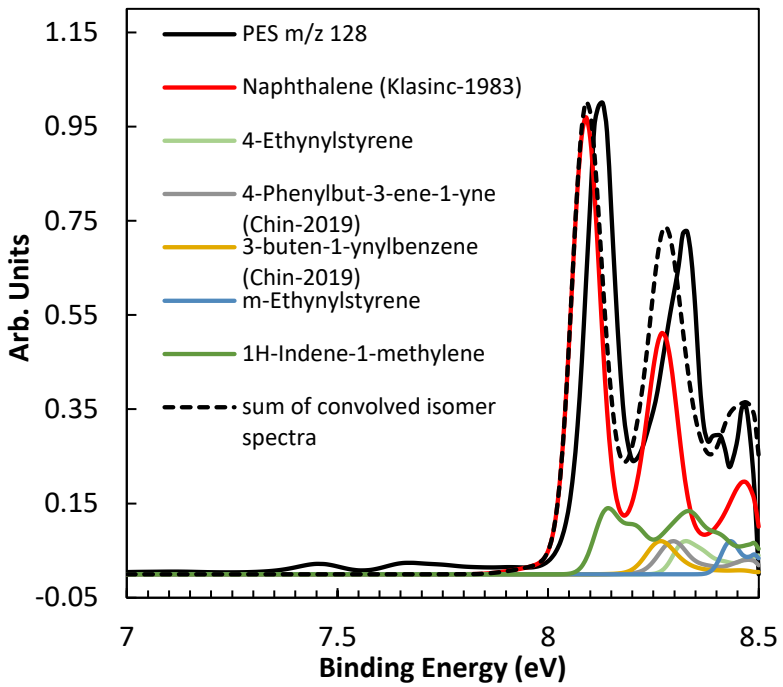

b)

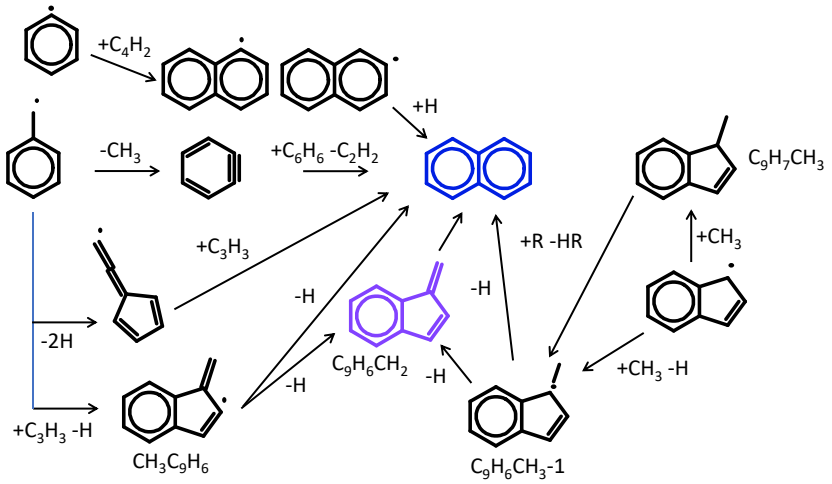

***Figure** 5-23. a) Experimental and reference photoelectron spectra for m/z 128 obtained at 8.5 eV, b) main pathways to the formation of naphthalene in toluene pyrolysis.*

Two possible isomers at m/z 128 were found in the literature, 3-buten-1-ynylbenzene ($C_6H_5CCCHCH_2$, [286]) and 4-Phenylbut-3-ene-1-yne ($C_6H_5CHCHCCH$, [286]). Additionally to these, simulations for 4-ethynylstyrene, m-ethynylstyrene ($C_6H_4(C_2H_3)C_2H$) and 1H-indene-1-methylene ($C_9H_6CH_2$) were included in the analysis as shown in the **Figure** 5-23a. 3-buten-1-ynylbenzene and 4-Phenylbut-3-ene-1-yne can be formed from the reaction of the phenyl radical with vinylacetylene (C_4H_6) while the ethynylstyrenes from the acetylene addition to the styrene radicals. The simulated PES for 1H-Indene-1-methylene (PI=8.14 eV) was found to have a significant impact (signal contribution of 10%) increasing the convolved signal in the region around 8.2 eV in order to best fit the overall experimental signal. This is in agreement with single pulse/GC experiments where 1H-Indene-1-methylene was identified among benzene pyrolysis products [65]. The 4-ethynylstyrene (PI=8.32 eV), 3-buten-1-ynylbenzene (PI=8.26 eV, [286]) and 4-Phenylbut-3-ene-1-yne (PI=8.29 eV, [286]) isomers contribute to the second peak at 8.31 eV in order to keep the same relative height with respect to the first peak at 8.12 eV. Finally, according to the convolved spectra some small contribution comes from m-ethynylstyrene (PI = 8.43 eV) in correspondence with the last peak at 8.45 eV. The ratio of all the contributions to the overall signal was found to be 70 : 5 : 5 : 5: 5 : 10 for naphthalene : 4-ethynylstyrene : 4-Phenylbut-3-ene-1-yne : 3-buten-1-ynylbenzene: m-ethynylstyrene : 1H-Indene-1-methylene, respectively.

5.3.2.4 Species at m/z 130

This is a minor peak in both mass spectra obtained at 10 eV and 8.5 eV. However, the identification of two candidates were evaluated here. Literature PES for 1,2-dihydronaphthalene ($C_{10}H_{10}$, [27]) was compared with the overall signal in **Figure** 5-24, finding that its photoionization energy (8.01 ± 0.01eV) corresponds to the first shoulder located at around 8 eV. The PES for 1-methylindene ($C_9H_7CH_3$) was also calculated. The corresponding profile shows a photoionization energy of 8.13 ± 0.05 eV, which is within the

uncertainty of the experimental peak observed at 8.1 eV. 1-Methylindene is a PAH compound included in the model developed in previous study on toluene pyrolysis using SPST/GC-GC/MS. The peak located at 8.34 eV is also captured by the simulated PES for 1-methylindene. 1,2-dihydronaphthalene should be formed from the hydrogeneration of naphthalene, while 1-methylindene from the recombination reaction of the indenyl radical with CH_3.

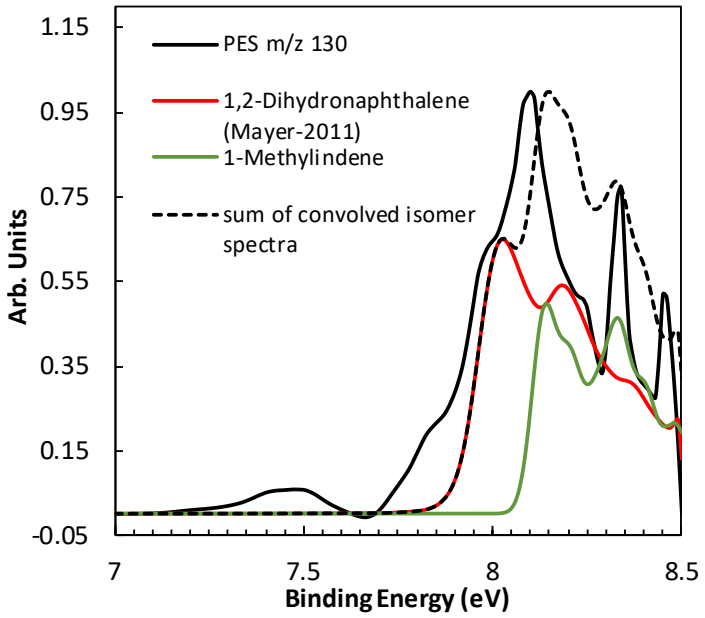

***Figure** 5-24. Experimental and reference photoelectron spectra for m/z 130 obtained at 8.5 eV.*

The uncertainties in the PESs of the two selected isomers do not allow a better fit of the experimental PES with the convolved one. In particular, the first shoulder located at 7.83 eV is not perfectly captured as well as the last peak at around 8.45 eV. The signal contribution was determined to be 57: 43 for 1,2-dihydronaphthalene: 1-methylindene, respectively.

5.3.2.5 Species at m/z 140

The m/z 140 ($C_{11}H_8$) is one of the biggest peaks in both mass spectra (**Figure** 5-16 and **Figure** 5-20). Surprisingly, only one possible candidate among the $C_{11}H_8$ isomers, 1H-cyclopropa[b]naphthalene [287], has been studied in the past for the determination of the corresponding photoelectron spectra. Thus, more than 30 isomers were considered in the ab-initio study. Since the simultaneous analysis of all the calculated PES is very challenging, nine different graphs are presented in **Figure** 5-25 for clarity purpose where the experimental PES signal for m/z 140 is compared with different groups of isomers.

Two different binning procedures were performed to the raw data in order to get the experimental PESs shown in the **Figure**s. One PES, named “2 binning” in the graphs, is less binned than the other (“4 binning”)

and this allows the derivation of sharper peaks for easier isomer identification. However, even if both data have consistent spectral features, the less binned data is preferred because of its bigger S/N characteristics. The PES calculations are not binned in the **Figure**s but for the convolution process that will be presented later they will be binned to match the resolution of the experimental PES.

Figure 5-25a compares two cyclopropanaphthalene isomers to the experimental profile. These species can be formed starting from the reaction of the methyl radical with the naphthyl radical and subsequent H-losses and rearrangements. The PES for 1H-cyclopropa[b]naphthalene from the literature ($PI_{vertical}$ = 8.03 ± 0.02 eV, [287]) and the calculated PES for the same compound (PI = 8.12 ± 0.2 eV) well corresponds. The literature PES will be used in the convolution procedure. The first peak in the profile closely matches the peak of the experimental PES located at 8.13 eV. 1H-cyclopropa[a]naphthalene is the only PAH available among all the PES simulations that has features in correspondence with the first rise in the experimental profile observed starting at around 7.85 eV. This means that 1H-cyclopropa[a]naphthalene is one of the major m/z 140 products, which is surprising since this PAH species has not been reported in the literature as a possible product of pyrolytic or soot related studies.

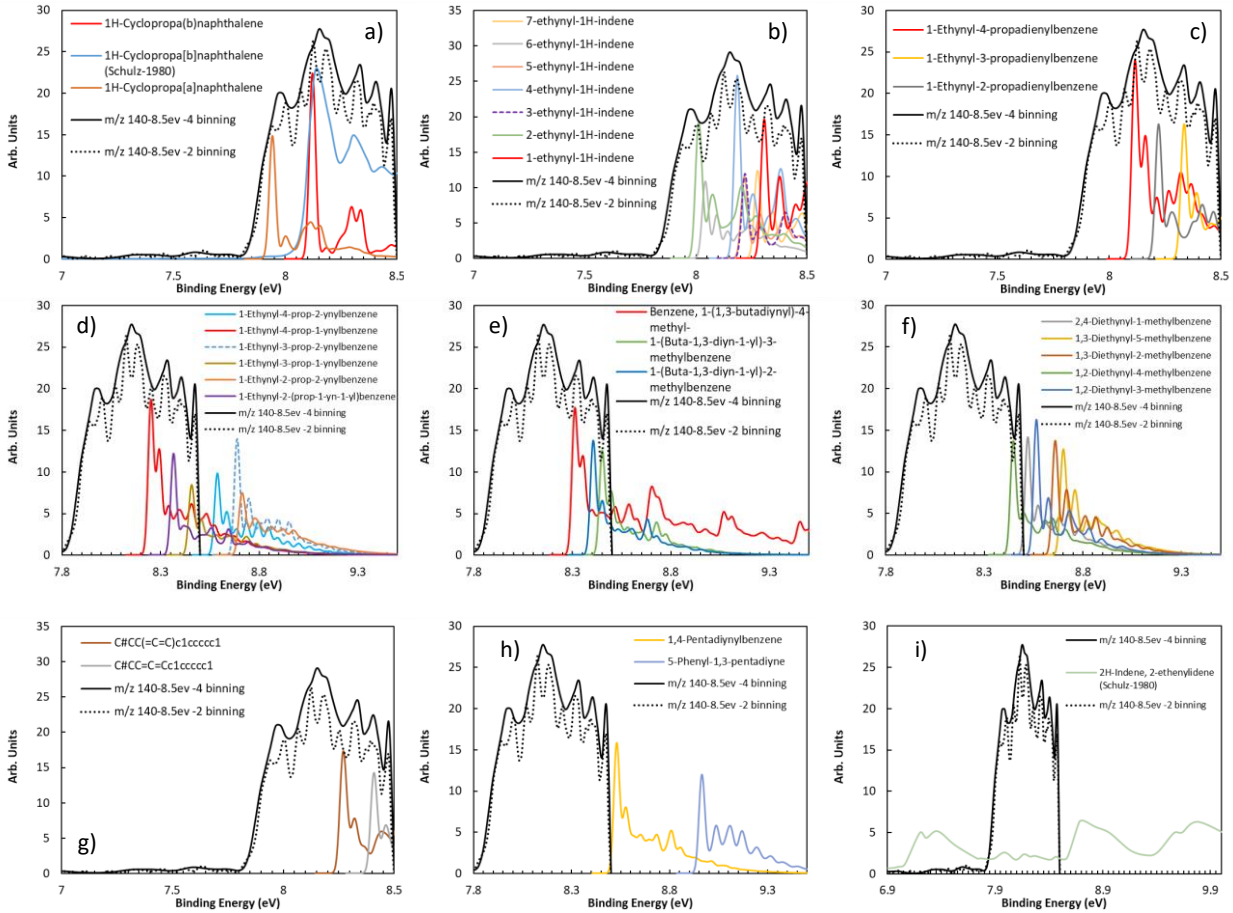

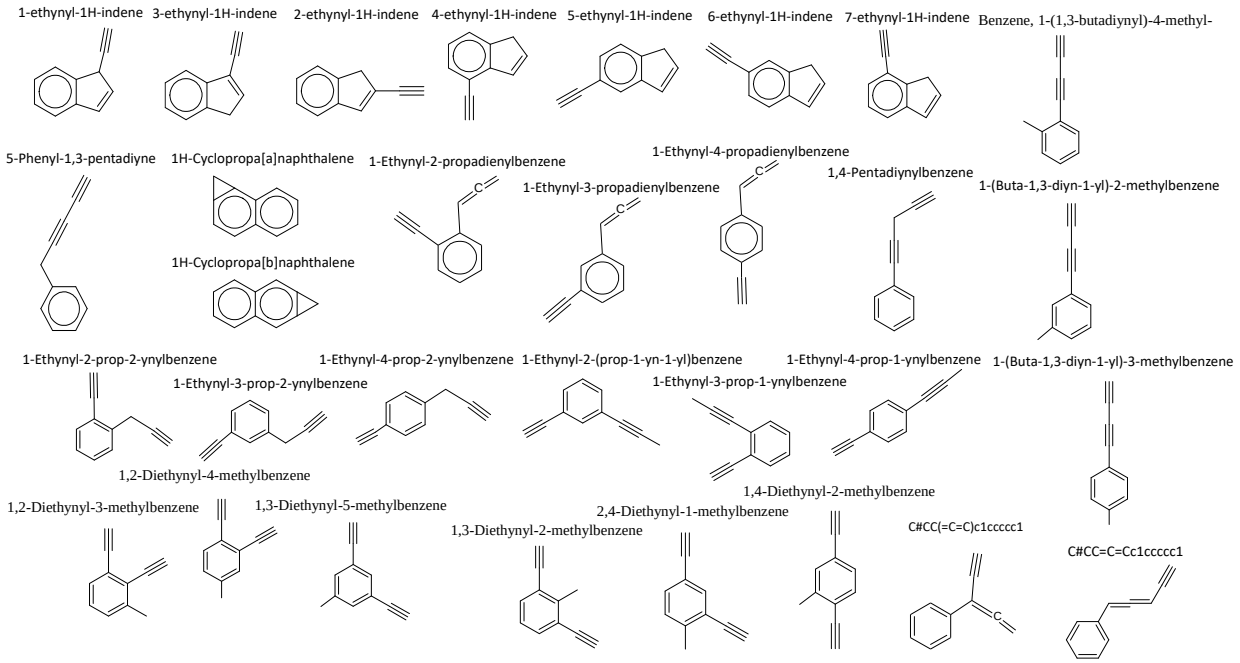

***Figure** 5-25. Experimental and reference photoelectron spectra for m/z 140 obtained at 8.5 eV among with the nomenclature of the PAH studied at m/z 140.*

Ethynyl-indene isomers ($C_9H_7C_2H$) can be produced from reactions of indene radicals (including indenyl radical) with C_2H_2. Both species are present in large amounts in the current kinetic system. All the possible isomers are compared to the experimental PES in **Figure** 5-25b. Considering the calculation uncertainties, 2-ethynyl-1H-indene and 6-ethynyl-1H-indene have similar profiles, while three compounds have PI between 8.15 and 8.25 eV (4-ethynyl-1H-indene, 5-ethynyl-1H-indene, and 3-ethynyl-1H-indene). Finally, 1-ethynyl-1H-indene and 7-ethynyl-1H-indene have higher PI energies. By matching the exact peak location of the experimental profile, the isomers which are more likely to be present are 1-ethynyl-1H-indene (PI = 8.31 ± 0.05 eV) matching with the peak at 8.33 eV, 2-ethynyl-1H-indene (PI = 8.01 ± 0.05 eV vs the peak at 8.0 eV in the experimental profile) and 4-ethynyl-1H-indene (PI = 8.19 ± 0.05 eV) in coincidence with the peak at 8.18 eV. The presence of the other isomers cannot be completely excluded due to the related uncertainties.

Three ethynyl-propadienyl-benzene isomers were also compared to the experimental PES for m/z 140 (**Figure** 5-25c). Ethynyl-propadienyl-benzenes can be formed from the reaction of the phenylacetylene radicals with C_3H_3. The 1-ethynyl-4-propadienylbenzene profile (PI = 8.12 ± 0.20 eV) seems to peak at the same position of 1H-cyclopropa[b]naphthalene and in correspondence with the peak located at 8.13 eV in the experimental profile. However, after the profiles are binned, the corresponding shapes might slightly change, as shown in the analysis of m/z 90 where the relative heights between the first and second peaks are affected by the binning procedure. 1-Ethynyl-3-propadienylbenzene (PI = 8.33 ± 0.05 eV) is also a possible isomer as its profile peaks as the experimental PES at 8.33 eV competing with 1-ethynyl-1H-indene. On the other hand, the PES of ethynyl-1H-indene has a second large peak at 8.38 eV which helps

the construction of the experimental profile around 8.4 eV. For this reason, a higher contribution from 1-ethynyl-1H-indene is expected compared to 1-ethynyl-3-propadienylbenzene.

Six ethynyl-prop-ynyl-benzene isomers (which could be formed once again from the reaction of the phenylacetylene radicals with C_3H_3) are presented in the **Figure** 5-25d but no significant contributions were estimated for the overall PES signal. This is due to the fact that none of the simulated PESs contains peaks that match major peaks of the experimental PES. The contributions from the buta-diyn-yl-methylbenzene isomers are also minor (**Figure** 5-25e). These species could be formed by methylation of phenyldiacetylene ($C_6H_5C_4H_2$) as produced in high concentrations based on the analysis of m/z 126. The profiles of benzene,1-(1,3-butadiynyl)-4-methyl- and 1-(buta-1,3-diyn-1-yl)-2-methylbenzene (8.41 ± 0.20 eV) have peaks which match with the peaks in the experimental PES located at 8.33 eV and 8.4 eV, respectively.

Six diethynyl-methylbenzene isomers were also considered as possibly formed from the methylation of the diethynyl-benzene isomers (**Figure** 5-25f). Only 1,2-diethynyl-4-methylbenzene (8.45 ± 0.20 eV) was found to ionize below 8.5 eV. The contribution from this group of isomers cannot be then confirmed or confuted based on the current measurements. However, since the formation of the buta-diyn-yl-methylbenzene isomers has been proven to be negligible, the one of the diethynyl-methylbenzenes should be even lower as the concentration of phenyldiacetylene is higher compared to the diethynyl-benzenes (see m/z 126). In addition to the diethynyl-methylbenzene isomers, three other isomers were discarded from the analysis (**Figure** 5-25h and i). This is the case for 1,4-pentadiynylbenzene (possibly from phenylacetylene + propargyl) and 5-phenyl-1,3-pentadiyne (possibly from benzyl + diacetylene) as well as for 2H-indene, 2-ethenylidene whose PES is available in the literature [287]. The first two ionize at energies higher than 8.5 eV, while the third does not have any feature which can correspond to the experimental m/z 140 profile (plus the species is not likely to be formed from a kinetic perspective).

Finally, two isomers *phenyl allenyl acetylene* ($C_6H_5CHCCHCCH$, 8.41 ± 0.05 eV) and *C#CC(=C=C)c1ccccc1* (a branched alkylated aromatic, PI = 8.27 ± 0.05 eV) were also simulated and compared to the experimental PES (**Figure** 5-25g). *C#CC=C=Cc1ccccc1* seems to well capture the two last peaks located at 8.4 eV and 8.48 eV although the peak at 8.48 eV could be an artifact of the energy cut at 8.5 eV. Anyway, this species may be influencing the formation of the peak at 8.4 eV.

Due to the fact that some of the compounds ionize after or before the region of interest for m/z 140, only 21 isomers were considered for the optimization of the convolved isomer spectrum. Of these 21, only nine isomers were found to have some impact on the overall signal (> 1 % contribution). These 9 isomers are presented in **Figure** 5-26. The list of species is also presented in **Table 5-3**

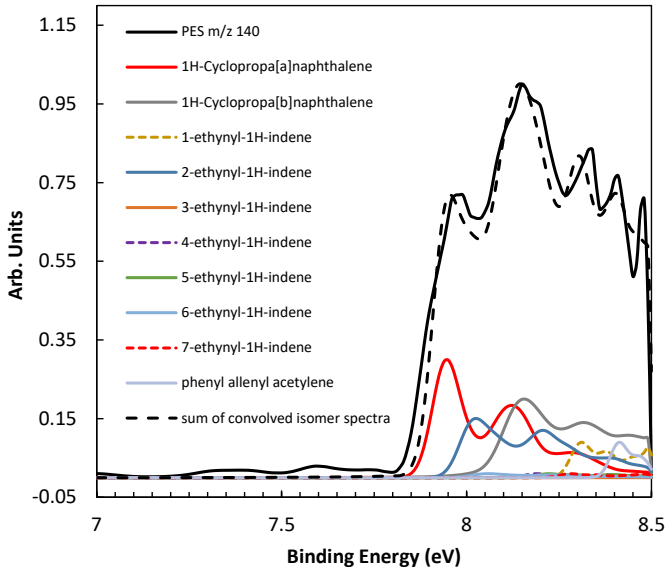

***Figure** 5-26. Comparison of experimental, reference and convolved isomer photoelectron spectra for m/z 140 obtained at 8.5 eV.*

***Table 5-3**. List of PAH species influencing in the formation of m/z 140.*

1H-cyclopropa[a]naphthalene	34.4%
1H-cyclopropa[b]naphthalene	23.0%
1-ethynyl-1H-indene	10.3%
2-ethynyl-1H-indene	17.2%
4-ethynyl-1H-indene	1.1%
5-ethynyl-1H-indene	1.1%
6-ethynyl-1H-indene	1.1%
7-ethynyl-1H-indene	1.1%
phenyl allenyl acetylene	5.3%

5.3.2.6 Species at m/z 142

Similar to m/z 130, the m/z 142 ($C_{11}H_{10}$) peak is small in both 10 eV and 8.5 eV mass spectra but the signal is large enough in the 8.5 eV dataset to allow identification of the two possible isomers proposed here. In this case, two different binned experimental PESs are presented in **Figure** 5-27, the first one (on the left) more binned than the second one (right graph). The PES of 2-methylnaphthalene is taken from the literature measurements [288] while the one of 1-methylnaphthalene was calculated. Isomers of methylnaphthalene are identified according to the peaks present in the less binned PES. Methylnaphthalenes are produced from methylation of naphthalene ($C_{10}H_8 + CH_3$) and as presented in the PES comparison the first peak found at 7.90 eV corresponds to 2-methylnaphthalene ($PI_{vertical}$ = 7.83 ± 0.02 eV) while the one located at 7.97 eV can be attributed to 1-methylnaphthalene since the photoionization energy for this PAH is 8.00 ± 0.05 eV. The more binned experimental PES demonstrates that keeping the same signal contribution between the two molecules provides a reasonable approximation of the

experimental PES although part of the main peak at 8.13 eV is not perfectly captured by the convolved profile. Additionally, the peaks located at 8.29 eV and 8.35 eV are also not captured by the spectral features of the fitting curve which means that additional isomers should be present at m/z 142 but they are not considered in the present analysis. In addition, very small peaks located at 7.59 eV and 7.73 eV correspond to some missing minor compounds, although the signal level is just above the oscillations of the baseline. The relative signal contribution of 1-methylnaphthalene and 2-methylnaphthalene was set to be equal to 44 : 56.

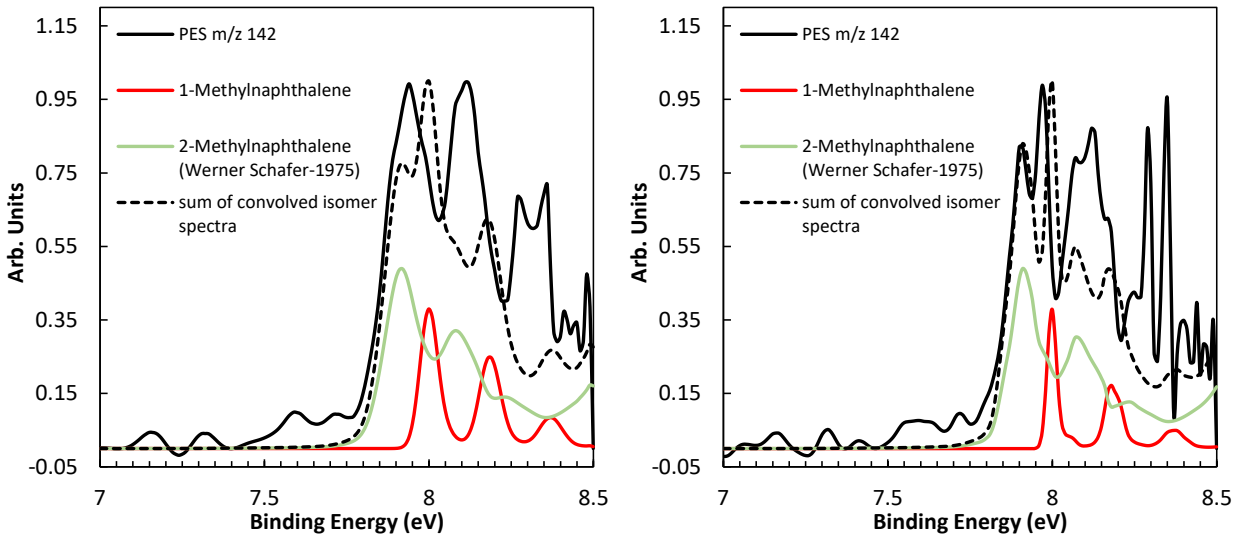

***Figure** 5-27. Comparison of experimental, reference and convolved isomer photoelectron spectra for m/z 142 obtained at 8.5 eV.*

5.3.2.7 Species at m/z 152

This is a common peak in PAH studies usually associated with the presence of acenaphthylene ($AC_{12}H_8$). Acenaphthylene is an important PAH that can be produced from different pathways as already mentioned in the introduction, i.e. by multiple hydrogen abstractions and acetylene additions steps (HACA) to the benzene radical, phenyl (C_6H_5). Indeed, according to the previous study on toluene pyrolysis using single pulse shock tube coupled to GC-GC/MS, acenaphthylene was one of the most abundant species from the pyrolysis of toluene. In reality, at the conditions considered in the present study, the pathway through the formation of biphenyl (from C_6H_5+C_6H_6, C_6H_5+C_6H_5) followed by H-abstraction to the biphenyl radical or directly to the biphenyl radical (from C_6H_5+o-C_6H_4) followed by isomerization reactions [63] is one of the dominant formation mechanism, together with the HACA route from the naphthyl radical. Another minor pathway involves addition reactions of indenyl radical (C_9H_7) with the propargyl radical (C_3H_3). The **Figure** 5-28 presents the main pathways to the m/z 152 species.

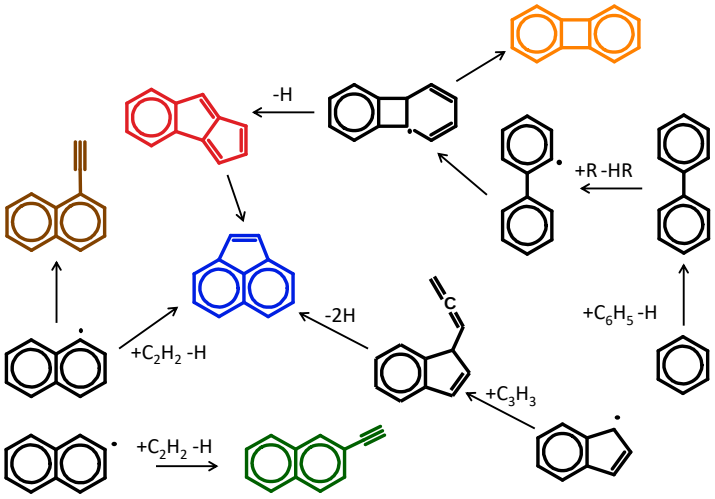

***Figure** 5-28. Main pathways to the formation of m/z 152 species.*

The convolved isomer spectra in **Figure** 5-29 show a large contribution coming from the binned literature PES of acenaphthylene (PI = 8.012 ± 0.014 eV[91]) which peaks as the experimental PES for m/z 152 at around 7.99 eV. Another major isomer is 2-ethynylnaphthalene (PI = 8.11 ± 0.02 eV[289]) which accounts for the experimental peak at 8.13 eV. 2-Ethynylnaphthalene is produced from the reaction of the 2-naphthyl radical with acetylene. The corresponding 1-ethynylnaphthalene contributes much less to the convolved spectrum as the reaction between 1-naphthyl radical with acetylene mainly leads to acenaphthylene. The experimental profile shows features for binding energies lower than 7.8 eV. Isomers whose PESs have signals in this energy range include biphenylene ($C_6H_4C_6H_4$, PI = 7.61 ±0.02 eV[290]) and cyclopenta[a]indene (PI = 7.55 eV) from the theoretical calculations. A priori, both compounds can be formed. Biphenylene can be produced from the isomerization and H-loss starting from the biphenyl radical and, in minor proportion, from the self-recombination of o-benzyne (o-C_6H_4) radicals which are possible candidates of m/z 76 peak observed at 10 eV. Cyclopenta[a]indene is an intermediate in the isomerization of the biphenyl radical to acenaphthylene. The fact that similar spectral characteristics appear in the binned PESs of cyclopenta[a]indene and biphenylene does not allow the differentiation between these two compounds whose photoionization starts at around 7.5 eV matching the same region of the experimental PES. A 50%/50% relative proportion is assumed here but this hypothesis requires further validation in future studies or with different techniques.

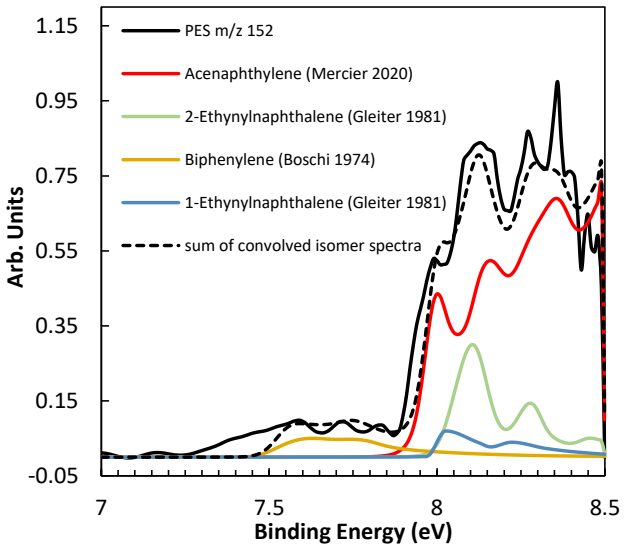

***Figure** 5-29. Comparison of experimental, reference and convolved isomer photoelectron spectra for m/z 152 obtained at 8.5 eV.*

The relative signal contribution of acenaphthylene : 2-ethynylnaphthalene : biphenylene : cyclopenta[a]indene : 1-ethynylnaphthalene was determined as 61 : 25 : 4 : 4 : 6, respectively.

5.3.2.8 Species at m/z 154

Several isomers found in literature were evaluated to identify the possible PAH species of m/z 154 ($C_{12}H_{10}$). For instance, in the **Figure** 5-30a, the literature PES for biphenyl ($C_6H_5C_6H_5$[291]) confirms that this is an important PAH product at the current conditions as its first peak at 8.40 eV correspond to the marked shoulder of the experimental PES at 8.38 eV, approximately. Biphenyl is produced from the reaction of the phenyl radical with benzene and the H ipso-addition to methylbiphenyl ($C_6H_5C_6H_4CH_3$), mainly, but also from the reaction of toluene with the cyclopentadienyl radical (C_5H_5) and the phenyl radical, the recombination between the fullvenallenyl radical (C_7H_5, from toluene thermal decomposition) and C_5H_5, and the self-recombination reactions of phenyl radicals (C_6H_5). The phenyl radical is produced in large amounts during benzene (C_6H_6) decomposition as reported in the previous shock tube study using laboratory-based measurements [65], while the main pathway to $C_6H_5C_6H_4CH_3$, is the reaction between toluene and the phenyl radical. The dominance of the biphenyl isomer is confirmed from the PES obtained in the 10 eV dataset (**Figure** 5-30c), where, despite the lower resolution for this experimental PES, the general spectral characteristics of the profile are sufficiently highlighted. Considering other isomers, the resolution of the experimental PES obtained at 10 eV for m/z 154 is not enough to determine the relative contributions from the vinylnaphthalene isomers which mainly come from the reaction of indenyl radical with the propargyl radical, based on the modeling results. In the **Figure** 5-30a, the experimental PES obtained at 8.5 eV is compared with the literature PES for 1-vinylnaphthalene ($PI_{vertical}$ = 7.89 ± 0.02 eV[289]) and the simulated PES for 2-vinylnaphthalene (7.93 ± 0.05 eV). The features of the literature PES for 1-vinylnaphthalene contain a very broad peak which a priori does not allow to separate its contribution

from the one of 2-vinylnaphthalene. Thus, a calculation was performed on 1-vinylnaphthalene (graph at the center) which clearly show the presence of two distinguished peaks the first being at 7.86 eV. This is consistent with the literature PI of 7.89 ± 0.02 eV. Thus, the first part of the experimental profile is influenced almost entirely by 1-vinylnaphthalene, while around the first experimental peak both 1-vinylnaphthalene and 2-vinylnaphthalene contribute to the convolved profile.

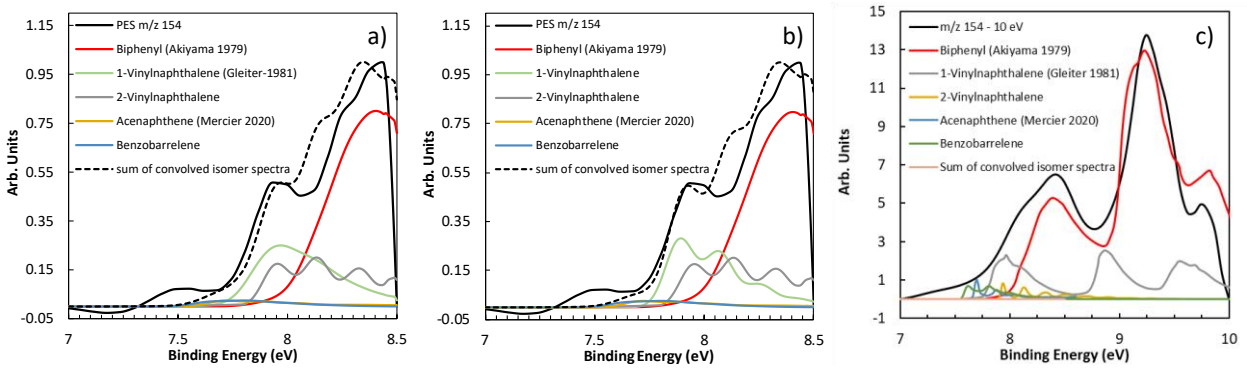

***Figure** 5-30. Comparison of experimental, reference and convolved isomer photoelectron spectra for m/z 154. a) using literature PES for 1-vinylnaphthalene and at 8.5 eV, b) using calculated PES for 1-vinylnaphthalene and at 8.5 eV, c) using literature PES for 1-vinylnaphthalene and at 10 eV.*

Additionally, the simulated PES benzobarrelene (PI = 7.58 eV) and the literature PES for acenaphthene (7.7 ± 0.014[91]) were considered in the determination of the sum of convolved isomer spectra. Their contribution is only minor. The results showed that either using the simulated or literature PES for 1-vinylnaphthalene, the changes in the relative signal contributions from all the PAH isomers are nearly identical. The ratio between acenaphthene/biphenyl (2/62) in m/z 154 is small at the pyrolytic conditions studied, different to the recent low-pressure $CH_4/N_2/O_2$ sooting flame study with i^{2}PEPICO where similar signal contributions were reported for acenaphthene and biphenyl (31/26) at a height above burner (HAB) of 9 mm [91].

The signal contributions for biphenyl : 1-vinylnaphthalene : 2-vinylnaphthalene : acenaphthene : benzobarrelene were found to be 61.5 : 19.2 : 15.4 : 1.9 : 1.9 when literature PES for 1-vinylnaphthalene was implemented in the optimization procedure, while the signal contributions when the calculated PES for 1-vinylnaphthalene was used were found to be 60.2 : 21 : 15 : 1.9 : 1.9, respectively.

5.3.2.9 Species at m/z 156

Although this is a very small peak in the mass spectrum obtained at 8.5 eV, an attempt for the identification of the PAH compounds is presented in **Figure** 5-31. The only available PESs found in literature that could be related to this mass are: 1,8-dimethylnaphthalene [292], 1,4-dihydro-1,4-ethanonaphthalene [293], 6-methyl-1,4-dihydro-1,4-methanonaphthalene [294], and 2-ethylnaphthalene [279]. 2-Ethylnaphthalene and 1,8-dimethylnaphthalene could be contributing at the beginning of the overall signal but their contribution cannot be confirmed due to the low S/N in this region. Specifically, the 1,8-dimethylnaphthalene profile could be used to match the peak at 7.77 eV but its photoionization energy is 7.5 eV. 2-Ethylnaphthalene has a $PI_{vertical}$ of 7.95 eV which is quite far from the experimental peak at 7.77 eV.

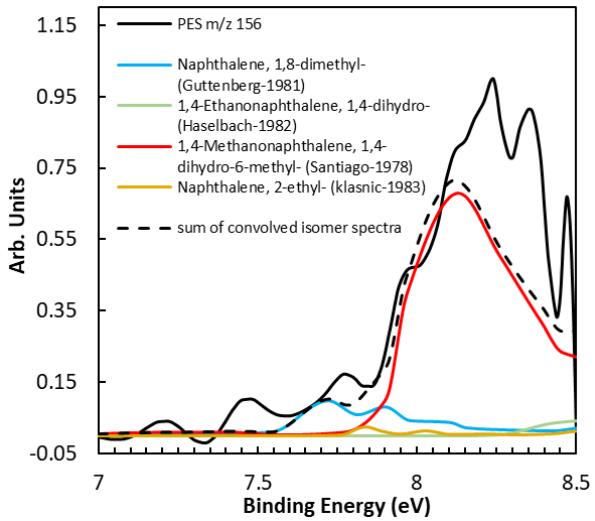

***Figure** 5-31. Comparison of experimental, reference and convolved isomer photoelectron spectra for m/z 156 at 8.5 eV.*

For m/z 156, mostly 1,4-dihydro,1,4-ethanonaphthalene could be a potential candidate to contribute to the experimental signal since its photoionization peak of 8.12 eV coincides with the same of the experimental PES. 1,4-dihydro,1,4-ethanonaphthalene could be produced from cycloaddition of benzene and o-benzyne followed by hydrogenation. A contribution of nearly 85 % is obtained for 1,4-dihydro,1,4-ethanonaphthalene in the current analysis, but more studies should be performed in order to complete the study of m/z 156, e.g. calculations on 1-ethylnaphthalene and other possible candidates which might account for the experimental features at higher energies.

5.3.2.10 Species at m/z 166

This peak is the biggest signal present in the mass spectrum of **Figure** 5-20. According to the literature review, the only available PES for the m/z 166 isomers corresponds to fluorene ($FC_{13}H_{10}$[291], [295]). Fluorenyl radical was also detected in m/z 165 as evidenced in the mass spectrum. In previous study on toluene pyrolysis with single pulse shock tube coupled to GC-GC/MS, fluorene was detected and modeled [65]. At the current conditions, fluorene is mainly formed from the recombination of fuel radical benzyl with phenyl (C_7H_7 + C_6H_5) and subsequent dehydrogenation of diphenylmethane ($C_6H_5CH_2C_6H_5$) as well as from the dehydrogenization of $C_{13}H_{11}$ from the reaction between the benzyl radical and m-benzyne. Based on results of the previous study on toluene-propyne co-pyrolysis where major $C_{13}H_{10}$ isomers were identified [74], several species were selected as possible candidates for the identification of m/z 166 and ab-initio calculations on the corresponding PESs were performed. The sum of the convolved isomer spectra that best fit the experimental PES for m/z 166 is shown in **Figure** 5-32 along with the binned PESs that mainly contribute to the overall signal.

The biggest contribution to the m/z 166 comes from fluorene profile that peaks at 7.944 ± 0.05 eV, in correspondence with the peak located at 7.92 eV in the experimental PES signal. Taking advantage of the calculated PESs, other species can be attributed to the remaining peaks of the experimental signal. At low photon energies, a small shoulder around 7.5 eV relates to the simulated PES for 1H-phenalene ($PC_{13}H_{10}$, PI=7.5 ± 0.05 eV) followed by 3H-benz[e]indene ($C_{13}H_{10}$, PI=7.60 ± 0.05 eV) that peaks at around 7.6 eV. 1H-Phenalene derives mainly from the ring-expansion of $C_{12}H_7CH_2$, while 3H-benz[e]indene from the reaction of 1-methylnaphthalene radical ($C_{10}H_7CH_2$) with acetylene. Addition of a small amount of 1h-benz[f]indene ($C_{10}H_7$CYC5–2, PI = 7.72 ± 0.05 eV) helped improving the fit in the curvature around 7.72 eV, while the contribution from 1-(1-naphthyl)-1-propyne (1-$C_{10}H_7CCCH_3$, PI=7.84 ± 0.05 eV) provided the signal necessary to complete the shoulder located at around 7.84 eV, just before the biggest peak corresponding to fluorene. The corresponding 2-propynyl naphthalene (2-$C_{10}H_7CCCH_3$, PI=7.92 ± 0.05 eV) is also present in considerable concentrations. The photoionization energy is very similar to the one of fluorene, but its contribution is mainly essential to fit experimental features at higher energies, as the two peaks at 8.11 eV and 8.31 eV match with the experimental shoulder at 8.10 eV and the small peak at 8.30 eV, respectively. The two species can be produced by the reactions of the 1-,2-naphthyl radicals with propyne and the 1-,2-ethynylnaphthalenes with the methyl radical.

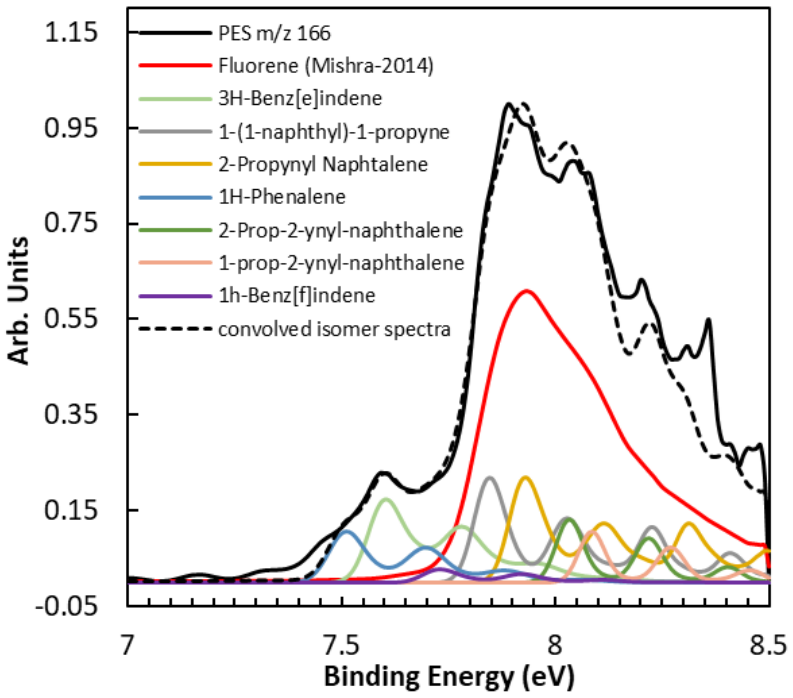

***Figure** 5-32. Comparison of experimental, reference and convolved isomer photoelectron spectra for m/z 156 at 8.5 eV*

Two additional isomers were employed to improve the fitting of the region near the second highest experimental peak. The photoionization of 2-prop-2-ynyl-naphthalene (2-$C_{10}H_7CH_2CCH$, PI = 8.03 ± 0.05 eV) matches exactly with the peak located around 8.05 eV with less than 20 meV difference. The second isomer, 1-prop-2-ynyl-naphthalene (1-$C_{10}H_7CH_2CCH$, PI=8.08 ± 0.05 eV), was also included in the sum of convolved spectra helping to complete the profile near the previous peak. These two isomers are formed from the reactions of the naphthyl radicals with C_3H_3 and C_3H_4.

The relative signal contributions are presented in **Table** 5-4.

***Table 5-4**. List of PAH species influencing in the formation of m/z 166.*

fluorene	39%
3H-benz[e]indene	11%
1-(1-naphthyl)-1-propyne	14%
2-propynyl naphthalene	14%
1H-phenalene	7%
2-prop-2-ynyl-naphthalene	8%
1-prop-2-ynyl-naphthalene	7%
1H-benz[f]indene	2%

If the simulation is run several times considering a different number of isomers or a different combination of isomers, the signals contributions from **Table** 5-4 may slightly change. In the specific case, for the major species, fluorene, the signal contribution varies around 37 ± 2.6 %.

5.3.2.11 Species at m/z 168

This is a small peak in the mass spectrum. This is mainly due to the fact that the most abundant isomer, diphenylmethane, ionize at 9.1 eV [296]. The dominance of the diphenylmethane isomer is confirmed from the PES obtained in the 10 eV dataset (**Figure** 5-33b), where, despite the lower resolution for this experimental PES, the general spectral characteristics of the profile are sufficiently highlighted. Concerning the contribution to the measured PES at 8.5 eV, the most probable species are the methylbiphenyl isomers. Unfortunately, the literature PESs for these compounds do not present sharp peaks. However, a fitting was obtained as in the **Figure** 5-33a, where it is shown how 2-methylbiphenyl (around 17%) is the minor species in this case. On the other hand, the relative signal contributions of 3-methylbiphenyl and 4-methylbiphenyl have similar values (around 42%).

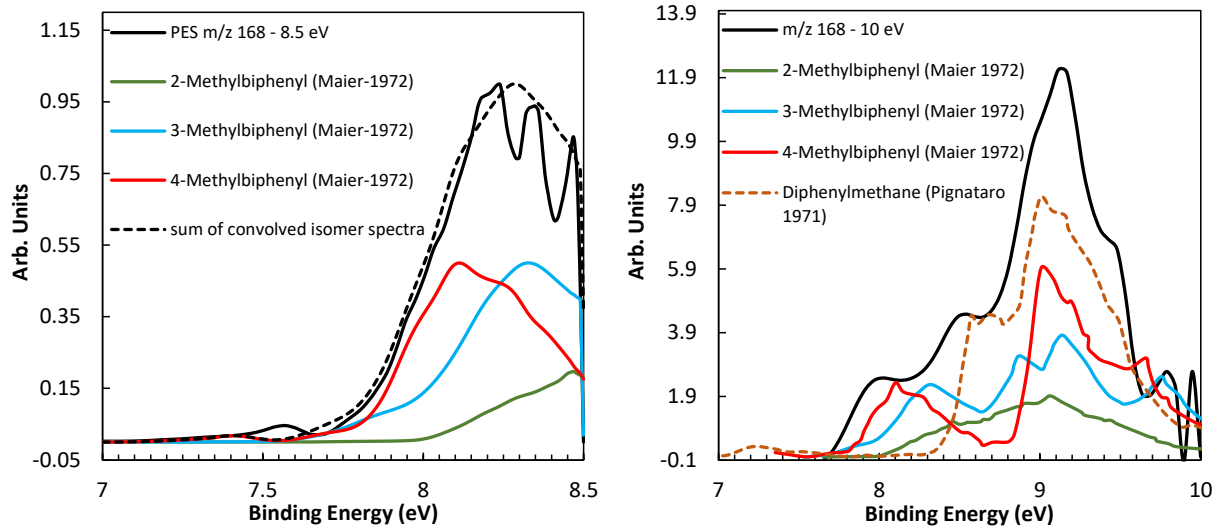

***Figure** 5-33. a) Comparison of experimental, reference and convolved isomer photoelectron spectra for m/z 168 at 8.5 eV, b) PES comparisons with 10 eV data.*

5.3.2.12 Species at m/z 176

This is a relatively large peak in the mass spectrum of **Figure** 5-16 and **Figure** 5-20, so analyses with a lower binning can be performed to help the identification when a large number of isomers needs to be distinguished in the experimental photoelectron signal, like in this case. In particular, 18 isomers were considered for the analysis, with 16 PESs from ab initio calculations and 2 from literature data.

In the **Figure** 5-34a, four isomers of ethynylacenaphthylene are compared with the experimental PES of m/z 176 along with pyracyclene (PI = 7.564 ± 0.05 eV) and cyclopenta[bc]acenaphthylene (PI = 7.56 ± 0.20 eV). The origin of all these species is common, as they can be formed from the reaction of the acenaphthylene radicals with C_2H_2. Pyracyclene and cyclopenta[bc]acenaphthylene could contribute to the low energy part of the spectrum although the oscillations in the experimental signal do not allow a clear identification of the corresponding features. The two species have similar PESs and the signal level in that region is too small to be able to differentiate between them, so equal contributions are attributed to pyracyclene and cyclopenta[bc]acenaphthylene. On the other hand, the ethynylacenaphthylene isomers have higher PI and the features of their PESs match with several peaks in the experimental profile. 4-Ethynylacenaphthylene (PI = 8.03 ± 0.05 eV) and 3-ethynylacenaphthylene (PI = 8.06 ± 0.05 eV) contribute not only to the largest peak of the experimental PES located at 8.06 eV, but also to other minor peaks at 8.20 eV, 8.12 eV and at 8.26 eV. Nevertheless, the reference PES for 3-ethynylacenaphthylene cannot reproduce the relative heights between the two experimental peaks at 8.06 eV and 8.12 eV, which means that necessarily contributions from other isomers are present. For example, the PES of 5-ethynylacenaphthylene (PI = 8.14 ± 0.05 eV) contains features which correspond to the peaks located at 8.12 eV and 8.30 eV. A smaller contribution from 1-ethynylacenaphthylene (PI = 7.91 ± 0.05 eV) influences the fitting profile around the shoulder located at 7.9 eV in the experimental PES.

The second group of isomers include the diethynylnaphthalenes, from the reactions of the ethynylnaphthalene radicals with acetylene. These isomers are presented in **Figure** 5-34b and c. The two available PESs in the literature for 1,8-diethynylnaphthalene (PI 7.88 ± 0.02 eV[289]) and 1,5-diethynylnaphthalene (PI 7.91 ± 0.02 eV[289]) might contribute to the signal near the experimental peak located at 7.84 eV, but this needs to be confirmed by additional analyses. The other species in **Figure** 5-34b have photoionization energies which are higher. In particular, the PESs of 1,2-diethynylnaphthalene (PI = 8.03 ± 0.10 eV), 1,3-diethynylnaphthalene (PI = 8.05 ± 0.10 eV) and 1,6-diethynylnaphthalene (PI = 8.07 ± 0.10 eV) show peaks around the highest experimental peak.

Additional diethynyl-naphthalene isomers are compared to the experimental PES in **Figure** 5-34c. Among these species, 1,4-diethynylnaphthalene is the one with lowest photoionization energy (PI = 7.96 ± 0.20 eV) which perfectly corresponds to the first major peak at 7.97 eV in the experimental profile. As 1,4-diethynylnaphthalene is the only isomer contributing to this peak, its relative contribution to the m/z 176 signal will be significant. The PESs of 2,6-diethynylnaphthalene (PI 8.07 ± 0.20 eV) and 1,7-diethynylnaphthalene have peaks which corresponds to the main experimental peak at 8.06 eV, similarly to 1,3-diethynylnaphthalene. Finally, 2,3-diethynylnaphthalene has a photoionization energy (PI = 8.12 ± 0.20 eV) which corresponds to peaks with 8.12 eV and 8.29 eV on the experimental PES.

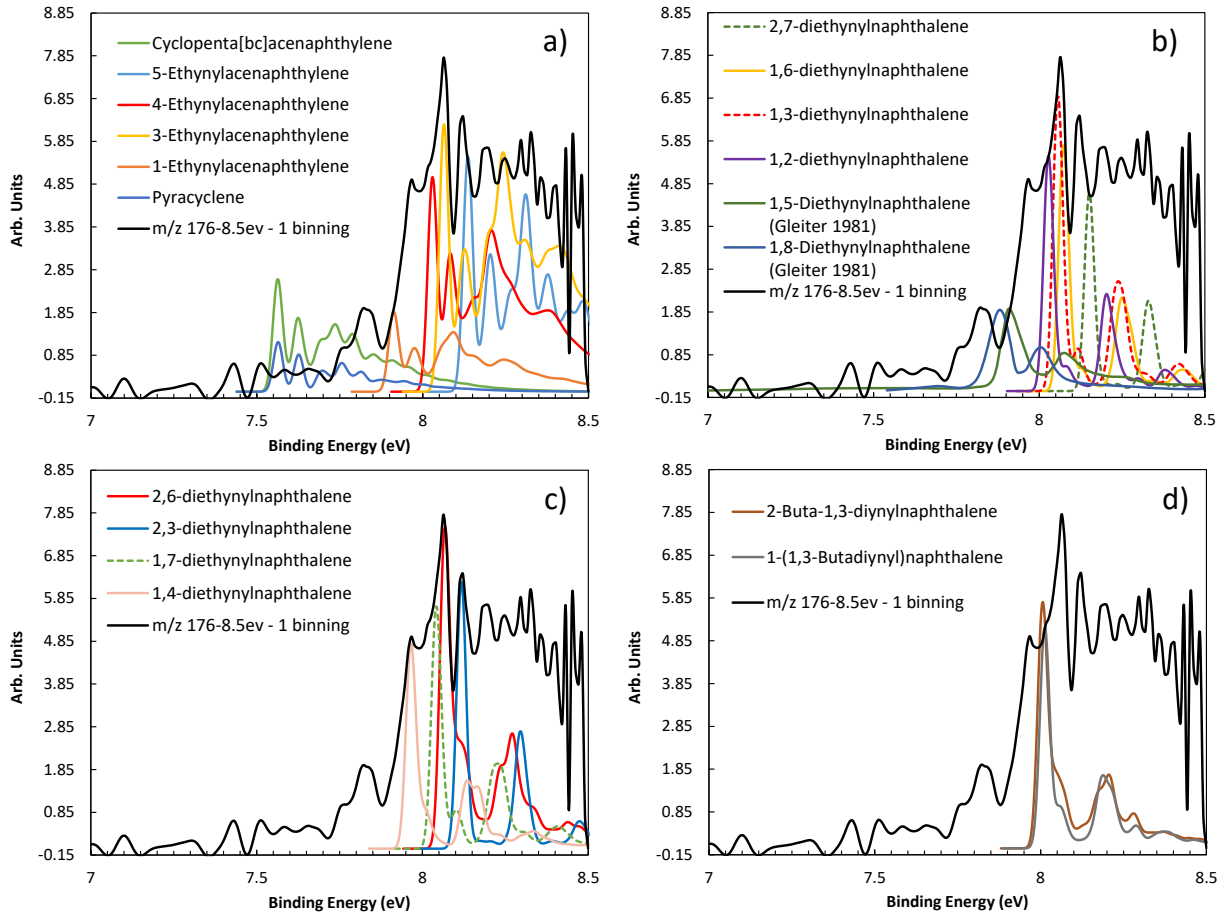

***Figure** 5-34. Comparison of experimental and reference photoelectron spectra for m/z 176 at 8.5 eV.*

Butadiynyl-naphthalene isomers were also considered in the isomer selective identification of m/z 176, as possibly produced from the reaction of the naphthyl radicals with diacetylene. According to the PES comparison presented in **Figure** 5-34d, PES simulations for 1-(1,3-butadiynyl)naphthalene (PI = 8.01 ± 0.05 eV) and 2-buta-1,3-diynylnaphthalene (PI = 8.00 ± 0.05 eV) present very similar photoelectron spectra both peaking with the peaks located at 8.02 eV and 8.20 eV of the experimental PES. Some contribution coming from these two isomers is evidenced.

The sum of convolved isomer spectra considering the 18 isomers discussed above is presented in **Figure** 5-35. As expected 1,4-diethynylnaphthalene highly contributes to the overall signal among all the diethynylnaphthalene isomers. Also, contributions from ethynylacenaphthylenes and butadiynyl-naphthalene is clearly evidenced. An excellent fitting between the convolved curve and the experimental PES of m/z 176 is evidenced in the **Figure** 5-35. The specific signal contribution for each PAH molecule is presented in the **Table 5-5**:

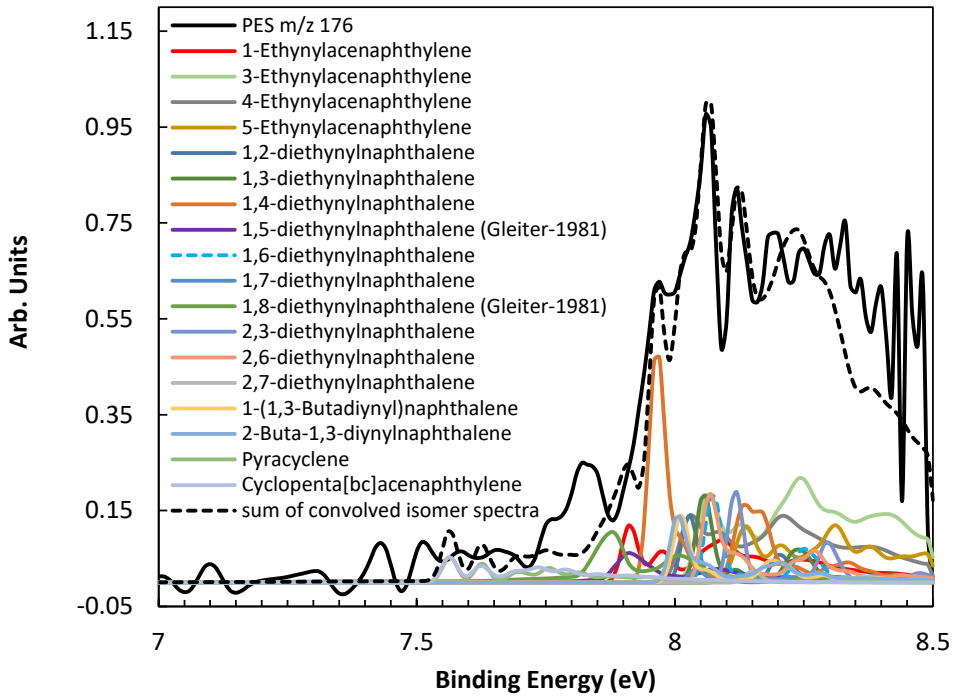

***Figure** 5-35. Comparison of experimental, reference and convolved isomer photoelectron spectra for m/z 176 at 8.5 eV.*

***Table 5-5**. List of PAH species influencing in the formation of m/z 176.*

1-Ethynylacenaphthylene	4.6%
3-Ethynylacenaphthylene	8.4%
4-Ethynylacenaphthylene	5.4%
5-Ethynylacenaphthylene	4.6%
1,2-Diethynylnaphthalene	5.4%
1,3-Diethynylnaphthalene	7.2%
1,4-Diethynylnaphthalene	18.9%
1,5-Diethynylnaphthalene	2.7%
1,6-Diethynylnaphthalene	7.2%
1,7-Diethynylnaphthalene	1.1%
1,8-Diethynylnaphthalene	4.1%
2,3-Diethynylnaphthalene	7.4%
2,6-Diethynylnaphthalene	7.2%
2,7-Diethynylnaphthalene	0.9%
1-(1,3-Butadiynyl)naphthalene	5.4%
2-Buta-1,3-diynylnaphthalene	5.4%
Pyracyclene	2.0%
Cyclopenta[bc]acenaphthylene	2.0%

5.3.2.13 Species at m/z 178

This group of compounds contains some of the most common PAH intermediates involved in soot formation. This is the case of anthracene ($AC_{14}H_{10}$) and phenanthrene ($C_{14}H_{10}$) who are the most abundant species present in the experimental PES for m/z 178. According to the model developed in previous shock tube works on toluene pyrolysis [65], phenanthrene can be produced from several routes depending on the reaction time. These include the isomerization of anthracene, the recombination reaction between two toluene radicals ($C_6H_4CH_3$) and between two fullvenallenyl radicals (C_7H_5), and the isomerization fragmentation of $C_{13}H_9CH_2$ and isomerization of 9H-fluorene, 9-methylene ($C_{13}H_8CH_2$). $C_{13}H_9CH_2$ is mainly formed from the reaction of the benzyl radical with the fullvenallenyl radical and in a minor way from a combination between fluorenyl radical ($C_{13}H_9$, m/z 165) with methyl (CH_3). A minor contribution to $C_{14}H_{10}$ comes from the decomposition of $C_6H_5CCHC_6H_5$ (from subsequent dehydrogenizations of bibenzyl) directly or through the formation of diphenylacetylene ($C_6H_5CCC_6H_5$). Anthracene is mainly produced from the recombination of toluene radicals ($C_6H_4CH_3$) with benzyl radical ($C_6H_5CH_2$). All these reaction pathways are reported in the scheme of **Figure** 5-36. Diphenylacetylene and 9H-fluorene, 9-methylene are also possible stable intermediates contributing the experimental PES.

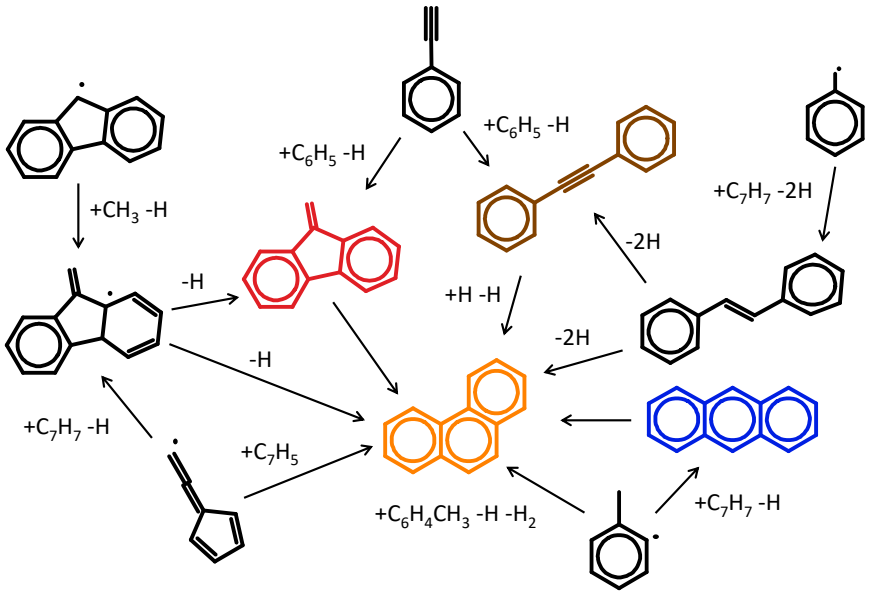

***Figure** 5-36. Main pathways to the formation of m/z 178 isomers in toluene pyrolysis.*

From the comparison of reference PES to the experimental PES for m/z 178 in **Figure** 5-37 it can be noticed that there is a shift of 60 meV between the literature PES for anthracene ($PI_{vertical}$=7.43 ± 0.03 eV[297]) and the first peak found in the experimental PES which is 7.37 eV. Despite this inconsistency, just outside the experimental uncertainties, the features of the experimental profile below 7.5 eV can be attributed with confidence to anthracene.

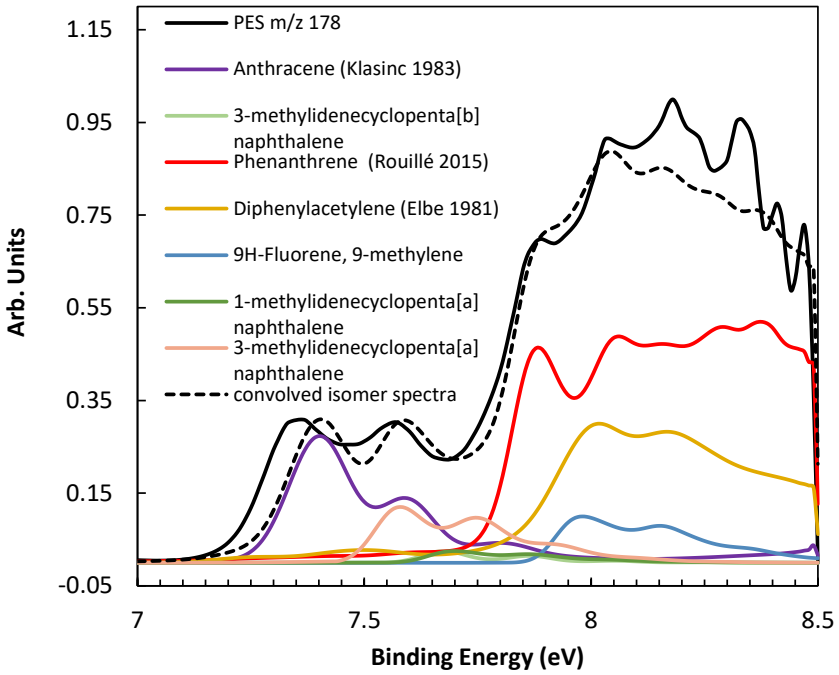

***Figure** 5-37. Comparison of experimental, reference and convolved isomer photoelectron spectra for m/z 178 at 8.5 eV.*

The next peak found in the experimental PES of m/z 178 is located at 7.56 eV coinciding with the higher-level threshold energy determination for isomer 3-methylidenecyclopenta[a]naphthalene which is 7.56 ± 0.05 eV. The formation of this species comes from the addition of methyl radical to 3H-benz[e]indene and subsequent dehydrogenization. 3H-benz[e]indene is a major compound detected in m/z 166. The isomers 3-methylidenecyclopenta[b]naphthalene and 1-methylidenecyclopenta[a]naphthalene are instead present in very small amounts, which agrees with the small contributions from the corresponding 1H-benz[e]indene and 1H-benz[f]indene, respectively. The molecular structures of these isomeric species are presented among with the related formation routes in **Figure** 5-38.

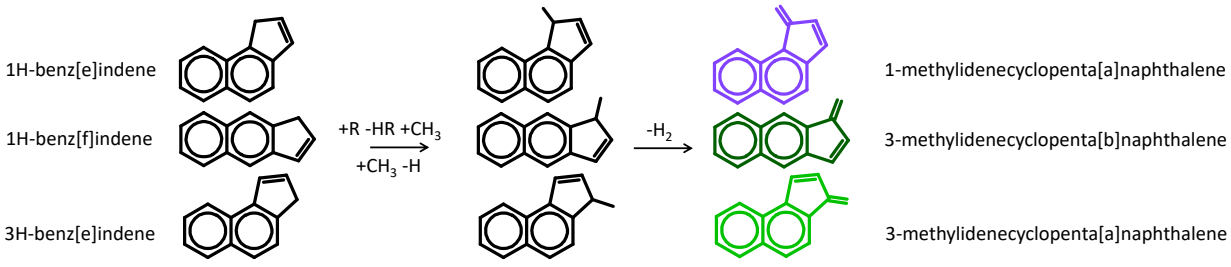

***Figure** 5-38. Molecular structures and related pathways for the formation of mehtylenebenzoindenes.*

The peak at 7.89 eV in the experimental PES is attributed to phenanthrene (PI = 7.88 ± 0.035 eV[298]) according to the convolved spectra. In order to keep the same height ratio between peak at 7.89 eV and the next one at 8.04 eV of the convolved profiles compared to the experimental one, the literature profile for diphenylacetylene (PI = 7.95 eV [259]) and the simulated PES for 9H-fluorene, 9-methylene (PI = 7.95 ± 0.05 eV) were used. Diphenylacetylene ($C_{14}H_{10}$) is mainly produced from the di-dehydrogenization of bibenzyl and then $C_6H_5C_2H_2C_6H_5$, and only from a minor contribution by combination of phenylacetylene (C_8H_6) with phenyl (C_6H_5), while 9H-fluorene, 9-methylene from the reaction between the phenyl radical and phenylacetylene and the thermal decomposition of $C_{13}H_9CH_2$. $C_{13}H_9CH_2$ forms by recombination between fluorenyl radical and CH_3 radical and subsequent rearrangement, and reaction between the benzyl radical with C_7H_5. Diphenylacetylene and 9H-fluorene, 9-methylene have similar PES shapes, with a difference of 0.15 eV in their peak location. However, lower signal contribution was assigned to 9H-fluorene, 9-methylene because the early ionization of this molecule would reduce the fitting accuracy (minimum squared root) in the region between 7.89 eV and 8.04 eV.

Considering the selected isomers, the overall fit for this mass is very good and the individual signal contributions are as it follows:

***Table 5-6**. List of PAH species influencing in the formation of m/z 178.*

Anthracene	20.0%
3-Methylidenecyclopenta[b]naphthalene	1.8%
Phenanthrene	38.2%
Diphenylacetylene	22.0%
9H-Fluorene, 9-methylene	7.3%
1-Methylidenecyclopenta[a]naphthalene	1.8%
3-Methylidenecyclopenta[a]naphthalene	8.8%

5.3.2.14 Species at m/z 180

This peak appears to be very small in the mass spectrum acquired at 10 eV over 8 ms time but it is big enough in the mass spectrum acquired in continuous mode at 8.5 eV, so that identification can be carried out. This difference in relative importance in the two mass spectra may be due either to the different photon energies or to the fact that in continuous acquisition mode reactions might continue after 8 ms. Based on the kinetic analyses presented below, the first hypothesis is the most probable. In fact, the main contributions for the m/z profile come from the stilbenes. Stilbenes are formed from the dehydrogenization of bibenzyl, which is the main recombination product between benzyl radicals, thus produced at early times in the toluene thermal decomposition. Two stilbene isomers are here considered, the trans- and the cis- configurations [299]. Despite the fact the literature PESs are not characterized by sharp features, the overall experimental profile is quite well reproduced (**Figure** 5-39). Here, the peak at 7.82 eV was attributed to literature PES of (E)-stilbene (PI = 7.87 ± 0.02 eV, $C_6H_5C_2H_2C_6H_5$[299]), while the latest part of the profile to (Z)-stilbene (PI = 8.17 ± 0.02 eV[299]). The PES of 1,1-diphenylethylene (PI = 8.00 ± 0.01 eV, [255]) is quite similar to the one of (Z)-stilbene, especially considering the fact that the two

PESs are quite spread over the binding energy range. However, the optimization procedure indicates that (Z)-stilbene has a major contribution compared to 1,1-diphenylethylene.

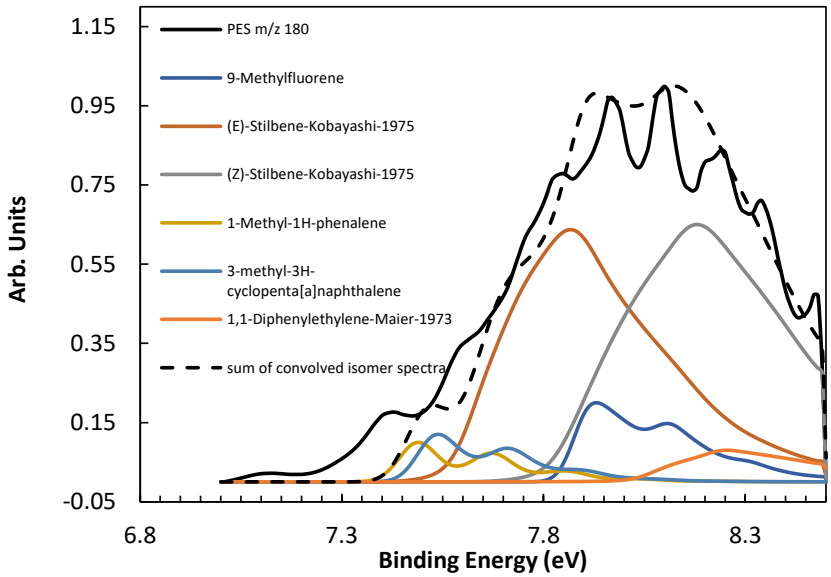

***Figure** 5-39. Comparison of experimental, reference and convolved isomer photoelectron spectra for m/z 180 at 8.5 eV.*

Other isomers of m/z 180 are present, including 9-methylfluorene (PI = 7.87 ± 0.05 eV), which is an important intermediate to the $C_{14}H_{10}$ isomers, produced from the reaction of fluorene with CH_3. In particular, the experimental peak at 7.96 eV is attributed to 9-methylfluorene. In order to capture the small peak evident at 7.42 eV, PES simulations for 1-methyl-1H-phenalene (PI = 7.48 ± 0.10 eV), 3-methyl-3H-cyclopenta[a]naphthalene (PI = 7.53 ± 0.10 eV), 3-methyl-3H-cyclopenta[b]naphthalene (PI 7.68 ± 0.10 eV) and 1-methyl-1H-cyclopenta[a]naphthalene (PI = 7.61 ± 0.10 eV) were included in the analysis. According to the uncertainties of less than 0.1 eV associated with these calculations, 1-methyl-1H-phenalene and 3-methyl-3H-cyclopenta[b]naphthalene are species far to be associated to the peak located at 7.42 eV and could be also contributors to the shoulders found between 7.51 eV and 7.79 eV. 1-methyl-1H-cyclopenta[a]naphthalene seems to match exactly with the shoulder located at 7.61 eV in the experimental PES, but its formation should be minor as the corresponding precursor, 1H-benz[e]indene (see m/z 166), is present in small amounts. Similar for 1-methyl-1H-cyclopenta[a]naphthalene. Thus, 1H-benz[e]indene and 1-methyl-1H-cyclopenta[a]naphthalene were not included in the analyses.

Due to the small differences in shape at the rising part of the sum of convolved isomer spectra with respect to the experimental PES for m/z 180, a hypothesis could be that the peak of the experimental PES located at 7.42 eV could mostly correspond to 1-methyl-1H-phenalene (PI = 7.48 eV), and the first shoulder located at 7.61 eV corresponds to 1-methyl-1H-cyclopenta[a]naphthalene (PI = 7.61 eV). On the other hand, more accurate simulations or measurements on PESs of these species need to be performed or additional isomers considered in order to have a better fitting of the experimental PES. The proposed considerations are quite reasonable with respect to the current knowledge on the photoionization energies of these compounds. 1,8-Diethenylnaphthalene is also reported in the literature [289]. The PI

energy of this compound (7.72 eV, error not reported) is very similar to the shoulder located at 7.75 eV in the experimental PES. On the other hand, the formation of this species is not probable, thus it was not considered here. The relative signal contributions for the studied compounds are listed in the **Table** 5-7.

***Table 5-7**. List of PAH species influencing in the formation of m/z 180.*

9-Methylfluorene	11.2%
(E)-Stilbene	35.6%
(Z)-Stilbene	36.4%
1-Methyl-1H-phenalene	5.6%
3-Methyl-3H-cyclopenta[a]naphthalene	6.7%
1,1-Diphenylethylene	4.5%

5.3.2.15 Species at m/z 182

Isomers of m/z 182 were analyzed including literature PES for 3-3-dimethylbiphenyl, 2,2-dimethylbiphenyl and 1,1-biphenyl, 2-ethyl [300]. Due to the rise on the experimental PES near 8.5 eV (**Figure** 5-40), the convolved spectra favored the contribution of 2,2-dmethylbiphenyl to the signal while 3-3-dimethylbiphenyl is associated to the peak evidenced at 8.12 eV. Only a small amount of 1,1-biphenyl, 2-ethyl was included which increased the accuracy of the fitting near 8.5 eV. However, due to the low signal intensity for the peak at m/z 182 only the two isomers of dimethylbiphenyl can be confirmed here. The relative signal contribution was set to be 30 : 60 : 10 for 3-3-dimethylbiphenyl : 2,2-dimethylbiphenyl : 1,1-biphenyl, 2-ethyl-, respectively.

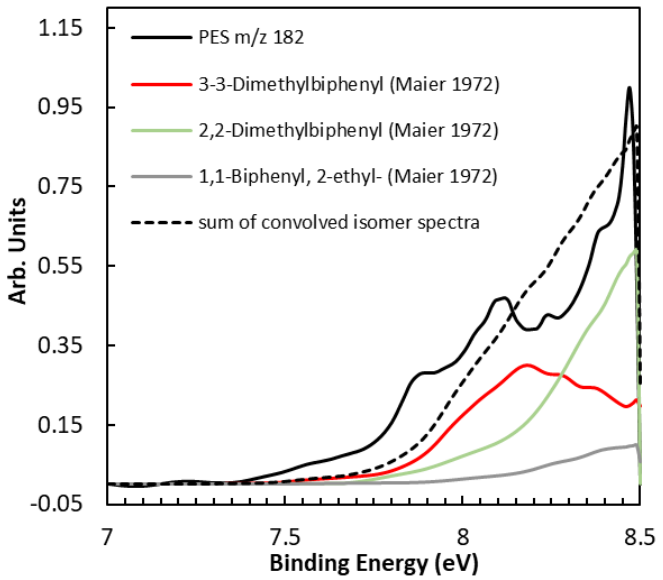

***Figure** 5-40. Comparison of experimental, reference and convolved isomer photoelectron spectra for m/z 182 at 8.5 eV.*

5.3.2.16 Species at m/z 202

This is the biggest peak among the PAH molecules larger than three rings. It is usually associated to pyrene ($PC_{16}H_{10}$, [27]) and fluoranthene ($FC_{16}H_{10}$, [91]) in previous PAH formation studies. The literature PESs for these two compounds are well known. According to the laboratory-based shock tube study on toluene pyrolysis [65], pyrene is mainly produced by the HACA route through phenanthrenyl ($C_{14}H_9 + C_2H_2$), while fluoranthene by the isomerization of phenylnaphthalene and H_2 elimination, as well as the reactions of fluorenyl radical ($C_{13}H_9$) with propargyl radical. The photoelectron spectrum of a third isomer, diphenyldiacetylene ($C_6H_5C_4C_6H_5$), has been measured by Elbel [259], while several $C_{16}H_{10}$ compounds were calculated by ab-initio calculations. It is the case of the ethynylanthracenes and aceanthrylene from the reactions of the anthracene radical with C_2H_2, as well as the benzene, 1-ethynyl-x-(phenylethynyl)-isomers from the HACA route starting from diphenylacetylene. The corresponding PESs are presented in **Figure** 5-41a together with the curves for pyrene [27] and diphenyldiacetylene [259].

The literature PES for diphenyldiacetylene seems to have similar shape to the experimental PES, although the curve does not contain very sharp features, as reflected in the uncertainty for the determination of its photoionization energy which is 7.9 ± 0.08 eV. On the other hand, the peak of this species's PES located at 8.1 eV almost coincides with a minimum on the experimental PES, while the drop in the experimental PES above 8.25 eV is not present in the PES features for diphenyldiacetylene. These facts significantly reduce the contribution of diphenyldiacetylene as it will be demonstrated in the analyses of the final convolved isomer spectrum. Pyrene, on the other hand, is characterized by a photoelectron spectrum with two marked peaks at 7.4 eV and at 8.25 eV, in correspondence with marked features of the experimental PES. Ethynylanthracenes and aceanthrylene have very similar PESs, with photoionization energy of 7.35-7.45 eV. Benzene, 1-ethynyl-2-(phenylethynyl) and benzene, 1-ethynyl-4-(phenylethynyl) have also similar PESs, and their contributions should be minor in view of the fact that their peak does not coincide with any feature of the experimental PES. On the other hand, benzene, 1-ethynyl-3-(phenylethynyl) has a photoionization energy of around 8.0-8.1 eV (0.1 eV uncertainty) coinciding with the peak located at 8.05 eV of the experimental PES. Its contribution will then be relevant based on the optimization routine, although from a kinetic point of view its formation should not be favored compared to the benzene, 1-ethynyl-2-(phenylethynyl) and benzene, 1-ethynyl-4-(phenylethynyl) isomers. This discrepancy could be due to uncertainties in the theoretical calculations, and further analyses are required to clarify this hypothesis. Two different optimization results will be presented, with or without benzene, 1-ethynyl-3-(phenylethynyl).

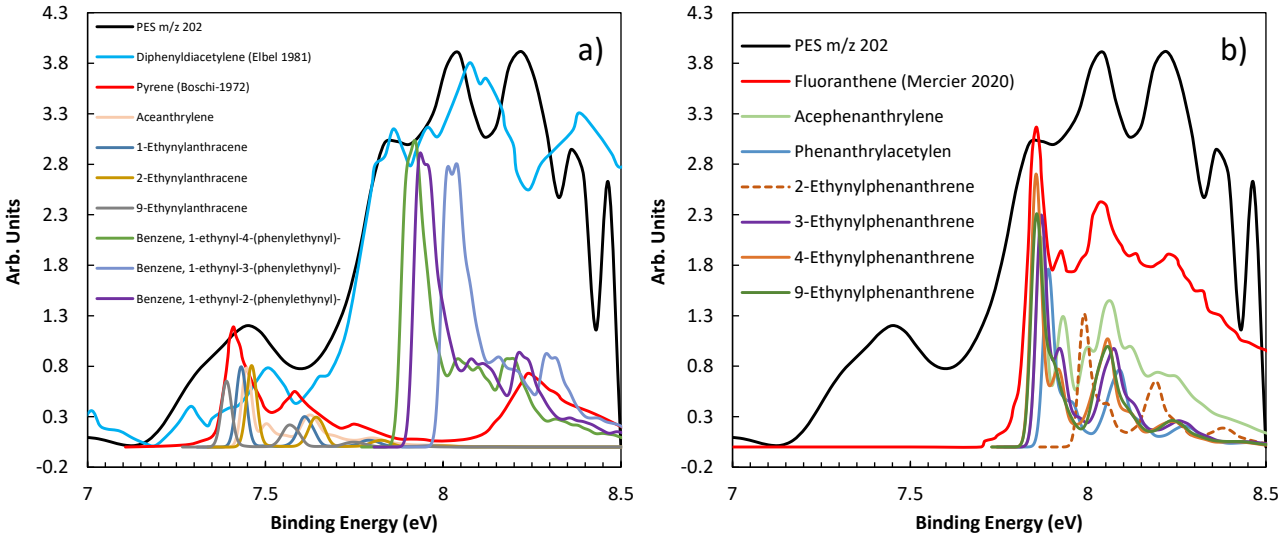

***Figure** 5-41. Comparison of experimental and reference photoelectron spectra for m/z 202 at 8.5 eV.*

The second group of isomers is presented in **Figure** 5-41b. Six photoelectron spectra for the ethynylphenanthrene isomers and for acephenanthrylene (all possibly formed by acetylene addition to the phenanthryl radical) were simulated and compared to the experimental PES, along with the literature PES of fluoranthene (PI = 7.86 ± 0.014 eV[91]). Excluding 2-ethynylphenanthrene, whose photoionization energy is around 8 eV, the remaining compounds are characterized by similar PIs and in correspondence with the first major peak of the experimental profile. On the other hand, the general profile of fluoranthene does not show a considerable drop above 7.9 eV as the other isomers, better reproducing the behavior of the measured PES. Additionally, literature PES for fluoranthene contains three peaks matching the three main peaks of the experimental PES which are located at 7.87 eV, 8.05 eV and 8.22 eV.

The resulting sum of convolved isomer spectra from the optimization software is presented in the **Figure** 5-42. Fluoranthene and pyrene were found to be the most abundant species according to the presented results. A simulated PES was included in the analysis finding that 4,5-vinylidenephenanthrene added some contribution in the shoulder around 7.7 eV significantly improving the shape of the convolved spectra. Two isomers were found to help in the rising of the second peak at 8.05 eV. These were Benzene, 1-ethynyl-3-(phenylethynyl)- and 2-Ethynylphenanthrene. The relative signal contributions for all the species including the minor ones in this optimization are presented in the **Table** 5-8.

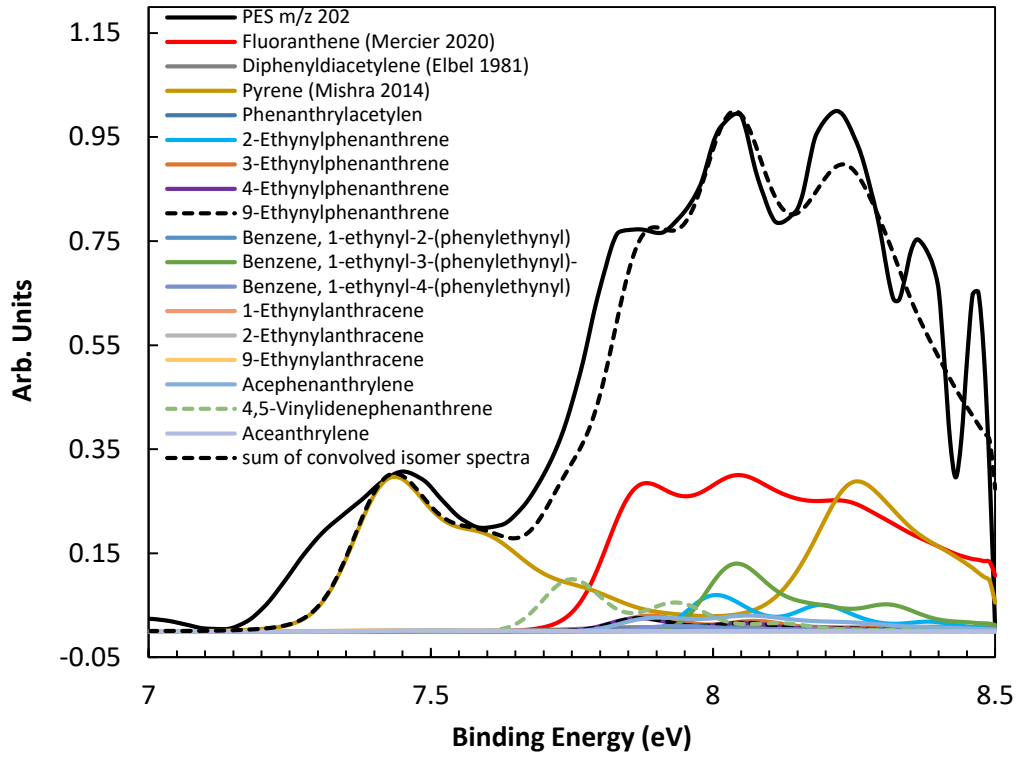

***Figure** 5-42. Comparison of experimental, reference and convolved isomer photoelectron spectra for m/z 202 at 8.5 eV. Case of study considering benzene, 1-ethynyl-3-(phenylethynyl) as big contributor.*

***Table 5-8**. List of PAH species influencing in the formation of m/z 202. Case of study considering benzene, 1-ethynyl-3-(phenylethynyl) as big contributor.*

Fluoranthene	32.1%
Diphenyldiacetylene	1.1%
Pyrene	19.8%
Phenanthrylacetylen	0.5%
2-Ethynylphenanthrene	7.5%
3-Ethynylphenanthrene	3.2%
4-Ethynylphenanthrene	2.7%
9-Ethynylphenanthrene	2.7%
Benzene, 1-ethynyl-2-(phenylethynyl)	1.1%
Benzene, 1-ethynyl-3-(phenylethynyl)	13.9%
Benzene, 1-ethynyl-4-(phenylethynyl)	1.1%
1-Ethynylanthracene	0.1%
2-Ethynylanthracene	0.1%
9-Ethynylanthracene	0.1%
Acephenanthrylene	3.2%
4,5-Vinylidenephenanthrene	10.7%
Aceanthrylene	0.1%

As mentioned above, if we consider chemical kinetic considerations, benzene, 1-ethynyl-3-(phenylethynyl) should not be favored compared to the other positional isomers. Thus, another analyses was performed reducing the contribution from this isomer (**Figure** 5-43). In this case, the fitting is less accurate, in particular the relative heights of the three main peaks is not well reproduced by the convolved signal. On the other hand, this fitting has more sense from a chemical point of view. The different contribution percentages are reported in

Table **5-9**. There is not a significant modification in the relative signal contributions of the main species, including pyrene, fluoranthene, ethynylphenanthrenes and 4,5-vinylidenephenanthrene. Thus, we can assume that, based on the current knowledge, these percentages are quite good estimates considering the uncertainties of the technique. Future work will have to be focused on more accurate determination of the PESs and energetics of the possible kinetic pathways to clarify the results obtained here.

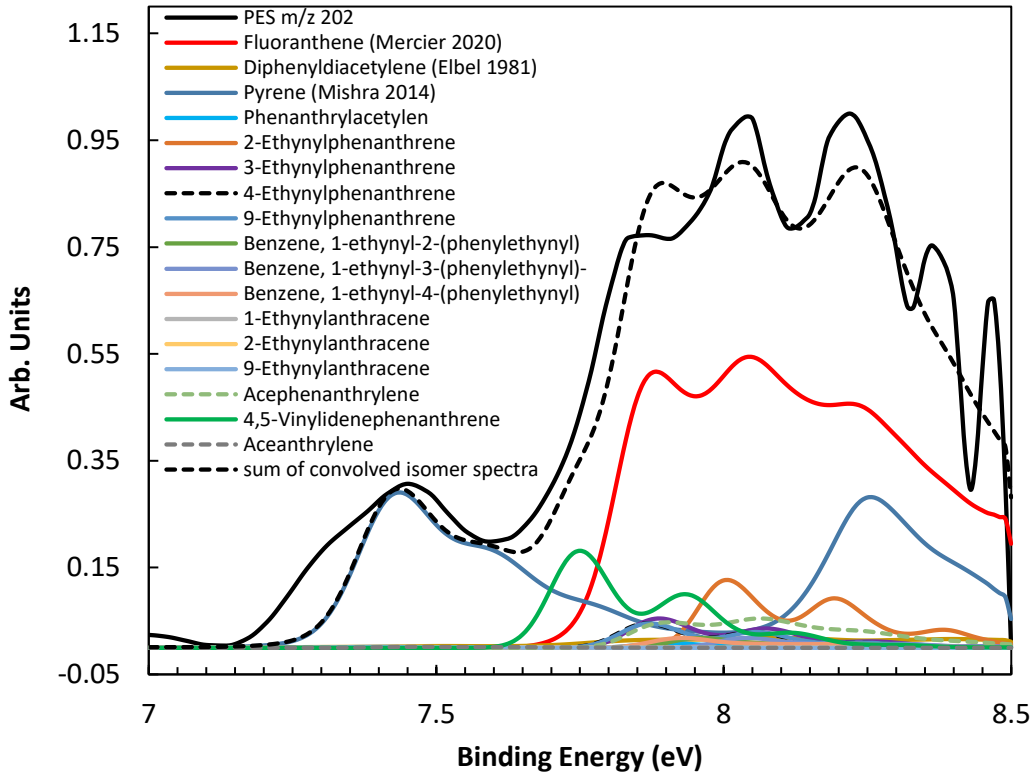

***Figure** 5-43. Comparison of experimental, reference and convolved isomer photoelectron spectra for m/z 202 at 8.5 eV. Case of study reducing contribution from benzene, 1-ethynyl-3-(phenylethynyl).*

***Table 5-9**. List of PAH species influencing in the formation of m/z 202. Case of study reducing contribution from benzene, 1-ethynyl-3-(phenylethynyl).*

Fluoranthene	38.0%
Diphenyldiacetylene	1.3%
Pyrene	20.3%
Phenanthrylacetylen	0.6%
2-Ethynylphenanthrene	8.9%
3-Ethynylphenanthrene	3.8%
4-Ethynylphenanthrene	3.2%
9-Ethynylphenanthrene	3.2%
Benzene, 1-ethynyl-2-(phenylethynyl)	1.3%
Benzene, 1-ethynyl-3-(phenylethynyl)	1.3%
Benzene, 1-ethynyl-4-(phenylethynyl)	1.3%
1-Ethynylanthracene	0.1%
2-Ethynylanthracene	0.1%
9-Ethynylanthracene	0.1%
Acephenanthrylene	3.8%
4,5-Vinylidenephenanthrene	12.7%
Aceanthrylene	0.1%

5.3.2.17 Species at m/z 226

This peak corresponds to some of the largest molecules that could be identified with the experimental PES, even if the signal levels in both mass spectra were low. Literature PESs were used to identify the PAH species, finding that 1-ethynylpyrene peaks at 7.41 ± 0.02 eV [298] and could potentially correspond with the experimental peak at 7.45 eV (**Figure** 5-44). Additionally, there is another peak in the experimental PES at 8.34 eV also present in the literature PES of 1-ethynylpyrene which supports the high possibilities for the presence of this species. Benzo(ghi)fluoranthene, a four-ring species commonly attributed to soot nucleation process, was also identified here as a highly possible isomer since the shoulder evidenced at 7.87 eV coincides with the photoionization energy of this molecule (7.874 ± 0.014 eV[91]). The two compounds can be produced by reactions of pyrene and fluoranthene radicals with acetylene, respectively. There are of course many additional possible isomers, and, as a consequence, the experimental PES is not fully reproduced by the convolved curve, e.g. around the peak at 8.1 eV. On the other hand, the presence of 1-ethynylpyrene and benzo(ghi)fluoranthene highlights the importance of the HACA mechanism for PAH growth kinetics.

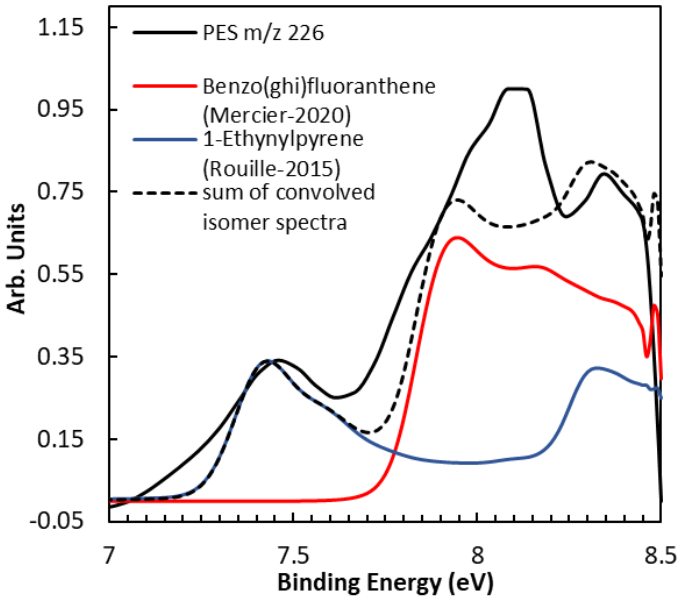

***Figure** 5-44. Comparison of experimental, reference and convolved isomer photoelectron spectra for m/z 226 at 8.5 eV.*

5.3.2.18 Species at m/z 228

A very low signal level was obtained for this peak in the mass spectrum of **Figure** 5-20. However, the sum of convolved isomer spectra provides an insight on the most probable species present at m/z 228. For this, literature PESs for chrysene[301], 1,2-benz[a]anthracene[301], triphenylene[290], and 1-(phenylethynyl)naphthalene[302] were used and compared to the experimental PES after being binned to the adequate resolution.

The most abundant species was found to be triphenylene from the point of view of signal contribution since its photoionization energy of 7.89 ± 0.04 eV coincides with the peak at 7.86 eV (**Figure** 5-45). In previous investigations on phenyl radical pyrolysis, Comandini et al.[63] suggested that triphenylene can be formed by reactions of o-benzyne with biphenylene, in addition to the isomerization of o-terphenyl (which on the other hand is associated to relatively high activation energies, 84.7 kcal/mol based on [101]) or the more probable HACA route from phenanthrene through 9-ethynylphenanthrene. 1,2-Benz[a]anthracene could also be present as its PES is characterized by a large peak at 7.45 eV; on the other hand, its contribution is limited by the absence of a peak in the experimental profile in correspondence with the 1,2-benz[a]anthracene profile peak at 8.1 eV. Finally, the fitting procedure predicts the presence of both chrysene and 1-(phenylethynyl)naphthalene. The latter can be formed from the reaction between the naphthyl radical with phenylacetylene, while 1,2-benz[a]anthracene and chrysene from the HACA route starting from the three-ring compounds anthracene and phenanthrene. The relative contributions from the presented isomers was set to be 10.4 : 11.3 : 56.5 : 21.7 for chrysene : 1,2-benz[a]anthracene : triphenylene : 1-(phenylethynyl)naphthalene, respectively.

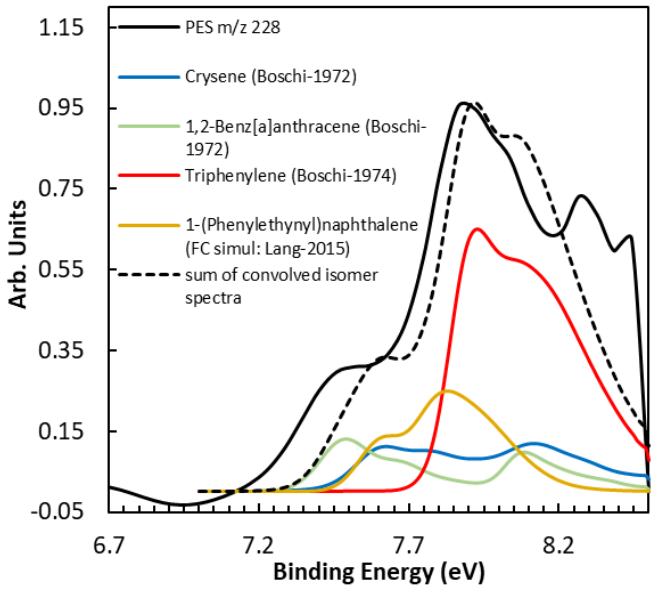

***Figure** 5-45. Comparison of experimental, reference and convolved isomer photoelectron spectra for m/z 228 at 8.5 eV.*

It is also interesting to mention here that the contributions needs to be corrected by the photoionization cross sections but such contributions may not vary considerably for large isomers. For instance, Y. Li [265] estimated that at 8.5 eV the PICS for chrysene is 12.4 Mb and for 1,2-benz[a]anthracene 14.4 Mb, while at 10 eV these are 51.5 Mb and 55.1 Mb, respectively. The proposed percentages should be quite representative of the actual species proportions.

5.3.2.19 Species at m/z 230

The photoelectron spectra of m/z 230 was mainly related to the presence of terphenyl isomers covering the three major peaks at 7.97 eV, 8.18 eV, and 8.34 eV (**Figure** 5-46). Comandini et al.[63] reported that that these species can be formed during reactions of biphenyl ($C_{12}H_{10}$) with phenyl (C_6H_5) as well from reactions of biphenyl radical (o-m-p$C_{12}H_9$) with phenyl (C_6H_5). Unfortunately, the literature PES for the three isomers was not sharp enough and the most rational consideration was to attribute contributions from m-terphenyl[303] to the peaks located at 7.97 eV and 8.34 eV while o-terphenyl[303] and p-terphenyl[304] to the one at 8.18 eV. This lack of sharpness in the literature PES, does not allow to recreate a well-defined sum of convolved isomer spectra and further studies should be addressed in order to reduce the uncertainty in the determination of the relative signal contributions of these species. Actually, from the signal level for m/z 230 the identification starts becoming quite challenging. The available PES for Naphtho[1,8',8:c,d]cycloundeca-1,5-diyne [305] could be used to explain the small peak at 7.45 eV since the photoionization energy for this molecule is 7.5 eV. Nevertheless, the presence of this species is very unprovable from the chemistry point of view, plus the uncertainty for this measurement of PI for Naphtho[1,8',8:c,d]cycloundeca-1,5-diyne is unknown which leaded to the decision of excluding it from

the analysis. The signal contributions for the considered species are 27.2 : 18.5: 54.3 for p-Terphenyl : o-Terphenyl : m-Terphenyl.

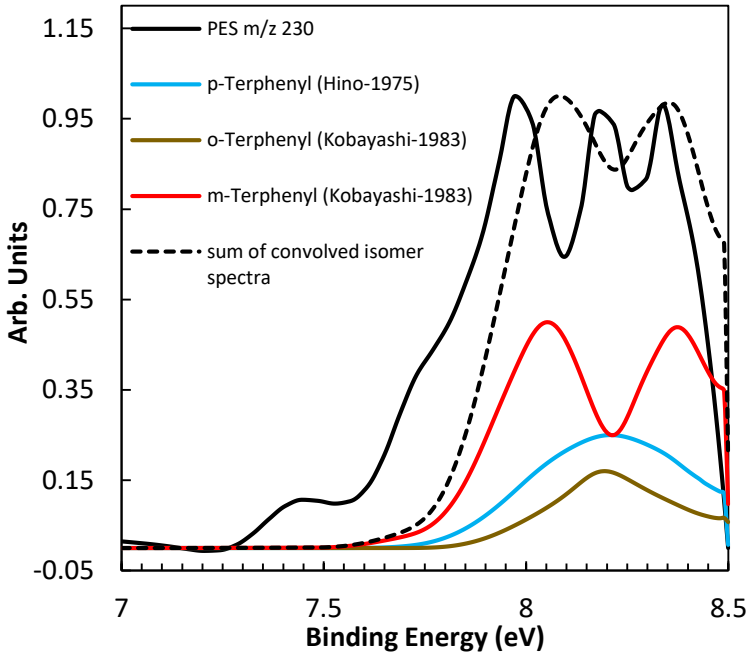

***Figure** 5-46. Comparison of experimental, reference and convolved isomer photoelectron spectra for m/z 230 at 8.5 eV.*

5.3.3 Detection of larger polycyclic aromatic hydrocarbons and kinetic considerations

Based on the results discussed in the previous paragraphs, several common pathways can be identified, including the HACA route, the addition of resonantly stabilized radicals (C_3H_3, C_7H_7), addition of the phenyl radical and cyclization, methylation, and diacetylene addition to aromatic radicals. By integrating the peaks in **Figure** 5-16, the general exponential trend in terms of signal response for the different m/z can be obtained as in **Figure** 5-47. In this figure, the full dots represent the species with higher signals in the specific m/z range. The analyses performed in previous sections provide information on the major isomeric components for each m/z up to ~ 230. Some of the isomers are reported in the figure, starting from benzene, phenylacetylene, naphthalene and acenaphthylene which have been identified as predominant isomers. For larger masses, the analyses become more complicated as the number of possible compounds increases almost exponentially with the number of carbon atoms, while the signal level decreases.

On the other hand, looking at the global trends, it is clear how the major peaks are separated by m/z 24 and 26, corresponding to the HACA mechanisms, e.g. acetylene addition to aromatic radicals followed by H-elimination or formation of an additional ring after H addition, respectively. **Figure** 5-16 contains examples of isomers which can be produced through such mechanisms up to m/z 426 ($C_{34}H_{18}$). The species have been chosen based on the hypothesis that the main contributions would come from reactions

involving smaller species with higher concentrations (thus, other smaller species corresponding to the full dots). Of course, the list is far from being exhaustive, especially considering that each large species has also a considerable number of positional isomers. On the other hand, this simplified view gives an idea of the possible pathways and intermediate structures. In particular, the current analysis is limited to the reactions starting with phenanthrene, the main $C_{14}H_{10}$ intermediate (m/z 178). H-abstraction and C_2H_2 addition can lead to the formation of pyrene and 9-ethynylphenanthrene, observed as main compounds for m/z 202 (section 5.3.2.16), while a subsequent HACA step to m/z 226 and 228. In the specific case, 1-ethynylpyrene and triphenylene were observed in sections 5.3.2.17 and 5.3.2.18 as main intermediates. The following growth to larger PAHs follows the same kinetics of the small species. For example, m/z 276 can be produced from m/z 252 with the addition of acetylene followed by H-elimination (formation of an ethynyl moiety – route R1 in **Figure** 5-48, or of a C5 ring – route R2, or another ring in case of a bay in the PAH structure – route R3). In addition, the formation of an additional ring is possible in case of reaction with a compound which already contains an ethynyl moiety (reaction path R7). These mechanisms can generate two main type of structures, fused with up to 10 rings or elongated, depending on the specific growth sites. The compounds can also contain ethynyl moieties and C5 ring structures. In addition to the HACA mechanism, the major m/z species can also be formed through reactions involving the phenyl radical, similar to the reaction leading to the formation of fluoranthene and phenylnaphthalene from the naphthyl radical + phenyl. These possible isomeric compounds are presented in blue in **Figure** 5-47, with an example in **Figure** 5-48 (R8). There could be other isomers possible from the reactions of aromatic radicals with diacetylene. On the other hand, the results described for smaller molecules suggest that these pathways would be minor compared to the reactions of the same radicals with acetylene, so they were not considered in the analyses.

The second series of species presented in **Figure** 5-49 concerns minor peaks in **Figure** 5-16. Above m/z 350, the signal for these minor peaks is not as sharp as for lower m/z values, thus the associated errors become larger in terms of integration. On the other hand, these data provide a qualitative understanding of the larger structures. As for previous analyses, in order to simplify the results, only possible formation reactions involving major intermediates presented in **Figure** 5-47 are considered. In particular, the different isomers were selected based on various reaction pathways observed in the chemistry of small intermediates: 1) HACA routes as in R1, R2, R3, R7 in **Figure** 5-48 (black species in **Figure** 5-49), including also addition of C_4H_2 to aromatic radicals, similar to the reaction between phenyl radical with diacetylene forming phenyldiacetylene + H; 2) methylation as in R4 (green species); 3) formation of 5-member rings from i) propargyl radical addition / ring-closure and H-elimination (R6), and ii) acetylene addition to benzyl group / ring-closure and H-elimination (R5), similar to the formation pathways for indene formation from the benzene (red species); 4) addition of a phenyl radical or a benzyl radical (R8 and R9, blue species), similar to the reaction of C_6H_5 + $C_{10}H_8$ to fluoranthene/phenylnaphthalene and C_7H_7 + C_6H_6 to fluorene/diphenylmethane.

Each growth reaction corresponds to a specific m/z addition, for example methylation will generate an increment of 14 in the m/z. By looking at the m/z values in **Figure** 5-49 and **Figure** 5-47, it is possible to derive a map of possible associations based on the m/z differences. When a reaction involves a species with multiple isomers (for example, methylation of m/z 276 (see **Figure** 5-47 for possible structures) to form m/z 290), only one example is considered (usually referring to fused structures). Thus, as for **Figure** 5-47, the current analysis contains only a simplified scheme of few possible isomers formed from toluene

pyrolysis with the goal of providing a schematic view of the different kinetic pathways based on considerations of the m/z values observed experimentally. In addition, the minor species can also be formed from the HACA route from smaller compounds as they can be divided by a m/z of 24 or 26. **Figure** 5-50 shows an example of possible competition between benzyl radical additions and HACA route for the formation of a m/z 290 isomer ($C_{23}H_{14}$).

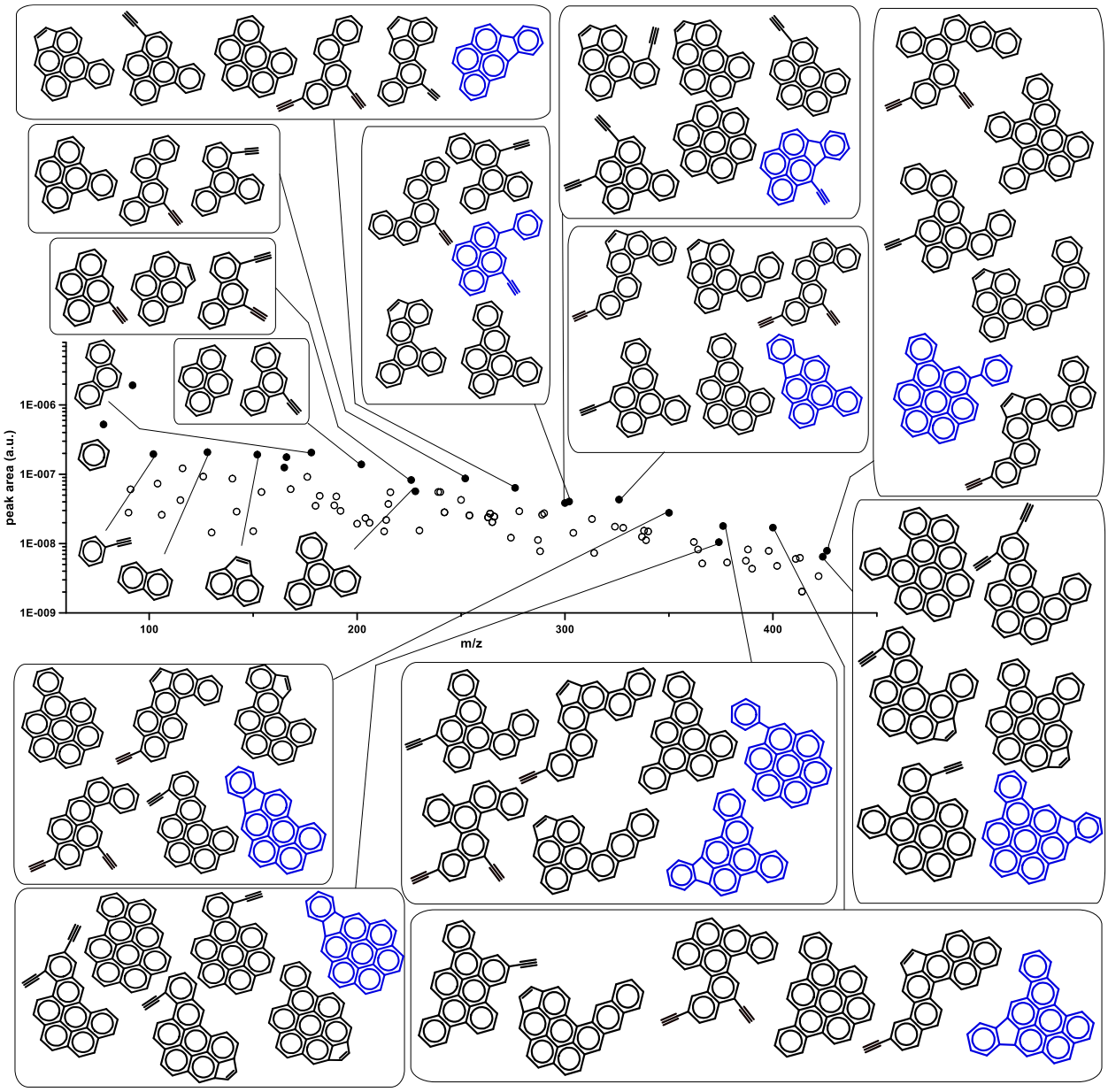

***Figure** 5-47. Exponential trend from integrating peak areas for the different m/z along with examples of isomers which can be produced through HACA (black) and phenyl mechanisms (blue).*

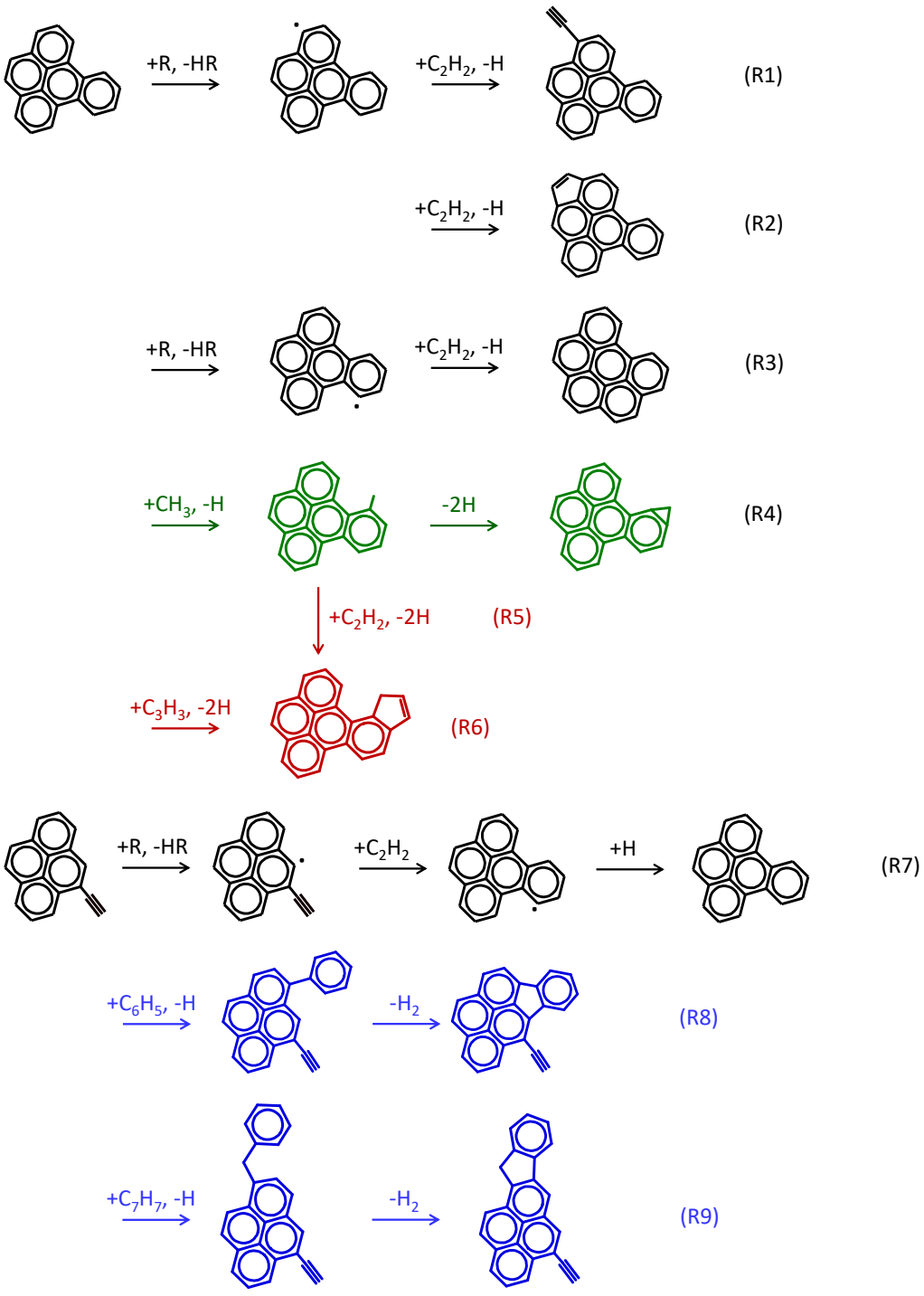

***Figure** 5-48. Examples of different routes implied in the formation and growth of large PAH compounds like HACA mechanism (black), reaction with methyl (green), propargyl (red), phenyl and benzyl (blue).*

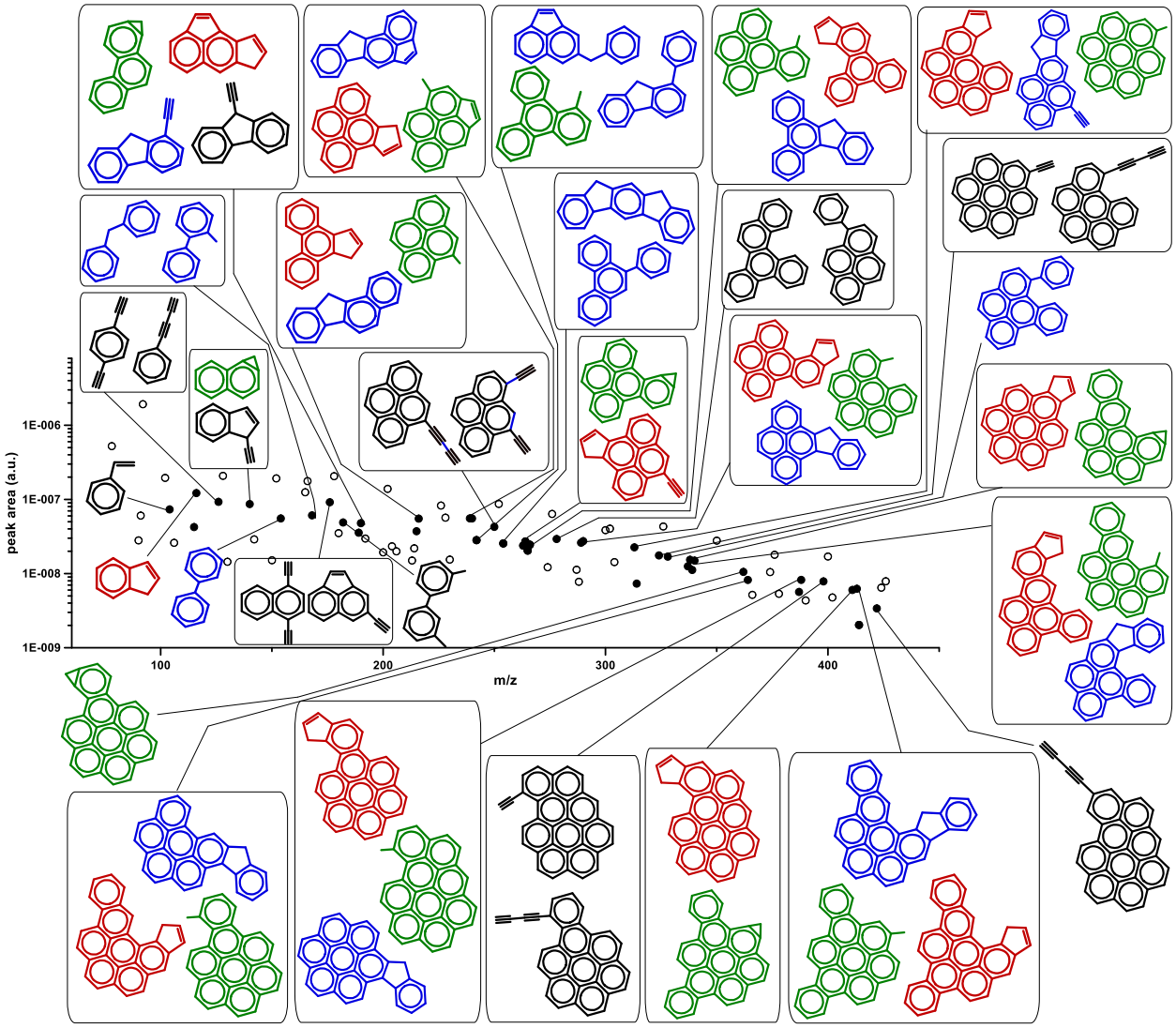

***Figure** 5-49. Exponential trend from integrating peak areas for the different m/z along with examples of isomers which can be produced through HACA mechanism (black), reaction with methyl (green), propargyl (red), phenyl and benzyl (blue).*

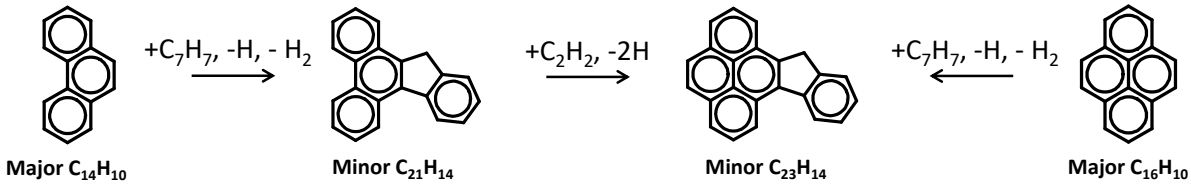

***Figure** 5-50. Example of possible competition between benzyl radical additions and HACA route for the formation of a m/z 290 isomer ($C_{23}H_{14}$).*

It is also important to notice how the majority of the m/z peaks are associated with a second peak at m/z -1. This is the case for species which can decompose to resonantly stabilized radicals, such as indene (m/z 116) to the indenyl radical (m/z 115) or methylbiphenyls and diphenylmethane (m/z 168) which can lose an H from the CH_3 and the CH_2 moieties, respectively. In general, all the species from the methylation processes (R4) or from the reactions with the benzyl radical (R9) or with a C5 ring (R5-R6) will form resonantly stabilized radicals. And this is confirmed in the current analyses, as all the m/z of possible radical structures correspond to stable molecules which can be formed from the above-mentioned reaction pathways (R4, R5, R6, R9). In addition, as mentioned above, the HACA route involving the minor products can play a key role for the molecular growth as shown in **Figure** 5-50. Only few m/z peaks in **Figure** 5-49 are not associated to radical peaks, such as for example m/z 250, 324, or 398. These compounds can be produced through HACA routes (R1, R2, R3, R7) or phenyl radical addition (R8), which is similar to what has been observed in the cases analyzed in **Figure** 5-47. In general, the majority of the minor products can be associated to isomers from various kinetic pathways. The identification of the predominant pathways will require development of detailed or lumped kinetic models for such large species and further kinetic analyses, which will be the focus of future studies.

As shown in **Figure** 5-49, there exist other species produced in even smaller quantities, which can derive from minor pathways involving the m/z isomers present in larger amounts **Figure** 5-47 or the minor products of **Figure** 5-49. The mechanisms should be similar to the ones presented in R1 to R9.

5.3.4 Conclusive remarks

The identification of a large number of polycyclic aromatic hydrocarbon compounds produced from toluene pyrolytic decomposition using the HRRST/i^{2}PEPICO configuration was presented in this chapter. This information constitutes a substantial progress for the understating of the first gas-phase steps of soot formation chemistry, complementing the data obtained with conventional laboratory-based techniques in terms of isomer identification and detection of large molecules. These new results also illustrate the capabilities of such innovative experimental technique that cannot be achieved with regular analytical studies in the laboratory. These exhaustive studies should be extended to other important soot intermediate molecules and fuel components. Thus, in the following chapters, the ICARE-HRRST/i^{2}PEPICO technique is used to analyze the pyrolytic decomposition from ethylbenzene (C_8H_{10}) and styrene (C_8H_8), and the results compared with respect to the toluene data.

5.4 Pyrolysis of ethylbenzene using HRRST/i^{2}PEPICO

The study performed on toluene pyrolysis using the HRRST/DELICIOUS III-i^{2}PEPICO combination was extended to ethylbenzene (ETB, $C_6H_5C_2H_5$, m/z = 106), the smallest among the alkylated aromatic hydrocarbons and an important fuel component. Initially, a comparative study between ethylbenzene and toluene results will be presented in terms of MS peak areas so that a qualitative analysis can be performed on the influence of the side chain length on the pyrolytic product distribution. This analysis is essential for understanding the different reaction pathways involved in the thermal decomposition of the different fuels, and for the future model developments for surrogate fuel chemistry.

Two different experimental conditions were considered in the study on ethylbenzene pyrolysis. A set of 27 042 experiments were averaged using the *pulsed* acquisition mode in order to perform chemical kinetic analysis. The pyrolytic decomposition of 0.1 % ETB diluted in argon bath was evaluated at T_5 = 1327±19 K, P_5 = 6.7±0.2 bar, and photon energy of 10 eV. The conditions are relatively close to the ones used in toluene pyrolysis in order to perform valid comparisons. The repetition rate used was 1 Hz, the spectral data was recorded during 8 ms comprising the pre-shock and post-shock regions, the skimmer 1 and skimmer 2 have orifices diameters of 1 and 2 mm, respectively. The employed nozzle has a 400 µm orifice and the distance between the nozzle and the skimmer 1 tips was kept at 9.5 mm.

The same experimental set-up was implemented for the second part of the ETB study. Around 29 019 experiments were averaged using the so-called *continuous* acquisition mode at photon energy of 8.5 eV. A concentration of 0.1 % ETB diluted in argon was once again considered and thermal pyrolytic decomposition was studied at similar conditions of 1339±14 K, 6.8±0.2 bar. The information obtained from ETB pyrolytic decomposition was used to obtain a large number of experimental PESs for identification of PAH isomers over a wide range of m/z's as in the toluene pyrolysis study. The experimental PESs are then compared to the convolved isomer photoelectron spectra and compared to the respective experimental mass-selected PESs from toluene pyrolysis at similar conditions. The comparison will further highlight the effects of the side chain on product distribution based on the relative isomer abundancy and contributions to each PES signal.

5.4.1 Mass spectrum and identification of small aromatic products

The comparison between mass spectra obtained at 10 eV from the experiments on the thermal decomposition of toluene and ethylbenzene can be done only after normalization of the raw data by the number of experiments of each specific experimental set. In fact, the signal is proportional to the number of experiments and the number of experiments is not the same for the toluene and ETB studies. Additionally, since all the kinetic analyses presented in this work are focused on reaction times of around 1.2 ms after the shock wave arrival at the endwall, the mass spectra obtained at 10 eV presented here were extracted from the first 1.2 ms of the reflected post-shock region. This reduces the S/N ratio of the experimental profiles, but it provides more accurate information for the comparison between the ETB and the toluene results. The comparison between mass spectra obtained for ETB and toluene pyrolysis at similar reaction conditions and at 10 eV of photon energy is presented in **Figure** 5-51.

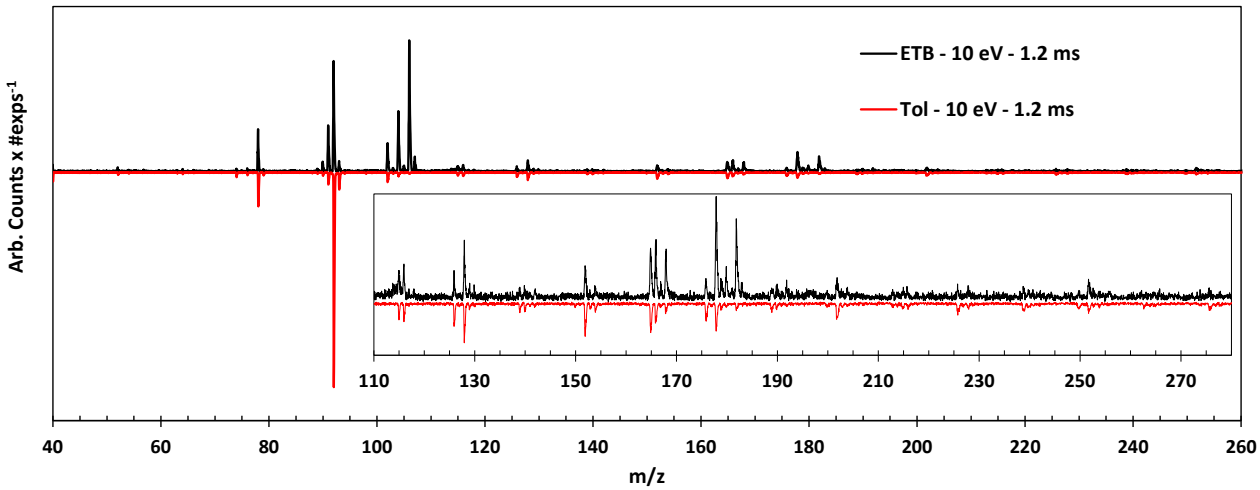

***Figure** 5-51. Mass spectrum obtained in pulsed mode during 1.2 ms of post-shock region. Data is normalized by number of experiments. 0.1% Ethylbenzene and 0.1 % toluene in argon, photon energy 10 eV.*

The figure shows large differences between the two mass spectra. Regarding the major species, ETB, the fuel molecule (m/z 106), represents the largest peak of the spectrum as it is the case of m/z = 92 in toluene pyrolysis. On the other hand, the products peak heights relative to fuel peak are much larger for ETB than for toluene, and this is once again due to the faster thermal decomposition of ETB. In particular, the large peak at m/z 92 is nearly of the same height of the fuel peak, suggesting the pathway from ETB to toluene as the main decomposition reaction. Also, large amounts of styrene (m/z 104), phenylacetylene (m/z 102), and benzene (m/z 78) are produced compared to toluene. Overall, for m/z higher than 108, ETB seems to produce larger amounts of PAH species. This might be due to the specific propensity of the fuel molecule to produce PAHs, the slightly higher carbon concentration for the same initial fuel mole fraction, and the different fuel stability. Indeed, despite the fact that the average temperature of the ETB dataset is around 36 K lower than the toluene case, ETB rapidly decomposes as presented in the external calibration method section (**Figure** 5-15). In addition, ETB consumes completely, while part of the toluene remains unreacted.

Regarding the products present in smaller concentrations, a more detailed comparison can be realized by considering the increase or decrease of the respective peak areas in the ETB spectrum with respect to the toluene one. The relative ratio A_{etb}-A_{tol}/A_{tol} for the different m/z's in **Figure** 5-51 is presented in **Figure** 5-52, where a variation in the ratio is in first approximation proportional to the increase/decrease of the specific product concentration. Positive values imply that the specific m/z is produced in larger amounts from ETB pyrolysis, negative from toluene pyrolysis. This information is very useful for qualitative analyses. For instance, according to the present analysis, the increase on the peak area of m/z 116 and m/z 128 are 0.97 (thus almost a factor 2 between the area in the ETB case compared to toluene) and 0.3, respectively. These masses have been previously attributed to indene (m/z 116) and naphthalene (m/z 128) and were also measured in the previous work on ETB pyrolysis using conventional shock tube techniques [68]. According to the quantitative analysis discussed is section 5.2, their maximum mole fractions increase from toluene to ETB by a factor of 1.0 (from around $1x10^{-5}$ mol/mol to $2 x10^{-5}$) and 0.2 (from $2.5x10^{-5}$ to $3x10^{-5}$), respectively. This example shows that the analysis presented here, despite

deriving from the integrated mass spectra, is consistent with the relation between calibrated mole fraction profiles for the different fuels. Of course, the integrated values will also be influenced by the species time histories (different time of appearance of the products in the two cases), from which the slight difference in the current results and the ones presented in section 5.2. It is important to underline the fact that, if the species distribution for a specific m/z is similar in both datasets, then the corresponding photoionization cross section will be similar, causing a small error in the comparative analyses.

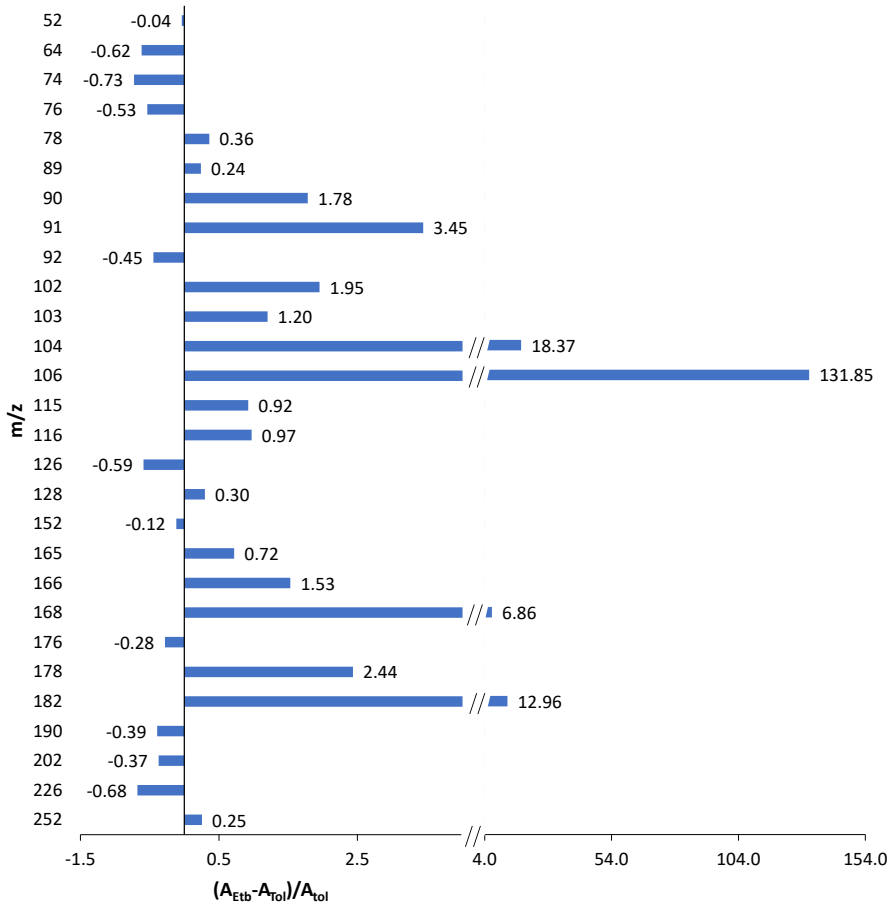

***Figure** 5-52. Peak area increase (A_{etb}-A_{tol}/A_{tol}) in ETB mass spectrum (10 eV-pulsed mode) compared to toluene mass spectrum (10 eV-pulsed mode) for m/z ranging from 52 to 252.*

The analysis can be extended to other product peaks present in the mass spectrum, including the PAH compounds for which the detailed analysis of the photoelectron spectra will be performed in the next section based on the data obtained with *continuous* acquisition mode at 8.5 eV. Despite the number of experiments is substantially lower for ETB pyrolysis compared to the toluene study (27 000 vs 107 000), which results in lower S/N ratio, the resolution of the presented data is enough to obtain meaningful results for most products, especially for major species, as presented in **Figure** 5-52. As commented above, the thermal decomposition of ETB leads to large mole fractions of styrene and phenylacetylene compared

to toluene pyrolysis (peak area increase of 18.37 and 1.95, respectively), as for the latter case these species will be only formed from the recombination of the benzyl radical with methyl followed by fragmentation of the resulting ETB product. Benzyl radicals (m/z 91) are also formed directly from the thermal decomposition of ETB, thus present in large amounts, together with fulvenallene (m/z 90) from subsequent decomposition. Benzene is also produced in larger amounts in ETB pyrolysis as hydrogen atoms are produced in larger concentrations for ipso-addition to the fuel. It is also interesting to notice how the related m/z 76 (possibly o-benzyne) and m/z 74 (triacetylene) are lower for ETB compared to toluene, and this can be mainly attributed to the difference in temperature condition (higher T favors ring fragmentation). Concerning PAH compounds, m/z 116 and 128 have been already discussed. Other common products deriving directly or indirectly from the reactions between two aromatic rings are also favored in the case of ETB, mainly by the higher reactivity of the fuel compared to toluene. These include m/z 166 (1.53), m/z 168 (6.86), m/z 178 (2.44), m/z 182 (2.44). On the contrary, other species which are mainly from HACA steps show negative peak area ratios, such as m/z 126 (-0.59), m/z 152 (-0.12), and m/z 176 (-0.28). This different behavior is influenced mainly by the different temperature condition, as acetylene formation will be favored at higher temperatures. Similar considerations for larger m/z, i.e. 202 and 226. The only exception is m/z 252, which is produced in larger amounts during ETB decomposition. This specific case will require further detailed analyses based on kinetic simulations which at the moment are not available.

In addition, the ETB data at 10 eV were used to derive photoelectron spectra and identify most of the major single-ring aromatic species and smaller intermediates as shown in **Figure** 5-53. Also in this case, the reduced number of experiments compared to toluene does not strongly influence the quality of the data. Indeed, the resolution of the PES for the major species is enough to identify the products of small mass with strong spectral characteristics including vinylacetylene (m/z 52), 1,3,5-hexatriyne (triacetylene, m/z 74), fulvenallene (m/z 90, obtained at 8.5 eV), toluene (m/z 92), phenylacetylene (m/z 102), and the fuel molecule ethylbenzene (m/z 106). In this case, different from toluene pyrolysis, no presence of o-m-p-xylene isomers can be identified as shown in the comparison of literature and experimental PES for m/z 106. This is reasonable as the toluene concentrations are much lower and thus its reaction with CH_3 inhibited. On the other hand, the signal from ETB is very large, so it could cover the signal from the xylenes. Similar to toluene, in ETB pyrolysis a small amount of xylylene isomers could be noticed as shown in the comparison of 10 eV and 8.5 eV data for m/z 104, where the major species identified is styrene. Finally, although m/z 78 is mainly attributed to benzene, a small amount less than 5 % of the signal contribution could be assigned to fulvene as shown in the PES figure for m/z 78.

The information presented in this section complements the data previously obtained using a well-stablished technique based on conventional single pulse shock tube coupled to GC-GC/MS system [68]. In that work, experiments on ETB decomposition were conducted at a nominal pressure of 20 bar over a temperature range of 950–1700 K. The experimental and modeling results revealed that ETB decomposes mainly to benzyl radical (m/z 91) and subsequently part of it leads to the formation of toluene (m/z 92) by H addition, diphenylmethane (m/z 168) by reaction with single-ring aromatic, and bibenzyl (m/z 182) by self-recombination, three peaks that were also detected in the present study. ETB can also produce benzene (m/z 78) via ipso-addition reaction ($C_6H_5C_2H_5$ + H -> C_6H_6+C_2H_5) while styrene is mainly produced from dehydrogenization of the fuel and the fuel radical ($C_6H_5C_2H_4$). Styrene can then decompose to form phenylacetylene. If the complete range of temperatures studied is taken into consideration, the order of the major single-ring aromatic products in the HPST study based on the related mole fractions was found

to be toluene (44.5 ppm max) > benzene (21 ppm max) > styrene (13.5 ppm max) > phenylacetylene (3.5 ppm max). These mole fractions represent the value at the end of the 4 ms reaction times, thus their ratios can be considered proportional in first approximation to the ratios of the mole fractions integrated over the 4 ms time, and consequently to the importance of the related kinetic pathways. This approximation would be correct if all the products appeared at the same time. More importantly, the maximum mole fractions are reached at different temperatures, thus a direct comparison between these values and the ones derived from the integrated peak areas in **Figure** 5-52 is not possible. Indeed, it is important to obtain the mole fractions at the same temperature of the present HRRST/i^{2}PEPICO ETB pyrolysis study. Specifically, in order to be able to compare the present mass spectrum information to the HPST results, for a temperature of around 1327 K the literature study provided the following order based on the species concentration profiles vs temperature: toluene (19 ppm) > styrene (12.5 ppm) > benzene (3.7 ppm) > phenylacetylene (0.25 ppm). In a more simplified way, the relative proportion is 3.8 : 2.5 : 0.74 : 0.05. These proportions are very similar to the ones extracted in the HRRST/i^{2}PEPICO study with T_5 = 1327 K, P_5 = 6.7 bar. In the latter case, the results are toluene : styrene : benzene : phenylacetylene as 3.8 : 2.2 : 1.3 : 1.0, respectively, after considering the cross sectional areas of the main isomers. Thus, in addition to the kinetic profiles which can be derived applying the calibration procedure as in Chapter 5.2, the integrated peaks can provide indicative information on the relative importance of the different reaction pathways in complex kinetic schemes. In this perspective, the synchrotron information complements quite well the results obtained in conventional systems.

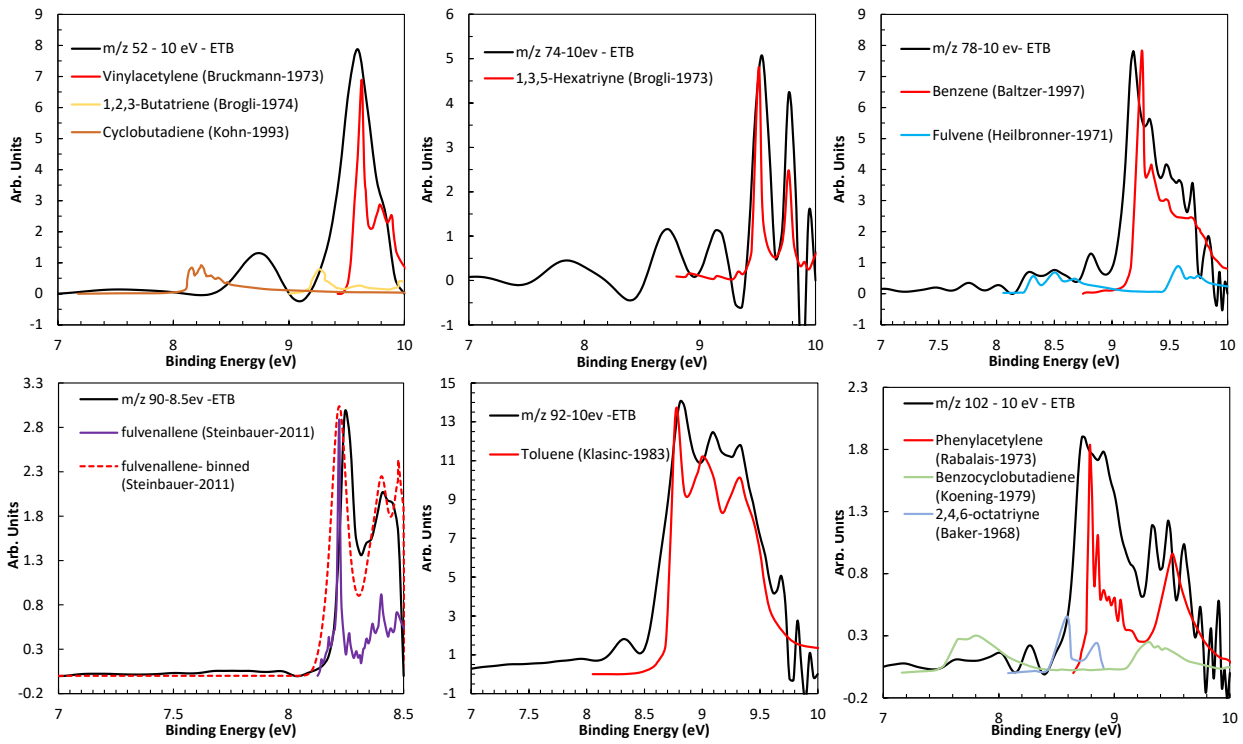

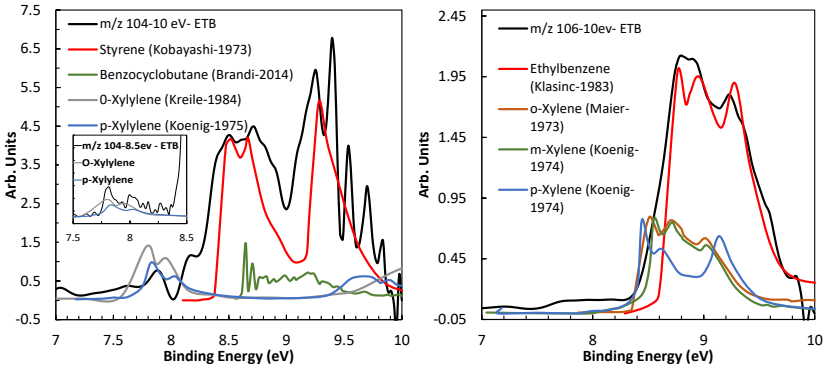

***Figure** 5-53. Photoelectron spectra of product molecules with m/z ranging from 52 to 106. Photon energy of 10 eV except for m/z 90 that was acquired at 8.5 eV.*

5.4.2 Mass selected identification of polycyclic aromatic hydrocarbons

The mass spectrum obtained for ETB pyrolysis at 8.5 eV and *continuous* mode was also compared to the mass spectrum of toluene obtained at similar conditions. In this case, the mass spectra are collected over the entire shock tube cycle, thus they will be affected by multiple passages of the shock wave before the opening of the valves for exhausting the gases. In addition, certain PAH species will not ionize at 8.5 eV, and the cross sections might significantly vary between 10 eV and 8.5 eV. Thus, certain differences with the data at 10 eV are expected. The mass spectra were normalized by the number of experiments of the respective dataset and are presented in **Figure** 5-54. It can be noticed how the peaks for the fuel molecules are absent; this is essential for the reduction of the background noise caused by the false coincidences and the ability to measure intermediate species present in small concentrations, as the PAHs.

Among the main single-ring aromatics and small fuel decomposition products, toluene (m/z 92, PI = 8.83 eV), vinylacetylene (m/z 102, PI = 8.78 eV), benzene (m/z 78, PI = 9.24 eV), and ETB (m/z 106, PI = 8.77 eV) have ionization energies which are higher than 8.5. Only styrene (m/z 104, PI= 8.46 eV) and fulvenallene (m/z 90, PI = 8.22 eV) are ionized, and major peaks at the corresponding m/z can be observed in **Figure** 5-54. The distribution of the PAH products is very similar to the one observed for toluene, although it is clear at first sight that the ETB pyrolysis leads to larger product concentrations between m/z 160 to 200, as also observed in the data obtained at 10 eV. The data obtained with *continuous* acquisition mode also allow to clearly identify the presence of larger PAHs, up to a m/z 330 for the ETB dataset. Indeed, this mode leads to a substantial improvement of the S/N compared to the *pulsed* mode integrated over 1.2 ms. For example, m/z 202 obtained by the two acquisition modes are presented in **Figure** 5-55. For the larger PAHs, certain compounds are produced in larger concentrations from ETB thermal decomposition, others in the toluene case. As mentioned above, this should be linked to the different pathways, aromatic recombination favored for ETB due to the higher reactivity of the fuel vs HACA route favored at the slightly higher temperatures of the toluene dataset. Chemical kinetic analyses including detailed mechanisms for the formation of such large products would be necessary to clarify this hypothesis, with simulations considering the entire pressure time-histories inside the HRRST. At the moment, this is beyond the scope of the present work.

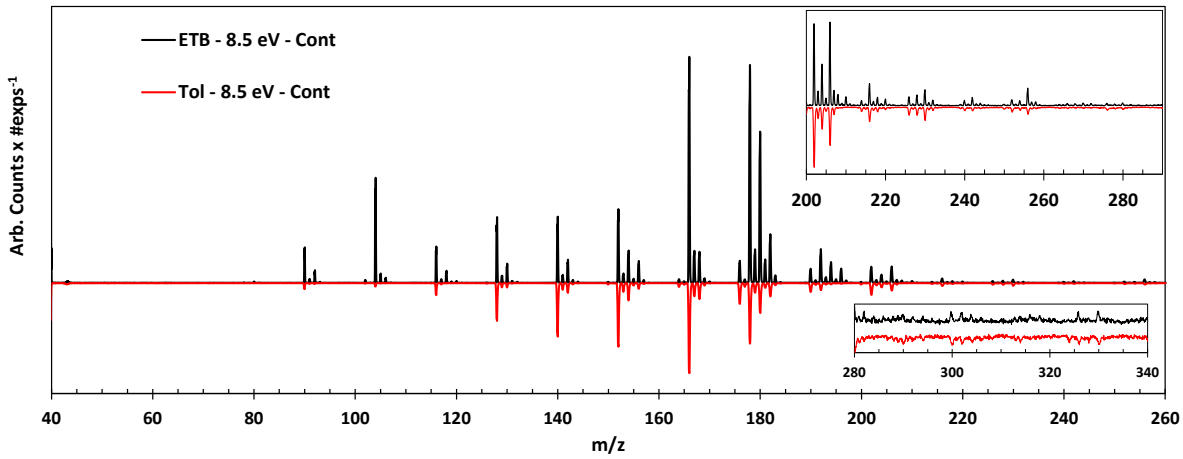

***Figure** 5-54. Mass spectrum obtained in continuous mode, averaging around 29 019 experiments for ETB and 41 000 for toluene. Data is normalized by number of experiments. 0.1% Ethylbenzene and 0.1 % toluene in argon, photon energy 8.5 eV.*

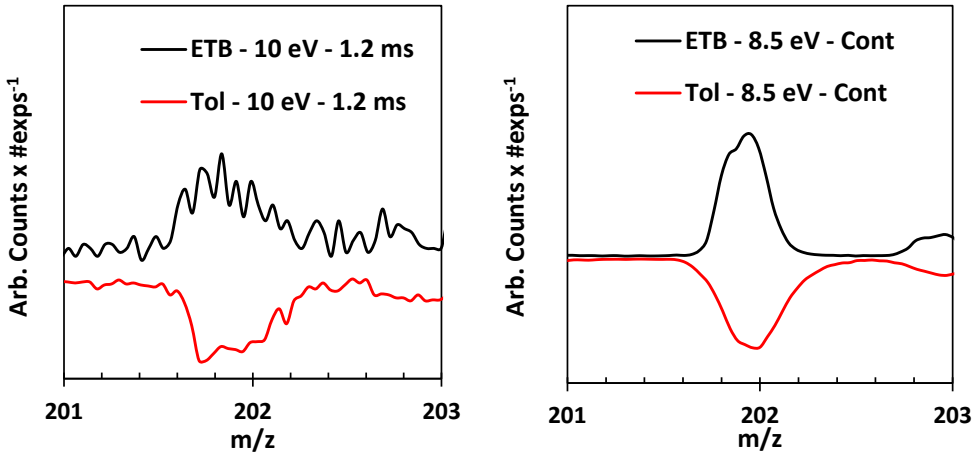

***Figure** 5-55. Comparison between mass spectrum data obtained at 10 eV with pulsed mode during 1.2 ms of acquisition time and mass spectrum data acquired at 8.5 eV with continuous mode for small concentration species m/z 202.*

The dataset at 8.5 eV and *continuous* mode does not only improve the MS S/N, but also the quality of the derived photoelectron spectra, for identification of PAHs up to a m/z of around 230. In **Figure** 5-54 the major PAH species are at m/z 166 and m/z 178. For m/z 166 the peak area in toluene pyrolysis is increased by around 80% in ETB pyrolysis. In order to derive the isomer distribution from ETB pyrolysis and compare it with the toluene case, the experimental (black line) and simulated (dashed line) spectra for m/z 166 are compared to the toluene experimental PES (red line). The same notation is used for all the masses that are analyzed in the present chapter.

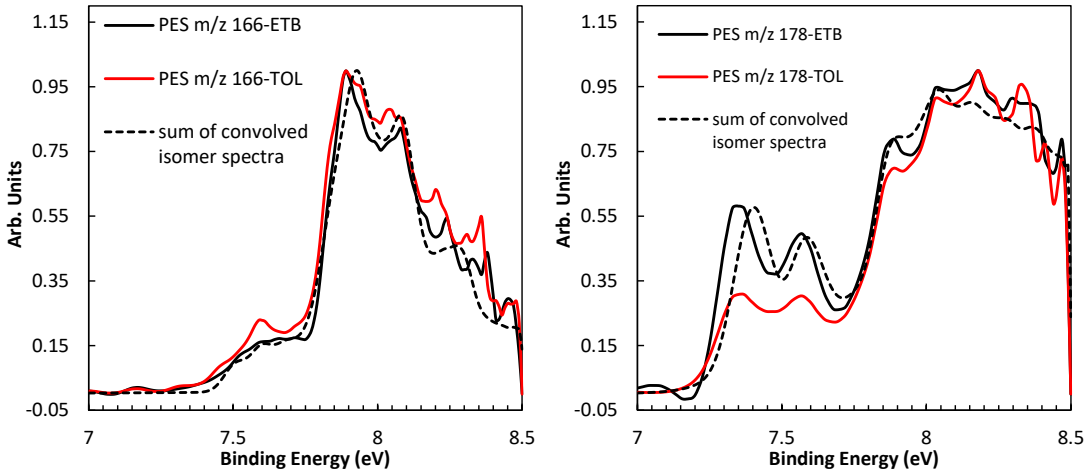

***Figure** 5-56. Photoelectron spectra for m/z 166 and m/z 178 obtained at 8.5 eV and continuous data acquisition mode. Each figure contains experimental PES for ETB and toluene pyrolysis and sum of convolved isomer spectra for ETB pyrolysis.*

First, even if m/z 166 MS signal increased from toluene to ETB pyrolysis, the overall shape of the photoelectron spectra did not significantly change between the two cases. One important difference can be evidenced at the beginning of the spectra at around 7.6 eV binding energy. Compared to toluene, ETB pyrolysis reduces the production of 3H-Benz[e]indene ($C_{13}H_{10}$, PI = 7.60±0.05 eV) and it suggests the formation of one additional isomer of m/z 166 whose PES was simulated: 1h-Benz[e]indene ($C_{13}H_{10}$, PI = 7.69±0.05 eV). The contribution of the latter is in any case quite small (around 2%), thus it could be affected by errors. For the remaining PES profile at higher binding energies, the changes compared to toluene pyrolysis are not perceptible, so presenting the relative contributions to the overall signal becomes more useful for the analysis (**Table** 5-10).

***Table 5-10**. Relative contributions to the m/z 166 overall signal for ethylbenzene and toluene.*

	toluene	***ETB***
fluorene	39%	45%
3H-benz[e]indene	11%	8%
1-(1-naphthyl)-1-propyne	14%	6%
2-propynyl naphthalene	14%	17%
1H-phenalene	7%	6%
2-prop-2-ynyl-naphthalene	8%	3%
1-prop-2-ynyl-naphthalene	7%	14%
1H-benz[f]indene	2%	0%
1H-benz[e]indene	0%	2%

During ETB decomposition, fluorene is still the most abundant species. According to the method proposed here and taking into consideration an overall 83 % (A_{etb}/A_{tol}=1.83) increase of the m/z 166 production and the internal change on the relative signal contribution for fluorene from 39% in toluene PES to 45% in ETB PES, this gives a total increase of around a factor 2.1 (1.83×[0.45/0.39]) in the amount of fluorene in ETB pyrolysis compared to toluene pyrolysis. As a general rule, the combined effects need to be considered. There is still the need of accounting for the PICS of the species present at m/z 166 in order to bring this signal values to concentration units but the information provided in this analysis is of special relevance for chemical kinetic model developments. The remaining isomer contributions vary but within the uncertainties of the method. For example, $C_{10}H_7CCCH_3$ isomers (1-(1-naphthyl)-1-propyne and 2-propynyl naphthalene) provide an overall contribution of 23% (vs 28% toluene), $C_{10}H_7CH_2CCH$ (1-prop-2-ynyl-naphthalene and 2-prop-2-ynyl-naphthalene) 17% (vs 15% in toluene).

For m/z 178, whose respective PESs are presented in **Figure** 5-56b, the peak area increases 1.59 times from toluene to ETB pyrolysis according to **Figure** 5-54. When analyzing the PES for this m/z, there is an evident increase in the contribution of anthracene since the peaks mostly attributed to anthracene located at the beginning of the photoelectron spectra are higher in the ETB PES compared to the toluene PES. The convolution process determines the correspondence anthracene : phenanthrene to be 9.2 : 10 in ETB pyrolysis versus 5.2 : 10 in toluene pyrolysis, which represents a large overall increase of 4 times (2.59x[31.5/20]) in the amount of anthracene in ETB pyrolysis compared to toluene pyrolysis. Phenanthrene does not seem to change much as anthracene since the overall signal change is determined to be 2.3 times (2.59x[34.1/38.2]) in ETB compared to the toluene case. The proportion anthracene : phenanthrene might be strongly affected by the difference in temperature condition between the two datasets. Considering an activation energy of around 65 kcal/mol for the isomerization from anthracene to phenanthrene as in [37], a 15 K drop in temperature leads to a decrease in the reaction rate by a factor 1.4-1.7 at the current conditions. The toluene *continuous* set was obtained at average T of 1351 K, the ETB set at 1339 K. The species with smaller contribution in ETB pyrolysis appears to be diphenylacetylene with a total signal increase of 1.84 times (2.59x[15.7/22]) compared to toluene pyrolysis, but a smaller total percentage contribution. For m/z 178, the individual signal contributions to the ETB PES are listed in **Table** 5-11:

Table 5-11*. Relative contributions to the m/z 178 overall signal for ethylbenzene and toluene.*

	toluene	***ETB***
Anthracene	20.0%	31.5%
3-Methylidenecyclopenta[b]naphthalene	1.8%	1.5%
Phenanthrene	38.2%	34.1%
Diphenylacetylene	22.0%	15.7%
9H-Fluorene, 9-methylene	7.3%	6.4%
1-Methylidenecyclopenta[a]naphthalene	1.8%	1.5%
3-Methylidenecyclopenta[a]naphthalene	8.8%	9.3%

Two other major PAH peaks that have been analyzed are m/z 152 and m/z 140. The experimental PES for both masses in ETB and toluene pyrolysis are presented in **Figure** 5-57 along with the sum of convolved

isomer spectra for ETB pyrolysis. An overall good fitting between the experimental PES for ETB and the convolved curve was obtained for m/z 152. The convolution procedure provides the following relative contributions to the signal for m/z 152, acenaphthylene : 2-ethynylnaphthalene : biphenylene : cyclopenta[a]indene: 1-ethynylnaphthalene 61.4 : 26.3 : 4.4 : 4.4 : 3.5, compared to the ones in toluene pyrolysis previously determined as 61 : 25 : 4 : 4 : 6, respectively. Thus, no significant changes in the isomer distribution is observed. The only difference between the two fuel molecules is that the MS peak area is larger by around 20% for toluene pyrolysis as also presented for the results in **Figure** 5-52, where a 12% increase was found for the data in *pulsed* acquisition mode and 10 eV photon energy.

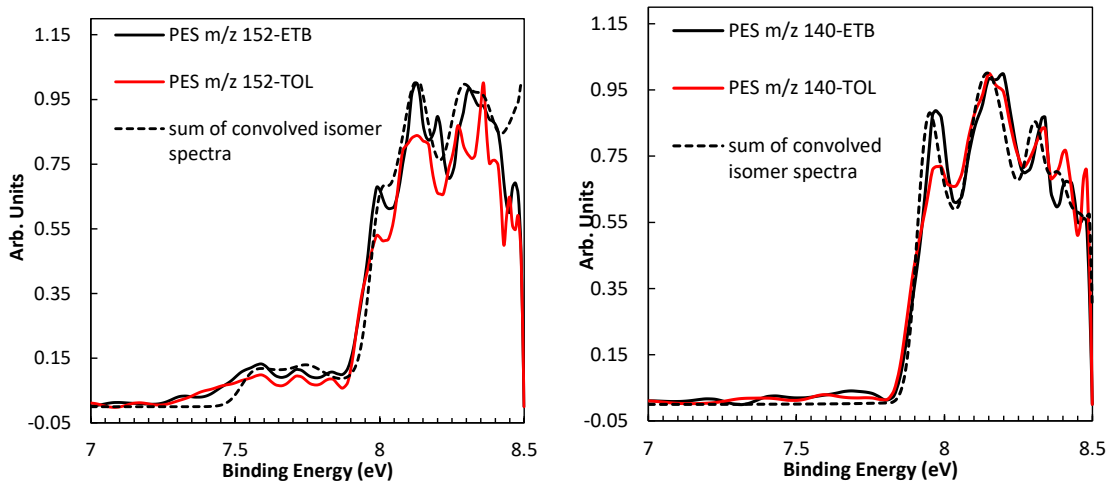

***Figure** 5-57. Photoelectron spectra for m/z 152 and m/z 140 obtained at 8.5 eV and continuous data acquisition mode. Each figure contains experimental PES for ETB and toluene pyrolysis and sum of convolved isomer spectra for ETB pyrolysis.*

For m/z 140, the peak areas in **Figure** 5-54 are very similar for toluene and ETB pyrolysis. On the other hand, the internal distribution of the isomeric species changes. Observing the general fit of the sum of convolved isomer spectra, the simulated spectra perfectly match the experimental ETB data. By using this fit, the resulting relative PES signal contributions considering a large number of isomers are presented in **Table 5-12**.

***Table 5-12**. Relative contributions to the m/z 140 overall signal for ethylbenzene and toluene.*

	toluene	***ETB***
1H-cyclopropa[a]naphthalene	34.4%	42.5%
1H-cyclopropa[b]naphthalene	23.0%	17.7 %
1-ethynyl-1H-indene	10.3%	13.3%
2-ethynyl-1H-indene	17.2%	13.0%
4-ethynyl-1H-indene	1.1%	4.4%
5-ethynyl-1H-indene	1.1%	0.9%
6-ethynyl-1H-indene	1.1%	0.9%
7-ethynyl-1H-indene	1.1%	0.9%
phenyl allenyl acetylene	5.3%	5.3%

In both cases, 1H-cyclopropa[a]naphthalene, 1H-cyclopropa[b]naphthalene, 1-ethynyl-1H-indene and 2-ethynyl-1H-indene are the species that contribute more to the PES signal but some changes in the relative percentage contributions between ETB and toluene pyrolysis need to be highlighted. Mainly, the contribution of 1H-cyclopropa[a]naphthalenes isomer was slightly increased for ETB (from 34% to 43%), while the one of 1H-cyclopropa[b]naphthalene decresed from 23% to 18%. The other isomers include the ethynyl-indenes which globally contribute to 32% of the total signal (vs 33% for toluene pyrolysis), and phenyl allenyl acetylene whose contribution remains unchanged.

Further advancing in the selective identification of isomers produced during the pyrolytic decomposition of ETB at 1339 K and 6.8 bar, other masses can be identified in the mass spectrum presented in **Figure** 5-54. Two other peaks are found to be major contributors to the mass spectrum and these are m/z 128 and m/z 180. The experimental PESs for ETB and toluene are compared in the **Figure** 5-58 together with the sum of convolved isomer spectra for the respective m/z.

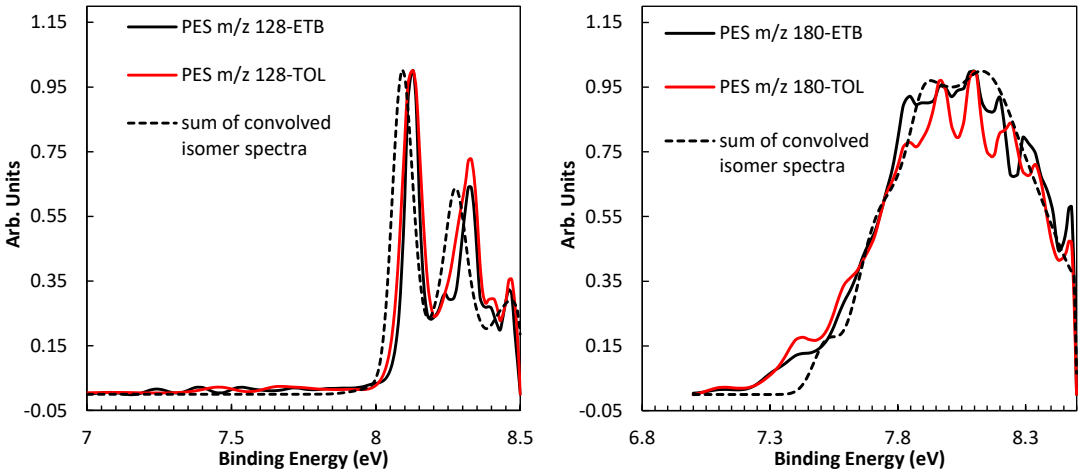

***Figure** 5-58. Photoelectron spectra for m/z 128 and m/z 180 obtained at 8.5 eV and continuous data acquisition mode. Each figure contains experimental PES for ETB and toluene pyrolysis and sum of convolved isomer spectra for ETB pyrolysis.*

The agreement between the experimental and convolved PES is quite good for for m/z 128 in ETB pyrolysis and some differences in the distribution of isomers can be observed with respect to the case of toluene decomposition. Mostly, naphthalene and 1H-indene-1-methylene were found to be the main products in ETB pyrolysis accounting for the 92.8% of the contribution to the overall signal of m/z 128 compared to 80% in toluene pyrolysis. The list of all the species considered for the PES analysis in m/z 128 are naphthalene : 4-ethynylstyrene : 3-buten-1-ynylbenzene : 4-phenyl-1-butene-3-yne : m-ethynylstyrene : 1H-indene-1-methylene. The relative contributions for these species were determined to be 81.1 : 1.7 : 1.7 : 1.7 : 2.2 : 11.7, respectively, compared to 70 : 5 : 5 : 5 : 5 : 10 in toluene pyrolysis. The reduction in the height of the second peak in the experimental profile (at around 8.35 eV) leads to a decrease in the

contributions from the minor isomers 3-buten-1-ynylbenzene ($C_6H_5CCCHCH_2$), 4-phenyl-1-butene-3-yne ($C_6H_5CHCHCCH$), and the ethynylstyrenes.

For m/z 180, fitting a convolved curve is quite challenging due to the lack of sharpness in the literature PES of the most abundant species used for this mass, i.e. the stilbene isomers. However, the PES peaks associated to each species were assigned in toluene study and as can be seen in the experimental PES of m/z 180 for ETB, the corresponding peak linked to (E)-stilbene located at 7.8 eV is slightly increased. This should result in an increment of the relative PES signal contribution from this species.

Other isomers of m/z 180 also presented changes in the relative signal contribution while observing the comparison between both experimental PES, for ETB and toluene. The list of species associated to m/z 180 are presented in **Table** 5-13.

***Table 5-13**. Relative contributions to the m/z 180 overall signal for ethylbenzene and toluene.*

	toluene	***ETB***
9-Methylfluorene	11.2%	6.2%
(E)-Stilbene	35.6%	40.4%
(Z)-Stilbene	36.4%	37.3%
1-Methyl-1H-phenalene	5.6%	3.1%
3-Methyl-3H-cyclopenta[a]naphthalene	6.7%	7.3%
1,1-Diphenylethylene	4.5%	5.6%

According to **Figure** 5-54 for ETB the increase in m/z 180 peak area is 2.78 with respect to toluene pyrolysis. This value can be used to calculate the signal change for a single isomer between the two different fuels. For instance, the most abundant species in m/z 180, (E)-stilbene, was globally increased by 3.3 times while (Z)-stilbene and 9-methylfluorene increased by 2.9 and 1.1 times, respectively. Thus, the pathways to the stilbenes are enhanced in the case of ETB. This is mainly due to the higher reactivity of ETB compared to toluene and the formation of large concentrations of benzyl radicals and consequently of bibenzyl, the precursor of stilbene. Analogously, concerning the less abundant isomers in ETB pyrolysis for m/z 180, 1-methyl-1H-phenalene was increased by 1.1 times and 1,1-diphenylethylene increased by 3.7 times as for the stilbenes.

The last among the larger PAH peaks is m/z 116 in **Figure** 5-54. The corresponding photoelectron spectra are presented in **Figure** 5-59. The comparison between the experimental PES and the shape of the literature PES for indene indicates that only indene is produced from ETB pyrolysis. This differs from toluene pyrolysis where also a small contribution (around 10%) coming from phenylpropadiene ($C_6H_5CHCCH_2$) is to m/z 116. Considering that m/z 116 peak area in the mass spectrum of 8.5 eV for ETB pyrolysis increased 2.29 times related to the peak area in toluene pyrolysis (A_{etb}/A_{tol}), the global amount of signal increase for the major species, indene, is determined to be 2.6 times the one present in toluene pyrolysis.

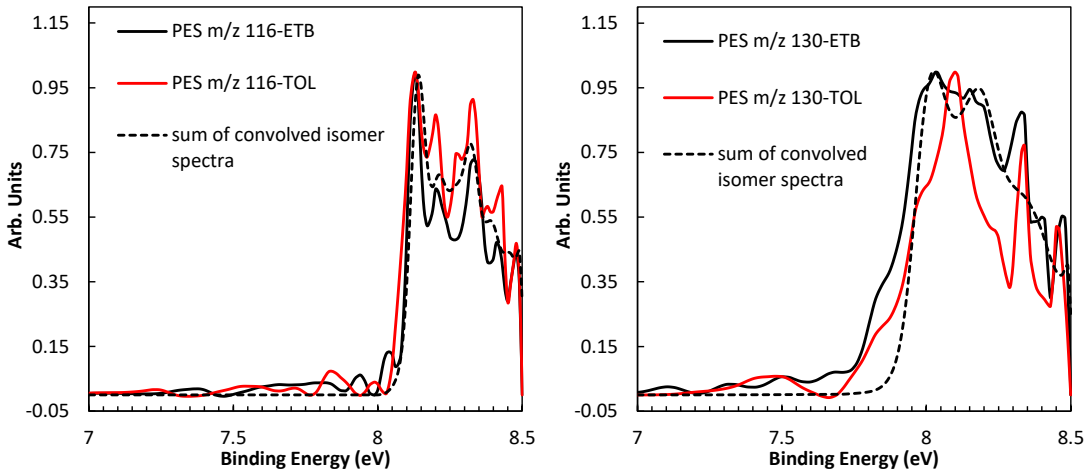

***Figure** 5-59. Photoelectron spectra for m/z 116 and m/z 130 obtained at 8.5 eV and continuous data acquisition mode. Each figure contains experimental PES for ETB and toluene pyrolysis and sum of convolved isomer spectra for ETB pyrolysis.*

For m/z 130, only two probable isomers where considered in the identification as was established in toluene pyrolysis. These are 1,2-dihydronaphthalene and 1-methylindene. Although **Figure** 5-59 shows a good agreement between the convolved and the experimental PESs for ETB m/z 130, the peak located at a binding energy of 8.33 eV is still not well captured. This means that possibly, one or more isomer is missing, fact that is confirmed later in the analysis of styrene pyrolysis where for m/z 130, the peak located at 8.33 eV significatively grows and a lack of experimental or simulated PES limits the full isomer identification. The PES signal contributions of 87.9 : 12.1 were obtained for 1,2-dihydronaphthalene : 1-methylindene for the case of ETB compared to the contributions previously determined for toluene pyrolysis of 56.5 : 43.5 for the same species.

The m/z 130 presented a considerable peak area increase of 2.36 in ETB pyrolysis compared to toluene. Thus, the overall increase in the signal from the major species, 1,2-dihydronaphthalene, was determined to be 5.23 times the amount present in toluene pyrolysis. The presence of long chain and additional H-atoms in the system favors the hydrogeneration processes. On the other hand, the production of 1-methylindene is very similar to the toluene case.

The PES analysis for m/z 142 and m/z 154 are presented in **Figure** 5-60. In m/z 142 the PESs of 1-methylnaphthalene and 2-methylnaphthalene were considered in the construction of a convolved isomer spectrum. Fitting the simulated PES to the experimental one is challenging since reference PESs seem to be slightly shifted compared to the peaks of the experimental curve, unless other isomers are missing in the analysis. The relative signal contributions were kept similar as for toluene, 46 : 54. However, the peak areas in **Figure** 5-54 shows how in the case of ETB pyrolysis the formation of the methylnaphthalene isomers is enhanced by a factor 1.76.

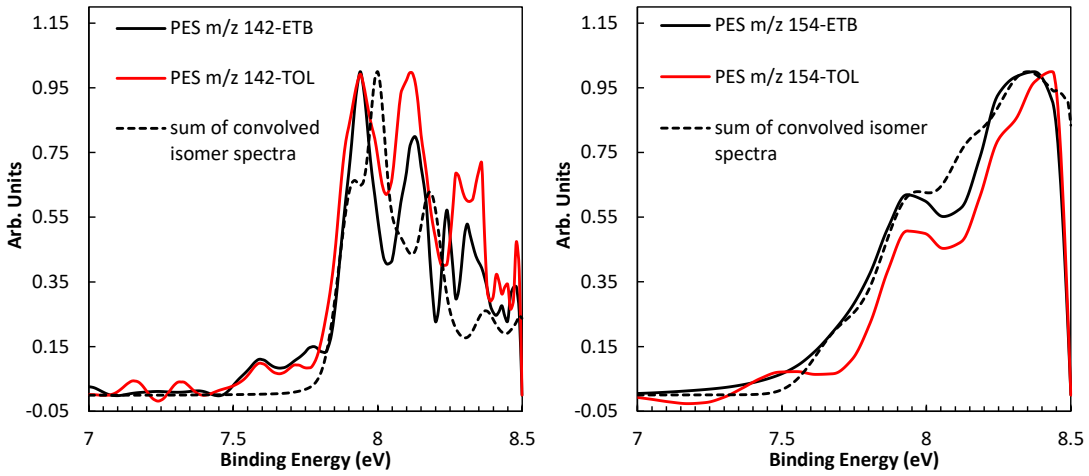

***Figure** 5-60. Photoelectron spectra for m/z 142 and m/z 154 obtained at 8.5 eV and continuous data acquisition mode. Each figure contains experimental PES for ETB and toluene pyrolysis and sum of convolved isomer spectra for ETB pyrolysis.*

For m/z 154 in **Figure** 5-60, a slight increase on the first peak of the ETB experimental PES is evidenced. The isomer distribution for ETB pyrolysis is 54.4 : 21.8 : 10.2 : 6.8 : 6.8 for biphenyl : 1-vinylnaphthalene : 2-vinylnaphthalene : acenaphthene : benzobarrelene, compared to the one found for toluene of 61.5 : 19.2 : 15.4 : 1.9 : 1.9. The results show how the contributions from acenaphthene and benzobarrelene are slightly higher (from 2% to 7%) while the one from biphenyl decreases from 62% to 54%. Overall, the distribution is similar between ETB and toluene.

Other relatively small peaks of similar size in the mass spectrum obtained from ETB pyrolysis (**Figure** 5-54) are m/z 156 and m/z 168. This time, the signal increase from toluene to ETB pyrolysis was found to be a factor of 2.86 and 1.45, respectively. The PES comparisons are presented in **Figure** 5-61. In the case of m/z 156, the sum of convolved isomer spectra does not seem to represent the full experimental PES, similar to the toluene case. More PES calculations will be required to solve this m/z.

In the case of m/z 168, the experimental PES signal for ETB pyrolysis seems to be reduced in the region around 8.23 eV compared to the toluene case. For 2-Methylbiphenyl : 3-Methylbiphenyl : 4-Methylbiphenyl the determined signal contributions for ETB pyrolysis are 5.6 : 55.6 : 38.9 compared to 16.7 : 41.7 : 41.7 in toluene pyrolysis.

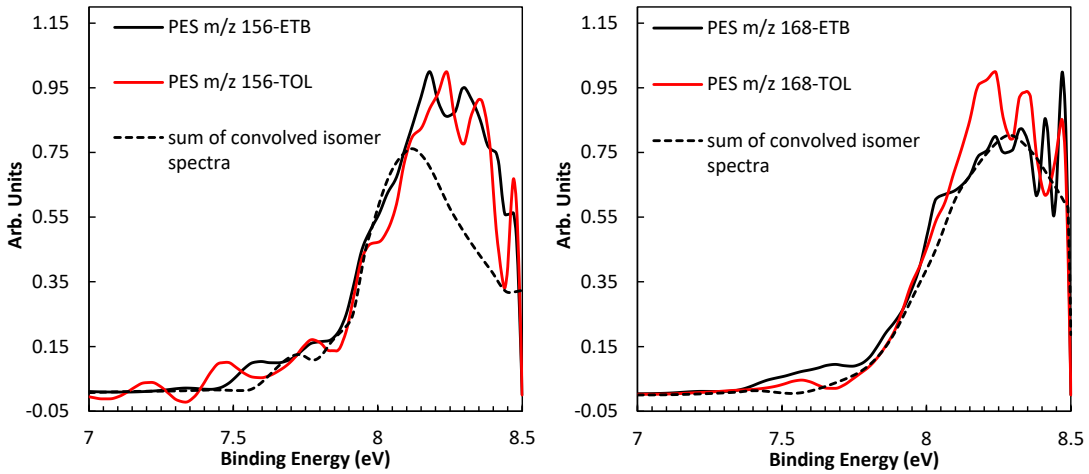

***Figure** 5-61. Photoelectron spectra for m/z 156 and m/z 168 obtained at 8.5 eV and continuous data acquisition mode. Each figure contains experimental PES for ETB and toluene pyrolysis and sum of convolved isomer spectra for ETB pyrolysis.*

For m/z 176 the peak areas were found to be reduced when ETB is pyrolyzed compared to toluene (variation by a factor 1.23). The PESs are presented in in **Figure** 5-62. The peak around 8.06 eV is very reduced compared to toluene which reveals some changes on the isomer distribution, although overall the main species are similar. For example, the main isomer in both cases is 1,4-diethynylnaphthalene (18.9% for toluene, 19.8% for ETB), while the sum of all the diethynylnaphthalenes is around 53% for ETB and 62% for toluene. On the contrary, the total contribution from the ethynylacenaphthylene is lower for toluene pyrolysis (23%) compared to the ETB case (34%). The ratio between the contributions ethynylacenaphthylenes : diethynylnaphthalenes in ETB pyrolysis is 1 : 1.53 compared to the ratio for toluene pyrolysis equal to 1 : 2.68. Other minor species are present in both cases.

***Table 5-14**. Relative contributions to the m/z 176 overall signal for ethylbenzene and toluene.*

	toluene	***ETB***
1-Ethynylacenaphthylene	4.6%	9.9%
3-Ethynylacenaphthylene	8.4%	7.3%
4-Ethynylacenaphthylene	5.4%	10.6%
5-Ethynylacenaphthylene	4.6%	6.6%
1,2-Diethynylnaphthalene	5.4%	9.5%
1,3-Diethynylnaphthalene	7.2%	1.1%
1,4-Diethynylnaphthalene	18.9%	19.8%
1,5-Diethynylnaphthalene	2.7%	6.6%
1,6-Diethynylnaphthalene	7.2%	1.1%
1,7-Diethynylnaphthalene	1.1%	2.1%
1,8-Diethynylnaphthalene	4.1%	6.0%
2,3-Diethynylnaphthalene	7.4%	4.0%
2,6-Diethynylnaphthalene	7.2%	1.1%
2,7-Diethynylnaphthalene	0.9%	1.3%

1-(1,3-Butadiynyl)naphthalene	5.4%	3.2%
2-Buta-1,3-diynylnaphthalene	5.4%	3,2%
Pyracyclene	2.0%	3.3%
Cyclopenta[bc]acenaphthylene	2.0%	3.3%

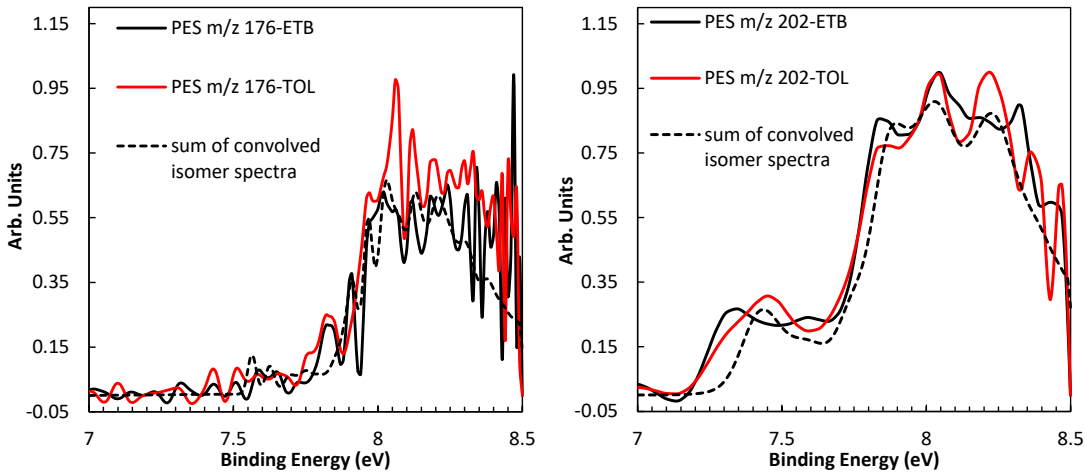

***Figure** 5-62. Photoelectron spectra for m/z 176 and m/z 202 obtained at 8.5 eV and continuous data acquisition mode. Each figure contains experimental PES for ETB and toluene pyrolysis and sum of convolved isomer spectra for ETB pyrolysis.*

For m/z 202, a neglectable peak area change of -0.01 was determined based on **Figure** 5-54. Overall, the isomer distributions are also very similar when comparing the ETB experimental m/z 202 PES to the one of toluene (**Figure** 5-62b). For this analysis, 17 isomeric species were considered like in toluene and the relative signal contributions for both fuels are compared in Table **5-15.**

Specifically, differences in the shape of the region normally associated to pyrene (starting from 7.22 eV) can be evidenced in the **Figure** 5-62. However, based on the uncertainties of the measurements and the large number of isomers analyzed here, this behavior is unlikely to be due to the presence of an unknown isomer. The changes captured by the convolution procedure showed a resulting sum of convolved isomer spectrum that well fitted the experimental PES for m/z 202. A remarkable change noticed when comparing the ETB PES to the toluene one is the more pronounced peak at around 7.85 eV. This change is considered by the convolution process as an increased relative contribution from fluoranthene. In ETB pyrolysis, pyrene shows a slight decrease in the signal contribution, 4,5-vinylidenephenanthrene remains almost constant while 2-ethynylphenanthrene iss slightly increased to fit the region at 8.05 eV. Ethynylphenanthrenes account for the 21 % of the signal contribution in ETB pyrolysis.

***Table 5-15**. Relative contributions to the m/z 202 overall signal for ethylbenzene and toluene.*

	toluene	***ETB***
Fluoranthene	38.0%	38.3%
Diphenyldiacetylene	1.3%	1.2%
Pyrene	20.3%	18.5%
Phenanthrylacetylen	0.6%	0.6%
2-Ethynylphenanthrene	8.9%	11.1%
3-Ethynylphenanthrene	3.8%	3.7%
4-Ethynylphenanthrene	3.2%	3.1%
9-Ethynylphenanthrene	3.2%	3.1%
Benzene, 1-ethynyl-2-(phenylethynyl)	1.3%	1.2%
Benzene, 1-ethynyl-3-(phenylethynyl)	1.3%	1.2%
Benzene, 1-ethynyl-4-(phenylethynyl)	1.3%	1.2%
1-Ethynylanthracene	0.1%	0.1%
2-Ethynylanthracene	0.1%	0.1%
9-Ethynylanthracene	0.1%	0.1%
Acephenanthrylene	3.8%	3.7%
4,5-Vinylidenephenanthrene	12.7%	12.4%
Aceanthrylene	0.1%	0.1%

Two of the largest masses for which the PESs have sufficient S/N for isomer identification are m/z 226 and m/z 228. Based on the mass spectrum in **Figure** 5-54, the peak area for m/z 226 reduces by a factor of 1.24 compared to the toluene case, while similar areas were obtained for m/z 228.

For m/z 226, the experimental PESs for benzo(ghi)fluoranthene and 1-ethynylpyrene were considered in the binning and convolution process. The sum of convolved isomer spectra for m/z 226 is compared to the experimental PES for ETB pyrolysis in **Figure** 5-63. The relative signal contributions for benzo(ghi)fluoranthene : 1-ethynylpyrene is 76.9 : 23.1 in ETB pyrolysis compared to 65.3 : 34.7 in toluene. Still, the fit between the convolved spectrum and the experimental PES for m/z 226 is partial, and more species should be included in the analysis. The determination of reference photoelectron spectra for this and other masses are subject of future works.

The PESs of m/z 228 presented in **Figure** 5-63b show differences between the experimental PES obtained in ETB pyrolysis and the one for toluene pyrolysis. The sum of convolved isomer spectra obtained with the aim to replicate the experimental PES for m/z 228 leads to the following relative signal contributions for ETB pyrolysis: 31.8 : 4.5 : 31.8 : 31.8 for chrysene : 1,2-benz[a]anthracene : triphenylene : 1-(phenylethynyl)naphthalene, respectively, compared to the ones for toluene pyrolysis at similar conditions: 10.4 : 11.3 : 56.5 : 21.7. A clear increase in the production of chrysene is evidenced for ETB pyrolytic chemistry compared to toluene. Considering the relative percentages and the MS area ratios, the chrysene production increases 1.9 times compared to the toluene case. On the other hand, 1,2-benz[a]anthracene and triphenylene formation decreases by 1.62 times and 1.47 times, respectively, while 1-(phenylethynyl)naphthalene increases by 1.39 times from toluene pyrolysis to ETB.

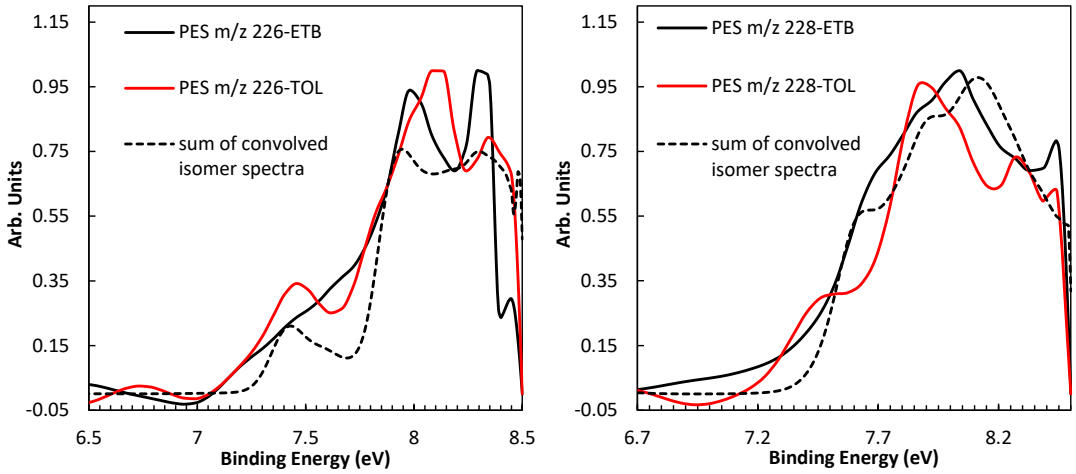

***Figure** 5-63. Photoelectron spectra for m/z 226 and m/z 228 obtained at 8.5 eV and continuous data acquisition mode. Each figure contains experimental PES for ETB and toluene pyrolysis and sum of convolved isomer spectra for ETB pyrolysis.*

Other two small peaks in the ETB mass spectrum corresponding to large PAH compounds are m/z 230 and m/z 182 whose signal level starts becoming relatively low, making more difficult the isomer identification process. The comparisons between experimental PES and convolved isomer photoelectron spectra for both masses are presented in **Figure** 5-64. The fitted PESs correctly describe the general characteristics of the experimental curves.

For the case of m/z 230, the convolution procedure determined individual contributions to the experimental PES signal from p-terphenyl : o-terphenyl : m-terphenyl to be 24.1 : 15.7 : 60.2, respectively. The three terphenyl isomers kept their contributions to the overall signal almost the same compared to the ones for toluene (27.2 : 18.5 : 54.3). Sharper photoelectron spectra (e.g ab-initio simulations) would allow to recreate a better-defined convolved spectrum in order to reduce the uncertainties in the determination of the signal contributions for m/z 230.

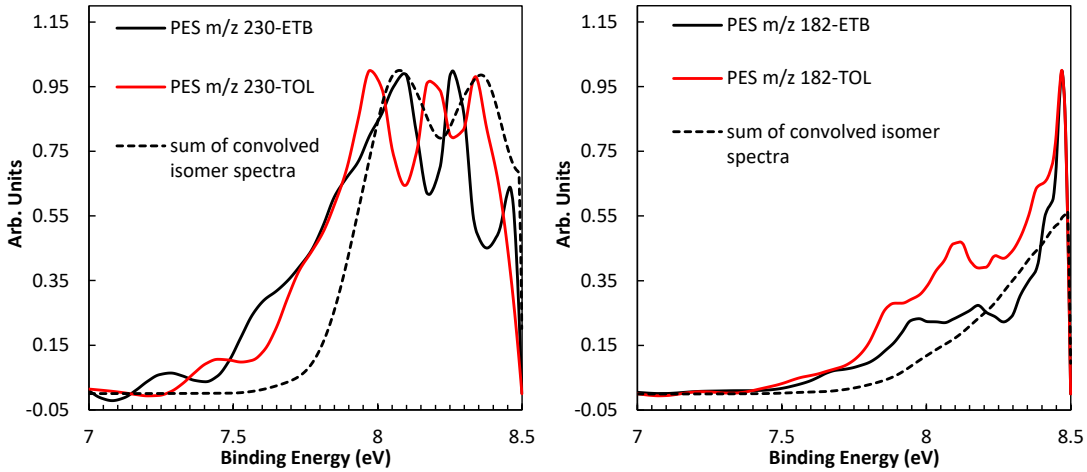

***Figure** 5-64. Photoelectron spectra for m/z 230 and m/z 182 obtained at 8.5 eV and continuous data acquisition mode. Each figure contains experimental PES for ETB and toluene pyrolysis and sum of convolved isomer spectra for ETB pyrolysis.*

Concerning m/z 182, there are significant differences in the shape of the experimental PES for ETB and toluene that are evidenced in the relative contributions from the different isomers. The contributions from 3-3-dimethylbiphenyl : 2,2-dimethylbiphenyl : 1,1-biphenyl,2-ethyl- are 16.7 : 75.0 : 8.3, compared to the ones for toluene pyrolysis that were determined to be 30 : 60 : 10, for the same group of isomers. The ETB decomposition also favors the formation of the m/z 182 isomers, with an increase in the peak area by 2.70 times. It is very important to highlight that bibenzyl was observed as a major PAH species produced from ETB pyrolytic decomposition in the work realized by Wenyu Sun. et al. [68]. Bibenzyl (PI = 9.1 eV[306]), a species whose photoelectron spectra is known in the literature, was not identified in the present work since its photoionization energy is higher than the photon energy of 8.5 eV. Future experiments should be performed using the *continuous* data acquisition mode at energies greater than 9 eV in order to obtain accurate PESs revealing the presence of this important PAH and the relative importance compared to the above mentioned minor isomers.

The identification of a large number of polycyclic aromatic hydrocarbon compounds produced from the pyrolytic decomposition of ethylbenzene using the HRRST/i^{2}PEPICO configuration was presented in this chapter for the first time. Two different series of experiments have been performed: (i) with *pulsed* mode (reflected shock time identified) with more than 27 000 runs and (ii) *continuous* acquisition mode with more than 29 000 runs. Well defined mass spectra were obtained from light species up to 5-member rings in the pulsed acquisition mode at an ionization level of 10 eV averaging data over 1.2 ms of shock reflected reaction conditions. In the *continuous* mode, at an ionization level of 8.5 eV, photoelectron spectra were obtained for numerous PAHs which allowed the isomer identification which could not have been done without i^{2}PEPICO. The results were presented in comparison with the toluene pyrolysis dataset presented in Chapter 0. These novel results complement the experimental databases available in the literature from laboratory-based conventional techniques, for improved understanding of the chemistry of alkylated hydrocarbons and validation of detailed chemical kinetic models.

This kind of exhaustive studies should be also extended to other important soot intermediate molecules and fuel components. For instance, as evidenced in the present ETB study, several aromatic products like styrene and phenylacetylene are produced in large concentrations and the related PAH formation chemistry is of special interest for improvement of soot models. In the following chapter, the HRRST/i^{2}PEPICO is used to analyze the pyrolytic decomposition of styrene (C_8H_8, $C_6H_5C_2H_3$).

5.5 Pyrolysis of styrene using HRRST/i^{2}PEPICO

Styrene, $C_6H_5C_2H_3$, m/z 104, referred in the figures of this section as STY, has been identified in the previous chapter as an abundant byproduct of ethylbenzene (ETB) pyrolysis and a key intermediate for the formation of large PAH molecules. In fact, as reported in previous studies on ethylbenzene pyrolysis using single pulse shock tube connected to GC/MS [68], styrene reactions with phenyl radical (C_6H_5) play an important role in the formation of phenanthrene through the production of dihydro-phenanthrene. Thus, studying the detailed pyrolytic chemistry of $C_6H_5C_2H_3$ is essential in the development of the gas-phase models of soot precursors. A recent investigation on the high temperature decomposition of styrene using a miniature HRRST (ANL-HRRST) coupled to VUV-PIMS has been performed with the aim of providing kinetic information on the initiation reactions of styrene [83]. However, the detailed speciation from styrene pyrolysis, including formation of polycyclic aromatic hydrocarbons has never been reported.

In this chapter, the first pyrolytic study on the thermal decomposition of styrene using the HRRST/i^{2}PEPICO combination is presented, taking advantage of the capabilities of such technique specifically in relation to the PAH formation chemistry. Styrene has a similar structure than ethylbenzene, although it presents a double bond in its side alkyl chain. In view of the analogy and to highlight the influence of bond saturation on the product distribution, the STY data are compared to the ethylbenzene results.

Similarly to toluene and ethylbenzene, two different experimental conditions were considered. A set of 22 021 experiments were averaged using the *pulsed* data acquisition mode in order to perform chemical kinetic analyses (mass spectra and species profiles). The pyrolytic decomposition of 0.1 % styrene diluted in argon bath was evaluated at T_5= 1345±34 K, P_5 = 6.5±0.3 bar and photon energy of 10 eV. In order to perform valid comparisons, the reaction conditions were chosen to be very close to the ones used in toluene and ethylbenzene pyrolysis. The configuration of the shock tube also remained unvaried. The repetition rate used was 1 Hz for most of the experiments, even if few runs were performed at 1.5 Hz. At this repetition rate, the HRRST tends to heat up quite fast inside the vacuum chamber, beyond what we consider as safe for the mechanical functioning of the vent valve. The spectral data was recorded during 8 ms comprising the pre-shock and post-shock regions but averaging during a time period of 1.2 ms was performed for mass spectrum comparisons between styrene and ETB.

Keeping the configuration unchanged, in the second experimental condition, 41 297 experiments were averaged using the *continuous* data acquisition mode at photon energy of 8.5 eV in order to focus on the identification of PAH molecules through their PESs. A concentration of 0.1 % styrene diluted in argon was considered and its thermal decomposition was studied at conditions similar to the ones used in pulsed mode, i.e. 1355±26 K, 6.5±0.2 bar. The data were used to identify a large number of PAH species at each m/z by using the respective mass-selected photoelectron spectra (PESs), and compared to the respective experimental mass-selected PESs obtained from ETB pyrolysis at similar conditions.

5.5.1 Mass spectrum and identification of small aromatic products

A comparison between the two mass spectra obtained from ETB and STY pyrolysis with the *pulsed* data acquisition mode, at photon energy of 10 eV, during 1.2 ms at reflected shock wave conditions is presented in **Figure** 5-65. The black color line represents the mass spectrum for styrene pyrolysis while the red line for ETB pyrolysis. At similar reaction conditions, the mass spectra are normalized by the number of experiments. It is clear at a first sight that styrene produces larger amount of products lighter than m/z 80 compared to ETB as well as phenylacetylene (m/z 102), while toluene (m/z 92), benzyl (m/z 91) and fulvenallene (m/z 90) appear to be reduced in the styrene case. For species equal and larger than ethylbenzene (m/z 106) the peak differences can be either negative or positive, suggesting an influence of the growth mechanisms related to the specific fuel structure.

The m/z peak areas from styrene pyrolysis compared to the respective peak areas in ETB pyrolysis were used to calculate the relative increase or decrease through the equation $(A_{Sty}-A_{Etb})/A_{Etb}$. The resulting values are presented in the **Figure** 5-66. If there are peaks in one mass spectrum that is not common to the other, then the peak is not included in the analysis of **Figure** 5-66. For instance, in the normalized 10 eV mass spectrum of styrene pyrolysis, the peak at m/z 91 is not detectable. On the contrary, m/z 91 exists in the toluene mass spectrum. Similar for other species, i.e. m/z 90 etc.

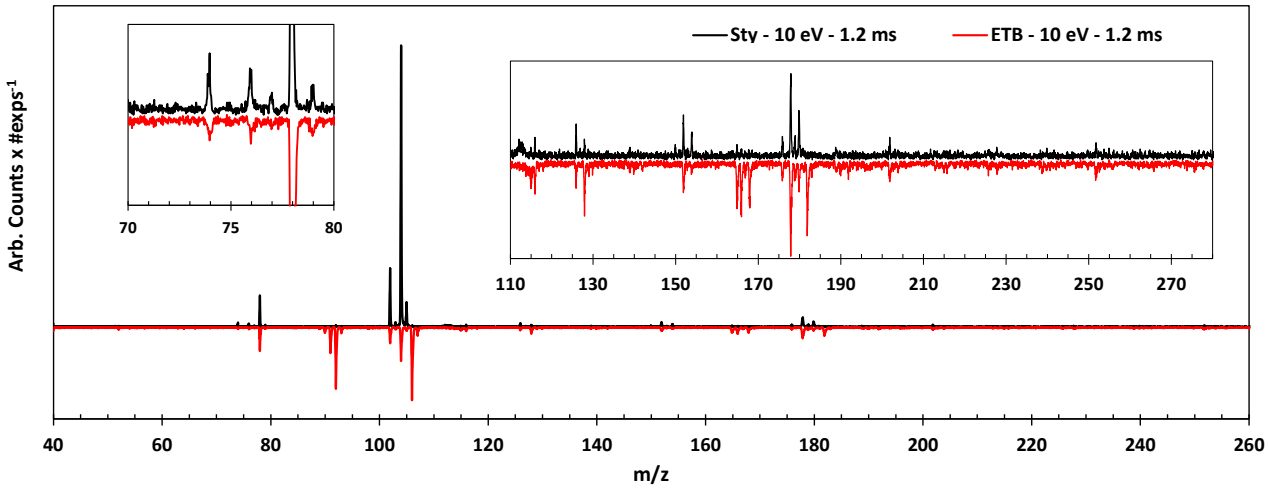

***Figure** 5-65. Mass spectrum obtained in pulsed mode during 1.2 ms of post-shock region. Data is normalized by number of experiments. 0.1% styrene and 0.1 % ethylbenzene (ETB) in argon, photon energy 10 eV.*

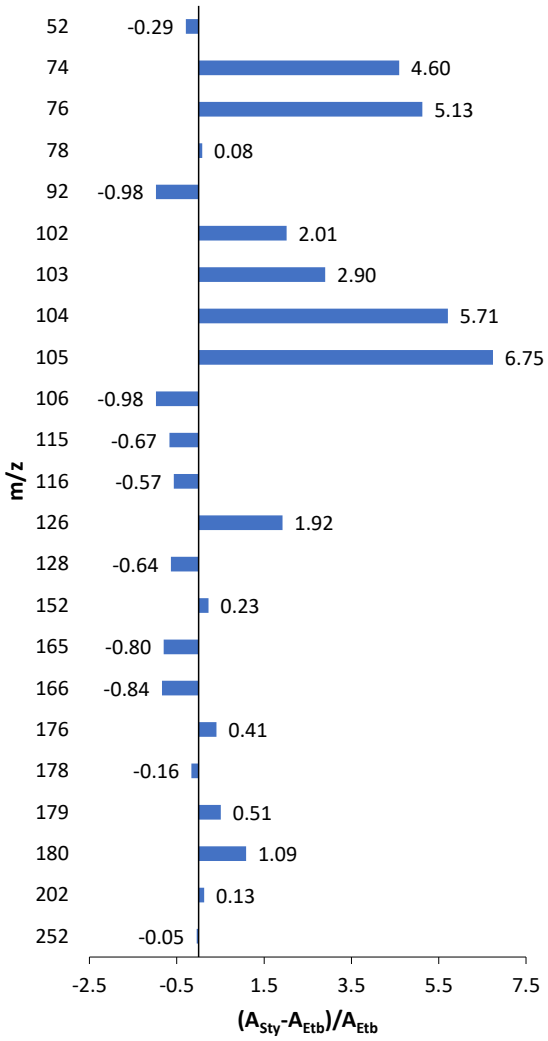

***Figure** 5-66. Peak area increase (A_{Sty}-A_{Etb}/A_{Etb}) in styrene mass spectrum (10 eV-pulsed mode) compared to ethylbenzene mass spectrum (10 eV-pulsed mode) for m/z ranging from 52 to 252.*

Regarding the small mass species, the mass spectrum from styrene pyrolysis contains products at m/z 52, m/z 74, m/z 76, m/z 77, m/z 78, m/z 79, m/z 92, m/z 100, m/z 102, m/z 103, m/z 104, m/z 105 and m/z 106. Some of these peaks are in common with the previous study on initiation reactions for 0.06% styrene pyrolysis in argon bath gas realized with ANL-HRRST coupled to VUV-PIMS, T = 1710-2260 K and P = 10.8-12.9 atm [83]. In that study, m/z 74 was assigned to triacetylene (1,3,5-hexatriyne), m/z 76 to o-benzyne, m/z 78 to benzene, and m/z 102 to phenylacetylene. The results shown in the present work complement the ANL-HRRST/VUV-PIMS study with confirmation of the isomer identification through the related PESs [83]. In particular, the comparison between experimental and literature PESs for several hydrocarbon and monoaromatic molecules (MAH) in the m/z range 52-106 is presented in **Figure** 5-67. In order to obtain more defined PESs, this information was obtained averaging not 1.2 ms as in **Figure** 5-65 but 8 ms of acquisition time. It is confirmed that m/z 52 can be attributed to vinylacetylene, m/z 74 is effectively 1,3,5-hexatriyne and m/z 78 corresponds to benzene, but this time a small contribution coming from fulvene

can be evidenced when the reference PES for fulvene is compared to the overall PES signal for m/z 78. Specifically, fulvene contributes to the signal in the initial region of the experimental PES in the range of 8.3 eV - 8.8 eV and in the final part of the spectrum, around the peak located at 9.6 eV. An estimated maximum signal contribution of 13 % to the overall PES signal for m/z 78 can be attributed to fulvene in styrene pyrolysis. In terms of peak area change, in styrene pyrolysis, 1,3,5-hexatriyne (m/z 74) and m/z 76 (possibly o-benzyne, to be confirmed) increased by 4.6 and 5.13 times compared to ETB pyrolysis. This suggests that the ring opening might be different for STY decomposition compared to ETB. The m/z 78 peak (mainly benzene) is similar in the two cases. This is influenced by two main reaction pathways, the ipso-addition to the fuel for ETB and the thermal decomposition of styrene to benzene + H2CC. The other main aromatic intermediate, toluene, is negligible from STY pyrolysis, as no direct pathways of alkyl side chain breaking exists leading to the formation of the benzyl radical (and consequently toluene) as for ethylbenzene.

Although it has a small signal, fulvenallene (C_7H_6) was also clearly identified in the pyrolysis of styrene as a minor product as shown in the comparison of the reference PES for this species with the experimental PES of m/z 90 obtained at 8.5 eV with the continuous acquisition mode. This mass appears to be reduced by half compared to ETB pyrolysis, but in the latter case fulvenallene comes directly from the benzyl radical decomposition, pathway which should not be present for styrene. Thus, a different formation mechanism still to be clarified is responsible for fulvenallene formation from styrene. For m/z 102, a peak area increment by 2.01 is obtained as reported in **Figure** 5-66. A clear correspondence between the reference PES for phenylacetylene and the experimental PES for m/z 102 is observed. Nevertheless, in the PES comparison presented in **Figure** 5-67, a possible contribution from benzocyclobutadiene to the experimental PES for m/z 102 obtained at 10 eV is possible. This fact is confirmed when the literature PES for benzocyclobutadiene is compared with the experimental PES for m/z 102 obtained with continuous mode at 8.5 eV (same figure). However, due to signal limitations in the experimental PES obtained at 10 eV, the signal contribution ratio between phenylacetylene and benzocyclobutadiene cannot be clearly defined. Although the contribution from benzocyclobutadiene to the m/z 102 signal is expected to be minor compared to the one of phenylacetylene, the presence of benzocyclobutadiene is in itself a very interesting finding as it highlights the presence of possible alternative pathways, although minor, for the styrene pyrolytic chemistry.

Regarding m/z 104, as expected being the fuel molecule, styrene is the main species in the respective 10 eV photoelectron spectrum. Additionally, different to ETB and toluene pyrolysis, no presence of o-p-xylylene isomers could be identified in m/z 104 as shown in the inset. Finally, m/z 106 is found to be produced in very small concentrations during styrene pyrolysis and a low S/N for the experimental m/z 106 PES was obtained. In reality, there is probably production of xylene isomers together with ethylbenzene, but a higher signal is required to accurately address this hypothesis.

For masses larger than the fuel molecule (m/z 104), m/z 178 and m/z 180 were found to be the biggest peaks as shown in the mass spectrum obtained at 10 eV. The signals for data obtained in pulsed mode are too small to extract PESs and perform accurate PAH identification, thus the additional experimental set focused only on PAH products will be discussed in the next section with the use of spectral information acquired continuously at 8.5 eV. However, large masses like m/z 116, m/z 128, m/z 152, m/z 166, m/z 178, m/z 180 and m/z 202 are common peaks between styrene and ETB products and the peak area changes in 10 eV data were found to be -0.57, -0.64, 0.23, -0.84, -0.16, 1.09, 0.13, respectively. In general,

ethylbenzene pyrolysis leads to the formation of larger PAH concentrations, partly due to the higher reactivity of the molecule compared to styrene (as already discussed in the comparison between ethylbenzene and toluene). The higher concentrations of m/z 152 and 202 are probably related to the slightly higher temperature conditions for styrene (~1345 K) compare to ETB (~1327 K) as related to the HACA routes being favored at higher temperatures. Similar considerations apply for m/z 126 and 176. The main m/z which is clearly related to the styrene specific chemistry is 180 ($C_{14}H_{12}$), possibly from the reaction of the fuel molecule with C_6H_5. This will be clarified in the following section.

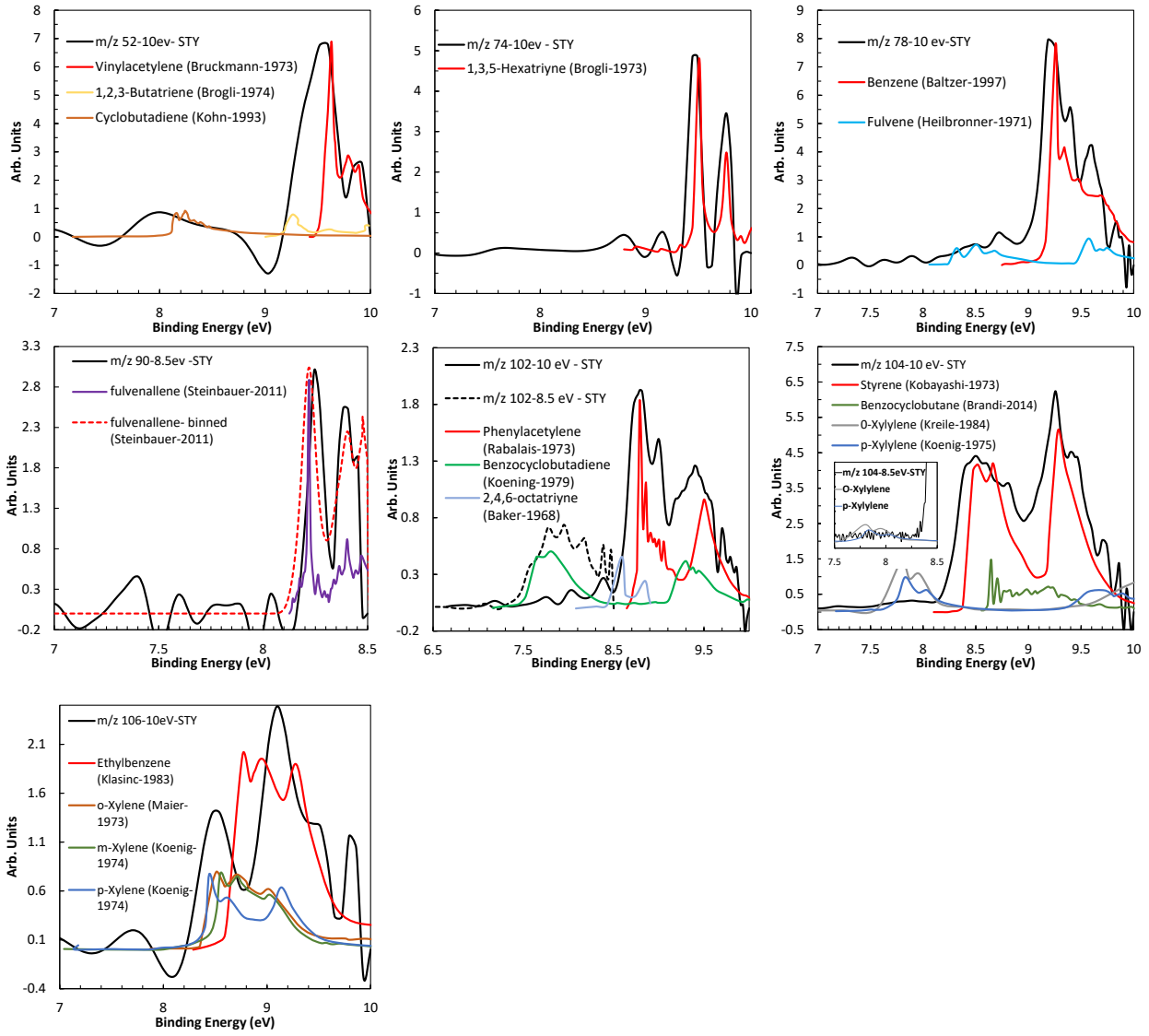

***Figure** 5-67. Photoelectron spectra of product molecules with m/z ranging from 52 to 106. Photon energy of 10 eV except for m/z 90 that was obtained at 8.5 eV.*

5.5.2 Mass selected identification of polycyclic aromatic hydrocarbons

The normalized mass spectra obtained with the continuous data acquisition mode at 8.5 eV for styrene and ethylbenzene pyrolysis are compared in **Figure** 5-68. A large peak located at m/z 104 corresponding to the ionization of fuel molecule is of course the biggest peak in the mass spectrum for the case of styrene. Other monoaromatic aromatic species are detectable, i.e. m/z 102 (as discussed above, mainly benzocyclobutadiene) and m/z 106 (partial ionization of ETB). On the other hand, the data at 8.5 eV for these species are only partial, and the data at 10 eV should be used for the analyses. The remaining m/z signals correspond to PAH species.

As discussed in the previous subsection, m/z 178 and m/z 180 are the largest peaks produced from styrene pyrolysis. The mass spectrum obtained at 10 eV showed that these two species change by 0.84 and 2.09 times, respectively. Similarly, in the mass spectrum in **Figure** 5-68 the peaks corresponding to m/z 178 and m/z 180 are also the largest and the increase with respect to ETB was determined to be 0.75 and 1.68, respectively. These values are within the uncertainties of the method, considering the different integration times between the two datasets.

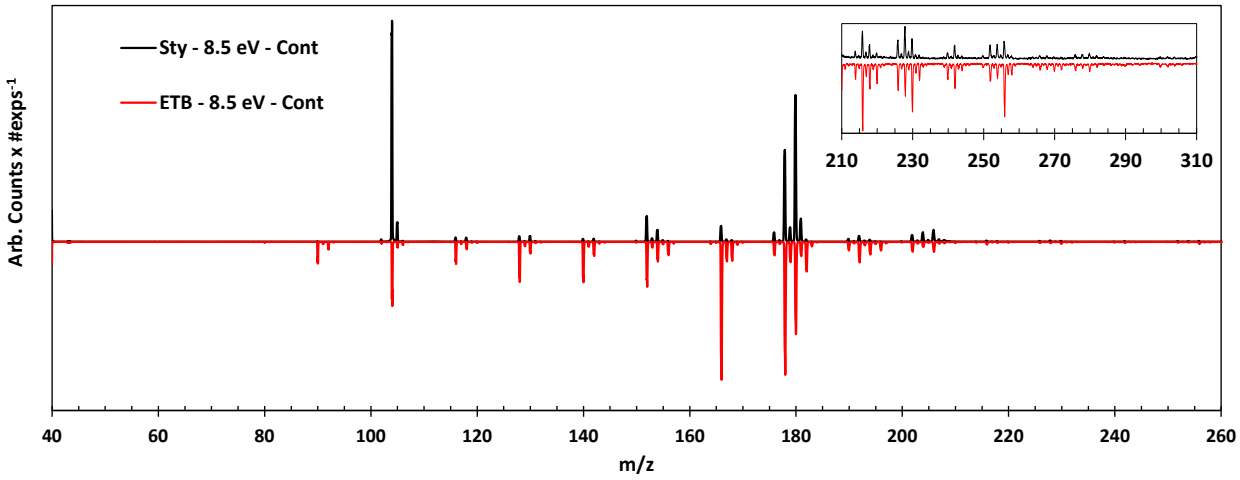

***Figure** 5-68. Mass spectrum obtained in continuous mode, averaging around 41 297 for styrene and 29 019 experiments for ETB. Data is normalized by number of experiments. 0.1% styrene and 0.1 % ethylbenzene in argon, photon energy 8.5 eV.*

The PES comparison presented in **Figure** 5-69 for m/z 178 leads to the conclusion that it is possible that such decrease of peak signal could be associated to the relative decrease in the production of anthracene, one of the major isomers for m/z 178. Based on the fitting procedure in **Figure** 5-69 the ratio between anthracene and phenanthrene is 1:4 in styrene pyrolysis and 1:1.1 in ETB pyrolysis. Considering the global change in the peak signal, anthracene mole fraction was found to decrease by -0.74 times while phenanthrene mole fraction is almost the same (-0.037). For all the considered species, the signal contributions are as presented in **Table** 5-16.

***Table 5-16**. Relative contributions to the m/z 178 overall signal for styrene and ethylbenzene.*

	STY	***ETB***
Anthracene	11.0%	31.5%
3-Methylidenecyclopenta[b]naphthalene	0.4%	1.5%
Phenanthrene	43.8%	34.1%
Diphenylacetylene	29.6%	15.7%
9H-Fluorene, 9-methylene	10.9%	6.4%
1-Methylidenecyclopenta[a]naphthalene	0.4%	1.5%
3-Methylidenecyclopenta[a]naphthalene	3.8%	9.3%

Two other important isomers whose relative contributions increase in styrene pyrolysis with respect to ETB are diphenylacetylene (2.41) and 9H-fluorene, 9-methylene (2.28). Based on the species distribution in **Figure** 5-65, the reactions between phenylacetylene (main product of the thermal decomposition of styrene) and the phenyl radical are the main candidate for the production of these two species, together with phenanthrene as a byproduct. On the other hand, the reactions between toluene and its radicals are suppressed, including the main pathway to the formation of anthracene ($C_6H_4CH_3+C_7H_7=AC_{14}H_{10}+H$). The contributions from the other isomers become nearly negligible.

Among all the PAH, the m/z 180 represents the biggest peak of the mass spectrum in **Figure** 5-68 for styrene pyrolysis. More importantly, the production of this peak is greater in styrene than in ETB. Compared to ETB, the peak area for m/z 180 increased by 1.68 times according to the 8.5 eV data and by 2.09 according to the 10 eV data. The reference PESs of nine isomers were considered. **Figure** 5-69 shows the comparison between the experimental PESs for m/z 180 in STY and ETB pyrolysis together with the sum of convolved isomer spectra for the styrene case. E-Stilbene contribution seem to be decreased compared to ETB since the region from 7.8 eV to 8.0 eV decreased while (Z)-stilbene increased considerably becoming the major one. For all the considered species, the signal contributions are as presented in **Table** 5-17.

***Table 5-17**. Relative contributions to the m/z 180 overall signal for styrene and ethylbenzene.*

	STY	***ETB***
9-Methylfluorene	10.7%	6.2%
(E)-Stilbene	28.9%	40.4%
(Z)-Stilbene	49.6%	37.3%
1-Methyl-1H-phenalene	1.7%	3.1%
3-Methyl-3H-cyclopenta[a]naphthalene	1.7%	7.3%
1,1-Diphenylethylene	7.4%	5.6%

Taking into account the peak increase for m/z 180 and its internal isomer distribution, 9-methylfluorene and (Z)-stilbene globally increase by 1.9 and 1.2 times their value compared to ETB pyrolysis. E-Stilbene relative global contribution does not vary significantly in the two cases. The above-mentioned molecules represent the 90 % of the signal contribution according to the analysis proposed here.

The m/z 166 is one of the main peaks for ethylbenzene and toluene, while the formation of these isomers from styrene is strongly reduced. Compared to ETB, the peak area of m/z 166 for styrene is 0.13 times smaller. The biggest contribution in all the studied cases comes from fluorene, which is mainly produced by reactions of the benzyl radical in toluene and ethylbenzene pyrolysis. In general, the $C_{13}H_{10}$ isomers comes from the C7+C6 reactions. Since in styrene pyrolysis toluene and its radicals are minor products, the C13 will consequently be reduced. Concerning the relative contributions from the different isomers presented in the table below, these are very similar with the ETB base, despite the slight reduction in the fluorene percentage (from 45% for ETB to 37% for STY).

***Table 5-18**. Relative contributions to the m/z 166 overall signal for styrene and ethylbenzene.*

	STY	***ETB***
fluorene	37%	45%
3H-benz[e]indene	11%	8%
1-(1-naphthyl)-1-propyne	11%	6%
2-propynyl naphthalene	17%	17%
1H-phenalene	7%	6%
2-prop-2-ynyl-naphthalene	10%	3%
1-prop-2-ynyl-naphthalene	7%	14%
1H-benz[f]indene	1%	0%
1H-benz[e]indene	0%	2%

For m/z 152, the experimental PES shows marked features below 7.9 eV, in correspondence with the photoionization of cyclopenta[a]indene and biphenylene (**Figure** 5-69). These two species are mostly related to the biphenyl radical, as presented in section related to toluene pyrolysis. Thus, these results suggest predominant pathways to $C_{12}H_9$ in the case of styrene pyrolysis. The PES relative signal contributions were determined by using the sum of convolved isomer spectrum that better fits the experimental PES as shown in **Figure** 5-69 (black dotted line). The calculated values are 47.3 : 33.0 : 8.8 : 8.8 : 2.2 for acenaphthylene : 2-ethynylnaphthalene : cyclopenta[a]indene : biphenylene : 1-ethynylnaphthalene , while the values obtained in ETB pyrolysis were 61.4 : 26.3 : 4.4 : 4.4 : 3.5, respectively. As for the ETB case, the relative percentage between cyclopenta[a]indene and biphenylene was kept the same, as the corresponding PESs are very similar which makes the exact identification impossible for the current S/N values.

Other important isomers in toluene and ETB pyrolysis are the ones associated with m/z 140. In the case os styrene pyrolysis, the production of these isomers is strongly reduced compared to the other fuels, as demonstrated by a MS peak area decrease of 0.07 compared to the ETB case. In addition, the PES analysis presented in **Figure** 5-69 shows that, for the case of styrene, the first peak at around 7.95 eV is reduced with respect to the ETB case. This fact, and other differences in peak sizes and curvatures are well captured by the sum of convolved isomer spectra considering a large number of PAH isomers. The fitted curve is shown in black dotted lines in the same figure and the extracted constants are presented in **Table** 5-19:

***Table 5-19**. Relative contributions to the m/z 140 overall signal for styrene and ethylbenzene.*

	STY	***ETB***
1H-cyclopropa[a]naphthalene	33.2%	42.5%
1H-cyclopropa[b]naphthalene	36.9%	17.7 %
1-ethynyl-1H-indene	7.4%	13.3%
2-ethynyl-1H-indene	7.7%	13.0%
4-ethynyl-1H-indene	1.8%	4.4%
5-ethynyl-1H-indene	1.8%	0.9%
6-ethynyl-1H-indene	1.8%	0.9%
7-ethynyl-1H-indene	1.8%	0.9%
phenyl allenyl acetylene	5.5%	5.3%

The main changes in this isomer distribution concern the formation of 1H-cyclopropa[a]naphthalene and 1H-cyclopropa[b]naphthalene which are the most abundant species in m/z 140 with around 70 % of the signal contribution to the PES signal. Specifically, , the global signal change was found to be -0.95 times and -0.85 times for 1H-cyclopropa[a]naphthalene and 1H-cyclopropa[b]naphthalene, respectively, compared to the values found for ETB. The contribution from the ethynyl-indene isomers also decreases from 33% to 22%.

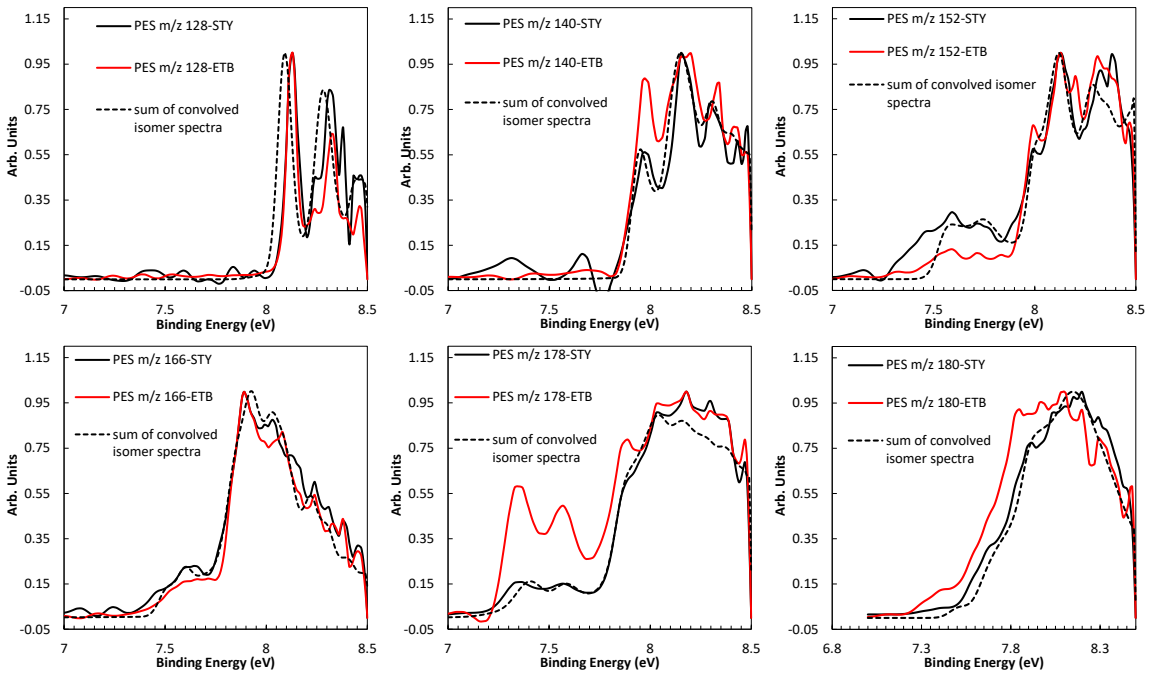

***Figure** 5-69. Photoelectron spectra for m/z 128, m/z 140, m/z 152, m/z 166, m/z 178 and m/z 180 obtained at 8.5 eV and continuous data acquisition mode. Each figure contains experimental PESs for styrene and ethylbenzene pyrolysis and the sum of convolved isomer spectra for styrene pyrolysis.*

The experimental photoelectron spectra comparison for m/z 128 is also presented in **Figure** 5-69. The results show that the second peak in the experimental profile is larger in styrene pyrolysis. This fact means that the contribution coming from naphthalene, the most abundant species, is probably reduced compared to ETB pyrolysis. The sum of convolved isomer spectra also presented in the PES analysis well fits the experimental curve. The relative signal contributions to m/z 128 from the different isomers are 61.4 : 8.5 : 8.5 : 8.5 : 8.5 : 4.4 for naphthalene : 4-ethynylstyrene : 3-buten-1-ynylbenzene : 4-phenyl-1-butene-3-yne : m-ethynylstyrene : 1H-Indene-1-methylene. In ETB pyrolysis, the relative signal contributions for the same species are 81.1 : 1.7 : 1.7 : 1.7 : 2.2 : 11.7, respectively. Overall, the contributions from 4-ethynylstyrene, 3-buten-1-ynylbenzene, 4-phenyl-1-butene-3-yne and m-ethynylstyrene are increased in percentage, but if we consider that the peak area for m/z 128 decreases by a factor 0.36 compared to ETB (**Figure** 5-66), the production of these species from styrene thermal decomposition is reduced compared to the ETB case. For naphthalene, such reduction is even more significant (-0.73 times less).

Moving to minor PAH species, the m/z 116 peak size is lower by 0.43 times compare to the peak obtained for ETB pyrolysis, thus the mole fractions of the related isomers are much lower. Indene is still the major species in m/z 116 during styrene decomposition at the evaluated temperatures. For all the studied species the signal contributions are 94.3 : 2.9 : 1.4 : 1.4 for indene : phenylpropadiene : p-methylphenylacetylene : 1-propynylbenzene (1-Phenyl-1-propyne) compared to a value of 100% indene in ETB pyrolysis.

The PES analysis for m/z 130 presented in **Figure** 5-70 indicates that, as mentioned in the analysis for ethylbenzene pyrolysis, there is a peak located at 8.33 eV that represents an important part of the spectrum and it is not captured by the available reference PESs available in this thesis work. However, part of the experimental PES at low binding energies is well described by the sum of convolved isomer spectra (dotted black line). The relative contributions for this part of the signal coming from 1,2-dihydronaphthalene and 1-methylindene are 66.7 : 33.3, respectively, in contrast to the ones found in ETB that were 87.9 : 12.1. Future efforts in determining reference PESs for other isomers of m/z 130 should be addressed in order to determine the correspondence of the two proposed isomers here with the unknown one(s) related to the peak located at 8.33 eV.

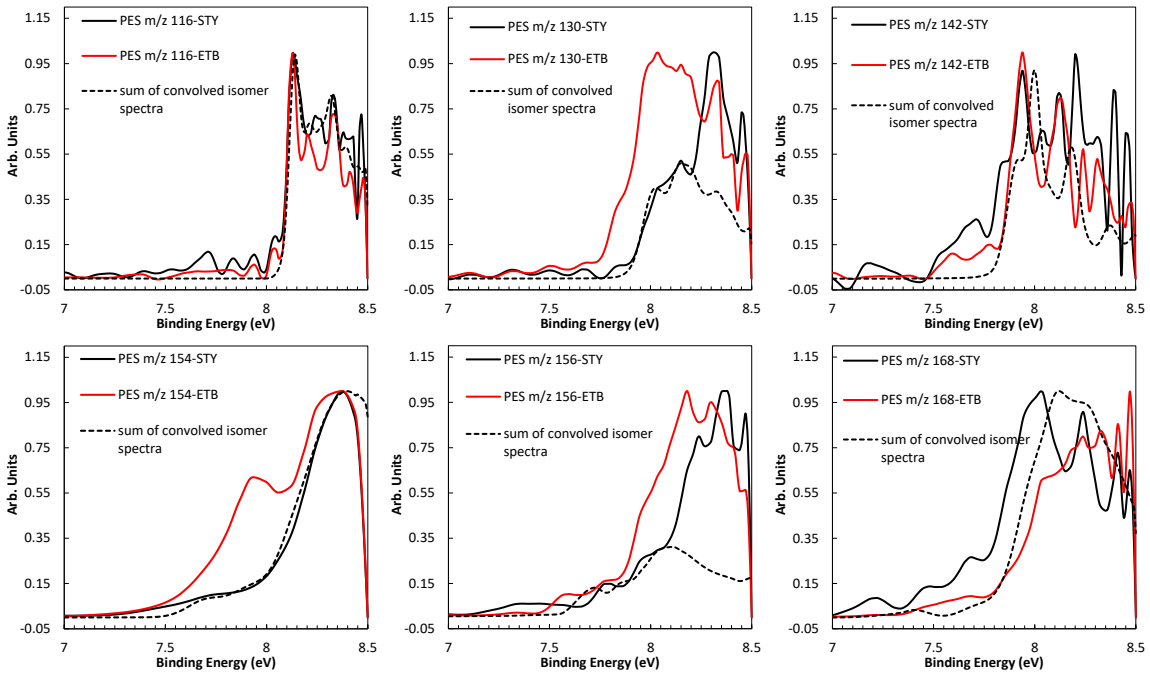

***Figure** 5-70. Photoelectron spectra for m/z 116, m/z 130, m/z 142, m/z 154, m/z 156 and m/z 168 obtained at 8.5 eV and continuous data acquisition mode. Each figure contains experimental PESs for styrene and ethylbenzene pyrolysis and the sum of convolved isomer spectra for styrene pyrolysis.*

For the case of m/z 142, the experimental PES signal for styrene is noisier as shown of **Figure** 5-70. This is due to the fact that m/z 142 peak is very small with respect to ETB, thus the formation of methylnaphthalenes is not a major pathway in styrene pyrolysis. This is linked to the reduced formation of naphthalene, the precursor molecules for methylnaphthalene. The relative contributions from 1-methylnaphthalene and 2-methylnaphthalene are 56 : 44, in contrast to the ones for ETB (46 : 54).

The PES comparisons between styrene and ETB presented in **Figure** 5-70 for m/z 154 clearly reveals that in styrene pyrolysis at the conditions studied, the production of 1-vinylnaphthalene is strongly reduced relative to biphenyl, the major species, as the correspondent peak at 7.95 eV almost disappear. Considering that in styrene pyrolysis the peak area for m/z 154 is reduced by 0.66 times compared to ETB pyrolysis, the global decrease in the concentration of 1-vinylnaphthalene is by a factor -0.93. The relative contributions to the overall signal of m/z 154 are 87.9: 2.2: 2.2 : 3.8 : 3.8 for all the studied species: biphenyl : 1-vinylnaphthalene : 2-vinylnaphthalene : acenaphthene : benzobarrelene, compared to ETB where the relative signal contributions are 54.4 : 21.8 : 10.2 : 6.8 : 6.8, respectively. Once again, the reduced production of $C_{10}H_8$ isomers should be the reason for the reduced vinylnaphthalene concentrations.

Similar to m/z 130, only a partial fitting of the overall experimental PES signal for m/z 156 could be obtained due to the lack of reference PESs with marked features above 8.1 eV binding energy. This can be observed in the PES comparisons presented in **Figure** 5-70. The corresponding peak in the mass spectrum is reduced by 0.06 times the value in ETB pyrolysis, and the convolution procedure provides the following relative signal contributions 21.0 : 8.1: 61.3 : 9.7 for 1,8-dimethylnaphthalene : 1,4-ethanonaphthalene :

1,4-dihydro,1,4-methanonaphthalene : 6-methyl-1,4-dihydro : 2-ethylnaphthalene, respectively. The values found in ETB pyrolysis are 9.4 : 3.9 : 82.0 : 4.7. In both cases, the initial part of the spectrum is mainly dominated by the presence of 1,4-dihydro,1,4-methanonaphthalene.

For m/z 168, the species whose PESs are available in the literature are the methylbiphenyl isomers ($C_{12}H_9CH_3$) as the photoionization energy of diphenylmethane (possibly the main product from aromatic-aromatic reactions) is higher than 8.5 eV. The relative PESs are presented in **Figure** 5-70. The fitting procedure provides relative signal contributions 4.4 : 10.5 : 85.1 for 2-methylbiphenyl : 3-methylbiphenyl : 4-methylbiphenyl compared to the ones obtained in ETB pyrolysis which are 5.6 : 55.6 : 38.9, respectively. On the other hand, the major peak at 8.03 eV is slightly shifted compared to the peak in the convolved curve, while the initial rise in the experimental curve is not very well captured. It is possible that other isomers might contribute in the case of styrene pyrolysis compared to ETB, but the signal in the case of STY pyrolysis is quite low compared to ETB (reduction by a factor 0.08) indicating that m/z is a very minor product in styrene chemistry.

The experimental photoelectron spectrum obtained in styrene pyrolysis for m/z 176 is compared to the one from ETB thermal decomposition in **Figure** 5-71. The two profiles are very similar. The relative contribution constants and the considered PAH species are presented in the **Table** 5-20.

***Table** 5-20. Relative contributions to the m/z 176 overall signal for styrene and ethylbenzene.*

	STY	***ETB***
1-Ethynylacenaphthylene	5.1%	9.9%
3-Ethynylacenaphthylene	8.0%	7.3%
4-Ethynylacenaphthylene	7.3%	10.6%
5-Ethynylacenaphthylene	7.3%	6.6%
1,2-Diethynylnaphthalene	6.6%	9.5%
1,3-Diethynylnaphthalene	2.8%	1.1%
1,4-Diethynylnaphthalene	17.9%	19.8%
1,5-Diethynylnaphthalene	7.3%	6.6%
1,6-Diethynylnaphthalene	2.8%	1.1%
1,7-Diethynylnaphthalene	1.5%	2.1%
1,8-Diethynylnaphthalene	4.4%	6.0%
2,3-Diethynylnaphthalene	4.4%	4.0%
2,6-Diethynylnaphthalene	2.8%	1.1%
2,7-Diethynylnaphthalene	1.5%	1.3%
1-(1,3-Butadiynyl)naphthalene	7.3%	3.2%
2-Buta-1,3-diynylnaphthalene	7.3%	3,2%
Pyracyclene	2.9%	3.3%
Cyclopenta[bc]acenaphthylene	2.9%	3.3%

The total contribution from the diethynylnaphthalenes remains nearly constant (52% for styrene, 53% for ethylbenzene), the remaining isomers are formed from the reactions of the acenaphthylene radicals with C_2H_2, thus their overall contribution remains unchanged too.

Concerning another minor peak, the experimental PES for m/z 182 is also partially reproduced by the fitting curve as shown in **Figure** 5-71. The two PESs for styrene and ethylbenzene pyrolysis are quite different, in particular the early rise in the STY case suggests the presence of a different isomer distribution compared to ETB. Based on the current literature data, the dimethylbiphenyls have been associated to m/z 182, but their contributions cannot provide a correct description of the experimental PES for styrene pyrolysis. Future theoretical calculations will have to be performed to further improve our understanding of the isomer distribution for this m/z.

The PES analysis of m/z 202 is represented in **Figure** 5-71. The sum of convolved isomer spectrum (black dotted line) seems to well represent the experimental PES in styrene pyrolysis. The relative signal contributions for all the considered species in m/z 202 are presented in **Table** 5-21.

Table 5-21*. Relative contributions to the m/z 202 overall signal for styrene and ethylbenzene.*

	STY	***ETB***
Fluoranthene	36.6%	38.3%
Diphenyldiacetylene	1.2%	1.2%
Pyrene	19.5%	18.5%
Phenanthrylacetylen	0.6%	0.6%
2-Ethynylphenanthrene	12.2%	11.1%
3-Ethynylphenanthrene	3.7%	3.7%
4-Ethynylphenanthrene	3.1%	3.1%
9-Ethynylphenanthrene	3.1%	3.1%
Benzene, 1-ethynyl-2-(phenylethynyl)	1.2%	1.2%
Benzene, 1-ethynyl-3-(phenylethynyl)	1.2%	1.2%
Benzene, 1-ethynyl-4-(phenylethynyl)	1.2%	1.2%
1-Ethynylanthracene	0.1%	0.1%
2-Ethynylanthracene	0.1%	0.1%
9-Ethynylanthracene	0.1%	0.1%
Acephenanthrylene	3.7%	3.7%
4,5-Vinylidenephenanthrene	12.2%	12.4%
Aceanthrylene	0.1%	0.1%

Few differences between the experimental curves for styrene and ETB pyrolysis are obtained in the convolution procedure. As can be noticed, for the case of styrene the major species are still fluoranthene, pyrene, 2-ethynylphenanthrene, and 4,5-vinylidenephenanthrene accounting for the 81% of the overall PES signal. Taking into account a MS peak area decrease of 0.75 times compared to ETB, the concentrations of the mentioned major species in m/z 202 globally changed by -0.28, -0.21, -0.18 and -0.26, thus in a similar fashion. This means that the isomeric distribution did not significantly change for

styrene compared to ETB pyrolysis, as also observed in **Table** 5-21, although the styrene pyrolysis leads to lower m/z 202 products based on the integrated mass spectra.

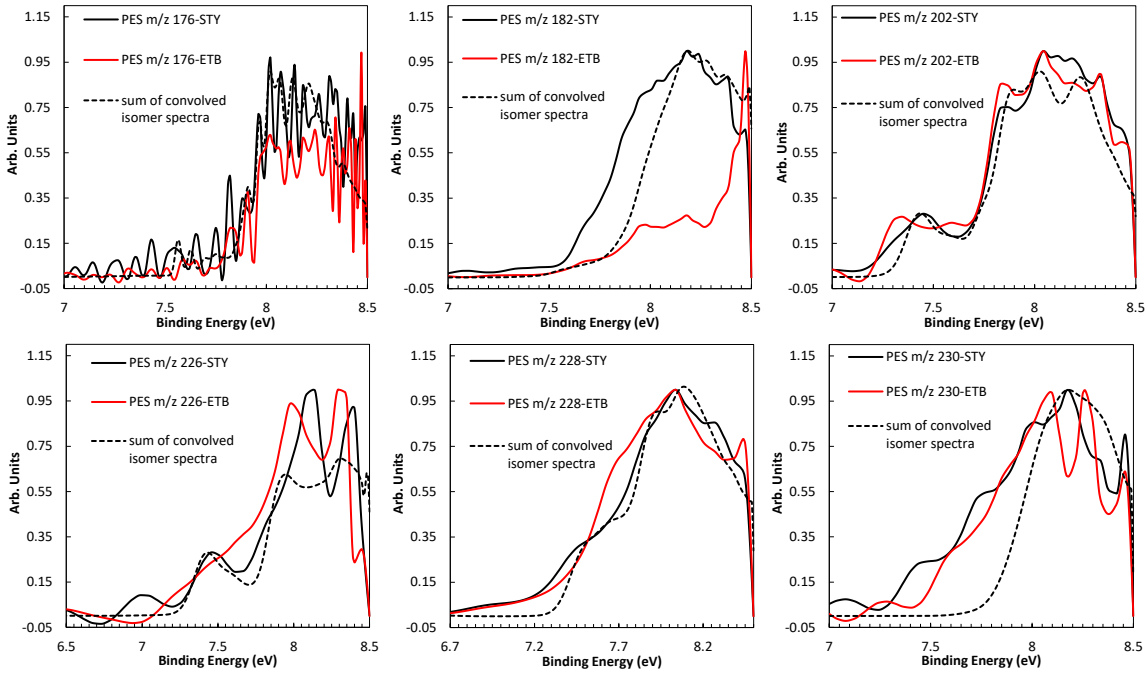

***Figure** 5-71. Photoelectron spectra for m/z 176, m/z 182, m/z 202, m/z 226, m/z 228, and m/z 230 obtained at 8.5 eV and continuous data acquisition mode . Each figure contains experimental PESs for styrene and ethylbenzene pyrolysis and the sum of convolved isomer spectra for styrene pyrolysis.*

The PES comparison for m/z 226 is also presented in **Figure** 5-71. The convolved curve captures part of the experimental PES for this mass. The signal contributions are 66.3 : 33.7 for benzo(ghi)fluoranthene and 1-ethynylpyrene, respectively, compared to the constants obtained in the case of ETB pyrolysis which are 76.9 : 23.1. In both cases, the most abundant species for m/z 226 is benzo(ghi)fluoranthene. Based on the peak size in **Figure** 5-68, the concentration of benzo(ghi)fluoranthene is expected to decrease by a factor -1.23 compared to the ETB case, while the one of pyrene to increase by a factor 1.30. Still, there is part of the experimental PES around 8.09 eV that require further refinements, and future calculations on reference PES for other PAH molecules should be addressed in order to clarify this part of the spectrum.

Even if the signals become relatively small, the PES comparison for m/z 228 presented in **Figure** 5-71 demonstrate that PAH isomers can be identified though the convolution procedure. The contribution constants for chrysene : 1,2-benz[a]anthracene : triphenylene : 1-(phenylethynyl)naphthalene are 2.5 : 20.5 : 45.1 : 32.0, respectively, and for ETB are 31.8 : 4.5 : 31.8 : 31.8. This information indicates that, in styrene pyrolysis, the percentage related to chrysene has strongly decreased in correspondence with an increase of 1,2-benz[a]anthracene formation. This might indicate specific pathways to the m/z 228 from styrene pyrolysis compared to the ethylbenzene case. The major species of m/z 228 is triphenylene followed by 1-(phenylethynyl)naphthalene.

Figure 5-71 shows in detail the experimental PES comparison for m/z 230 obtained in styrene and ETB pyrolysis. The fit obtained by means of the sum of convolved isomer spectra has determined the relative contribution for the considered species. p-Terphenyl, o-terphenyl and m-terphenyl were found to contribute 44.4 : 33.3 : 22.2 to the PES signal, respectively, which means that with respect to ETB, p-terphenyl and o-terphenyl are more prominent species. In ETB pyrolysis the relative PES signal contribution for the same group of isomers is found to be 24.1 : 15.7 : 60.2. However, a global decrease is found for these species since this mass has suffered a decrease in the peak area of 0.48 times the value observed in ETB.

To summarize the results presented in this chapter, two different series of experiments have been performed (i) with pulsed mode (reflected shock time identified) averaging more than 22 000 runs and (ii) with continuous acquisition mode averaging more than 41 000 runs. For the experiments at 10 eV, well defined mass spectra were obtained from light species up to 5-member rings in the pulsed acquisition mode averaging data over 1.2 ms of shock reflected reaction conditions. At photon energy of 8.5 eV, photoelectron spectra were measured for the main PAH products in the *continuous* mode that allowed the isomer identification. The results were compared to the ethylbenzene ones. Despite the qualitative nature of the current analyses, the datasets constitute an important benchmark for improving our fundamental understanding on the complex chemistry from styrene pyrolysis, and for the development of detailed chemical kinetic models for soot precursor chemistry. Finally, a comparative study between the synchrotron-based shock tube techniques and the conventional laboratory-based shock tube techniques is realized in the frame of this thesis in order to highlight the complementarity of the different set-ups. Specifically, the first pyrolytic study on styrene decomposition using the HPST single pulse shock tube coupled to GC/GC-MS is presented in the next sections, together with preliminary model simulations for products up to four rings. Future experimental campaigns at SOLEIL and SLS will focus on other important fuel components and intermediates, i.e. phenylacetylene, benzene, xylenes, and mixtures with small aliphatics.

5.6 Pyrolysis of Styrene using HPST/ GC-MS

In the previous chapter the HRRST/i^{2}PEPICO coupling has been employed to measure and identify several products formed during the styrene pyrolytic decomposition ranging from m/z = 52 up to m/z = 230. In the present chapter new measurements on styrene pyrolysis using the ICARE single pulse shock tube coupled to gas chromatographic systems and mass spectrometry (SPST/GC/GC-MS) will be presented, including measurements of PAH products up to four rings, for comparison with the HRRST data. This will evidence the complementary between these two kinetic techniques. Additionally, several important aspects related to the PAH chemistry during the thermal decomposition of styrene are discussed based on chemical kinetic modeling.

The single pulse experiments were performed at a temperature range of 1168 – 1734 K and a nominal pressure of P_5 = 20 bar with reaction time of around 4 ms. The initial fuel concentration is 92 ppm (styrene from Sigma-Aldrich, 98% putity) diluted in argon (Air Liquid, 99.9999%) as bath gas, while the driver gas was helium (Air Liquid, 99.995%). The error associated to the measurement of the temperature is estimated to be ±30 K, the uncertainty on the measurement of small species mole fraction is not more than 5 %, and for PAH not more than 15 %.

The experimental results are accompanied by numerical simulation results that were obtained with the most updated version of the ICARE chemical kinetic model for PAH formation and growth. The simulations were run using the homogeneous batch reactor module in CHEMKIN Pro. The validated styrene model serves as a sub mechanism for a more comprehensive chemical kinetic model that has been already validated against speciation profiles obtained with single pulse shock tube. The fuels considered in previous studies include single fuels like toluene, benzene, alkylbenzene, xylenes, phenylacetylene, cyclopentene, n-heptane and reactions with C2-C3 small hydrocarbons, at nominal pressure of 20 bar and temperature range of 1000 - 1800 K.

5.6.1 Small hydrocarbon and mono-ring aromatic species

Figure 5-72 presents the experimental species profiles (in symbols) for small hydrocarbon and mono-ring aromatic species produced from styrene ($C_6H_5C_2H_3$) decomposition. The current model results are shown in solid lines. The model presents an overall good agreement with the experiments including the fuel decay and the formation of aliphatic species like acetylene (C_2H_2), ethylene (C_2H_4), diacetylene (C_4H_2) and small single-ring aromatics like benzene (C_6H_6), toluene (C_7H_8) and phenylacetylene ($C_6H_5C_2H$), validating the proposed reaction pathways.

According to the experimental results, styrene starts decomposing at 1226 - 1283 K similar to toluene which decomposes above 1240 K [65]. Additionally, for both fuels, the decay slope is similar. Benzene (C_6H_6) is one of the main byproducts of styrene pyrolysis (**Figure** 5-72e). This aromatic compound starts to be produced at the same temperatures as styrene starts decomposing and its maximum concentration is located at a temperature of 1516-1553 K (~25 ppm). According to the model, almost 90% of the benzene production comes directly from the decomposition of styrene ($C_6H_5C_2H_3$) though reactions with H atoms producing also vinyl radical (C_2H_3). The remaining 10% mainly comes from H-abstraction reactions of the phenyl radical (C_6H_5) with styrene. Phenyl radical is formed from the thermal decomposition of 2-

phenylethyl ($C_6H_5CH_2CH_2$), one species produced from the addition reaction of styrene with hydrogen atoms. The addition step leads also to 1-phenylethyl ($C_6H_5CHCH_3$) that is also accounted in the current model [83].

Large amounts of phenylacetylene ($C_6H_5C_2H$) were also detected in the single pulse shock tube experiments as shown in **Figure** 5-72g. This mono-ring compound reaches the peak of concentration at 1496 K with a value of ~11 ppm. After styrene breakdown initiated by C-H bond fission on the vinyl moiety, unimolecular decomposition reactions give place to mono-aromatic species like phenylacetylene and other products like o-benzyne (o-C_6H_4) and ethylene (C_2H_4). This last species is also measured with the GC and presented in **Figure** 5-72b. The breakdown of styryl radicals participate in the formation of phenylacetylene but in a minor amount compared to the unimolecular reaction $C_6H_5C_2H_3=C_6H_5C_2H+H_2$.

Toluene (C_7H_8) is the last mono-aromatic compound detected using the HPST/GC coupling, it is produced in small amounts during styrene pyrolysis reaching values less than 1 ppm as presented in the **Figure** 5-72f. This fact has also been proven in the previous chapter using HRRST/i^{2}PEPICO coupling where toluene production during the decomposition of styrene is very reduced compared to ethylbenzene, for example. Toluene may be formed when benzyl radical reacts with a hydrogen atom. On the other hand, the benzyl radical is produced in small amounts from the recombination of o-benzyne (o-C_6H_4) with methyl (CH_3) and not from a direct decomposition step as for ethylbenzene.

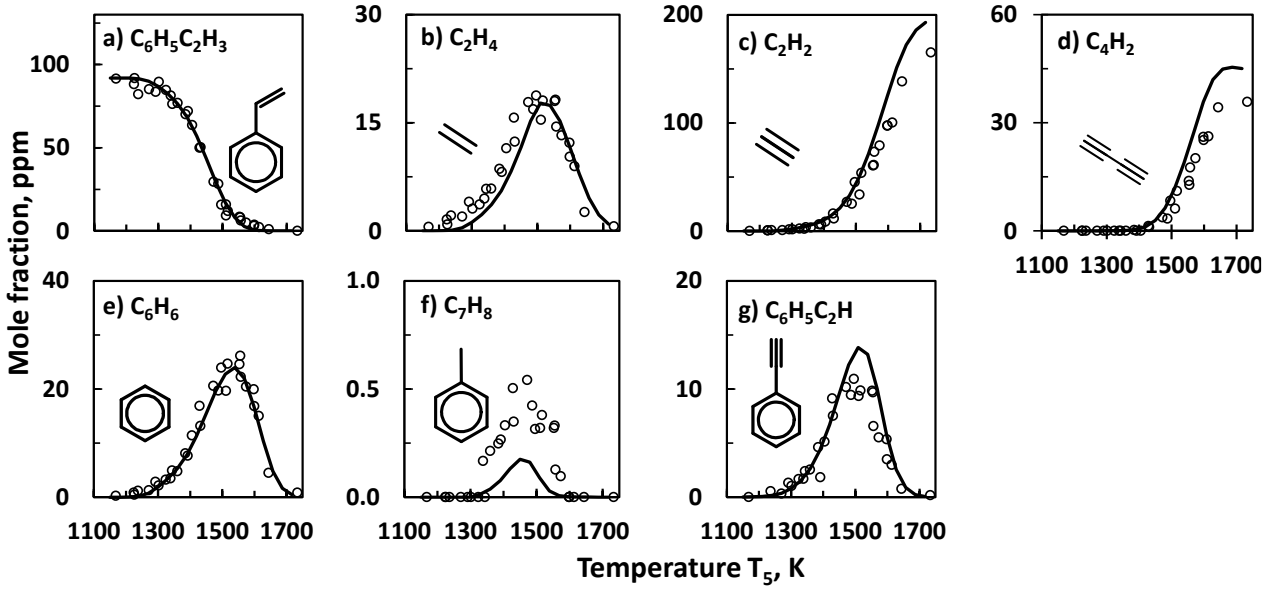

***Figure** 5-72. Styrene decomposition, mole fractions of small hydrocarbons and mono-ring aromatic products as a function of T_5 at nominal pressure P_5 of 20 bar. The symbols are the experimental results while the solid lines are numerical results with the current ICARE model for PAH formation and growth.*

The comparison between the concentrations of the main monoaromatic products obtained with the GC-MS system and with the HRRST/i^{2}PEPICO system may provide an additional confirmation of the validity of the new synchrotron-based methodology. For instance, at T_5= 1350 K, 20 bar, and 92 ppm of styrene, the relative concentration for small aromatic species produced in the decomposition of styrene in the HPST

for benzene : toluene : phenylacetylene is 64 : 3 : 33. At similar temperatures $T_{5,average}$= 1345 K, $P_{5,average}$ = 6.5 bar, 0.1% styrene using the HRRST/i^{2}PEPICO coupling, the relative concentrations from the respective m/z peak areas in the mass spectra of 1.2 ms (thus area corrected by the cross-section at a photon energy of 10 eV (A_x/σ_x)) are 48.8 : 2.7 : 48.5 for benzene : toluene : phenylacetylene, respectively. This is a reasonable agreement considering the differences in the experimental conditions especially in terms of non-idealities and temperature rise behind the reflected shock waves in the HRRST. If we consider, based on the adiabatic compression simulations based on the measured pressure profile, the temperature within the first 600 µs increases by around 200 K before dropping. The average temperature is around 1450 K then. If we consider the HPST result at 1452 K, the ratio becomes 61 : 2 : 37, which is very close to what is obtained in the HRRST. In addition, the m/z 102 area might be affected by the presence of benzocyclobutadiene, as shown in the previous chapter, whose contribution need to be eliminated for a more accurate analysis.

5.6.2 Polycyclic aromatic hydrocarbons

Regarding the larger species, including the PAH products, the experimental species profiles vs temperature are presented in **Figure** 5-73. The figure contains the information for species ranging from two, up to four-member rings starting from very common PAH compounds like indene and naphthalene until pyrene. Other species were also detected in this work but they are not included in the analysis due to the small signal levels and, for the largest molecular weight compounds, due to possible condensation inside the transfer lines. The results are discussed in the following paragraphs in order of the molecular weight, from the smaller to the larger PAHs.

Indene (C_9H_8) was produced in low concentrations compared to other PAH compounds, and its behavior is well captured by the model. As shown in **Figure** 5-73a, the formation window for this species starts at around 1323 K reaching a peak of ~0.3 ppm at 1496 K-1556 K. According to the current model, the production of this species can be attributed to reactions between phenylacetylene ($C_6H_5C_2H$) and methyl (CH_3). Naphthalene ($C_{10}H_8$) maximum mole fraction was found to be ~1 ppm at ~1557 K, **Figure** 5-73b. This common PAH species starts appearing at around 1400 K and as previously mentioned, its formation is related to the reactions between o-benzyne (o-C_6H_4) with benzene (C_6H_6) via BICYCLO intermediate giving also place to the formation of acetylene C_2H_2, which is a measured species presented in **Figure** 5-72c . The model can accurately reproduce the species profile considering the measurement errors for the concentration and temperature which are less than 15 % and 30 K, respectively.

1-Ethynylnaphthalene ($C_{10}H_7C_2H$) is produced in smaller concentrations than naphthalene, as expected. Its maximum concentration of ~0.2 ppm is reached at ~1555 K as shown in **Figure** 5-73c. In fact, ethynylnaphthalene is mainly produced from naphthalene reaction with ethynyl radical ($C_{10}H_8 + C_2H = C_{10}H_7C_2H + H$). The current version of the model overpredicts the concentrations for this species, and this may be due to the lack of consumption reactions or uncertainties in the related kinetic parameters.

The concentration versus temperature profile for acenaphthylene ($AC_{12}H_8$) is showed in detail in **Figure** 5-73d. The peak of concentration for this species is located at ~1573 K taking a value of ~0.8ppm. According to the model, which well reproduces acenaphthylene concentration profile, the main contribution for the formation of this species is due to hydrogen loss and ring closure of biphenyl ($C_{12}H_{10}$)

intermediate which is produced from the reaction between two phenyl (C_6H_5) radicals. A minor pathway involves 1-ethynylnaphthalene which may react with a free hydrogen to produce acenaphthylene ($AC_{12}H_8$) through the reaction $C_{10}H_7C_2H + H = AC_{12}H_8 + H$.

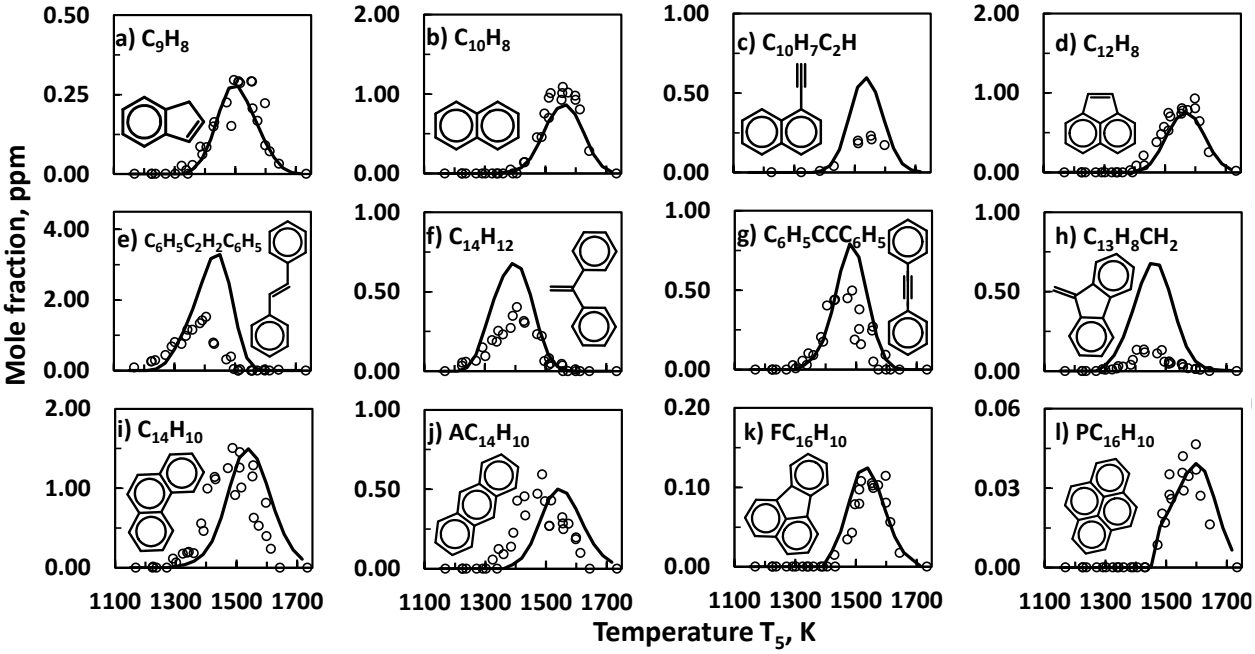

***Figure** 5-73. Experimental concentration profiles vs temperature for polycyclic aromatic hydrocarbon compounds detected using SPST/GC/GC-MS system at nominal pressure P_5 of 20 bar. The symbols are the experimental results while the solid lines are numerical results produced with the current version of ICARE model for PAH formation and growth.*

Stilbene ($C_6H_5C_2H_2C_6H_5$, also $C_{14}H_{12}$) is one of the most predominant PAH compounds produced during styrene pyrolysis according to detection and measurement with GC. The concentration profile for this species presented in **Figure** 5-73e shows that a peak value of ~1.5 ppm was found at ~1400 K evidencing an early formation of this species, starting at around ~1237 K. The formation of stilbene ($C_6H_5C_2H_2C_6H_5$) can come from the addition of radical phenyl (C_6H_5) to styrene ($C_6H_5C_2H_3$), producing two kind of $C_{14}H_{13}$ species, either $C_6H_5CH(\dot{C}H_2)C_6H_5$ and $C_6H_5\dot{C}HCH_2C_6H_5$. Specifically, $C_6H_5\dot{C}HCH_2C_6H_5$ can release a hydrogen to produce stilbene. Additionally and similar to stilbene, from $C_6H_5CH(\dot{C}H_2)C_6H_5$ decomposition it can be produced another $C_{14}H_{12}$ isomer: 1,1-diphenyl-ethylene ($C_6H_5C(CH_2)C_6H_5$) which was also measured as depicted in **Figure** 5-73f with a maximum concentration of ~0.4 ppm at ~1405 K. Additional studies on the different pathways related to styrene pyrolysis should clarify these kinetic steps as the current version of the model overpredicts the formation of stilbene and 1,1-diphenyl-ethylene.

Regarding $C_{14}H_{10}$ isomers, the presence of diphenylacetylene ($C_6H_5CCC_6H_5$) was investigated. **Figure** 5-73g shows that this species reaches a maximum concentration of ~0.5 ppm at ~1487 K. Overall, the model can predict the rising temperature and level of concentration with relatively good accuracy within the experimental uncertainties. Diphenylacetylene can be produced from phenyl (C_6H_5) addition to phenylacetylene ($C_6H_5C_2H$). On the other hand, 9-methylenefluorene ($C_{13}H_8CH_2$), whose species profiles is

presented in **Figure** 5-73h, can be directly produced from the decomposition of 1,1-diphenyl-ethylene ($C_6H_5C(CH_2)C_6H_5$) already discussed with the analysis of **Figure** 5-73f. The current model overpredicts the relative mole fractions which reach a maximum value of ~0.14 ppm.

Phenanthrene ($C_{14}H_{10}$) is one of the main PAH compounds produced in styrene pyrolysis. Similar to stilbene, the phenanthrene mole fractions reach ~1.5 ppm at ~1487 K as shown in **Figure** 5-73i. The model exhibits a good prediction for the phenanthrene profile within the measurement uncertainties. According to the kinetic analyses, phenanthrene is being mainly produced from the decomposition of 1,1-diphenyl-ethylene ($C_6H_5C(CH_2)C_6H_5$) which produces 9-methylenefluorene ($C_{13}H_8CH_2$) and 1,2-diphenyl-ethenyl radical ($C_6H_5CCHC_6H_5$) which subsequently form phenanthrene ($C_{14}H_{10}$). Also, phenanthrene can be produced from phenyl addition to phenylacetylene through the reaction route $C_6H_5C_2H + C_6H_5 = C_{14}H_{10} + H$, however this pathway is only minor in styrene pyrolysis.

Anthracene ($AC_{14}H_{10}$) was found to be almost three times less abundant than phenanthrene ($C_{14}H_{10}$) with a maximum concentration of ~0.6 ppm at ~1470 K. Analyzing **Figure** 5-73j, it can be noticed that the current version of the model cannot well reproduce the temperature window for this species since it predicts a delayed appearance and consumption of anthracene compared to the measurements. However, the magnitude of concentration for the gaussian shaped curve is well captured. Anthracene ($AC_{14}H_{10}$) may be produced from stilbene ($C_6H_5C_2H_2C_6H_5$) which decomposes into radical $C_6H_4C_2H_2C_6H_5$ that subsequently produces anthracene.

Larger PAH compounds were measured with the aid of the HPST/GC system including four-ring isomeric species of $C_{16}H_{10}$. For instance, pyrene ($PC_{16}H_{10}$), whose experimental profile is presented in **Figure** 5-73l, seems to be mostly produced from the combination of phenylacetylene radical ($C_6H_4C_2H$) with styrene ($C_6H_5C_2H_3$). Another possible pathway for the formation of this large PAH is the reaction between phenylacetylene radical ($C_6H_4C_2H$) with phenylacetylene ($C_6H_5C_2H$) but this route has a small contribution to the overall pyrene formation. The concentration of pyrene in the mixture starts to increase at a late temperature of ~1450 K with a maximum of ~0.05 ppm located at ~1597 K.

Fluoranthene ($FC_{16}H_{10}$) concentration was found to be larger than pyrene. It reaches a maximum of ~0.1 ppm at a temperature of ~1560 K as evidenced in the graph of **Figure** 5-73k. The formation of fluoranthene is also late in temperature as pyrene, starting to be produced at around 1431 K. According to the most recent version of the ICARE PAH model, fluoranthene may be produced through two main routes. The first one is the reactions between fluorenyl radical ($C_{13}H_9$) with propargyl radical (C_3H_3). Fluorenyl ($C_{13}H_9$) comes from the decomposition of 9-methyl-9H-fluorene ($C_{13}H_9CH_3$) which is a stepwise result of the combination of styrene ($C_6H_5C_2H_3$) and phenyl (C_6H_5). Such reaction yields the radical $C_6H_5CH(\dot{C}H_2)C_6H_5$ which can also produce 1,1-diphenyl-ethylene ($C_6H_5C(CH_2)C_6H_5$). Propargyl (C_3H_3) is a minor product of styrene decomposition from the reaction $C_6H_5C_2H_3 = C_5H_5+C_3H_3$. The second route to the production of fluoranthene is the unimolecular decomposition of phenyl naphthalene ($C_{10}H_7C_6H_5$) which is formed from the reaction between benzene (C_6H_6) and naphthyl radical ($C_{10}H_7$).

A qualitative comparison between the results from the HPST experiments in **Figure** 5-73 and the HRRST results can be performed by considering the integrated mass spectrum obtained at 10 eV (**Figure** 5-65). The PAH products will be the focus of the present analysis. First, the biggest m/z peaks correspond to m/z 178 and 180, similar to the HPST results where maximum total mole fractions of around 2.7 ppm and 2 ppm were obtained, respectively, by considering the sum of the single mole fractions of the different

isomers. Among the $C_{14}H_{10}$ isomers, the order based on the HPST maximum mole fractions is phenanthrene > diphenylacetylene ~ anthracene > 9H-fluorene, 9-methylene, while stilbene is clearly the major isomer among the $C_{14}H_{12}$ species. The stilbene isomers, (E)- and (Z)-, provide the main contributions to the experimental PES of m/z 180 in the HRRST experiments, although the anthracene contribution is reduced in this case and similar to the one of 9H-fluorene,9-methylene. This difference might be due to the different T conditions considered (the HRRST P and T profiles vary over time as discussed above), the different reaction times (4 ms for the HPST vs 1.2 ms integration time for the HRRST), or the initial fuel concentration which varies by an order of magnitude. These hypotheses require further validation by chemical kinetic analyses.

Among other major products, naphthalene and acenaphthylene are clearly the most important in both cases, although the HRRST experiments show major contributions from other isomers which are negligible in the case of the single-pulse shock tube experiments. For example, the contributions to m/z 152 from acenaphthylene and ethynylnaphthalenes are 47% and 35%, respectively, while the concentration of ethynylnaphthalenes in the HPST results is around ¼ of that of acenaphthylene. In addition, several isomers were detected for m/z 128, i.e. the ethynylstyrenes, which are not detectable in the HPST signals. This difference is probably due to the initial fuel concentrations, much higher in the HRRST experiments, which leads to an increased importance of the secondary chemistry. For the same reason, certain m/z such as 126 and 176 (mainly diethynylbenzenes and diethynylnaphthalenes) are major products in the HRRST mass spectrum and not in the GC measurements.

Finally, for the largest molecular weight PAHs, the ratio between the mole fractions of fluoranthene and pyrene is around 2.5 : 1 in **Figure** 5-73, while the in the case of HRRST this ratio of the contributions to the PES is 1.9 : 1. In addition, other products in the HRRST results include the ethynylphenanthrenes and 4,5-vinylidenephenanthrene which are not detectable in the HPST results.

These results show how, overall, the two experimental techniques provide data which are consistent with each other. On the other hand, the possibility to perform experiments with higher initial mole fractions in the HRRST coupled to the high-sensitivity and isomer selectivity of the synchrotron diagnostics, provides complementary information compared to the laboratory-based techniques.

5.6.3 Styrene pyrolysis compared to toluene and ethylbenzene pyrolysis

In order to compare the styrene pyrolytic products to the ones produced in toluene and ethylbenzene pyrolysis, **Figure** 5-74 presents the measured mole fractions of small species, monocyclic aromatic hydrocarbon (MAH) species, and polycyclic aromatic hydrocarbons (PAHs) . The nominal pressure P_5 is 20 bar, the temperatures T_5 between 1000 K and 1700 K, reaction time of around 4 ms for mixtures of 92 ppm of styrene (black circle symbols), 105 ppm of toluene (blue triangle symbol) and 101 ppm of ethylbenzene (red squared symbols) all diluted in argon bath gas.

In **Figure** 5-74a, a rapid fuel decay occurring at relatively low temperatures is evidenced for ETB decomposition compared to styrene and toluene which present similar decomposition rates and temperature windows, evidencing that ETB has a higher reactivity compared to the other two fuels. As a consequence, MAH intermediates like toluene and styrene are produced in larger amounts and present a

wider temperature window in ETB pyrolysis. Additionally, these compounds start forming at very early stages in ETB decomposition as can be seen in **Figure** 5-74e and g.

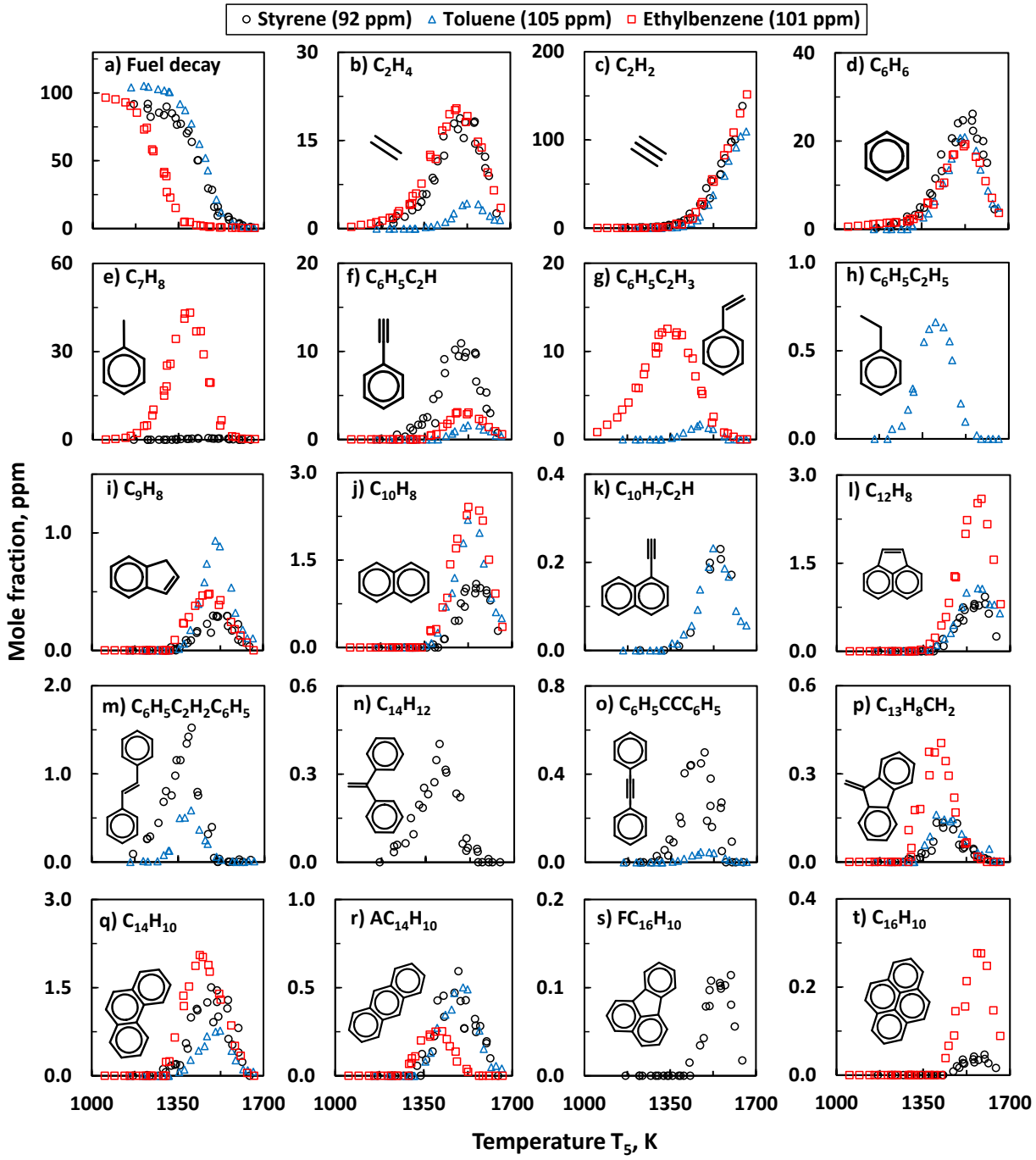

***Figure** 5-74. Measured mole fractions for small species, monocyclic aromatic hydrocarbons (MAHs), and polycyclic aromatic hydrocarbons (PAHs) from 92 ppm of styrene (black circle symbols), 105 ppm of toluene (blue triangle symbol), 101 ppm of ethylbenzene (red squared symbols) diluted in argon. Nominal pressure P_5 of 20 bar, reaction time of around 4 ms.*

On the contrary, as evidenced in **Figure** 5-74f the production of phenylacetylene is predominant in styrene pyrolysis from the direct dehydrogenization of the fuel, followed by ETB and by toluene. Similarly, the pathways to the decomposition into benzene are slightly more favored in styrene pyrolysis rather than in ETB and toluene decomposition which present very similar mole fractions as in **Figure** 5-74d. Indeed, together with the ipso-addition fuel+H=benzene+(C_2H_3, C_2H_5, or CH_3), in styrene pyrolysis benzene can be produced also by the reaction $C_6H_5C_2H_3=C_6H_6+H_2CC$. Finally, ethylbenzene was not detected in styrene pyrolysis but only in the case of toluene pyrolysis (**Figure** 5-74h). Thus, considering the MAH intermediate species, ethylbenzene mainly decomposes into benzene, toluene, and styrene and, in a minor way, to phenylacetylene, while toluene pyrolysis produces mainly benzene, and small amounts of phenylacetylene, styrene, and ethylbenzene. For the case of styrene, its decomposition pathways favors the production of benzene and phenylacetylene, while the production of toluene is very reduced.

The distribution of MAH species affects the formation of PAH products. In general, most of the main multi-ring species reach higher mole fractions from ETB pyrolysis, including acenaphthylene (**Figure** 5-74l), 9-methylenefluorene (**Figure** 5-74p), phenanthrene (**Figure** 5-74q), and pyrene (**Figure** 5-74t) the concentrations are clearly higher in ETB pyrolysis. As benzene profiles are very similar, this intermediate species can not be responsible for the different propensity of ETB to form PAHs (it is relatively stable at these conditions, its thermal fragmentation leads to the opening of the ring at high temperatures). The fact that ETB decomposes at lower temperatures to form toluene, styrene, and the corresponding radicals, which can react with the fuel molecule directly to form larger products, is possibly the main reason for an enhanced propensity to form PAHs. A similar general behavior was also observed in the experimental results obtained with the HRRST/i^2PEPICO technique (**Figure** 5-53).

Considering the different compounds, naphthalene production is slightly reduced from ETB to toluene pyrolysis, while a significant drop in the corresponding concentrations is observed for styrene (**Figure** 5-74j). Indene (**Figure** 5-74i) is primarily produced from the reaction of the benzyl radical with C_2H_2, thus it follows the same order as for the mole fractions of the benzyl radical produced (toluene > ETB > STY). The mole fractions of the other main two-ring fused product, acenaphthylene (**Figure** 5-74l), are similar for toluene and STY pyrolysis, but lower almost by a factor 2.5 compared to the ETB case. As shown in the previous chapters, the reactions of styrene and its radicals lead to the formation of $C_{14}H_{12}$ isomers, primarily stilbene (**Figure** 5-74m) and, in minor proportion, 1,1-diphenylethylene (**Figure** 5-74n). With regards to other fuels, only toluene decomposition leads to the formation of stilbene from the dehydrogenization of bibenzyl, produced in large concentrations in this case. Further dehydrogenization of stilbene produces diphenylacetylene, whose relative concentrations are proportional to the ones of stilbene. Finally, the $C_{14}H_{10}$ isomers are the ones which exhibits different behaviors. In fact, while phenanthrene (**Figure** 5-74) and 9H-Fluorene, 9-methylene (**Figure** 5-74p) are formed primarily during ETB pyrolysis, anthracene (**Figure** 5-74o) production seems to be very similar in styrene and toluene pyrolysis but higher than the concentrations found in ETB pyrolysis. Further detailed kinetic analyses will be required to explain this fuel-dependent behavior.

To conclude this chapter, new experimental information on styrene thermal decomposition and speciation up to four ring PAH structures were obtained using single-pulse shock tube coupled to GC/MS system. The ICARE PAH formation kinetic model was validated against the experimental data and the most updated version with a styrene sub-mechanism was used here. The model is capable to reproduce the majority of the species concentration versus temperature profiles for small hydrocarbon, mono-ring

species, and PAH compounds aiding the analysis of the experimental results. It was also illustrated how the information obtained using the HRRST coupled to i^{2}PEPICO detector can complement and confirm the results obtained with well-stablished conventional techniques, but still giving more insight in the formation chemistry of large PAH species as discussed in previous chapters. The present results constitute one important contribution to the field of soot chemistry because of the important role that styrene plays on the formation of PAHs from typical real and surrogate fuels.

5.7 Pyrolysis of ethylbenzene and styrene using HST/LS

The previous chapters have been focused mostly on the PAH chemistry from three important aromatic fuels, toluene, ethylbenzene, and styrene. Complementary experimental results from both laboratory-based and synchrotron-based techniques were presented to highlight the different formation kinetics as function of the fuel properties with the support of model analyses and chemical intuition. In particular, the three fuels are correlated as ethylbenzene, the smallest alkylbenzene representative of this class of hydrocarbons often implemented in surrogate formulations, undergoes thermal decomposition to styrene and benzyl radical (from which toluene is formed), among the others, from dehydrogenization and C-C bond scission. The propensity of ethylbenzene to form PAH intermediates has been highlighted. On the other hand, the pathway to the carbon nanoparticles and their growth includes additional steps which needs to be clarified based on complementary techniques focused on the solid-phase chemistry. In particular, the ICARE heated shock tube and laser extinction technique (HST/LS) were implemented in order to obtain time-history optical density profiles from the pyrolysis of styrene and ethylbenzene, and compared to the toluene data from previous works. The overall output of this chapter constitutes an important contribution as experimental benchmark for the development of the on-going ICARE soot model which is intended to be a comprehensive multi-phase pyrolytic model for simulation of a wide number of fuels and intermediates, aliphatic and aromatic, and their mixtures.

Around 76 experiments for the two fuels were performed with an initial carbon concentration [C] used in previous study on toluene pyrolysis (3.2–4.0x10^{17} atoms·cm^{-3}), which correspond to molar concentrations of 0.0613% ethylbenzene (ETB) and styrene (STY) in argon bath gas. The reflected conditions were kept at nominal pressure of 17.6 bar with small standard deviation of ± 0.6 bar in ETB tests and 17.9 bar ± 0.3 bar for styrene. The temperature range varied between 1567 K and 1942 K for STY, between 1560 K and 1939 K for ETB.

The following discussion is based on the analysis of the soot optical densities at shocked conditions before the arrival of the rarefaction waves, in particular at two different times, 2 ms ($D_{633nm,2ms}$) and 4 ms ($D_{633nm,4ms}$). The optical densities were chosen instead of the soot volume fractions as independent from the particle refractive index which is of difficult evaluation and which introduces considerable uncertainties in the final qualitative measurements. The induction delay times (τ_{ind}) will also be presented, providing an estimate of the fuel tendency to more or less quickly form the first nascent nanoparticles.

5.7.1 Optical densities

Figure 5-75 contains plots of the measured optical densities versus time for the three analyzed fuels at different temperature conditions. Styrene and ethylbenzene are compared to the reference optical densities reported in [128] for toluene keeping the same initial carbon concentration, temperature, and pressure conditions. All the plots share the same scale for a better comparison. **Figure** 5-75a to c clearly show that 0.07% toluene can reach higher optical densities followed by 0.0613% styrene and 0.0613% ethylbenzene. Toluene as well presents a wider temperature window compared to the other two fuels. A more detailed evolution of the temporal optical densities with the temperature comparing the three fuels can be found in **Figure** 5-75d to **Figure** 5-75i. **Figure** 5-75d exemplifies how at low temperatures (~1565 K), the optical densities are low for all fuels, styrene being the one less prompt to produce soot compared to ethylbenzene and toluene, in the order. Also styrene seems to be the slowest to produce soot at low

temperatures. As the temperature increases the level of soot for all the three fuels significantly increases (**Figure** 5-75e). Specifically, the optical densities for styrene becomes similar to the ones of ethylbenzene at around ~1655 K while the ones for toluene remains higher over the whole time interval. At around ~1710 K the optical densities are still high for all the fuels but at this point styrene starts producing more soot than ethylbenzene, reaching optical densities slightly lower than toluene (**Figure** 5-75f). Moreover, **Figure** 5-75g to **Figure** 5-75i show how toluene and styrene produce soot at similar initial times at high temperatures while at the same time the optical densities start gradually decreasing for the three fuels being ethylbenzene always the slower and the one with lower optical densities.

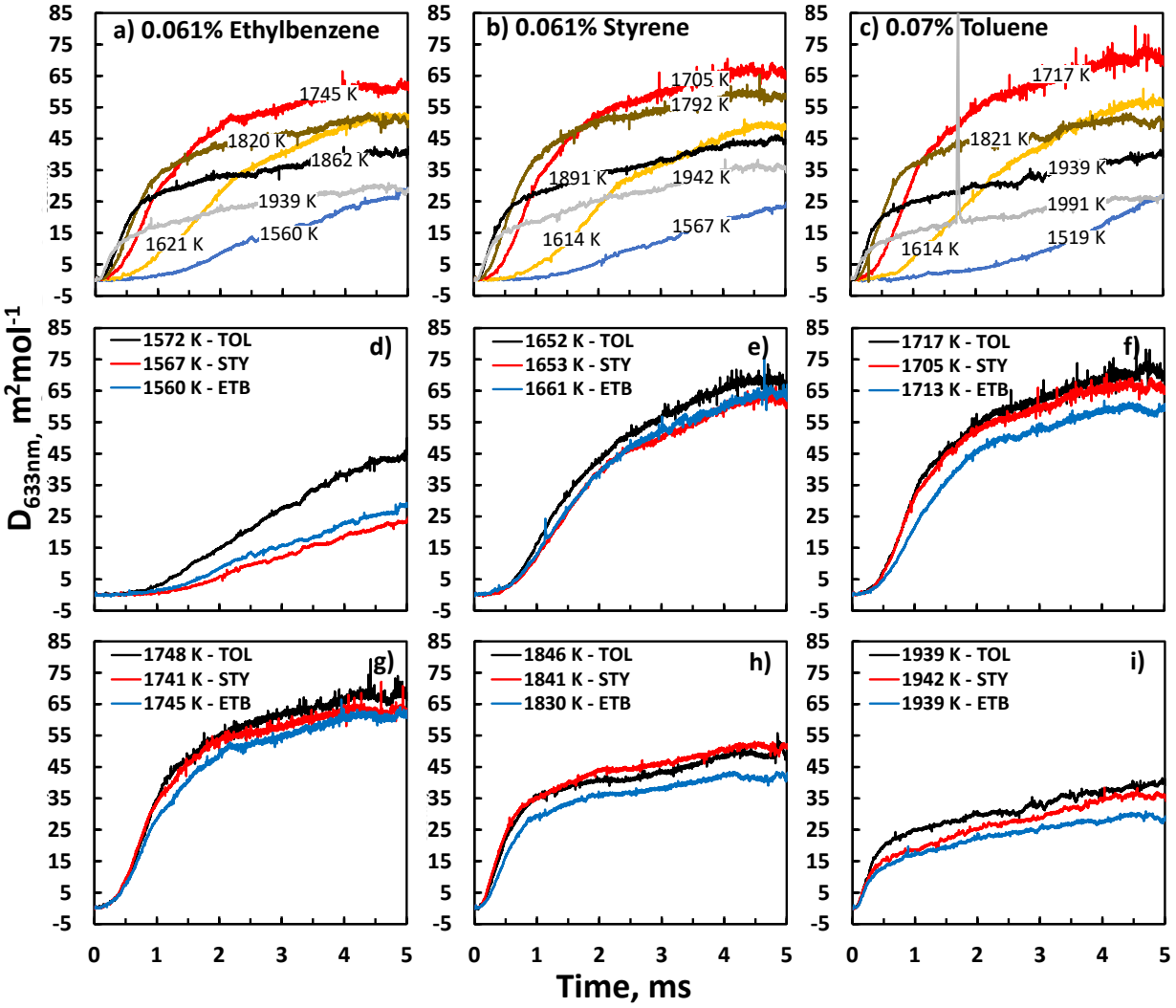

***Figure** 5-75. Optical densities versus time for a) 0.0613% ethylbenzene at different temperatures, b) 0.0613% styrene at different temperatures, c) 0.07% toluene at different temperatures, d) ~1565 K for the three fuels, e) ~1655 K for the three fuels, f) ~1710 K for the three fuels, g) ~1745 K for the three fuels, h) ~1840 K for the three fuels and, i) ~1940 K for the three fuels.*

In a more visual representation, **Figure** 5-76 compares the optical densities vs temperature obtained in this work for ethylbenzene (in blue) and styrene (in red) to the reference ones for toluene (in black). The temperature dependent shape for optical densities obtained at 2 ms and 4 ms are in concordance with the behavior for soot yield previously observed [55], [307]. The optical density plots show that overall, toluene tendency to produce soot particles is higher than styrene and ethylbenzene.

In particular, the graphs can be divided into two regions, the one at relatively low temperatures and the high-temperature region. Below 1600-1650 K, the soot formation and growth is dominated by the reaction between aromatic compounds and radicals, in particular the resonantly stabilized radicals as the benzyl radical. It is for this reason that the order in the optical densities follow the same order as the benzyl radicals concentrations from the thermal decomposition of the three fuels, thus toluene > ethylbenzene > styrene. At higher temperatures, the chemistry is driven by the reactions between small aliphatics and PAH/particles, in particular the HACA mechanisms. In this case, the C/H ratio in the fuel plays an important role. The results for toluene are comparable with the ones from styrene pyrolysis and higher than the ethylbenzene case, ethylbenzene being the fuel with the lower C/H ratio.

Concerning the maximum values of optical densities measured, for the case of ethylbenzene, the peak in the 4 ms profile is located around 1713 K with a value of ~60 m^2/mol. This is lower to the one obtained for toluene which peaks at very similar temperatures with a maximum optical density of ~70 m^2/mol. For the case of styrene, the temperature dependent optical densities measured at 4 ms indicate that the maximum peak is located at around 1705 K-1726 K, similarly to toluene and ethylbenzene, with a value of ~66 m^2/mol, thus between the other two profiles. At 2 ms, the maximum optical densities of toluene and styrene are nearly identical (~52 m^2/mol), while the ones for the ETB case are lower by around 10%.

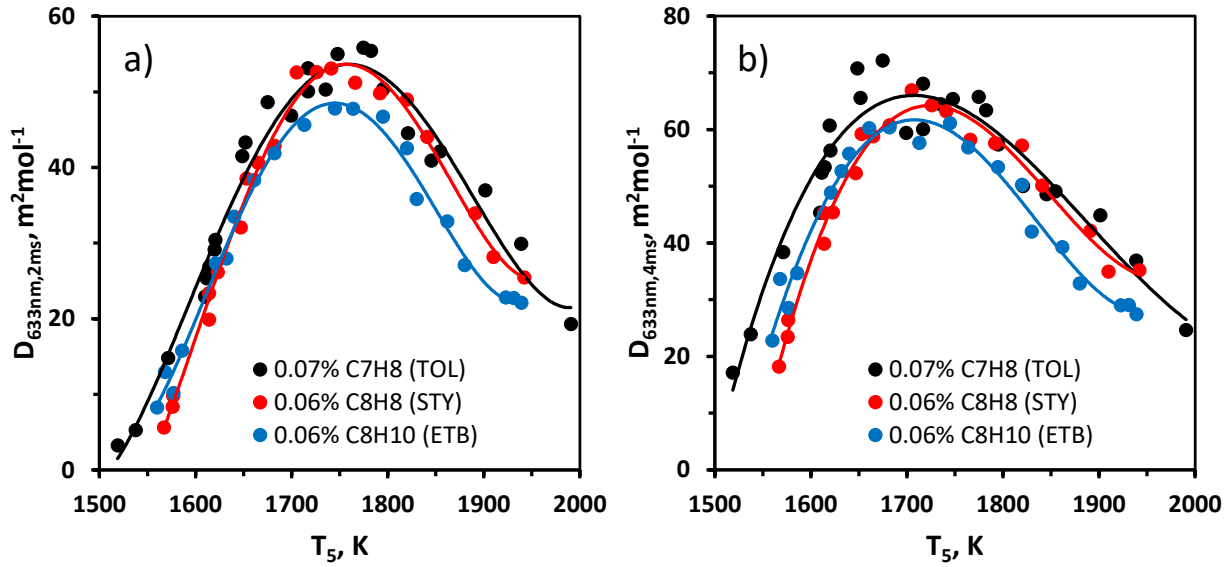

***Figure** 5-76. Optical densities vs temperature for 0.0613% ethylbenzene (blue), 0.0613% styrene (red), 0.07% toluene (black,* [128]*) diluted in argon: a) measured at 2 ms after shock arrival; b) measured at 4 ms after shock arrival.*

5.7.2 Induction delay times

Another important parameter that can be derived from the optical density time-profiles is the induction delay time, which indicates the time necessary for the appearance of the first detectable particles. This parameter is linked to the nucleation phase. The results are presented in **Figure** 5-77. which is divided in four parts for better visualization. **Figure** 5-77a and b present the processed induction delay times in a logarithmic scale vs the inverse of temperature for ethylbenzene and styrene, respectively, while **Figure** 5-77c shows the data previously reported for toluene. The comparison of all the three fuels is presented in **Figure** 5-77d.

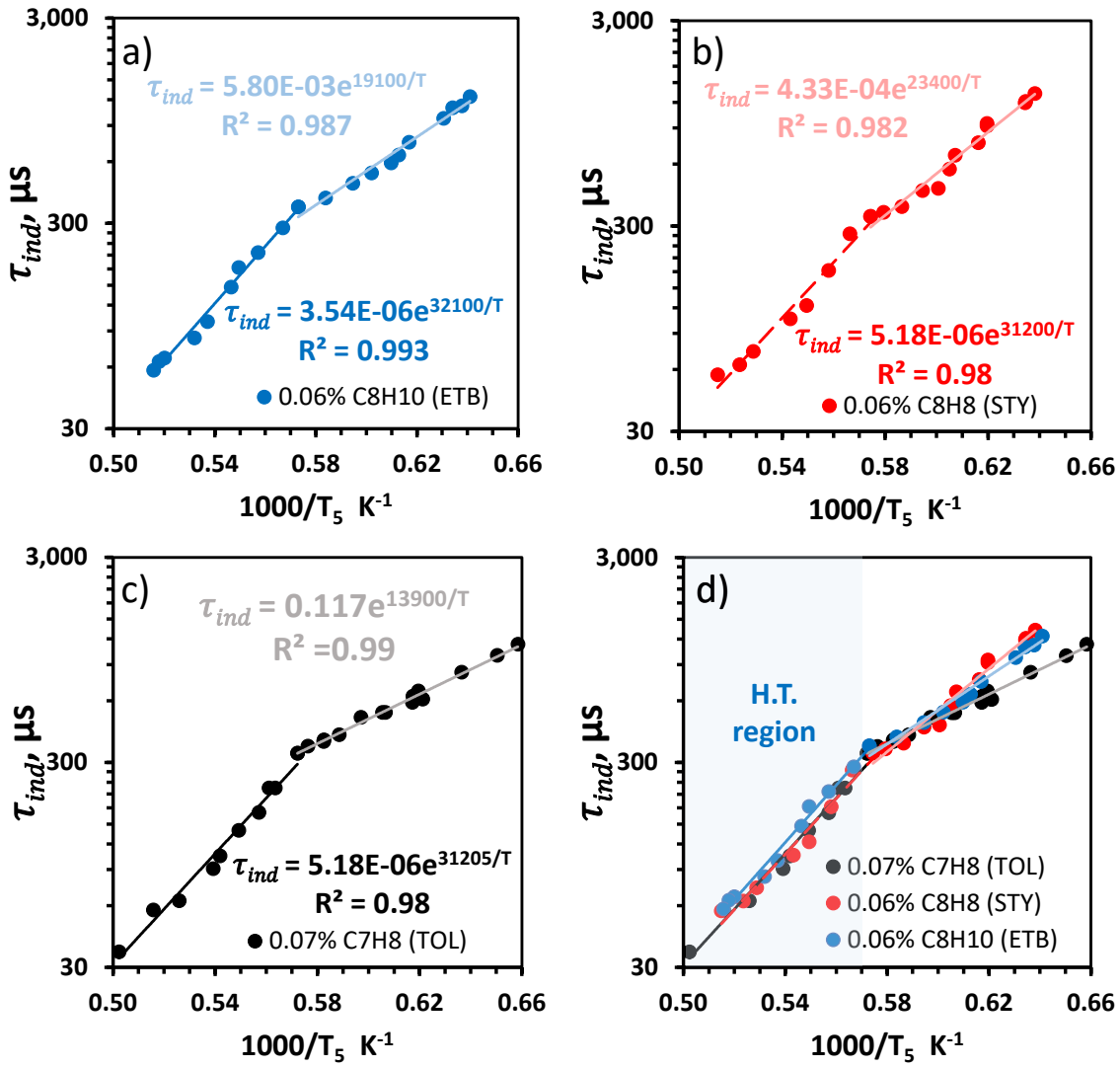

***Figure** 5-77. Induction delay times vs 1000/temperature (1000·K-1) for a) 0.0613% ethylbenzene (blue), b) 0.0613% styrene (red), c) 0.07% toluene (black;,* [128]*), diluted in argon d) comparison between the three datasets.*

For all the cases, there is a double slope in the induction delay time profiles. The temperature at which the change in slope occurs corresponds to the condition where the production of soot is maximized (1720 K - 1750 K). The reason for the presence of the two regions is linked to the different mechanisms governing soot formation at low and high temperatures, i.e. aromatic-aromatic recombination and aromatic-aliphatic reactions, respectively. The experiments have been fitted with exponential curve in Arrhenius form [118]. The slope of the curve is proportional to the activation energy of the global process (slope multiplied by the gas constant R). In the high-temperature regions, the three activation energies are very similar, 63±1 kcal/mol. On the other hand, the activation energies in the low temperature regions increase from 28 kcal/mol to 38 kcal/mol and 47 kcal /mol from toluene to ETB and STY, respectively. Again, as for the analyses performed on the optical densities, the different slopes are related the concentrations of the benzyl radical availability in the product pools, the higher the benzyl mole fraction the lower the induction delay times, thus the higher the propensity to form the primary particles.

When comparing the three curves in **Figure** 5-77d, other differences are perceptible. Ethylbenzene induction delay times in the high temperature region, are slightly higher than the ones of toluene and styrene despite the similar slopes. This can be linked to the C/H ratio, as ETB is the fuel among the three which has the lowest ratio. Toluene and styrene curves are characterized by similar induction delay times in this region. The curves will then cross towards the low-temperature region, where the different slopes lead to the above-mentioned ranking, $\tau_{STY} > \tau_{ETB} > \tau_{TOL}$. For example, in ETB pyrolysis the maximum value in induction delay times is 1243 µs at 1560 K, while at similar conditions (T_5 = 1571 K) the induction delay time for toluene is 827 µs, thus around 30% lower.

5.7.3 Preliminary kinetic modeling considerations

Work is ongoing at ICARE with the goal of developing a detailed soot chemical kinetic model for particle chemistry from pyrolytic reactions of aromatic fuels. In particular, the results show that toluene has a higher propensity to form soot than styrene and ethylbenzene. In general, two factors influence the soot chemistry based on the data analyses, i) the formation of resonantly stabilized radicals from the thermal decomposition of the fuel molecule in the low-temperature region; ii) the C/H ratio in the high-temperature region. The datasets presented in the previous section provide essential information for improving our understanding of the different processes responsible for soot formation from key fuels, depending on the temperature conditions and fuel structure/chemistry, and for the estimation of the corresponding kinetic parameters.

Preliminary considerations can be withdrawn from the current ICARE PAH model developed for simulating the PAH chemistry from pyrolysis reactions of aromatic fuels. The model does not contain the detailed chemistry of the particles, but only the lumped species BIN1A and BIN1B, which corresponds to C20 species with different C/H ratios. On the other hand, the bigger BINs which represent the soot particles will build upon the BIN1, thus they will be proportional to the BIN1 concentrations. **Figure** 5-78a contains the simulation results for BIN1B for the three fuels, at representative temperature and pressure conditions of 1750 K and 18 bar, respectively, and fuel concentrations as in the experiments of previous sections. The simulations are not capable to reproduce the experimental behavior as styrene is predicted to produce more particles over the entire reaction time compared to toluene and ethylbenzene. On the

other hand, **Figure** 5-76 indicates that at these conditions, styrene and toluene should produce similar soot mole fractions while ETB lower values.

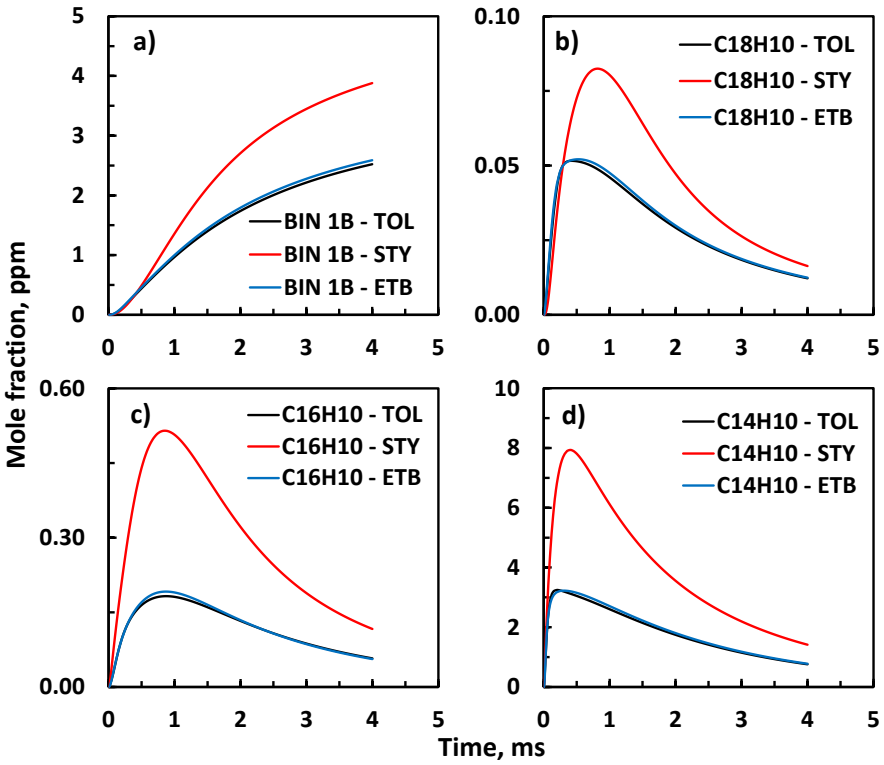

***Figure** 5-78. Simulation results using the ICARE PAH model for a) BIN1B b) $C_{18}H_{10}$, c) $C_{16}H_{10}$, c) $C_{14}H_{10}$. For the three fuels, at representative temperature and pressure conditions of 1750 K and 18 bar, respectively, and fuel concentrations as in the experiments of previous sections.*

Further model developments are then required. In particular, in the three cases, the reaction pathways to the BIN1s species are common, based on rate-of-production analyses. The main formation mechanism is the HACA route $C_{16}H_{10}$ / $FC_{16}H_{10}$ → $C_{18}H_{10}$ → BIN1B, where $C_{16}H_{10}$ is pyrene and $FC_{16}H_{10}$ fluoranthene, while $C_{18}H_{10}$ the lumped C18 species. A third pathway to $C_{18}H_{10}$ involves the reaction between the indenyl radical C_9H_7 and the naphthyl radical $C_{10}H_7$ (global reaction based on CRECK model from Politecnico di Milano). $C_{16}H_{10}$ is mainly formed through HACA step from $C_{14}H_{10}$ (phenanthrene), while $FC_{16}H_{10}$ derives from the reactions between $C_{13}H_9$ ($C_{10}H_7$+C_3H_3 main reaction to $C_{13}H_{10}$) and C_3H_3 and the isomerization of $C_{10}H_7C_6H_5$ (which is the result of the C10+C6 reactions). Among these intermediate species, two main pathways are responsible for the phenanthrene production: i) the one starting from the reaction between the phenyl radical and phenylacetylene to form diphenylacetylene, which then isomerize to phenanthrene; ii) the pathway $C_{13}H_9$+CH_3 → $C_{13}H_9CH_3$ → $C_{13}H_8CH_2$ → $C_{14}H_{10}$. Considering all these main mechanisms, the two main PAH building blocks are naphthalene and indene, from which $C_{10}H_7$ and C_9H_7 derive. Naphthalene also derives from reactions of the indenyl radical with the methyl radical, following

the pathway $C_9H_7+CH_3 \rightarrow C_9H_7CH_3 \rightarrow C_9H_6CH_2 \rightarrow C_{10}H_8$. Indene is mainly formed from the reaction of benzene/phenyl with the C3 intermediates, mainly the propargyl radical.

As mentioned above, these mechanisms are responsible for BIN1 formation from the three fuels, with different relative importance based on the specific fuel chemistry. In particular, the enhanced production of BIN1B from styrene is due to the pathway starting with the phenylacetylene reaction with the phenyl radical to form first diphenylacetylene, and then phenanthrene through isomerization. The subsequent HACA steps to the BIN species are quite relevant compared to the ethylbenzene and the toluene cases. Thus, the future model developments will need to address the question if the latter pathway is overestimated or if other pathways from toluene and ethylbenzene needs to be added/enhanced. The behavior of ethylbenzene pyrolysis compared to toluene will have also to be analyzed in detail to match the experimental findings.

6 Conclusions

Our fundamental understanding on the complex chemical and physical processes involved in soot formation and growth needs to be refined in order to develop predictive chemical kinetic models that can be used for the design of next-generation combustion devices. Recent efforts have focused the attention on improving the conventional experimental techniques to allow the measurement of soot precursor molecules, the so-called polycyclic aromatic hydrocarbon (PAH), and to evaluate the solid-phase chemistry. However, the conventional techniques present some limitations that can be overcome only by developing innovative solutions based on up-to-date diagnostics.

This thesis work used three shock tubes of different scales coupled to both laboratory-based and synchrotron-based techniques, to experimentally investigate PAH and soot particle chemistry from key real and surrogate fuel components and intermediates. In particular, a fully functional, new miniature high repetition rate shock tube (ICARE-HRRST) is here presented for the first time. The ICARE-HRRST was developed based on previous design by Tranter and Lynch (ANL-HRRST) in order to access double imaging photoelectron/photoion coincidence spectroscopy (i^2PEPICO) detectors located in different European synchrotron facilities (SOLEIL and SLS). Its design and operation were discussed in detail together with the characterization of its performances. In particular, the miniature shock tube, characterized by an internal diameter of 8 mm, is built in a modular fashion that allows length variation from ~84 cm. The test gas and product gases are loaded/evacuated to/from the driven section of the shock tube by means of five custom made pneumatic valves (one to fill and four to evacuate) which are key components of the system. The fill valve used to introduce the mixtures is equipped with two reservoirs to ensure that pressure P_1 is nearly constant during continuous operation. The two reservoirs are connected to a 6 L tank that is automatically filled with new mixture when needed. The fresh mixture is prepared with the use of three mass flow controllers and a bubbling system. The shock tube is equipped with 8 pressure transducers equally spaced and located along the driven section axis in order to measure time passage of the shock wave, while velocity is extrapolated to the end wall in order to compute T_5 and P_5 by solving the conservation equations. The shock tube can be equipped at the end wall either with a PCB pressure transducer to measure pressure time-histories or with a stainless-steel divergent nozzle coupling by molecular beam sampling to synchrotron detectors. The automatic operation of the HRRST is guaranteed by a LabVIEW software which also manages the data acquisition. The ICARE-HRRST can operate at rates up to around 1.5 Hertz.

The performances of the HRRST system were characterized with pressure time history measurements by a PCB transducer located at the end-wall. The results highlighted how larger dP/dt's (due to boundary layer growth behind reflected shock waves) compared to conventional systems are present in the mini shock tube experiments which is the main drawback of the size reduction. This is not detrimental for the quality of the results as pressure time-histories can be accounted for during the kinetic simulations. The laboratory experiments demonstrated excellent reproducibility of the experimental conditions, nor only for the temperature T_5 and pressure P_5, with standard deviations usually less than 20 K and 0.15 bar, respectively, but also for the pressure histories. This is an essential for the subsequent signal averaging required when using low S/N ratio diagnostics as the synchrotron ones.

The coupling between the HRRST with i^{2}PEPICO detectors at SOLEIL and PSI has been carried out with success, although experimental results of PSI campaign were only preliminary and they are not presented in this thesis. The mechanical alignment between the HRRST and the SAPHIRS end station located in the branch A of VUV monochromator DESIRS beamline at SOLEIL synchrotron was one of the main challenges together with the HRRST safe operations inside the vacuum chamber. A differential vacuum chamber separated the main chamber, where the HRRST is inserted, and the DELICIOUS III i^{2}PEPICO mass spectrometer vacuum chamber for efficient products extraction reducing risk of damaging the mass spectrometer instruments. The optimization of the experimental technique was obtained empirically, including selection of the best nozzle and skimmers models as well as the distance between them, for safe pressure levels inside the mass spectrometer chamber during HRRST operation and good quality molecular beam with enough signal levels. The alignment between the HRRST nozzle and the SAPHIRS skimmers was also refined with the design of a *birdcage/clamp* system and the use of high precision aluminum rails for accurate insertion/extraction of the HRRST with reproducibility of the alignment. The coupling between the ICARE-HRRST and the X04DB SLS/VUV beamline is also presented, including main challenges and future developments.

The first experimental campaign at SOLEIL was focused on ethanol pyrolysis, the current main biofuel. In general, four experimental conditions including more than 54 000 experiments were discussed demonstrating several functionalities of the HRRST/i^{2}PEPICO coupling in a wide range of conditions of temperatures (1232 K – 1525 K), pressures (6.2 bar-7.5 bar), fuel concentrations (0.25%-2.7%), repetition rates (1Hz-1.5Hz), and photon energies (10.0 eV-11.0 eV). The spectral data was recorded by using *pulsed* data acquisition mode at pre-shock and post-shock conditions. Simulations performed with CRECK chemical kinetic model helped the interpretation of the experimental results showing the great potential of this technique for the kinetic study of complex mixtures of isomeric gaseous species. For each experimental dataset, ion/electron time of flight matrices and mass-selected photoelectron images could be obtained, which allowed the extraction of mass spectra, time kinetic profiles, and, additionally, mass-selected photoelectron spectra (PES), unique feature for isomeric species identification.

Nevertheless, two challenges were identified in order to improve the experimental capabilities. First, the need to obtain quantitative datasets of temporal species profiles was highlighted in the first campaign at SOLEIL, despite the value of the qualitative information. Specifically, the quantitative measurements must take into consideration the pressure variations inside the mass spectrometer chamber in order to correct the signal from the dynamic behavior of the shock tube. The other problem concerns the limited PES signal levels in the *pulsed* data acquisition mode, even with optimized alignment. This limitation makes difficult the identification of several isomers, especially for minor species like PAHs.

In order to overcome these limitations, new solutions were implemented in the following campaign at SOLEIL focused on toluene, ethylbenzene and styrene pyrolysis. More than 300 000 HRRST experiments were realized in this campaign at average temperature of ~1350 K, pressure of ~6.6 bar and two photon energies: 10 eV using the *pulsed* acquisition mode, obtaining kinetic profiles including for the fuel molecule and main products, and 8.5 eV with the *continuous* mode, focused on the identification of the PAH molecules. First, an external calibration technique to solve the problematic of pressure fluctuations inside the mass spectrometer chamber was developed allowing the conversion of the raw data into concentration profiles. The method utilizes CO_2 as an external standard gas to correct for initial pressure rise in the mass spectrometer due to the inherent dynamic behavior of the HRRSTs and the following

pressure-time history non-idealities. The validity of the method was evaluated based on experiments for the thermal decomposition of toluene and ethylbenzene. The corrected profiles for fuels and main products resulted in excellent agreement with simulations obtained employing the most updated version of the ICARE PAH model, demonstrating the reliability of the procedure. The external standard method is a versatile technique to obtain kinetic information from HRRST/TOF-MS experiments conducted at synchrotrons, including the HRRST/i^{2}PEPICO coupling.

In addition, the above mentioned *continuous* data acquisition mode of the i^{2}PEPICO detector was employed and exploited in order to obtain higher signal levels. This mode does not allow for extracting kinetic information because the information is acquired continuously without a reference to the shock wave arrival. However, well defined mass spectra and sharper PESs were obtained for large PAHs allowing the isomer identification which could not have been obtained without i^{2}PEPICO.

The mass-selected identification of a large number of polycyclic aromatic hydrocarbon compounds produced from toluene pyrolytic decomposition using the HRRST/i^{2}PEPICO configuration was presented and compared to experimental results previously reported using the ICARE single pulse shock tube coupled to GC/GC-MS. This was possible thanks to the development of a new analytical methodology that implements ab-initio quantum chemistry calculations on the detailed spectral characteristics of possible isomers. Based on the results and the current kinetic knowledge, several common pathways were identified, including the HACA route, the addition of resonantly stabilized radicals (C_3H_3, C_7H_7), addition of the phenyl radical and cyclization, methylation, and diacetylene addition to aromatic radicals. In addition, the detection of large PAH products up to m/z 426 was possible, providing qualitative information on the growth to the large soot precursors. The information constitutes a substantial progress for the understanding of the first gas-phase steps of soot formation chemistry, complementing the data obtained with conventional laboratory-based techniques in terms of isomer identification and detection of large molecules. These new results also illustrate the capabilities of such innovative experimental technique that cannot be achieved with regular analytical studies in the laboratory.

This exhaustive study using the ICARE-HRRST/i^{2}PEPICO technique was extended to other important soot intermediate molecules and fuel components. Specifically, the results of the pyrolytic decomposition from ethylbenzene (C_8H_{10}) and styrene (C_8H_8) were compared with respect to the toluene data in order to highlight the influence of the fuel structure on the PAH growth. These novel results complement the experimental databases available in the literature from laboratory-based conventional techniques, for improved understanding of the complex chemistry from alkylated hydrocarbons and styrene pyrolysis and the validation of detailed chemical kinetic models for soot precursor chemistry.

Moreover, a comparative study between the synchrotron-based shock tube techniques and the conventional laboratory-based shock tube techniques was realized in the frame of this thesis in order to highlight the complementarity of the different set-ups. Specifically, the first pyrolytic study on styrene decomposition using the ICARE single pulse shock tube coupled to GC/GC-MS was presented together with preliminary model simulations for products up to four rings (species profiles). It was illustrated how the information obtained using the HRRST coupled to i^{2}PEPICO detector can complement and confirm the results obtained with well-stablished conventional techniques, but still giving more insight in the formation chemistry of large PAH species. The results constitute one important contribution to the field of soot chemistry because of the important role that styrene plays on the formation of PAHs from typical

real and surrogate fuels. Additionally, these new data, together with the results on toluene and ethylbenzene from the literature, provide the benchmark for model validation, as well as a reference for comparison with the HRRST results. Finally, shock tube/laser extinction time-history data from ethylbenzene and styrene pyrolysis are compared to previous toluene data, serving together with PAH data to clarify the main mechanisms related to soot formation from these fuels, for future chemical kinetic model developments, part of the ongoing activities of the ICARE group.

Appendix

A 1. *Isometric views of part of the facility showing the two plate P1 and P2 assembled for removal of the shock tube from SAPHIRS (left) and configuration with only P1 as during experiments (right).*

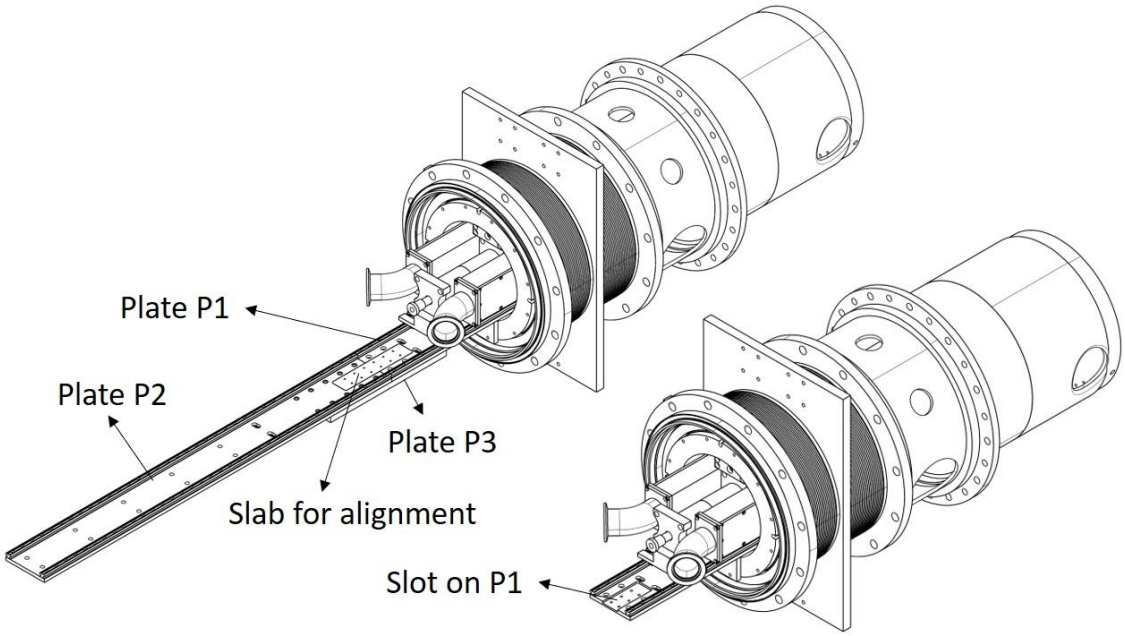

A 2. *2.7% ethanol in argon, $T_{5,avg}$ = 1232 K, $P_{5,avg}$ = 7.4 bar, photon energy = 11.0 eV*

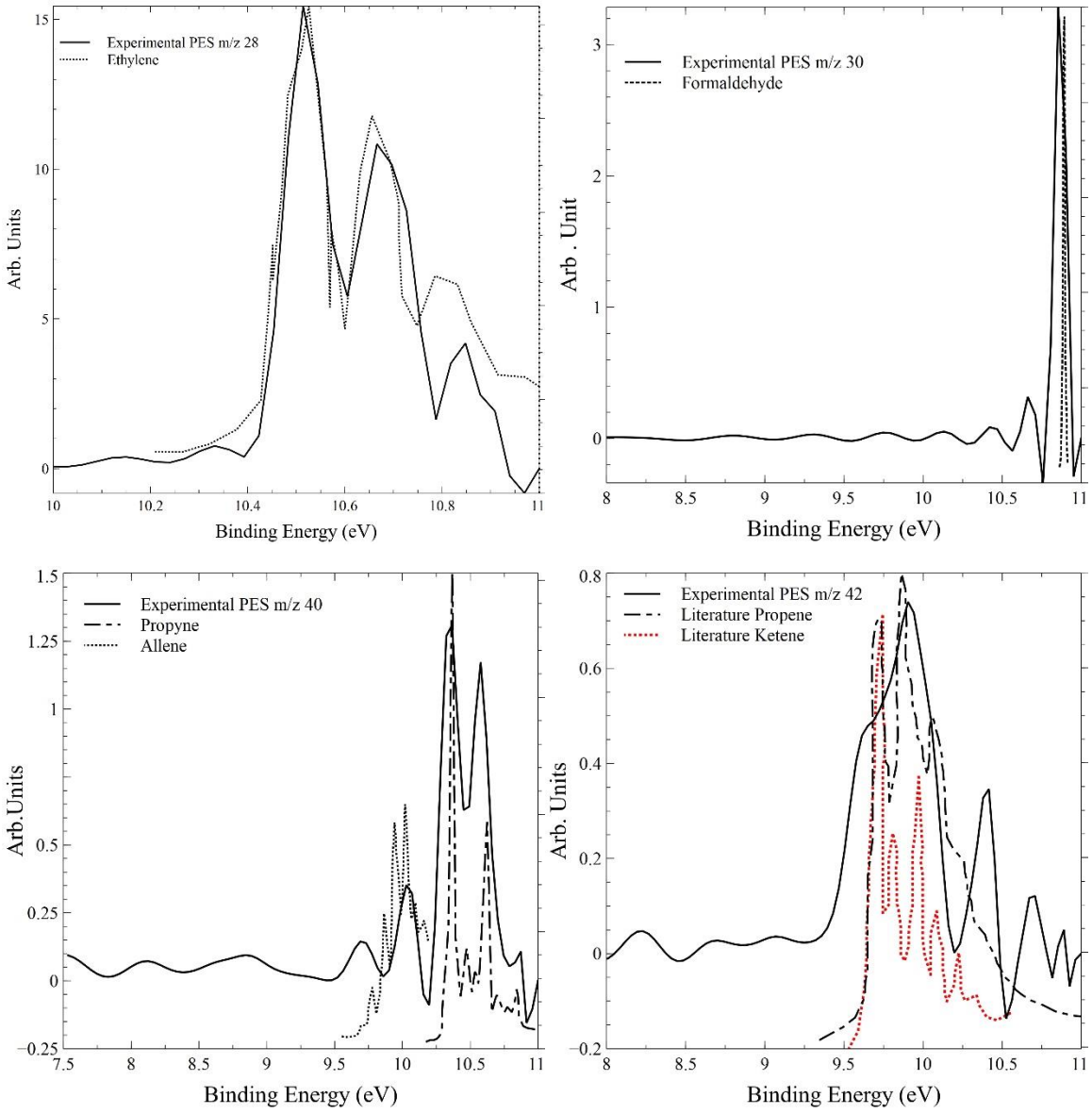

Photoelectron spectrums of product molecules with mass ranging from 28 to 42.

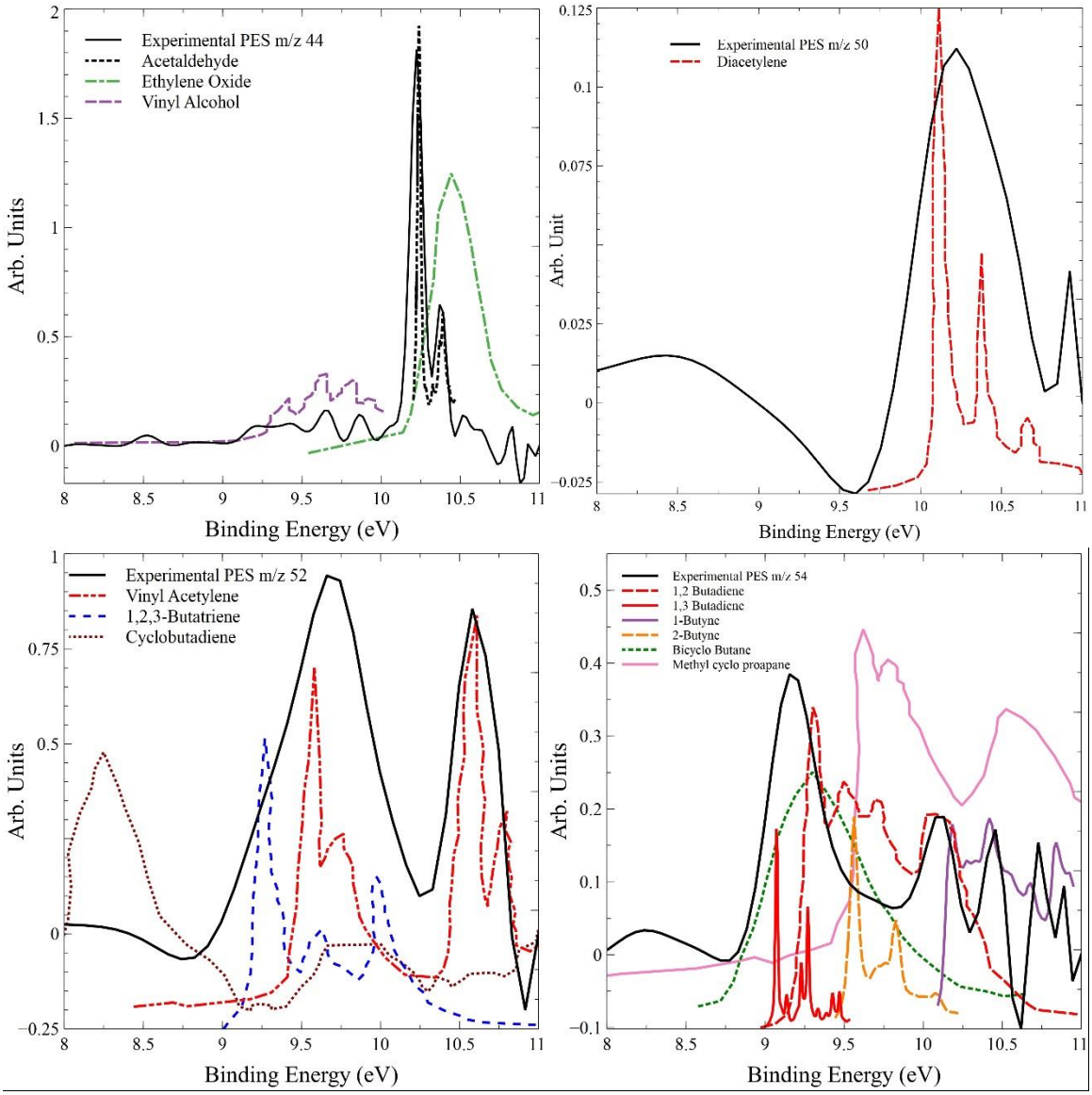

Photoelectron spectrums of product molecules with mass ranging from 44 to 54.

A 3. *2.7% ethanol in argon, $T_{5,avg}$ = 1234 K, $P_{5,avg}$ = 7.5 bar, photon energy = 10.0 eV*

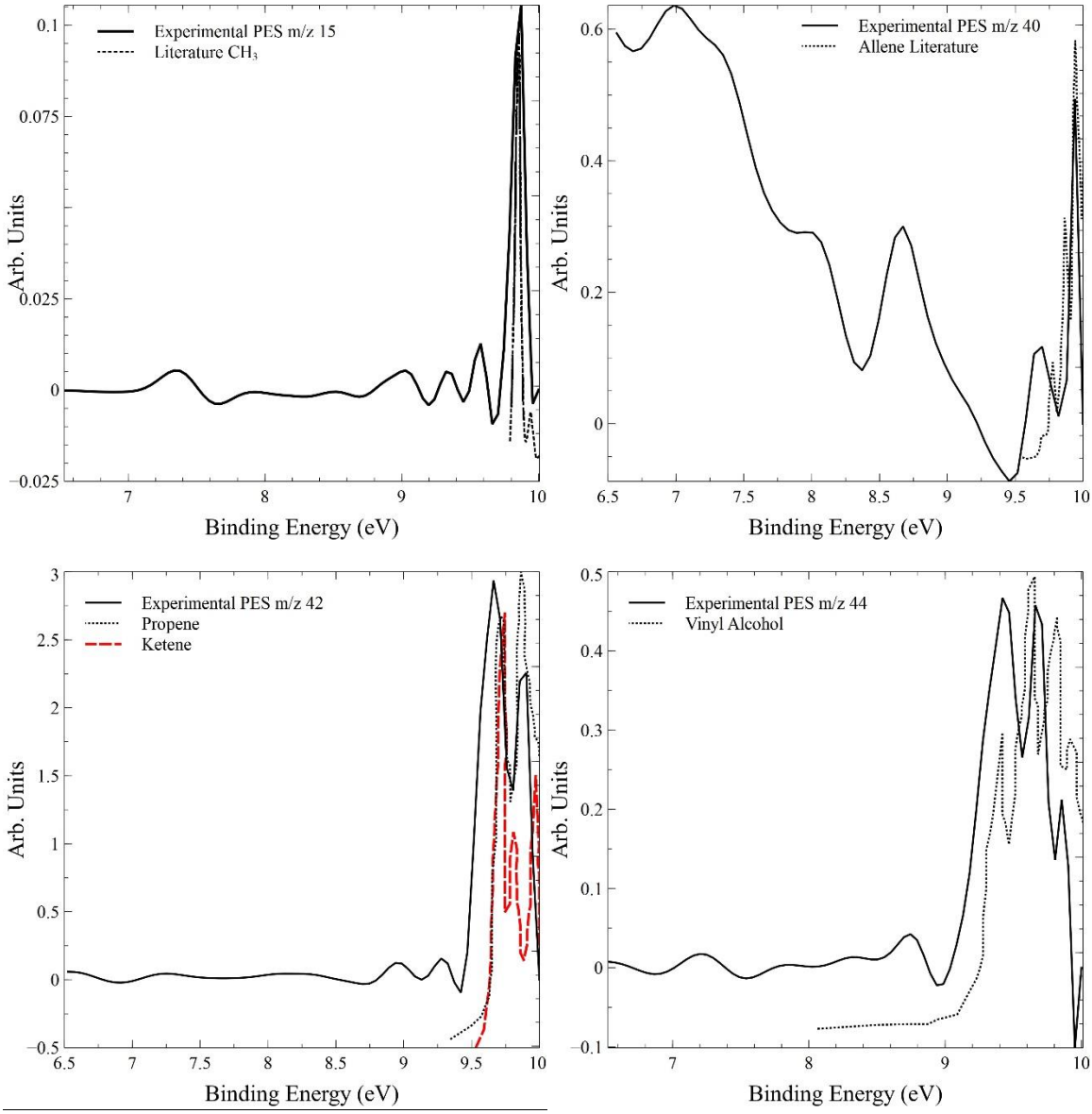

Photoelectron spectrums of product molecules with mass ranging from 15 to 44.

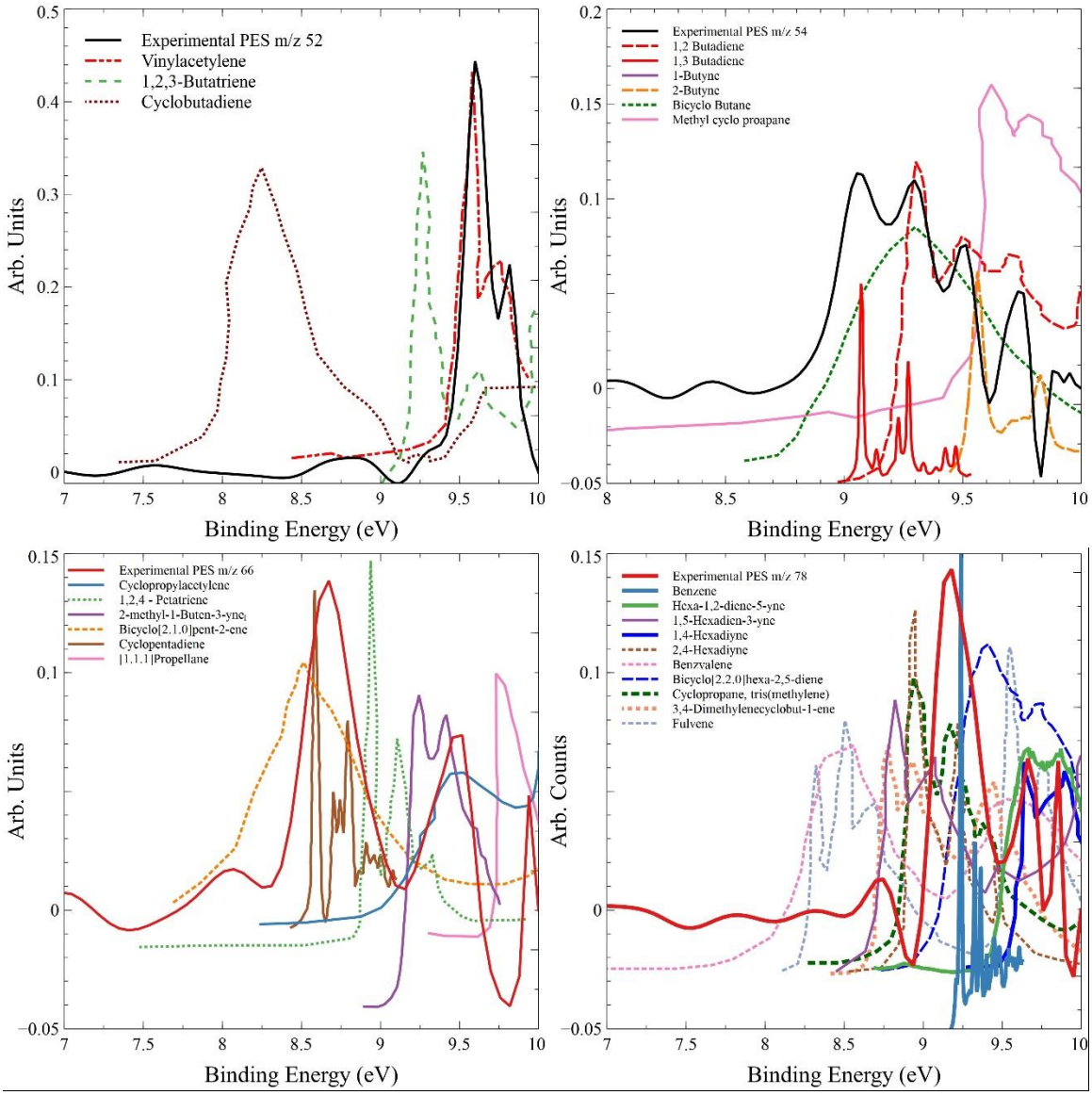

Photoelectron spectrums of product molecules with mass ranging from 52 to 78.

A 4. *2.7% ethanol in argon, $T_{5,avg}$ = 1525 K, $P_{5,avg}$ = 7.5 bar, photon energy = 10.0 eV*

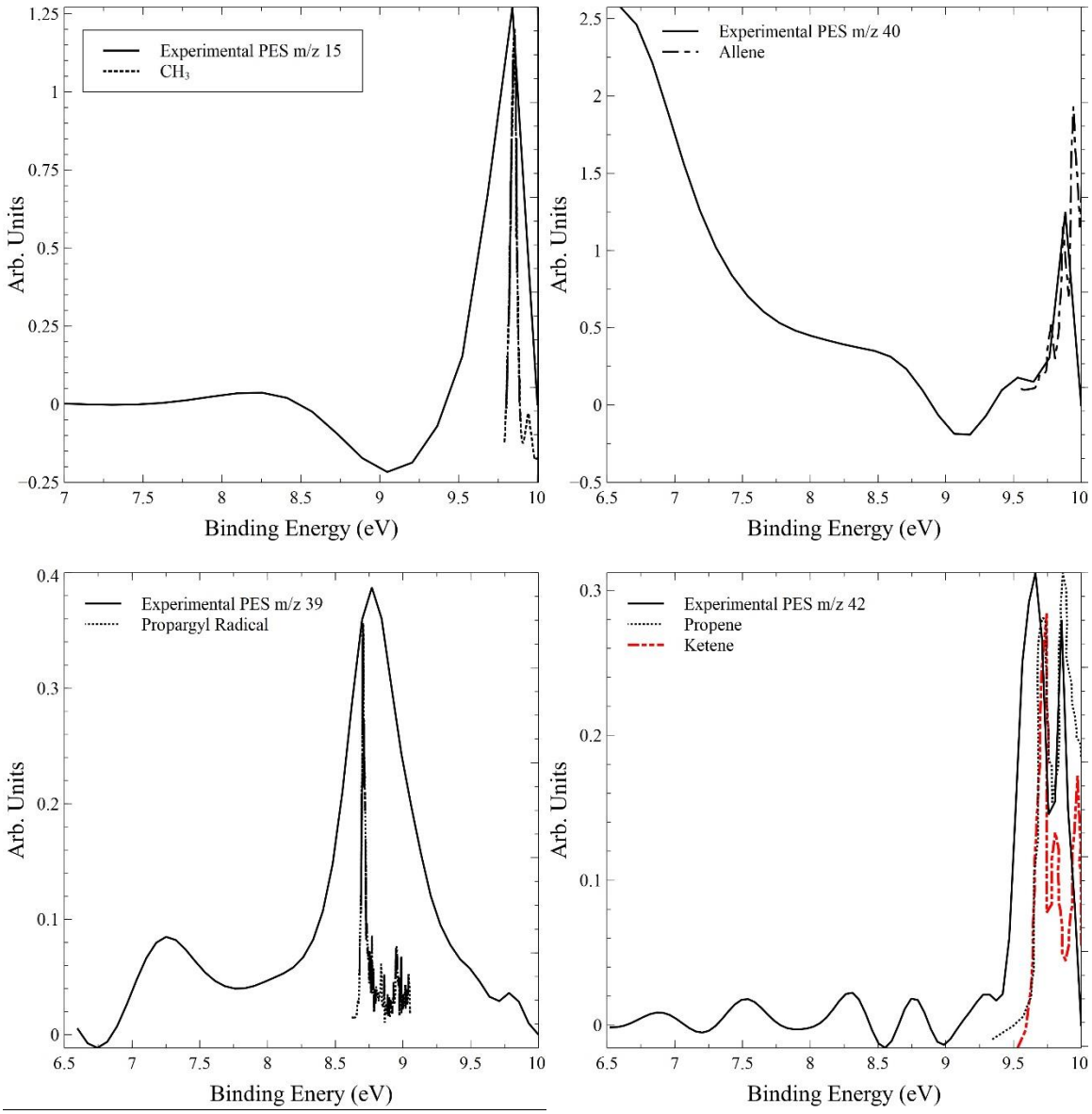

Photoelectron spectrums of product molecules with mass ranging from 15 to 42.

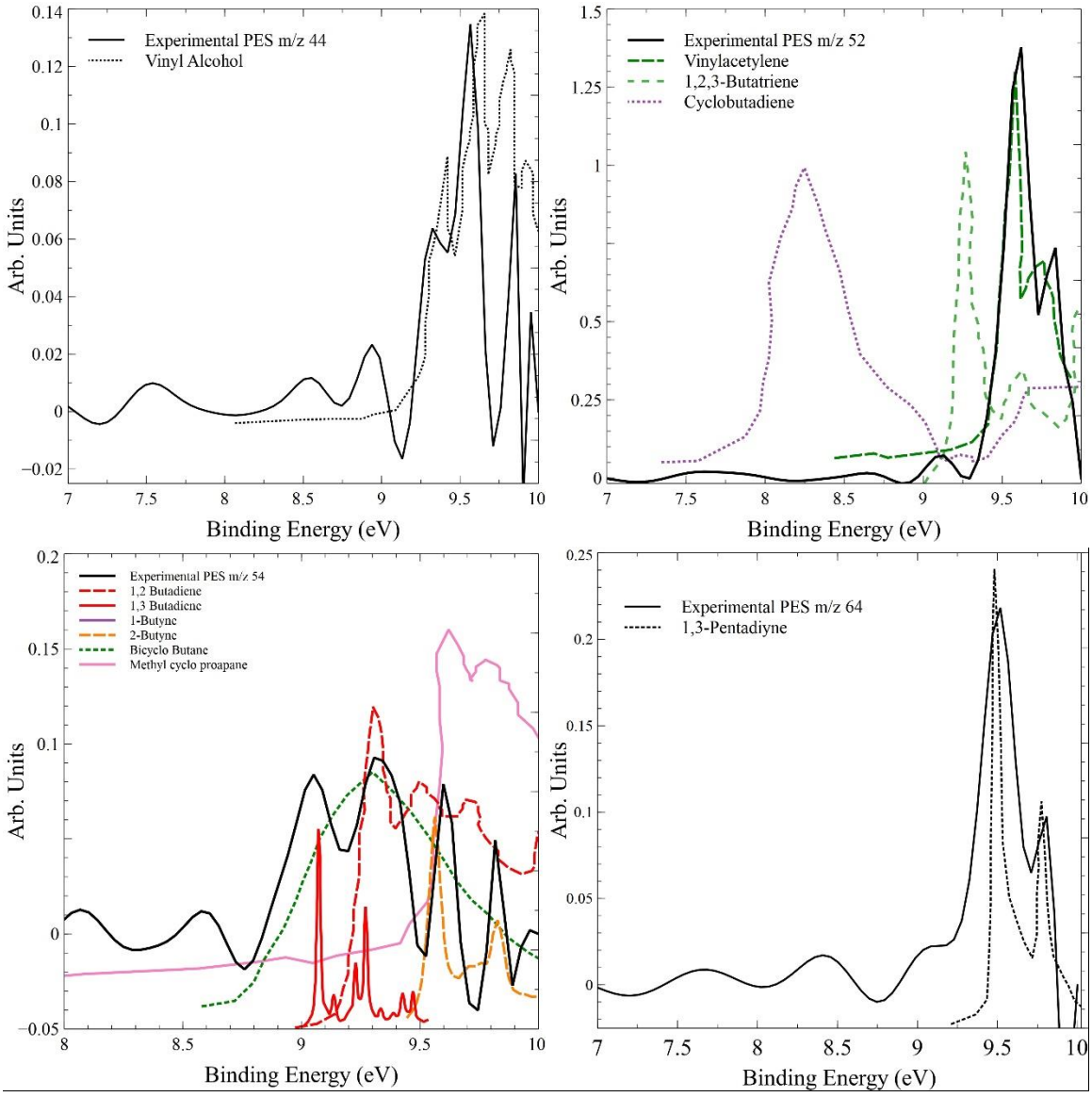

Photoelectron spectrums of product molecules with mass ranging from 44 to 64.

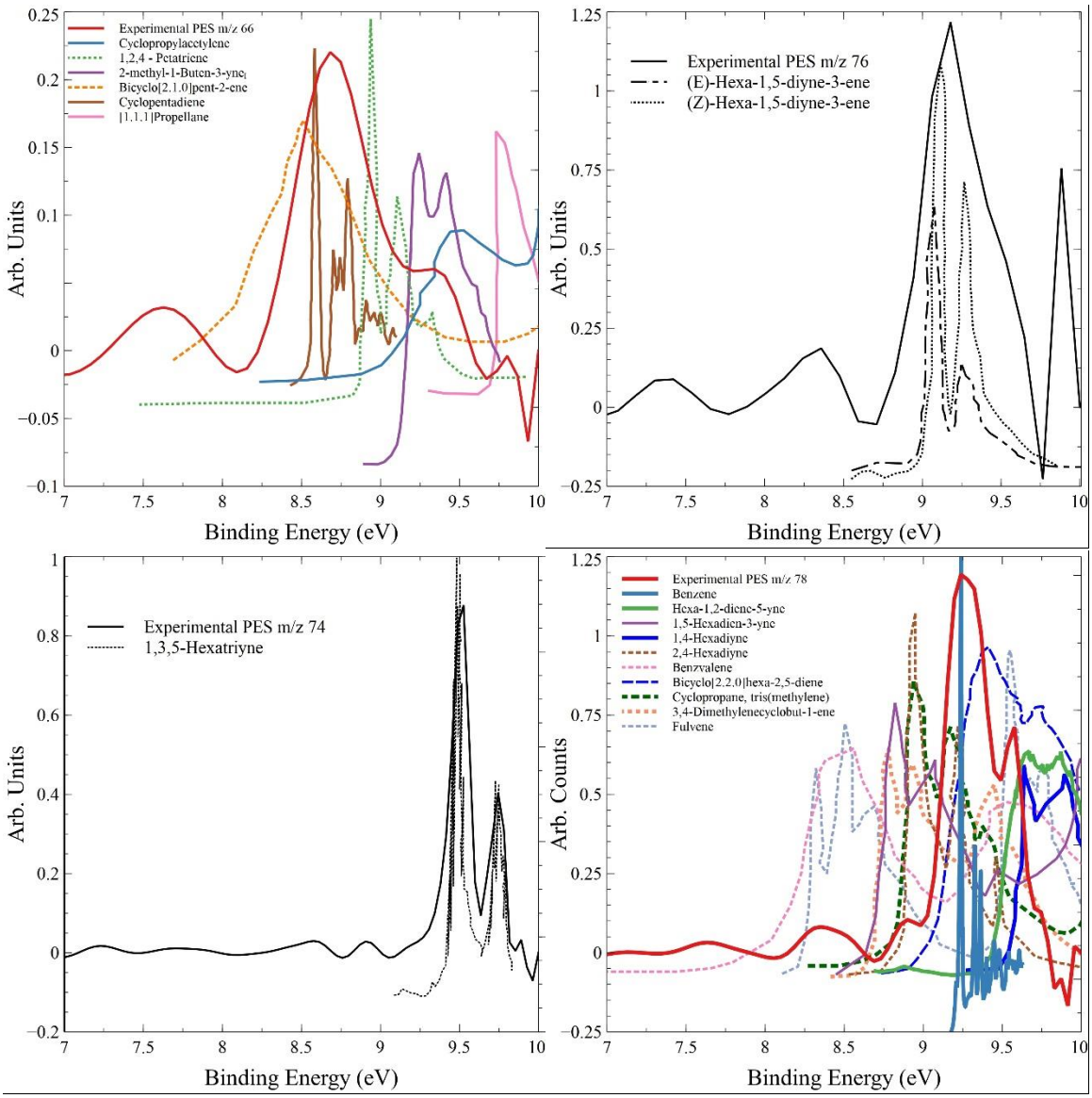

Photoelectron spectrums of product molecules with mass ranging from 66 to 78.

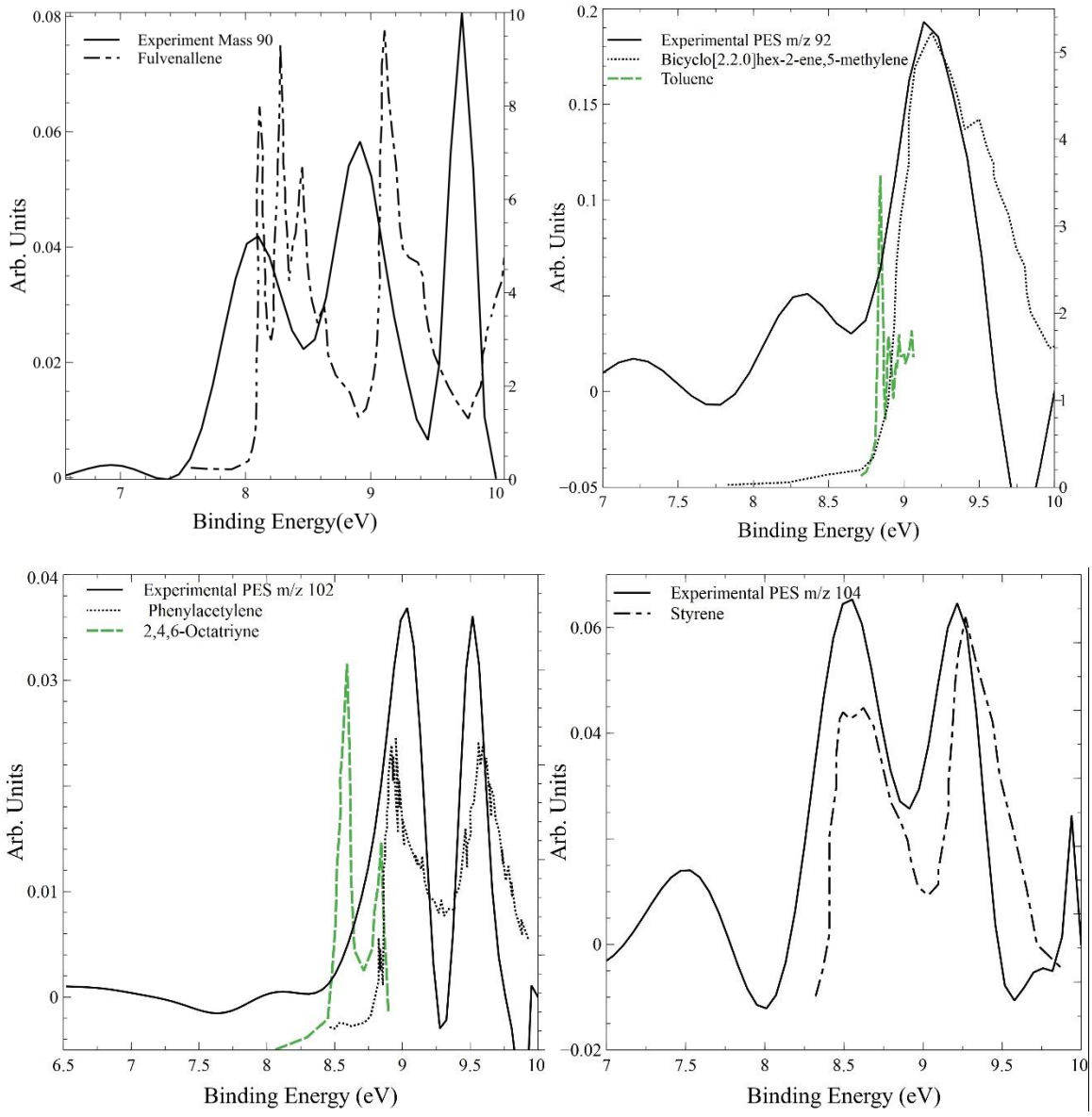

Photoelectron spectrums of product molecules with mass ranging from 90 to 104.

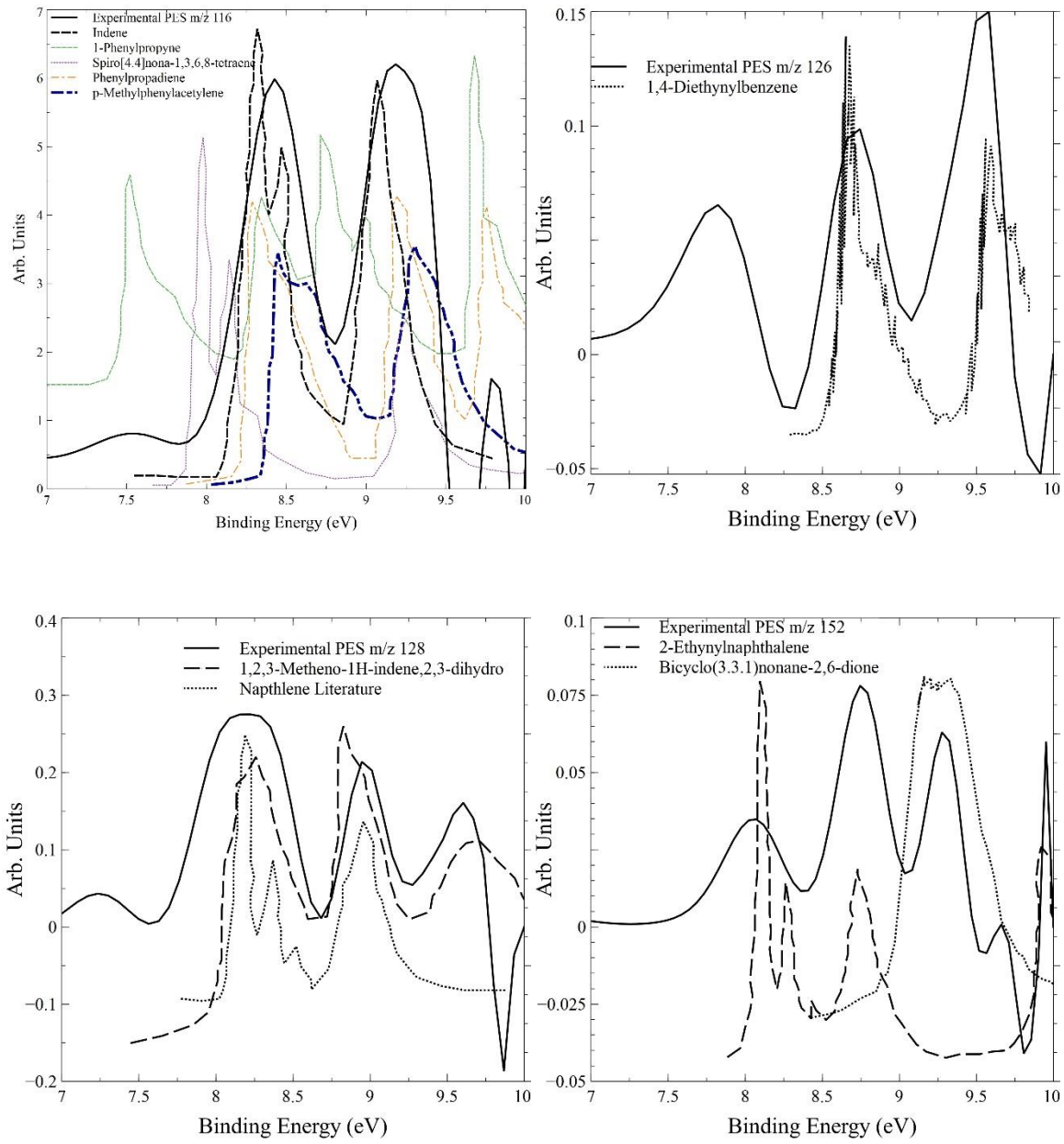

Photoelectron spectrums of product molecules with mass ranging from 116 to 152.

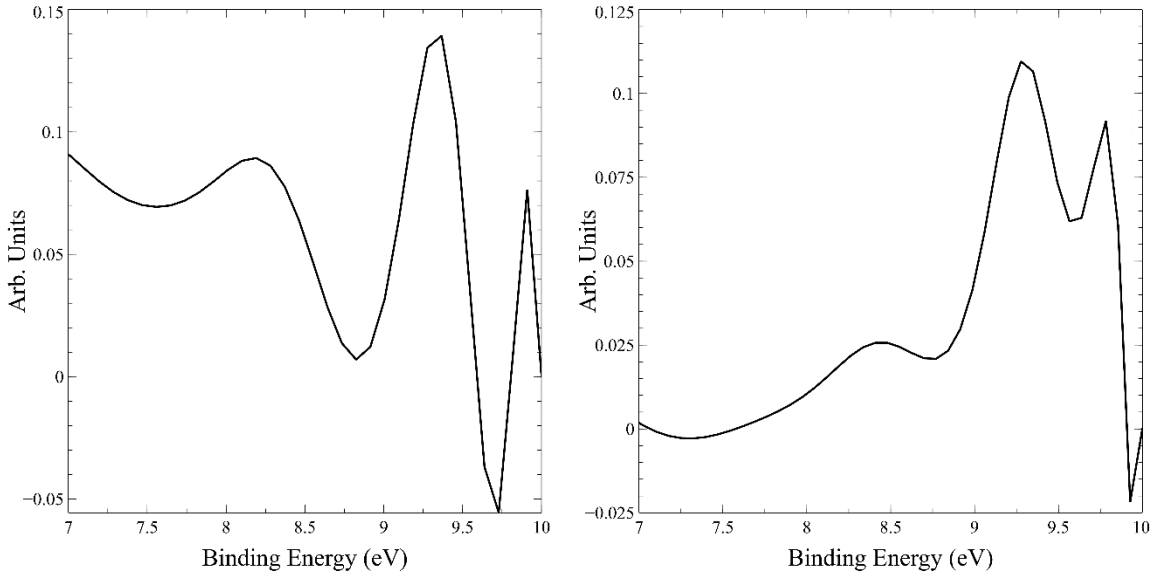

Experimental PESs corresponding masses 38 (left) and 98 (right)

A 5. *0.25% ethanol in argon, $T_{5,avg}$ = 1354 K, $P_{5,avg}$ = 6.2 bar, photon energy = 11.0 eV*

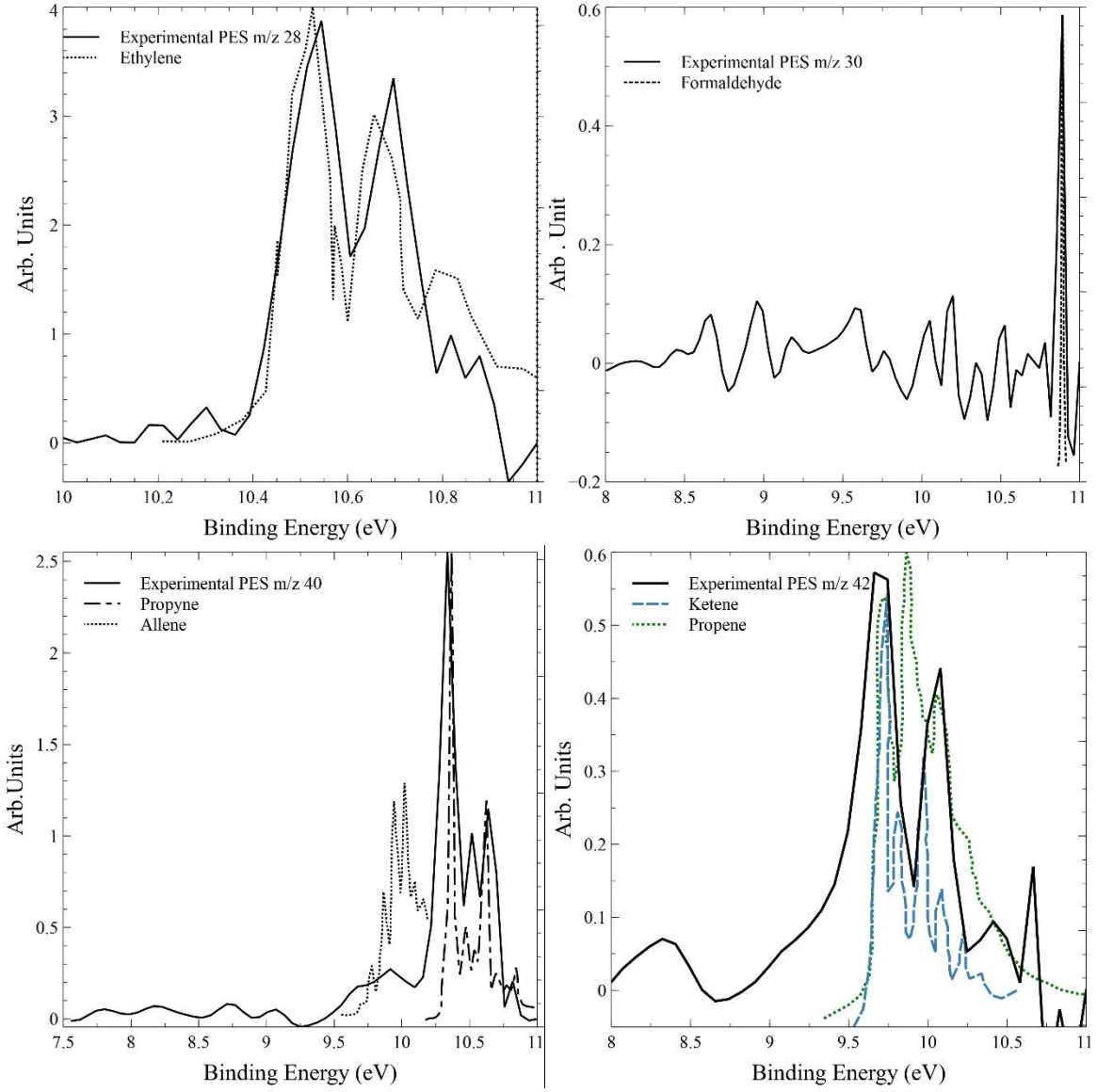

Photoelectron spectrums of product molecules with mass ranging from 28 to 42.

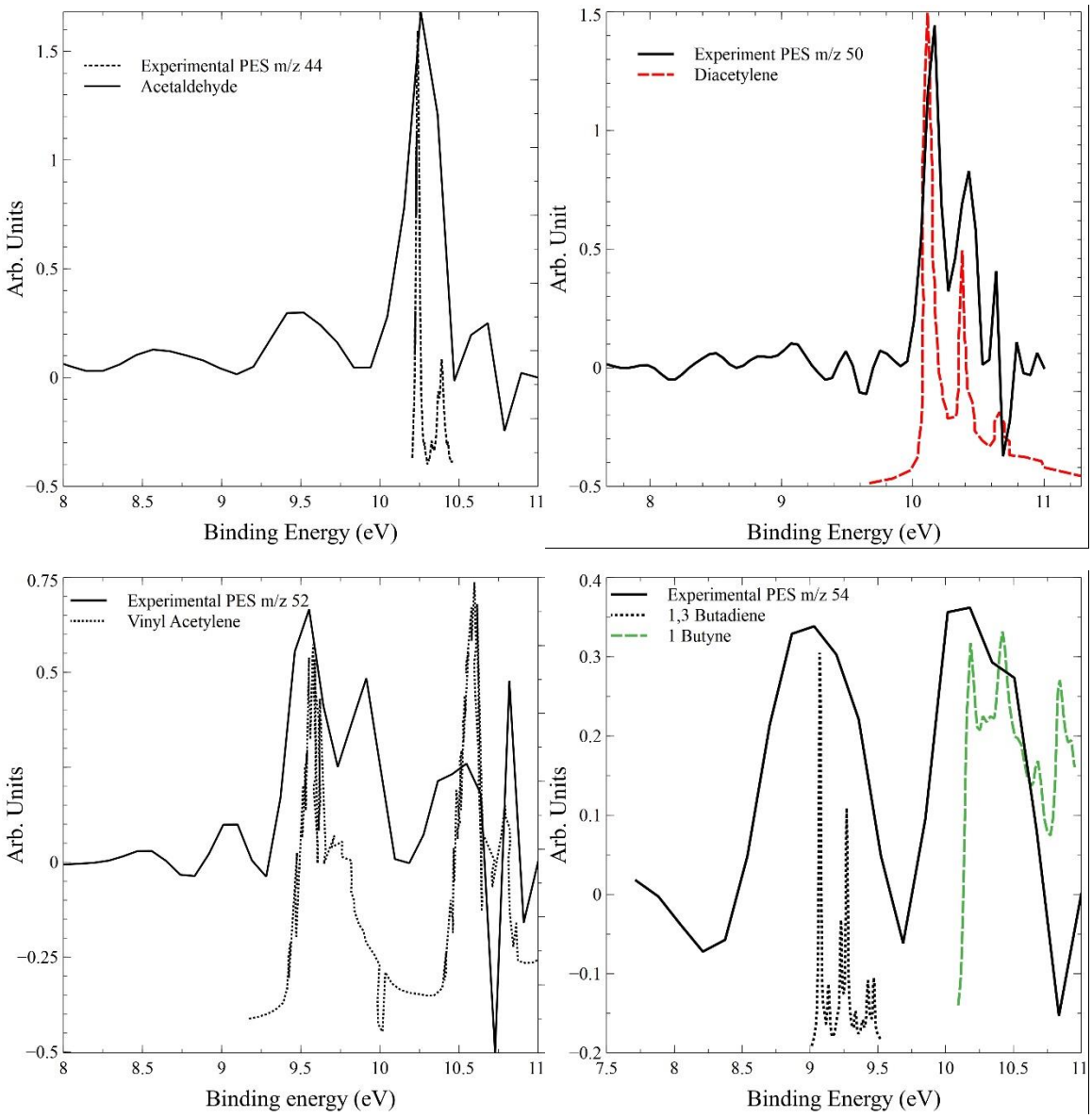

Photoelectron spectrums of product molecules with mass ranging from 44 to 54.

A 6. *List of photoionization cross section used in this work*

	PICS (Mb)	**Photon energy (eV)**	**Reference**
benzene	23.42	10.0	Rennie et al. [264]
toluene	26.17	10.0	Zhou et al. [263]
phenylacetylene	52.40	10.0	Zhou et al. [263]
styrene	32.08	10.0	Zhou et al. [263]
ethylbenzene	25.85	10.0	Zhou et al. [263]
indene	40.58	10.0	Zhou et al. [263]
naphthalene	39.81	10.0	Estimated. [265]
CO2	13.72	14.5	Hitchcock et al. [266]

A 7. *Nomenclature and structure for species involved in the mass-selected isomer identification*

m/z	***Formula***	***Name***	***Structure***
52	C_4H_4	Cyclobutadiene	
52	C_4H_4	Vinylacetylene	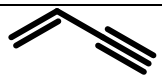
52	C_4H_4	1,2,3-Butatriene	
54	C_4H_6	Methylene Cyclo Propane	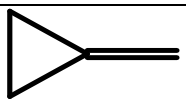
54	C_4H_6	1,2 Butadiene	
54	C_4H_6	Bicyclo Butane	
54	C_4H_6	Cyclobutene	
54	C_4H_6	1,3 Butadiene	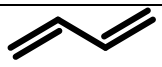
54	C_4H_6	2-Butyne	
64	C_5H_4	1,3-Pentadiyne	
74	C_6H_2	1,3,5-Hexatriyne "Triacetylene"	

78	C_6H_6	Benzene	
78	C_6H_6	Fulvene	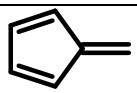
90	C_7H_6	Fulvenallene	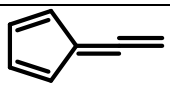
92	C_7H_8	Toluene	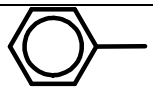
102	C_8H_6, $C_6H_5C_2H$	Phenylacetylene	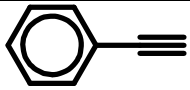
102	C_8H_6	Benzocyclobutadiene	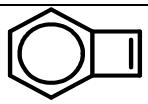
102	C_8H_6	2,4,6-octatriyne	
104	C_8H_8, $C_6H_5C_2H_3$	Styrene	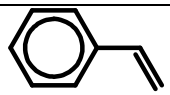
104	C_8H_8	Benzocyclobutane	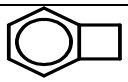
104	p-C_8H_8	p-Xylylene	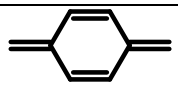
104	o-C_8H_8	o-Xylylene	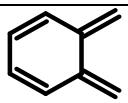
106	C_8H_{10}, $C_6H_5C_2H_5$	Ethylbenzene	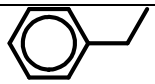
106	o-C_8H_{10}	o-Xylene	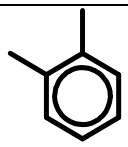
106	m-C_8H_{10}	m-Xylene	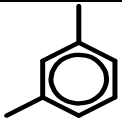

106	p-C_8H_{10}	p-Xylene	
116	C_9H_8	Indene	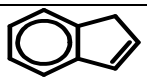
116	C_9H_8	p-methylphenylacetylene	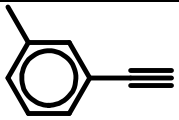
116	C_9H_8	Phenylpropadiene	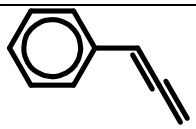
116	C_9H_8	1-propynylbenzene (1-Phenyl-1-propyne)	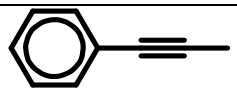
116	C_9H_8	Propargylbenzene	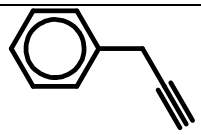
126	$C_{10}H_6$	1,2-Diethynylbenzene	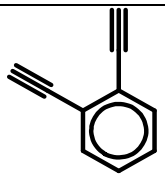
126	$C_{10}H_6$	1,4-Diethynylbenzene	
126	$C_{10}H_6$	1,3-Diethynylbenzene	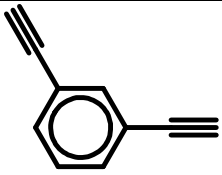
126	$C_{10}H_6$	phenyldiacetylene (1,3-Butadiyn-1-ylbenzene)	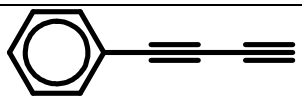
126	$C_{10}H_6$	1,2-Didehydronaphthalene	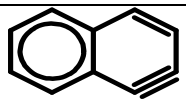
126	$C_{10}H_6$	2,3-Didehydronaphthalene	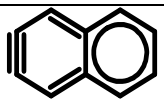

126	$C_{10}H_6$	1,3-Didehydronaphthalene	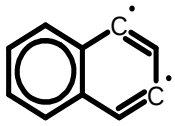
128	$C_{10}H_8$	Naphthalene	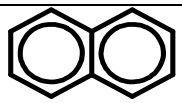
128	$C_{10}H_8$, $C_6H_5CCCHCH_2$	3-buten-1-ynylbenzene	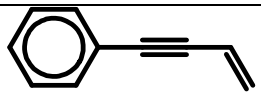
128	$C_{10}H_8$, $C_6H_5CHCHCCH$	4-Phenylbut-3-ene-1-yne	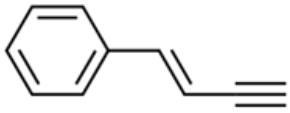
128	$C_{10}H_8$	1H-Indene-1-methylene	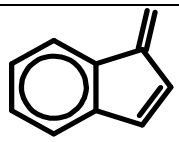
128	$C_{10}H_8$	2-Ethynylstyrene	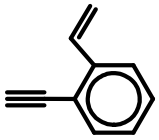
128	$C_{10}H_8$	m-Ethynylstyrene	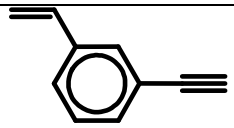
128	$C_{10}H_8$	4-Ethynylstyrene	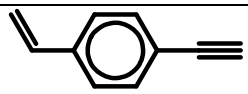
128	$C_{10}H_8$	Azulene	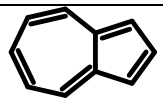
130	$C_{10}H_{10}$	1,2-Dihydronaphthalene	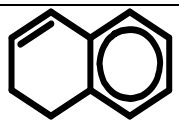
130	$C_{10}H_{10}$	1-Methylindene	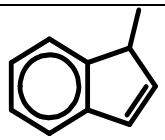
140	$C_{11}H_8$	1H-cyclopropa[a]naphthalene	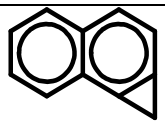

140	$C_{11}H_8$	1H-cyclopropa[b]naphthalene	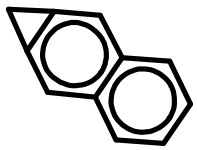
140	$C_{11}H_8$	1-ethynyl-1H-indene	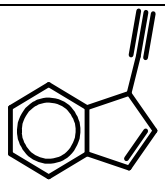
140	$C_{11}H_8$	2-ethynyl-1H-indene	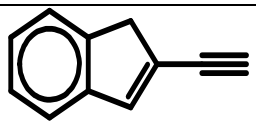
140	$C_{11}H_8$	3-ethynyl-1H-indene	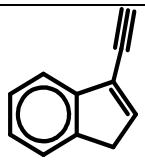
140	$C_{11}H_8$	4-ethynyl-1H-indene	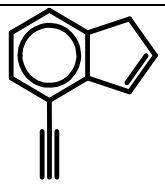
140	$C_{11}H_8$	5-ethynyl-1H-indene	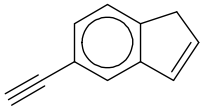
140	$C_{11}H_8$	6-ethynyl-1H-indene	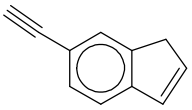
140	$C_{11}H_8$	7-ethynyl-1H-indene	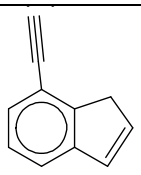
140	$C_{11}H_8$	1-(buta-1,3-diyn-1-yl)-2-methylbenzene	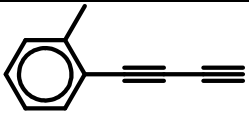
140	$C_{11}H_8$	1-(buta-1,3-diyn-1-yl)-3-methylbenzene	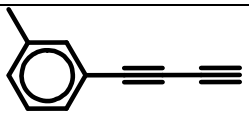

140	$C_{11}H_8$	benzene, 1-(1,3-butadiynyl)-4-methyl-	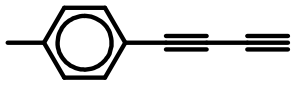
140	$C_{11}H_8$	1-ethynyl-2-propadienylbenzene	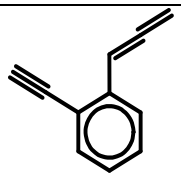
140	$C_{11}H_8$	1-ethynyl-3-propadienylbenzene	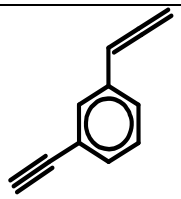
140	$C_{11}H_8$	1-ethynyl-4-propadienylbenzene	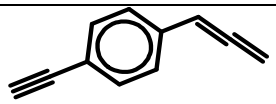
140	$C_{11}H_8$	1-ethynyl-2-(prop-1-yn-1-yl)benzene	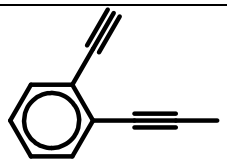
140	$C_{11}H_8$	1-ethynyl-3-prop-1-ynylbenzene	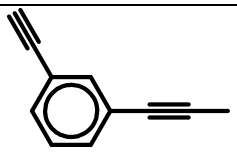
140	$C_{11}H_8$	1-Ethynyl-2-prop-2-ynylbenzene	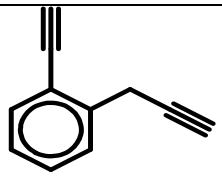
140	$C_{11}H_8$	1-Ethynyl-3-prop-2-ynylbenzene	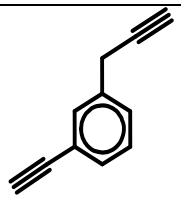
140	$C_{11}H_8$	1-Ethynyl-4-prop-2-ynylbenzene	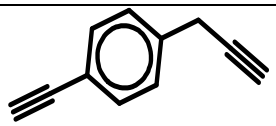
140	$C_{11}H_8$	1-ethynyl-4-prop-1-ynylbenzene	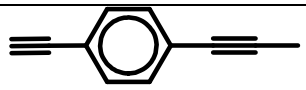

140	$C_{11}H_8$	1,2-diethynyl-4-methylbenzene	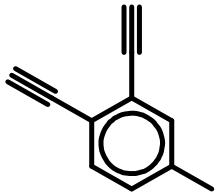
140	$C_{11}H_8$	C#CC=C=Cc1ccccc1	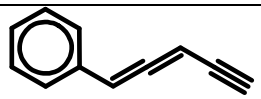
140	$C_{11}H_8$	C#CC(=C=C)c1ccccc1	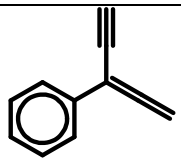
140	$C_{11}H_8$	5-Phenyl-1,3-pentadiyne	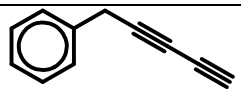
140	$C_{11}H_8$	(Penta-3,4-dien-1-yn-1-yl)benzene	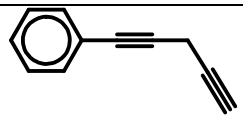
140	$C_{11}H_8$	(Penta-3,4-dien-1-yn-1-yl)benzene	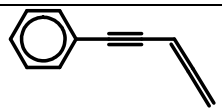
140	$C_{11}H_8$	Penta-1,4-diyn-3-ylbenzene	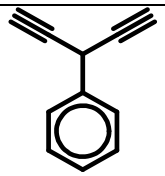
142	$C_{11}H_{10}$	1-Methylnaphthalene	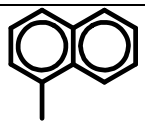
142	$C_{11}H_{10}$	2-Methylnaphthalene	
152	$C_{12}H_8$, $AC_{12}H_8$	Acenaphthylene	

152	$C_{12}H_8$	2-Ethynylnaphthalene	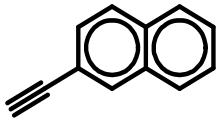
152	$C_{12}H_8$, $C_6H_4C_6H_4$	Biphenylene	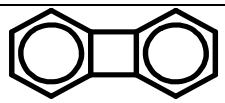
152	$C_{12}H_8$, $C_{10}H_7C_2H$	1-Ethynylnaphthalene	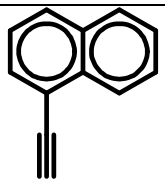
152	$C_{12}H_8$	Cyclopenta[a]indene	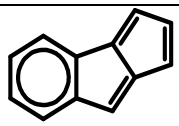
154	$C_{12}H_{10}$	Biphenyl	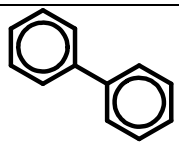
154	$C_{12}H_{10}$	Acenaphthene	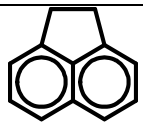
154	$C_{12}H_{10}$	1-Vinylnaphthalene	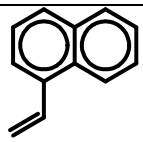
154	$C_{12}H_{10}$	2-Vinylnaphthalene	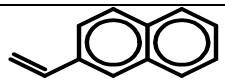
154	$C_{12}H_{10}$	Benzobarrelene	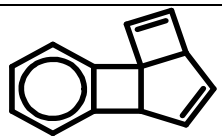
156	$C_{12}H_{12}$	Naphthalene, 1,8-dimethyl-	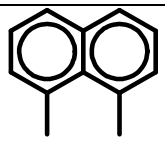
156	$C_{12}H_{12}$	1,4-Ethanonaphthalene, 1,4-dihydro-	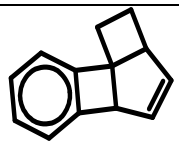

156	$C_{12}H_{12}$	1,4-Methanonaphthalene, 1,4-dihydro-6-methyl-	
156	$C_{12}H_{12}$	Naphthalene, 2-ethyl-	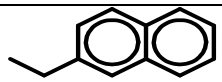
166	$C_{13}H_{10}$, $FC_{13}H_{10}$	fluorene	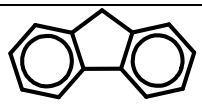
166	$C_{13}H_{10}$	3H-benz[e]indene	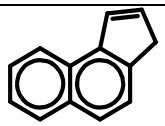
166	$C_{13}H_{10}$, $1\text{-}C_{10}H_7CCCH_3$	1-(1-naphthyl)-1-propyne	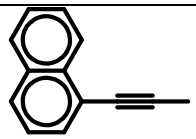
166	$C_{13}H_{10}$, $2\text{-}C_{10}H_7CCCH_3$	2-propynyl naphthalene	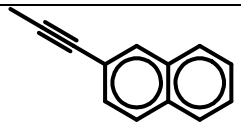
166	$C_{13}H_{10,}$ $PC_{13}H_{10}$	1H-phenalene	
166	$C_{13}H_{10,}$	2-prop-2-ynyl-naphthalene	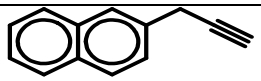
166	$C_{13}H_{10,}$	1-prop-2-ynyl-naphthalene	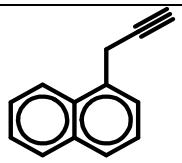
166	$C_{13}H_{10}$, $C_{10}H_7CYC5{-}2$	1h-benz[f]indene	
166	$C_{13}H_{10}$	1H-Benz[e]indene	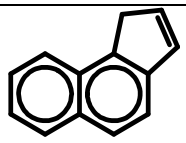
168	$C_{13}H_{10}$, $C_6H_5C_6H_4CH_3$	2-Methylbiphenyl	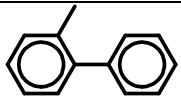

168	$C_{13}H_{12}$	3-Methylbiphenyl	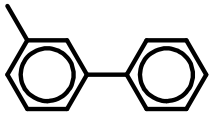
168	$C_{13}H_{12}$	4-Methylbiphenyl	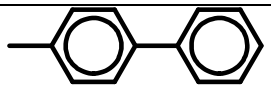
168	$C_{13}H_{12}$	Diphenylmethane	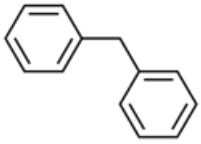
176	$C_{14}H_8$	1-Ethynylacenaphthylene	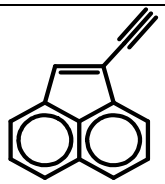
176	$C_{14}H_8$	3-Ethynylacenaphthylene	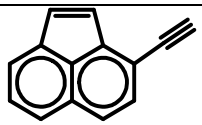
176	$C_{14}H_8$	4-Ethynylacenaphthylene	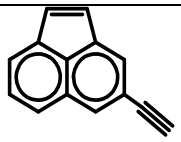
176	$C_{14}H_8$	5-Ethynylacenaphthylene	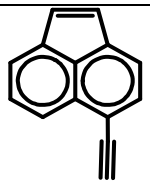
176	$C_{14}H_8$	1,2-Diethynylnaphthalene	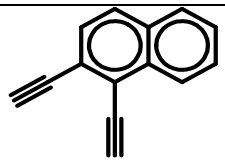
176	$C_{14}H_8$	1,3-Diethynylnaphthalene	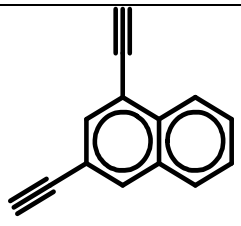

176	$C_{14}H_8$	1,4-Diethynylnaphthalene	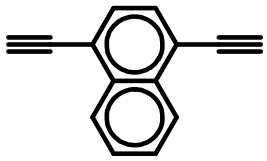
176	$C_{14}H_8$	1,5-Diethynylnaphthalene	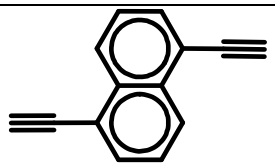
176	$C_{14}H_8$	1,6-Diethynylnaphthalene	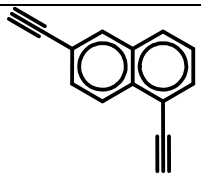
176	$C_{14}H_8$	1,7-Diethynylnaphthalene	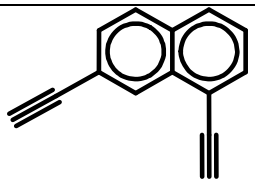
176	$C_{14}H_8$	1,8-Diethynylnaphthalene	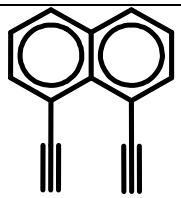
176	$C_{14}H_8$	2,3-Diethynylnaphthalene	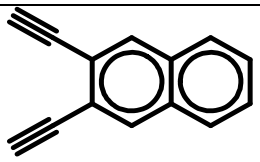
176	$C_{14}H_8$	2,6-Diethynylnaphthalene	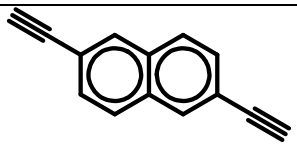
176	$C_{14}H_8$	2,7-Diethynylnaphthalene	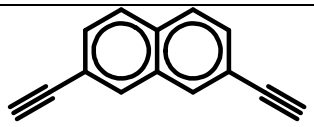
176	$C_{14}H_8$	1-(1,3-Butadiynyl)naphthalene	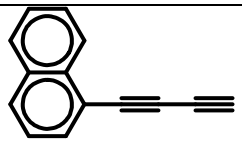

176	$C_{14}H_8$	2-Buta-1,3-diynylnaphthalene	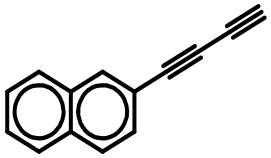
176	$C_{14}H_8$	Pyracyclene	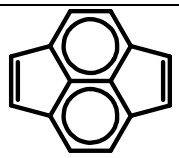
176	$C_{14}H_8$	Cyclopenta[bc]acenaphthylene	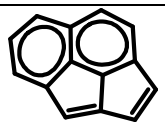
178	$AC_{14}H_{10}$	Anthracene	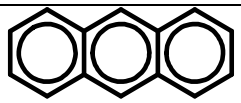
178	$C_{14}H_{10}$	1-methylidenecyclopenta[a]naphthalene	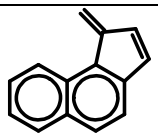
178	$C_{14}H_{10}$	Phenanthrene	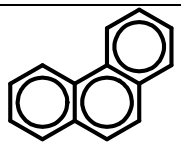
178	$C_{14}H_{10}$, $C_6H_5CCC_6H_5$	Diphenylacetylene	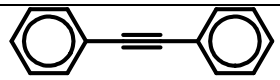
178	$C_{14}H_{10}$, $C_{13}H_8CH_2$	9H-Fluorene, 9-methylene	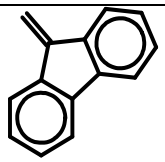
178	$C_{14}H_{10}$	3-methylidenecyclopenta[a]naphthalene	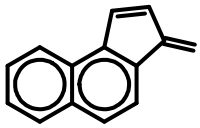
178	$C_{14}H_{10}$	3-methylidenecyclopenta[b]naphthalene	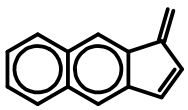

180	$C_{14}H_{12}$	9-Methylfluorene	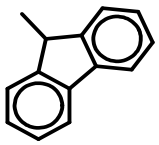
180	$C_{14}H_{12}$, $C_6H_5C_2H_2C_6H_5$	(E)-Stilbene	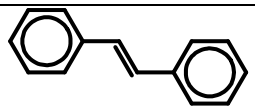
180	$C_{14}H_{12}$	(Z)-Stilbene	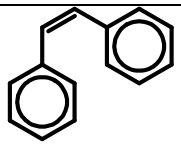
180	$C_{14}H_{12}$	1-Methyl-1H-phenalene	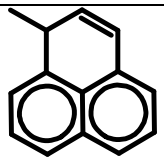
180	$C_{14}H_{12}$	3-Methyl-3H-cyclopenta[a]naphthalene	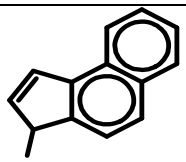
180	$C_{14}H_{12}$	3-Methyl-3H-cyclopenta[b]naphthalene	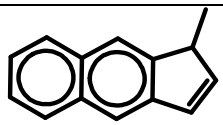
180	$C_{14}H_{12}$, $C_6H_5C(CH_2)C_6H_5$	1,1-Diphenylethylene	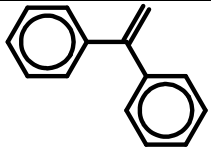
180	$C_{14}H_{12}$	1,8-Diethenylnaphthalene	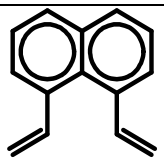
180	$C_{14}H_{12}$	1-Methyl-1H-cyclopenta[a]naphthalene	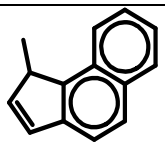
182	$C_{14}H_{14}$	3,3'-Dimethylbiphenyl	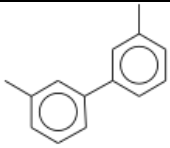

182	$C_{14}H_{14}$	2,2'-Dimethylbiphenyl	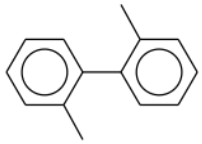
182	$C_{14}H_{14}$	1,1'-Biphenyl, 2-ethyl-	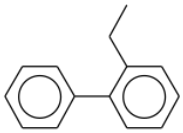
202	$C_{16}H_{10}$, $FC_{16}H_{10}$	Fluoranthene	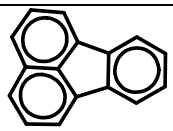
202	$C_{16}H_{10}$, $C_6H_5C_4C_6H_5$	Diphenyldiacetylene	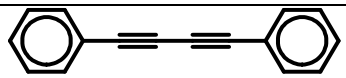
202	$C_{16}H_{10}$, $PC_{16}H_{10}$	Pyrene	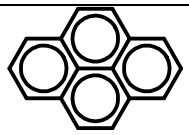
202	$C_{16}H_{10}$	Phenanthrylacetylen	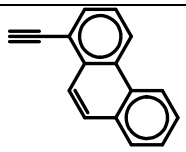
202	$C_{16}H_{10}$	2-Ethynylphenanthrene	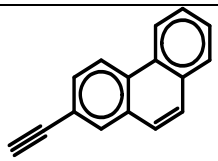
202	$C_{16}H_{10}$	3-Ethynylphenanthrene	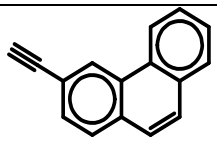
202	$C_{16}H_{10}$	4-Ethynylphenanthrene	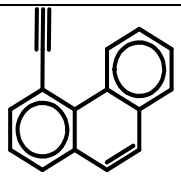
202	$C_{16}H_{10}$	9-Ethynylphenanthrene	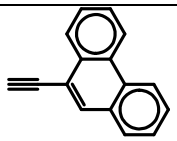

202	$C_{16}H_{10}$	Benzene, 1-ethynyl-2-(phenylethynyl)	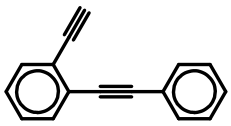
202	$C_{16}H_{10}$	Benzene, 1-ethynyl-3-(phenylethynyl)	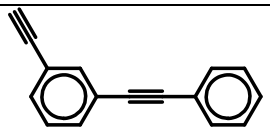
202	$C_{16}H_{10}$	Benzene, 1-ethynyl-4-(phenylethynyl)	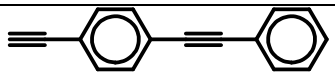
202	$C_{16}H_{10}$	1-Ethynylanthracene	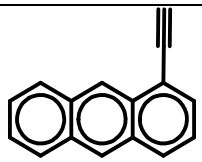
202	$C_{16}H_{10}$	2-Ethynylanthracene	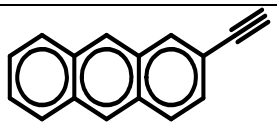
202	$C_{16}H_{10}$	9-Ethynylanthracene	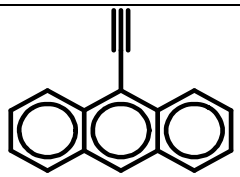
202	$C_{16}H_{10}$	Acephenanthrylene	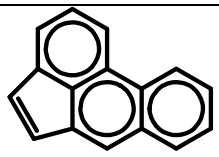
202	$C_{16}H_{10}$	4,5-Vinylidenephenanthrene	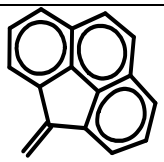
202	$C_{16}H_{10}$	Aceanthrylene	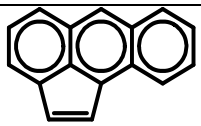
226	$C_{18}H_{10}$	1-ethynylpyrene	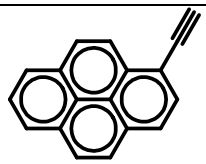

226	$C_{18}H_{10}$	benzo(ghi)fluoranthene	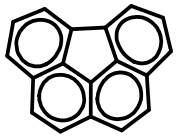
228	$C_{18}H_{12}$	Crysene	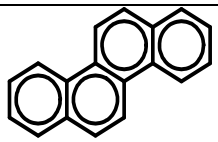
228	$C_{18}H_{12}$	1,2-Benz[a]anthracene	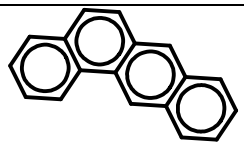
228	$C_{18}H_{12}$	Triphenylene	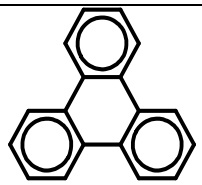
228	$C_{18}H_{12}$	Naphthacene	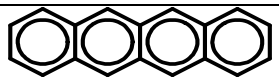
228	$C_{18}H_{12}$	1-(Phenylethynyl)naphthalene	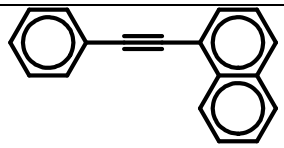
230	p-$C_{18}H_{14}$	p-Terphenyl	
230	o- $C_{18}H_{14}$	o-Terphenyl	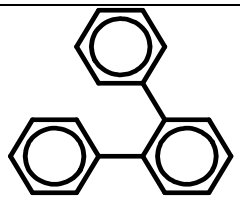
230	m- $C_{18}H_{14}$	m-Terphenyl	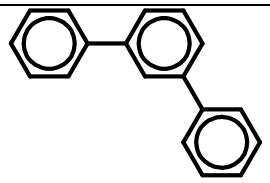
230	$C_{18}H_{14}$	Naphtho[1,8',8:c,d]cycloundeca-1,5-diyne	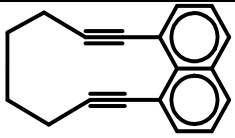

Bibliography

[1] A. Lewis, S. J. Moller, and D. Carslaw, “Non-exhaust emissions from road traffic,” 2019.

[2] D. Fino, S. Bensaid, M. Piumetti, and N. Russo, “A review on the catalytic combustion of soot in Diesel particulate filters for automotive applications: From powder catalysts to structured reactors,” *Appl. Catal. A Gen.*, vol. 509, pp. 75–96, 2016, doi: 10.1016/j.apcata.2015.10.016.

[3] M. K. Khair, “A review of diesel particulate filter technologies,” *SAE Tech. Pap.*, no. 724, 2003, doi: 10.4271/2003-01-2303.

[4] K. Kitamori, T. Manders, R. Dellink, and A. A. Tabeau, “OECD environmental outlook to 2050: the consequences of inaction,” OECD, 2012.

[5] H. Bockhorn, *Soot formation in combustion: mechanisms and models*, vol. 59. Springer Science & Business Media, 2013.

[6] J. A. S. Lighty, J. M. Veranth, and A. F. Sarofim, “Combustion aerosols: Factors governing their size and composition and implications to human health,” *J. Air Waste Manag. Assoc.*, vol. 50, no. 9, pp. 1565–1618, 2000, doi: 10.1080/10473289.2000.10464197.

[7] M. Frenklach and A. M. Mebel, “On the mechanism of soot nucleation,” *Phys. Chem. Chem. Phys.*, vol. 22, no. 9, pp. 5314–5331, 2020.

[8] “G. Ben-Dor, O. Igra, A. Lifshitz (Eds.), Handbook of Shock Waves, Academic Press, New York, 2001.”

[9] A. Lifshitz, *Shock waves in chemistry*. New York: Marcel Dekker Incorporated, 1981.

[10] P. Vieille, “Sur les discontinuités produites par la détente brusque de gaz comprimés,” *Comptes Rendus*, vol. 129, no. 1228, p. 68, 1899.

[11] “P. Vieille, Etude sur les roles des discontinuites dans les phenomenes de propagation, Mémorial des Poudres et Salpêtres 10 (1899) 177–260.”

[12] J. A. Miller *et al.*, “Combustion chemistry in the twenty-first century: Developing theory-informed chemical kinetics models,” *Prog. Energy Combust. Sci.*, vol. 83, p. 100886, 2021.

[13] S. J. Klippenstein, “From theoretical reaction dynamics to chemical modeling of combustion,” *Proc. Combust. Inst.*, vol. 36, no. 1, pp. 77–111, 2017.

[14] A. Comandini, T. Malewicki, and K. Brezinsky, “Online and offline experimental techniques for polycyclic aromatic hydrocarbons recovery and measurement,” *Rev. Sci. Instrum.*, vol. 83, no. 3, p. 34101, 2012.

[15] R. S. Tranter, B. R. Giri, and J. H. Kiefer, “Shock tube/time-of-flight mass spectrometer for high temperature kinetic studies,” *Rev. Sci. Instrum.*, vol. 78, no. 3, 2007, doi: 10.1063/1.2437150.

[16] S. H. Dürrstein, M. Aghsaee, L. Jerig, M. Fikri, and C. Schulz, “A shock tube with a high-repetition-rate time-of-flight mass spectrometer for investigations of complex reaction systems,” *Rev. Sci.*

Instrum., vol. 82, no. 8, p. 84103, 2011.

[17] R. K. Hanson and D. F. Davidson, "Recent advances in laser absorption and shock tube methods for studies of combustion chemistry," *Prog. Energy Combust. Sci.*, vol. 44, pp. 103–114, 2014.

[18] S. De Iuliis, N. Chaumeix, M. Idir, and C.-E. E. Paillard, "Scattering/extinction measurements of soot formation in a shock tube," *Exp. Therm. fluid Sci.*, vol. 32, no. 7, pp. 1354–1362, 2008, doi: 10.1016/j.expthermflusci.2007.11.008.

[19] T. A. Cool *et al.*, "Photoionization mass spectrometer for studies of flame chemistry with a synchrotron light source," *Rev. Sci. Instrum.*, vol. 76, no. 9, 2005, doi: 10.1063/1.2010307.

[20] A. R. Milosavljević *et al.*, "VUV synchrotron radiation: A new activation technique for tandem mass spectrometry," *J. Synchrotron Radiat.*, vol. 19, no. 2, pp. 174–178, 2012, doi: 10.1107/S0909049512001057.

[21] A. G. Gaydon and I. R. Hurle, *The shock tube in high-temperature chemical physics*. Chapman and Hall, 1963.

[22] R. S. Tranter and P. T. Lynch, "A miniature high repetition rate shock tube," *Rev. Sci. Instrum.*, vol. 84, no. 9, 2013, doi: 10.1063/1.4820917.

[23] P. T. Lynch, T. P. Troy, M. Ahmed, and R. S. Tranter, "Probing combustion chemistry in a miniature shock tube with synchrotron VUV photo ionization mass spectrometry," *Anal. Chem.*, vol. 87, no. 4, pp. 2345–2352, 2015.

[24] G. A. Garcia, B. K. Cunha De Miranda, M. Tia, S. Daly, and L. Nahon, "DELICIOUS III: A multipurpose double imaging particle coincidence spectrometer for gas phase vacuum ultraviolet photodynamics studies," *Rev. Sci. Instrum.*, vol. 84, no. 5, p. 53112, 2013, doi: 10.1063/1.4807751.

[25] P. Bréchignac *et al.*, "Photoionization of cold gas phase coronene and its clusters: Autoionization resonances in monomer, dimer, and trimer and electronic structure of monomer cation," *J. Chem. Phys.*, vol. 141, no. 16, 2014, doi: 10.1063/1.4900427.

[26] B. West, A. Sit, A. Bodi, P. Hemberger, and P. M. Mayer, "Dissociative photoionization and threshold photoelectron spectra of polycyclic aromatic hydrocarbon fragments: An imaging photoelectron photoion coincidence (iPEPICO) study of four substituted benzene radical cations," *J. Phys. Chem. A*, vol. 118, no. 47, pp. 11226–11234, 2014, doi: 10.1021/jp5085982.

[27] P. M. Mayer, V. Blanchet, and C. Joblin, "Threshold photoelectron study of naphthalene, anthracene, pyrene, 1,2-dihydronaphthalene, and 9,10-dihydroanthracene," *J. Chem. Phys.*, vol. 134, no. 24, 2011, doi: 10.1063/1.3604933.

[28] Y. Wang *et al.*, "Observation of incipient particle formation during flame synthesis by tandem differential mobility analysis-mass spectrometry (DMA-MS)," *Proc. Combust. Inst.*, vol. 36, no. 1, pp. 745–752, 2017.

[29] H. Richter and J. B. Howard, *Formation of polycyclic aromatic hydrocarbons and their growth to soot-a review of chemical reaction pathways*, vol. 26, no. 4. 2000.

[30] M. Frenklach, "Reaction mechanism of soot formation in flames," *Phys. Chem. Chem. Phys.*, vol. 4, no. 11, pp. 2028–2037, 2002.

[31] H. Böhm, H. Jander, D. Tanke, H. Bohm, H. Jander, and D. Tanke, “Pah Growth and Soot Formation in the Pyrolysis of Acetylene and Benzene At High Temperatures and Pressures : Modeling,” *Combust. Inst.*, pp. 1605–1612, 2000.

[32] D. S. N. Parker, R. I. Kaiser, B. Bandyopadhyay, O. Kostko, T. P. Troy, and M. Ahmed, “Unexpected chemistry from the reaction of naphthyl and acetylene at combustion-like temperatures,” *Angew. Chemie Int. Ed.*, vol. 54, no. 18, pp. 5421–5424, 2015.

[33] J. A. Miller and C. F. Melius, “Kinetic and thermodynamic issues in the formation of aromatic compounds in flames of aliphatic fuels,” *Combust. Flame*, vol. 91, no. 1, pp. 21–39, 1992.

[34] N. M. Marinov, W. J. Pitz, C. K. Westbrook, M. J. Castaldi, and S. M. Senkan, “Modeling of aromatic and polycyclic aromatic hydrocarbon formation in premixed methane and ethane flames,” *Combust. Sci. Technol.*, vol. 116, no. 1–6, pp. 211–287, 1996.

[35] M. J. Castaldi *et al.*, “Experimental and modeling investigation of aromatic and polycyclic aromatic hydrocarbon formation in a premixed ethylene flame,” in *Symposium (International) on Combustion*, 1996, vol. 26, no. 1, pp. 693–702.

[36] M. Lu and J. A. Mulholland, “Aromatic hydrocarbon growth from indene,” *Chemosphere*, vol. 42, no. 5–7, pp. 625–633, 2001.

[37] M. B. Colket and D. J. Seery, “Reaction mechanisms for toluene pyrolysis,” *Symp. Combust.*, vol. 25, no. 1, pp. 883–891, 1994, doi: 10.1016/S0082-0784(06)80723-X.

[38] K. O. Johansson, M. P. Head-Gordon, P. E. Schrader, K. R. Wilson, and H. A. Michelsen, “Resonance-stabilized hydrocarbon-radical chain reactions may explain soot inception and growth,” *Science (80-.).*, vol. 361, no. 6406, pp. 997–1000, 2018, doi: 10.1126/science.aat3417.

[39] J. B. Howard, “Carbon addition and oxidation reactions in heterogeneous combustion and soot formation,” in *Symposium (International) on Combustion*, 1991, vol. 23, no. 1, pp. 1107–1127.

[40] J. T. Mckinnon and J. B. Howard, “The roles of PAH and acetylene in soot nucleation and growth,” in *Symposium (International) on Combustion*, 1992, vol. 24, no. 1, pp. 965–971.

[41] H. Hepp, K. Siegmann, and K. Sattler, “New aspects of growth mechanisms for polycyclic aromatic hydrocarbons in diffusion flames,” *Chem. Phys. Lett.*, vol. 233, no. 1–2, pp. 16–22, 1995.

[42] H. Richter, W. J. Grieco, and J. B. Howard, “Formation mechanism of polycyclic aromatic hydrocarbons and fullerenes in premixed benzene flames,” *Combust. Flame*, vol. 119, no. 1–2, pp. 1–22, 1999.

[43] B. Shukla and M. Koshi, “A highly efficient growth mechanism of polycyclic aromatic hydrocarbons,” *Phys. Chem. Chem. Phys.*, vol. 12, no. 10, pp. 2427–2437, 2010.

[44] B. Shukla and M. Koshi, “Comparative study on the growth mechanisms of PAHs,” *Combust. Flame*, vol. 158, no. 2, pp. 369–375, 2011.

[45] B. Shukla and M. Koshi, “A novel route for PAH growth in HACA based mechanisms,” *Combust. Flame*, vol. 159, no. 12, pp. 3589–3596, 2012.

[46] B. Shukla, A. Miyoshi, and M. Koshi, “Role of methyl radicals in the growth of PAHs,” *J. Am. Soc. Mass Spectrom.*, vol. 21, no. 4, pp. 534–544, 2010.

[47] C. S. McEnally and L. D. Pfefferle, “An experimental study in non-premixed flames of hydrocarbon growth processes that involve five-membered carbon rings,” *Combust. Sci. Technol.*, vol. 131, no. 1–6, pp. 323–344, 1998.

[48] C. S. McEnally and L. D. Pfefferle, “Improved sooting tendency measurements for aromatic hydrocarbons and their implications for naphthalene formation pathways,” *Combust. Flame*, vol. 148, no. 4, pp. 210–222, 2007.

[49] A. Lifshitz, C. Tamburu, A. Suslensky, and F. Dubnikova, “Decomposition, isomerization, and ring expansion in 2-methylindene: Single-pulse shock tube and modeling study,” *J. Phys. Chem. A*, vol. 108, no. 16, pp. 3430–3438, 2004.

[50] A. Comandini and K. Brezinsky, “Theoretical study of the formation of naphthalene from the radical/π-bond addition between single-ring aromatic hydrocarbons,” *J. Phys. Chem. A*, vol. 115, no. 22, pp. 5547–5559, 2011.

[51] B. Shukla, K. Tsuchiya, and M. Koshi, “Novel products from C6H5+ C6H6/C6H5 reactions,” *J. Phys. Chem. A*, vol. 115, no. 21, pp. 5284–5293, 2011.

[52] A. Comandini and K. Brezinsky, “Radical/π-bond addition between o-benzyne and cyclic C5 hydrocarbons,” *J. Phys. Chem. A*, vol. 116, no. 4, pp. 1183–1190, 2012.

[53] A. Comandini, S. Abid, and N. Chaumeix, “Polycyclic aromatic hydrocarbon growth by diradical cycloaddition/fragmentation,” *J. Phys. Chem. A*, vol. 121, no. 31, pp. 5921–5931, 2017.

[54] R. D. Kern, H. J. Singh, M. A. Esslinger, and P. W. Winkeler, “PRODUCT PROFILES OBSERVED D U R I N G THE PYROLYSES OF TOLUENE , B E N Z E N E , B U T A D I E N E , AND ACETYLENE,” pp. 1351–1358, 1982.

[55] S. C. Graham, J. B. Homer, and J. L. J. Rosenfeld, “The formation and coagulation of soot aerosols generated by the pyrolysis of aromatic hydrocarbons,” *Proc. R. Soc. London. A. Math. Phys. Sci.*, vol. 344, no. 1637, pp. 259–285, 1975.

[56] T. S. Wang, R. A. Matula, and R. C. Farmer, “Combustion kinetics of soot formation from toluene,” in *Symposium (International) on Combustion*, 1981, vol. 18, no. 1, pp. 1149–1158.

[57] K. M. Pamidimukkala, R. D. Kern, M. R. Patel, H. C. Wei, and J. H. Kiefer, “High-temperature pyrolysis of toluene,” *J. Phys. Chem.*, vol. 91, no. 8, pp. 2148–2154, 1987.

[58] K. M. Pamidimukkala and R. D. Kern, “The high temperature pyrolysis of ethylbenzene,” *Int. J. Chem. Kinet.*, vol. 18, no. 12, pp. 1341–1353, 1986, doi: 10.1002/kin.550181206.

[59] A. Laskin and A. Lifshit, “Thermal decomposition of benene. Single-pulse shock-tube investigation,” *Symp. Combust.*, vol. 26, no. 1, pp. 669–675, 1996, doi: 10.1016/S0082-0784(96)80274-8.

[60] R. Sivaramakrishnan, K. Brezinsky, and R. S. Tranter, “Combustion Science and Technology A SHOCK-TUBE STUDY OF THE HIGH-PRESSURE THERMAL DECOMPOSITION OF BENZENE,” no. May 2013, pp. 37–41, 2007.

[61] R. Sivaramakrishnan, R. S. Tranter, and K. Brezinsky, “High pressure pyrolysis of toluene. 1. Experiments and modeling of toluene decomposition,” *J. Phys. Chem. A*, vol. 110, no. 30, pp. 9388–9399, 2006, doi: 10.1021/jp060820j.

[62] R. Sivaramakrishnan, R. S. Tranter, and K. Brezinsky, “High pressure pyrolysis of toluene. 2. Modeling benzyl decomposition and formation of soot precursors,” *J. Phys. Chem. A*, vol. 110, no. 30, pp. 9400–9404, 2006.

[63] A. Comandini, T. Malewicki, and K. Brezinsky, “Chemistry of polycyclic aromatic hydrocarbons formation from phenyl radical pyrolysis and reaction of phenyl and acetylene,” *J. Phys. Chem. A*, vol. 116, no. 10, pp. 2409–2434, 2012, doi: 10.1021/jp207461a.

[64] S. Gudiyella and K. Brezinsky, “The high pressure study of n-propylbenzene pyrolysis,” *Proc. Combust. Inst.*, vol. 34, no. 1, pp. 1767–1774, 2013, doi: 10.1016/j.proci.2012.05.007.

[65] W. Sun, A. Hamadi, S. Abid, N. Chaumeix, and A. Comandini, “Probing PAH formation chemical kinetics from benzene and toluene pyrolysis in a single-pulse shock tube,” *Proc. Combust. Inst.*, vol. 38, no. 1, pp. 891–900, 2021.

[66] W. Sun, A. Hamadi, F. E. C. Ardila, S. Abid, N. Chaumeix, and A. Comandini, “Insights into pyrolysis kinetics of xylene isomers behind reflected shock waves,” *Combust. Flame*, vol. 244, p. 112247, 2022, doi: 10.1016/j.combustflame.2022.112247.

[67] W. Sun, A. Hamadi, S. Abid, N. Chaumeix, and A. Comandini, “An experimental and kinetic modeling study of phenylacetylene decomposition and the reactions with acetylene/ethylene under shock tube pyrolysis conditions,” *Combust. Flame*, vol. 220, pp. 257–271, 2020, doi: 10.1016/j.combustflame.2020.06.044.

[68] W. Sun, A. Hamadi, S. Abid, N. Chaumeix, and A. Comandini, “A comparative kinetic study of C8–C10 linear alkylbenzenes pyrolysis in a single-pulse shock tube,” *Combust. Flame*, vol. 221, pp. 136–149, 2020, doi: 10.1016/j.combustflame.2020.07.031.

[69] A. Hamadi, L. Piton Carneiro, F.-E. Cano Ardila, S. Abid, N. Chaumeix, and A. Comandini, “Probing PAH Formation from Heptane Pyrolysis in a Single-Pulse Shock Tube,” *Combust. Sci. Technol.*, vol. 195, no. 7, pp. 1526–1542, 2023.

[70] A. Hamadi, L. C. Piton, S. Abid, N. Chaumeix, and A. Comandini, “Combined high-pressure experimental and kinetic modeling study of cyclopentene pyrolysis and its reactions with acetylene,” *Proc. Combust. Inst.*, 2022.

[71] W. Sun, A. Hamadi, S. Abid, N. Chaumeix, and A. Comandini, “A comprehensive kinetic study on the speciation from propylene and propyne pyrolysis in a single-pulse shock tube,” *Combust. Flame*, vol. 231, p. 111485, 2021, doi: 10.1016/j.combustflame.2021.111485.

[72] A. Hamadi, W. Sun, S. Abid, N. Chaumeix, and A. Comandini, “An experimental and kinetic modeling study of benzene pyrolysis with C2− C3 unsaturated hydrocarbons,” *Combust. Flame*, vol. 237, p. 111858, 2022.

[73] W. Sun, A. Hamadi, S. Abid, N. Chaumeix, and A. Comandini, “Detailed experimental and kinetic modeling study of toluene/C2 pyrolysis in a single-pulse shock tube,” *Combust. Flame*, vol. 226, pp. 129–142, 2021.

[74] W. Sun, A. Hamadi, S. Abid, N. Chaumeix, and A. Comandini, “Influences of propylene/propyne addition on toluene pyrolysis in a single-pulse shock tube,” *Combust. Flame*, vol. 236, p. 111799, 2022.

[75] L. Nahon *et al.*, “DESIRS: A state-of-the-art VUV beamline featuring high resolution and variable polarization for spectroscopy and dichroism at SOLEIL,” *J. Synchrotron Radiat.*, vol. 19, no. 4, pp. 508–520, 2012, doi: 10.1107/S0909049512010588.

[76] X. Tang, G. A. Garcia, J. F. Gil, and L. Nahon, “Vacuum upgrade and enhanced performances of the double imaging electron/ion coincidence end-station at the vacuum ultraviolet beamline DESIRS,” *Rev. Sci. Instrum.*, vol. 86, no. 12, 2015, doi: 10.1063/1.4937624.

[77] F. Qi, “Combustion chemistry probed by synchrotron VUV photoionization mass spectrometry,” *Proc. Combust. Inst.*, vol. 34, no. 1, pp. 33–63, 2013.

[78] Y. Li and F. Qi, “Recent applications of synchrotron VUV photoionization mass spectrometry: Insight into Combustion Chemistry,” *Acc. Chem. Res.*, vol. 43, no. 1, pp. 68–78, 2010, doi: 10.1021/ar900130b.

[79] X. Yang, A. W. Jasper, J. H. Kiefer, and R. S. Tranter, “The dissociation of diacetyl: A shock tube and theoretical study,” *J. Phys. Chem. A*, vol. 113, no. 29, pp. 8318–8326, 2009, doi: 10.1021/jp903716f.

[80] X. Yang, C. Franklin Goldsmith, and R. S. Tranter, “Decomposition and vibrational relaxation in CH 3i and self-reaction of CH 3 radicals,” *J. Phys. Chem. A*, vol. 113, no. 29, pp. 8307–8317, 2009, doi: 10.1021/jp903336u.

[81] J. B. Randazzo, R. Sivaramakrishnan, A. W. Jasper, T. Sikes, P. T. Lynch, and R. S. Tranter, “An experimental and theoretical study of the high temperature reactions of the four butyl radical isomers,” *Phys. Chem. Chem. Phys.*, vol. 22, no. 33, pp. 18304–18319, 2020, doi: 10.1039/d0cp02404j.

[82] C. Banyon, T. Sikes, and R. S. Tranter, “Reactions of propyl radicals: A shock tube–VUV photoionization mass spectrometry study,” *Combust. Flame*, vol. 224, no. xxxx, pp. 14–23, 2021, doi: 10.1016/j.combustflame.2020.10.024.

[83] T. Sikes *et al.*, “Initiation reactions in the high temperature decomposition of styrene,” *Phys. Chem. Chem. Phys.*, vol. 23, no. 34, pp. 18432–18448, 2021, doi: 10.1039/d1cp02437j.

[84] B. Brehm and E. von Puttkamer, “Koinzidenzmessung von photoionen und photoelektronen bei methan,” *Zeitschrift für Naturforsch. A*, vol. 22, no. 1, pp. 8–10, 1967.

[85] T. Baer, J. Booze, and K.-M. Weitzel, “Photoelectron photoion coincidence studies of ion dissociation dynamics,” in *Vacuum ultraviolet photoionization and photodissociation of molecules and clusters*, World Scientific, 1991, pp. 259–296.

[86] J. H. D. Eland, *Photoelectron spectroscopy: an introduction to ultraviolet photoelectron spectroscopy in the gas phase*. Elsevier, 2013.

[87] X. Tang *et al.*, “A threshold photoelectron-photoion coincidence spectrometer with double velocity imaging using synchrotron radiation,” *Rev. Sci. Instrum.*, vol. 80, no. 11, pp. 0–10, 2009, doi: 10.1063/1.3250872.

[88] A. Bodi, P. Hemberger, T. Gerber, and B. Sztáray, “A new double imaging velocity focusing coincidence experiment: I 2PEPICO,” *Rev. Sci. Instrum.*, vol. 83, no. 8, 2012, doi: 10.1063/1.4742769.

[89] T. Bierkandt, P. Hemberger, P. Oßwald, M. Köhler, and T. Kasper, “Insights in m-xylene decomposition under fuel-rich conditions by imaging photoelectron photoion coincidence spectroscopy,” *Proc. Combust. Inst.*, vol. 36, no. 1, pp. 1223–1232, 2017, doi: 10.1016/j.proci.2016.06.143.

[90] Z. Pan, A. Puente-Urbina, A. Bodi, J. A. van Bokhoven, and P. Hemberger, “Isomer-dependent catalytic pyrolysis mechanism of the lignin model compounds catechol, resorcinol and hydroquinone,” *Chem. Sci.*, vol. 12, no. 9, pp. 3161–3169, 2021, doi: 10.1039/d1sc00654a.

[91] X. Mercier *et al.*, “Selective identification of cyclopentaring-fused PAHs and side-substituted PAHs in a low pressure premixed sooting flame by photoelectron photoion coincidence spectroscopy,” *Phys. Chem. Chem. Phys.*, vol. 22, no. 28, pp. 15926–15944, 2020, doi: 10.1039/d0cp02740e.

[92] J. Bouwman, A. Bodi, and P. Hemberger, “Nitrogen matters: The difference between PANH and PAH formation,” *Phys. Chem. Chem. Phys.*, vol. 20, no. 47, pp. 29910–29917, 2018, doi: 10.1039/c8cp05830j.

[93] Z. Hu *et al.*, “Elucidating the photodissociation fingerprint and quantifying the determination of organic hydroperoxides in gas-phase autoxidation,” *Proc. Natl. Acad. Sci.*, vol. 120, no. 10, p. e2220131120, 2023.

[94] P. Hemberger, A. Bodi, T. Bierkandt, M. Köhler, D. Kaczmarek, and T. Kasper, “Photoelectron Photoion Coincidence Spectroscopy Provides Mechanistic Insights in Fuel Synthesis and Conversion,” *Energy and Fuels*, vol. 35, no. 20, pp. 16265–16302, 2021, doi: 10.1021/acs.energyfuels.1c01712.

[95] K. C. Hou and H. B. Palmer, “The kinetics of thermal decomposition of benzene in a flow system,” *J. Phys. Chem.*, vol. 69, no. 3, pp. 863–868, 1965.

[96] R. D. Smith, “A direct mass spectrometric study of the mechanism of toluene pyrolysis at high temperatures,” *J. Phys. Chem.*, vol. 83, no. 12, pp. 1553–1563, 1979.

[97] O. S. L. L. Bruinsma and J. A. Moulijn, “The pyrolytic formation of polycyclic aromatic hydrocarbons from benzene, toluene, ethylbenze,e, styrene, phenylacetylene and n-decane in relation to fossil fuels utilization,” *Fuel Process. Technol.*, vol. 18, no. 3, pp. 213–236, 1988, doi: 10.1016/0378-3820(88)90048-3.

[98] B. Shukla, A. Susa, A. Miyoshi, and M. Koshi, “In situ direct sampling mass spectrometric study on formation of polycyclic aromatic hydrocarbons in toluene pyrolysis,” *J. Phys. Chem. A*, vol. 111, no. 34, pp. 8308–8324, 2007.

[99] B. Shukla, A. Susa, A. Miyoshi, and M. Koshi, “Role of phenyl radicals in the growth of polycyclic aromatic hydrocarbons,” *J. Phys. Chem. A*, vol. 112, no. 11, pp. 2362–2369, 2008.

[100] T. Zhang *et al.*, “An experimental and theoretical study of toluene pyrolysis with tunable synchrotron VUV photoionization and molecular-beam mass spectrometry,” *Combust. Flame*, vol. 156, no. 11, pp. 2071–2083, 2009.

[101] L. Zhang, J. Cai, T. Zhang, and F. Qi, “Kinetic modeling study of toluene pyrolysis at low pressure,” *Combust. Flame*, vol. 157, no. 9, pp. 1686–1697, 2010.

[102] Y. Zhang *et al.*, “Pyrolysis of n-butylbenzene at various pressures: influence of long side-chain

structure on alkylbenzene pyrolysis," *Energy & Fuels*, vol. 31, no. 12, pp. 14270–14279, 2017.

[103] Y. Zhang *et al.*, "Flow reactor pyrolysis of iso-butylbenzene and tert-butylbenzene at various pressures: Insight into fuel isomeric effects on pyrolysis chemistry of butylbenzenes," *Proc. Combust. Inst.*, vol. 38, no. 1, pp. 1423–1432, 2021.

[104] Y. Zhang *et al.*, "Experimental and kinetic modeling investigation on sec-butylbenzene combustion: Flow reactor pyrolysis and laminar flame propagation at various pressures," *Combust. Flame*, vol. 211, pp. 18–31, 2020.

[105] W. Yuan, Y. Li, P. Dagaut, J. Yang, and F. Qi, "Investigation on the pyrolysis and oxidation of toluene over a wide range conditions. I. Flow reactor pyrolysis and jet stirred reactor oxidation," *Combust. Flame*, vol. 162, no. 1, pp. 3–21, 2015.

[106] W. Yuan, Y. Li, P. Dagaut, J. Yang, and F. Qi, "Investigation on the pyrolysis and oxidation of toluene over a wide range conditions. II. A comprehensive kinetic modeling study," *Combust. Flame*, vol. 162, no. 1, pp. 22–40, 2015.

[107] W. Yuan, Y. Li, G. Pengloan, C. Togbé, P. Dagaut, and F. Qi, "A comprehensive experimental and kinetic modeling study of ethylbenzene combustion," *Combust. Flame*, vol. 166, pp. 255–265, 2016.

[108] W. Yuan, Y. Li, P. Dagaut, Y. Wang, Z. Wang, and F. Qi, "A comprehensive experimental and kinetic modeling study of n-propylbenzene combustion," *Combust. Flame*, vol. 186, pp. 178–192, 2017.

[109] W. Yuan *et al.*, "Exploring pyrolysis and oxidation chemistry of o-xylene at various pressures with special concerns on PAH formation," *Combust. Flame*, vol. 228, pp. 351–363, 2021.

[110] H. Jin *et al.*, "An experimental study of indene pyrolysis with synchrotron vacuum ultraviolet photoionization mass spectrometry," *Phys. Chem. Chem. Phys.*, vol. 21, no. 10, pp. 5510–5520, 2019, doi: 10.1039/c8cp07285j.

[111] H. Jin *et al.*, "Experimental and kinetic modeling study of α-methyl-naphthalene pyrolysis: Part I. Formation of monocyclic aromatics and small species," *Combust. Flame*, vol. 233, no. xxxx, p. 111587, 2021, doi: 10.1016/j.combustflame.2021.111587.

[112] H. Jin *et al.*, "Experimental and kinetic modeling study of α-methyl-naphthalene pyrolysis: Part II. PAH formation," *Combust. Flame*, vol. 233, no. xxxx, p. 111530, 2021, doi: 10.1016/j.combustflame.2021.111530.

[113] C. Shao *et al.*, "Polycyclic aromatic hydrocarbons in pyrolysis of gasoline surrogates (n-heptane/iso-octane/toluene)," *Proc. Combust. Inst.*, vol. 37, no. 1, pp. 993–1001, 2019.

[114] C. Shao, G. Kukkadapu, S. W. Wagnon, W. J. Pitz, and S. M. Sarathy, "PAH formation from jet stirred reactor pyrolysis of gasoline surrogates," *Combust. Flame*, vol. 219, pp. 312–326, 2020.

[115] Z. Liu *et al.*, "Synergistic effects in toluene/C3H4 isomers co-pyrolysis: Formation of indene and naphthalene," *Proc. Combust. Inst.*, 2022.

[116] A. C. Eckbreth, *Laser diagnostics for combustion temperature and species*, vol. 3. CRC press, 1996.

[117] R. Di Sante, "Laser extinction technique for measurements of carbon particles concentration during combustion," *Opt. Lasers Eng.*, vol. 51, no. 6, pp. 783–789, 2013, doi:

10.1016/j.optlaseng.2013.01.019.

[118] V. G. Knorre, D. Tanke, T. Thienel, and H. G. Wagner, “Soot formation in the pyrolysis of bezene/acetylene and acetylene/hydrogen mixtures at high carbon concentrations,” in *Symposium (international) on combustion*, 1996, vol. 26, no. 2, pp. 2303–2310, doi: 10.1016/S0082-0784(96)80058-0.

[119] M. Frenklach, M. K. Ramachandra, and R. A. Matula, “Soot formation in shock-tube oxidation of hydrocarbons,” in *Symposium (International) on Combustion*, 1985, vol. 20, no. 1, pp. 871–878.

[120] M. Evans and A. Williams, “Shock tube studies on the formation of soot from the combustion and pyrolysis of some hydrocarbons,” *Fuel*, vol. 60, no. 11, pp. 1047–1056, 1981.

[121] I. Naydenova, M. Nullmeier, J. Warnatz, and P. A. Vlasov, “Detailed kinetic modeling of soot formation during shock-tube pyrolysis of C6H6: Direct comparison with the results of time-resolved laser-induced incandescence (LII) and CW-laser extinction measurements,” *Combust. Sci. Technol.*, vol. 176, no. 10, pp. 1667–1703, 2004.

[122] G. L. Agafonov, P. A. Vlasov, and V. N. Smirnov, “Soot formation in the pyrolysis of benzene, methylbenzene, and ethylbenzene in shock waves,” *Kinet. Catal.*, vol. 52, pp. 358–370, 2011.

[123] G. L. Agafonov, V. N. Smirnov, and P. A. Vlasov, “Shock tube and modeling study of soot formation during the pyrolysis and oxidation of a number of aliphatic and aromatic hydrocarbons,” *Proc. Combust. Inst.*, vol. 33, no. 1, pp. 625–632, 2011.

[124] A. Drakon, A. Eremin, E. Mikheyeva, B. Shu, M. Fikri, and C. Schulz, “Soot formation in shock-wave-induced pyrolysis of acetylene and benzene with H2, O2, and CH4 addition,” *Combust. Flame*, vol. 198, pp. 158–168, 2018, doi: 10.1016/j.combustflame.2018.09.014.

[125] K. C. Utsav, M. Beshir, A. Farooq, U. KC, M. Beshir, and A. Farooq, “Simultaneous measurements of acetylene and soot during the pyrolysis of ethylene and benzene in a shock tube,” *Proc. Combust. Inst.*, vol. 36, no. 1, pp. 833–840, 2017, doi: 10.1016/j.proci.2016.08.087.

[126] S. Bauerle *et al.*, “Soot formation at elevated pressures and carbon concentrations in hydrocarbon pyrolysis,” *Symp. Combust.*, vol. 25, no. 1, pp. 627–634, 1994, doi: 10.1016/S0082-0784(06)80694-6.

[127] D. Nativel, J. Herzler, S. Krzywdziak, S. Peukert, M. Fikri, and C. Schulz, “Shock-tube study of the influence of oxygenated additives on benzene pyrolysis: Measurement of optical densities, soot inception times and comparison with simulations,” *Combust. Flame*, vol. 243, no. xxxx, p. 111985, 2022, doi: 10.1016/j.combustflame.2022.111985.

[128] A. C. Letícia CARNEIRO PITON, “Experimental study on particle formation using shock tubes,” Universite D’Orleans, 2023.

[129] A. Alexiou and A. Williams, “Soot formation in shock-tube pyrolysis of toluene, toluene-methanol, toluene-ethanol, and toluene-oxygen mixtures,” *Combust. Flame*, vol. 104, no. 1–2, pp. 51–65, 1996.

[130] T. E. Parker, R. R. Foutter, and W. T. Rawlins, “Soot initiation and particle growth in the pyrolysis of toluene at high inert gas pressures,” in *AIP Conference Proceedings*, 1990, vol. 208, no. 1, pp. 481–486.

[131] G. L. Agafonov, V. N. Smirnov, and P. A. Vlasov, “A shock-tube and modeling study of soot formation during pyrolysis of propane, propane/toluene and rich propane/oxygen mixtures,” *Combust. Sci. Technol.*, vol. 182, no. 11–12, pp. 1645–1671, 2010.

[132] J. D’Alessio *et al.*, “Absorption spectroscopy of toluene pyrolysis,” *Opt. Lasers Eng.*, vol. 37, no. 5, pp. 495–508, 2002, doi: 10.1016/S0143-8166(01)00122-1.

[133] L. Y. Xian, Y. L. Li, J. N. He, C. H. Zhang, P. Li, and X. Y. Li, “Measurement of Soot Yield from the Pyrolysis of Toluene at High Temperatures by Laser Extinction Method,” *Guang pu xue yu Guang pu fen xi= Guang pu*, vol. 36, no. 11, pp. 3481–3484, 2016.

[134] D. Nativel *et al.*, “Shock-tube study on the influence of oxygenated co-reactants on ethylene decomposition under pyrolytic conditions,” *Proc. Combust. Inst.*, 2022.

[135] D. Nativel *et al.*, “Impact of Methanol and Butanol on Soot Formation in Gasoline Surrogate Pyrolysis: A Shock-Tube Study,” *J. Phys. Chem. A*, vol. 127, no. 5, pp. 1259–1270, 2023.

[136] O. Mathieu, N. Djebaïli-Chaumeix, C.-E. Paillard, and F. Douce, “Experimental study of soot formation from a diesel fuel surrogate in a shock tube,” *Combust. Flame*, vol. 156, no. 8, pp. 1576–1586, 2009.

[137] A. V. Martin and N. T. D. Loh, “X-ray Free-Electron Lasers: Illuminating a New Path to Single Particle Imaging,” *Synchrotron Radiat. News*, vol. 26, no. 2, pp. 11–19, 2013, doi: 10.1080/08940886.2013.771069.

[138] C. Lou, C. Chen, Y. Sun, and H. Zhou, “Review of soot measurement in hydrocarbon-air flames,” *Sci. China Technol. Sci.*, vol. 53, no. 8, pp. 2129–2141, 2010, doi: 10.1007/s11431-010-3212-4.

[139] L. A. Melton, “Soot diagnostics based on laser heating,” *Appl. Opt.*, vol. 23, no. 13, pp. 2201–2208, 1984.

[140] R. L. Vander Wal, T. M. Ticich, and A. B. Stephens, “Can soot primary particle size be determined using laser-induced incandescence?,” *Combust. Flame*, vol. 116, no. 1–2, pp. 291–296, 1999.

[141] D. R. Snelling, K. A. Thomson, G. J. Smallwood, and Ö. L. Gülder, “Two-dimensional imaging of soot volume fraction in laminar diffusion flames,” *Appl. Opt.*, vol. 38, no. 12, pp. 2478–2485, 1999.

[142] C. P. Arana, M. Pontoni, S. Sen, and I. K. Puri, “Field measurements of soot volume fractions in laminar partially premixed coflow ethylene/air flames,” *Combust. Flame*, vol. 138, no. 4, pp. 362–372, 2004.

[143] D. R. Snelling, K. A. Thomson, G. J. Smallwood, O. L. Guider, E. J. Weckman, and R. A. Fraser, “Spectrally resolved measurement of flame radiation to determine soot temperature and concentration,” *AIAA J.*, vol. 40, no. 9, pp. 1789–1795, 2002.

[144] H. Zhao and N. Ladommatos, “Optical diagnostics for soot and temperature measurement in diesel engines,” *Prog. energy Combust. Sci.*, vol. 24, no. 3, pp. 221–255, 1998.

[145] C. S. McEnally, Ü. Ö. Köylü, L. D. Pfefferle, and D. E. Rosner, “Soot volume fraction and temperature measurements in laminar nonpremixed flames using thermocouples,” *Combust. Flame*, vol. 109, no. 4, pp. 701–720, 1997.

[146] R. A. Dobbins and C. M. Megaridis, “Morphology of flame-generated soot as determined by

thermophoretic sampling," *Langmuir*, vol. 3, no. 2, pp. 254–259, 1987.

[147] Ü. Ö. Köylü, C. S. McEnally, D. E. Rosner, and L. D. Pfefferle, "Simultaneous measurements of soot volume fraction and particle size/microstructure in flames using a thermophoretic sampling technique," *Combust. Flame*, vol. 110, no. 4, pp. 494–507, 1997.

[148] B. D. Ratner and D. G. Castner, "Electron spectroscopy for chemical analysis," *Surf. Anal. Princ. Tech.*, vol. 2, pp. 374–381, 2009.

[149] R. J. Santoro, H. G. Semerjian, and R. A. Dobbins, "Soot particle measurements in diffusion flames," *Combust. Flame*, vol. 51, pp. 203–218, 1983.

[150] R. J. Samson, G. W. Mulholland, and J. W. Gentry, "Structural analysis of soot agglomerates," *Langmuir*, vol. 3, no. 2, pp. 272–281, 1987.

[151] B. Quay, T.-W. Lee, T. Ni, and R. J. Santoro, "Spatially resolved measurements of soot volume fraction using laser-induced incandescence," *Combust. Flame*, vol. 97, no. 3–4, pp. 384–392, 1994.

[152] R. L. Vander Wal and K. J. Weiland, "Laser-induced incandescence: development and characterization towards a measurement of soot-volume fraction," *Appl. Phys. B*, vol. 59, pp. 445–452, 1994.

[153] R. L. Vander Wal, T. M. Ticich, and A. B. Stephens, "Optical and microscopy investigations of soot structure alterations by laser-induced incandescence," *Appl. Phys. B*, vol. 67, pp. 115–123, 1998.

[154] R. L. Vander Wal, Z. Zhou, and M. Y. Choi, "Laser-induced incandescence calibration via gravimetric sampling," *Combust. Flame*, vol. 105, no. 4, pp. 462–470, 1996.

[155] S. Will, S. Schraml, and A. Leipertz, "Two-dimensional soot-particle sizing by time-resolved laser-induced incandescence," *Opt. Lett.*, vol. 20, no. 22, pp. 2342–2344, 1995.

[156] P.-E. Bengtsson and M. Aldén, "Soot-visualization strategies using laser techniques: Laser-induced fluorescence in C 2 from laser-vaporized soot and laser-induced soot incandescence," *Appl. Phys. B*, vol. 60, pp. 51–59, 1995.

[157] M.-Y. Choi, G. W. Mulholland, A. Hamins, and T. Kashiwagi, "Comparisons of the soot volume fraction using gravimetric and light extinction techniques," *Combust. Flame*, vol. 102, no. 1–2, pp. 161–169, 1995.

[158] F. Xu, P. B. Sunderland, and G. M. Faeth, "Soot formation in laminar premixed ethylene/air flames at atmospheric pressure," *Combust. Flame*, vol. 108, no. 4, pp. 471–493, 1997.

[159] Z.-Q. Zhou, T. U. Ahmed, and M. Y. Choi, "Measurement of dimensionless soot extinction constant using a gravimetric sampling technique," *Exp. Therm. fluid Sci.*, vol. 18, no. 1, pp. 27–32, 1998.

[160] G. Skillas, H. Burtscher, K. Siegmann, and U. Baltensperger, "Density and fractal-like dimension of particles from a laminar diffusion flame," *J. Colloid Interface Sci.*, vol. 217, no. 2, pp. 269–274, 1999.

[161] B. Zhao *et al.*, "Measurement and numerical simulation of soot particle size distribution functions in a laminar premixed ethylene-oxygen-argon flame," *Combust. Flame*, vol. 133, no. 1–2, pp. 173–188, 2003.

[162] H. Bladh *et al.*, "Influence of soot particle aggregation on time-resolved laser-induced

incandescence signals," *Appl. Phys. B*, vol. 104, pp. 331–341, 2011.

[163] S. Chowdhury, W. R. Boyette, and W. L. Roberts, "Time-averaged probability density functions of soot nanoparticles along the centerline of a piloted turbulent diffusion flame using a scanning mobility particle sizer," *J. Aerosol Sci.*, vol. 106, pp. 56–67, 2017.

[164] D. J. Bryce, N. Ladommatos, and H. Zhao, "Quantitative investigation of soot distribution by laser-induced incandescence," *Appl. Opt.*, vol. 39, no. 27, pp. 5012–5022, 2000.

[165] B. Axelsson, R. Collin, and P.-E. Bengtsson, "Laser-induced incandescence for soot particle size measurements in premixed flat flames," *Appl. Opt.*, vol. 39, no. 21, pp. 3683–3690, 2000.

[166] W. Merchan-Merchan, S. G. Sanmiguel, and S. McCollam, "Analysis of soot particles derived from biodiesels and diesel fuel air-flames," *Fuel*, vol. 102, pp. 525–535, 2012.

[167] M. Sirignano, D. Bartos, M. Conturso, M. Dunn, A. D'Anna, and A. R. Masri, "Detection of nanostructures and soot in laminar premixed flames," *Combust. Flame*, vol. 176, pp. 299–308, 2017.

[168] H. Bladh, P.-E. Bengtsson, J. Delhay, Y. Bouvier, E. Therssen, and P. Desgroux, "Experimental and theoretical comparison of spatially resolved laser-induced incandescence (LII) signals of soot in backward and right-angle configuration," *Appl. Phys. B*, vol. 83, pp. 423–433, 2006.

[169] M. Charwath, R. Suntz, and H. Bockhorn, "Influence of the temporal response of the detection system on time-resolved laser-induced incandescence signal evolutions," *Appl. Phys. B*, vol. 83, pp. 435–442, 2006.

[170] S. S. Iyer, T. A. Litzinger, S.-Y. Lee, and R. J. Santoro, "Determination of soot scattering coefficient from extinction and three-angle scattering in a laminar diffusion flame," *Combust. Flame*, vol. 149, no. 1–2, pp. 206–216, 2007.

[171] S. De Iuliis, F. Migliorini, F. Cignoli, and G. Zizak, "2D soot volume fraction imaging in an ethylene diffusion flame by two-color laser-induced incandescence (2C-LII) technique and comparison with results from other optical diagnostics," *Proc. Combust. Inst.*, vol. 31, no. 1, pp. 869–876, 2007.

[172] T. C. Williams, C. R. Shaddix, K. A. Jensen, and J. M. Suo-Anttila, "Measurement of the dimensionless extinction coefficient of soot within laminar diffusion flames," *Int. J. Heat Mass Transf.*, vol. 50, no. 7–8, pp. 1616–1630, 2007.

[173] R. Hadef, K. P. Geigle, W. Meier, and M. Aigner, "Soot characterization with laser-induced incandescence applied to a laminar premixed ethylene–air flame," *Int. J. Therm. Sci.*, vol. 49, no. 8, pp. 1457–1467, 2010.

[174] Q. N. Chan, P. R. Medwell, P. A. M. Kalt, Z. T. Alwahabi, B. B. Dally, and G. J. Nathan, "Simultaneous imaging of temperature and soot volume fraction," *Proc. Combust. Inst.*, vol. 33, no. 1, pp. 791–798, 2011.

[175] F. Migliorini, K. A. Thomson, and G. J. Smallwood, "Investigation of optical properties of aging soot," *Appl. Phys. B*, vol. 104, pp. 273–283, 2011.

[176] B. Yang and U. O. Koylu, "Detailed soot field in a turbulent non-premixed ethylene/air flame from laser scattering and extinction experiments," *Combust. Flame*, vol. 141, no. 1–2, pp. 55–65, 2005.

[177] B. Yang and U. O. Koylu, “Soot processes in a strongly radiating turbulent flame from laser scattering/extinction experiments,” *J. Quant. Spectrosc. Radiat. Transf.*, vol. 93, no. 1–3, pp. 289–299, 2005.

[178] Y. N. Mishra *et al.*, “Application of frame for simultaneous LIF and LII imaging in sooting flames using a single camera,” *Sensors*, vol. 20, no. 19, p. 5534, 2020.

[179] M. Mannazhi, S. Török, J. Gao, and P.-E. Bengtsson, “Soot maturity studies in methane-air diffusion flames at elevated pressures using laser-induced incandescence,” *Proc. Combust. Inst.*, vol. 38, no. 1, pp. 1217–1224, 2021.

[180] L. Xu, M. Zhou, Y. Wang, and D. Liu, “Probing sooting limits in counterflow diffusion flames via multiple optical diagnostic techniques,” *Exp. Therm. Fluid Sci.*, vol. 136, p. 110679, 2022.

[181] C. Zhang, Y. Wu, B. Liu, Z. Wang, and L. Zhou, “Investigation of soot particles morphology and size distribution produced in a n-heptane/anisole laminar diffusion flame based on TEM images,” *Combust. Flame*, vol. 244, p. 112234, 2022.

[182] S. L. Manzello *et al.*, “On the use of a well stirred reactor to study soot inception,” in *Fourth Joint Meeting of the US Sections of the Combustion Institute, Philadelphia, Pa*, 2005, pp. 20–23.

[183] S. L. Manzello *et al.*, “Soot particle size distributions in a well-stirred reactor/plug flow reactor,” *Proc. Combust. Inst.*, vol. 31, no. 1, pp. 675–683, 2007.

[184] D. B. Lenhert and S. L. Manzello, “Effects of benzene and naphthalene addition on soot inception in a well-stirred reactor/plug flow reactor,” *Proc. Combust. Inst.*, vol. 32, no. 1, pp. 657–664, 2009.

[185] C. Crua, D. A. Kennaird, and M. R. Heikal, “Laser-induced incandescence study of diesel soot formation in a rapid compression machine at elevated pressures,” *Combust. Flame*, vol. 135, no. 4, pp. 475–488, 2003.

[186] I. Kitsopanidis and W. K. Cheng, “Soot formation study in a rapid compression machine,” 2006.

[187] J. E. Ketterer and W. K. Cheng, “A study of soot formation in a rapid compression machine at conditions representative of cold-fast-idle in spark ignition engines,” *Int. J. engine Res.*, vol. 20, no. 6, pp. 670–677, 2019.

[188] M. Kasper, K. Siegmann, and K. Sattler, “Evaluation of an in situ sampling probe for its accuracy in determining particle size distributions from flames,” *J. Aerosol Sci.*, vol. 28, no. 8, pp. 1569–1578, 1997.

[189] R. L. Vander Wal and K. A. Jensen, “Laser-induced incandescence: excitation intensity,” *Appl. Opt.*, vol. 37, no. 9, pp. 1607–1616, 1998.

[190] W. PAYMAN and W. C. SHEPHERD, “Explosion waves and shock waves; the disturbance produced by bursting diaphragms with compressed air.,” *Proc. R. Soc. Lond. A. Math. Phys. Sci.*, vol. 186, no. 1006, pp. 293–321, 1946, doi: 10.1098/rspa.1946.0045.

[191] A. Hertzberg and A. Kantrowitz, “Studies with an aerodynamically instrumented shock tube,” *J. Appl. Phys.*, vol. 21, no. 9, pp. 874–878, 1950, doi: 10.1063/1.1699776.

[192] E. F. Greene, G. R. Cowan, and D. F. Hornig, “The thickness of shock fronts in argon and nitrogen and rotational heat capacity lags,” *J. Chem. Phys.*, vol. 19, no. 4, pp. 427–434, 1951, doi:

10.1063/1.1748241.

[193] R. W. Nlcholls and W. H. Parkinson, “Shock excitation of atomic and molecular spectra,” *J. Chem. Phys.*, vol. 26, no. 2, pp. 423–424, 1957, doi: 10.1063/1.1743313.

[194] K. A. Bhaskaran and P. Roth, *The shock tube as wave reactor for kinetic studies and material systems*, vol. 28, no. 2. 2002.

[195] W. J. M. Rankine, “XV. On the thermodynamic theory of waves of finite longitudinal disturbance,” *Philos. Trans. R. Soc. London*, no. 160, pp. 277–288, 1870.

[196] H. Hugoniot, “Memoir on the propagation of movements in bodies, especially perfect gases (first part),” *J. l’Ecole Polytech.*, vol. 57, no. 3, 1887.

[197] W. Tang and K. Brezinsky, “Chemical kinetic simulations behind reflected shock waves,” *Int. J. Chem. Kinet.*, vol. 38, no. 2, pp. 75–97, 2006.

[198] X. Han, J. M. Mehta, and K. Brezinsky, “Temperature approximations in chemical kinetics studies using single pulse shock tubes,” *Combust. Flame*, vol. 209, pp. 1–12, 2019.

[199] L. A. Mertens, I. A. Awan, D. A. Sheen, and J. A. Manion, “Evaluated site-specific rate constants for reaction of isobutane with H and CH3: shock tube experiments combined with bayesian model optimization,” *J. Phys. Chem. A*, vol. 122, no. 49, pp. 9518–9541, 2018.

[200] M. F. Campbell, T. Parise, A. M. Tulgestke, R. M. Spearrin, D. F. Davidson, and R. K. Hanson, “Strategies for obtaining long constant-pressure test times in shock tubes,” *Shock Waves*, vol. 25, pp. 651–665, 2015.

[201] Z. Hong, G. A. Pang, S. S. Vasu, D. F. Davidson, and R. K. Hanson, “The use of driver inserts to reduce non-ideal pressure variations behind reflected shock waves,” *Shock Waves*, vol. 19, pp. 113–123, 2009.

[202] W. D. Erickson, G. C. Williams, and H. C. Hottel, “Light scattering measurements on soot in a benzene air flame,” *Combust. Flame*, vol. 8, no. 2, pp. 127–132, 1964.

[203] W. H. Dalzell and A. F. Sarofim, “Optical constants of soot and their application to heat-flux calculations,” 1969.

[204] S. Chippett and W. A. Gray, “The size and optical properties of soot particles,” *Combust. Flame*, vol. 31, pp. 149–159, 1978.

[205] H. Bockhorn, F. Fetting, U. Meyer, R. Reck, and G. Wannemacher, “Measurement of the soot concentration and soot particle sizes in propane oxygen flames,” in *Symposium (International) on Combustion*, 1981, vol. 18, no. 1, pp. 1137–1147.

[206] S. C. Lee and C. L. Tien, “Optical constants of soot in hydrocarbon flames,” in *Symposium (international) on combustion*, 1981, vol. 18, no. 1, pp. 1159–1166.

[207] H. Chang and T. T. Charalampopoulos, “Determination of the wavelength dependence of refractive indices of flame soot,” *Proc. R. Soc. London. Ser. A Math. Phys. Sci.*, vol. 430, no. 1880, pp. 577–591, 1990.

[208] B. S. Haynes and H. Gg, “Wagner, soot formation,” *Prog. Energy Combust. Sci.*, vol. 7, no. 4, pp.

229–273, 1981.

[209] H. Mätzing and H. G. Wagner, “Measurements about the influence of pressure on carbon formation in premixed laminar C2H4-air flames,” in *Symposium (International) on Combustion*, 1988, vol. 21, no. 1, pp. 1047–1055.

[210] H. Böhm, C. Feldermann, T. Heidermann, H. Jander, B. Lüers, and H. G. Wagner, “Soot formation in premixed C2H4-air flames for pressures up to 100 bar,” in *Symposium (International) on Combustion*, 1992, vol. 24, no. 1, pp. 991–998.

[211] O. Mathieu *et al.*, “Characterization of adsorbed species on soot formed behind reflected shock waves,” *Proc. Combust. Inst.*, vol. 31, no. 1, pp. 511–519, 2007.

[212] A. Emelianov *et al.*, “Time and temperature dependence of carbon particle growth in various shock wave pyrolysis processes,” *Proc. Combust. Inst.*, vol. 30, no. 1, pp. 1433–1440, 2005.

[213] R. S. Tranter and T. Sikes, “Solenoid actuated driver valve for high repetition rate shock tubes,” *Rev. Sci. Instrum.*, vol. 91, no. 5, 2020, doi: 10.1063/5.0006010.

[214] R. A. Alpher and D. R. White, “Flow in shock tubes with area change at the diaphragm section,” *J. Fluid Mech.*, vol. 3, no. 5, pp. 457–470, 1958.

[215] A. Dalmiya, J. M. Mehta, R. S. Tranter, and P. T. Lynch, “High pressure, high flow rate batch mixing apparatus for high throughput experiments,” *Rev. Sci. Instrum.*, vol. 92, no. 11, p. 114104, 2021.

[216] P. T. Lynch, “Note: An improved solenoid driver valve for miniature shock tubes,” *Rev. Sci. Instrum.*, vol. 87, no. 5, p. 56110, 2016, doi: 10.1063/1.4953115.

[217] A. Matsugi, “A high-repetition-rate shock tube for transient absorption and laser-induced fluorescence studies of high-temperature chemical kinetics,” *Rev. Sci. Instrum.*, vol. 91, no. 5, p. 54101, 2020.

[218] L. S. Nadolski *et al.*, “SOLEIL Update Status,” in *12th International Particle Accelerator Conference*, 2021, p. THPAB078.

[219] G. A. Garcia, L. Nahon, and I. Powis, “Two-dimensional charged particle image inversion using a polar basis function expansion,” *Rev. Sci. Instrum.*, vol. 75, no. 11, pp. 4989–4996, 2004, doi: 10.1063/1.1807578.

[220] C. A. Taatjes, N. Hansen, D. L. Osborn, K. Kohse-Höinghaus, T. A. Cool, and P. R. Westmoreland, “‘Imaging’ combustion chemistry via multiplexed synchrotron-photoionization mass spectrometry,” *Phys. Chem. Chem. Phys.*, vol. 10, no. 1, pp. 20–34, 2008.

[221] A. Bodi, M. Johnson, T. Gerber, Z. Gengeliczki, B. Sztáray, and T. Baer, “Imaging photoelectron photoion coincidence spectroscopy with velocity focusing electron optics,” *Rev. Sci. Instrum.*, vol. 80, no. 3, 2009, doi: 10.1063/1.3082016.

[222] R. Choudhary, Y. Peng, J. Shao, D. F. Davidson, and R. K. Hanson, “Multi-species time history measurements during ethanol pyrolysis behind reflected shock waves,” 2019.

[223] J. Kiecherer, C. Bänsch, T. Bentz, and M. Olzmann, “Pyrolysis of ethanol: A shock-tube/TOF-MS and modeling study,” *Proc. Combust. Inst.*, vol. 35, no. 1, pp. 465–472, 2015.

[224] J. Li, A. Kazakov, and F. L. Dryer, “Ethanol pyrolysis experiments in a variable pressure flow reactor,” *Int. J. Chem. Kinet.*, vol. 33, no. 12, pp. 859–867, 2001.

[225] R. Sivaramakrishnan, M.-C. Su, J. V Michael, S. J. Klippenstein, L. B. Harding, and B. Ruscic, “Rate constants for the thermal decomposition of ethanol and its bimolecular reactions with OH and D: reflected shock tube and theoretical studies,” *J. Phys. Chem. A*, vol. 114, no. 35, pp. 9425–9439, 2010.

[226] C.-W. Wu, H. Matsui, N.-S. Wang, and M.-C. Lin, “Shock tube study on the thermal decomposition of ethanol,” *J. Phys. Chem. A*, vol. 115, no. 28, pp. 8086–8092, 2011.

[227] M. Aghsaee, D. Nativel, M. Bozkurt, M. Fikri, N. Chaumeix, and C. Schulz, “Experimental study of the kinetics of ethanol pyrolysis and oxidation behind reflected shock waves and in laminar flames,” *Proc. Combust. Inst.*, vol. 35, no. 1, pp. 393–400, 2015.

[228] J. Park, R. S. Zhu, and M.-C. Lin, “Thermal decomposition of ethanol. I. Ab Initio molecular orbital/Rice–Ramsperger–Kassel–Marcus prediction of rate constant and product branching ratios,” *J. Chem. Phys.*, vol. 117, no. 7, pp. 3224–3231, 2002.

[229] L. Xing, S. Li, Z. Wang, B. Yang, S. J. Klippenstein, and F. Zhang, “Global uncertainty analysis for RRKM/master equation based kinetic predictions: A case study of ethanol decomposition,” *Combust. Flame*, vol. 162, no. 9, pp. 3427–3436, 2015.

[230] A. G. Vandeputte, L. B. Harding, Y. Georgievskii, and S. J. Klippenstein, “Roaming radical kinetics in the pyrolysis and combustion of ethanol,” 2013.

[231] J. L. Holmes and F. P. Lossing, “Ionization energies of homologous organic compounds and correlation with molecular size,” *Org. mass Spectrom.*, vol. 26, no. 6, pp. 537–541, 1991.

[232] D. A. Krause, J. W. Taylor, and R. F. Fenske, “An analysis of the effects of alkyl substituents on the ionization potentials of n-alkenes,” *J. Am. Chem. Soc.*, vol. 100, no. 3, pp. 718–723, 1978.

[233] D. R. Miller, “Atomic and molecular beam methods,” *At. Mol. Beam Methods*, vol. 1, p. 14, 1988.

[234] V. K. Potapov and V. V Sorokin, “Kinetic energies of products of dissociative pho-toionization of molecules. I,” *Aliphatic ketones alcohols, Khim. Vys. Energ*, vol. 6, pp. 387–391, 1972.

[235] G. R. Branton, D. C. Frost, T. Makita, C. A. McDowell, and I. A. Stenhouse, “Photoelectron Spectra of Ethylene and Ethylene-d 4,” *J. Chem. Phys.*, vol. 52, no. 2, pp. 802–806, 1970.

[236] P. Bruckmann and M. Klessinger, “Photoelektronenspektren organischer verbindungen: III. Photoelektronenspektren acetylensubstituierter kleiner ringe,” *J. Electron Spectros. Relat. Phenomena*, vol. 2, no. 3, pp. 341–354, 1973.

[237] F. Brogli *et al.*, “The photoelectron spectrum of butatriene,” *Chem. Phys.*, vol. 4, no. 1, pp. 107–119, 1974.

[238] J. Kreile, N. Münzel, A. Schweig, and H. Specht, “Uv photoelectron spectrum of cyclobutadiene. free cyclobutadiene stable up to high temperatures,” *Chem. Phys. Lett.*, vol. 124, no. 2, pp. 140–146, 1986.

[239] F. Brogli, J. K. Crandall, E. Heilbronner, E. Kloster-Jensen, and S. A. Sojka, “The photoelectron spectra of methyl-substituted allenes and of tetramethyl-bisallenyl,” *J. Electron Spectros. Relat.*

Phenomena, vol. 2, no. 5, pp. 455–465, 1973.

[240] J. Krüger *et al.*, "Photoelectron-photoion coincidence spectroscopy for multiplexed detection of intermediate species in a flame," *Phys. Chem. Chem. Phys.*, vol. 16, no. 41, pp. 22791–22804, 2014, doi: 10.1039/c4cp02857k.

[241] R. Bombach, J. Dannacher, J. -P Stadelmann, and R. Neier, "Fundamental Aspects of Ionic Dissociations: The Fragmentation Pathways of Excited Bicyclobutane Cations," *Helv. Chim. Acta*, vol. 66, no. 2, pp. 701–717, 1983, doi: 10.1002/hlca.19830660234.

[242] K. B. Wiberg, G. B. Ellison, J. J. Wendoloski, C. R. Brundle, and N. A. Kuebler, "Electronic states of organic molecules. 3. Photoelectron spectra of cycloalkenes and methylenecycloalkanes," *J. Am. Chem. Soc.*, vol. 98, no. 23, pp. 7179–7182, 1976.

[243] H. KG, "COSILAB The Combustion Simulation Laboratory, Rotexo GmbH & Co. Germany." 2009.

[244] W. Pejpichestakul *et al.*, "Examination of a soot model in premixed laminar flames at fuel-rich conditions," *Proc. Combust. Inst.*, vol. 37, no. 1, pp. 1013–1021, 2019.

[245] P. Oßwald *et al.*, "In situ flame chemistry tracing by imaging photoelectron photoion coincidence spectroscopy," *Rev. Sci. Instrum.*, vol. 85, no. 2, p. 25101, 2014.

[246] K. Johnson, I. Powis, and C. J. Danby, "A photoelectron—photoion coincidence study of acetaldehyde and ethylene oxide molecular ions," *Chem. Phys.*, vol. 70, no. 3, pp. 329–343, 1982.

[247] J. C. Person and P. P. Nicole, "Isotope effects in the photoionization yields and the absorption cross sections for ethylene and n-butane," *J. Chem. Phys.*, vol. 49, no. 12, pp. 5421–5426, 1968.

[248] T. A. Cool *et al.*, "Selective detection of isomers with photoionization mass spectrometry for studies of hydrocarbon flame chemistry," *J. Chem. Phys.*, vol. 119, no. 16, pp. 8356–8365, 2003.

[249] L. G. Dodson *et al.*, "VUV photoionization cross sections of HO2, H2O2, and H2CO," *J. Phys. Chem. A*, vol. 119, no. 8, pp. 1279–1291, 2015.

[250] L. Åsbrink, E. Lindholm, and O. Edqvist, "Jahn-Teller effect in the vibrational structure of the photoelectron spectrum of benzene," *Chem. Phys. Lett.*, vol. 5, no. 9, pp. 609–612, 1970.

[251] E. Heilbronner, R. Gleiter, H. Hopf, V. Hornung, and A. De Meijere, "Photoelectron-Spectroscopic Evidence for the Orbital Sequence in Fulvene and 3, 4-Dimethylene-cyclobutene," *Helv. Chim. Acta*, vol. 54, no. 3, pp. 783–794, 1971.

[252] P. Bischof, R. Gleiter, H. Hopf, and F. T. Lenich, "Photoelectron spectra of open chain C6H6 isomers," *J. Am. Chem. Soc.*, vol. 97, no. 19, pp. 5467–5472, 1975.

[253] F. Brigoli, J. Wirz, E. Kloster-Jensen, R. G. Bergmann, K. P. C. Vollhardt, and A. J. Ashe, "The Consequences of sigma and pi Conjugative Interactions in Mono-, Di- and Triacetylenes," *Helv. Chim. Acta*, vol. 58, no. 286, pp. 2620–2645, 1975.

[254] G. Bieri *et al.*, "Dewar Benzene and Some of its Derivatives. A photoelectron spectroscopic analysis [1]," *Helv. Chim. Acta*, vol. 59, no. 8, pp. 2657–2673, 1976.

[255] J. P. Maier and D. W. Turner, "Steric inhibition of resonance studied by molecular photoelectron spectroscopy. Part 2.—Phenylethylenes," *J. Chem. Soc. Faraday Trans. 2 Mol. Chem. Phys.*, vol. 69,

pp. 196–206, 1973.

[256] C. Baker and D. W. Turner, “High resolution molecular photoelectron spectroscopy. III. Acetylenes and aza-acetylenes,” *Proc. R. Soc. London. Ser. A. Math. Phys. Sci.*, vol. 308, no. 1492, pp. 19–37, 1968, doi: 10.1098/rspa.1968.0205.

[257] M. Yamazaki, N. Kishimoto, and K. Ohno, “Collision-energy-resolved Penning ionization electron spectroscopy of styrene, 2-vinylpyridine, and 4-vinylpyridine with He*(2 3 S) metastable atoms,” *Eur. Phys. J. D-Atomic, Mol. Opt. Plasma Phys.*, vol. 38, pp. 47–57, 2006.

[258] J. H. D. Eland and C. J. Danby, “Inner ionization potentials of aromatic compounds,” *Zeitschrift für Naturforsch. A*, vol. 23, no. 3, pp. 355–357, 1968.

[259] S. Elbel, K. Lienert, A. Krebs, and H. T. Dieck, “Photoelektronenspektren von Phenylethinen, I. Phenylethin-Mustersonde für Substituenteneffekte,” *Liebigs Ann. der Chemie*, vol. 1981, no. 10, pp. 1785–1797, 1981.

[260] W. Runge, W. Kosbahn, and J. Kroner, “The molecular structure of allenes and ketenes II [1] photoelectron spectra, absorption spectra, and CNDO/S-calculations of phenyl and methyl substituted Allenes,” *Berichte der Bunsengesellschaft für Phys. Chemie*, vol. 79, no. 4, pp. 371–381, 1975.

[261] R. Griebel, G. Hohlneicher, and F. Dörr, “A photoelectron spectroscopic study of benzonitrile, ethynylbenzene and some of its substituted derivatives,” *J. Electron Spectros. Relat. Phenomena*, vol. 4, no. 3, pp. 185–206, 1974, doi: 10.1016/0368-2048(74)80050-2.

[262] B. Gans *et al.*, “Determination of the absolute photoionization cross sections of CH 3 and i produced from a pyrolysis source, by combined synchrotron and vacuum ultraviolet laser studies,” *J. Phys. Chem. A*, vol. 114, no. 9, pp. 3237–3246, 2010, doi: 10.1021/jp909414d.

[263] Z. Zhou, M. Xie, Z. Wang, and F. Qi, “Determination of absolute photoionization cross-sections of aromatics and aromatic derivatives,” *Rapid Commun. Mass Spectrom. An Int. J. Devoted to Rapid Dissem. Up-to-the-Minute Res. Mass Spectrom.*, vol. 23, no. 24, pp. 3994–4002, 2009.

[264] E. E. Rennie, C. A. F. Johnson, J. E. Parker, D. M. P. Holland, D. A. Shaw, and M. A. Hayes, “A photoabsorption, photodissociation and photoelectron spectroscopy study of C6H6 and C6D6,” *Chem. Phys.*, vol. 229, no. 1, pp. 107–123, 1998.

[265] Edited by JiuZhong Yang and Combustion Team., “Photonionization Cross Section Database (Version 2.0). http://flame.nsrl.ustc.edu.cn/database/. National Synchrotron Radiation Laboratory, Hefei, China.,” *Estim. data Provid. by YuYang Li, JiuZhong Yang ZhanJun Cheng.*, 2017.

[266] A. P. Hitchcock, C. E. Brion, and M. J. Van der Wiel, “Absolute oscillator strengths for valence-shell ionic photofragmentations of N2O and CO2 (8–75 eV),” *Chem. Phys.*, vol. 45, no. 3, pp. 461–478, 1980.

[267] D. M. P. Holland *et al.*, “An experimental and theoretical study of the valence shell photoelectron spectrum of butadiene,” *J. Phys. B At. Mol. Opt. Phys.*, vol. 29, no. 14, p. 3091, 1996.

[268] F. Brogli, E. Heilbronner, V. Hornung, and E. Kloster-Jensen, “Die Photoelektronen-Spektren methyl-substituierter Acetylene,” *Helv. Chim. Acta*, vol. 56, no. 7, pp. 2171–2178, 1973.

[269] J. Zador, M. D. Fellows, and J. A. Miller, “Initiation reactions in acetylene pyrolysis,” *J. Phys. Chem. A*, vol. 121, no. 22, pp. 4203–4217, 2017.

[270] D. W. Kohn and P. Chen, “Vibrational structure in the photoelectron spectrum of cyclobutadiene as a probe of structure,” *J. Am. Chem. Soc.*, vol. 115, no. 7, pp. 2844–2848, 1993.

[271] D. Polino, A. Famulari, and C. Cavallotti, “Analysis of the reactivity on the C7H6 potential energy surface,” *J. Phys. Chem. A*, vol. 115, no. 27, pp. 7928–7936, 2011.

[272] M. Steinbauer, P. Hemberger, I. Fischer, and A. Bodi, “Photoionization of C7H6 and C7H 5: Observation of the fulvenallenyl radical,” *ChemPhysChem*, vol. 12, no. 10, pp. 1795–1797, 2011, doi: 10.1002/cphc.201000892.

[273] C. Cavallotti, M. Derudi, and R. Rota, “On the mechanism of decomposition of the benzyl radical,” *Proc. Combust. Inst.*, vol. 32 I, no. 1, pp. 115–121, 2009, doi: 10.1016/j.proci.2008.06.203.

[274] M. Derudi, D. Polino, and C. Cavallotti, “Toluene and benzyl decomposition mechanisms: Elementary reactions and kinetic simulations,” *Phys. Chem. Chem. Phys.*, vol. 13, no. 48, pp. 21308–21318, 2011, doi: 10.1039/c1cp22601k.

[275] A. M. Mebel, Y. Georgievskii, A. W. Jasper, and S. J. Klippenstein, “Temperature-and pressure-dependent rate coefficients for the HACA pathways from benzene to naphthalene,” *Proc. Combust. Inst.*, vol. 36, no. 1, pp. 919–926, 2017.

[276] J. W. Rabalais and R. J. Colton, “Electronic interaction between the phenyl group and its unsaturated substituents,” *J. Electron Spectros. Relat. Phenomena*, vol. 1, no. 1, pp. 83–99, 1972, doi: 10.1016/0368-2048(72)85006-0.

[277] T. Koenig, I. Daniel, and J. A. Hoobler, “He(I) Photoelectron Spectrum of Benzocyclobutadiene,” *J. Am. Chem. Soc.*, vol. 101, no. 21, pp. 6446–6447, 1979, doi: 10.1021/ja00515a057.

[278] T. Kobayashi, K. Yokota, and S. Nagakura, “Photoelectron spectra of styrenes,” *J. Electron Spectros. Relat. Phenomena*, vol. 2, no. 5, pp. 449–454, 1973, doi: 10.1016/0368-2048(73)80059-3.

[279] L. Klasinc, B. Kovac, and H. Gusten, “Photoelectron spectra of acenes. Electronic structure and substituent effects,” *Pure Appl. Chem.*, vol. 55, no. 2, pp. 289–298, 1983, doi: 10.1351/pac198855020289.

[280] J. Kreile, N. Münzel, R. Schulz, and A. Schweig, “Uv photoelectron spectrum of o-xylylene—detection of a low-energy non-koopmans (shake-up) ionization,” *Chem. Phys. Lett.*, vol. 108, no. 6, pp. 609–612, 1984.

[281] T. Koenig, R. Wielesek, W. Snell, and T. Baile, “Helium(I) Photoelectron Spectrum of p-Quinodimethane,” *J. Am. Chem. Soc.*, vol. 97, no. 11, pp. 3225–3226, 1975, doi: 10.1021/ja00844a055.

[282] T. Koenig, M. Tuttle, and R. A. Wielesek, “The HE (I) photoelectron spectra of xylenes and metacyclophanes. A reassignment of the lowest ionic state of [2.2] metacyclophane.,” *Tetrahedron Lett.*, vol. 15, no. 29, pp. 2537–2540, 1974.

[283] H.-S. Kim, D. R. Wagner, and R. J. Saykally, “Single photon infrared emission spectroscopy of the gas phase pyrene cation: support for a polycyclic aromatic hydrocarbon origin of the unidentified

infrared emission bands," *Phys. Rev. Lett.*, vol. 86, no. 25, p. 5691, 2001.

[284] M. K. Spencer, M. R. Hammond, and R. N. Zare, "Laser mass spectrometric detection of extraterrestrial aromatic molecules: Mini-review and examination of pulsed heating effects," *Proc. Natl. Acad. Sci.*, vol. 105, no. 47, pp. 18096–18101, 2008.

[285] R. Griebel, G. Hohlneicher, and F. Dörr, "A photoelectron spectroscopic study of benzonitrile, ethynylbenzene and some of its substituted derivatives," *J. Electron Spectros. Relat. Phenomena*, vol. 4, no. 3, pp. 185–206, 1974.

[286] C. H. Chin, T. Zhu, and J. Z. H. Zhang, "Theoretical investigations of photoionization efficiency of naphthalene," *ChemRxiv*, pp. 1–28, 2019, doi: 10.26434/chemrxiv.7665620.

[287] R. Schulz, A. Schweig, C. Wentrup, and H. Winter, "2-Vinylidene-2H-indene," *Angew. Chemie Int. Ed. English*, vol. 19, no. 10, pp. 821–822, 1980.

[288] W. Schäfer, A. Schweig, H. Vermeer, F. Bickelhaupt, and H. De Graaf, "On the nature of the 'free electron pair' on phosphorus in aromatic phosphorus compounds: The photoelectron spectrum of 2-phosphanaphthalene," *J. Electron Spectros. Relat. Phenomena*, vol. 6, no. 2, pp. 91–98, 1975, doi: https://doi.org/10.1016/0368-2048(75)80001-6.

[289] R. Gleiter, W. Schäfer, and M. Eckert-Maksić, "Transannulare Wechselwirkungen zwischen Acetylenen – Photoelektronenspektroskopische Untersuchungen an 1,8-Diethinylnaphthalin und cyclischen Derivaten von 2,2'-Diethinylbiphenyl," *Chem. Ber.*, vol. 114, no. 6, pp. 2309–2321, 1981, doi: 10.1002/cber.19811140627.

[290] R. Boschi, E. Clart, and W. Schmidt, "Photoelectron spectra of polynuclear aromatics. III. the effect of nonplanarity in sterically overcrowded aromatic hydrocarbons," *J. Chem. Phys.*, vol. 4406, no. 1974, pp. 4406–4418, 1974, doi: 10.1063/1.1680919.

[291] B. Ruščić, B. Kovač, L. Klasinc, and H. Güsten, "Photoelectron Spectroscopy of Heterocycles. Fluorene Analogues," *Zeitschrift für Naturforsch. A*, vol. 33, no. 9, pp. 1006–1012, 1978.

[292] H. G. Guttenberger, H. J. Bestmann, F. L. Dickert, F. S. Jorgensen, and J. P. Snyder, "Molecules with a helix structure. 3. Sulfur-bridged peri-naphthalenes: synthesis, conformational analysis, and photoelectron spectroscopy of the mono-, di-, and trisulfides of 1,8-dimethylnaphthalene," *J. Am. Chem. Soc.*, vol. 103, no. 1, pp. 159–168, Jan. 1981, doi: 10.1021/ja00391a029.

[293] E. Haselbach, L. Neuhaus, R. P. Johnson, K. N. Houk, and M. N. Paddon-Row, "π-Orbital Interactions in Möbius-Type Molecules as Studied by Photoelectron Spectroscopy," *Helv. Chim. Acta*, vol. 65, no. 6, pp. 1743–1751, 1982, doi: 10.1002/hlca.19820650609.

[294] C. Santiago, E. J. McAlduff, K. N. Houk, R. A. Snow, and L. A. Paquette, "Photoelectron Spectra of Ortho-and Meta-Substituted Benzonorbornadienes. Relationships to Regioselectivities in Triplet Di-π-methane Rearrangements," *J. Am. Chem. Soc.*, vol. 100, no. 19, pp. 6149–6156, 1978, doi: 10.1021/ja00487a031.

[295] P. M. Mishra, L. Avaldi, P. Bolognesi, K. C. Prince, R. Richter, and U. R. Kadhane, "Valence shell photoelectron spectroscopy of pyrene and fluorene: Photon energy dependence in the far-ultraviolet region," *J. Phys. Chem. A*, vol. 118, no. 17, pp. 3128–3135, 2014, doi: 10.1021/jp502445d.

[296] S. Pignataro, V. Mancini, J. N. A. Ridyard, and H. J. Lempka, “Photoelectron energy spectra of molecules having classically non-conjugated π-systems,” *J. Chem. Soc. D Chem. Commun.*, no. 3, pp. 142–143, 1971, doi: 10.1039/C29710000142.

[297] L. Klasinc, B. Kovač, S. Schoof, and H. Gusten, “Photoelectron Spectroscopy of 9-Substituted Anthracenes,” *Croat. Chem. Acta*, vol. 51, no. 4, pp. 307–315, 1978.

[298] G. Rouillé *et al.*, “DISSOCIATIVE PHOTOIONIZATION of POLYCYCLIC AROMATIC HYDROCARBON MOLECULES CARRYING AN ETHYNYL GROUP,” *Astrophys. J.*, vol. 810, no. 2, p. 114, 2015, doi: 10.1088/0004-637X/810/2/114.

[299] T. Kobayashi, K. Yokota, and S. Nagakura, “Photoelectron Spectra of the cis-and trans-Isomers of Some Ethylene Derivatives,” *Bull. Chem. Soc. Jpn.*, vol. 48, no. 2, pp. 412–415, 1975.

[300] J. P. Maier and D. W. Turner, “Steric inhibition of resonance studied by molecular photoelectron spectroscopy: Part 1. - Biphenyls,” *Gen. Discuss. Faraday Soc.*, vol. 54, pp. 149–167, 1972, doi: 10.1039/DC9725400149.

[301] R. Boschi, J. N. Murrell, and W. Schmidt, “Photoelectron spectra of polycyclic aromatic hydrocarbons,” *Faraday Discuss. Chem. Soc.*, vol. 54, pp. 116–126, 1972.

[302] M. Lang, “Valence Shell Photoionization of Soot Precursors with Synchrotron Radiation,” Universität Würzburg, 2015.

[303] T. Kobayashi, “Conformational Analysis of Terphenyls By Photoelectron Spectroscopy.,” *Bulletin of the Chemical Society of Japan*, vol. 56, no. 11. pp. 3224–3229, 1983, doi: 10.1246/bcsj.56.3224.

[304] S. Hino, K. Seki, and H. Inokuchi, “Photoelectron spectra of p-terphenyl in gaseous and solid states,” *Chem. Phys. Lett.*, vol. 36, no. 3, pp. 335–339, 1975.

[305] R. Gleiter, W. Schafer, and A. Flatow, “Interaction between Triple Bonds in 1,8-Diethynylnaphthalenes,” *J. Org. Chem.*, vol. 49, no. 2, pp. 372–374, 1984, doi: 10.1021/jo00176a029.

[306] S. Pignataro, V. Mancini, G. Innorta, and G. Distefano, “Ionization Energies and Ring Orbital Interaction in Diarylmethanes and Diarylethanes,” *Zeitschrift fur Naturforsch. - Sect. A J. Phys. Sci.*, vol. 27, no. 3, pp. 534–536, 1972, doi: 10.1515/zna-1972-0324.

[307] M. Frenklach, S. Taki, and R. A. Matula, “A conceptual model for soot formation in pyrolysis of aromatic hydrocarbons,” *Combust. Flame*, vol. 49, no. 1–3, pp. 275–282, 1983.